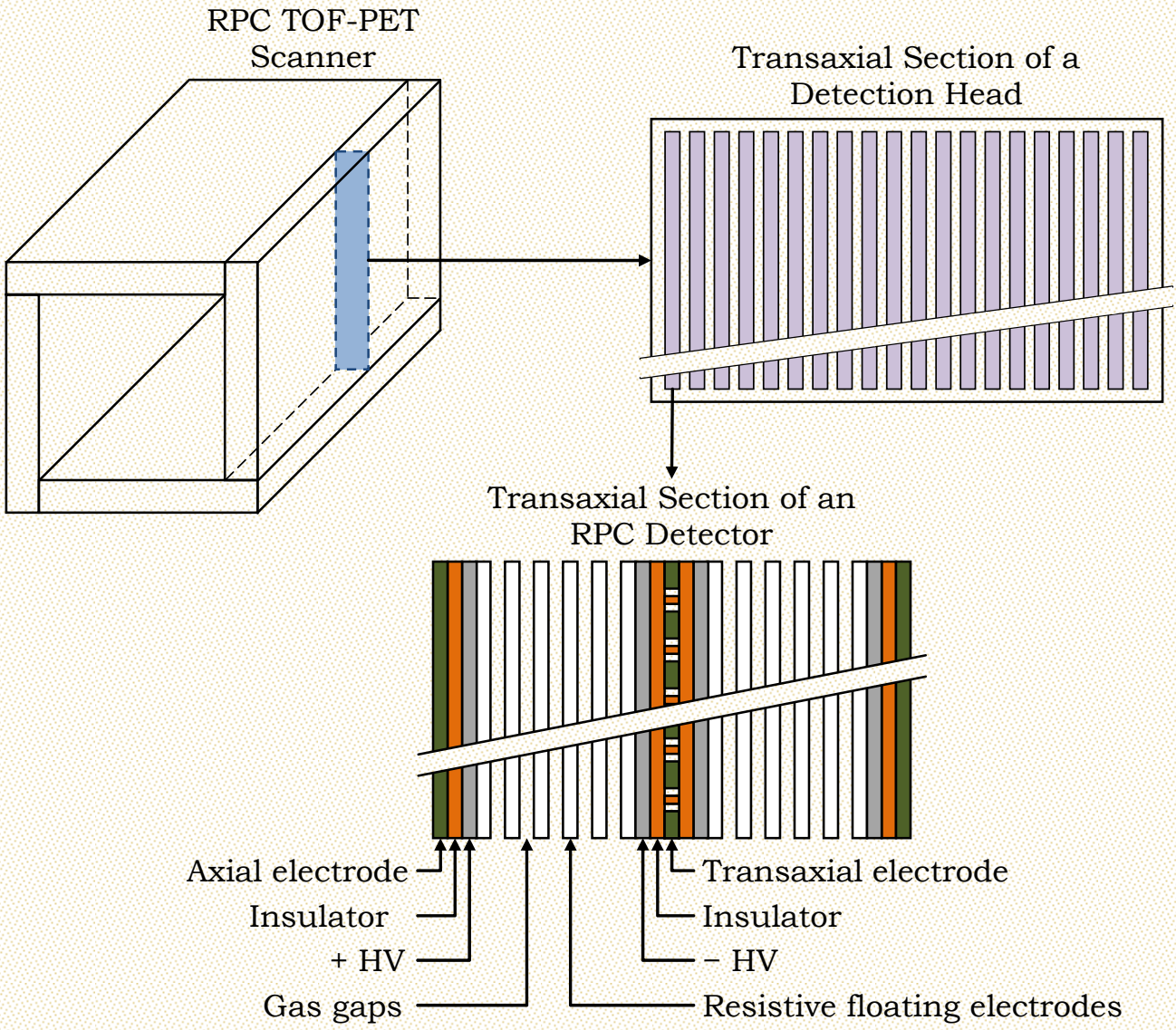

Jorge Miguel Tavares Couceiro de Sousa

SIMULATION STUDY OF A WIDE AXIAL FIELD OF VIEW POSITRON EMISSION TOMOGRAPHY SYSTEM BASED ON RESISTIVE PLATE CHAMBER DETECTORS

Tese de Doutoramento em Física, Especialidade de Física Tecnológica
orientada por: Prof. Doutor Paulo Jorge Ribeiro da Fonte
Prof. Doutor Rui Ferreira Marques
e apresentada ao Departamento de Física
da Faculdade de Ciências e Tecnologia
da Universidade de Coimbra

31 de Julho/2013

· U C ·

UNIVERSIDADE DE COIMBRA

• U  C •

FCTUC FACULDADE DE CIÊNCIAS
E TECNOLOGIA
UNIVERSIDADE DE COIMBRA

Departamento de Física

SIMULATION STUDY OF A WIDE AXIAL FIELD OF VIEW POSITRON EMISSION TOMOGRAPHY SYSTEM BASED ON RESISTIVE PLATE CHAMBER DETECTORS

Tese de Doutoramento em Física, Especialidade de Física Tecnológica, orientada por Prof. Doutor Paulo Jorge Ribeiro da Fonte e Prof. Doutor Rui Ferreira Marques, e apresentada ao Departamento de Física da Faculdade de Ciências e Tecnologia da Universidade de Coimbra

Jorge Miguel Tavares Couceiro de Sousa

Coimbra

2013

ACKNOWLEDGMENTS

This dissertation is the result of several years of work, during which I received support in many different ways. In the next lines, I will try to not forget all those who directly or indirectly helped and supported me. If I do, please accept my sincere apology.

I thank to the Portuguese Foundation for Science and Technology, for the financial support in the form of two scholarships with the references SFRH/BD/42217/2007 and SFRH/PROTEC/49822/2009.

I thank to the Laboratory of Instrumentation and Experimental Particle Physics of Coimbra (LIP-Coimbra), in the persons of the Directors of Board, for having accepted and supported me as a PhD student for the last years, and also for the numerous facilities granted to me in order to make possible the completion of this work.

I thank to the Polytechnic Institute of Coimbra and the Coimbra Institute of Engineering, in the persons of the Directors of Boards, the numerous facilities and support, including the reduction of teaching service, without which it would have been harder to finish the current work.

I thank to the Laboratory of Advanced Computing of the University of Coimbra, for the generous computing time provided in the *milipeia* HPC cluster, without which it would have been almost impossible to carry out the present work.

I thank to Professor Paulo Jorge Ribeiro da Fonte, the opportunity given to me to work under his wise guidance, his prompt availability, support, help and friendship. It sincerely was an honour and a pleasure to work under his supervision, as well as having him as a teaching colleague in the Coimbra Institute of Engineering.

I thank to Professor Rui Ferreira Marques, the opportunity to work under his wise co-guidance, as well as his prompt availability, support, help and friendship. It was a pleasure to work with him again, just as during my years as a student of Physics Engineer in the Physics Department of the University of Coimbra.

I thank to Professor Paulo Alexandre Vieira Crespo, for the numerous fruitful scientific discussions, his prompt availability for helping in what was needed, and his friendship.

I thank to Doctor Alberto Blanco Castro, for his support and generous contribution in the form of supplementary experimental data, and consent to use some of his material.

I thank to my colleagues and friends at LIP-Coimbra, for the support and cooperation in everything that was needed throughout these years.

I thank to Professor Francisco José Santiago Fernandes Amado Caramelo, for his friendship, valuable personal support, and his availability at all times. Without him, it would have been difficult to end this dissertation.

I thank to Professor Milton Augusto Morais Sarmento Pato de Macedo, for his friendship, all his useful advices, and the time he spared to help and support he gave me at work during deadlines. It has been a pleasure to work with him all these years.

I thank to Professor Susete Teresa Gaspar do Fetal, for her support and friendship, so important, and the help she gave me at work during deadlines. It is a pleasure to share the office with her.

I thank to MSc. Marisa Marques Manso, for her support, friendship, and the help she gave me.

I thank to Doctor Miguel Afonso Oliveira, for his friendship and support, so important to me.

I thank to Professor Francisco José Cerqueira Alves, for all the support, help, and friendship given to me during this work.

I thank to Professor Nuno David de Sousa Chichorro da Fonseca Ferreira, for his availability to help with reviewing the background information as well as all the support given and his friendship.

I thank to Doctor Antero José Pena Afonso de Abrunhosa, for all the help given, in the form of investigative information and data discussion.

I thank to Professor António Miguel Lino Santos Morgado, for his friendship, valuable personal support, and his availability at all times.

I thank to all my colleagues at the Physics and Mathematics Department of the Coimbra Institute of Engineering, of the Polytechnic Institute of Coimbra, for their understanding and constant support, helping me with class preparation, paperwork, and exam duties. It has been my privilege to work with them.

I thank to my wife, Elsa Maria Ferreira Virgolino Couceiro, my son, Pedro Miguel Virgolino Couceiro de Sousa, and my daughter, Marta Virgolino Couceiro de Sousa, for their patience during the process of investigating and writing, their support, their help, and most of all, their love, returned in kind tenfold.

I thank to my sister, Maria Alexandra Tavares Couceiro de Sousa, for her support, friendship and love.

I thank to my father, Carlos Manuel Couceiro Neto de Sousa, for his support, friendship and love, and for the determination he always taught me to have, without which I would not have finished this work.

I thank to my mother, Maria Manuela Lopes Tavares Couceiro de Sousa, for the determination she always taught me to have, all the memories I have of her, and all the love, pride and support I still feel she has for me. I only wished that she could be present to share this moment, and that cancer had not taken her so young.

LIST OF ACRONYMS

Acronym	Meaning
2D	Two Dimensional
3D	Three Dimensional
AACP	All Accepted Coincidence Pairs
ADC	Analog to Digital Converter
AFOV	Axial Field Of View
ALARA	As Low As Reasonably Achievable
AMCP	Accepted Multiple Coincidence Pairs
APD	Avalanche PhotoDiodes
ASCP	Accepted Single Coincidence Pairs
ASIC	Application-Specific Integrated Circuit
BGO	Bismuth Germanium Oxide
BP	Back Projection
BR	Branching Ratio
BREP	Boundary REPresented solid
CAD	Computer-Aided Design
CERN	European Organization for Nuclear Research
CSDA	Continuous Slowing Down Approximation
CSG	Constructive Solid Geometry
CT	Computed Tomography
DAWN	Fukui renderer Drawer for Academic WritiNgs

Acronym	Meaning
DOI	Depth Of Interaction
EAP	Electron Assignment Point
EDP	Electron Detection Point
EEDL	Evaluated Electron Data Library
EEP	Electron Extraction Point
ENSDF	Evaluated Nuclear Structure Data File
EPDL	Evaluated Photons Data Library
FBP	Filtered Back Projection
FOV	Field Of View
FWHM	Full Width at Half Maximum
FWTM	Full Width at Tenth Maximum
GATE	GEANT4 Application for Tomographic Emission
GE	General Electric
GEANT4	GEometry ANd Tracking 4
GR	Geometric Rejection
GSO	Gadolinium OxyorthoSilicate
GTOFR	Geometric TOF Rejection
HPC	High Performance Computing
LEP	Low Energy Package
LLD	Low Level Discrimination
LLNL	Lawrence Livermore National Laboratory

Acronym	Meaning
LOR	Line Of Response
LSO	Lutetium OxyorthoSilicate
LTF	Live Time Fraction
LYSO	Lutetium-Yttrium OrthoSilicate
MC	Monte Carlo
MIF	Misidentified Fraction
MLEM	Maximum Likelihood Expectation Maximization
MRI	Magnetic Resonance Imaging
MTW	Multiple Time Window
MWPC	MultiWire Proportional Chamber
NCAT	NURBS-based CArdiac-Torso
NECR	Noise Equivalent Count Rate
NEMA	National Electrical Manufacturers Association
NM	Nuclear Medicine
NURBS	Non-Uniform Rational B-Splines
OpenGL	Open Graphics Library
OSEM	Ordered Subset Expectation Maximization
PEACP	Pileup Event Acceptance with Coarse Position
PEP	Photon Entry Point
PER	Pileup Event Rejection
PET	Positron Emission Tomography

Acronym	Meaning
PF	PhotoFraction
PIP	Photon Interaction Point
PMMA	PolyMethyl MethAcrylate
PMT	PhotoMultiplier Tube
PSF	Point Spread Function
QE	Quantum Efficiency
ROI	Region Of Interest
RPC	Resistive Plate Chamber
SEP	Standard Electromagnetic Package
SF	Scatter Fraction
SimSET	Simulation System for Emission Tomography
SiPM	Silicon PhotoMultiplier
SNR	Signal to Noise Ratio
SPECT	Single Photon Emission Computed Tomography
SPET	Single Photon Emission Tomography
SSRB	Single Slice ReBinning
STEP	STandard for the Exchange of Product model data
STW	Single Time Window
TDC	Time to Digital Converter
TOF	Time-Of-Flight
ULD	Upper Level Discrimination

Acronym	Meaning
VRML	Virtual Reality Modelling Language
WMER	With Multiple Events Removal
WoMER	Without Multiple Events Removal

RESUMO

O presente trabalho teve por objectivo avaliar, através de simulações em GEANT4 (GEometry ANd Tracking 4), os parâmetros de desempenho de um tomógrafo de Tomografia por Emissão de Positrões (PET) com 2400 mm de comprimento do Campo de Visão Axial (AFOV – *Axial Field Of View*), baseado em detectores do tipo Câmaras de Placas Resistivas (RPC - *Resistive Plate Chamber*).

Para estabelecer uma base de comparação para esse estudo, investigou-se a dependência da sensibilidade a coincidências verdadeiras de um tomógrafo baseado em detectores de germanato de bismuto (BGO) em função do ângulo polar de aceitação e do comprimento do AFOV, segundo a versão de 1994 das normas NU2 da *National Electrical Manufacturers Association* (NEMA). O tomógrafo foi definido como um anel de tungsténio de modo a obter os pontos de entrada dos fotões, tendo-se usado factores de correcção para ter em conta a fracção de empacotamento e a eficiência de detecção em função da segmentação do tomógrafo Advance da General Electric (GE). Concluiu-se que a sensibilidade para eventos verdadeiros é dominada pelo ângulo sólido, aumentando significativamente com o comprimento do AFOV e com o ângulo polar de aceitação, enquanto a Fracção de Radiação Dispersa (SF - *Scatter Fraction*), se revelou quase independente da geometria, dependendo no entanto do ângulo polar de aceitação. A sensibilidade para coincidências verdadeiras obtida para um AFOV de 2400 mm e plena aceitação no ângulo polar foi cerca de 100 vezes maior que a do tomógrafo GE Advance. Complementarmente desenvolveu-se um modelo analítico simples para a sensibilidade a coincidências verdadeiras que revelou um acordo razoável com os dados de simulação.

De seguida fez-se um estudo semelhante para um tomógrafo baseado em detectores de RPC, tendo o mesmo sido definido de maneira análoga. As eficiências de detecção foram obtidas simulando uma pilha de 121 placas de vidro (400 μm de espessura) separadas por 120 camadas de gás (350 μm de espessura). Verificou-se que a sensibilidade para coincidências verdadeiras seguia a mesma tendência apresentada pelo tomógrafo baseado em detectores de BGO, atingindo para os 2400 mm de AFOV, e plena aceitação no ângulo polar, uma sensibilidade cerca de 20 (5) vezes mais elevada do que no caso do tomógrafo GE Advance usando um ganho devido à informação de tempo de voo (TOF – *Time-Of-Flight*) de 4,4 (sem ganho de TOF), e uma SF de 46,4%, excluindo a dispersão no detector.

Procedeu-se então a simulações detalhadas com vista à optimização do detector RPC a usar num tomógrafo PET de forma paralelepipédica definido por quatro cabeças

de detecção com um AFOV de 2400 mm. Cada cabeça de detecção contém uma pilha de 20 detectores RPC, cada um com dois módulos de detecção com 5 camadas de gás (350 μm de espessura) delimitados por 6 placas de vidro. Definiram-se os materiais e as espessuras para as camadas isoladoras, os eléctrodos de alta tensão e os de recolha de sinal, tendo-se obtido uma espessura óptima de 200 μm para as placas de vidro para detecção de fotões de 511 keV, e uma fracção de eventos mal identificados de 32% para uma distância das Linhas de Resposta (LORs) ao ponto de aniquilação igual ou inferior a 2 mm.

Estudou-se também a resolução espacial do referido tomógrafo com simulações detalhadas em GEANT4. Os dados de simulação foram processados por forma a ter em conta a electrónica de leitura dos protótipos de RPCs desenvolvidos para teste. As coincidências foram efectuadas recorrendo a um classificador de coincidências de janela temporal simples, aceitando-se as LORs com ângulo polar igual ou inferior a 9º. Avaliou-se a resolução especial de acordo com as recomendações das normas NEMA NU2-2001, mas considerando apenas uma fonte pontual com 1 μm de diâmetro localizada no centro de uma esfera de polymetil-metacrilato com 2 mm de diâmetro, que foi posicionada no plano transaxial central, desviada 100 mm do eixo segundo as duas direcções do referido plano. A resolução espacial encontrada foi de 0,9, 1,4 e 2,1 mm, respectivamente, para uma segmentação do detector de, respectivamente, 0, 1 e 2 mm nas direcções transaxial e axial, e de 3,44 mm na direcção radial.

Estudou-se ainda a SF, as taxas de contagem e a Taxa de Contagem Equivalente de Ruído (NECR - *Noise Equivalent Count Rate*) do tomógrafo já descrito, seguindo as normas NEMA NU2-2001. Os dados de simulação foram processados de modo a ter em conta a electrónica de leitura do detector. O melhor esquema de processamento para optimizar o NECR consistiu em efectuar as coincidências recorrendo a um classificador de coincidências do tipo janela temporal múltipla, aceitação total no ângulo polar, rejeição das LORs cujo ponto reconstruído directamente por TOF cai fora de uma região de interesse com 2 cm de margem relativamente às dimensões do fantoma, e aceitando todos os possíveis pares de coincidências, incluindo todas as combinação possíveis retiradas das coincidências múltiplas. Considerando um tempo morto para a leitura em posição de 3,0 μs e para o fantoma NEMA NU2-2001, obteve-se uma SF de 51,8% e um pico de NECR de ~167 kcps a $\sim 7{,}6\ \mathrm{kBq\,cm^{-3}}$. Para um fantoma similar mas estendido axialmente até aos 1800 mm, a SF obtida foi de 53,7% e o pico de NECR de ~164 kcps a $\sim 3{,}0\ \mathrm{kBq\,cm^{-3}}$.

ABSTRACT

The aim of the present work was to assess the performance parameters of a Positron Emission Tomography (PET) scanner with 2400 mm long Axial Field of View (AFOV), based on Resistive Plate Chamber (RPC) detectors, by means of simulations performed with the GEometry ANd Tracking 4 (GEANT4) toolkit.

The dependence of the sensitivity to True coincidences of a Bismuth Germanate Oxide BGO based scanner with the polar acceptance angle and the length of the AFOV, was studied by simulations performed in GEANT4, and following the National Electrical Manufacturers Association (NEMA) NU2-1994 standards. The scanner was defined as a tungsten annulus for retrieving the photon entry points and a set of correction factors were applied to account for packing fraction and detection efficiency according to the segmentation of the GE Advance tomograph. It was found that the sensitivity to True events is dominated by the solid angle, growing strongly with the AFOV and with the polar acceptance angle, while the Scatter Fraction (SF) was found to be almost independent of the geometry. The Trues sensitivity for a 2400 mm long AFOV with full acceptance on the polar angle was found to be 100 times greater than that presented by the GE Advance scanner. Complementary, a simple mathematical model of the sensitivity to True coincidences for the NEMA NU2-1994 sensitivity phantom was developed and a reasonable agreement with the simulation data was found.

A similar study was conducted for a scanner based on RPC detectors. The scanner was defined as mentioned above, and the detection efficiencies considered where obtained by simulation of a stack of 121 glass plates (400 μm thick each) separated by 120 gas gaps (350 μm thick each). The sensitivity to True coincidences was found to follow the same trends as those found for the BGO based PET scanner, with the sensitivity for a 2400 mm long AFOV with full acceptance on the polar angle being up to 20 (5) times higher than that of the GE Advance if a Time-Of-Flight (TOF) gain of 4.4 was considered (without TOF gain), with a SF of 46.4% that do not include scatter in the detector.

Following the above mentioned simulations, the optimization of an RPC detector to be employed in the development of a human PET scanner with a parallelepipedic shape defined by four detection heads and an AFOV with 2400 mm long, was performed by detailed simulations in GEANT4. The detection head contained a stack of 20 RPC detectors consisting of two detection modules, each with 5 gaps (350 μm thick), delimited by 6 glass plates. The layers of isolators, high voltage electrodes and

signal pickup electrodes with the correct thicknesses and materials were also defined. The thickness for the glass plates and the simulated geometry that maximized the detection efficiency of 511 keV photons was found to be of 200 μm, with the Fraction of Misidentified events (MIF) being of about 32% for a 2 mm binning on the distance of the Lines Of Response (LORs) to the annihilation points.

The spatial resolution of the above mentioned scanner, with the detection heads containing a stack of 40 single module RPC detectors with dimensions equal to those of each detection module defined above, was also addressed by means of detailed simulations performed with GEANT4. The simulation data was processed to account for detector readout as implemented in RPCs for testing proposes, the coincidences were performed by a Single Time Window coincidence sorter, and only those Lines Of Response (LORs) traversing the scanner bore with a polar angle equal to, or less than, 9° were accepted. The spatial resolution was assessed according to the prescriptions of the NEMA NU2-2001 standards, but considering a single point source with 1 μm diameter enclosed by a 2 mm diameter shell of Polymethyl methacrylate. The point source was placed in the central slice and 100 mm off-axis in both directions of the transaxial plane. The spatial resolution was found to be of 0.9, 1.4 and 2.1 mm for detector binning of, respectively, 0, 1 and 2 mm along the transaxial and axial directions, the binning along the radial direction being of 3.44 mm.

The SF, count rates and the Noise Equivalent Count Rate (NECR) of the scanner described in the optimization of the glass thickness was assessed by simulations performed with GEANT4 and following the NEMA NU2-2001 standards. Simulation data was processed to account for detector readout. The best processing scheme to maximize NECR consisted in performing the coincidences with a Multiple Time Window coincidence sorter, full acceptance on the polar angle, rejection of LORs for which the direct TOF reconstructed point fall outside of a tight cylinder enclosing the phantom, and by accepting all possible pairs of coincidences, including all the possible combinations contained in Multiple coincidences. For a value of 3.0 μs for the dead time for position signals, and for the standard NEMA NU2-2001 phantom, the SF was of 51.8% and the peak NECR was of ~167 kcps at $\sim 7.6\,\mathrm{kBq\,cm^{-3}}$. For an axially extended version of the NEMA NU2-2001 phantom with 1800 mm long, the SF was found to be of 53.7% and the peak NECR was found to be of ~164 kcps at $\sim 3.0\,\mathrm{kBq\,cm^{-3}}$.

TABLE OF CONTENTS

CHAPTER 1
INTRODUCTION

Positron Emission Tomography (PET) is a medical imaging technique that makes use of molecules, targeted to the biological process under study, labelled with a radionuclide that undergoes β^+ decay (emission of positrons), and usually having short half-lives (e.g., Carbon - ${}^{11}_{6}\mathrm{C}$, Nitrogen - ${}^{13}_{7}\mathrm{N}$, Fluorine - ${}^{18}_{9}\mathrm{F}$). The labelled molecules (radiopharmaceutical hereinafter) are administered to the patient, which, in some cases, may need to rest lying down for a given period of time so that the radiopharmaceutical, transported by the blood stream, reaches the tissues or organs for which it is targeted, be uptaken and establishes a stable bound. The patient is then placed in the PET scanner, usually a cylindrical annulus on the surface of which several detectors are distributed.

The positrons emitted by the radioisotopes undergoing β^+ decay will lose energy by successive collisions with atomic electrons and nuclei of the medium reaching then thermal equilibrium with it. This process is known as thermalisation, after which the positron, which is the antimatter of the electron, interacts with the latter leading to the annihilation of both particles. In this process generally two photons, each with energy equal to ~511 keV, are emitted in almost opposite directions being then detected in temporal coincidence defined by a time window of a few nanoseconds on the detection times of the two photons.

Since the two photons are emitted in almost opposite directions, the line joining the detection points of the two annihilation photons, which is named a Line Of Response (LOR), will presumably pass near the point of annihilation. By acquiring a large number of LORs, and employing appropriate reconstruction algorithms, a three dimensional (3D) distribution of the annihilation points can be obtained, which is in direct correlation with the biodistribution of the radiopharmaceutical.

The ability of using several radiopharmaceuticals for targeting different physiological functions, combined with the capability of detecting minute concentrations of the radiopharmaceutical, makes PET unique. For instance, Fluorodeoxyglucose labelled with Fluorine 18 (${}^{18}_{9}\mathrm{F}$-FDG), which is probably the radiopharmaceutical most commonly employed in PET, is an analogous of glucose

used to assess the cellular metabolism, being employed mainly in oncology to detect increased cellular activity of cancer cells, and also in neurology where hypometabolic regions may be identified. Currently, many other radiopharmaceuticals are being used to trace different physiological functions or specific receptors. In fact, applications of PET are virtually endless as long as molecules suitable to assess biological functions can be labelled with a suitable positron emitter.

Current commercial PET scanners for human whole-body applications employ detectors consisting of a pixelated block of scintillator material coupled to an array of single channel Photomultiplier Tubes (PMTs) which, along with dedicated electronic circuitry for coincidence processing, compose the detection system of a PET scanner.

The use of scintillator detectors have long been the rule on PET scanners. Among the major reasons for this are their high detection efficiencies for 511 keV photons and good energy resolution allowing rejecting photons that have undergone interaction in the patient body or in the detection system prior to the final interaction leading to detection. This is considered to be a key point in PET, since these photons suffer deviation from their initial flight path leading then to the detection of LORs that do not pass close to the site of annihilation and that contribute with a blurring to the final reconstructed image.

However, the use of pixelated scintillator detectors limits the maximum achievable spatial resolution (currently ranging from about 2 mm to 4 mm) and the temporal resolution (typically greater than 500 ps for photon pairs for the currently available state of the art commercial PET scanners). The improvement of the spatial resolution could be achieved by using detectors with smaller individual detection elements, and highly segmented photodetectors. However this leads to a decrease in sensitivity between any given pair of detector elements and an increase in the total cost of the PET scanner, which is reflected in the final cost.

The aforementioned cost issues also limit the length of PET scanners along their axial direction, also known as Axial Field of View (AFOV), which drastically reduces their sensitivity. Enlarging the AFOV would increase the geometric efficiency of PET scanners, which, combined with the increase of the photons detected per unit time, would lead to an overall increase of the sensitivity, with the consequent reduction of the total activity administered to the patient, the reduction of the time needed to perform a full acquisition and the improvement of the Signal to Noise Ratio (SNR). Besides, extending the AFOV to lengths close to that of the human height would permit to perform all body acquisitions in a single bed position, which is particularly important for quantification, motion correction and dynamic acquisition protocols.

Moreover, the increase in the AFOV and the reduction of the total activity administered to patients would lead also to a higher throughput and a lower cost per exam, thus allowing PET to be used for large scale oncological screening programs for the general population, similarly to what already occurs with conventional X-ray mammography and Computed Tomography (CT), with the added benefit of increased specificity. However, and as long as the cost of scintillator detectors remain at the present levels, the increase of the AFOV of PET scanners can only be achieved by employing more affordable detectors based on different technologies and requiring less electronics for readout per unit area available for detection. One of the detectors that may meet these requirements is the Resistive Plate Chamber (RPC).

Developed for High Energy Physics experiments, the RPC is a gaseous detector consisting of two or more flat layers of a resistive material separated by small and precise gaps, placed inside a gas-tight box which is then filled with an appropriate gas mixture so that the gaps become also filled with it. Charged particles passing through the gas gaps will eventually ionize the gas there contained creating primary electron/positive ion pairs (ionization clusters) which, under the influence of an electric field established in the gaps by a pair of opposing electrodes, will drift toward the anode and cathode, respectively, eventually producing more pairs of electrons/positive ions in a cascade process known as an avalanche.

The flow of the charge carriers in the gas gaps leads to electronic and ionic currents that induce currents in a set of appropriate readout electrodes, for instance, two sets of strips aligned orthogonally to each other and placed on top of the outer surfaces of the detector. The signal induced in the pickup electrodes can then be readout by appropriate electronics holding information on the fast transit times of electrons in the gaps, leading to a fast time signal, and on the total charge collected in the electrodes, from which the accurate position of the centroid of the avalanches can be obtained.

The processes described above apply strictly to charged particles. For the detection of photons, these have to be first converted into charged particles that must reach the gas gaps. This process is carried out in the resistive plates in which the primary photons to be detected will eventually interact with the subsequent extraction of electrons into the gas gaps, where they will then undergo the amplification process previously mentioned.

RPC detectors present several advantages relative to scintillator detectors: are much less expensive, can be produced in large areas at small costs, have an excellent intrinsic spatial resolution and a time resolution that allows the use of the so called

Time-Of-Flight (TOF) information. However, RPC detectors have two major drawbacks when compared to scintillator detectors: the detection efficiency of a single practical RPC detector is two orders of magnitude lower than those presented by scintillator detectors, and do not have energy resolution to permit the rejection of photons that have undergone interaction in the patient body or in the detection system. As to the latter, it is partially compensated by a detection efficiency that depends on the energy of the incident photons, leading to a detection efficiency that is sensitive to the energy of the incoming photons. As to the former, it can eventually be compensated by stacking several RPC detectors so as to achieve an overall detection efficiency that is high enough to permit the use of RPC detectors in PET scanners. However, stacking several RPC detectors increases the number of photons that undergo interaction in the detector prior to detection, with the consequent increase of the number of detected photons that have suffered deviations from their initial flight path, which may compromise the spatial resolution and SNR on the final reconstructed image.

The aim of the present work was to study the feasibility of a full-body length PET scanner based on RPC detectors with a time resolution of 90 ps σ for Single events and a coincidence time resolution of 300 ps Full With at Half Maximum (FWHM), by means of simulations performed with the GEometry ANd Tracking 4 (GEANT4) toolkit accounting for the detailed geometry of the foreseen RPC TOF-PET scanner, depicted in Fig. 1.1 (along with a scheme of currently available commercial PET scanners), by assessing the expected performance of the RPC TOF-PET scanner by means of the National Electrical Manufacturers Association (NEMA) NU2 standards for performance measurements of PET scanners.

The Thesis is divided in eleven Chapters, the first being the present one, followed by four Chapters devoted to bibliographic revision and by five Chapters related with the work done on the scope of the present Thesis, a Chapter for conclusions, after which the Bibliographic references are given, and ending with some Appendixes.

In Chapter 2, “Physical Principles Relevant to Positron Emission Tomography and Associated Detectors”, the structure of matter, the nuclear decay and the interaction of radiation with matter will be first revised.

In Chapter 3, “γ-Ray Detectors Employed in Clinical Positron Emission Tomography Systems”, the requirements for successful PET detectors, the mechanisms of scintillation, the photodetectors employed in current or proposed PET detectors, and the main designs of current PET detectors will be addressed.

In Chapter 4, “Positron Emission Tomography”, the basics of PET will be

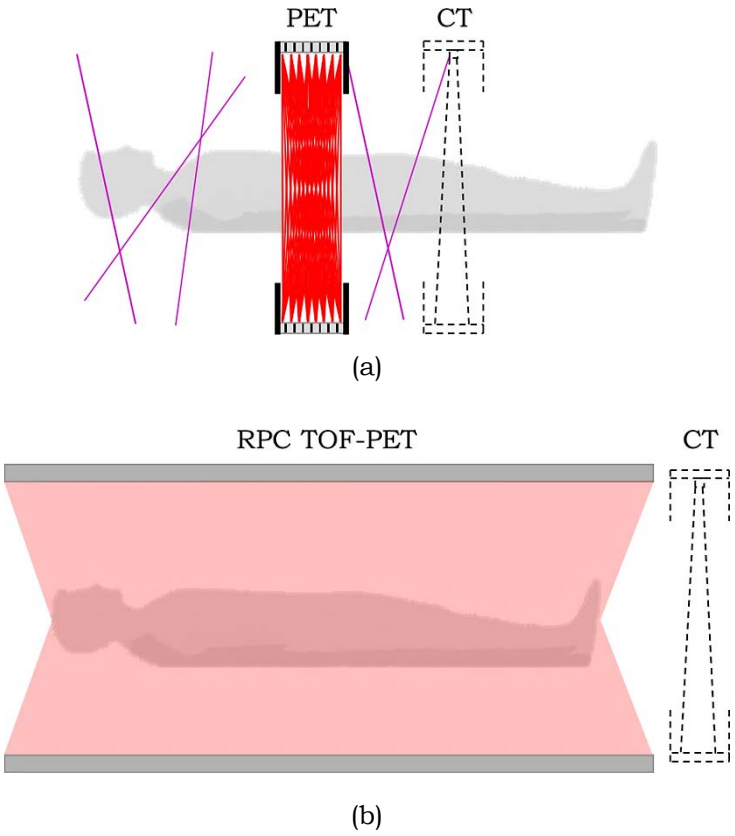

Fig. 1.1: Schematic representation of (a) conventional PET scanner for human whole-body studies, and (b) the RPC TOF-PET scanner.
(Adapted from personal presentations kindly ceded by Prof. Nuno Chichorro Ferreira).

addressed starting with a very brief review of the radionuclides employed in current radiopharmaceuticals, the basics of PET scanning systems, the corrections commonly performed to the acquired data prior to image reconstruction and this latter, the advantages of TOF information, followed by the performance tests as defined by the NEMA NU2-2001 standards and the current state of the art PET scanners will be revised.

In Chapter 5, "Resistive Plate Chamber Detectors Developed for Positron Emission Tomography", the basics of a single gap RPC detector, the signal induction in the pickup electrodes, the structure and advantages of multi-gap RPC detectors, the readout of time and position signals, and the sources of dead time will be briefly mentioned.

In Chapter 6, "Software Developed for the Simulation of a Positron Emission Tomography System Based on Resistive Plate Chamber Detectors", the GEANT4 toolkit will be briefly addressed so that the structure of the program developed to perform the simulations can be explained and the options taken addressed. After these, the

software developed for processing simulation data to account for decay times, and hence detection instants, detector readout, and coincidence processing are first explained, after which the software developed for processing coincidence data to obtain the final set of data for the performance tests will be explained.

In Chapter 7, "Optimization of the Resistive Plate Chamber Detector and Preliminary Tests of the Resistive Plate Chamber Time-Of-Flight Positron Emission Tomography Scanner", the setup employed in simulations will be given, after which the optimization of the thickness of the resistive electrodes for the detection of 511 keV photons considering a complete detection head of the scanner will be presented after a very brief summary of the results previously obtained by Alberto Blanco. Then, the energy spectrum of detected photons and the number of interactions that each photon undergoes in the detectors until its detection will be presented. At the end of the Chapter, the results obtained concerning the effects of dead time on the Single events rate will be given.

In Chapter 8, "Sensitivity of Wide-Axial Field of View Positron Emission Tomography Scanners Based on Scintillation And Resistive Plate Chamber Detectors, Assessed by Simulations, Following a NEMA-Like Measurement", the NEMA NU2-1994 sensitivity to True coincidences for a wide AFOV PET scanner based on inorganic scintillation detectors and a wide AFOV PET scanner based on Resistive Plate Chamber detectors, will be addressed by means of simulations.

In Chapter 9, "Spatial Resolution " the spatial resolution of a full-body length RPC TOF-PET scanner will be addressed by means of detailed simulation of the RPC TOF-PET scanner, and following the NEMA NU2-2001 standards.

In Chapter 10, "Scatter Fraction, Count Rates and Noise Equivalent Count Rate, of A Full-Body Length Resistive Plate Chamber Time-Of-Flight Positron Emission Tomography Scanner, Assessed by Means of Detailed Simulations", the complete set of parameters employed in the processing of simulation data will be first given, followed by the complete set of parameters used for processing the coincidence data, to then present and discuss the results for the Scatter Fraction (SF), count rate, and Noise Equivalent Count Rate (NECR) obtained according with NEMA NU2-2001 standards.

In Chapter 11, "Conclusions", the main conclusions of the present work will be given.

The Bibliographic references can be found after the previously mentioned Chapter, followed by a set of Appendixes in which the complete set of parameters, data structures, and stored variables employed in the software developed, are given.

CHAPTER 2
PHYSICAL PRINCIPLES RELEVANT TO POSITRON EMISSION TOMOGRAPHY AND ASSOCIATED DETECTORS

Electromagnetic radiation (commonly termed light) with frequency ν (or wavelength $\lambda = c/\nu$, where c is the light speed[1]) has a dual nature, viz., in some phenomena (ex. refraction and diffraction) light must be treated as a wave propagating in space with velocity c, while in other phenomena, such as photoelectric absorption and Compton effect, light must be treated as a beam of particles (photons) each having an energy

$$E = h\nu \quad \Leftrightarrow \quad E = \frac{hc}{\lambda}. \tag{2.1}$$

where h is the Planck's constant[2].

Other important equation is the Einstein relation between the mass of a particle and its energy

$$E = mc^2 \quad \Leftrightarrow \quad E = \gamma m_0 c^2, \tag{2.2}$$

where m is the mass of a particle with velocity v, m_0 is the particle rest mass, viz., for $v = 0\ \mathrm{m\,s^{-1}}$, and γ is the Lorentz factor given by

$$\gamma = \frac{1}{\sqrt{1-\beta^2}} \quad \text{with} \quad \beta = \frac{v}{c}. \tag{2.3}$$

The energy unit commonly used in particle physics is the electron-Volt (eV)[3], or one of its multiples (keV, MeV, ...), which is defined as the kinetic energy acquired by an elementary charge (denoted by e)[4] when accelerated through a potential difference of 1 Volt. So, the mass of a particle can be expressed in units of energy per squared light speed $\left(\mathrm{eV/c^2}\right)$.

From Eq. (2.2) and Eq. (2.3), the relativistic relation between the particle energy E and the magnitude of its linear momentum p is given by

---

1 $c = 299792458\ \mathrm{m\,s^{-1}}$ [Mohr et al., 2012].

2 $h = 6.62606957(29)\times10^{-34}\ \mathrm{J\,s}$ [Mohr et al., 2012].

3 $1\ \mathrm{eV} = 1.602176565(35)\times10^{-19}\ \mathrm{J}$. [Mohr et al., 2012]

4 $e = 1.602176565(35)\times10^{-19}\ \mathrm{C}$. [Mohr et al., 2012]

$$E^2 = p^2 c^2 + m_0^2 c^4 \quad \Leftrightarrow \quad p = \frac{\sqrt{E^2 - m_0^2 c^4}}{c}. \tag{2.4}$$

For photons, which have zero rest mass, Eq. (2.2) gives the equivalent photon mass for a given photon energy, and from equation (2.4) the linear momentum of a photon is simply given by the quotient between its energy and the light speed.

Such as light, matter also has a dual nature, viz., in some phenomena (ex. collisions) matter particles are better treated as particles with linear momentum *p*, while in other phenomena (ex. diffraction) matter particles must be treated as waves with wavelength γ (or frequency $\nu = \upsilon/\lambda$, where υ is the magnitude of the particle velocity), the two quantities being related by the de Broglie equation

$$\lambda = \frac{h}{p}. \tag{2.5}$$

2.1 THE STRUCTURE OF MATTER

In general, matter is composed of molecules[5], formed by atoms consisting of a nucleus containing *Z* protons, each carrying an elementary charge *e* and rest mass $m_{0,p} \approx 1.007\,276\ \mathrm{u}$[6] [Mohr et al., 2012], *N* neutrons[7], each with no charge and rest mass $m_{0,n} \approx 1.008\,665\ \mathrm{u}$ [Mohr et al., 2012], surrounded by a cloud of electrons, each with a charge symmetric to the elementary charge $(-e)$ and rest mass $m_{0,e} \approx 0.000\,549\ \mathrm{u}$ [Mohr et al., 2012]. Table 2.1 resumes the abovementioned properties of the particles that constitute the atom.

In the nucleus, protons and neutrons are collectively named nucleons, and their sum $(Z+N)$ is called the mass number, denoted by *A*, which is equal to the nearest integer of the atomic mass expressed in atomic mass units [Eisberg & Resnick, 1985]. The *Z* number of protons of an atom is called the atomic number, and defines the atom chemical properties, corresponding to a well-determined position in the periodic table of the elements. Since the atom is electrically neutral, the number of electrons is equal to the *Z* number of protons[8].

Atoms with the same atomic number and different mass number have the same

---

5 Exception made for noble gases and crystals. However, crystals can be regarded as large molecules [Eisberg & Resnick, 1985].

6 $1\ \mathrm{u} = \frac{1}{12}\mathrm{M}_{^{12}\mathrm{C}} = 1.660538921(73)\times10^{-27}\ \mathrm{kg} = 931.494061(21)\ \mathrm{MeV/c^2}$, where $\mathrm{M}_{^{12}\mathrm{C}}$ is the mass of Carbon 12 atom [Mohr et al., 2012]. u is called the atomic mass unit.

7 Exception made to the Hydrogen atom, the nucleus of which has only a proton.

8 An atom with unequal number of protons and electrons is called an ion, being negative if it has more electrons than protons, and positive if it has more protons than electrons.

TABLE 2.1: PHYSICAL PROPERTIES OF ATOM CONSTITUTIVE PARTICLES.

Particle	Charge (multiple of *e*)	Rest mass [u]	Rest mass $[\mathrm{MeV/c^2}]$
Proton	+1	1.007 276	938.272
Neutron	0	1.008 665	939.565
Electron	-1	0.000 549	0.511

chemical properties and hence occupy the same position in the periodic table of the elements, being called isotopes[9]. Atoms with different atomic numbers but the same mass number are termed isobars[10], and atoms with different atomic and mass numbers but with the same number of neutrons are designated by isotones[11].

Atoms and nuclei can be represented as ${}^{A}_{Z}X_{N}$, where X is the atom chemical symbol. However, since $N = Z - A$, it is preferable to use the notation ${}^{A}_{Z}X$, or even the more compact notation ${}^{A}X$, since the atomic symbol univocally defines the atomic number Z.

Concerning the dimensions, the nucleus can roughly be considered as a sphere with radius given by $R = r_0 \sqrt[3]{A}$ [Krane, 1988], where $r_0 = 0.9541(6) \pm 0.1309$ fm [12] [Angeli, 1999]. As to the average atomic radius, is in the order of magnitude of 10^5 fm [Born, 1990; Eisberg & Resnick, 1985; Krane, 1988]. So, the atom can be viewed as containing a very small nucleus with high mass density[13], surrounded by vacuum in which electrons are spread.

Each atomic electron is bound to the atom by the Coulomb potential created by the nucleus and the remaining electrons, having a total energy equal to the sum of its potential and kinetic energies, that can be obtained by quantum mechanics, which, making use of the concept of matter waves referred to on page 8, seeks for the stationary solutions of a wave equation operating on a complex wave function. Those solutions, corresponding to stationary waves, lead to electron stationary states for which the atomic electron energy is quantized, viz., can only assume discrete values that depend on a set of four quantum numbers. The most used set of quantum numbers include the principal quantum number *n*, assuming integer values such that

9 From the Greek *isos* - equal, and *topos* - place.

10 From the Greek *isos* - equal, and *baros* - weight.

11 Name derived from isotopes by replacing the *p* by *n* (for neutrons) [Brucer, 1978].

12 $1\,\mathrm{fm(fentometer)} = 10^{-15}$ m is a conventional length unit in nuclear physics, also named Fermi.

13 Given the values of Table 2.1 and previous nuclear radius equation, the nucleus density can be found to be $\sim 10^{14}\ \mathrm{g\,cm^{-3}}$.

$n = 1, 2, 3, \cdots$, the orbital quantum number[14] ℓ, assuming integer values given by $\ell = 0, 1, 2, \cdots, n-1$, the magnetic quantum number m_ℓ, assuming the integer values $m_\ell = -\ell, -\ell+1, \cdots, \ell-1, \ell$, and the spin quantum number m_s, which can only take two semi-integer values $m_s = \pm 1/2$. Besides, according to the Pauli Exclusion Principle, in a quantized system, two identical particles cannot have the same set of quantum numbers, which means that in atoms two electrons cannot have the same set of quantum numbers.

The electron energy depends on all the four quantum numbers. However, that dependency is higher for the principal and orbital quantum numbers, the principal quantum number giving a measure of the most probable distance of the electron to the nucleus [Eisberg & Resnick, 1985]. So, the higher the principal quantum number, the farther from (and less attached to) the nucleus the electron is, and the higher its energy[15] is. For this, the atom is said to be arranged in shells, termed *K*, *L*, *M*, *N*, ..., which are assigned to the principal quantum numbers $n = 1, 2, 3, 4, \cdots$. The orbital quantum number gives the angular distribution of electrons around the nucleus defining the orbital shape in a given shell. So, each atomic shell contains one or more subshells of different shapes, termed *s*, *p*, *d*, *f*, ..., corresponding to the orbital quantum numbers $\ell = 0, 1, 2, 3, \cdots$, with a lower energy increase with the increase in the orbital quantum number than that observed for the principal quantum number. Concerning the magnetic and spin quantum numbers, they define the atomic orbital orientation in space and the electron intrinsic angular momentum, respectively, and together account for the splitting of subshell energy levels.

So, quantum mechanics applied to atoms leads to a set of distinct quantum numbers for each atomic electron, corresponding to different energy levels, predicting also that only some transitions between electronic states have non-negligible probability of occurrence. The electronic energy levels corresponding to atomic shells and subshells can be schematically represented as in Fig. 2.1.

If the atomic electrons occupy energy levels such that the atomic energy is the lowest possible, the atom is said to be in the ground state, otherwise is said to be in an excited state. Atoms in the ground or in an excited state can undergo discontinuous excitation transitions by absorption of energy from incident radiation (both photons and particles) with the discontinuous promotion of electrons from lower to higher energy levels. Likewise, an atom in an excited state can, and will, return to the ground state by discontinuous demotion of electrons from higher to lower energy

[14] The orbital quantum number is also termed azimuthal or angular momentum quantum number.

[15] The energy of a bonded atomic electron is negative, being zero when the electron is removed from the atom staying unbonded with zero kinetic energy.

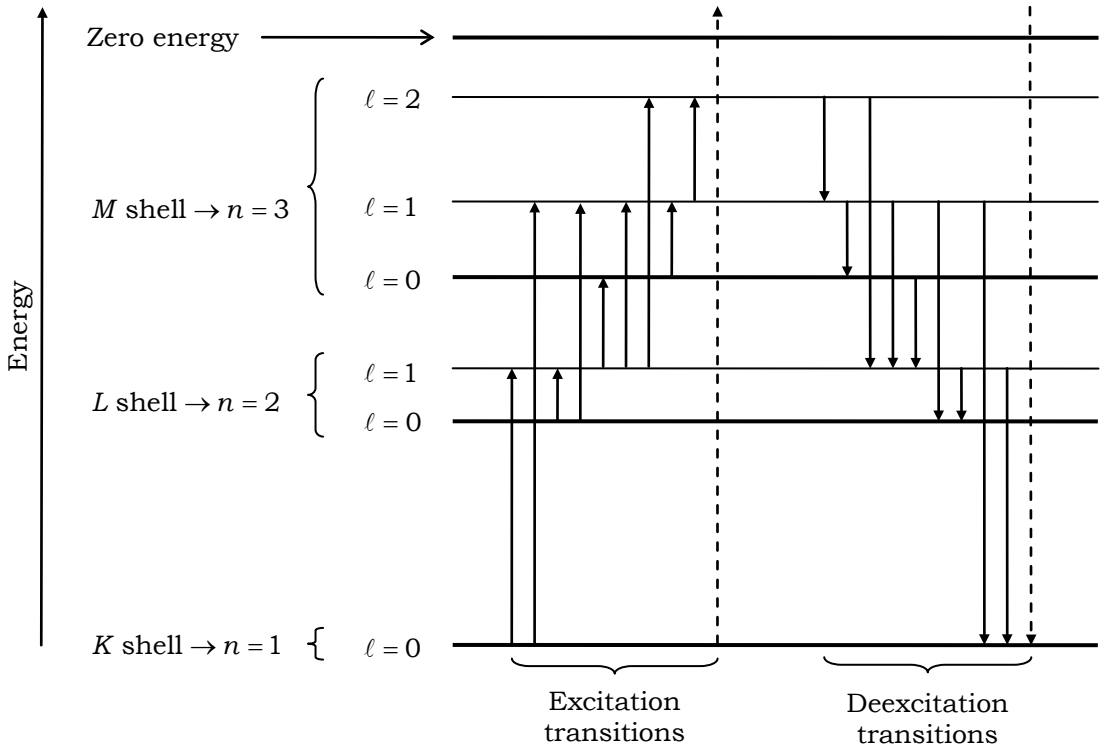

Fig. 2.1: Schematic diagram of atomic electronic energy levels, along with some illustrative excitation and deexcitation transitions.

levels, with emission of a photon with energy equal to the energy difference between the electron's initial and final states, which is called a characteristic X-ray photon. Alternatively, the energy associated with electron deexcitation can be directly transferred to an atomic electron which is then ejected from the atom, named Auger electron. [Born, 1990; Eisberg & Resnick, 1985].

What was said about energy quantization in atoms also holds for nuclei, molecules and solids, as in all of them the energy is quantized. However, molecules and solids, namely crystals, have a different energy level structure.

2.2 NUCLEAR DECAY

In the nucleus, protons and neutrons (recall footnote 7 on page 8) are confined in a very small volume[16], being subjected to two distinct forces: the Coulomb force, and the nuclear force. The first is a long range repulsive force which is exerted between protons, while the second is a short range force acting between neighbouring nucleons.

The nuclear force is charge independent[17], and is repulsive for very short

[16] Using the nuclear radius expression on page 6, nuclear volumes range from $\sim 3.6\ \text{fm}^3$ to $\sim 1000\ \text{fm}^3$.
[17] The nuclear force is the same for proton-proton, proton-neutron, and neutron-neutron interaction.

distances (~0.5 fm), maintaining nucleons at a minimum distance, being attractive and much stronger than the Coulomb force for distances of ~1 fm, becoming negligible at distances larger than the nuclear radius. So, nucleons can roughly be viewed as particles moving in a net square potential well. [Krane, 1988]

Since the nuclear force acts between neighbouring nucleons, its effective range is less than the nuclear radius and, as the atomic number increases, the repulsive Coulomb force exerted on a given proton by non-neighbouring protons becomes increasingly stronger, challenging the attractive nuclear force sensed by that same proton. To overcome the net proton-proton repulsive forces, neutrons have to be added to nuclei in order to increase the nuclear force, leading to nuclear stability. So, when atomic number increases one can expect that the number of neutrons also increases more than the number of protons[18]. This does not mean that, for a given number of protons, the nucleus will be more stable if it has an arbitrarily high number of neutrons, as it will be clear soon.

Nuclear stability ultimately depends on the binding energy per nucleon, which can be computed through the mass-energy difference between a given nucleus and its constituent particles, given (in MeV) by

$$E_B = \frac{931.50 \times \left[Z\, M\left({}^{1}_{1}\mathrm{H}\right) + (A-Z)\, m_{0,n} - M\left({}^{A}_{Z}X\right) \right]}{A}, \tag{2.6}$$

where $M\left({}^{A}_{Z}X\right)$ is the mass of isotope ${}^{A}_{Z}X$, and unified atomic mass units should be used for all masses. [Krane, 1988]

The binding energy per nucleon of a given nucleus can also be obtained by

$$E_B = \frac{1}{A}\left[a_v\, A - a_s\, A^{2/3} - a_c\, Z(Z-1)\, A^{-1/3} - a_{sym}\, \frac{(A-2Z)^2}{A} + \delta \right], \tag{2.7}$$

where the first term in brackets accounts for the total binding energy associated with the nucleus spherical volume, the second one reduces the total binding energy due to nucleons on the surface of the spherical nuclear volume which have less neighbouring nucleons to bind to than those on the core of the spherical nuclear volume, the third term accounts for the Coulomb repulsion between protons, the forth favours nucleus with the same number of protons and neutrons, and the fifth term is due to the tendency of nucleons to be paired in more stable configurations[19], and is given by

[18] The number of neutrons is roughly given by $N \approx 0.6\,Z$ [Eisberg & Resnick, 1985].

[19] Of the 254 nuclides marked as stable, 102 have an odd number of nucleons and 152 have an even number of nucleons. Of this 152, 5 have an odd number of neutrons and protons, the remaining 147 having an even number of neutrons and protons.

$$\delta = \begin{cases} -a_p A^{-3/4} & \text{even } A \rightarrow \text{with odd } Z \text{ and } N \\ 0 & \text{odd } A \\ a_p A^{-3/4} & \text{even } A \rightarrow \text{with even } Z \text{ and } N \end{cases} . \tag{2.8}$$

The constants a_v, a_s, a_c, a_{sym} and a_p are adjustable and proper values lead to a very good agreement between Eq. (2.6) and Eq. (2.7). [Krane, 1988]

What was said is resumed in Fig. 2.2 which depicts a plot of the binding energy per nucleon computed by Eq. (2.6) for all known nuclei along with a plot of the binding energy for stable nuclei, as well as two insets with the plot of the binding energy for all isobars with $A = 18$ and $A = 22$, defined by the two vertical dashed lines, and two insets for all nuclides with $Z = 9$ and $Z = 11$. It can be clearly seen that stable nuclides have an optimum ratio between the number of protons and neutrons.

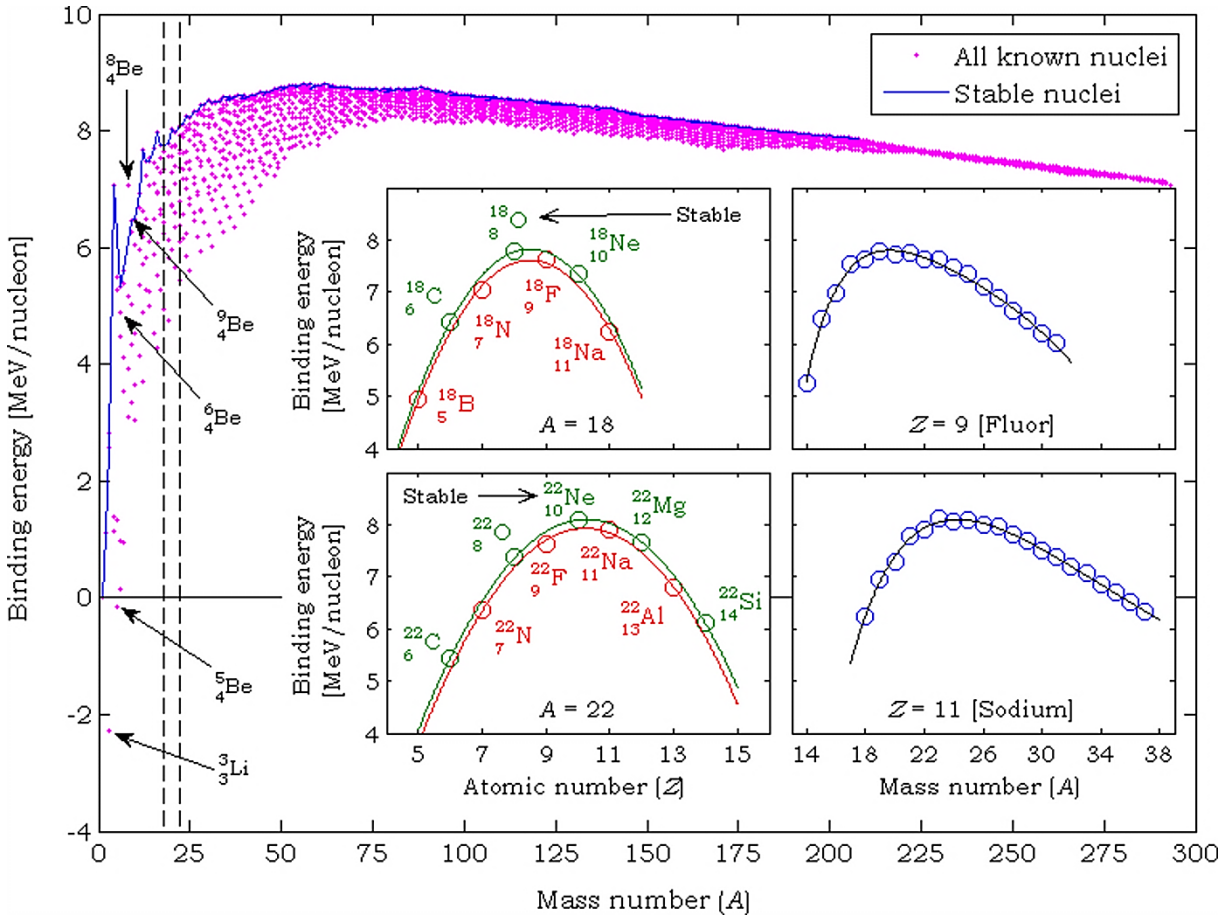

Fig. 2.2: Average binding energy per nucleon for all known nuclei (magenta dots) along with the energy of stable nuclei (solid blue line), computed by Eq. (2.6), with two insets depicting the quadratic dependence of the binding energy per nucleon obtained by Eq. (2.7), with δ given by Eq. (2.8), for all known nuclides with $A = 18$ and $A = 22$, and two insets depicting the dependence of the total binding energy per nucleon with the mass number A for all known nuclides with $Z = 9$ and $Z = 11$, with $\delta = 0$. (Data retrieved from [Coursey et al., 2011].)

Due to the difference in binding energy per nucleon, radionuclides tend to suffer transmutation processes in order to achieve the highest possible binding energy per nucleon. These transmutation processes, along with transitions of nucleons from excited nuclear states to the ground state, are named nuclear decay.

2.2.1 Nuclear Decay Laws

All processes through which nuclei can undergo decay share the same statistical nature and laws. For this, it is useful to introduce those laws before proceeding to the individual nuclear decay modes.

Considering that a given sample contains N radioactive nuclei of the same nuclide[20] at a given time t, the number of nuclei dN undergoing radioactive decay in the time interval $[t, t+dt]$ is given by

$$-\frac{dN}{dt} = \lambda N \quad \Leftrightarrow \quad N(t) = N_0\, e^{-\lambda t}, \tag{2.9}$$

where N_0 is the number of nuclei present at a time $t_0 = 0\,\mathrm{s}$, λ is a constant specific for each radionuclide and decay process, named decay constant, that represents the probability of decay of a single nucleus per unit time, and the minus sign is due to the fact that the number of radioactive nuclei diminish with time. Since the first part of Eq. (2.9) only depends on the number of nuclei present in the sample at a given time t, one can conclude that this probability is constant throughout time, viz., is independent of the number of radioactive nuclei present in the sample at any given time t. [Krane, 1988]

The rate of decay represented in the first part of Eq. (2.9), is named *activity* and represents the number of decays per unit time undergone by a radionuclide sample with N radioactive nuclei at time t, and is written as

$$A(t) = A_0\, \mathrm{e}^{-\lambda t}, \tag{2.10}$$

where $A_0 = \lambda N_0$ is the activity at a given time taken as the initial time $t = 0\,\mathrm{s}$. The SI unit of activity is the Becquerel (Bq), and is defined as being equal to one disintegration per second. Another commonly used unit of activity is the Curie (Ci) defined as $1\mathrm{Ci} = 3.7\times10^{10}\,\mathrm{Bq}$. In PET, activities are usually given in multiples of Becquerel (kBq for very low activities, and MBq for clinically used activities), or in submultiples of Curie (μCi for very low activities, and mCi for activities used in clinical practice).

Being statistical in nature, radioactive decay can be associated with a *mean*

[20] A nuclide which undergoes radioactive decay is also named radionuclide.

lifetime τ (usually simply referred to as *lifetime*) for an individual nucleus to exist without undergoing decay, which can be computed using Eq.(2.9) or Eq. (2.10) by

$$\tau = \frac{\int_0^\infty \left[t\,N(t)\right]dt}{\int_0^\infty \left[N(t)\right]dt} \quad \Leftrightarrow \quad \tau = \frac{\int_0^\infty \left[t\,A(t)\right]dt}{\int_0^\infty \left[A(t)\right]dt} \quad \Leftrightarrow \quad \tau = \frac{1}{\lambda}. \tag{2.11}$$

From Eq. (2.9) one can also compute the time needed for the number of radioactive nuclei present in a given sample to be reduced to half of its value, or, equivalently, the time needed to reduce the activity to half of its initial value. This time is called the *half-life* $T_{1/2}$ (or period) and is given by

$$N(t) = \frac{N_0}{2} \quad \Leftrightarrow \quad N_0\,\mathrm{e}^{-\lambda T_{1/2}} = \frac{N_0}{2} \quad \Leftrightarrow \quad T_{1/2} = \frac{\ln(2)}{\lambda}. \tag{2.12}$$

It may happen that a given radionuclide decays by more than one process, each with a characteristic decay constant. Let λ_a, λ_b, λ_c, ..., be the decay constants associated with the decay processes *a*, *b*, *c*, ... The total decay constant for the radioactive sample is equal to the sum of the decay constants of individual decay processes, and one can write

$$N(t) = N_0\,\mathrm{e}^{-(\lambda_a+\lambda_b+\lambda_c+\cdots)t} \quad \Leftrightarrow \quad N(t) = N_0\,\mathrm{e}^{-\lambda_t t} \quad \text{with} \quad \lambda_t = \lambda_a + \lambda_b + \lambda_c + \cdots. \tag{2.13}$$

When nuclei decay by two or more processes with different decay constants, it is usual to use the total decay constant distinguishing the different decay modes by their fractions relative to the total decay. These fractions are named *branching fractions* or *branching ratios* (BR). Decay constants, lifetimes and half-lives of each decay process can then be obtained by

$$\begin{cases} \lambda_a = BR_a \times \lambda_t \\ \lambda_b = BR_b \times \lambda_t \\ \quad \vdots \end{cases} \qquad \begin{cases} \tau_a = \tau_t / BR_a \\ \tau_b = \tau_t / BR_b \\ \quad \vdots \end{cases} \qquad \begin{cases} T_{1/2,a} = T_{1/2,t} / BR_a \\ T_{1/2,b} = T_{1/2,t} / BR_b \\ \quad \vdots \end{cases}, \tag{2.14}$$

and the number of nuclei present in a sample at time *t* and decaying by a given decay process *i*, or the activity of a given decay process *i*, can be expressed by

$$\begin{cases} N_i(t) = BR_i \times N_0\,\mathrm{e}^{-\lambda_t t} \\ A_i(t) = BR_i \times A_0\,\mathrm{e}^{-\lambda_t t} \end{cases}, \tag{2.15}$$

The number of nuclei that decayed in the time interval $[t_s, t_e]$ can be computed directly from Eq. (2.9). However, since the number of radioactive nuclei present in a given sample is usually unknown, Eq. (2.10) must be used:

$$\Delta N = \int_{t_s}^{t_e} A(t)\,dt \quad \Leftrightarrow \quad \Delta N = \int_{t_s}^{t_e} A_0\,\mathrm{e}^{-\lambda_t t}\,dt \quad \Leftrightarrow \quad \Delta N = \frac{A_0}{\lambda_t}\left(\mathrm{e}^{-\lambda_t t_s} - \mathrm{e}^{-\lambda_t t_e}\right). \tag{2.16}$$

In the case of multiple decay modes, the number of nuclei ΔN_i that undergone a specific decay mode i in the time interval $[t_s, t_e]$ is given by

$$\Delta N_i = BR_i \times \frac{A_0}{\lambda_t}\left(\mathrm{e}^{-\lambda_t t_s} - \mathrm{e}^{-\lambda_t t_e}\right). \tag{2.17}$$

Besides the multiple decay processes, a given radionuclide can undergo decay with the resultant nuclide being also radioactive. Moreover, the decay of a given initial radionuclide may origin a chain of radioactive products. The initial radionuclide is referred to as the parent nuclide and the succeeding radionuclides are called the daughter, granddaughter, and so on [Krane, 1988]. Denoting by 1, 2, 3, ..., the successive generations of radionuclides, and assuming that at time $t = 0\,\mathrm{s}$ only a N_0 number of the parent radionuclide is present in the sample, the number of nuclides of the n^{th} generation present in the sample will be given by the Bateman equations, which can be written as [Krane, 1988]

$$\begin{aligned} N_n(t) &= N_0 \sum_{i=1}^{n} a_i \,\mathrm{e}^{-\lambda_i t} \quad \text{with} \quad a_i = \frac{\prod_{j=1}^{n-1} \lambda_j}{\prod_{\substack{j=1 \\ j\neq i}}^{n} \left(\lambda_j - \lambda_i\right)} \\ A_n(t) &= N_0 \sum_{i=1}^{n} b_i \,\mathrm{e}^{-\lambda_i t} \quad \text{with} \quad b_i = \frac{\prod_{j=1}^{n} \lambda_j}{\prod_{\substack{j=1 \\ j\neq i}}^{n} \left(\lambda_j - \lambda_i\right)} \end{aligned}, \tag{2.18}$$

If the decay constants of the successive generations are such that $\lambda_1 > \lambda_2 > \lambda_3 > \cdots > \lambda_n$, then, as time increases, the exponential terms of all generations previous to the last one will tend to zero more quickly than the exponential term of the last generation nuclide. After a sufficient long time, which depends on the lifetimes of the last but one nuclide, the last nuclide in the decay chain will decay with a simple exponential law, with a decay constant given by the term b_n of Eq. (2.18).

If the decay constants of the successive generations of nuclides are such that $\lambda_1 < \lambda_2 < \lambda_3 < \cdots < \lambda_n$, with the decay constants not being negligible when compared with each other, as time increases the exponential terms of a given nuclide generation will tend to zero more quickly than the exponential term of the previous generation, and, after a sufficient long time that depends on the values of the decay constants, the activities of all nuclides became equal, and all radionuclides will decay with an effective decay constant equal to that of the parent nuclide. This is called transient equilibrium, and is verified, for instance, in the ${}^{99}_{42}\mathrm{Mo} \rightarrow {}^{99m}_{43}\mathrm{Tc}$ generator widely used

in Single Photon Emission Tomography (SPET) and Single Photon Emission Computed Tomography (SPECT), or the ${}^{68}_{32}\mathrm{Ge} \rightarrow {}^{68}_{31}\mathrm{Ga}$ and ${}^{82}_{38}\mathrm{Sr} \rightarrow {}^{82}_{37}\mathrm{Rb}$ generators used in PET.

If $\lambda_1 << \lambda_2 << \lambda_3 << \cdots << \lambda_n$ the activities of the all the radionuclides generations tend to a constant value, equal to the activity of the parent nuclide, viz., $\lambda_1 N_1 = \lambda_2 N_2 = \lambda_3 N_3 = \cdots = \lambda_n N_n$. This is called *secular equilibrium*.

2.2.2 Nuclear Decay Processes

The transmutation process through which nuclei decay depends on how fast the stability is attained and on the total energy released which can be written as

$$Q = \left[M\left({}^{A}_{Z}X_N\right) - M\left({}^{A'}_{Z'}Y_{N'}\right) - m \right] c^2 > 0 . \tag{2.19}$$

where $M\left({}^{A}_{Z}X_N\right)$ is the mass of the parent nuclide, $M\left({}^{A'}_{Z'}Y_{N'}\right)$ is the mass of the daughter nuclide, or the sum of all daughter nuclide masses, and m represents the sum of all nuclear particles emitted in the transmutation process. However, it is not sufficient that a given transmutation process is energetically favourable for the nuclide to be marked as undergoing that same transmutation. It is also necessary that the decay constant associated to the process is high enough so that the process can be detected. If not, the nuclide is not marked as undergoing the corresponding decay process, even if theoretically possible or expectable [Krane, 1988]. Fig. 2.3 depicts a plot of all known nuclides, colour coded with the corresponding decay modes. The black coded band is named the *stability belt*.

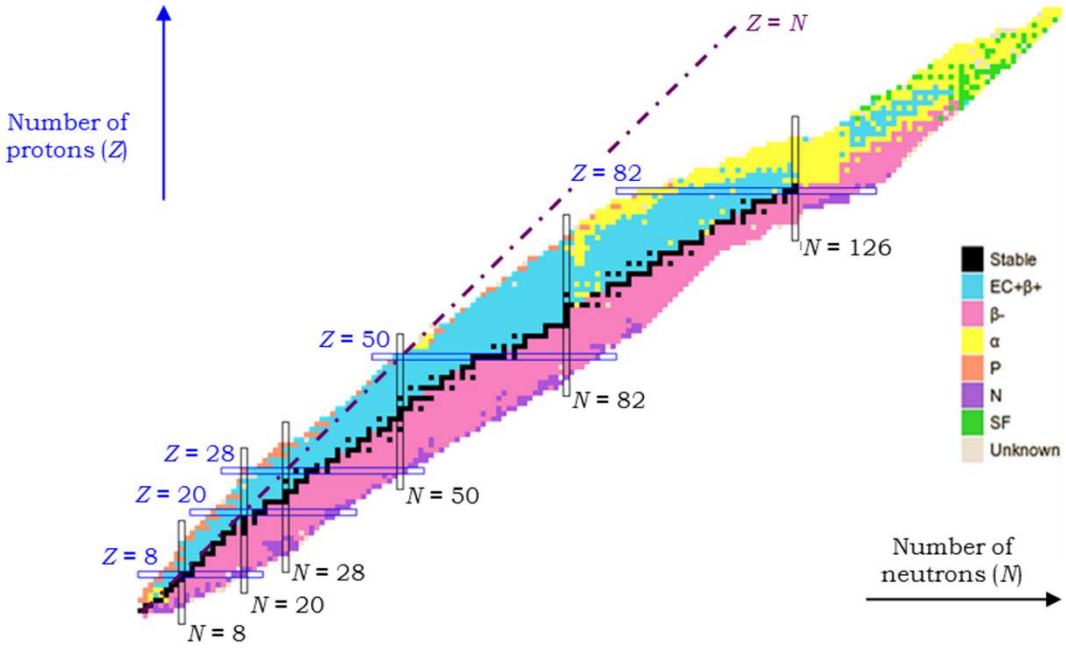

Fig. 2.3: Chart of nuclei plotted as $Z(N)$, colour coded with the corresponding decay modes. (Retrieved and adapted from [Sonzogni, 2013].)

2.2.2.1 α, Proton and Neutron Decay, and Spontaneous Fission

Some of the processes through which a nuclide can achieve higher stability involve the loss of nucleons and, with the exception of neutron decay, are explained by the probability of the emitted particles to tunnel the potential barrier resulting from the overlap of the Coulomb potential with the nuclear potential well [Krane, 1988].

This is the case of alpha decay (α decay, for short), which consist on the emission of an α particle (a ${}^{4}_{2}\mathrm{He}$ nucleus), the daughter nucleus becoming ${}^{A-4}_{Z-2}Y_{N-2}$, and starts to be a dominant decay process for nuclides with $Z > 82$. However, it can also occur for low Z nuclei, as in the case of ${}^{8}_{4}\mathrm{Be}$, signalled in Fig. 2.2 (page 13), for which $Q \simeq 91.8\ \mathrm{keV}$ [Krane, 1988].

Another process involving the loss of nucleons is spontaneous fission, which is similar to α decay, but resulting in two heavy nuclei, usually with identical mass numbers [Krane, 1988]. Due to the high number of neutrons in nuclides undergoing spontaneous fission, this process is usually accompanied with the emission of neutrons [Krane, 1988].

The two other transmutation processes involving the loss of atomic mass are the decays through emission of free neutrons or protons. In all these processes, which are unimportant for PET, the energy released in transmutation is shared between the daughter nuclei, in the form of recoil kinetic energy, and the emitted particles.

2.2.2.2 β Decay

Besides of the abovementioned transmutation processes involving a change of the number of nucleons, other transmutation process can also occur which do not involve a change in the atomic mass number *A*. These process is known as beta decay (β decay, for short), and is explained by the weak interaction[21]. The process involves nuclei undergoing transmutation along (and/or between) quadratic curves as those presented in the two left insets of Fig. 2.2 (page 13). So, two β decay modes are possible.

If a given nuclide undergoing β decay has an atomic number lower than the one corresponding to the isobar with higher binding energy per nucleon, a neutron may decay into a proton with the emission of a β^- particle (an electron) and an antineutrino ($\bar{\upsilon}$), which is an uncharged particle and, for practical proposes, can be considered as massless. This decay mode is called β^- decay, and is represented by

$$ {}^{A}_{Z}X_{N} \rightarrow {}^{A}_{Z+1}Y_{N-1} + \beta^- + \bar{\upsilon}\,. \tag{2.20} $$

[21] The *weak interaction*, along with the *strong nuclear force*, *electromagnetic interaction* and *gravitation*, constitute the four fundamental forces in nature.

If the nuclide undergoing β decay has an atomic number higher than that of the corresponding isobar with higher binding energy per nucleon, a proton decays into a neutron with the emission of a positron (e^+)[22], also known as β^+ particle, and a neutrino (υ), also uncharged and massless for practical proposes [Krane, 1988]. This decay mode is called β^+ decay, and can be represented by

$$ {}^{A}_{Z}X_N \rightarrow {}^{A}_{Z-1}Y_{N+1} + \beta^+ + \upsilon . \tag{2.21} $$

This is the decay mode with relevance for PET.

So, β^- decay can occur with radionuclides located below the stability belt represented in Fig. 2.3 (page 17), and β^+ decay can occur with nuclides located above that line. However, some radionuclides located along the stability belt can decay both by β^- and β^+ emission. This is the case of ${}^{64}_{29}\mathrm{Cu}$, which is located right in the middle of the stability belt, as depicted in Fig. 2.4.

In both cases (β^- and β^+ decay), the processes only occur if the total energy released during the decay, and given by

$$ Q = \begin{cases} \left[M\left({}^{A}_{Z}X_N\right) - M\left({}^{A}_{Z+1}Y_{N-1}\right) \right] c^2 & \beta^- \text{ decay} \\ \left[M\left({}^{A}_{Z}X_N\right) - M\left({}^{A}_{Z-1}Y_{N+1}\right) - 2m_e \right] c^2 & \beta^+ \text{ decay} \end{cases} , \tag{2.22} $$

is positive. This energy, which is quantized, is shared by all the decay products, viz., the daughter nuclide in the form of kinetic recoil energy, which can be neglected for practical proposes[23], the β particle and the neutrino[24]. As a consequence, β particles present a continuous energy spectrum, which is described by the Fermi theory of β decay and that is given by

Fig. 2.4: Decay modes of ${}^{64}_{29}\mathrm{Cu}$. (Retrieved and adapted from [Sonzogni, 2013].)

[22] The positron is the anti-matter of the electron, having a positive elementary charge.

[23] Free neutrons decay into a proton and a β^- particle with a half-life of ~10 min, the recoil energy of the proton being ~1.7% of the total energy released in the decay process. Free protons are stable particles that do not decay. [Krane, 1988]

[24] In this context, neutrino refers indistinctly to neutrino and antineutrino.

$$N(T) = g_W F(Z,T)\sqrt{T^2 + 2T m_{\beta,0} c^2}\left(T + m_{\beta,0}c^2\right)\left(T_{\max} - T\right)^2, \tag{2.23}$$

where g_W is the coupling constant of the week interaction[25], T is the kinetic energy of the emitted β particle, $T_{\max}$ is the maximum kinetic energy of the β particle, $m_{\beta,0} = 0.511\,\text{MeV}$ is the β particle rest mass, and $F(Z,T)$ is the Fermi function which accounts for the Coulomb interaction between the β particle and the daughter nucleus and is given by

$$F(Z,T) = \frac{2\pi\eta(Z,T)}{1 - e^{-2\pi\eta(Z,T)}} \qquad \text{with} \qquad \eta(Z,T) = \pm Z\alpha\frac{\left(T + m_{\beta,0}c^2\right)}{\sqrt{T^2 + 2T m_{\beta,0} c^2}} \tag{2.24}$$

with α the fine structure constant[26], Z the atomic number of the daughter nucleus, and the plus sign is to be used for β^- decay while the minus sign holds for β^+ decay [Krane, 1988; Srivastava, 2005].

Fig. 2.5 depicts the energy spectrum of β decay for $^{64}_{29}\text{Cu}$, showing the influence of the Coulomb field on β^- and β^+ particles. Table 2.2 depicts some properties of positron emitters relevant to PET and Fig. 2.6 the corresponding positron energy spectra.

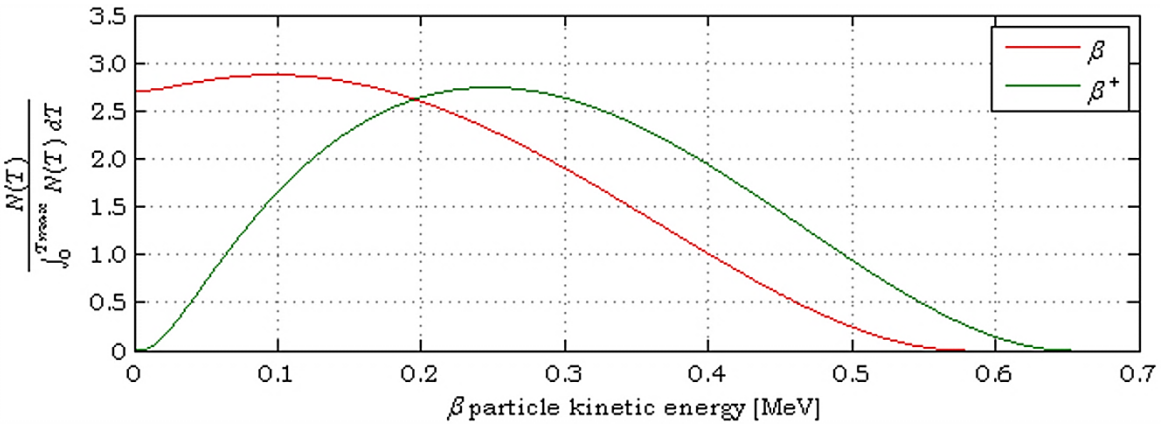

Fig. 2.5: Energy spectra of β^- and β^+ particles emitted in $^{64}_{29}\text{Cu}$ β decay, showing the effect of the Coulomb force exerted by the nucleus on β particles, shifting the kinetic energy of β^- toward lower energy values and the β^+ kinetic energy toward higher energy values.

2.2.2.3 Electron Capture

Another process through which nuclides with an excess of protons relative to the isobar with higher binding energy per nucleon can decay is by capturing an inner shell atomic electron which draws the conversion of a proton into a neutron, with the

[25] $g_W = 0.6295$ [Griffiths, 2008].
[26] $\alpha = 7.297352569\,8(24)\times10^{-3}$ [Mohr et al., 2012].

emission of a neutrino. This process, also explained by the weak interaction and which competes with β^+ decay, is called electron capture and can be represented by

$$ {}^{A}_{Z}X_N + e^- \rightarrow {}^{A}_{Z-1}Y_{N+1} + \upsilon \,. \tag{2.25} $$

Again, the process can only occurs if the energy released, and given by Eq. (2.22) for the β^+ decay, is positive. Since the nuclear mass is several orders of magnitude larger than that of the neutrino, this energy is essentially transferred to the neutrino.

After the decay by electron capture, the daughter atom will generally be in an excited state, returning to the ground state by the processes referred at the end of Section 2.1 (page 8).

TABLE 2.2: SOME PROPERTIES OF RADIONUCLIDES UNDERGOING β^+ DECAY AND USED IN PET.

Radionuclide	**Half-Life**	T_{max} **[MeV]**	**branching ratio**
$^{22}_{11}$Na	2.6 years	0.546	0.90
$^{18}_{9}$F	109.8 min	0.634	0.97
$^{11}_{6}$C	20.4 min	0.960	1.00
$^{13}_{7}$N	9.8 min	1.199	1.00
$^{15}_{8}$O	2.0 min	1.732	1.00
$^{68}_{31}$Ga	67.6 min	1.899	0.89
$^{82}_{37}$Rb	1.3 min	3.378	0.96

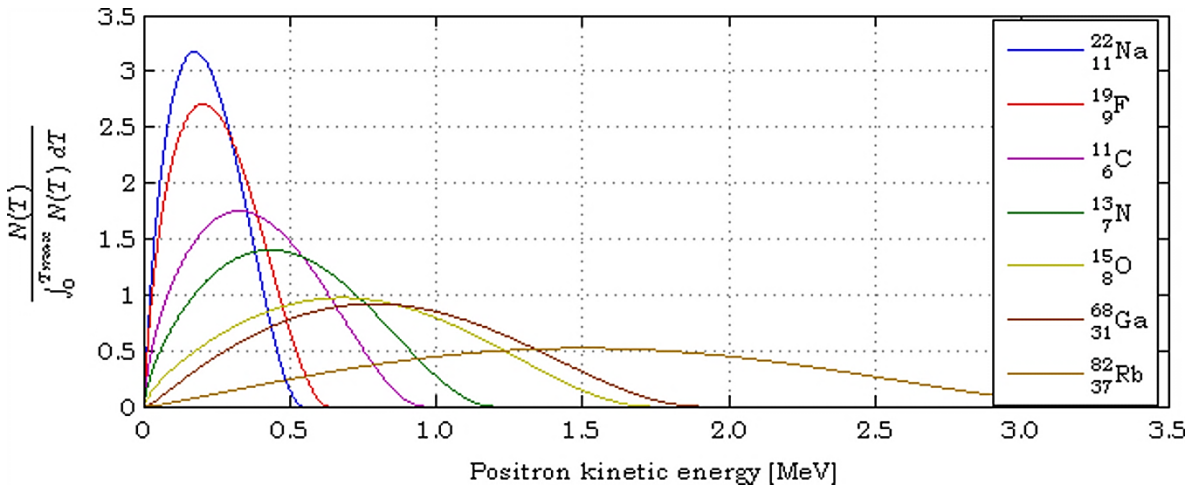

Fig. 2.6: Positron energy spectra of some radionuclides used in PET, computed by Eq. (2.23), with $F(Z,T)$ given by Eq. (2.24).

2.2.2.4 γ Decay and Internal Conversion

After a transmutation process, daughter nuclei can be in an excited state. This excess of energy is lost by transitions of nucleons from higher to lower energy levels. Two processes can then occur: the excess energy is released in the form of a detectable photon, also called a gamma-ray or gamma-photon[27] (γ-ray or γ-photon, for short), or the excess energy lost by the nucleus in returning from the excited to the ground state is directly transferred to an atomic electron which is then ejected from the atom. In this latter case, called internal conversion, the decay is followed by the emission of characteristic X-rays or Auger electrons due to atomic deexcitation. So, γ decay and internal conversion are competitive processes.

The emission of γ-photons is observed, for instance, in the decay of $^{22}_{11}\mathrm{Na}$ to $^{22}_{10}\mathrm{Ne}$ which remains in an excited state, decaying to the ground state with the emission of a γ photon with energy of ~1.275 MeV.

2.3 INTERACTION OF RADIATION WITH MATTER

If a beam of radiation (particles or photons) is fired onto a material, the beam may interact with matter modifying it in several different ways, and the matter affects the beam by scattering it, slowing it down or absorbing it. The physical processes that govern the beam interaction with matter depend on the beam nature and energy.

For radiation wavelengths longer than the atomic dimensions, interatomic distances in molecules, or interatomic planes in condensed media, radiation interacts with bulk matter as a whole, revealing its wave nature. As the wavelength of the incident radiation decreases and becomes of the order of, or shorter than, atomic dimensions, interatomic distances in molecules or interatomic planes in condensed matter, radiation interacts with individual atoms revealing its particle nature.

The energies at which radiation can be regarded as interacting with individual atoms of matter depends on the type of radiation (electromagnetic or particles), and it is not well defined. However, since atomic dimensions are of the order of one angstrom and interatomic distances in condensed matter of the order of a few angstroms, electromagnetic radiation can roughly be considered to interact with individual atoms for energies above a few keV and electrons for energies above a few hundreds of eV. These are energies well below those of interest in PET, and for practical proposes radiation interacts with individual atoms.

[27] The name gamma photon is used to distinguish the radiation origin. γ radiation has its origin in nuclear deexcitation transitions or annihilation processes, while X-rays have their origin in atomic electrons deexcitation (characteristic X-rays) or free electrons passing near the Coulomb field of the nucleus or atomic electrons (Bremsstrahlung radiation).

Interactions of charged particles, like protons, α particles or heavy ions, can occur due to collisions with the nucleus transferring some or all of the particles energy to the nucleus in the form of recoil kinetic energy, eventually causing its displacement in a solid, or allowing for nuclear reactions leading to nuclear transmutation. Charged particles can also interact with the Coulomb potential created by the nucleus with emission of electromagnetic radiation, called bremsstrahlung radiation or continuous X-rays, or yet through Coulomb interactions with atomic electrons causing excitation or ionization of multiple atoms. For this, charged particles are said to be directly ionizing radiation.

Uncharged particles, like neutrons and photons, interact with matter by direct collisions with nuclei causing their excitation and/or transmutation, or even pair production, in the case of photons, or through direct collisions with electrons causing their excitation and/or ionization. Fragments resulting from nuclear transmutation can further interact with other nuclei or with atomic electrons, and charged particles resulting from the uncharged particle interactions can also interact with matter causing further transmutation processes or atomic ionization. For this, uncharged particles are said to be indirectly ionizing radiation.

The probability of interaction of a given particle with matter is given by a quantity named *cross section* (σ) which corresponds to an effective area for collision per atom, and depends on the atomic number and particle energy (E), viz., $\sigma \equiv \sigma(Z,E)$. For charged particles, which interact with nearly all atoms of matter along their paths, $\sigma \sim 10^{-16}\,\mathrm{cm}^2/\mathrm{atom}$, while for uncharged particles, which interact relatively infrequently with matter, $\sigma \sim 10^{-24}\,\mathrm{cm}^2/\mathrm{atom}$ to $\sigma \sim 10^{-20}\,\mathrm{cm}^2/\mathrm{atom}$ [Carron, 2007]. Another unit used for atomic cross sections is the barn[28]. Cross sections can also be given in units of area per unit mass. For a single isotope with molar mass $m\left({}^{A}_{Z}X\right)\left[\mathrm{g\,mol}^{-1}\right]$ the conversion from area per atom to area per unit mass is given by

$$\sigma\left[\mathrm{cm}^2/\mathrm{g}\right] = \frac{N_A}{m\left({}^{A}_{Z}X\right)}\,\sigma\left[\mathrm{cm}^2/\mathrm{atom}\right]. \tag{2.26}$$

where N_A is the Avogadro's number[29].

Generally, three different cross sections can be defined: the *total collision cross section* (σ_c), expressing the probability of any kind of collision between the incident radiation beam and the target material, the *scattering cross section* (σ_s), representing the fraction of the incident energy which is scattered, and the *absorption cross section* (σ_a), representing the fraction of energy transferred from the incident particle to the

[28] $1\ \mathrm{barn} = 10^{-28}\ \mathrm{m}^2$

[29] $N_A = 6.02214129(27)\times 10^{23}\ \mathrm{mol}^{-1}$ [Mohr et al., 2012].

medium. The three cross sections are related by

$$\sigma_c = \sigma_s + \sigma_a . \tag{2.27}$$

The difference between these three quantities can be understood by recurring to Fig. 2.7. In the case of Fig. 2.7 (a), the detector, with a small cross sectional area, is placed far apart from the matter sample, and hence detects only those particles of the incident beam that pass through matter without interacting. In this case, the quotient between the radiation intensity[30] measured by the detector in the presence of the matter sample, *I*, and the intensity of the radiation beam without the matter sample, I_0, is a function of the total collisional cross section σ_c and the matter sample thickness *x*, viz., $I/I_0\big|_t = f(\sigma_c, x)$. As to the case of Fig. 2.7 (b), the detector virtually surrounds the matter sample and all radiation emerging from it will be detected, which includes unscattered and scattered particles, and the quotient I/I_0 is a function of both the absorption cross section σ_a and the matter sample thickness *x*, viz., $I/I_0\big|_a = f(\sigma_a, x)$. The intensity of the scattered beam can thus be obtained by making the difference between the two intensity quotients already mentioned, and can be written in functional form as $I/I_0\big|_s = f(\sigma_s, x)$.

Closely related to the cross section is the differential cross section, which can be defined as the probability of finding a scattered particle within a given solid angle Ω, and is expressed as $d\sigma/d\Omega$. The differential cross section can be computed both for the incident particle which is scattered in the collision process, and for the particles resulting from the collision process. Considering the differential cross section for a given interaction process, the corresponding total cross section can be computed from

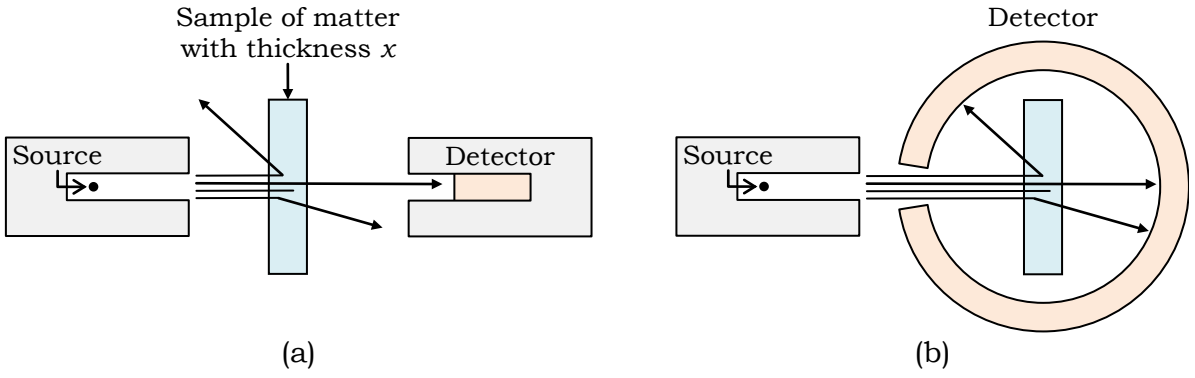

Fig. 2.7: Configuration for measuring radiation (a) attenuation and (b) absorption.

[30] The intensity of a given radiation beam is equal to the total beam energy per unit area perpendicular to the beam trajectory per unit time. In SI units $\left[\mathrm{J\,m^{-2}\,s^{-1}}\right]$. So, for a monoenergetic radiation beam containing *n* particles each with energy E_0, passing through a cross sectional area *S* of matter, the incident beam intensity is given by $I_0 = nE_0/S$, and the emerging beam intensity is given by $I = \int_0^\infty (n(E)dE)/S$, where $n(E)dE$ represents the number of particles detected with energies in the range $[E, E+dE]$.

$$\sigma = \int_{\Omega} \left(\frac{d\sigma}{d\Omega} d\Omega \right). \tag{2.28}$$

Another practical quantity closely related to the cross section and also used to describe the interaction of particles with matter is the *mean free path*, also called the *interaction length*, which is equal to the average distance travelled by a particle in matter before undergoing an interaction given by

$$\ell = \frac{1}{\sum_i \left[n_i \, \sigma(Z_i, E) \right]}, \tag{2.29}$$

where n_i is the number of atoms per unit volume of the i^{th} element with atomic number Z_i present in the matter with which the interaction occurs, and is given by

$$n_i = \frac{w_i \, N_A \, \rho}{m\left({}^{A_i}_{Z_i}X\right)}, \tag{2.30}$$

where w_i is the fraction by mass of the i^{th} element with molar mass $m\left({}^{A_i}_{Z_i}X\right)$, N_A is the Avogadro's number, and ρ is the medium bulk density. The inverse of the interaction length of a material is called the *macroscopic cross section* and have units of inverse length [Geant4 Collaboration, 2008b], which, divided by the bulk density of the material, holds the macroscopic cross section in units of area per unit mass.

2.3.1 Interaction of Photons with Matter

For the photon energies involved in PET, which go up to 511 keV, photons can interact with matter essentially in three different ways: elastic scattering, also named *coherent* scattering or Rayleigh scattering, inelastic scattering, also named incoherent scattering or Compton scattering, and photoelectric absorption.

2.3.1.1 Rayleigh Scattering

Rayleigh scattering consists in the elastic scattering of a photon by the atom as a whole, the energy of the scattered photon being equal to the energy of the incident photon, with the only change in the photon direction. So, Rayleigh scatter is simply a scattering process without energy absorption, the absorption cross section being zero, and the total collision cross section being equal to the scattering cross section. For this, Rayleigh scattering contributes only to the total mass attenuation coefficient.

The atomic differential cross section for elastic collision of a photon is conventionally written in terms of the differential collision cross section for collision from a single isolated electron, which is known as Thomson scattering cross section, and is independent of the incident photon energy, which is given by [Carron, 2007]

$$\frac{d_e\sigma_T(\theta)}{d\Omega} = \frac{1+\cos^2(\theta)}{2} r_0^2, \tag{2.31}$$

where the subscript e before σ_T denotes electron cross section $\left[\text{cm}^2/\text{electron}\right]$, θ is the angle between the incident and scattered beam directions, and r_0 is the classical electron radius[31]. Fig. 2.8 presents a polar plot of the Thomson differential cross section in barns per steradian.

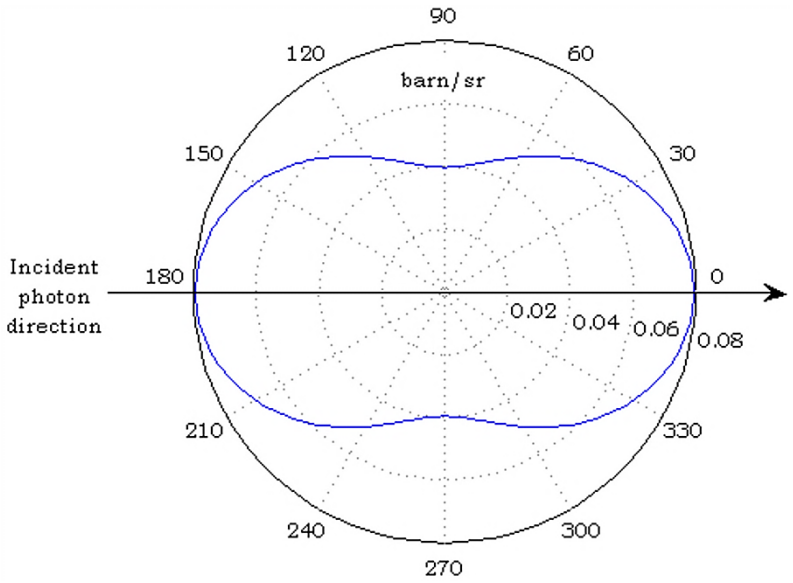

Fig. 2.8: Thomson differential cross section for a single electron in barns per steradian.

From Eq. (2.31), the electron cross section for Thomson scattering is given by [Hubbell et al., 1975; Carron, 2007]

$$_e\sigma_T = \frac{8}{3}\pi r_0^2. \tag{2.32}$$

To account for the scattering from an atom with Z electrons, the Rayleigh differential cross section is written as [Carron, 2007]

$$\frac{d_a\sigma_R}{d\Omega} = \frac{d_e\sigma_T}{d\Omega} F^2(q,Z), \tag{2.33}$$

where $F(q,Z)$ is the atomic form factor[32], which depends on the atomic number Z and the linear momentum transferred from the photon to the atom or electron and, in the Born approximation (see Section 2.3.1.3 on page 37), is given by [Carron, 2007]

$$\hbar q = 2\sin(\theta/2)\frac{h\nu_0}{m_{0,e}c^2}. \tag{2.34}$$

[31] $r_0 = 2.817940\,3267(27)$ fm [Mohr et al., 2012].

[32] Values of $F(q,Z)$ are tabulated for several atomic numbers and linear momentum transferred as in [Hubbell & Øverbø, 1979], for instance.

One of the effects of the atomic form factors is to cause a very strong distortion on the atomic differential cross section for Rayleigh scattering, which is very strongly forward peaked for energies above a few keV, depending on the atomic number [Carron, 2007].

From Eq. (2.33) the Rayleigh cross section per atom can be computed by [Hubbell & Øverbø, 1979]

$$ {}_a\sigma_R = \int_{\theta=0}^{\theta=\pi} \left[d_e\sigma_T F^2(q,Z) \right] \quad \Leftrightarrow \quad {}_a\sigma_R = \frac{3}{8}\sigma_T \int_{-1}^{1} \left\{ \left[1+\cos^2(\theta) \right] F^2(q,Z)\, d\left[\cos(\theta)\right] \right\}. \qquad (2.35) $$

The result is a cross section per atom which, for photon energies above a few keV, is proportional to the square of the atomic number and inversely proportional to the square of the incident photon energy [Attix, 1986]

$$ {}_a\sigma_R \propto \frac{Z^2}{(h\nu_0)^2} \left[\mathrm{cm}^2/\mathrm{atom} \right] \quad \text{or} \quad {}_a\sigma_R \propto \frac{Z}{(h\nu_0)^2} \left[\mathrm{cm}^2/g \right]. \qquad (2.36) $$

The cross section for Rayleigh scattering is almost never larger than 10% of the total cross section (including photoelectric and Compton cross sections) at any energy, being maximum (close to 10%) for energies in the range of 10 keV to 100 keV, depending on the atomic number [Carron, 2007]. Fig. 2.9 depicts the cross sections for Rayleigh scattering for some materials of interest in PET and the present work.

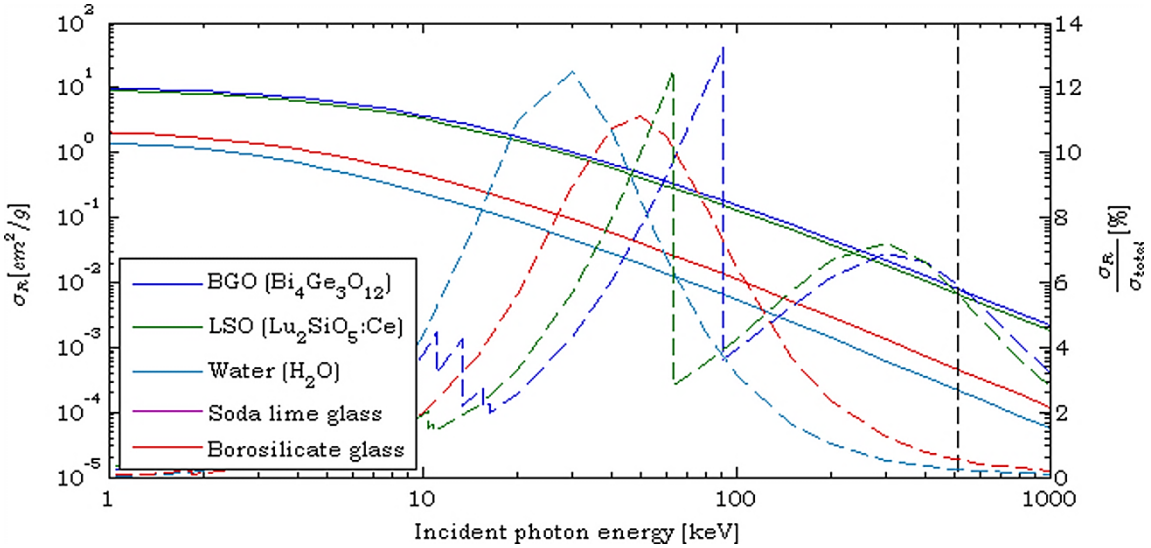

Fig. 2.9: Rayleigh scattering cross sections (solid lines - left *Y* axis) for several materials with relevance for PET and the present work. Also presented are the percentages of Rayleigh cross section relative to the total cross section (dashed lines - right *Y* axis, which is linear). The black vertical dashed line represents photon energy equal to 511 keV. Rayleigh scattering cross sections of Bismuth Germanate Oxide (BGO) and Cerium-doped Lutetium Oxyorthosilicate (LSO) are almost equal, as are the corresponding cross sections of borosilicate glass and soda lime glass. (Data retrieved from [Berger et al., 2011].)

2.3.1.2 Compton Scattering

Compton scattering is a two body interaction process consisting in the scattering of a photon by a free or bonded atomic electron. In the first case, the scattering is an elastic process since the total energy of the photon/electron system before and after the collision is conserved. In the case of bonded electrons, the process is inelastic, the difference in the total kinetic energy before and after the interaction being equal to the electron binding energy.

The probability of Compton scattering is much higher for electrons which looks like free electrons when compared with the incident photon energy, viz., with low binding energy when compared to the incident photon energy. For this, it is useful to study the case of free electrons, introducing then corrections for the case of bonded ones.

In practice, this only limits the results obtained for electrons with binding energies much lower than that of the incident photon [Evans, 1955]. Since the cases where the binding energies should be taken into account correspond to high Z materials and low photon energies, where photoelectric absorption (to be treated in Section 2.3.1.3 on page 37) dominates over Compton scattering, the errors introduced by this approach are usually disregarded in PET physics.

Fig. 2.10 depicts the general scheme of Compton interaction with a free electron considering that the electron initial velocity is zero. By applying the appropriate Lorentz transformations the analysis can be extended to the case where the electron initial velocity is different from zero [Evans, 1955].

From the conservation of linear momentum and energy, and defining $a = h\nu_0 / \left(m_{e,0} c^2\right)$, one can deduce the following relations for the energy of the scattered photon $\left(E = h\nu\right)$, the kinetic energy of the scattered electron $\left(T\right)$ and the maximum possible kinetic energy of the scattered electron $\left(T_{\max.}\right)$ for a given incident photon energy $\left(E_0 = h\nu_0\right)$, which is equal to the maximum energy that a photon can

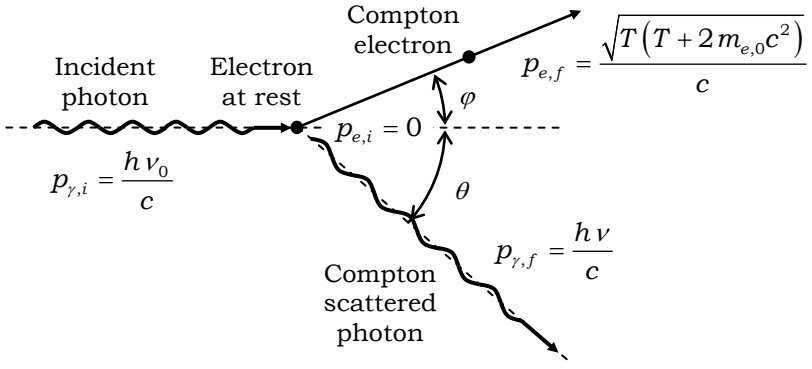

Fig. 2.10: Schematic representation of Compton interaction kinematics.

transfer to the electron and is called the Compton edge:

$$h\nu = \frac{h\nu_0}{1+a[1-\cos(\theta)]}, \tag{2.37}$$

$$T = h\nu_0 \frac{a[1-\cos(\theta)]}{1+a[1-\cos(\theta)]}, \tag{2.38}$$

$$T_{\max.} = \frac{2h\nu_0}{2+a^{-1}}. \tag{2.39}$$

Three different cross sections can be obtained from the corresponding differential cross sections [Evans, 1955]: the collision (or total) cross section $\left({}_e\sigma_c\right)$, the scattering cross section $\left({}_e\sigma_s\right)$, and the absorption cross section $\left({}_e\sigma_a\right)$.[33]

The differential collision cross sections for Compton scattering by free electrons $\left(d\,{}_e\sigma_c/d\Omega\right)$, expressed in units of $\left[\mathrm{cm}^2/\mathrm{electron}\right]$, which express the total probability of scattering incident photons in a given direction θ, is given by the Klein-Nishina cross section [Evans, 1955; Attix, 1986; Carron, 2007]

$$\frac{d_e\sigma_c}{d\Omega} = \frac{r_0^2}{2}\left\{\frac{1}{1+a[1-\cos(\theta)]}\right\}^2\left\{1+\cos^2(\theta)+\frac{a^2[1-\cos(\theta)]^2}{1+a[1-\cos(\theta)]}\right\}. \tag{2.40}$$

Fig. 2.11 depicts the differential collision cross sections for photons scattered by free electrons for several incident photon energies, showing that, photons tend to be scattered in the forward direction as the incident photon energy increases.

Multiplying $d\,{}_e\sigma_c/d\Omega$ by the ratio between the scattered and incident photon energy $\left(h\nu/h\nu_0\right)$ the differential scattering cross section for free electrons is obtained, which represents the average fraction of incident photon energy contained in the scattered photon in the θ direction. [Evans, 1955; Attix, 1986; Carron, 2007]. Making use of Eq. (2.37) and Eq. (2.40)

$$\frac{d_e\sigma_s}{d\Omega} = \frac{h\nu}{h\nu_0}\frac{d_e\sigma_c}{d\Omega} = \frac{1}{1+a[1-\cos(\theta)]}\frac{d_e\sigma_c}{d\Omega}. \tag{2.41}$$

Fig. 2.12 depicts the differential scattering cross sections for photons scattered by free electrons for several incident photon energies, showing that the differential scattering cross section is even more peaked in the forward direction than the differential collision cross section (Fig. 2.11), meaning that forward scattered photons contain a higher fraction of the incident photon energy than backward scattered ones.

[33] The subscript *e* before the cross sections means that these are computed for free unbonded electrons, rather than for atomic bonded electrons.

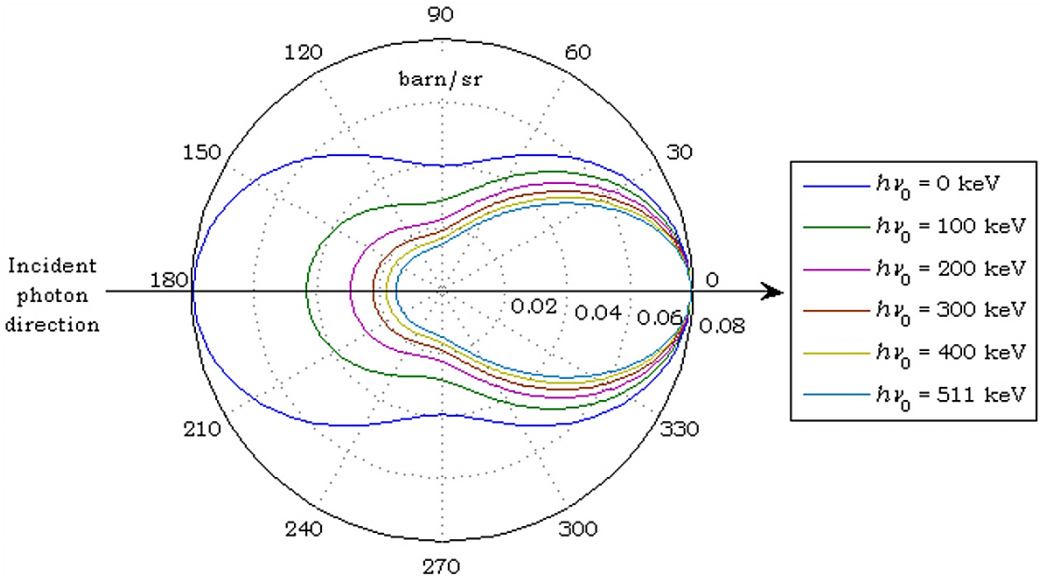

Fig. 2.11: Photon differential collision cross sections for Compton interactions with free electrons for several energies of the incident photons. The plot gives the probability of an incident photon with energy $E_0 = h\nu_0$ being scattered through a given angle θ, in units of barn per steradian. The case for which $E_0 = 0$ keV should be viewed as the limiting case of very low energies, for which the Klein-Nishina differential cross section reduces to the Thomson differential cross section given by Eq. (2.31).

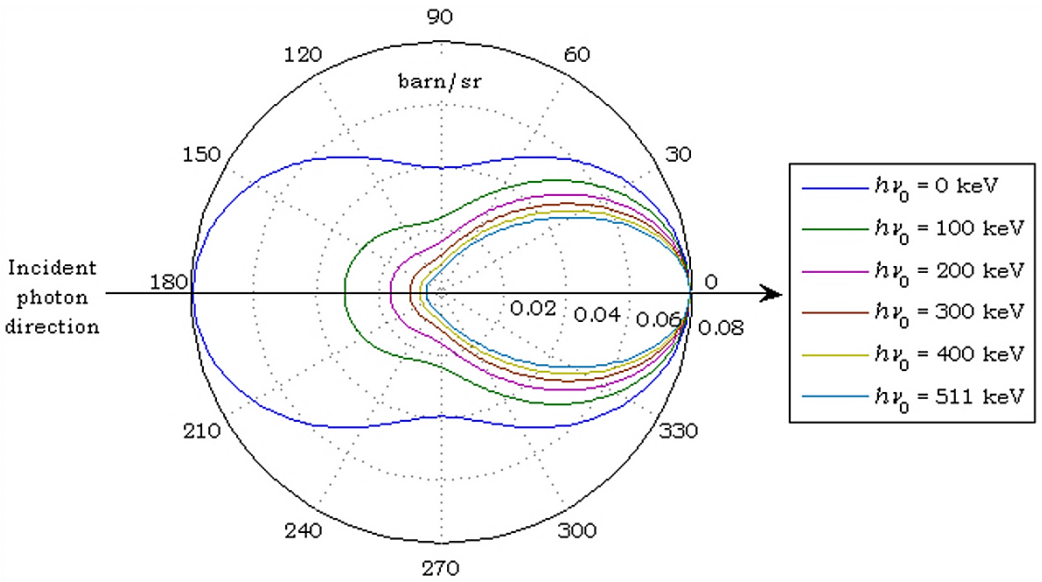

Fig. 2.12: Photon differential scattering cross sections for Compton interactions with free electrons for several energies of the incident photons. The plot gives the fraction of the incident photon energy contained in the scattered photon as a function of the photon scattering angle θ, in units of barn per steradian. The case for which $E_0 = 0$ keV should be viewed as the limiting case of very low energies, for which the differential scattering cross section is equal to the differential collision cross section, since no photon energy is transferred to the electron.

From the total and scattering differential cross sections for free electrons one can obtain the differential absorption cross section for free electrons, which represents the average fraction of incident photon energy transferred to the Compton electron. In the case of interaction with free electrons in a given material, the differential absorption cross section is related to the amount of energy absorbed by the material in a Compton interaction[34], and is given by

$$\frac{d_e\sigma_a}{d\Omega}=\frac{d_e\sigma_c}{d\Omega}-\frac{d_e\sigma_s}{d\Omega}\Leftrightarrow\frac{d_e\sigma_a}{d\Omega}=\frac{T}{h\nu_0}\frac{d_e\sigma_c}{d\Omega}\Leftrightarrow\frac{d_e\sigma_a}{d\Omega}=\frac{a[1-\cos(\theta)]}{1+a[1-\cos(\theta)]}\frac{d_e\sigma_c}{d\Omega}. \qquad (2.42)$$

Fig. 2.13 depicts the differential absorption cross sections for free electrons for several incident photon energies as a function of the scattered photon angle, showing that backward scattered photons have a higher probability of energy deposition in the material than forward scattered photons.

Photon differential cross sections can also be given in units of barn/degree, by replacing $d\Omega$ in Eq. (2.40), Eq. (2.41) and Eq. (2.42) by $d\Omega=2\pi\sin(\theta)d\theta$. Differential cross sections thus obtained are presented in Fig. 2.14, Fig. 2.15 and Fig. 2.16.

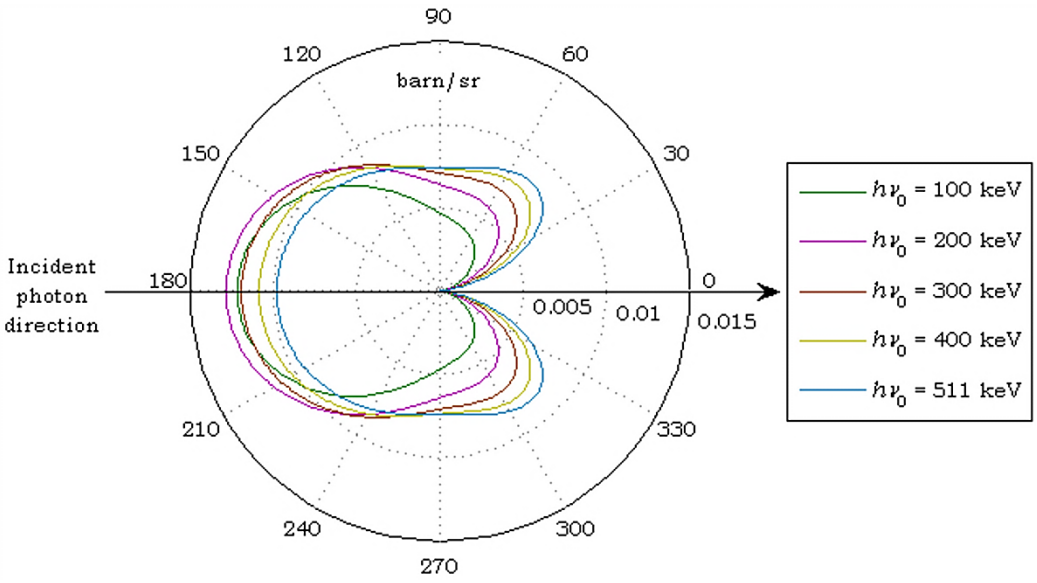

Fig. 2.13: Photon absorption scattering cross sections for Compton interactions with free electrons for several energies of the incident photons. The plot gives the probability of energy transfer to the electrons as a function of the scattered photon angle θ, in units of barn per steradian. In the limit of $E_0=0$ keV no energy is transferred to the electron.

[34] For thick materials, Compton electrons and electrons resulting from further ionizations are fully stopped in the material. In this case the Compton absorption cross section represents the probability of energy deposition in the material. For thin absorbers, low density materials (as gases), and interactions in the material surface, the electrons resulting from Compton interaction can escape the material, the energy transferred from the incident photon to the Compton electron not being totally deposited in the material, and one should instead refer to the differential energy-transfer cross section.

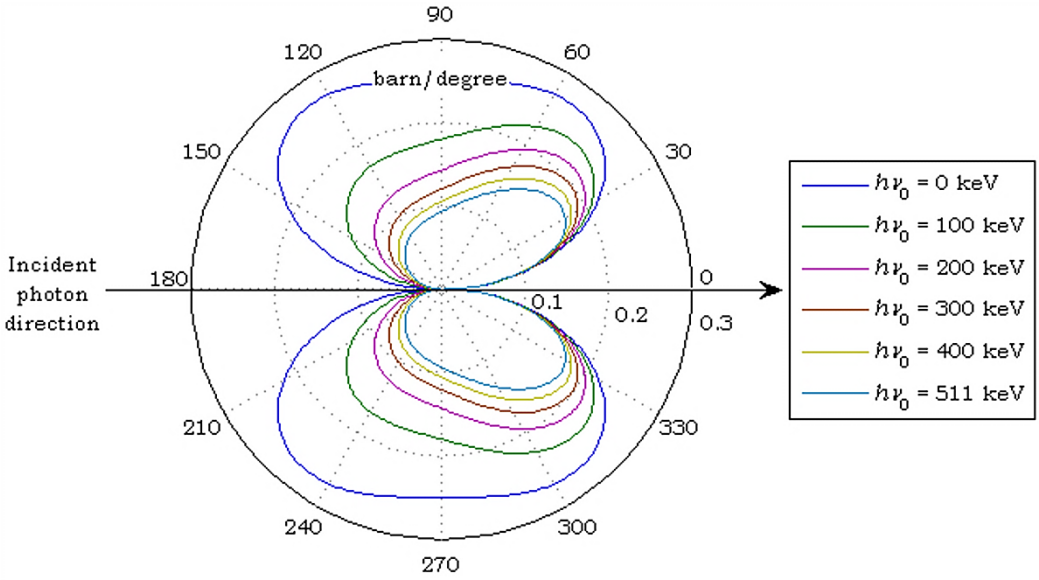

Fig. 2.14: Photon differential collision cross sections for Compton interactions with free electrons for several energies of the incident photons as a function of the scattered photon angle θ, in units of barn per degree.

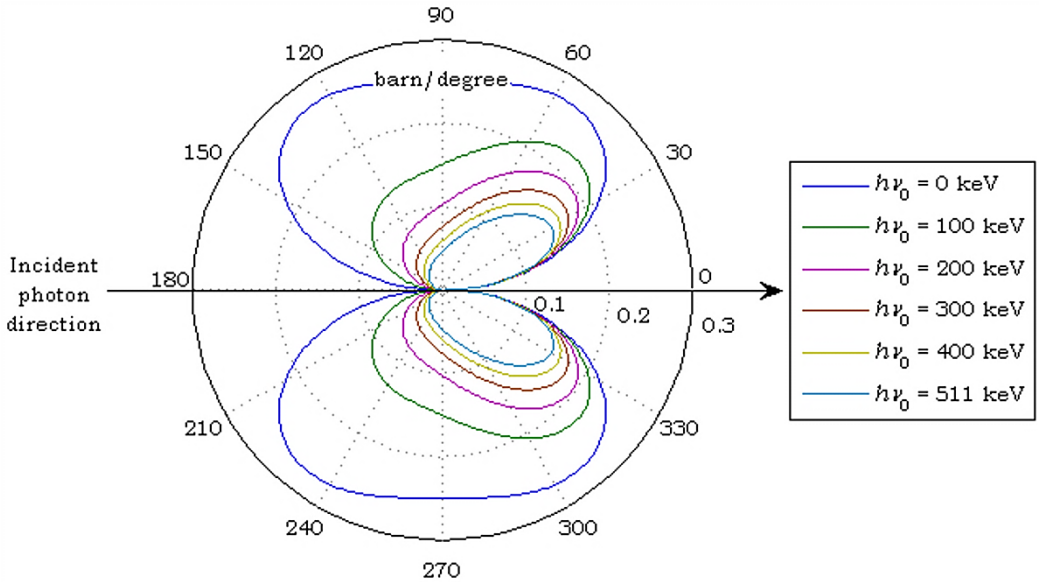

Fig. 2.15: Photon differential scattering cross sections for Compton interactions with free electrons for several energies of the incident photons as a function of the scattered photon angle θ, in units of barn per degree.

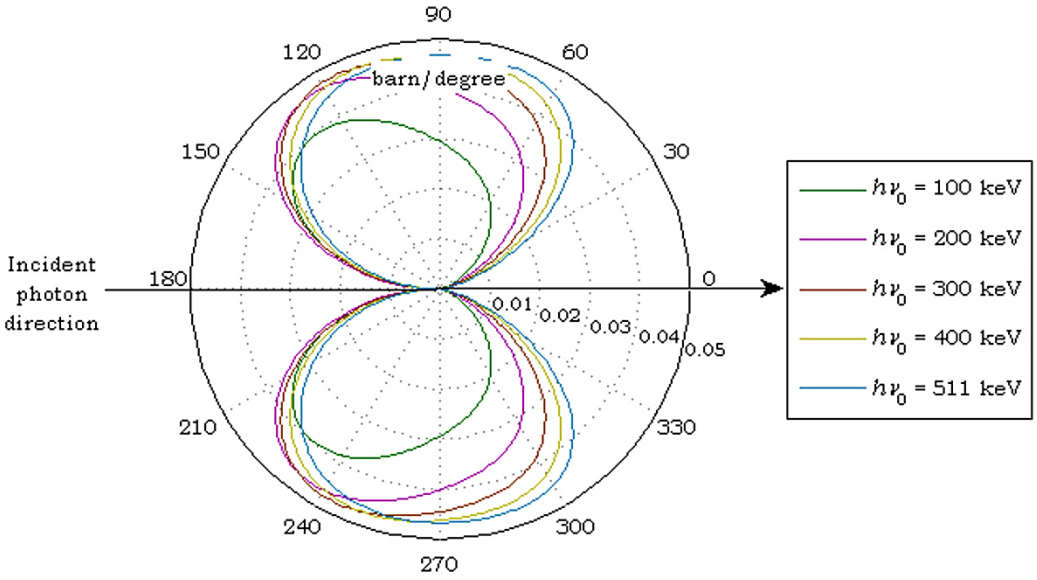

Fig. 2.16: Photon differential absorption cross sections for Compton interactions with free electrons for several energies of the incident photons as a function of the scattered photon angle θ, in units of barn per degree.

Photon cross sections for collision, scattering and absorption due to Compton interactions with free electrons can be obtained by integrating the corresponding differential cross sections through all the solid angle, which can be accomplished by replacing $d\Omega = 2\pi \sin(\theta) d\theta$ and integrating from $\theta = 0°$ to $\theta = 180°$. From Eq. (2.40), Eq. (2.41) and Eq. (2.42) the corresponding cross sections will be given by

$$ {}_e\sigma_c = 2\pi r_0^2 \left\{ \frac{1+a}{a^2}\left[\frac{2(1+a)}{1+2a} - \frac{\ln(1+2a)}{a} \right] + \frac{\ln(1+2a)}{2a} - \frac{1+3a}{(1+2a)^2} \right\}, \tag{2.43} $$

$$ {}_e\sigma_s = \pi r_0^2 \left\{ \frac{\ln(1+2a)}{a^3} + \frac{2(1+a)(2a^2-2a-1)}{a^2(1+2a)^2} + \frac{8a^2}{3(1+2a)^3} \right\}, \tag{2.44} $$

$$ {}_e\sigma_a = {}_e\sigma_c - {}_e\sigma_s . \tag{2.45} $$

Fig. 2.17 depicts the cross sections given by Eq. (2.43), (2.44) and (2.45).

Two other relevant quantities in Compton interaction when applied to radiation detection are the angular distributions of Compton electrons and their energy spectrum. The first can be given by [Evans, 1955; Attix, 1986; Carron, 2007]

$$ \frac{d_e\sigma}{d\Omega_\varphi} = \frac{(1+a)^2[1-\cos(\theta)]^2}{\cos^3(\varphi)} \frac{d_e\sigma_c}{d\Omega_\theta}, \tag{2.46} $$

where $d_e\sigma/d\Omega_\varphi$ is the differential cross section of the ejected electrons through angles $[\varphi, \varphi + d\varphi]$, $d_e\sigma_c/d\Omega_\theta$ is the photon differential collision cross section, expressed by

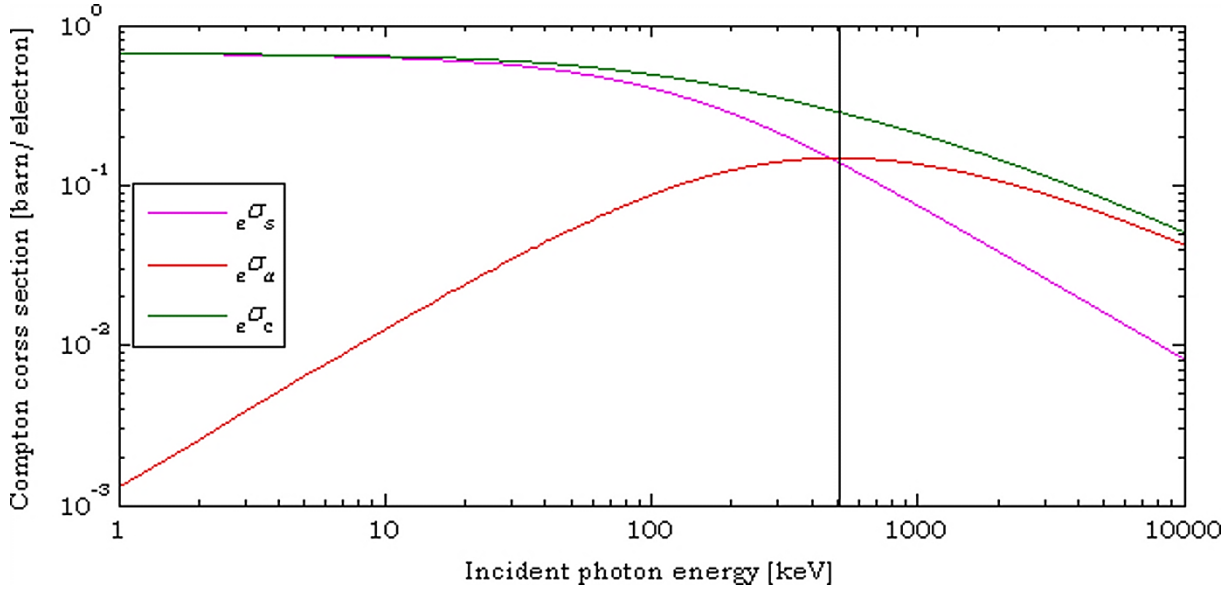

Fig. 2.17: Photon cross sections for Compton interaction with free electrons as a function of the incident photon energy. The vertical line corresponds to incident photon energy of 511 keV, for which the Compton absorption cross section for free electrons presents its maximum.

Eq. (2.40), and the relation between θ and φ can be obtained from Fig. 2.10 (page 28) and the linear momentum conservation, and is given by

$$\cot(\varphi) = (1+a)\tan\left(\frac{\theta}{2}\right) \quad \Leftrightarrow \quad \varphi = \operatorname{arccot}\left[(1+a)\tan\left(\frac{\theta}{2}\right)\right]. \tag{2.47}$$

Substituting Eq. (2.47) into Eq. (2.46), one finally obtains

$$\frac{d_e\sigma}{d\Omega_\varphi} = \frac{(1+a)^2\left[1-\cos(\theta)\right]^2}{\cos^3\left(\operatorname{arccot}\left[(1+a)\tan\left(\frac{\theta}{2}\right)\right]\right)}\frac{d_e\sigma_c}{d\Omega_\theta}. \tag{2.48}$$

Using the photon differential collision cross section one can obtain the distribution of the directions of the Compton electrons relative to the incident photon direction, expressed in units of barns/steradian, which is depicted in Fig. 2.18. Once again, the corresponding differential cross section in units of barn per degree can be obtained by noting that $d\Omega_\varphi = 2\pi\sin(\varphi)d\varphi$. Differential cross section thus obtained is presented in Fig. 2.19.

As to the energy distribution of Compton electrons, is given by [Evans, 1955]

$$\frac{d_e\sigma}{dT} = \frac{2\pi}{a^2 m_{e,0}c^2}\left[\frac{(1+a)^2 - a^2\cos^2(\varphi)}{(1+a)^2 - a(2+a)\cos^2(\varphi)}\right]^2 \frac{d_e\sigma_c}{d\Omega}, \tag{2.49}$$

where $d_e\sigma_c/d\Omega$ is given by Eq. (2.40) and φ can obtained from θ by Eq. (2.47). Fig. 2.20 depicts the Compton electron energy spectrum in units of barn per keV.

What was said is only valid for Compton interactions with free electrons. In atoms, electrons are bonded to the nucleus, and a fraction of the incident photon energy must be absorbed to overcome the electron binding energy, so that the conservation of energy leads to

$$h\nu_0 = h\nu + T + B_{shell}(Z), \tag{2.50}$$

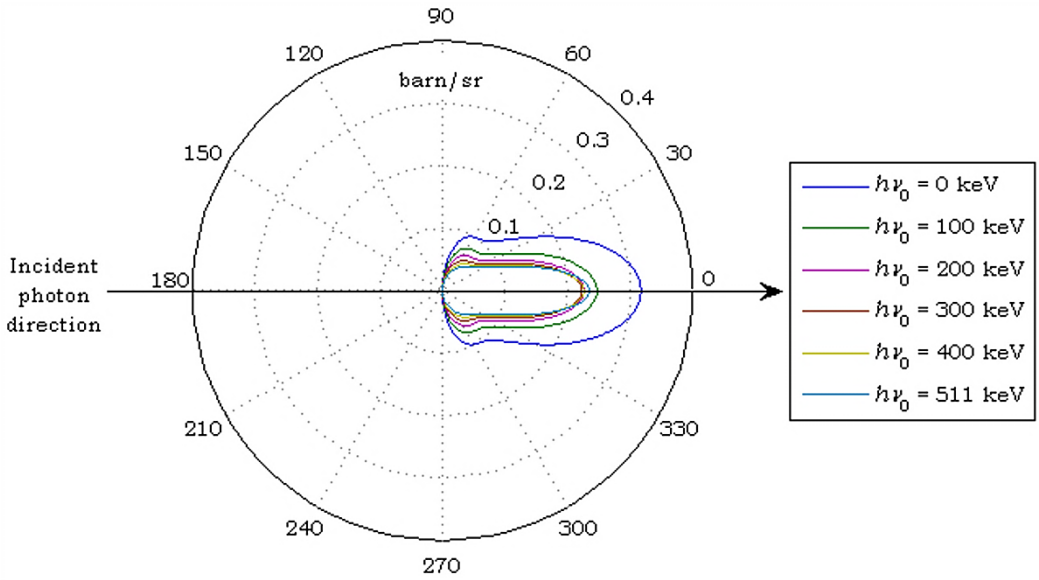

Fig. 2.18: Electron differential collision cross section for Compton interactions with free electrons for several energies of the incident photons. The plot gives the total angular distribution of Compton electrons relative to that of the incident photon as a function of the scattered electron angle φ, in units of barn per steradian.

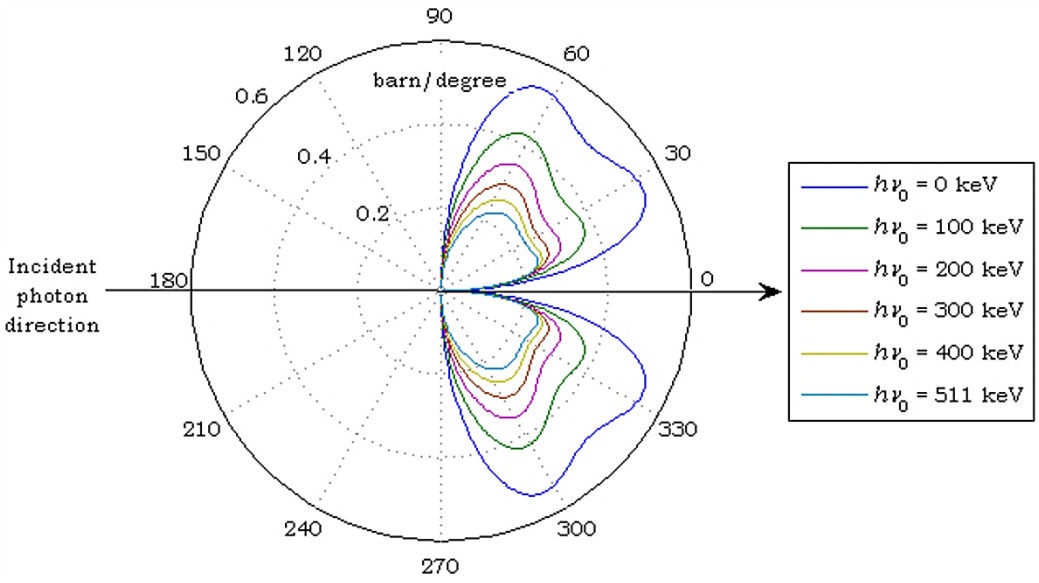

Fig. 2.19: Electron differential collision cross sections for Compton interactions with free electrons as a function of the photon scattering angle φ, in units of barn per degree.

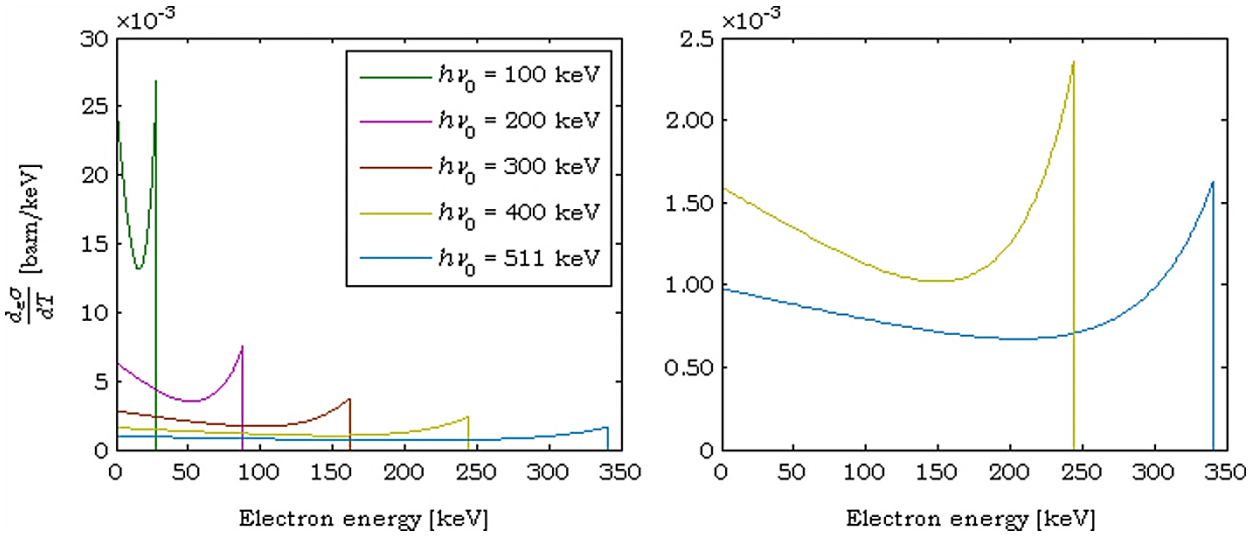

Fig. 2.20: Compton electron energy distribution for Compton interactions with free electrons.

where $B_{shell}(Z)$ is the binding energy of the electron with which the interaction occurs.

The binding energy and the atomic number of the atom with which the electron interacts is usually accounted for in the differential cross sections through the incoherent scattering function $S(q,Z)$, where $\hbar q$ is the magnitude of the momentum transferred to the recoiling electron, and is given by [Carron, 2007]

$$\hbar q = \frac{E}{c}\sqrt{1-2\alpha\cos(\theta)+\alpha^2}\ . \tag{2.51}$$

The differential cross sections are then written as [Carron, 2007]

$$\frac{d_a\sigma}{d\Omega} = \frac{d_e\sigma}{d\Omega}S(q,Z)\,, \tag{2.52}$$

where the subscript a before σ stands for atomic.

At high energy or high momentum transfer, the incoherent scattering function tends to Z, $S(q\to\infty,Z)\to Z$, and the atomic differential cross sections are simply equal to the product of the atomic number by the free electron cross sections [Carron, 2007]. So, in this limit, electron binding energies have no influence on the atomic cross sections [Carron, 2007]. As to the kinematics of Compton scattering, and considering high energy or high momentum transfer, the angular distribution of Compton photons is essentially the same as that obtained for free electron, except for very small angles near zero, for which the atomic differential collision cross section is equal to zero. This means that, even at high energy or high linear momentum transfer, photons cannot be scattered in the forward direction due to electron binding energies, and the differential collision cross section depicted in Fig. 2.11 (page 30) presents a

lack of photons in the forward direction [Carron, 2007]. This lack of photons in the forward direction is even more marked for low energy or low momentum transfer. However, the differential collision cross section for electron ejection in the forward directions does not vanish at very small angles near zero [Carron, 2007].

Fig. 2.21 depicts the total collision cross sections for Compton scattering for some materials of interest in PET, and the present work

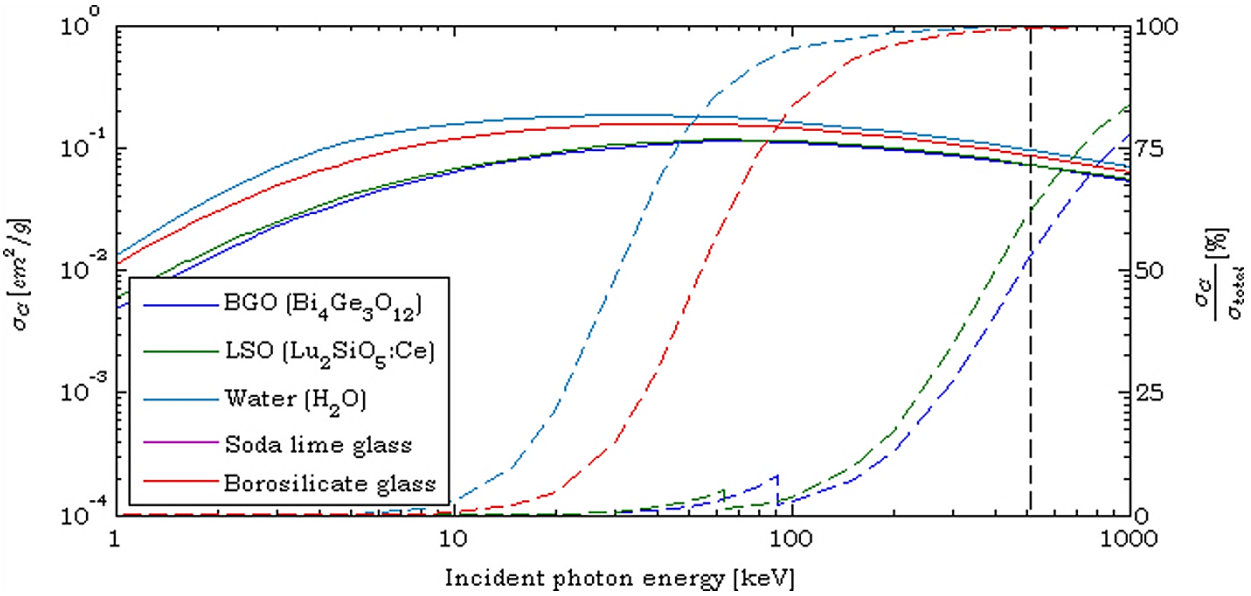

Fig. 2.21: Compton collisional cross sections (solid lines to be read at the left *Y* axis) for several materials with relevance for PET and the present work. Also presented are the percentages of Compton collision cross sections relative to the total cross section (dashed lines to be read at the right *Y* scale, which is linear). The black vertical dashed line represents photon energy equal to 511 keV. Compton collision cross sections for borosilicate glass and soda lime glass are superimposed. (Data retrieved from [Berger et al., 2011].)

2.3.1.3 Photoelectric Absorption

Free electrons cannot entirely absorb photons, but bonded electrons can. The process by which a bonded electron absorbs the entire energy of the incident photon being then ejected from the atom is named photoelectric absorption. If the incident photon energy is $E_0 = h\nu_0$ and the electron binding energy is equal to $B_{shell}(Z)$, then the electron will be ejected from the atom with kinetic energy given by

$$T_e = h\nu_0 - B_{shell}(Z). \tag{2.53}$$

So, for photoelectric absorption to occur the energy of the incident photon has to be equal to, or higher than, the electron binding energy, but not so higher that the atomic electron seems to be essentially free, in which case Compton interaction is

favoured over photoelectric absorption. On the other hand, with the increase of the atomic number, electron binding energies also increase, at least for those electrons of the inner shells, particularly those of the *K* shell. So, the cross section for photoelectric absorption must decrease with increasing energy, while increasing with the atomic number. Besides, since *K* shell electrons are those with the highest binding energy, the probability of occurrence of photoelectric absorption with *K* shell electrons is larger than that for electrons from any other shells. As a rule of thumb, the total cross section for photoelectric absorption, σ_{ph}, is about 5/4 of the cross section for photoelectric absorption for *K* shell electrons, $\sigma_{ph,K}$, for which some theoretical formulas of the photoelectric cross sections, valid for limited ranges of the incident photon energies and atomic numbers, were derived. [Evans, 1955; Carron, 2007]

Since the interaction probability depends on the specific binding energies of each atomic shell, there is no exact expression for the photoelectric absorption cross sections, as in the case of Rayleigh scattering and Compton effect, for which the atomic cross sections can be given, in a first approximation, by the product of the free electron cross section by the atomic number, with further corrections accomplished via the atomic form factor for the Rayleigh scattering, or the incoherent scattering function for the Compton effect. Though, several approximate expressions have been derived for interaction with *K* shell electrons, different incident photon energies and atomic numbers of the absorber. In one way or the other, all of them make use of the assumption that the electron binding energy is far less than the incident photon energy. This condition can be expressed mathematically by [Heitler, 2010]

$$T_e >> B_{shell}(Z) \quad \Leftrightarrow \quad \frac{Z e^2}{\hbar \nu_0} << 1 . \tag{2.54}$$

which implies that the obtained results are valid only for incident photon energies far greater than the electron binding energies.

For incident photon energies such that $h\nu_0 << m_{0,e}c^2$ and low atomic numbers, $\alpha Z << 1$ where α is the fine structure constant, the cross section for photoelectric absorption by the *K* shell electrons will be given by [Carron, 2007; Heitler, 2010]

$$\sigma_{ph,K} = 4\sqrt{2}\,\alpha^4 Z^5 \left(\frac{m_{0,e}c^2}{h\nu_0} \right)^{7/2} {}_e\sigma_T . \tag{2.55}$$

where ${}_e\sigma_T$ is the Thomson cross section for free electrons given by Eq. (2.32). The conditions imposed for the validity of Eq. (2.55) are known as the Born approximation. Despite of the condition $h\nu_0 << m_{0,e}c^2$ the error committed in using Eq. (2.55) is not meaningful for incident photon energies up to $m_{0,e}c^2/2$ [Heitler, 2010].

In the neighbourhood of the *K* absorption edge, the Born approximation is no longer valid as $h\nu_0 \simeq B_{K\ shell}(Z)$. In this case, the photoelectric cross section given by Eq. (2.55) must be multiplied by the factor [Heitler, 2010]

$$f(\xi) = 2\pi \sqrt{\frac{B_{K\ shell}}{h\nu_0}} \frac{e^{-4\xi \operatorname{arccot}(\xi)}}{1-e^{-2\pi\xi}} \qquad \text{with} \qquad \xi = \frac{Z e^2}{h\nu_0}. \tag{2.56}$$

For incident photon energies such that $h\nu_0 \sim m_{0,e}c^2$ or $h\nu_0 > m_{0,e}c^2$, the Born approximation no longer holds, and the photoelectric absorption cross section for light elements $(\alpha Z << 1)$ is approximately given by [Heitler, 2010]

$$\sigma_{ph,K} = \frac{3}{2}\alpha^4 \left(Z\frac{m_{0,e}c^2}{h\nu_0}\right)^5 {}_e\sigma_T \left(\gamma^2-1\right)^{3/2} \left\{\frac{4}{3} + \frac{\gamma(\gamma-2)}{\gamma+1}\left[1 - \frac{1}{2\gamma\sqrt{\gamma^2-1}}\log\left(\frac{\gamma+\sqrt{\gamma^2-1}}{\gamma-\sqrt{\gamma^2-1}}\right)\right]\right\}, \tag{2.57}$$

which, for the case of light elements and $h\nu_0 >> m_{0,e}c^2$ Eq. (2.57) reduces to [Carron, 2007; Heitler, 2010]

$$\sigma_{ph,K} = \frac{3}{2}\alpha^4 Z^5 \frac{m_{0,e}c^2}{h\nu_0} {}_e\sigma_T. \tag{2.58}$$

A more general expression for high energy photons, which is a good approximation for all values of *Z*, is given by [Heitler, 2010]

$$\sigma_{ph,K} = \frac{3}{2}\alpha^4 Z^5 \frac{m_{0,e}c^2}{h\nu_0} {}_e\sigma_T\, e^{-\pi\alpha Z + 2(\alpha Z)^2\left[1-\log(\alpha Z)\right]}. \tag{2.59}$$

Though the inexistence of a single expression which accounts for the photoelectric absorption cross section for all elements and energies, a useful approximation which allows acquainting for the general shape of the photoelectric cross section is given by [Evans, 1955; Attix, 1986]

$$\sigma_{ph} \propto \frac{Z^n}{(h\nu_0)^m}, \tag{2.60}$$

where *n* gradually increases from ~ 4 for $h\nu_0 = 0.1\,\text{MeV}$ to ~ 4.6 for $h\nu_0 = 3\,\text{MeV}$ [Evans, 1955; Attix, 1986], and *m* gradually decreases from ~ 3 for $h\nu_0 = 0.1\,\text{MeV}$ to ~ 1 for $h\nu_0 = 5\,\text{MeV}$ [Attix, 1986].

Eq. (2.60) holds for energies given in MeV, giving a cross section that, for a given atomic number, smoothly decreases with increasing incident photon energy. This is in accordance with what was said previously, namely, as the incident photon energy increases the ratio between electron binding energy and the incident photon energy

decreases toward zero, so that the electrons become essentially free when compared to the incident photon energy, and Compton effect is then favoured over photoelectric absorption. Since photoelectric absorption can only occur if the incident photon energy is larger than the electron binding energy, the continuous and smooth decrease in photoelectric cross section is strictly true for incident photon energies comprised between two consecutive atomic shells binding energies. As soon as the incident photon energy reaches the binding energy of a given shell, also named shell edge energy, photoelectric absorption can then take place with electrons bonded to that shell, and photoelectric absorption cross section rises abruptly.

More precise equations for the photoelectric absorption cross section used in particle transport simulation codes are usually given as functions fitted to tabulated experimental data, and account also for the electron binding energies. For instance, GEANT4 uses an inverse power series given by [Geant4 Collaboration, 2008b]

$$\sigma_{ph}(Z,h\nu_0)=\frac{a(Z,h\nu_0)}{h\nu_0}+\frac{b(Z,h\nu_0)}{(h\nu_0)^2}+\frac{c(Z,h\nu_0)}{(h\nu_0)^3}+\frac{d(Z,h\nu_0)}{(h\nu_0)^4}, \tag{2.61}$$

where a, b, c and d are tabulated coefficients based on experimental data.

Fig. 2.22 depicts the cross sections for photoelectric absorption for some materials of interest in PET and the present work.

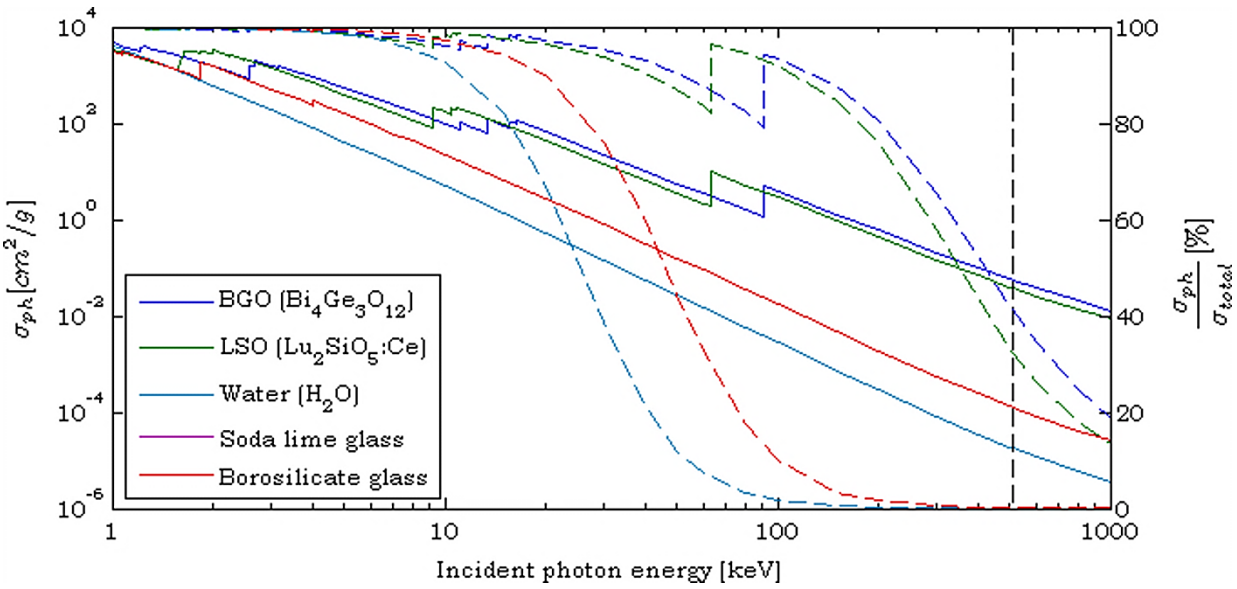

Fig. 2.22: Photoelectric absorption cross sections (solid lines to be read at the left Y axis) for several materials with relevance for PET and the present work. Also presented are the percentages of photoelectric absorption cross sections relative to the total cross section (dashed lines to be read at the right Y axis). The black vertical dashed line represents photon energy of 511 keV. Photoelectric absorption cross sections for borosilicate glass and soda lime glass are superimposed. (Data retrieved from [Berger et al., 2011].)

Photoelectrons resulting from the interaction of low energy photons $(h\nu_0 \leq 10\,\text{keV})$ tend to be ejected perpendicularly to the incident photon direction, while the direction of photoelectron emission for photoelectrons resulting from the interaction of higher energy photons $(h\nu_0 \geq 100\,\text{keV})$ is significantly shifted forward, but cannot occur in the exact direction of the incident photon [Carron, 2007]. For relativistic photoelectrons, the differential cross section for the photoelectrons angular distribution is given by the Sauter-Gavrila distribution for the *K* shell, which is only valid in zero order approximation in relation to αZ, and is given by [Carron, 2007]

$$\frac{d\sigma_{ph,K}}{d\Omega} \simeq \frac{\sin^2(\theta)}{\left[1-\beta\cos(\theta)\right]^4}\left\{\frac{1}{\gamma}+\frac{1}{2}(\gamma-1)(\gamma-2)\left[1-\beta\cos(\theta)\right]\right\}, \tag{2.62}$$

where β and γ are given by Eq. (2.3) and can be written as

$$\begin{aligned}\gamma &= \frac{T+m_{0,e}c^2}{m_{0,e}c^2}\\ \beta &= \frac{\sqrt{T^2+2m_{0,e}c^2T}}{T+m_0c^2}\end{aligned}. \tag{2.63}$$

In spite of the limited validity, the Sauter-Gavrila is used, for instance, in GEANT4 standard energy physics photoelectric model, to compute the photoelectron angular distribution [Geant4 Collaboration, 2008b]. Fig. 2.23 depicts the differential cross section for the angular distribution of photoelectrons, neglecting the electron binding energy, viz., assuming that in Eq. (2.53) $B_{shell}(Z)=0$, which is only approximately valid for low binding energies.

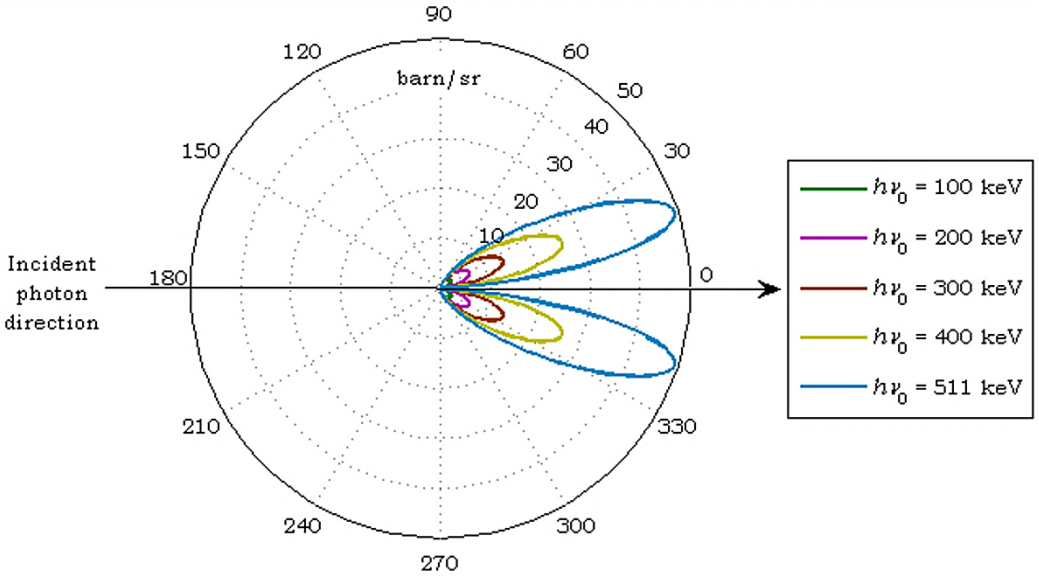

Fig. 2.23: Photoelectron differential absorption cross sections as a function of the electron scattering angle, in units of barn per steradian, assuming a negligible electron binding energy.

Upon photoelectric absorption, the atom is in an excited state and will return to the ground state by the processes mentioned in the end of Section 2.1 (page 8), namely the emission of characteristic X-rays or Auger electrons, which are low energy electrons, absorbed near their emission sites. The process of X-ray emission after photoabsorption is called fluorescence, and plays an important role in energy deposition. Since photoelectric absorption is far more probable to occur with electrons from the *K* shell than with electrons of any other shell (80% against 20%) and since the electronic deexcitation transitions will occur from less tightly bound shells, the energy of the fluorescence photon will be lower than the *K* shell energy edge, and the photoelectric absorption cross section of the fluorescence will abruptly decrease relative to that of the incident photon. As a consequence, the mean free path of the fluorescence photon will be larger than that of the incident photon, and will eventually deposit the energy far from the site of emission.

2.3.1.4 Attenuation and Absorption of a Photon Beam

Due to the fact that photons are scattered and absorbed in a single event, a well-collimated beam of photons presents an exponential attenuation when passing through matter [Evans, 1955]. This exponential attenuation, measured in experimental setups similar to that presented in Fig. 2.7 (a) (page 24), is given by

$$I = I_0 \, \mathrm{e}^{-\frac{x}{\ell}} \quad \Leftrightarrow \quad I = I_0 \, \mathrm{e}^{-\sigma x}, \tag{2.64}$$

where I_0 is the incident beam intensity, I is the emerging beam intensity, x is the material thickness traversed by the photon beam, ℓ is the *linear attenuation length*, and $\sigma = \ell^{-1}$ is the *macroscopic attenuation cross section*. Since ℓ, as well as σ, depends on the bulk density of the matter traversed by the incident beam, the intensity of the emerging photon beam will also depend on the bulk density of the matter it traverses. However, this dependency can be removed by dividing the macroscopic cross section by the bulk density of matter [Evans, 1955]. The coefficient thus obtained is named *mass attenuation coefficient*, which has the dimensions of a cross section expressed in units of area per unit mass, and is of more fundamental value than the linear attenuation coefficient [Evans, 1955], and is equal to the cross section in units of area per unit mass of the target material:

$$\mu = \frac{\sigma}{\rho} = \frac{1}{\rho \ell}. \tag{2.65}$$

Using the mass attenuation coefficient, Eq. (2.64) then becomes

$$I = I_0 \, \mathrm{e}^{-\mu \rho x} \quad \Leftrightarrow \quad I = I_0 \, \mathrm{e}^{-\mu X}, \tag{2.66}$$

where $X = \rho x$ is called the *mass thickness*.

Since photons can interact by more than one process when passing through matter, the total mass attenuation coefficient must be used, which is equal to the sum of the mass attenuation coefficients of all interaction processes that a photon can undergo when striking a target of a given material. For the energies with relevance in PET these are the interactions seen in the previous sections, and the total mass attenuation coefficient is then given by

$$\mu_{att.} = \mu_{pe} + \mu_{C,c} + \mu_R \qquad \Leftrightarrow \qquad \mu_{att.} = \sigma_{pe} + {}_a\sigma_{C,c} + {}_a\sigma_R \,, \tag{2.67}$$

where μ_{pe}, $\mu_{C,c}$ and μ_R are the total mass attenuation coefficients for photoelectric absorption, Compton scattering and Rayleigh scattering, and σ_{pe}, ${}_a\sigma_{C,c}$ and ${}_a\sigma_R$ are the total atomic cross sections in units of $\left[\mathrm{cm}^2/\mathrm{g}\right]$. In particular, $\mu_{C,c}$ and ${}_a\sigma_{C,c}$ represent the total collision cross section for Compton effect, which includes both scattering and absorption.[35]

Similarly, one can define the corresponding total absorption coefficients by considering only those processes that lead to energy absorption. In particular, the total mass absorption coefficient will be given by

$$\mu_{abs.} = \mu_{pe} + \mu_{C,a} \qquad \Leftrightarrow \qquad \mu_{abs.} = \sigma_{pe} + {}_a\sigma_{C,a} \,, \tag{2.68}$$

where $\mu_{C,a}$ and ${}_a\sigma_{C,a}$ represent, respectively, the mass absorption coefficient and the Compton absorption cross section given by Eq. (2.45). Absorption of electromagnetic radiation also follows the exponential law given by Eq. (2.66) [Evans, 1955].

Fig. 2.24 depicts the cross sections for some materials with relevance to PET and the present work and Fig. 2.25 depicts a plot of the relative importance of photoelectric absorption, Compton scattering and pair production[36] with the atomic number of target materials and photon energy.

2.3.2 Interaction of Electrons and Positron with Matter

Unlike neutral particles, which interact infrequently with individual atoms of the target material, charged particles interact with nearly all atoms along their path, losing some energy in each interaction [Carron, 2007]. Besides, heavy charged

[35] The mass attenuation coefficient for pair production was ignored, since for pair production to occur the energy of the incident photon has to be equal to twice the rest electron mass, viz., it has to be equal to at least 1.022 MeV, while the energies relevant to PET range up to 511 keV.

[36] Pair production consists in an interaction of an incident photon with the Coulomb field of the nucleus resulting in the conversion of the incident photon into an electron/positron pair. The effect has not been mentioned because it has no relevance for PET, being energetically possible only for photon energies above $2m_{e,0}c^2 = 1.022$ MeV.

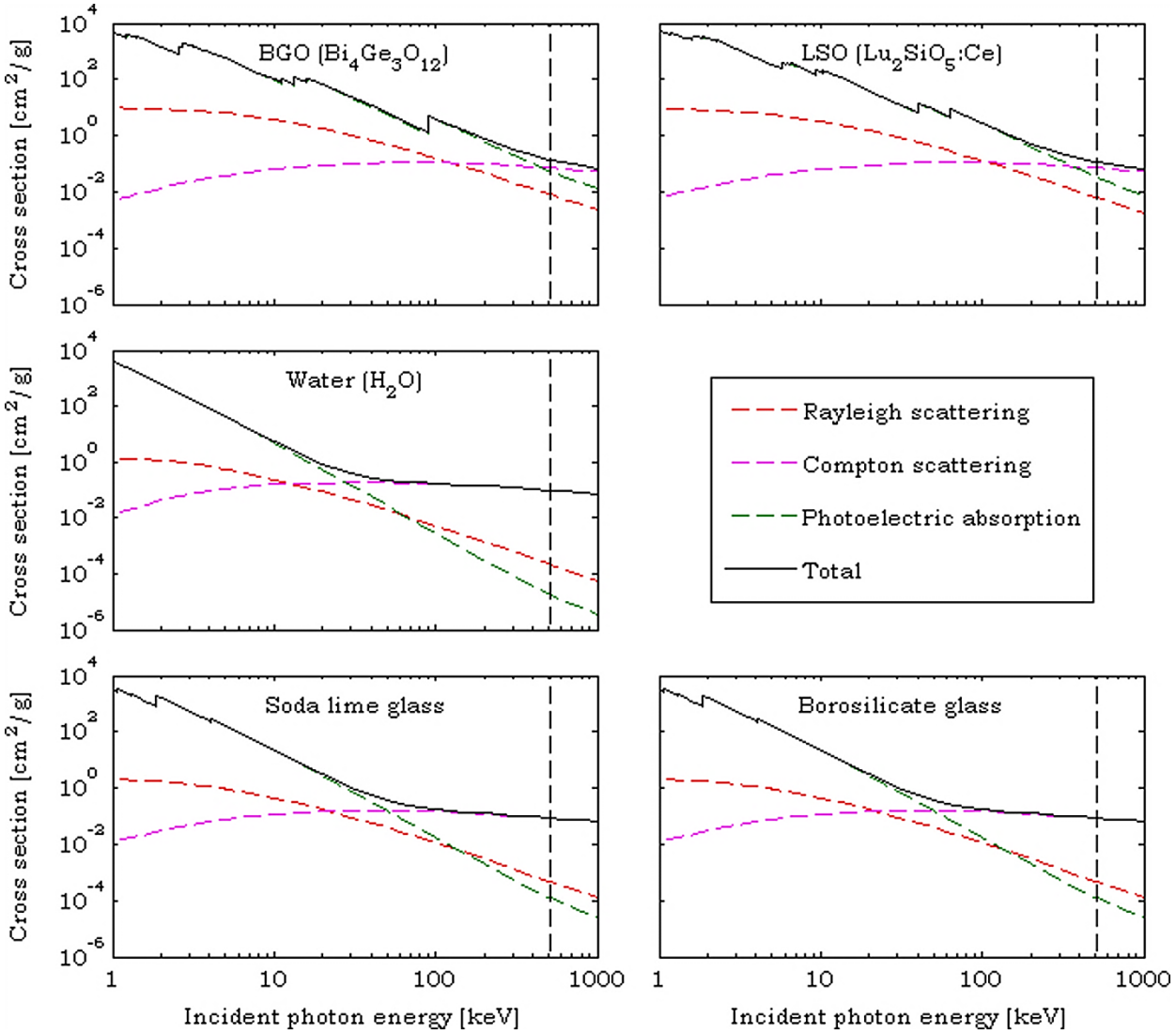

Fig. 2.24: Cross sections for several materials with relevance for PET and the present work. The black vertical dashed line represents photon energy equal to 511 keV.
(Data retrieved from [Berger et al., 2011].)

particles and relativistic electrons are only slightly deflected in each interaction [Carron, 2007]. So, when studying the interaction of charged particles with matter, the loss of particles from the incident beam is of little concern, as is the mean free path between successive collisions, the relevant parameters being rather the rate of energy loss and the total range of the particles along their initial directions [Carron, 2007]. Since protons, alpha particles and heavier charged ions are of no concern for PET physics[37], in what follows attention will be given only to the interaction of electrons and positrons with matter, the latter essentially focused on annihilation radiation.

The processes through which an electron can undergo interaction with matter

[37] With the exception in the production of positron emitters, which is not a subject of the present work.

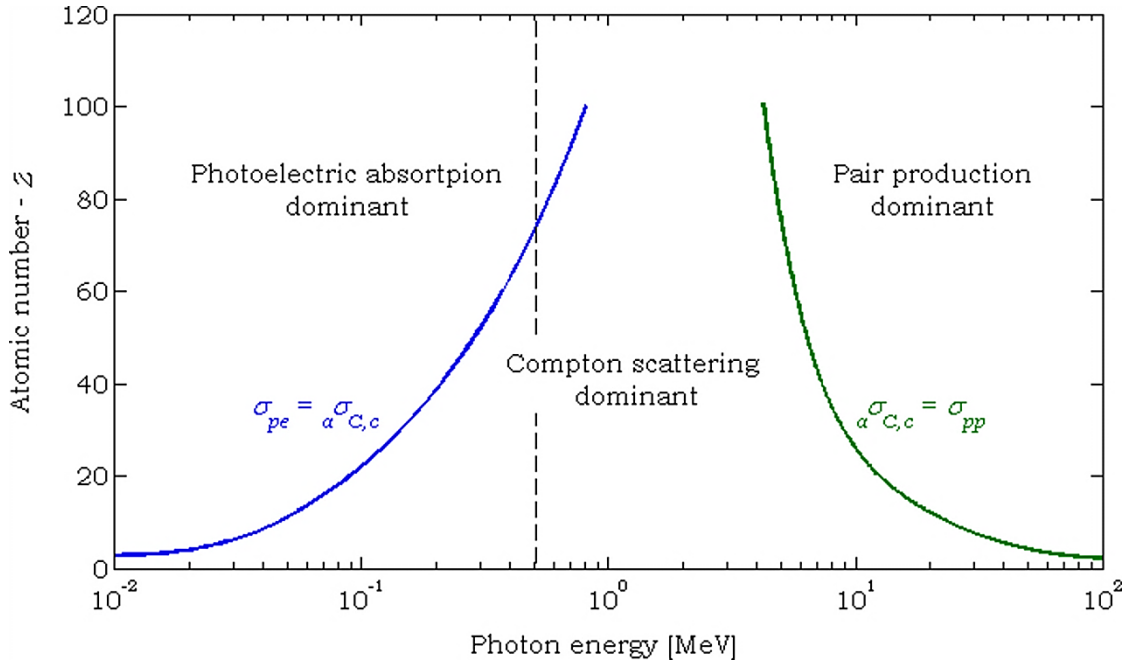

Fig. 2.25: Regions of dominant photon interaction processes as a function of atomic number and incident photon energy. The blue and green lines represent the equal probability lines for the photon interaction processes they separate. The black vertical dashed line represents photon energy of 511 keV. (Data retrieved from [Knoll, 2010] by using the *grabit* routine [Doke, 2007] developed for Matlab.)

are: (a) inelastic scattering with atomic electrons leaving the atom in an excited state or ionizing it [Evans, 1955; Carron, 2007], or by emitting a photon [Carron, 2007], (b) inelastic collisions with a nucleus with emission of a photon [Evans, 1955; Carron, 2007] or raising the nucleus to an excited state [Evans, 1955], (c) elastic scattering with atomic electrons [Evans, 1955] and (d) elastic scattering with the nucleus [Evans, 1955]. In all of the aforementioned interaction processes the incident electron is deflected from its initial trajectory [Evans, 1955; Carron, 2007].

2.3.2.1 Inelastic Scattering

Inelastic scattering processes are the main source of energy loss of electrons when passing through matter, the energy loss being described by the *stopping power* (dE/ds) which is the energy lost by electrons in the medium per unit path length and is usually given in units of $\mathrm{MeV\,cm^2\,g^{-1}}$ or $\mathrm{MeV\,cm^{-1}}$ [Carron, 2007]. Since the energy loss is a statistical process, the stopping power is usually described by two quantities: the *mean stopping power*, representing the average energy lost by electrons when passing through a medium, and the spread of the energy loss about the mean value which is called *straggling* [Carron, 2007]. So, the *stopping power* should be understood as the *mean stopping power*.

Two different stopping powers quantities can be defined: the *collisional stopping power*, due to inelastic collision leading to excitation and ionization, and the *radiative stopping power* due to inelastic collisions leading to the emission of bremsstrahlung radiation [Carron, 2007]. The *total stopping power* is then the sum of the collisional and radiative stopping powers [Evans, 1955; Carron, 2007]

$$\left(\frac{dE}{ds}\right)_{total} = \left(\frac{dE}{ds}\right)_{col} + \left(\frac{dE}{ds}\right)_{rad}. \tag{2.69}$$

For any charged particle with rest mass M_0 and kinetic energy T (expressed in MeV), traversing a medium with atomic number Z, the ratio of radiative to collisional stopping powers can be roughly given by [Evans, 1955]

$$\frac{(dE/ds)_{rad}}{(dE/ds)_{col}} \simeq \left(\frac{m_{e,0}}{M_0}\right)^2 \frac{Z\,T}{1400\,m_{0,e}\,c^2}, \tag{2.70}$$

which, for electrons $\left(M_0 = m_{e,0}\right)$ reduces to

$$\frac{(dE/ds)_{rad}}{(dE/ds)_{col}} \simeq \frac{Z\,T}{1400\,m_{0,e}\,c^2}, \tag{2.71}$$

and, finally, the fractions of energy loss due to collisional and radiative processes to the total energy loss can thus be roughly given by

$$f_{col}(Z,T) = \frac{(dE/ds)_{col}}{(dE/ds)_{tot}} \simeq \frac{1400\,m_{0,e}\,c^2}{1400\,m_{0,e}\,c^2 + Z\,T}, \tag{2.72}$$

$$f_{rad}(Z,T) = \frac{(dE/ds)_{rad}}{(dE/ds)_{tot}} \simeq \frac{Z\,T}{1400\,m_{0,e}\,c^2 + Z\,T}. \tag{2.73}$$

Fig. 2.26 depicts Eq. (2.72) and Eq. (2.73) for several values of Z as a function of the kinetic energy of the incident electron. It can be readily seen that for 511 keV photons interacting mainly by Compton scattering (the maximum energy of Compton electrons in this case is less than 350 keV – Fig. 2.20 on page 36), almost all energy lost by electrons is due to collisions.

The mean collisional stopping power of electrons with kinetic energy T traversing a medium with an atomic density $\rho_N\,[atoms/unit\ volume]$ for which the mean excitation energy[38] is equal to I, is given by the Bethe formula [Carron, 2007]

$$-\left(\frac{dE}{ds}\right)_c = \frac{2\pi\,\rho_N\,Z\,e^4}{m\,v^2}\left\{\ln\left[\frac{(\gamma+1)T^2}{2I^2}\right] - \left(\frac{2}{\gamma} - \frac{1}{\gamma^2}\right)\ln(2) + \frac{1}{\gamma^2} + \frac{1}{8}\left(1-\frac{1}{\gamma}\right)^2 - \delta\right\}. \tag{2.74}$$

[38] The mean excitation energy is an average energy for excitation and ionizations, which is computed taking into account the contributions of the different atomic shells. [Carron, 2007]

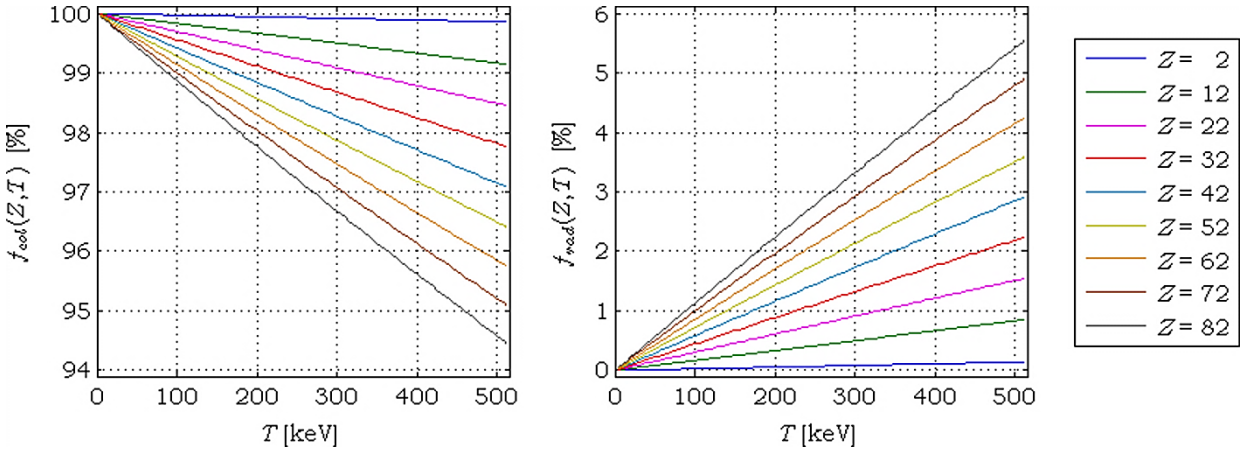

Fig. 2.26: Percentage of energy losses of electrons due to collisional and radiative inelastic scattering processes as a function of the kinetic energy of the electron for several values of the atomic number of the absorber material.

where v is the electron velocity and δ is the density effect parameter, which is more important for high density materials and for electrons with kinetic energies such that $\gamma \gg 1$ [Carron, 2007], which is not the case of those resulting from interactions of 511 keV photons. The Bethe formula is only accurate for electrons with kinetic energies above of a few keV for low density materials, being only accurate for energies above 100 keV in the case of lead [Carron, 2007]. Fig. 2.27 depicts the collisional and radiative stopping powers for borosilicate glass and Bismuth Germanate Oxide (BGO), as well as their relative contributions to the total stopping power for data retrieved from [Berger et al., 2005] instead of computed from Eq. (2.74). The density effect parameter for the same materials is presented in Fig. 2.28.

When incident electrons with kinetic energy T collide inelastically with atomic electrons and cause ionization, after the interaction the ejected electron may have energy higher or lower than the incident one. Since both electrons have exactly the same properties the only way to distinguish them is by means of their kinetic energies. As such, the electron with the higher energy is named the primary electron while the other is a secondary electron or δ-ray [Carron, 2007], and therefore δ-rays will always have energies in the range $[0, T/2]$. These δ-rays can further ionize the medium at some distance from the point where the first interaction occurred. The differential cross section for production of secondary electrons with kinetic energy w, large compared with the electron binding energy, when a single target electron is considered is given by [Carron, 2007]

$$\frac{d\sigma}{dw} = \frac{\sigma_0 \, m_{e,0} \, c^2}{\beta_0^2 \, w^2}, \tag{2.75}$$

where $\sigma_0 = 2\pi\left[e^2/\left(m_{0,e}c^2\right)^2\right] = 0.499[\text{barn}]$, and β_0 is the ratio of the primary electron velocity to that of light. This equation shows that in inelastic scattering will be than produced much more low energy δ-rays than higher energy ones.

By direct integration of Eq. (2.75), the distribution of δ-rays with energy above some value w produced in inelastic collisions can be obtained holding [Carron, 2007]

$$\eta(w) = \frac{N_g \sigma_0 m_{e,0} c^2}{\beta_0^2}\left(\frac{1}{w} - \frac{1}{T}\right), \tag{2.76}$$

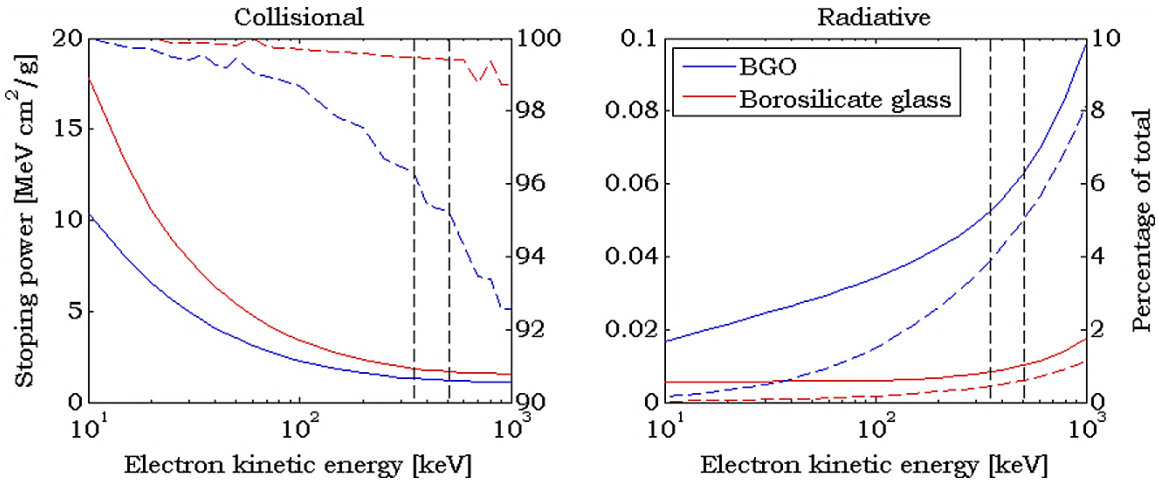

Fig. 2.27: Electron stopping powers for BGO and borosilicate glass (colour solid lines – left Y axis). Left pane depicts the collisional stopping power and right pane the radiative one. Also depicted is the percentage contribution of each stopping power to the total stopping power (colour dashed lines – right Y axis). Vertical black dashed lines represent electron kinetic energies of 350 and 511 keV. (Data retrieved from [Berger et al., 2005].)

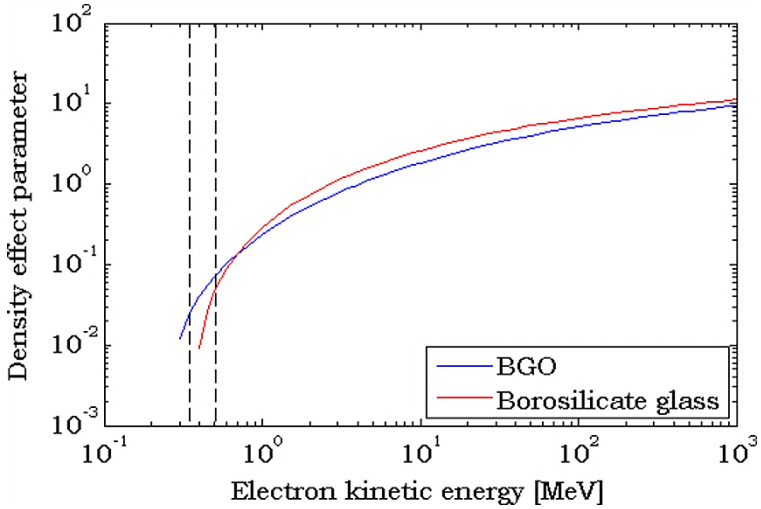

Fig. 2.28: Density effect parameter for BGO and borosilicate glass. Vertical black dashed lines represent electron kinetic energies of 350 and 511 keV.
(Data retrieved from [Berger et al., 2005].)

where N_g is the number of electrons per gram present in the material where the interaction occurs. The angular distribution of primary electrons and δ-rays is given by [Carron, 2007]

$$w = \frac{T\cos^2(\theta)}{1+\frac{T}{2m_{e,0}c^2}\sin^2(\theta)}, \tag{2.77}$$

Fig. 2.29 depicts plots of Eq. (2.76) and Eq. (2.77) for some values of T. For the plot of Eq. (2.76) the number of electrons per gram in a given material was roughly considered as half the mass number of the atoms of the material, such that $N_g = N_A/2$, with N_A the Avogadro number, which means that the plot is independent of the material. For the plot of Eq. (2.77) the Y axis represents the quantity w/T, which allows to distinguish between primary electrons and δ-rays, since, by the above definition, the latter have energies below half the kinetic energy of the incident electron [Carron, 2007].

As a consequence of inelastic collision of primary electrons with the medium, these will tend to progress through the material in the forward direction relative to that of incidence, while δ-rays tend to be spread about the direction of incidence of the primary electron. This, combined with the energy lost in the collisions and transferred to δ-rays, leads to a maximum penetration depth along the direction of incidence of the primary electron.

2.3.2.2 Elastic Scattering

While passing through matter, electrons can elastically scatter with the only

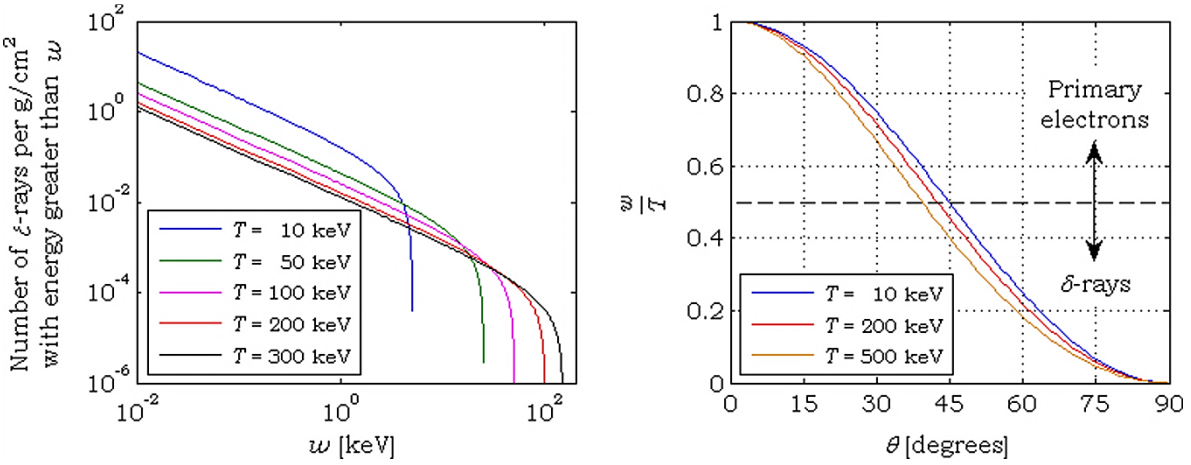

Fig. 2.29: Plots with the number of δ-rays produced by inelastic collision of primary electrons as a function of the δ-rays kinetic energy computed from Eq. (2.76) (left pane) and plot of the angular distribution of primary electrons and δ-rays computed from Eq. (2.77) (right pane), where primary electrons and δ-rays are those for which $w/T > 0.5$ and $w/T < 0.5$, respectively.

transfer of energy being due to momentum conservation. So, the effect of elastic scattering is the deflection of the primary electrons through a given angle. This deflection is given by the differential cross section for elastic scattering of electrons from a neutral atom with atomic number *Z*, which can be approximated by [Carron, 2007]

$$\frac{d\sigma}{d\Omega} = \left(\frac{Z r_0}{\gamma \beta^2}\right)^2 \frac{1-\beta^2 \sin^2(\theta/2)}{\left[1-\cos(\theta)+\frac{\theta_s^2}{2}\right]^2}, \tag{2.78}$$

where r_0 is the classical electron radius (recall footnote 31 on page 26), γ and β are defined by Eq. (2.3) or by Eq. (2.63), and θ_s is named the *screening angle*, given by[39] [Carron, 2007]

$$\theta_s = \sqrt{\frac{\alpha^2}{\gamma^2 \beta^2}\frac{Z^{2/3}}{(0.885)^2}\left[1.13+3.76\left(\frac{\alpha Z}{\beta}\right)^2 \sqrt{\frac{T}{T+m_{e,0}c^2}}\right]}, \tag{2.79}$$

While the differential cross section given by Eq. (2.78), with θ_s given by Eq. (2.79), holds the general shape of the angular distribution of the scattered electrons, it does not hold the correct values, especially for low energy electrons [Carron, 2007]. This can however be corrected for by obtaining the cross section for large angle scattering from tabulated data and then adjust the results obtained by Eq. (2.78) so that the function be continuous at the point for which large angle deflection is considered [Carron, 2007]. The value of the critical angle θ_c, which defines the transition from small to large angle deflection, is somewhat arbitrary, although some databases (for instance, the Electron Evaluated Data Library – EEDL, from the Lawrence Livermore National Laboratory – LLNL) set this value to $\theta_c = 0.081°$ [Carron, 2007].

Fig. 2.30 depicts the shape of the differential cross section computed directly from Eq. (2.78) with θ_s given by Eq. (2.79) without any corrections, just for illustrative proposes of the orders of magnitude of the deflection angle for inelastic scattering. As the plots show, the scattering angle can assume almost any value with equal probability for incident electrons with very small kinetic energies, while the scattering angle becomes markedly in the forward direction (very small angles deflection) as the kinetic energy of the incident electron increases.

Due to this high probability of forward scattering, even for relatively small kinetic energies of the incident electrons, and to the small mean free path for elastic

[39] Another approximation for the screening angle can also be given by this expression omitting the terms inside the square brackets (see, for instance, [Carron, 2007]).

scattering (< 1 μm), the simulation of each individual elastic interaction is a very inefficient and time consuming process [Carron, 2007]. Therefore, simulation codes intended to deal with the transport of electrons through matter (and of any other charged particle) implement models of multiple scattering which compute the angular distribution of incident electrons after a considerable number of inelastic collisions [Carron, 2007].

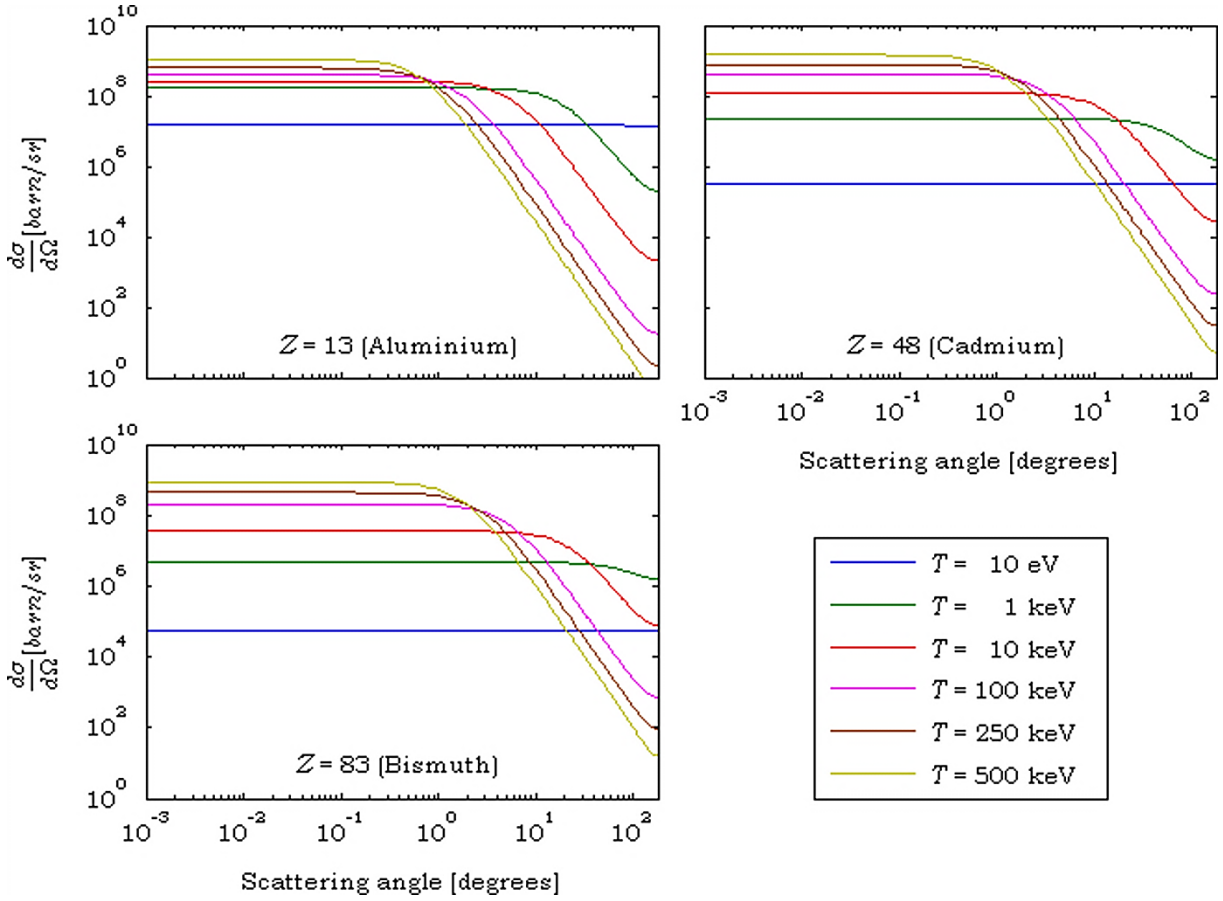

Fig. 2.30: General shape of the differential cross section for inelastic scattering of electrons in three different materials as given from Eq. (2.78) with θ_s given by Eq. (2.79), showing that the scattering angle can assume almost any value with equal probability for incident electrons with very small kinetic energies, and that the scattering is markedly in the forward direction and for very small angles as the kinetic energy of the incident electron increases.

2.3.2.3 Range

As a consequence of the energy loss of primary electrons undergoing inelastic and elastic collisions, and also the collisions undergone by the produced δ-rays that act as primary electrons once created, a well collimated and narrow monoenergetic beam of electrons impinging on a material will penetrate up to a maximum depth (see

Section 2.3.2.1). The range associated to this maximum penetration when working only with the mean stopping powers is named the Continuous Slowing Down Approximation (CSDA) range [Carron, 2007], which does not take into account the effects of straggling, which amounts from 10 to 15% of the CSDA range [Carron, 2007].

A useful empirical fit to the CSDA range for electrons with a kinetic energy T striking a target with atomic weight A and number Z is given by [Carron, 2007]

$$R_{CSDA}^{fit} = \frac{c_1}{B}\left[\frac{\ln\left(1+c_2\,\tau^{c_3}\right)}{c_2} - \frac{c_4\,\tau^{c_5}}{1+c_6\,\tau}\right], \tag{2.80}$$

with

$$B = 2\ln\left(\frac{\tau}{\frac{I}{m_{e,0}c^2}+c_7\,\tau}\right)+\ln\left(1+\frac{\tau}{2}\right), \tag{2.81}$$

where I is the mean excitation energy as in Eq. (2.74), $\tau = T/m_{e,0}c^2$, and c_1, ..., c_7 are given by

$$\begin{array}{llll} c_1 = d_1\dfrac{A}{Z^{d_2}} & c_2 = d_3\,Z^{d_4} & c_3 = d_5 - d_6\,Z & c_4 = d_7 - d_8\,Z \\ c_5 = d_9 - d_{10}\,Z & c_6 = \dfrac{d_{11}}{Z^{d_{12}}} & c_7 = d_{13}\,Z^{d_{14}} & \end{array}, \tag{2.82}$$

where d_1, ..., d_{14} are given in Table 2.3.

Another useful value is the *mean forward range* for which an empirical fit also exists in the form of the ratio between the mean forward range to the CSDA range. The empirical fit to this ratio, which is named *detour factor* and is less than unity, is given by [Carron, 2007]

TABLE 2.3: FITTING PARAMETERS TO BE USED IN EQ. (2.82). (DATA RETRIEVED FROM [CARRON, 2007].)

n	d_n	n	d_n	n	d_n
1	3.60	6	1.0803×10^{-4}	11	1.030
2	0.9882	7	0.99628	12	1.110×10^{-2}
3	1.191×10^{-3}	8	1.303×10^{-4}	13	1.10×10^{-6}
4	0.8662	9	1.02441	14	0.959
5	1.02501	10	1.2986×10^{-4}		

$$\frac{R_{mf}^{fit}}{R_{CSDA}} = \left[1 + \frac{c_1 (Z-1)^{c_2} (1 + c_3 \tau)}{1 + c_4 \tau^{c_5}}\right]^{-1}, \tag{2.83}$$

with

$$\begin{aligned} &c_1 = 0.3087 \qquad c_2 = 0.6384 \qquad c_3 = k_1 Z^{k_2 - k_3 \ln(Z)} \\ &c_4 = \frac{k_4}{Z^{k_5}} \qquad c_5 = k_6 Z^{k_7} \end{aligned}, \tag{2.84}$$

where k_1, ..., k_7 are given in Table 2.4.

TABLE 2.4: FITTING PARAMETERS TO BE USED IN EQ. (2.84). (DATA RETRIEVED FROM [CARRON, 2007].)

n	k_n	n	k_n	n	k_n
1	0.00585	4	0.1012	6	1.0576
2	0.547	5	0.1026	7	0.0234
3	0.0571				

The *most probable depth*, or most *probable projected range*, is defined as the depth at which occurs the maximum value of the mean forward range distribution, $r_{mf}(z)$, from which two other important quantities are also defined: the depth at which half of the primary electrons are stopped, named *median range*, given by

$$\int_0^{R_{med}} r_{mf}(z)\,dz = \frac{1}{2}\int_0^{\infty} r_{mf}(z)\,dz, \tag{2.85}$$

and the projected range straggling parameter, which is defined as the FWHM of the $r_{mf}(z)$ distribution [Carron, 2007].

2.3.2.4 Annihilation Radiation

Positrons have the same properties as electrons, differing only in the charge. So, the interaction processes and the energy loss of positrons when passing through matter are essentially the same as those previously described for electrons [Knoll, 2010] except in two aspects. First, positrons are always distinguishable from electrons due to their positive charge, which means that after a collision the positron is always the primary particle, even if the energy transferred to the medium is higher than half of its kinetic energy. Second, positrons can combine with electrons resulting in the annihilation of the positron/electron pair with emission of electromagnetic radiation. This process is named annihilation and is the basic principle on which PET relies.

The positron/electron annihilation occurs preferentially after the positron has lost almost all its kinetic energy and reached thermal equilibrium with the medium [Pedroso de Lima & Gordo, 2008]. Thus, the process of energy loss and stopping of the positron prior to annihilation is usually named *thermalisation*. In water, the annihilation occurs mostly (70%) between a free positron and a free electron, but can also occur after the formation of a structure called positronium that resembles a hydrogen atom. However, this bonded system is unstable and characterized by lifetimes of 125 ps if the spins of the electron and positron are anti-parallel (para-positronium), and of 142 ns if the spins of both particles are aligned (ortho-positronium) [Pedroso de Lima & Gordo, 2008]. So, the positronium system will also decay resulting in the annihilation of the positron/electron pair accounting for the remaining 30% of the annihilation radiation emitted by the positron/electron pair in water [Pedroso de Lima & Gordo, 2008]. From the annihilation of the positron with a free electron or the positronium system, any number of photons can result, with the exception of a single photon due to the conservation of linear momentum [Pedroso de Lima & Gordo, 2008]. However, the annihilation with emission of a pair of photons is far more probable than that with a higher number of photons (99.5% in water) [Pedroso de Lima & Gordo, 2008], and in what follows it will be considered that the positron/electron pair will always annihilate into a pair of photons.

If the annihilation occurred with the positron/electron pair at rest, then the conservation of linear momentum and energy would imply that the two annihilation photons where emitted in exactly opposite directions with exactly the same energy, equal to half the rest mass energy of the pair, viz., 511 keV. However, the linear momentum and kinetic energy of the positron/electron pair immediately before annihilation occurs is not zero, and the two photons will not be emitted in exactly opposite directions and with the same energy, but rather with an angular deviation between their directions as depicted in Fig. 2.31, which is related with the component of the linear momentum p_t by [Pedroso de Lima & Gordo, 2008]

$$\Delta\theta \simeq \frac{p_t}{m_0 c}, \tag{2.86}$$

and the difference in energy relative to that corresponding to the electron or positron rest mass is given by [Pedroso de Lima & Gordo, 2008]

$$\Delta E \simeq \frac{p_t c}{2}. \tag{2.87}$$

Moreover, the angular deviation $\Delta\theta$ and the energy difference can also be related by [Pedroso de Lima & Gordo, 2008]

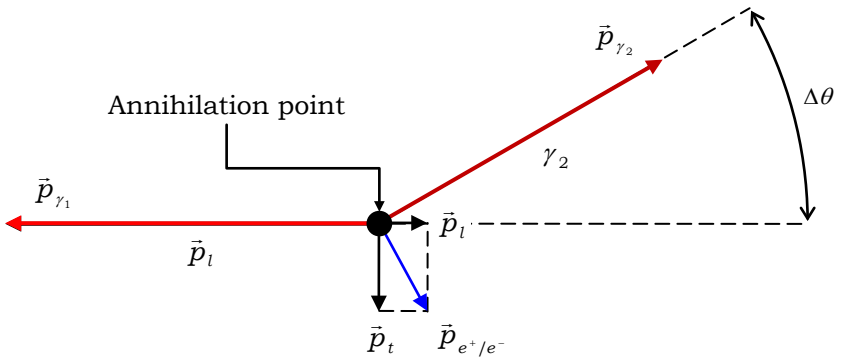

Fig. 2.31: Scheme of the annihilation process in the laboratory reference frame taken as the plane defined by the two annihilation photons, in which the residual momentum of the positron/electron pair before annihilation also lies.

$$\Delta\theta \simeq \frac{2\Delta E}{m_{e,0}c^2}. \tag{2.88}$$

This relation can be found in the treatment of positron annihilation in some simulation codes developed for PET, such as the GEANT4 Application for Tomographic Emission (GATE) [Jan et al., 2004], where the full angular deviation $(2\Delta\theta)$ is assumed to follow a Gaussian distribution with a standard deviation of ~0.25°, leading to a FWHM of 0.58° corresponding to experimental values measured in water [Jan et al., 2004]. As discussed in Section 4.6.1, the photon acollinearity is accepted to be one of the two physical limiting factors of the spatial resolution in PET [Moses, 2011].

The second physical limiting factor is related to the positron range [Moses, 2011]. Taking into account that positrons and electrons have a similar behaviour in what concerns the energy loss [Knoll, 2010], and can also be characterized by range parameters such as those referred to in the previous section. However, positrons arising from β^+ decay are emitted isotropically and with kinetic energies presenting a continuum that runs from zero to a maximum. So, the range is better defined in terms of the three dimensional distribution of annihilation points relative to the sites of β^+ decay, from which a one dimensional range distribution in any given direction and passing through the point of maximum intensity can be obtained. This distribution is called a Point Spread Function (PSF) and its FWHM characterizes the precision within which it is possible to localize the point where the β^+ decay occurred. Due to the considerable amount of positrons emitted with low energies which are stopped close to their site of emission, the PSF of the positron range has a cusplike shape that has been modelled by [Levin, 2004]

$$PSF(x) = C\,\mathrm{e}^{-k_1|x|} + (1-C)\,\mathrm{e}^{-k_2|x|}, \tag{2.89}$$

where C, k_1 and k_2 are fitting parameters for each radionuclide. Table 2.4 resumes the best fitting parameters obtained by simulation of positron ranges in water for $^{11}_{6}\mathrm{C}$, $^{13}_{7}\mathrm{N}$, $^{15}_{8}\mathrm{O}$ and $^{18}_{9}\mathrm{F}$, along with the FWHM and the Full Width at Tenth Maximum (FWTM), and Fig. 2.32 depicts the shape of the PSF for each of the aforementioned radionuclides.

TABLE 2.4: BEST-FIT PARAMETERS OF EQ. (2.89) FOR DATA SIMULATED IN WATER FOR SOME RADIONUCLIDES USED IN PET. (DATA RETRIEVED FROM [LEVIN, 2004].)

Parameter	$^{11}_{6}\mathbf{C}$	$^{13}_{7}\mathbf{N}$	$^{15}_{8}\mathbf{O}$	$^{18}_{9}\mathbf{F}$
C	0.49	0.43	0.38	0.52
k_1 [mm^{-1}]	23.8	20.2	18.1	37.9
k_2 [mm^{-1}]	1.81	1.42	0.90	3.1
FWHM	0.19	0.28	0.50	0.10
FWTM	1.86	2.53	4.14	1.03

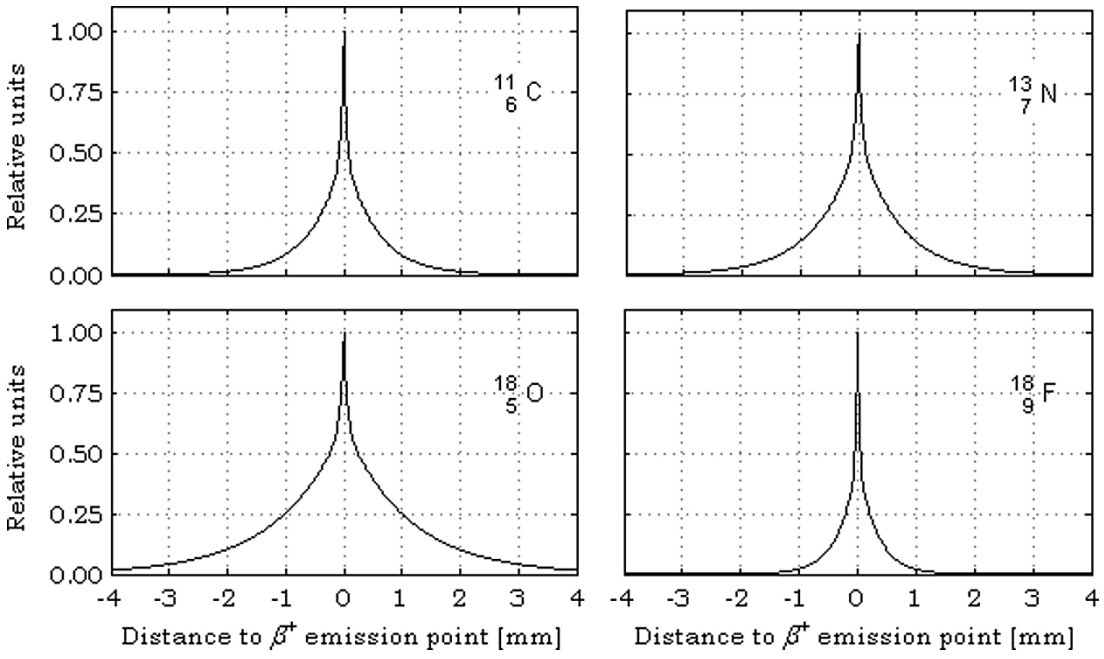

Fig. 2.32: PSF of the positron range for $^{11}_{6}\mathrm{C}$, $^{13}_{7}\mathrm{N}$, $^{15}_{8}\mathrm{O}$ and $^{18}_{9}\mathrm{F}$ obtained from Eq. (2.89) with the fitting parameters C, k_1 and k_2 from Table 2.4.

CHAPTER 3
γ-RAY DETECTORS EMPLOYED IN CLINICAL POSITRON EMISSION TOMOGRAPHY SYSTEMS

PET, which will be addressed in Chapter 4, relies on the ability to detect annihilation photons in temporal coincidence, determined by a time window of a few nanoseconds on the time difference between the two detected photons [Lewellen, 2008] resulting from positron annihilation, which, as seen in Section 2.3.2.4, have an energy of ~511 keV. Since the annihilation photons are almost anti-parallel, the two detection points will define a line along which the annihilation occurred, called LOR. By recording a high number of LORs and by using appropriate reconstruction algorithms, the volumetric distribution of the annihilation points can thus be obtained, which is in straight correlation with the biodistribution of the β^+ emitter.

Several aspects have to be considered when choosing materials and designing detectors for PET scanners, or more generally, when designing PET scanners. Some of those are intrinsically related with the physics processes of radiation interaction in the patient or object to be imaged and the primary physics processes of interaction in the detector medium, while others are intrinsically related with the physics processes following photon interaction in the detector and that serve as the primary source of signal for detection, which impose some requirements for the electronics employed in the detector as well as the overall design and segmentation of the detection system.

Although the existence of at least one pre-clinical PET scanner based on gaseous detectors [Schäfers et al., 2005] consisting of a Multi-Wire Proportional Chamber (MWPC) [Charpak et al., 1968] operating under the converter plate principle [Bateman et al., 1980] and at least a proposed system based on straw tubes[1] operating under the same principles [Shehad et al., 2006], scintillation detectors consisting in a scintillator material coupled to photodetectors, are the most common detectors used

[1] A straw tube is a radiation detection device combining the converter plate principle with that of the wire chamber. A tube acting as a photon/electron converter surrounds a single wire kept under tension. The tube is filled with an appropriate gas mixture for electron amplification (see Section 5.1.2 on page 151), the charge being then collected by the wire kept under tension. (See [Toki, 1990].)

in PET systems [Dahlbom, 2012]. For this, in the present Chapter attention will be devoted only to scintillation detectors.

3.1 REQUIREMENTS FOR POSITRON EMISSION TOMOGRAPHY DETECTORS

In the present section several aspects that dictate the requirements of a successful PET detector will be addressed shortly throughout the different subsections, and the requirements for PET detectors will be summarized in the last subsection.

3.1.1 Photon Interactions in the Patient Body

It was shown, by detailed simulations of the NCAT[2] phantom [Segars, 2001], performed in GEANT4, that at least 65.5% of the 511 keV photons emitted from the abdomen suffer some kind of interaction in the patient body [Reis, 2008]. Since ~56% of the human body is composed of water [Guyton, 1990], and considering the corresponding photon interaction cross sections presented in Fig. 2.9 (page 27), Fig. 2.21 (page 37), and Fig. 2.22 (page 40), it is clear that the main primary interaction process undergone by the 511 keV photons in the human body is Compton scattering[3], with partial absorption of energy. As such, PET detectors should, in principle, be able to discriminate the detected photon energy, or at least have some sort of energy sensitivity, in order to reject photons that suffered Compton scattering in the patient. However, since Compton scattering can occur with small fraction of energy transferred to the medium but with non-negligible photon deviation from its initial path (Fig. 2.14, page 32), the rejection of photons based solely on energy deposition in the detector does not completely eliminate photons that have undergone scattering in the patient. In fact, scatter rejection based on energy deposition is not very effective in PET [Dahlbom, 2012].

As to Rayleigh scattering, it is not possible to reject photons based on energy, since none is transferred in the scattering process. However, from Fig. 2.9 (page 27) it can be readily seen that, for 511 keV photons, the probability of Rayleigh scattering for water is ~0.22% of the total photon interaction probability[4] and, as such, Rayleigh scattering in the patient body is of little or no concern in PET.

---

2 NCAT stands for NURBS-based cardiac-torso, with NURBS meaning Non-Uniform Rational B-Splines.

3 For 511 keV photons, the total mean free path and the mean free path for Compton scattering in water are, respectively, 10.42 cm and 10.44 cm. (Computed from data retrieved from [Berger et al., 2011].)

4 For 511 keV photons, the mean free path for Rayleigh scattering in water is 4649 cm. (Computed from data retrieved from [Berger et al., 2011].)

Finally, as to the photoelectric absorption in the patient or object to be imaged, its only effect, in what detection is concerned, could be the reduction of the total number of detected photons. From Fig. 2.22 (page 40), it can be seen that the probability of photoelectric absorption for 511 keV photons in water is negligible[5] (~0.02%). Combining this with the aforementioned probability of Compton scattering for 511 keV photons in water, one may expect that the 8.52% of photons that do not escape the human body, reported by [Reis, 2008], are due to primary Compton scattering and/or Compton cascades followed then by photoelectric absorption, which means that, probably, photoelectric absorption of 511 keV photons has very little or even no effect on the total number of annihilation photons detected.

3.1.2 Photon Interactions in the Detectors

The ideal detector should effectively stop the 511 keV photons in the shortest distance possible, viz., the interaction length for 511 keV photons in the material of the detector should be as small as possible. Since the interaction length is inversely proportional to the product of the mass density of the material by the cross section (Eq. (2.29) and Eq. (2.30)), the ideal detector should have both a high mass density and a high cross section for photon interaction.

Besides, photons incoming from the patient body should, ideally, interact only by photoelectric absorption, since this is the only interaction process for which all the photon energy is deposited in the detector and, hence, combined with some sort of energy discrimination, is the only interaction process for which it is possible to reject Compton scattered photons in the patient body. This means that the detector should, in principle, have a high photofraction[6], which for 511 keV photons can only be achieved for materials with high atomic number (Fig. 2.25, page 45). However, and since photoelectric absorption is more probable for low energy photons, even for high atomic number (Z) elements or high effective atomic number $\left(Z_{eff}\right)$ compounds and mixtures[7], the fraction of 511 keV photons that interact in the detector by Compton scattering is not to be disregarded, as it can be seen in Fig. 2.21 (page 37) for BGO $\left(Z_{eff} = 74\right)$ and Cerium-doped Lutetium Oxyorthosilicate (LSO) $\left(Z_{eff} = 66\right)$, which are two of the materials commonly employed in PET detectors [Lewellen, 2008].

---

5 For 511 keV photons, the mean free path for photoelectric absorption in water is 56243 cm. (Computed from data retrieved from [Berger et al., 2011].)

6 The photofraction is the quotient between the photoelectric absorption cross section and the total cross section for interaction.

7 The effective atomic $\left(Z_{eff}\right)$ and mass $\left(A_{eff}\right)$ numbers of a compound or mixture are the atomic and mass numbers of a hypothetical single element that would reproduce the same photon interaction cross sections as those of the compound or mixture.

If the detector has some sort of energy discrimination, which is widely accepted as being fundamental (see for instance [Moses & Derenzo, 1996; Humm et al., 2003; Cherry & Dahlbom, 2006; Dahlbom, 2012]), primary photons interacting by Compton scattering in the detector and that did not suffer any energy loss in the patient body can be rejected if the energy deposition is below the threshold of energy acceptance. Recurring to Fig. 2.20 (page 36), it can readily be seen that the maximum energy that a 511 keV photon undergoing Compton scattering can transfer to the detector medium is slightly less than 350 keV, which, combined with the relative probability of Compton scattering for BGO and LSO (depicted in Fig. 2.21 on page 37), means that for energy thresholds above this value[8] a considerable number of unscattered photons in the patient and that suffer a single Compton interaction in a single detection unit[9] will be rejected by the detection system, hence reducing its sensitivity.

Unscattered photons coming from the patient can also undergo a single Compton interaction or a Compton cascade in a single detection unit, followed by a photoelectric interaction. In this case, the photon energy will be entirely deposited in the single detection unit and the event will be accepted as an unscattered one. Since the position of the interaction is computed on the basis of the centroid of energy deposition (see Section 3.4.2 on page 77) these events will introduce a bias in the detection position, contributing to the degradation of the spatial resolution on the reconstructed image.

Contrary to low density materials as water, the probability of Rayleigh scattering for 511 keV photons in high Z or Z_{eff} materials is not to be disregarded, as shown in Fig. 2.9 (page 27) for BGO and LSO. Photons undergoing Rayleigh scattering in the detection system, being then deviated from their incoming trajectories, can traverse it without suffering further interactions, or can interact in the same detection unit, or in a different one, by means of photoelectric absorption, by single Compton scattering or Compton cascades followed or not by photoelectric absorption. If the energy deposited by the interaction processes following Rayleigh scattering is below the threshold for detection, then Rayleigh scattering will reduce the number of detected photons and hence the overall detection efficiency. On the other hand, if the energy deposition is above the threshold for detection, then the centroid of the energy deposition will have a bias relative to the site where Rayleigh scattering occurred, eventually[10] contributing to the degradation of the spatial resolution on the final reconstructed image.

---

8 For PET systems with high energy resolution the energy threshold (also known as Low Level Discrimination – LLD) for acceptance of events is of ~400 keV [Dahlbom, 2012].

9 In the present context, a single detection unit should be understood as a single and independent readout unit for which the total energy deposited is used for rejecting scattered photons.

10 Recall that in Section 2.3.1.1 (page 27) it was said that, for photons with energies above 100 keV, Rayleigh scattering is strongly forward peaked.

3.1.3 Detector Dead Time

An important factor that determines the choice of materials and electronic devices to be employed in PET detectors, and also in the detector design, is the time needed for the detector to be available for detection of a given photon upon the detection of a previous one. This time is called *dead time* and can be described by two limiting models: the non-paralyzable and the paralyzable models [Eriksson et al., 1994; Knoll, 2010]. Fig. 3.1 depicts a scheme of both dead time models.

In the paralyzable model, upon the detection of a first event, the detector will be unavailable for a given time interval to detect further events arising at the detector. If a second event arises during the dead time interval started by a previous event, the dead time will be extended for a time interval equal to the dead time window. In the limit, if the true input rate[11] is too high, the detector may eventually saturate and become permanently unavailable for detection. For the paralyzable dead time model, the fraction of time during which the detector is available for detection (the Live Time Fraction – LTF) is given by [Eriksson et al., 1994]

$$LTF_{paralyzable} \approx k\,\mathrm{e}^{-R_t \tau_p}, \tag{3.1}$$

where k is a constant (≈ 1 [Eriksson et al., 1994]), R_t is the true input rate and τ_p is the paralyzable dead time.

In the non-paralyzable model the detector will also be unavailable to detect events arising in a given time interval after the first event has been detected. However, if an event arises during the dead time window started by a previous one, the dead time will not be extended. In this case, the LTF is given by [Eriksson et al., 1994]

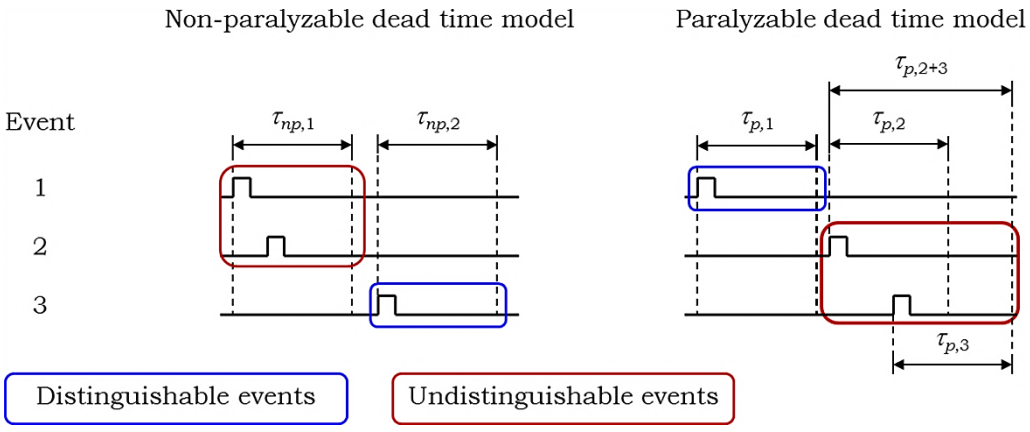

Fig. 3.1: Schemes of the two limiting dead time models, where τ_{np} and τ_p are, respectively, the non-paralyzable and paralyzable dead times.

[11] The rate at which detectable events arise at the detector.

$$LTF_{non-paralyzable} \approx k \frac{1}{1 + R_t \tau_{np}}, \tag{3.2}$$

with k and R_t defined as above and τ_{np} the non-paralyzable dead time.

More often, the dead time behaviour of a counting system is better described by a combination of these two limiting cases [Eriksson et al., 1994; Knoll, 2010]. A possible combination consists in the geometrical mean of both models with a LTF given by [Eriksson et al., 1994]

$$LTF_{combined} \approx k \sqrt{\frac{e^{-R_t \tau_p}}{1 + R_t \tau_{np}}}. \tag{3.3}$$

For PET scanners, the global dead time is a combination of the dead times of the detectors and the dead time of the data handling system [Eriksson et al., 1994], the former being more important than the latter [Eriksson et al., 1994; Cherry & Dahlbom, 2006], and dictates the overall performance of the scanner in what concerns the maximum achievable count rate [Eriksson et al., 1994].

3.1.4 Timing Performance

Since PET relies on the ability to detect two photons in temporal coincidence, the time performance of the detector is a critical factor that has to be taken into account. Moreover, if TOF information is desired (see Section 4.5 on page 115), the requirements for time performance are even more stringent than those required for coincidence detection.

The performance of a detector in terms of time resolution is not necessarily related to its dead time. Some detectors may use two different schemes for reading time and position. This is the case of RPC detectors in which the time signal directly rely on a fast component of the signal induced in the detector, with the position determined by integrating the slow components for a given period of time. (See Section 5.2 on page 151, and Section 5.4 on page 155.)

For the detectors currently employed in commercial clinical PET scanners, the signal at the output of the detector has a more or less fast rising from a reference value up to a maximum, then falling slowly down to the reference level. In this case, the dead time is determined by the time length of the fast rising portion of the signal and by a given fraction of the falling portion of the signal, while the time resolution is determined by the fast rising component of the output signal.

3.1.5 Spatial Resolution

The intrinsic spatial resolution of a PET detector is a key point to obtain a useful image of the biodistribution of the β^+ emitter, and strongly depends on the nature of the physics processes undergone in the detector leading to the primary source of signal, and on the segmentation of the detector and/or readout [St. James et al., 2004].

3.1.6 Final Considerations on the Requirements of Detectors for Positron Emission Tomography

From the previous sections it is clear that there is no such ideal detector and that the design of a PET detector is a compromise between all the above mentioned aspects, the desired image quality, which include not only spatial resolution but also the contrast, the radiation dose that must be administered to the patient and that must follow the ALARA[12] principle, respecting upper limits above which the risk of damages impaired by the radiation does not compensate the benefits of the exam, and, also important, the total cost of the system, which ultimately dictates its usefulness.

The requisites that a PET detector must fulfil, taking into account the several aspects mentioned from Section 3.1.1 (page 58) to Section 3.1.5 (page 63), have been summarized in the past by [Moses & Derenzo, 1996] with the following order of decreasing importance: (1) more than 85% of detection efficiency, (2) spatial resolution of at least 5 mm FWHM, (3) a low cost (less than ~$100 per square centimetre of detection surface area[13]), (4) low dead time (< 25.8 μs cm^2, where the figure of merit is the product of the detector dead time and the front surface area of the portion of the detector that is dead[14]), (5) a timing resolution better than 5 ns FWHM for non-TOF conventional PET scanners and better than 200 ps FWHM for TOF capable ones, and (6) an energy resolution higher than 100 keV FWHM. More recently [Humm et al., 2003] summarized the above mentioned requirements updating the spatial resolution to 4 mm, the cost of the detector to less than $\$400\,\mathrm{cm}^{-3}$, and with the energy resolution expressed as 20% of the energy of the annihilation photons (102.2 keV).

3.2 SCINTILLATORS

As with the above mentioned general characteristics that a PET detector must fulfil, the characteristics of a successful scintillator for PET detectors have also been summarized in the past by [Moses & Derenzo, 1996] and have been accepted to be, in

[12] As Low As Reasonably Achievable.

[13] Value of 1995, uncorrected for inflation rate, and converted from the original that states $< \$600\,\mathrm{in}^{-2}$.

[14] Value converted from the original that states $< 4\,\mu\mathrm{s\,in}^2$.

decreasing order of importance: (1) a high interaction cross section (short interaction length < 1.5 cm) for the interaction of 511 keV photons, which is to say a high effective atomic number and density, (2) a high photofraction (> 30%), (3) short scintillation decay time (< 500 ns) to reduce the dead time of the detector and improve its time resolution to allow shorter coincidence time windows and high TOF resolutions, (4) a low cost (< $20/cm^3)[15], and (5) a high light output (> 8000 ph/MeV).

Essentially three different mechanisms of scintillation can be observed in materials that may be suitable for PET detectors: that of single elements (noble-gases), that of organic compounds and that of inorganic crystals.

3.2.1 Noble-Gases Scintillators

The simplest mechanism of scintillation is that observed in single elements (noble-gases) and that is based on the electronic deexcitation to the ground state upon radiation absorption as mentioned in Section 2.1 (page 8). Liquid Xenon is one of those scintillators.

3.2.2 Organic Scintillators

The mechanism of scintillation of organic compounds has its origin in the molecular energy levels presented in Fig. 3.2, and that consist in a series of electronic singlet (S_1, S_2, ...) and triplet (T_1, T_2, ...) states[16] further decomposed in vibrational energy levels which are further subdivided in rotational energy ones. In the ground state, electrons are usually found in the first vibrational level of the S_0 singlet state (the S_{00} state) [Knoll, 2010].

When photons are absorbed, electrons may jump from the ground state to a given vibrational and rotational level of an excited singlet (S_1, S_2, ...) or triplet (T_1, T_2, ...) state, or may be ejected from the molecules loosing then energy and being trapped in one of the aforementioned excited states. Due to the small energy difference between rotational energy levels (from $\sim 10^{-4}$ to $\sim 10^{-3}$ eV for typical diatomic molecules [Eisberg & Resnick, 1985]) and vibrational levels (with energy spacing of the order of 0.15 eV [Knoll, 2010]), the excess of vibrational and rotational energy will be lost in a negligible short period of time, electrons reaching then the first vibrational energy level of the S_1 or T_1 electronic states (S_{10} or T_{10}) [Knoll, 2010] from where they will then undergo radiative deexcitation to a vibrational level of the S_0 singlet state [Knoll, 2010]. The transitions from the S_{10} state to the S_{0V} state, where the index V

[15] Values of 1995, uncorrected for inflation rate.

[16] In singlet states the total electronic spin (the sum of the spins of all electrons of the molecule) is equal to zero, while in triplet states the total spin is equal to one [Knoll, 2010].

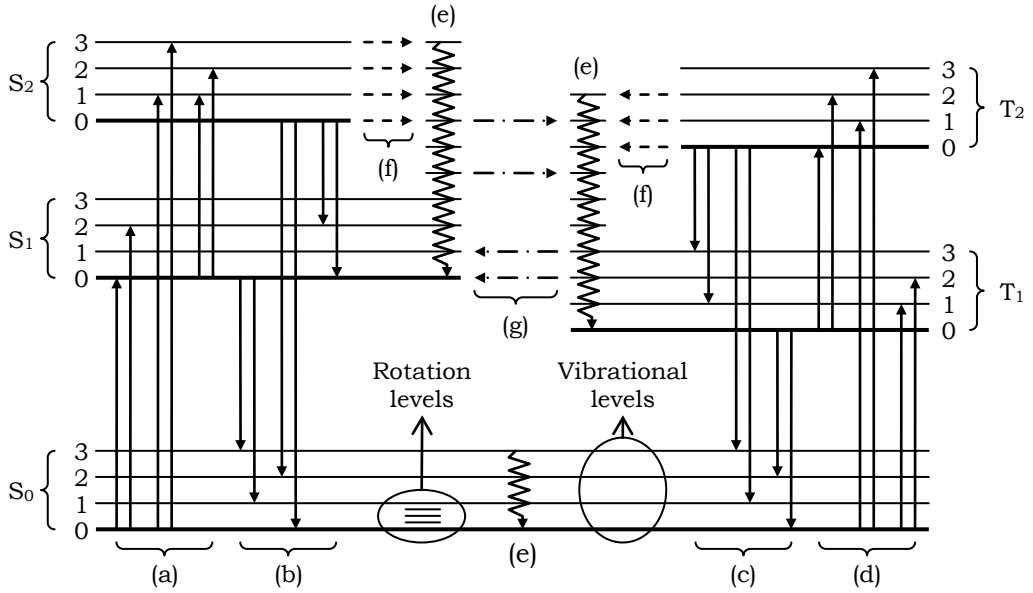

Fig. 3.2: Molecular energy levels: S_0 – singlet ground state; S_1 and S_2 – first and second singlet excited states; T_1 and T_2 – first and second excited triplet states; (a) and (d) – electronic excitation transitions; (b) and (c) – electronic deexcitation transitions; (e) – vibrational and rotational energy lost due to collisions with neighbouring molecules; (f) – internal conversion ; (g) inter-system crossing.

represents one of the vibrational energy levels of the S_0 electronic state, occurs in a few nanoseconds and correspond to the so called prompt fluorescence [Knoll, 2010], while the transition from the T_{10} state to the S_{0V} state correspond to the so called phosphorescence and is characterized by decay times as much as 1 μs [Knoll, 2010].

Due to the superposition of the rotational and vibrational energy levels of the singlet and triplet states, electrons in the latter can undergo a delayed transition to the formers from which will then undergo a radiative transition to the S_0 state, called delayed fluorescence [Knoll, 2010], and which can contribute to the spread of the total decay time of the scintillator. For molecules of interest as organic scintillators, the separation between the two levels involved in prompt and delayed fluorescence is of the order of 3 or 4 eV [Knoll, 2010] which correspond to wavelengths in the near ultraviolet and visible region of the electromagnetic spectrum (from 300 to 410 nm). As to the energy difference between the T_{10} and the S_{0V} energy states, is less than that between the S_{10} and the S_{0V} states [Knoll, 2010] and, as such, phosphorescence photons will have longer wavelengths than those of fluorescence.

3.2.3 Inorganic Crystal Scintillators

The scintillation mechanism of inorganic crystals is different from that of monoatomic molecules and organic compounds. Due to the tight packing of atoms in a

regular lattice, the energy levels of scintillation crystals consist of two continuous bands: the valence band representing those electrons that are essentially bound at lattice sites, and the conduction band representing those electrons that have sufficient energy to migrate throughout the crystal [Knoll, 2010]. The valence and conduction bands are separated by a gap of forbidden energies [Humm et al., 2003; Knoll, 2010], typically between 4 to 6 eV [Humm et al., 2003], as depicted in Fig. 3.3. Upon energy absorption from the interacting photon, electrons jump from the valence to the conduction band ((a) in Fig. 3.3) creating a given number of electron-hole pairs ((b) in Fig. 3.3) in the crystal [Humm et al., 2003; Knoll, 2010]. In a pure crystal, the direct deexcitation of the electrons from the conduction to the valence band with the emission of photons is an inefficient process [Knoll, 2010]. For the deexcitation with the emission of a photon in the visible region of the electromagnetic spectrum to be an efficient process it is necessary to introduce appropriate atoms in the crystal lattice that will act as activators[17] of the deexcitation process by creating energy levels in the forbidden energy gap of the crystal [Humm et al., 2003; Knoll, 2010].

Once electrons reach the conduction band and holes are left in the valence one, both will migrate across the crystal lattice ((c) in Fig. 3.3) eventually reaching the sites of an activator being then transferred non-radiatively to the ground (hole) and excited (electron) states of the activator ((d) in Fig. 3.3) [Knoll, 2010]. Once in an excited state

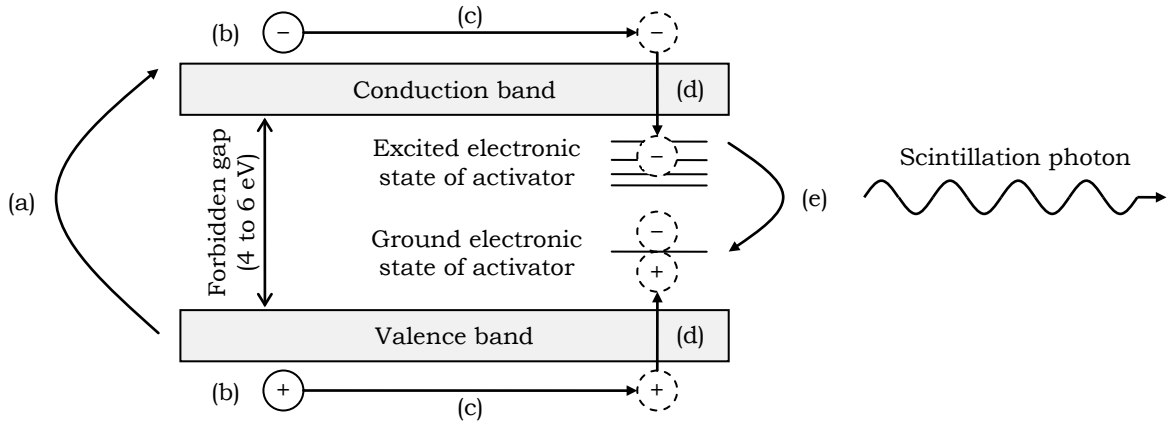

Fig. 3.3: Scheme of the processes involved in the emission of scintillation by inorganic crystals: (a) electronic excitation transition from the valance to the conduction band of the crystal upon energy absorption; (b) hole left in the valence band and electron raised to the conduction band; (c) migration of holes and electrons to the sites of the activators, (d) non-radiative transitions of holes and electrons from the valence and conduction bands to the ground and excited states of the activators, (e) electronic deexcitation transitions from the excited to the ground state of the activators with emission of scintillation photons.

[17] If the activator atoms are a major component of the crystal lattice the scintillator is said to be *self-activated* (BGO), otherwise the scintillator is said to be *activated* (NaI:Tl, LSO:Ce, …).

of the activator, electrons will undergo deexcitation to the ground state of the activator with the emission of a photon ((e) in Fig. 3.3) which, if the activator is properly selected, will have a wavelength in the visible region of the electromagnetic spectrum [Knoll, 2010].

Since the process of electron/hole creation, migration and capturing by the activator is fast when compared to the lifetimes of the activator excited states [Knoll, 2010], which can range from tenths to several hundred of nanoseconds [Humm et al., 2003], the timing characteristics of inorganic scintillators are entirely determined by the decay times of the activators [Knoll, 2010].

3.2.4 Final Considerations on Scintillators

Independently of the scintillation mechanism, photons interacting in the scintillator create primary electrons which have energies well above their excitation energy and will lose the excess of energy in collisions with atomic electrons producing further ionizations, the process continuing until further ionizations are not possible [Bell, 2012]. These processes take place in a time frame as short as 1 to 100 fs [Bell, 2012], after which the electrons lose energy to the medium [Bell, 2012]. The number of electrons surviving to this stage and that are available to undergo radiative deexcitation transitions is given by $E_0/(kE_g)$ where E_0 is the energy of the incident photon, E_g is the energy difference between the excited states and the ground state (or the energy of the forbidden gap in inorganic crystals), and k is a constant that varies between 1 to 2 for noble-gas scintillators, 3 to 4 for organic scintillators, and 1.5 to 2.0 for inorganic scintillators [Bell, 2012]). So, the number of scintillation photons emitted in the deexcitation process will then be proportional to the total energy deposited by the photon impinging the scintillator. As to the intensity of the emitted scintillation light, follows an exponential decay law given by

$$I(t) = I_0 \sum_{i=1}^{N} \mathrm{e}^{-\frac{t}{\tau_i}} . \tag{3.4}$$

with $I_0 \left[\text{photons}\,\text{MeV}^{-1}\,\text{ns}^{-1}\right]$ the initial intensity of scintillation light emitted by the scintillator, N the total number of decay components presented by the scintillator[18], and τ_i the lifetime of the excited state leading to the decay component i, and which are of the order of nanoseconds (far higher than the few femtoseconds needed to populate the radiative excited states) and thus determine the timing characteristics of the scintillator.

For scintillators with two or more decay components, the dead time of the

[18] The different number of excited states that are populated and decay with a characteristic life-time.

scintillator is influenced most by the one with the longest lifetime [Moses & Derenzo, 1996]. As to the time resolution, is determined by $I_0\left[\text{photons}\,\text{MeV}^{-1}\,\text{ns}^{-1}\right]$, viz., the number of scintillation photons emitted immediately after excitation [Moses & Derenzo, 1996], which, in the case of multiple radiative decay modes, is usually influenced by the one with the smallest lifetime [Moses & Derenzo, 1996]. For scintillators with a single radiative decay component the lifetime of the excited states dictates both the dead time and the time resolution.

Liquid Xenon has already been proposed for use in PET detectors [Blanco, 2011]. It has a high atomic number (54), a moderate mass density of $3\,\text{g}\,\text{cm}^{-3}$ [Blanco, 2011], a photofraction of 20.8% for 511 keV photons[19], a fast decay time of 3 to 30 ns and excellent time resolutions of about 300 ps [Blanco, 2011], a high light output of about 58000 photons/MeV[20] leading to an energy resolution of 17% to 20% [Blanco, 2011]. Moreover, a fraction of the energy deposited by the incident photons appears in the form of electron/ion pairs, allowing to acquire further information by collecting the charges produced with some secondary detector based on charge collecting electrodes such as MWPC [Blanco, 2011]. Although being dependent on the specific detector design, liquid Xenon based detectors present good detection efficiencies, of about 70%, as well as full 3D localization of interaction points with millimetric spatial resolutions [Blanco, 2011]. As a drawback, and since the melting and boiling points of Xenon are, respectively, 161.4 and 165.1 K [Winter, 2012], detectors based on liquid Xenon require very stable and precise cooling and pressure controlling systems.

Recently, PET scanners based on plastic scintillators (organic scintillators), have been proposed (the Strip-PET and the Matrix-PET [Moskal et al., 2012]). In general, organic scintillators have densities of about $1\,\text{g}\,\text{cm}^{-3}$ [Knoll, 2010; Bell, 2012], a negligible photofraction for 511 keV photons [Moskal et al., 2012], and a light output of about 10000 photons/MeV [Bell, 2012], comparable to that of some inorganic scintillators, a decay constant in general lower than 3 ns [Knoll, 2010; Bell, 2012], and an excellent TOF resolution that can be better than 100 ps for large detectors [Moskal et al., 2012].

Inorganic crystal scintillators have long been the ones of choice for PET scanners, and, along with photodetectors (Section 3.3), continue to be a very active area of research. This is mainly due to their high effective atomic number and density, presenting small interaction lengths and photofractions up to 40% [Humm et al., 2003], decay times ranging from a few tenth to hundreds of nanoseconds [Blanco,

19 Value computed from [Berger et al., 2011].
20 Value given as 30,000 photons/511 keV in the cited work.

2011], higher than those presented by organic scintillators [Bell, 2012], light outputs ranging from a few thousand to a few tenths of thousand photons per MeV of energy absorbed, good energy resolution and emission wavelengths in the visible region of the electromagnetic spectrum. As a drawback, inorganic scintillators are still expensive.

Table 3.1 resumes the main properties of the scintillators already used or proposed for use in PET scanners.

TABLE 3.1: PROPERTIES OF INORGANIC SCINTILLATOR CRYSTALS ALREADY USED OR CURRENTLY USED IN COMMERCIAL PET SCANNERS, ALONG WITH AN INORGANIC CRYSTAL USED IN A PROTOTYPE 3D TOF-PET SCANNER ($LaBr_3$:Ce) [KARP ET AL., 1990], AN ORGANIC PLASTIC SCINTILLATOR TARGETED FOR LARGE AREA TOF COUNTING SYSTEMS, AND LIQUID XENON.

Scintillator	ρ[b]	ℓ[b]	***PF***[c]	***LO***[d]	τ[b]	Δt[e]	ΔE[b]	**Price**[d]
Liquid Xenon	3.00[e]	3.68[h]	20.8[e]	58000[e]	3-30[e]	300	< 20[e]	-
BC-408[a]	1.032[f]	10.3[f]	0.01[g]	12800[f]	2.1[f]	-	-	< 0.4
NaI:Tl	3.67	2.88	17	37700	230	1500	7.8	6
BGO	7.13	1.05	40	8200	300	5000	20.0	35
GSO:Ce	6.71	1.43	25	12500	60	-	8.9	-
LSO:Ce	7.35	1.16	32	30000	40	600	< 9	60
LYSO:Ce	7.10	1.20	-	32000	41	600	11.0	70
$LaBr_3$:Ce	5.29	~2	13[g]	63000	25	400	7.5	~500

ρ: Mass density $\left[\mathrm{g/cm^3}\right]$.

ℓ: Interaction length (511 keV photons) [cm].

PF: Photofraction (511 keV photons) [%].

LO: Light output [photons/MeV].

τ: Decay constant [ns].

Δt: Time resolution (FWHM) (photon pairs) [ps].

ΔE: Energy resolution ($\mathrm{FWHM}_{@\,511\,\mathrm{keV}}$) [%].

Price: Estimative $\left[\mathrm{US\$/cm^3}\right]$.

[a] Plastic scintillator from [Saint-Gobain Crystals, 2011].

[b] Data retrieved from [Dahlbom, 2012], except where specified otherwise.

[c] Data retrieved from [Humm et al., 2003], except where specified otherwise.

[d] Data retrieved from [Bell, 2012], except where specified otherwise.

[e] Data retrieved from [Blanco, 2011], except where specified otherwise

[f] Data retrieved from [Saint-Gobain Crystals, 2011].

[g] Data computed from [Berger et al., 2011].

3.3 PHOTODETECTORS

Scintillation light, produced by the interaction of the primary particles to be detected, must be converted to a measurable signal. This is performed by coupling a photodetector to the scintillator. The one currently used in all human whole-body commercial PET scanners from the three main constructors (General Electric, Philips and Siemens) is the PMT [Blanco, 2011]. Other photodetectors used in specific PET applications or under study for clinical PET scanners are the Avalanche Photodiodes (APDs) and the Silicon Photomultipliers (SiPM) [Blanco, 2011].

3.3.1 Photomultiplier Tube

Fig. 3.4 depicts a scheme of a PMT, consisting of a vacuum tube usually made of glass [Blanco, 2011], with an entrance window made of a material transparent to the wavelengths of the photons to be detected [Križan, 2012], after which a photosensitive material (photocathode) is placed. Inside the vacuum tube a first focusing electrode is placed between the photocathode and the first of a series of electrodes[21] (dynodes). A high voltage is applied through a resistive voltage division chain connected to the photocathode and the dynodes in order to maintain an appropriate voltage drop between consecutive electrodes [Križan, 2012].

The photocathode is made of a material with a low work function[22] so that each photon impinging it can efficiently remove an electron from its surface[23] [Križan, 2012] to the vacuum region between the photocathode and the focusing electrode. The

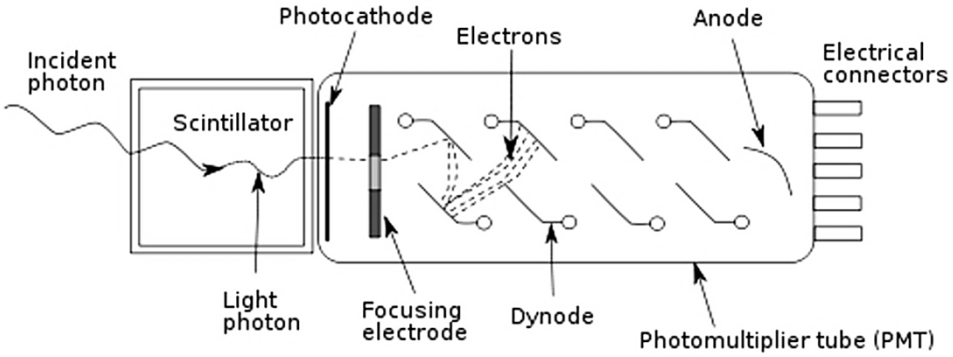

Fig. 3.4: Scheme of a scintillator coupled to a PMT along with the processes involved in the conversion of light into a measurable electric signal.
(Public domain figure retrieved from [Eberhardt, 2006].)

[21] Usually 10 [Križan, 2012].
[22] The minimum energy required to remove an electron from the surface of a material.
[23] This efficiency, which is called Quantum Efficiency (QE), can take values from 20 to 30% [Dahlbom, 2012] and is equal to the quotient of the number of photons that strike the photocathode and eject an electron by the total number of photons that strike the photocathode.

electron is then accelerated by the electric field established between the photocathode and the first dynode passing through the focusing electrode, the function of which is to guide the photoelectron toward the first dynode where secondary electrons (~5 [Križan, 2012]) are extracted and accelerated toward the second dynode by the electric field established between the two dynodes. The amplification process is repeated at the second dynode with the electrons extracted from it being accelerated toward the third dynode and so on, toward the last amplification stage performed at the last dynode from which 10^5 to 10^6 electrons per detected photon are extracted and collected at the anode [Križan, 2012].

The amplification process, with an almost constant gain per photoelectron ejected from the photocathode, combined with the proportionality between the energy deposited in the scintillator and the number of scintillation photons emitted, produces a signal at the output of the PMT that is proportional to the energy of the detected photon, and can thus be used to reject events on the basis of a preset energy threshold. The timing characteristics of the signal collected at the output of the PMT are determined by the timing properties of the scintillator, the time spread introduced by the PMT and that can range from a few hundred picoseconds to a few nanoseconds, depending on the structure of the dynodes, which depend on the pretended use [Križan, 2012], and also by the shaping performed to the output signal.

Among the advantages of PMTs are their availability in a wide range of shapes and sizes [Blanco, 2011], including position sensitive models with multichannel anode granularities as fine as $\approx 2 \times 2\ \mathrm{mm}^2$ [Križan, 2012], a high amplification gain leading to a high SNR [Blanco, 2011], a high stability and ruggedness [Blanco, 2011], and a fast response time. The disadvantages are that they are quite bulky and fairly expensive and susceptible to external magnetic fields [Blanco, 2011].

3.3.2 Semiconductor Photodetectors

Semiconductor photodetectors have been used or proposed for use in PET scanners. Their compactness and availability in high grained arrays allows designing much more compact detectors with higher spatial resolutions, and their immunity to external magnetic fields allows the development of imaging systems integrating the PET scanner and a Magnetic Resonance Imaging (MRI) device.

The basic principle of operation of these devices relies on the operation mode of photodiodes, schematically depicted in Fig. 3.5, which consist of a thin foil[24] of silicon

[24] Typically with a few hundred micrometres [Blanco, 2011].

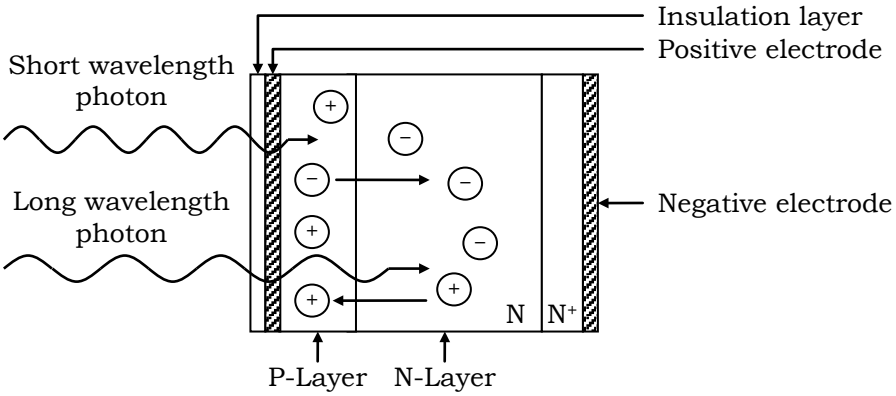

Fig. 3.5: Schematic operation of a photodiode. (Adapted from [Križan, 2012].))

doped to produce a PN junction through which a small voltage drop (of a few volts) is applied [Blanco, 2011]. A scintillation photon interacting in the PN junction often has sufficient energy to release an electron from the structure of the silicon, which will then drift towards the anode, creating then an electric current that can be measured [Blanco, 2011]. The Quantum Efficiency (QE) of conversion of scintillation photons into electrons is much higher than that of PMTs ranging up to 60 or 80% over a wide range of wavelengths [Blanco, 2011]. However, simple photodiodes have no internal gain leading to a low SNR (when compared to that of PMTs) requiring very low noise preamplifiers [Lewellen, 2008] and a much longer integration time degrading the time resolution [Blanco, 2011]. For this, photodiodes are generally not suitable for PET scanners [Lewellen, 2008].

If the voltage drop applied across the PN junction could be raised well above that employed in photodiodes, electrons drifting in the semiconductor would eventually acquire enough energy to release further electrons, leading then to an amplification process similar to that observed in PMTs [Blanco, 2011]. This is the case of APDs which are designed to operate with voltage drops ranging from 200 to 2000 V [Lewellen, 2008], presenting gains ranging from 10^2 to 10^3 [Lewellen, 2008] and that depended on the applied voltage [Lewellen, 2008], as well as QE similar to those of simple photodiodes [Blanco, 2011]. Preamplifiers are also needed although they do not have to be ultralow noise as in the case of simple photodiodes [Lewellen, 2008]. As a drawback, the gain is temperature dependent and can be significant for changes of temperature as low as 1 or 2 C [Lewellen, 2008]. Nevertheless, the performance in terms of energy resolution and timing is roughly equivalent to that of PMTs [Blanco, 2011], with the advantage of being very compact devices and insensitive to magnetic fields, allowing the development of more compact detectors than those allowed by PMTs and that can be operated in MRI devices [Blanco, 2011].

Another photodetector that is in active research for use in PET scanners is the SiPM, which consists basically on a series of APD micro-cells, with sizes ranging from 20 to 100 μm^2, packed in a single envelope containing from 100 to 10000 micro-cells per squared millimetre [Blanco, 2011]. Each cell is an independent Geiger-mode detector that is biased such that when a scintillation photon interacts in the cell, it discharges [Lewellen, 2008]. Ideally, a SiPM should produce the same size and shape of a current pulse from each cell, making each cell a digital detection device (on or off) [Lewellen, 2008]. When coupled to a scintillator, photons that are emitted by the scintillator interact in a large number of micro-cells resulting in an output pulse similar to that observed in PMTs [Lewellen, 2008]. The gains achieved for typical devices range from 10^5 to 10^7 with QE of about 20% and with time resolutions, obtained with scintillators, below the 500 ps [Blanco, 2011]. As APDs, SiPMs are insensitive to magnetic fields [Blanco, 2011], which allow to develop high performance detectors that can be used in MRI devices.

3.3.3 Final Considerations on Photodetectors

Two important aspects of photodetectors are the QE for the wavelengths of the scintillation light and a good matching of their refractive indexes to those of the scintillators.

The wavelength of the scintillation photons emitted by a given scintillator is given by [Bell, 2012]

$$\lambda[\text{mm}] = \frac{1240}{E[\text{eV}]}, \tag{3.5}$$

where E is the energy difference between the radiative excited states and the ground state, which, for plastic and inorganic crystal scintillators is roughly about 3 eV, thus leading to wavelengths of about 410 nm. As to the dependence of the QE of photodetectors with the wavelength of the radiation to be detected is given by [Bell, 2012]

$$QE(\lambda) = \frac{1.24}{\lambda} S(\lambda), \tag{3.6}$$

where $S(\lambda)$ is the sensitivity of the photosensor measured in mA W^{-1}, viz., the current liberated per unit incident power at a given wavelength [Bell, 2012]. Since $S(\lambda)$ is different for different materials, the photosensitive portion of the photodetector must be chosen carefully in order to maximize the signal at the output of the photosensor.

The wavelength of the scintillation photons of liquid Xenon is 178 nm [Solovov et al., 2000], the wavelength of maximum emission for most plastic scintillators is

comprised between 370 and 580 nm (425 nm for BC-408, presented in Table 3.1, page 69) [Saint-Gobain Crystals, 2011], and the wavelength of maximum emission of inorganic crystal scintillators commonly used in PET is roughly comprised between 380 ($LaBr_3$:Ce) and 480 nm (BGO) [Bell, 2012].

For PMTs coupled to inorganic crystal scintillators, this implies a bialkali photocathode with maximum sensitivities ranging roughly from 310 to 470 nm and borosilicate windows with transmittances ranging roughly from 80 to almost 100% for wavelengths greater than 350 nm [Križan, 2012]. Fortunately, PMTs with borosilicate windows and bialkali photocathodes are the less expensive ones [Moses & Derenzo, 1996; Humm et al., 2003; Križan, 2012]. As to APDs and SiPMs, the efficiency is high for a large range of wavelengths [Blanco, 2011].

As to the refractive index, a good match between those of the scintillator and of the photodetector is essential to minimize losses due to refraction and reflection at the scintillator-photodetector interface [Bell, 2012]. For normal incidence, the fractions of light reflected (R) and transmitted (T) at the interface between two dielectric mediums with refractive indexes n_1 and n_2 are given by [Bell, 2012]

$$R = \left(\frac{n_1 - n_2}{n_1 + n_2} \right)^2, \tag{3.7}$$

$$T = \frac{4 n_1 n_2}{\left(n_1 + n_2 \right)^2}. \tag{3.8}$$

The refractive indexes of plastic scintillators are ~1.58 [Saint-Gobain Crystals, 2011], those of inorganic crystal scintillators can range from 1.81 (Cerium-doped Lutetium Yttrium Orthosilicate - LYSO) to 2.15 (BGO) [Bell, 2012], and that of glass is ~1.52 [Bell, 2012]. So, the fraction of scintillation light with normal incidence in the PMT window and that is reflected is ~0.04% for organic plastic scintillators and ranges at least from ~0.8 to ~3% for inorganic crystal scintillators.

Despite the small fraction of reflected light at normal incidence, the mismatch between the refraction indexes of scintillators and photodetectors can have a significant effect on light collection [Bell, 2012]. The critical angle for acceptance of scintillation light when passing from a medium with high refractive index $\left(\eta_{high} \right)$, the scintillator medium, to one with lower refractive index $\left(\eta_{low} \right)$, the photodetector medium, is given by [Bell, 2012]

$$\theta_C = \arcsin\left(\frac{\eta_{low}}{\eta_{high}} \right), \tag{3.9}$$

which implies critical angles of ~74° for plastic scintillators and ranging from ~45°

(BGO) to ~57° (LYSO) for some inorganic crystal scintillators used in PET. So, light incident upon the scintillator-photodetector interface with angles outside the acceptance angle will be reflected, suffering then even more reflections at the scintillator walls, with the consequent lengthening of the optical path of the scintillation photons, leading to a delay in the detection with consequent increase in the apparent decay time, or can suffer self-absorption due to the overlap of emission and absorption bands of the scintillator, reducing then the total light collected by the photodetector [Bell, 2012].

To reduce the fraction of scintillation light reflected (hence to augment the fraction of light transmitted), scintillators are coupled to photodetectors by using index-matching substances such as glycerine and silicone greases [Bell, 2012].

3.4 COMMON CONFIGURATIONS OF DETECTORS FOR CLINICAL POSITRON EMISSION TOMOGRAPHY SCANNERS

The detectors employed in the first PET systems consisted of single crystals mounted on individual PMTs [Lewellen, 2008; Dahlbom, 2012]. While this solution allows to unambiguously identify the crystal where the interaction occurred, it limits the spatial resolution to (ideally) half the width of the crystal [Lewellen, 2008], suited for the smallest PMTs available, which are about 10 mm diameter [Dahlbom, 2012].

Considering a cylindrical scanner with a total of 15 cm length and 70 cm diameter, the number of individual crystals and PMTs would be of the order of 38000. So, and apart the cost of PMTs, each PMT had to have its own readout electronics which would increase the complexity of the detection system besides being very expensive [Dahlbom, 2012]. Moreover, this solution would also pose serious problems on the packing of PMTs due to their glass envelope [Lewellen, 2008], leading to a large fraction of dead space for detection (small packing fraction) [Lewellen, 2008] with consequent reduction of the overall detection efficiency.

To overcome this problem, and also to improve the spatial resolution, several approaches have been used or proposed, the most common of which are a large area scintillator read by an array of photosensors (Fig. 3.6 (a)), usually single-channel PMTs, and a small parallelepipedic block of crystal with saw cuts of variable depth (or an array of small individual crystals) read by an array of photosensors (Fig. 3.6 (b)), usually four single-channel PTMs. This last approach, referred to as block detectors, is the one used in most of the modern clinical PET scanners [Dahlbom, 2012]. Several other approaches have been proposed and used, but only these two will be considered.

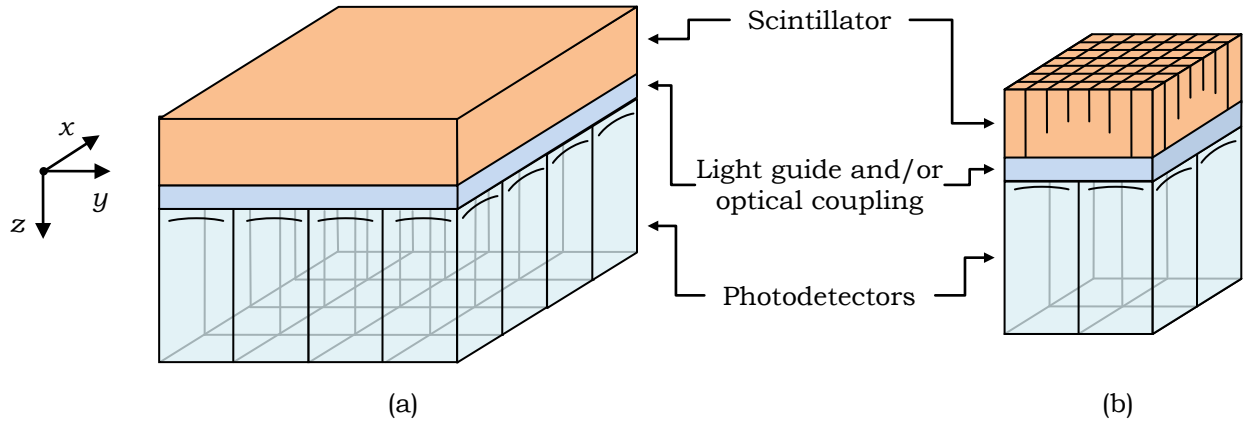

Fig. 3.6: Most common configurations of PET detectors employed in clinical PET scanners: (a) large area crystal coupled to an array of PMTs; (b) scintillator block with saw cuts, or an array of small individual crystals, coupled to an array (usually 4) of single-channel PMTs.

3.4.1 Continuous Detection Panel

Initially developed for use with NaI:Tl scintillator, the detector (Fig. 3.6 (a)) is an adaptation of the Anger gamma camera used in conventional nuclear medicine [Lewellen, 2008]. The low stopping power of NaI:Tl (refer to Table 3.1 on page 69) was a major disadvantage [Lewellen, 2008] and, although used in a PET scanner with curved NaI:Tl [Adam et al., 2001], and in gamma cameras with the ability to perform PET studies, it is no longer in use in PET detectors developed for human whole-body PET scanners [Lewellen, 2008]. However, the basic concept is still in use in commercial PET scanners [Lewellen, 2008] by Philips, first based on Gandulinum OxyorthoSilicate (GSO) crystals (the Allegro PET scanner [Surti & Karp, 2004]) and later extended to use LYSO crystals (the Gemini TF PET scanner [Surti et al., 2007]).

In this approach, a continuous scintillator is coupled to an array of PMTs through a light guide, the scintillation light being distributed among several PMTs [Cherry & Dahlbom, 2006]. One of the major problems with the original design is that the detector must handle multiple events arising simultaneously at very different positions, which requires special efforts in the readout [Cherry & Dahlbom, 2006]. Besides, a large number of PMTs are irradiated by scintillation light. If not handled properly, these two issues lead to dead time problems with the consequent degradation of the overall performance of the detector [Cherry & Dahlbom, 2006]. The last issue can be partially controlled by employing proper materials for coupling the crystal to the PMTs so that the cone of acceptance of scintillation light, discussed in Section 3.3.3 (page 73), is reduced leading to a smaller number of PMTs being irradiated by the scintillation light, while the former can be handled by using larger

PMTs, in a less compact packing, so that each of them can be read independently while maintaining the total cost at reasonable values (Fig. 3.7 (a)).

One of the advantages of this approach is that the signal is continuous along the *X* and *Y* directions [Cherry & Dahlbom, 2006], while the shape is dependent on the position along the *Z* direction (the Depth of Interaction - DOI) if the crystal is thick enough [Lewellen, 2008] (Fig. 3.7 (b)), thus allowing obtaining a continuous 3D position of the interaction of photons incoming from the patient with added improvements on the spatial resolution of the final reconstructed image [Lewellen, 2008]. However, the shape of the signal is also dependent on the scatter within the detector Fig. 3.7 (c)), which reduces the DOI resolution leading to the degradation of the spatial resolution of the final reconstructed image [Lewellen, 2008].

Detectors based on the continuous crystal panel approach achieved intrinsic spatial resolution of ~3 mm for 10 mm thick crystals, and of 4 to 5 mm for 25 mm thick crystals [Cherry & Dahlbom, 2006].

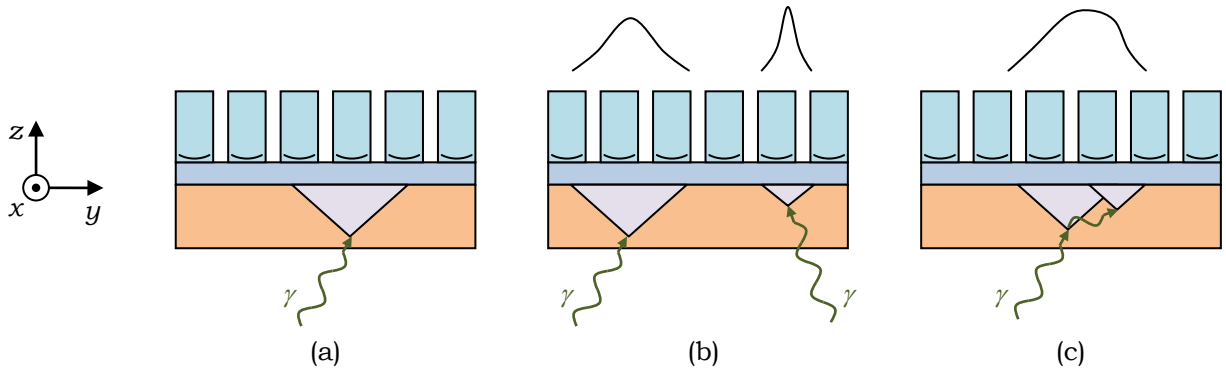

Fig. 3.7: Schemes of the interaction of radiation within the crystal: (a) aperture of the cone for scintillation light acceptance; (b) effect of the DOI on the shape of the readout signal; (c) effect of photon scatter within the detector on the shape of the readout signal.

3.4.2 The Block Detector

The block detector (Fig. 3.6 (b) and Fig. 3.8 (a)) can be made of a monolithic block of scintillator crystal with saw cuts of variable depth depending on the position within the crystal, the deeper ones near the corners and the less deep at the centre, the cuts being then filled with an appropriate reflective material in order to optically isolate the detection elements [Cherry & Dahlbom, 2006; Dahlbom, 2012]. Alternatively, single small cross sectional area scintillator crystal elements, with the faces of each element treated differently depending on their final position within the detector (see for instance [Johnston et al., 1994]), can be glued together to form a single block detector [Cherry & Dahlbom, 2006; Dahlbom, 2012]. In both cases, the block is optically

coupled to an array of four single-channel PMTs [Cherry & Dahlbom, 2006; Dahlbom, 2012]. Multichannel PMTs can also be employed, but their use has been largely limited to more specialized applications, such as breast cancer and animal imaging due to the quite high cost relative to single-channel ones [Cherry & Dahlbom, 2006].

The number of detection elements and total size of the detector block depends on the detector design and scintillation crystal employed [Dahlbom, 2012], but can typically range from $4\times4\ \text{cm}^2$ with 6×6 detection elements [Cherry & Dahlbom, 2006] to $5\times5\ \text{cm}^2$ with 13×13 detection elements [Dahlbom, 2012] in the *XY* plane, and with variable thickness along the *Z* direction (Fig. 3.6 (b) and Fig. 3.8 (a)), usually ranging from ~2 to ~3 cm [Cherry & Dahlbom, 2006], depending on the interaction length of 511 keV photons for the scintillation crystal employed and the scintillation crystal price (see Table 3.1 on page 69).

The different treatment of the surfaces of each small crystal element, or the different depth of the saw cuts, forces the scintillation light to produce a unique pattern in the four single-channel PMTs allowing the identification of the element in which most of the energy of the photons incoming from the patient is deposited [Dahlbom, 2012]. This identification is performed in two steps by recurring first to an Anger-like algorithm and then to a look-up tables from which the pixelated detection element is identified [Cherry & Dahlbom, 2006; Lewellen, 2008; Dahlbom, 2012]. Recurring to Fig. 3.8 (a), the coordinates of the centroid of energy deposition in the *XY* plane, X_{pos} and Y_{pos}, relative to the centre of the block detector, can be given by [Dahlbom, 2012]

$$\begin{aligned} X_{pos} &= \frac{\left(PMT_A + PMT_B\right) - \left(PMT_C + PMT_D\right)}{PMT_A + PMT_B + PMT_C + PMT_D} \\ Y_{pos} &= \frac{\left(PMT_A + PMT_C\right) - \left(PMT_B + PMT_D\right)}{PMT_A + PMT_B + PMT_C + PMT_D} \end{aligned}, \tag{3.10}$$

where PMT_i, with $i=\{A,B,C,D\}$, are the amplitudes of the signals at the outputs of the PMTs[25]. The denominator of Eq. (3.10) is simply the summed signal from all the PMTs and, thus, is proportional to the total energy deposited in the detector, being compared against a threshold in order to reject photons that were scattered [Humm et al., 2003] in the patient body, and eventually in the detection system (recall Section 3.1.1 on page 58, and Section 3.1.2 on page 59).

Since it is not possible to design the cuts (or the individual small crystals) such that the response is completely linear across the whole detector surface [Cherry &

[25] Recall from Section 3.3.1 (page 73) that the amplitude at the output of a PMT is proportional to the total number of scintillation photons produced in the portion of the crystal seen by the PMT.

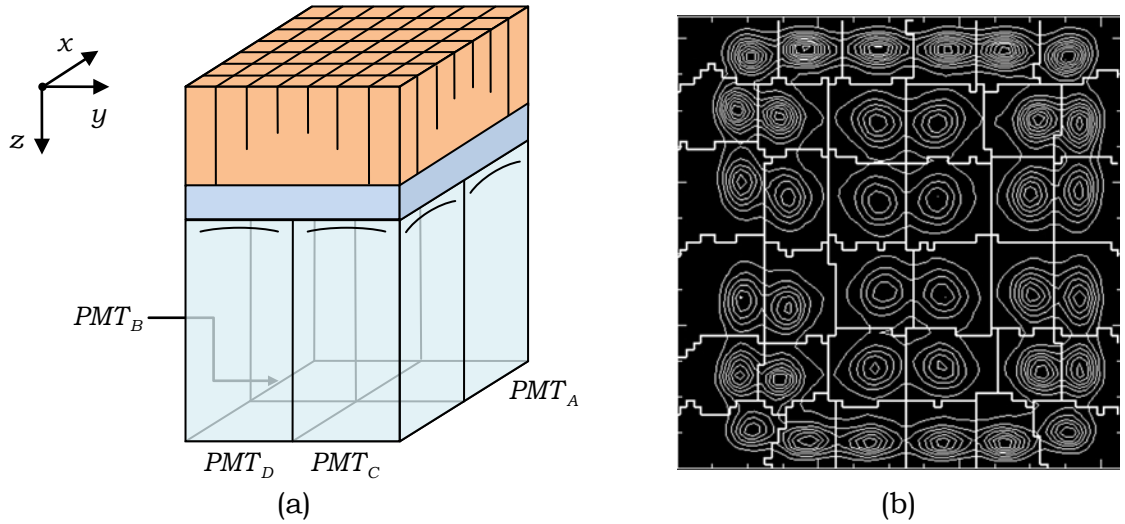

Fig. 3.8: (a) Identification of the PMTs of a block detector along the *X* and *Y* directions. (b) A block map of a 6×6 BGO crystal array viewed by four PMTs, showing iso-count curves indicating the relative light output, along with heavy white lines indicating the regions assigned to each crystal position (reproduced from [Lewellen, 2008] with consent).

Dahlbom, 2006] (with multichannel PMTs this response is linear [Cherry & Dahlbom, 2006]), the positions given by Eq. (3.10) are not used as the detection ones. Instead, the coordinates are used for comparison with a look-up table (obtained from a calibration scan), the detection being then attributed to the corresponding pixelated element of the block detector [Cherry & Dahlbom, 2006; Lewellen, 2008; Dahlbom, 2012]. Fig. 3.8 (b) shows such a map obtained for a BGO block detector, with the light white lines representing the iso-count curves and the heavy white lines delimiting the regions assigned to each crystal position.

One of the advantages of block detectors, over continuous panel ones, is that the dead time is considerably reduced. This is due to the fact that a given block is optically isolated from their neighbours, the scintillation photons being collected only by the four single-channel PMTs coupled to the block, instead of being spread among several PMTs as in the case of the continuous panel detector. Moreover, and since photodetectors are one of the most expensive components of a PET scanner [Cherry & Dahlbom, 2006], by reading a great number of pixelated elements with only four single-channel PMTs the block detector design allows to achieve higher intrinsic spatial resolutions at a reasonable cost [Cherry & Dahlbom, 2006]. Further reductions in the total cost can be achieved recurring to the so called quadrant sharing detector, in which larger PMTs are used such that the detectors placed at the outer faces of the block detector are shared by the contiguous block detectors, requiring then less PMTs and less readout channels [Cherry & Dahlbom, 2006; Dahlbom, 2012]. However, since

each of the shared PMTs must handle events from more than one detection block, this solution has the disadvantage of presenting a higher dead time, thus limiting the maximum achievable count rate [Cherry & Dahlbom, 2006; Dahlbom, 2012].

Ideally, the intrinsic spatial resolution of a pixelated block detector along the *X* and *Y* directions (Fig. 3.8 (a)), should be related to half the width of the single detection elements [Lewellen, 2008; Moses, 2011]. However, several effects limit the detector intrinsic spatial resolution. Some of the effects that may contribute to the degradation of spatial resolution are the scatter within the detection block [Lewellen, 2008], variations in the collection of scintillation photons [Lewellen, 2008], statistical variations in the signal from the photosensors [Lewellen, 2008], or even errors in the look-up table[26] [St. James et al., 2004].

Scatter in the detector leads to a clear degradation of spatial resolution (Fig. 3.9 (a)). Depending on the amount of energy transferred from the incident photons to the scintillator material in the first interaction, the interaction length of the scattered photons can be longer than the dimensions of the individual detection elements, the remaining energy being then transferred to the scintillator material in a detection element far from that where the first interaction occurred, leading to the misidentification of the detection element. This effect, which strongly depends on the amount of energy transferred to the crystal in each interaction, can be reduced by decreasing the thickness of the scintillation material along the *Z* direction, the scattered photon escaping then from the detector without a second interaction [Lewellen, 2008]. However, this also reduces the detection efficiency and impacts in the global sensitivity of the scanner [Lewellen, 2008].

Variations in light collection (Fig. 3.9 (b)) can occur due to variations in the reflectivity of each detection element [Dahlbom, 2012], multiple reflections of the scintillation photons, leading to self-absorption and/or different scintillation light distribution in the photodetectors, and due to interactions at different depths in the detector [St. James et al., 2004; St. James & Thompson, 2005].

Contrary to continuous detection panels, for which the shape of the detection signal can be used to determine the interaction depth within the crystal, block detectors as those presented so far are not able to resolve the DOI, and most systems assign the third coordinate of photon detection (along the *Z* axis of Fig. 3.6 (b) and Fig. 3.8 (a)) to a small distance from the front edge of the crystal identified as the source of the event [Lewellen, 2008]. This leads to an additional factor contributing to the

[26] During the calibration scan, the system performs a self-calibration of the crystal identification map of each block. However, sometimes it may be necessary to manually adjust the mapping for some blocks.

degradation of the spatial resolution of the reconstructed image [Cherry & Dahlbom, 2006]. Several schemes have been proposed to overcome this issue and resolve the DOI leading to the determination of the interaction point in 3D mode, two of which are presented in Fig. 3.10 (page 83).

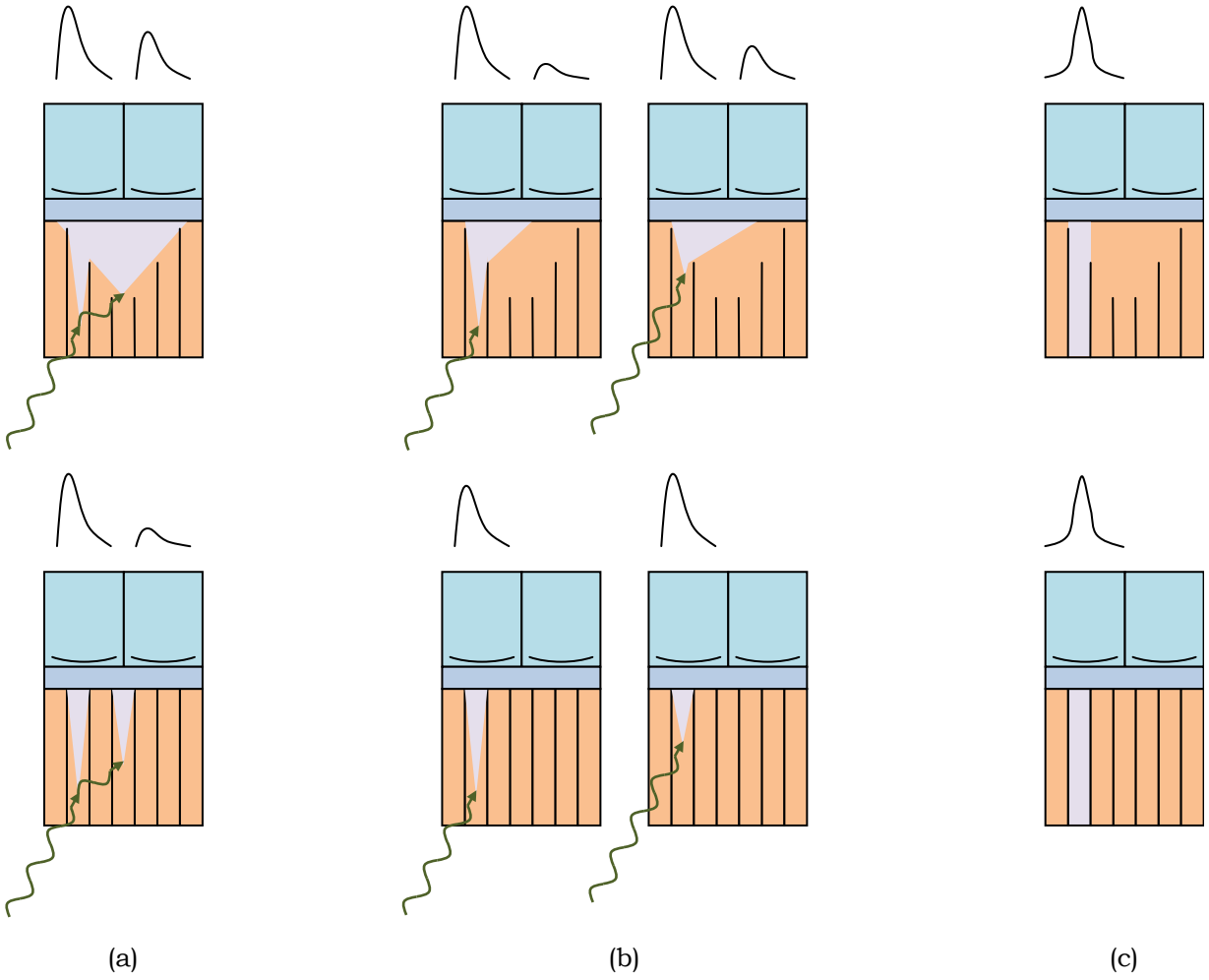

Fig. 3.9: Scheme of some sources of degradation of spatial resolution: (a) scatter within the detector; (b) efficiency of light collection and DOI; (c) statistical uncertainties on the position computed from Eq. (3.10) combined with the look-up table presented in Fig. 3.8 (b) (page 79).

3.4.2.1 Phoswitch Detectors

One of the schemes employed to address the DOI, known as *phoswitch detector* and depicted in Fig. 3.10 (a)[27], relies on the properties of different scintillator materials coupled to each other and read by the same set of PMTs [Humm et al., 2003; Cherry & Dahlbom, 2006; Lewellen, 2008]. The amplitude and time shape of the summed signal

[27] The presented scheme employs only two different scintillation materials thus allowing a limited DOI resolution. However, several layers of thinner scintillator materials can be employed.

of the PMTs depend, respectively, on the scintillation yield and decay times of each scintillator material. Both this dependences can be used for determining the scintillator module in which the interaction occurred [Humm et al., 2003], and thus to obtain a DOI resolution ideally equal to half the thickness of each scintillation module. However the phoswitch approach poses some problems.

First, the time response of the detector is determined by the scintillation material presenting the longer decay time, eventually rendering phoswitch not an attractive solution for detectors designed for TOF applications [Lewellen, 2008]. This can be partially solved by employing scintillators with shorter but still different enough decay times to allow the discrimination based on the time spectra, or by using scintillators with different enough scintillation yields to allow amplitude discrimination, or both.

Second, scattering in the detector leads to an output signal which is a combination of the outputs produced by each scintillation material, weighted by the energy deposited in each scintillator, which reduces the DOI accuracy [Lewellen, 2008]. However, time discrimination techniques allow the discrimination of scattered events [Humm et al., 2003].

A third problem arising in phoswitch detectors concerns the optical coupling between the different stacked scintillator detection elements which is critical for resolving the DOI [Humm et al., 2003] and leads to additional costs of fabrication due to the mechanical operations needed to assemble and match the crystals of both scintillation materials [Lewellen, 2008].

3.4.2.2 Dual Photosensor Detector

Another approach to determine the DOI consists in reading the scintillation light by using two photosensors placed at opposite sides of the scintillator [Humm et al., 2003; Lewellen, 2008], as depicted in Fig. 3.10 (b).

The rear end photosensor, commonly a single-channel PMT, covers the entire rear surface of the scintillator block and collects the fraction of scintillation light that reaches it, being used for energy discrimination and timing proposes [Humm et al., 2003; Lewellen, 2008]. The front end photosensor consists in a multichannel photodetector, usually an array of PIN diodes, APDs or SiPMs, with a one-to-one coupling to the pixelated elements of the detector, that collects the fraction of scintillation light reaching it, being used to identify the pixelated element where the interaction occurred [Humm et al., 2003; Lewellen, 2008].

Being A_R and A_F the summed amplitudes of the signal produced at the outputs of, respectively, the rear and front ends of the scintillation block, and rescaling the amplitude of one of the pulses to match the amplitude of the other, the position of the

interaction along the Z direction $\left(Z_{pos}\right)$ relative to the block centre can be obtained by [Humm et al., 2003]

$$Z_{pos} = \frac{A_F}{A_F + A_R} \qquad \text{or} \qquad Z_{pos} = \frac{A_R}{A_F + A_R}, \tag{3.11}$$

With this method, DOI resolution of ~2 mm has been achieved for single crystals illuminated from the side with a collimated beam of photons [Lewellen, 2008].

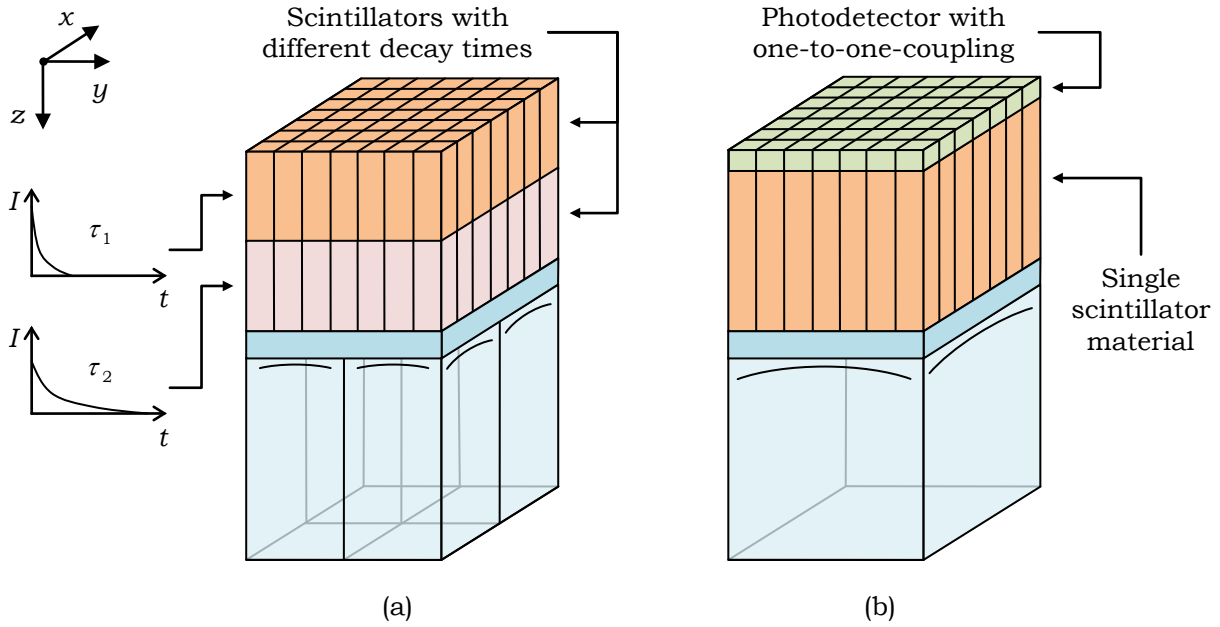

Fig. 3.10: Schemes for block detector readout with DOI information: (a) phoswitch detector read by four single-channel PMTs/photosensor; (b) single scintillator read by a single-channel PMT/photosensor and an one-to-one-coupling multichannel photosensor.

CHAPTER 4
POSITRON EMISSION TOMOGRAPHY

PET is a non-invasive medical imaging modality in which a molecule targeted to a biophysical, biochemical or physiological process is labelled with an appropriate radioactive isotope which undergoes β^+ decay. These molecules are commonly named as *radiotracers* or *radiopharmaceuticals*[1].

The radiopharmaceutical can be injected directly into the blood stream, taken orally and reach the blood stream due to absorption in the organism, or breathed in, passing to the blood stream by diffusion through the alveoli-capillary membrane. In this last case, the physiological process under study can be the lung ventilation, the permeability of the alveoli-capillary membrane, or simply be a path through which the radiopharmaceutical is administered in order to reach the blood stream. Once in the blood stream, the radiopharmaceutical is transported across the body to different organs and tissues, where it will be uptaken according to the biophysical, biochemical or physiological process to which it is targeted.

The radionuclide with which the radiopharmaceutical is labelled will undergo β^+ decay with the subsequent emission of two almost back-to-back photons with energy of ~511 keV (see Section 2.3.2.4 on page 53), which are then detected in temporal coincidence by an appropriate detection system that registers the line joining the two detectors in coincidence (the LOR), and, eventually, the time difference between the instants of detection of the two photons, called the TOF[2].

Acquired LORs can be saved in several two dimensional (2D) histograms, called *sinograms*, or can be stored in *list mode*, in which each individual LOR is recorded and

---

[1] A technical difference exists between radiotracers and radiopharmaceuticals. A radiotracer is any molecule labelled with a radioactive element and suited for the study of a biophysical, biochemical or physiological process. A radiopharmaceutical is a radiotracer that has been subjected to a pharmaceutical licencing process and obtained the required legal approval for human administration.

[2] Strictly speaking, the TOF of an annihilation photon is the time elapsed from the instant of positron annihilation to the instant of photon detection. Since it is not possible to know the exact instant of positron annihilation, the exact TOF of each annihilation photon cannot be determined. However, as will be seen later (Section 4.5, page 118), in PET the useful timing information is the time difference between the TOF of the annihilation photons detected. For that, in what follows, TOF will be used to refer to the time difference between the TOF of detected photons, as is usual in PET terminology.

retained for further processing (Section 4.2.2, page 92). Due to the photon interaction processes in the patient body and also in the detection system, registered LORs, both in sinogram or list modes, must be corrected for scatter, and also other effects, prior to be fed to an appropriate image reconstruction algorithm, which will produce a series of 2D images that are combined to produce a 3D visualization of the radiopharmaceutical biodistribution, or to an appropriate 3D image reconstruction algorithm which will give a 3D biodistribution of the radiopharmaceutical.

4.1 RADIONUCLIDES AND RADIOPHARMACEUTICALS TARGETED TO POSITRON EMISSION TOMOGRAPHY

Radionuclides used in PET are produced through suitable nuclear reactions carried out in cyclotrons, linear accelerators, nuclear reactors, or generators previously produced in one of the aforementioned systems. Due to the relative small size, less severe radioprotection requirements and much lower cost, dedicated cyclotrons are commonly used to produce radionuclides in PET centres, through the collision of charged particles (commonly proton or deuteron - ${}^{2}_{1}\mathrm{H}$) beams, accelerated to an energy usually ranging from ~9 MeV up to ~18 MeV, with a suitable target material. Linear accelerators or higher energy cyclotrons can be used to produce radionuclides by collision of charged particle beams with higher energies than those achieved by dedicated PET cyclotrons. Nuclear reactors, located in appropriate nuclear reactor facilities, may be used to produce radionuclides by nuclear reactions that involve the collision of neutrons with the target material. Generator available PET radionuclides are based in the transient equilibrium mentioned in Section 2.2.1 (page 14): the parent nuclide, produced in cyclotrons, linear accelerators or nuclear reactors, having a long half-life allowing the world-wide transportation for PET centres where the daughter nuclide is extracted by elution. After production, the radionuclide is sent to a radiochemistry facility where it undergoes an appropriate processing chain, including extraction and purification, labelling of the target molecule with the purified radionuclide, which is then submitted to a rigorous quality control process before being expedited to PET centres to be administrated to patients.

Of all the existing radiopharmaceuticals, the most used is the 2-deoxy-D-glucose molecule labelled with ${}^{18}_{9}\mathrm{F}$ and named 2-$[{}^{18}\mathrm{F}]$fluoro-2-deoxy-D-glucose, or simply FDG, which is targeted, for instance, to image glucose consumption by tumour cells. For that, an initial activity usually ranging from 185 MBq (5 mCi) to 370 MBq (10 mCi), depending on the patient weight, is intravenously injected into the patient, which then rests laying down during approximately one hour before the scanning is

made, in order for the radiopharmaceutical to be completely uptaken by the cancerous cells. Due to nuclear decay and biological excretion, at the time of examination the total activity of $\left[{}^{18}_{9}\mathrm{F}\right]$ present in the patient will be approximately half of that injected.

Some of the most common radionuclides used in PET imaging are summarized in Table 4.1, along with their physical properties, common production modes and common use in clinical practice.

TABLE 4.1: SOME RADIONUCLIDES USED IN PET ALONG WITH THEIR PHYSICAL PROPERTIES, PRODUCTION REACTIONS AND CLINICAL USES. THE MOST COMMON NUCLEAR REACTIONS USED IN THE PRODUCTION OF EACH RADIONUCLIDE ARE INDICATED AS ${}^{A}_{Z}X(a,b){}^{A'}_{Z'}Y$, WHERE ${}^{A}_{Z}X$ IS THE TARGET NUCLEUS WHICH IS BOMBARDED WITH a PARTICLES, RESULTING FROM THE NUCLEAR REACTION b PARTICLES AND THE RADIONUCLIDE ${}^{A'}_{Z'}Y$. (DATA RETRIEVED FROM [ABRUNHOSA & PRATA, 2008].)

Nuclide	$T_{1/2}$ **(min)**	β^+ **BR**	**Production**	**Radiopharmaceutical**	**Use**
${}^{11}_{6}\mathrm{C}$	20.4	99.8%	${}^{14}_{7}\mathrm{N}(\mathrm{p},\alpha){}^{11}_{6}\mathrm{C}$	$[{}^{11}\mathrm{C}]\ \mathrm{C_5H_{14}NO}$	Cellular proliferation
				$[{}^{11}\mathrm{C}]\ \mathrm{C_6H_{15}NO_2S^+}$	
				$[{}^{11}\mathrm{C}]\ \mathrm{CH_3CO_2^-}$	Oxidative metabolism
				$[{}^{11}\mathrm{C}]\ \mathrm{C_{16}H_{32}O_2}$	Fatty acids metabolism
${}^{13}_{7}\mathrm{N}$	9.97	100%	${}^{12}_{6}\mathrm{C}(\mathrm{d},\mathrm{n}){}^{13}_{7}\mathrm{N}$	$[{}^{13}\mathrm{N}]$ Ammonia	Blood flow
${}^{15}_{8}\mathrm{O}$	2.04	99.9%	${}^{14}_{7}\mathrm{N}(\mathrm{d},\mathrm{n}){}^{15}_{8}\mathrm{O}$	$[{}^{15}\mathrm{O}]$ Oxygen	Oxygen metabolism
				$[{}^{15}\mathrm{O}]$ Carbon Monoxide	Blood volume
				$[{}^{15}\mathrm{O}]$ Carbon Dioxide	Blood flow
				$[{}^{15}\mathrm{O}]$ Water	
${}^{18}_{9}\mathrm{F}$	109.8	97%	${}^{18}_{8}\mathrm{O}(\mathrm{p},\mathrm{n}){}^{18}_{9}\mathrm{F}$ ${}^{20}_{10}\mathrm{Ne}(\mathrm{d},\alpha){}^{18}_{9}\mathrm{F}$	$[{}^{18}\mathrm{F}]$ FMISO	Cellular hypoxia
				$[{}^{18}\mathrm{F}]$ ANXA5	Apoptosis
				$[{}^{18}\mathrm{F}]$ FDG	Oxidative metabolism
				$[{}^{18}\mathrm{F}]$ FLT	Cellular proliferation
				$[{}^{18}\mathrm{F}]$ FDOPA	Dopamine biosynthesis
${}^{64}_{29}\mathrm{Cu}$	762	17.86%	${}^{63}_{28}\mathrm{Ni}(\mathrm{p},\mathrm{n}){}^{64}_{29}\mathrm{Cu}$	$[{}^{64}\mathrm{Cu}]$ ATSM	Cellular hypoxia
${}^{68}_{31}\mathrm{Ga}$	67.8	89%	${}^{68}_{32}\mathrm{Ge} \rightarrow {}^{68}_{31}\mathrm{Ga}$ (generator)	$[{}^{68}\mathrm{Ga}]$ DOTA	Somatostatin receptor
${}^{82}_{37}\mathrm{Rb}$	1.26	95.5%	${}^{82}_{38}\mathrm{Sr} \rightarrow {}^{82}_{37}\mathrm{Rb}$ (generator)	$[{}^{82}\mathrm{Rb}]$ Chlorine Bromide	Cardiology

4.2 BASICS OF POSITRON EMISSION TOMOGRAPHY SCANNING SYSTEMS

Typically, human whole-body PET scanners consist of a series of detectors disposed along the surface of a cylindrical hole [Lewellen, 2008] which, for modern PET systems, can have a diameter ranging from ~80 cm to ~100 cm [Dahlbom, 2012], surrounding the patient (or object) to be imaged, as show in Fig. 4.1 (a). However, the first PET scanners, and yet some current ones developed for research proposes (e.g. Siemens P39-5H [Conti et al., 2006]) or brain imaging (e.g. PENN-PET [Karp et al., 1990]), use an hexagonal geometry as depicted in Fig. 4.1 (b), or other polygonal-like geometry, and some dual head SPECT gamma cameras, as depicted in Fig. 4.1 (c) along with the indication of dual head rotation, are also capable of PET imaging.

Despite the existence of at least one cylindrical PET systems with continuous curved detector panels (C-PET [Adam et al., 2001]), and more recently of at least two PET scanners with a set of pixelated blocks coupled to an annular light guide read by PMTs in a continuous Anger-logic design [Surti & Karp, 2004; Surti et al., 2007], scanners based on this geometry generally use a set of relatively small flat block detectors [Dahlbom, 2012], as described in Section 3.4.2 (page 77).

Generally, the terms *axial*, *transaxial* and *radial* are used to refer to three different directions [Blanco, 2011]. The axial direction is that of the scanner axis and the transaxial direction is contained in a plane perpendicular to the axial direction, named *transaxial plane* [Cherry & Dahlbom, 2006]. Due to the segmentation usually employed in PET detectors containing N_Z discrete detection elements along the axial direction, this direction is said to be divided in N_Z detection rings. As to the radial direction, is defined as that going from the scanner centre to the periphery, along a transaxial plane [Blanco, 2011]. The aforementioned directions are depicted in Fig. 4.1 (a), (b) and (c). Fig. 4.1 (d) depicts a cylindrical PET configuration along with the Cartesian coordinate system usually adopted in PET, in which the *z*-axis lies along the scanner axis, defining the axial direction, with the *XY*-plane defining the transaxial plane. Also presented are the angles ϕ and θ, referred to as the *azimuthal* and *polar angles*, respectively, the first measured from the positive portion of the *x*-axis along a transaxial plane, and the second measured from the positive portion of the *y*-axis in a direction perpendicular to the transaxial planes [Blanco, 2011].

The area of a transaxial plane comprised by the patient port is referred to as the transaxial Field Of View (FOV) while the axial length subtended by the scanner is named AFOV, usually ranging from 15 cm to 22 cm [Dahlbom, 2012]. As to the volume subtended by the patient port and the AFOV, equal to the product of the area of the transaxial FOV by the AFOV, is simply called the FOV.

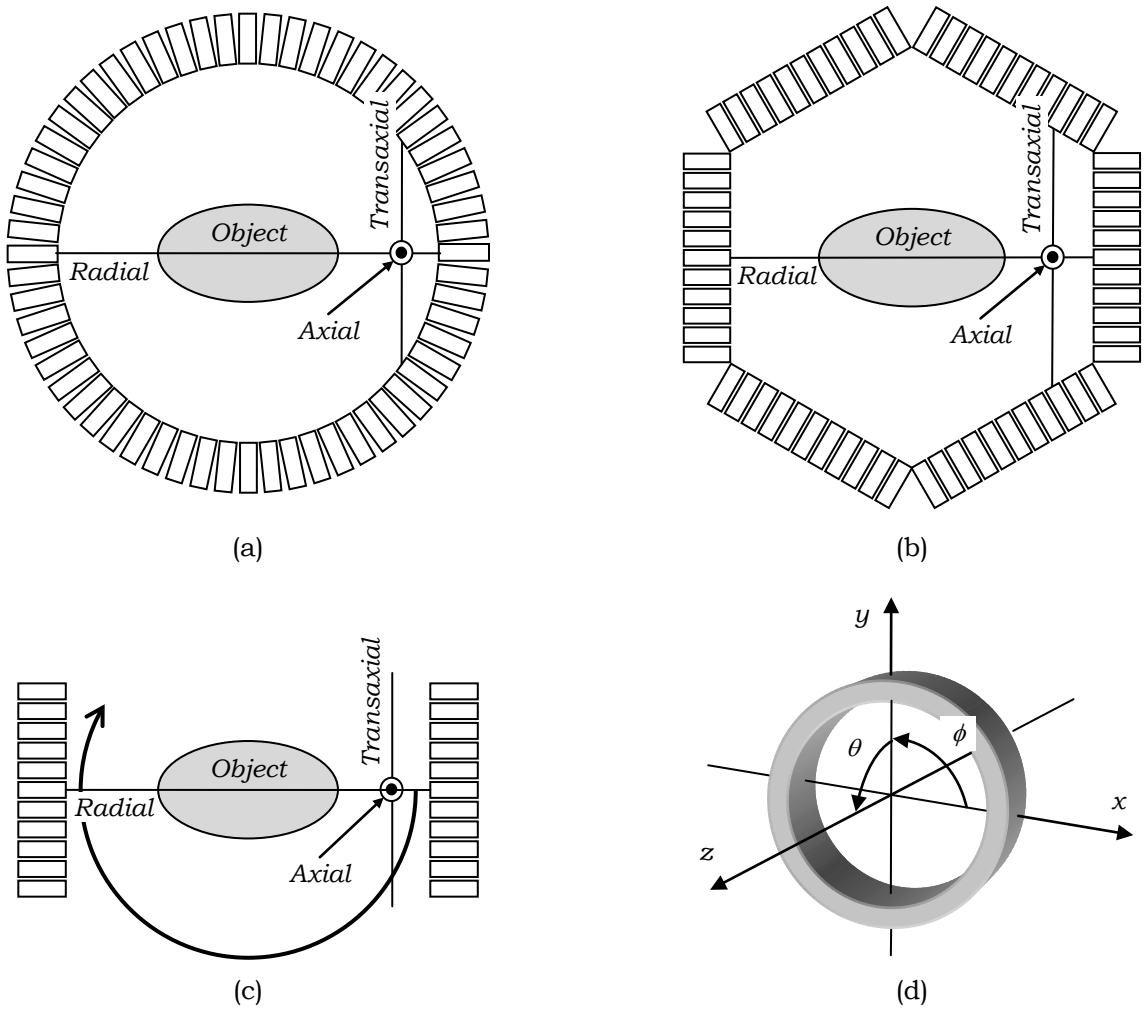

Fig. 4.1: Schemes of (a) a classical ring PET scanner, (b) a polygonal detector arrangement and (c) a dual head configuration. Also presented are the common axial, transaxial and radial directions defined in PET. A sketch of a full-ring geometry is presented in (d) along with the coordinate system commonly used to describe the system orientation as well as the azimuthal (ϕ). and polar (θ) angles, usually used to define orientations relative to *x*-axis and the *XY*-plane.

Usually, the dimensions of the opening available for patient motion in the transaxial and radial directions, commonly referred to as the *patient port*, are smaller than the scanner ring diameter and can range from 50 cm to 70 cm [Zanzonico, 2004]. This is mainly due to the existence of shields of tungsten placed outside both ends of the FOV, the propose of which is to reduce the number of photons incoming from points in the patient body located outside the FOV.

4.2.1 Coincidence Detection

Contrary to SPECT, which makes use of absorptive collimation, PET uses electronic collimation based on the time difference between the detection times of the

two annihilation photons[3] [Lewellen, 2008]. For that, in addition to the detection position, each detector generates timed pulses, with a time width τ_e, corresponding to photon detection instants which are then fed to an appropriate electronic coincidence circuitry that determines if there is an overlap between the time pulses arising from two different detectors [Cherry & Dahlbom, 2006], in which case a logic signal is generated and a coincidence is registered. Since each single pulse has a τ_e time width, the total time allowed for a coincidence to be registered, often referred to as the *coincidence time window*, is given by $\tau_c = 2\tau_e$ and can usually range from 4 to 12 ns in non-TOF systems [Cherry & Dahlbom, 2006].

Two main factors affect the choice of the width of the timed pulses generated for each Single event[4], and hence the coincidence time window: the time difference necessary for the two annihilation photons to reach the scanner detectors, which is entirely determined by the object size and scanner geometry, and the characteristic response time of the detectors and associated electronics [Cherry & Dahlbom, 2006], as mentioned in Sections 3.1.4 (page 62), 3.2.4 (page 67) and 3.3.1 (page 70). The former imposes a lower limit of ~4 ns to the coincidence time window [Moses, 2003], while the latter dictates the upper limit for the coincidence time window.

Since annihilation photons are almost anti-parallel, the detection points of the two photons in temporal coincidence allows defining the line along which the annihilation occurred (the LOR) [Cherry & Dahlbom, 2006]. By recording a large number of LORs and applying appropriate reconstruction algorithms, an image of the radiopharmaceutical biodistribution is obtained [Dahlbom, 2012]. Fig. 4.2 depicts a scheme of the coincidence detection, along with the LOR defined by the coordinates of the detection points.

Usually the coincidence circuitry does not check the triggering detector against all the remainder ones, but rather against a restrict set of opposing detectors [Cherry & Dahlbom, 2006], for which the corresponding LORs pass through the FOV. This is related both to cost issues and the dead time of the data handling system, briefly mentioned in Section 3.1.3 (page 61), and that is closely related to the segmentation of the coincidence sorter [Eriksson et al., 1994]. The more segmented the coincidence sorter is, viz., the more parallel data channels are available for coincidence processing, the smaller the load per coincidence segment and less events will be lost due to the dead time of the coincidence circuitry. As an example, Fig. 4.3 depicts the seven sets of detectors used for parallel coincidence processing of the GE Advance PET scanner, according to [Mertens & Bhend, 1993].

---

[3] Excluding SPECT systems with 511 keV rated parallel hole collimators [Lewellen, 2008].

[4] *Single events* are the individual events detected by each individual detector.

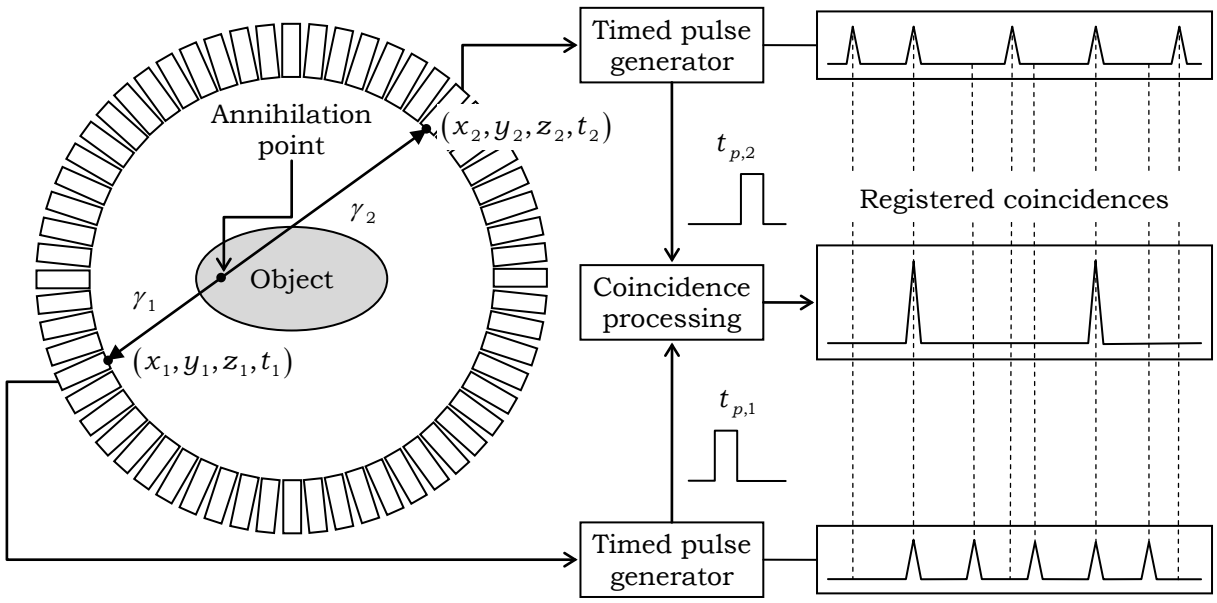

Fig. 4.2: Schematic of a PET scanner coincidence processing.
(Adapted from [Lewellen, 2008] with consent)

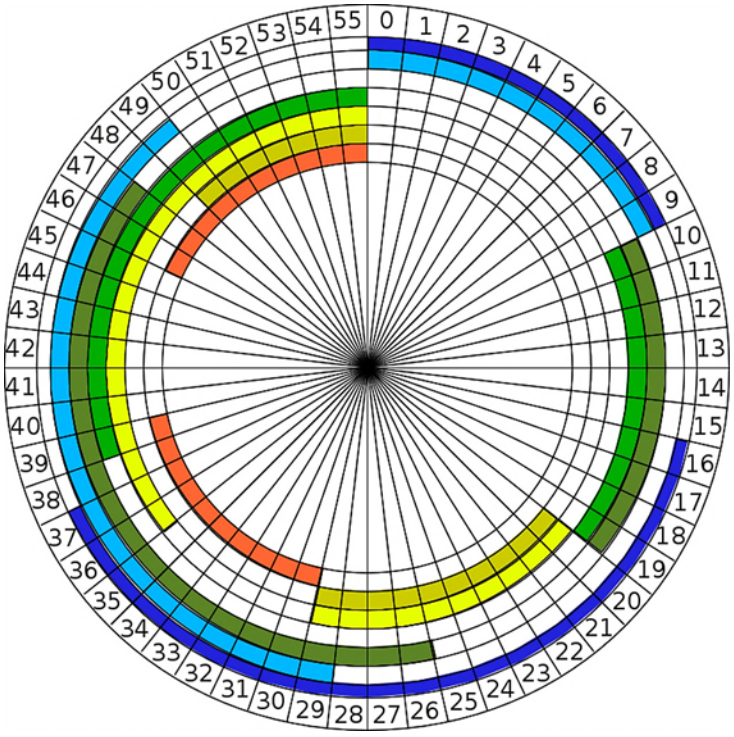

Fig. 4.3: Schemes of the segmentation of the coincidence processing circuitry employed in the GE Advance PET scanner according to [Mertens & Bhend, 1993], in which the single events coming from a set of 56 detection modules disposed along a ring, are fed to seven Application-Specific Integrated Circuits (ASICs) according to the colours presented.

Two basic schemes for coincidence detection, depicted in Fig. 4.4, are possible. In the first one, which will be referred to as *Single Time Window* (STW) *coincidence sorter* a coincidence time window is opened by the triggering event, and a new coincidence window is opened only after the first one is closed. In the second coincidence sorter, which will be referred to as the *Multiple Time Window* (MTW)*coincidence sorter*, each detected event functions as a triggering event and opens its own time window. Thus, for MTW a given event is always a triggering event and can also be a coincidence event falling in the coincidence time window opened by previous triggering events.

From what was said and from Fig. 4.4, one can conclude that the coincidence sorter (both STW and MTW) can form two distinct sets of coincidences: single coincidences, consisting of only two events detected in coincidence, and multiple coincidences, when two or more events fall in the same coincidence time window (Section 4.2.3.4, page 100).

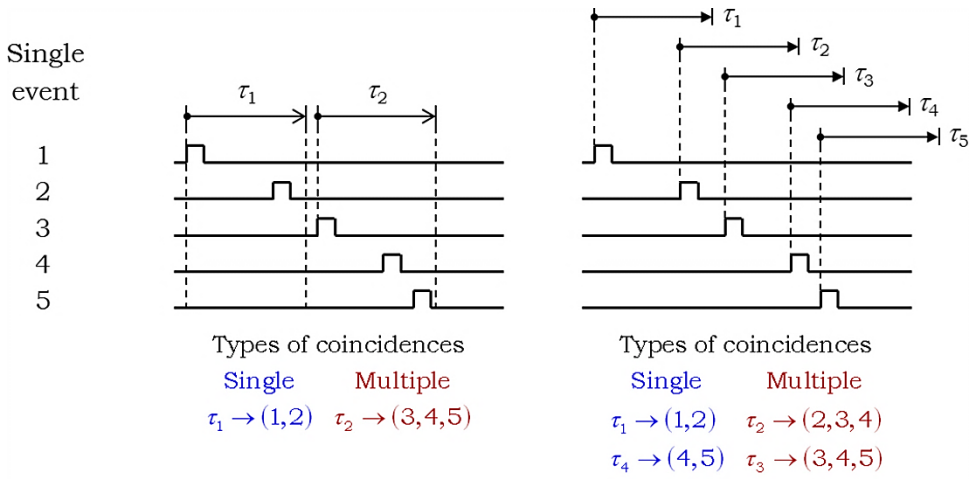

Fig. 4.4: Coincidence scheme of (a) single and (b) multiple time window coincidence sorters.

4.2.2 Data Acquisition, Representation and Storage

The first generation of PET scanners acquired data in what is known as the 2D mode, in which coincidences where registered only if occurring between detectors of the same detector ring (ring difference equal to zero), giving rise to the so called *direct* planes (or slices), and between detectors of contiguous rings (ring difference equal to ±1), giving rise to the so called *cross planes* (or slices) [Cherry & Dahlbom, 2006]. So, for a PET scanner with N_Z detection rings, a total of N_Z direct planes and $N_Z - 1$ cross planes could be defined, giving rise to a total of $2N_Z - 1$ slices [Zanzonico, 2004; Cherry & Dahlbom, 2006] with thicknesses equal to half the axial pitch between the discrete detection elements [Zanzonico, 2004]. To reduce the count rate due to

annihilation photons impinging the detectors at large angles, with the consequent increase of the LTF of the detectors and the reduction of the number of Random counts (Section 4.2.3.3, page 99), and also to reduce the number of detected photons that suffered scatter in the patient body, scanners used to have thin tungsten shields, known as *septa*, that where interposed between detection rings [Cherry & Dahlbom, 2006]. Fig. 4.5 depicts the 2D acquisition mode along with the inter-ring septa and lateral shields, as well as a view of a transaxial plane.

The decrease of the size of the detection elements led to a decrease of sensitivity (Section 4.6.2, page 124) for each direct and cross plane as defined above (ring differences of 0 and ±1) [Cherry & Dahlbom, 2006]. To overcome this problem, and hence improve the sensitivity (Section 4.6.2, page 124), direct and cross planes were still used, but larger ring differences of up to ±5 or ±6 were allowed [Cherry & Dahlbom, 2006], with the even ring differences contributing to the direct planes and the odd ones contributing to the cross planes.

The coincidence data was then acquired and stored in two dimensional matrix form, with one matrix for each plane, each element of the matrix representing the number of coincidences recorded between a specific pair of detectors for which the coincidences were checked against with, viz., along a given LOR [Cherry & Dahlbom, 2006]. The matrix was arranged such that each position within it corresponded to a well-defined combination of azimuthal angle (ϕ in Fig. 4.1 (d)) (page 89) and distance of the LOR to the scanner axis, as depicted in Fig. 4.6. This mode of acquiring, representing and storing coincidence data is known as *sinogram mode* [Cherry &

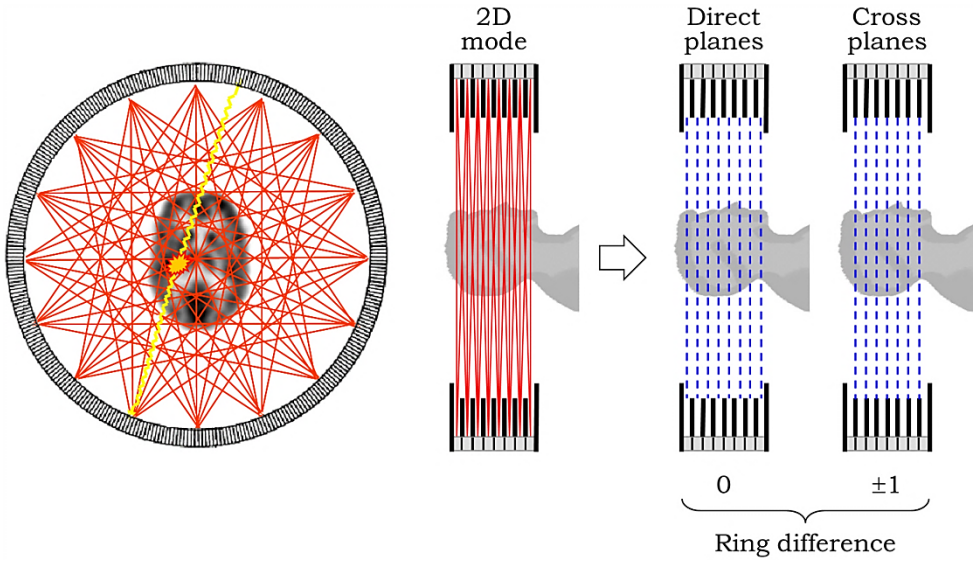

Fig. 4.5: Scheme depicting the 2D acquisition mode with LORs (red) defined in transaxial and sagittal planes, along with the direct and cross planes (blue).
(Adapted from original presentations kindly ceded by Prof. Nuno C. Ferreira)

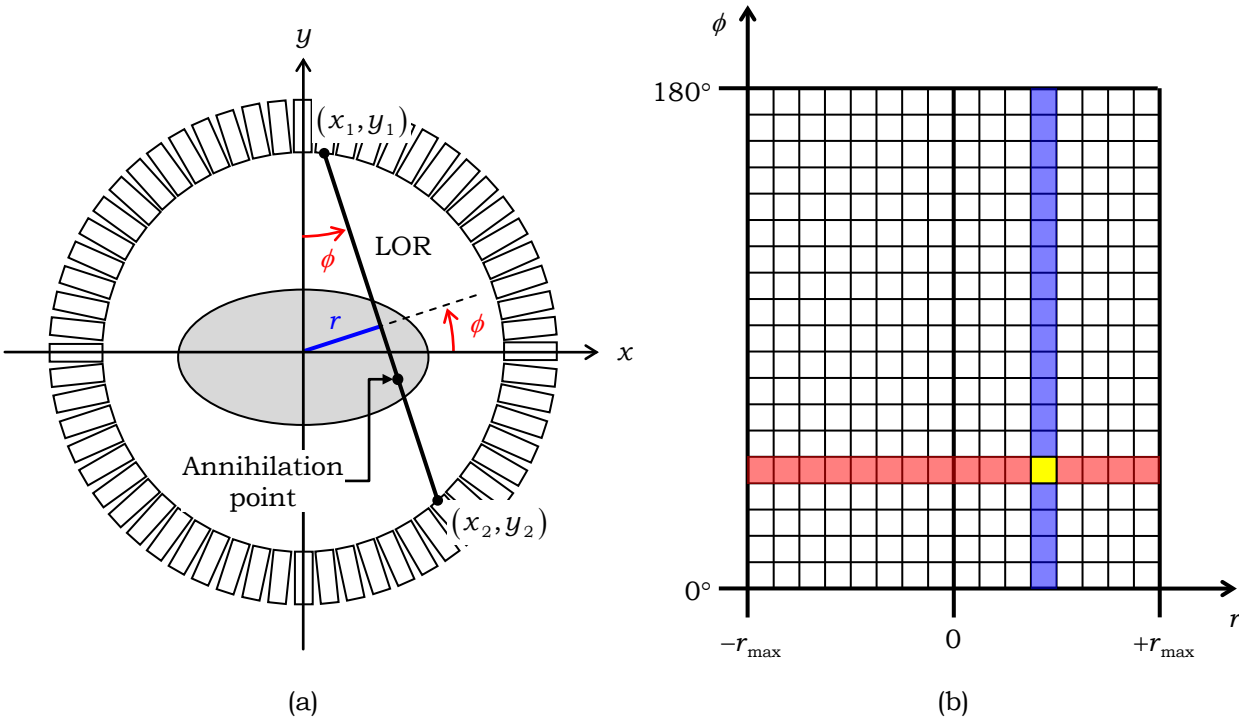

Fig. 4.6: Matrix form of acquisition and storage of coincidence data: (a) definition of the azimuthal angle and radial distance for a given LOR; (b) matrix used to store and represent coincidence data, known as sinogram. A PET scan acquisition in 2D mode has as much sinograms as the total number of slices (direct and cross).

Dahlbom, 2006]. The name comes from the relation between the radial distance, the azimuthal angle, and the coordinates of the annihilation point in the *XY* plane (x,y), given by

$$r = x\cos(\phi) + y\sin(\phi), \tag{4.1}$$

the point with coordinates (x,y) tracing a sinusoidal path in the matrix [Cherry & Dahlbom, 2006]. Fig. 4.7 depicts an object and the sinogram that would be obtained.

Instead of using the pair of detectors that register the coincidence to bin directly the data into a matrix, the sinogram, $S(r,\phi)$, can be obtained from the coordinates of the detection points of the two photons, (x_1,y_1) and (x_2,y_2), by first computing the azimuthal angle from

$$\phi = \begin{cases} \arccos\left(\dfrac{|y_1 - y_2|}{\ell}\right) & (x_1 - x_2)(y_1 - y_2) < 0 \\ 180° - \arctan\left(\dfrac{|y_1 - y_2|}{\ell}\right) & (x_1 - x_2)(y_1 - y_2) \geq 0 \end{cases}, \tag{4.2}$$

and then applying Eq. (4.1) with $(x,y) \equiv (x_1,y_1)$ or $(x,y) \equiv (x_2,y_2)$[5].

[5] Notice that any point along the LOR has always the same (r,ϕ) coordinates.

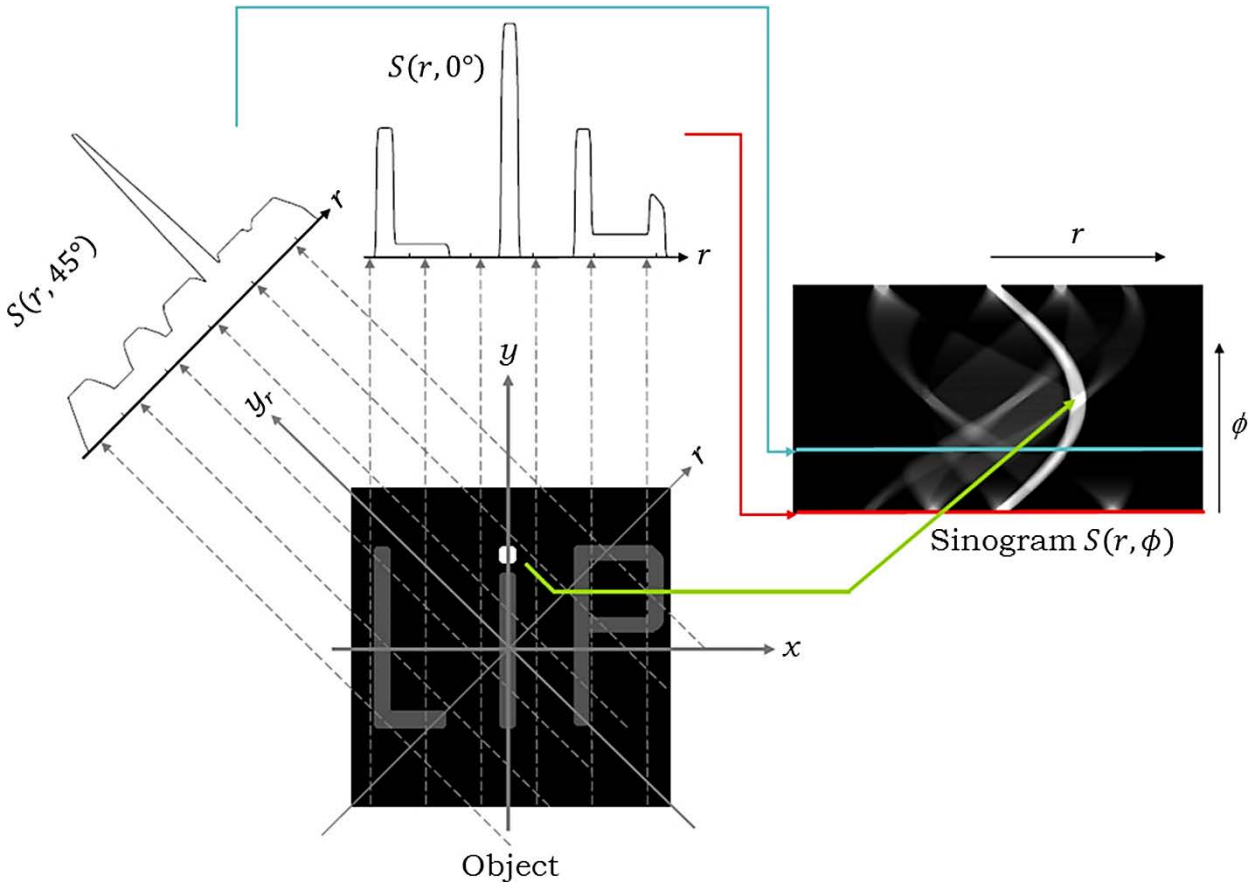

Fig. 4.7: Image of an object (LIP characters) and the corresponding sinogram showing the sinusoidal pattern produced by a point source (the most intense white line of the sinogram corresponds to the dot over the *I* character). Also given are the intensity profiles of the image obtained for $\phi = 0°$ and $\phi = 45°$, and their insertion in the sinogram.
(Adapted from [Blanco, 2011] with consent).

What was mentioned is also valid for the so called 3D mode of acquisition in which the septa between adjacent rings are removed in order to increase the scanner sensitivity (Section 4.6.2, page 124), and which is the only mode of operation of most modern PET scanners [Dahlbom, 2012]. However, now, in addition to the direct and cross planes, there are all possible oblique planes, as depicted in Fig. 4.8, in a total of N_z^2, which are stored in independent sinograms to avoid resolution loss for the source points located out of the scanner axis, leading to a considerable increase of the raw data to be saved [Cherry & Dahlbom, 2006]. For instance, for a PET scanner with 18 independent detection elements along the axial direction, acquiring data in 2D mode, a total number of 35 sinograms have to be stored for being then used by a 2D reconstruction algorithm that will produce an image for each transaxial plane which, when combined together, hold a 3D image of the radiopharmaceutical distribution. For a full 3D acquisition, the number of sinograms to be stored in order to avoid data loss

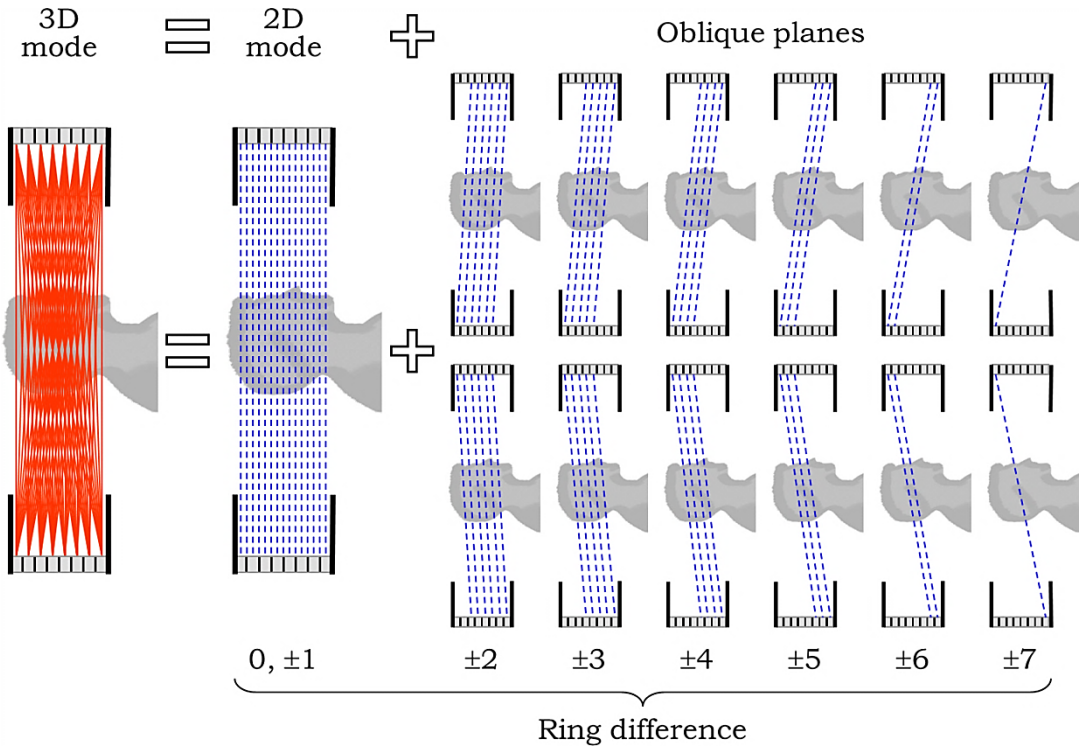

Fig. 4.8: Scheme depicting the 3D acquisition mode with the LORs (red) in a sagittal plane, along with the direct, cross and the oblique planes (blue).
(Adapted from original presentations kindly ceded by Prof. Nuno C. Ferreira)

increases to 324, which will then be used by an appropriate 3D reconstruction algorithm to produce a more accurate biodistribution of the radiopharmaceutical.

Each sinogram acquired in 3D mode has a ring difference associated with it, which can be positive or negative depending on the slope of the LORs relative to scanner axis (Fig. 4.8). This ring difference can be translated into an angle, commonly known as the polar acceptance angle, which for cylindrical PET scanners is given by

$$\theta = \pm \arctan\left(\frac{\Delta d_a \left|\Delta r\right|}{2R}\right), \tag{4.3}$$

where Δd_a is the width of each detection element along the axial direction, and $\Delta r = r_1 - r_2$ is the ring difference.

For dynamic studies, involving the visualization of the evolution of the biodistribution of the radiopharmaceutical along time, with acquisition in sinogram mode (both in 2D or 3D mode), a complete set of sinograms must be acquired over time, with each set corresponding to a fixed time length Δt (or frame) that must be specified prior to acquisition [Cherry & Dahlbom, 2006] and such that the statistics contained in each set of sinograms allow to reconstruct the image with the required quality. However, by specifying the time interval prior to acquisition, important time

information may eventually be lost. To overcome this problem, the time interval can, in principle, be made as small as wished and then, prior to reconstruction, the sinograms for several contiguous frames can be added to create a new set of frames with improved counting statistics while maintaining the relevant time information. In the limit, this can lead to complete sets of sinograms containing a very small number of counts leading then to a considerable amount of waste of storage space. So, instead acquiring data in sinogram mode it may be preferable to store the information of each acquired LOR, such as $(r,\phi,\Delta r,t)$ with t the time stamp at which the LOR was acquired, or $(x_1,x_2,y_1,y_2,z_1,z_2,t_1,t_2)$, where the indexes 1 and 2 represent the two detection points of the LOR. This mode of acquisition is known as *list mode* [Cherry & Dahlbom, 2006] and is the one used in modern PET scanners [Blanco, 2011]. The acquired LORs can then be used in a LOR based full 3D reconstruction algorithm or gathered to form the sets of sinograms representing each acquisition frame with the desired time width in case of dynamic studies, and the bins in the radial and azimuthal directions chosen to meet the requirements of the intended spatial resolution.

4.2.3 Types of Events in Positron Emission Tomography

Since PET systems rely on the ability to form LORs based on temporal coincidence between single events, there is no guarantee that a given registered coincidence corresponds to a pair of photons arising from the same annihilation, and even less that arising from the same annihilation the corresponding LOR passes through the annihilation point or even near it, with the deviation being exclusively due to detector intrinsic spatial resolution or photon acollinearity. In fact, there are four types of coincidences that can be formed by the detection system and that are commonly grouped under the names of *True*, *Scattered*, *Random* and *Multiple* coincidences or events. Fig. 4.9 depicts some examples of these four types of coincidences.

4.2.3.1 True Coincidences

From the previous sections, it is clear that the LORs that should be acquired in PET systems are those for which the two photons have their origin in the same annihilation and that do not suffer any interaction, neither in the object to be imaged nor in the detection system, prior to the one allowing their detection. These coincidences are called *True coincidences* or *True events*.

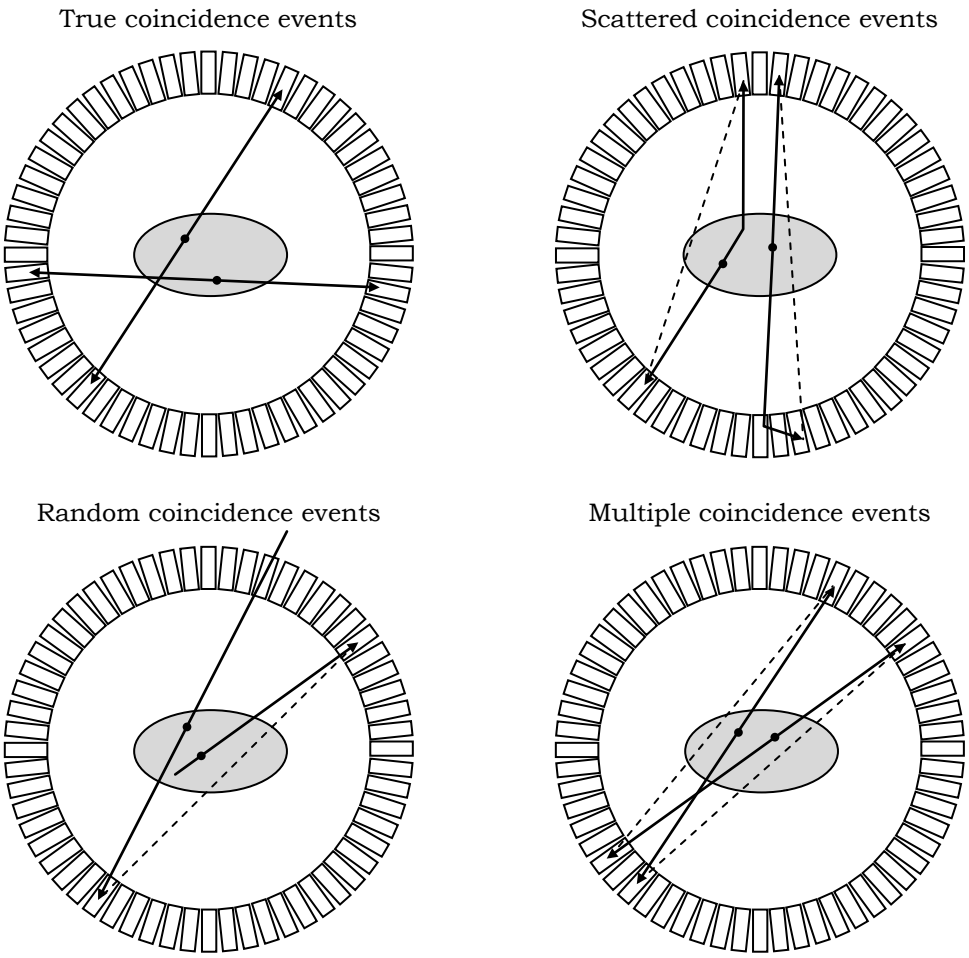

Fig. 4.9: Schemes of possible coincidence events in PET. Dots inside the object represent the annihilation points and full lines represent the trajectories of annihilation photons, with the arrows representing the detection points. Dashed lines represent detected LORs, with the exception for the True coincidence events, for which LORs coincides with the straight full lines representing the paths of annihilation photons, and the Multiple coincidence events for which, besides the two LORs indicated by the dashed lines, the full lines representing annihilation photon paths also represent possible LORs (Redrawn from [Blanco, 2011].)

4.2.3.2 Scattered Coincidences

As seen in Section 2.3.1 (page 25), photons can be partially absorbed and scattered when passing through matter, being deviated from their initial trajectories. For a 4 ns coincidence time window (the aforementioned lower limit) the maximum allowed difference in the distances travelled by both photons for still being detected in coincidence is ~120 cm. So, if both photons from the same annihilation are detected after one or both of them have suffered scatter in the patient body or in the scanner, it is most likely that they will be detected in coincidence. In this case, the LOR defined by the two annihilation photons is in fact a True event in the sense that both photons

have their origin in the same annihilation [Cherry & Dahlbom, 2006; Lewellen, 2008]. However, due to photon scatter, the LOR defined by the coincidence event, and which is named *Scattered coincidence* or *Scattered event*, do not contain the annihilation point, and will contribute to the degradation of spatial resolution and contrast in the final reconstructed image [Cherry & Dahlbom, 2006; Lewellen, 2008].

The degradation of the image spatial resolution and contrast due to Scattered coincidences can partially be reduced if the detection system has some sort of energy resolution and/or energy-dependent sensitivity. In the first case, which is the preferred one and that is used in current commercial PET systems for human studies, an appropriate energy window can be applied to Single events, thus rejecting those for which the total energy deposited in the detector is below a given threshold. In the case of scatter rejection from energy sensitivity, the rejection is governed solely by the cross sections of the materials from which the detectors are made of, which, as seen in Section 2.3.1 (page 25), depend on the incident photon energy. This is the case, for instance, of gaseous detectors without energy resolution, currently used in specific PET applications, such as the HIDAC small animal PET scanner [Jeavons et al., 1999] or the RPC TOF-PET system discussed in the current work. The amount of Scattered events accepted in a PET scan can also be reduced by using collimators, as mentioned in the previous section, with the consequent reduction of the overall system efficiency [Dahlbom, 2012].

Even with the above mentioned methods, and depending on the object size, scanner geometry, acquisition mode and detector technology, the percentage of Scattered coincidences detected in typical PET studies, can range from 15% to more than 50% of the total registered coincidences [Cherry & Dahlbom, 2006].

4.2.3.3 Random Coincidences

In common PET systems, 90% or more of the detected Single events are unpaired, in the sense that only one of the annihilation photons is detected, the other photon being absorbed in the object, not traversing the detection system or passing through it without interacting, interacting by Rayleigh scattering without being detected, or even interacting by Compton scattering but being rejected due to small energy deposition in the detector [Cherry & Dahlbom, 2006]. Since all the detected photons are fed into the coincidence circuitry, it may happen that two unpaired single events are found to be in temporal coincidence giving rise to a false LOR. This type of coincidence events are named *Accidental coincidences*, *Random coincidences* or *Random events*, and contribute to the degradation of the contrast in the final reconstructed image [Cherry & Dahlbom, 2006].

If the count rates of Single events detected by two detectors, for which coincidences are registered, are equal to R_1 and R_2, then the Random count rate in the LOR joining the two detectors is given by [Cherry & Dahlbom, 2006]

$$R = 2\tau_e R_1 R_2 \quad \Leftrightarrow \quad R = \tau_c R_1 R_2, \tag{4.4}$$

with τ_e and τ_c as defined in Section 4.2.1 (page 89).

The total Random count rate on a PET study is equal to the sum of the Random count rates extended to all possible detector pairs against with the coincidences are checked, and depend on the width of the coincidence time window, the total activity of the radiopharmaceutical present in the scanner FOV, the polar angle used for coincidence acceptance (Fig. 4.1 (d), page 89), and the scanner axial extent. The dependence on the total FOV activity and the width of the coincidence time window follows immediately from Eq. (4.4). As to the dependence on the polar acceptance angle and the scanner axial extent follows from the fact that, with the increase of any or both of them, the number of detector pairs available for coincidence triggering also increases with a consequent increase in the total Random events rate.

Random rejection can be performed during acquisition through Compton kinematics in PET scanners employing detectors with high spatial and energy resolutions [Chinn & Levin, 2008], or, in PET scanners with high TOF resolutions, through rejection of LORs for which direct TOF reconstructed point falls outside a tight region of interest surrounding the patient or object to be imaged (Section 10.4, page 275).

4.2.3.4 Multiple Coincidences

Multiple coincidences, already briefly referred to in Section 4.2.1 (page 89), can occur when three or more events are detected in coincidence. The events in coincidence can be due to photons from unrelated annihilations, to two or more True or Scattered LORs, or from a Scattered or, often [Cherry & Dahlbom, 2006], a True event and a third photon from an unrelated annihilation. In any of the aforementioned cases, it may happen that the several LORs that can be formed from the multiple coincidences can pass through the FOV or, more restrictively, through the object. Since it is not possible to unambiguously determine which of those LORs correspond to True events, Multiple events are usually discarded in current PET systems [Cherry & Dahlbom, 2006; Dahlbom, 2012]. However, since many of the Multiple coincidences contain True events, they are a source of data loss or dead time [Dahlbom, 2012]. For this, in some circumstances, it may be preferable to accept some of those LORs corresponding to Multiple events, for instance, based on the energy deposited by each

photon in the detector, or randomly selecting one out of the multiple LORs formed by Multiple coincidences [Cherry & Dahlbom, 2006].

For scanners with detectors capable of providing a detection position in full 3D mode and with high spatial and energy resolution, the kinematics of Compton interactions can be used to select one out of the multiple possible LORs formed by Single events in multiple coincidence [Chinn & Levin, 2008]. For detectors with high TOF resolution, the TOF information can be used to accept the LOR with the lowest time difference [Yoshida & Yamaya, 2013], or those LORs for which the direct TOF reconstructed point falls inside a tight region of interest surrounding the patient or object to be imaged [Couceiro et al., 2012].

4.2.3.5 Prompt Coincidences

Prompt coincidences consist in the complete set of coincidences registered by the PET system, and include the True, Scatter and Random coincidences. For scanners retaining some of the multiple coincidences, these will be included in one of the three previous mentioned coincidence sets.

4.3 DATA CORRECTION

Data acquired by a PET system, both in sinogram or list mode, must first be corrected for several factors, which contribute to the loss of spatial resolution or degradation of image quality, prior to be fed to a reconstruction algorithm. Those factors, and the order in which they are usually corrected for [Blanco, 2011], include non-uniformity of the sampling along the radial direction, Random counts, dead time, non-uniformity of detection efficiency throughout the scanner FOV, attenuation of detected LORs in the patient body or object that is to be imaged, and scatter. The methods employed in the aforementioned corrections may rely on data collected for correction, analytical models, or even simulation techniques. In what follows the corrections for all these effects will be briefly addressed.

4.3.1 Arc Correction

For cylindrical PET scanners based on discrete detection elements, as those of a block detector without DOI information, for which the detection points are assigned to a small distance from the detector surfaces, the LOR density along the radial direction is related to the spacing between the LORs contained in the transaxial plane. For a given value of the projection angle ϕ, this leads to a non-uniform LOR density in the radial direction, as depicted in Fig. 4.10, for which the distance between two LORs is

given by [Defrise & Kinahan, 1998]

$$\Delta r_i = \Delta d_t \sqrt{1-\left(\frac{r_i}{R}\right)^2}\,, \tag{4.5}$$

where Δr_i and r_i are, respectively, the width and distance to the centre of the sinogram of the i^{th} bin, Δd_t is the width of each detection element along the transaxial direction and R is the radius of the scanner. For acquisition in sinogram mode, data is interpolated so that the radial bins of the sinogram have a uniform spacing equal to $\Delta r = \Delta d_t/2$, with the binning along the azimuthal angle being $\Delta\phi = \Delta\varphi$ [Defrise & Kinahan, 1998]. For list mode of acquisition, the LORs may also be resampled so that the LOR density across the transaxial FOV is constant. The resampling with interpolation of the radial direction so that the radial bins of the sinograms have the same width is known as *arc correction* [Defrise & Kinahan, 1998].

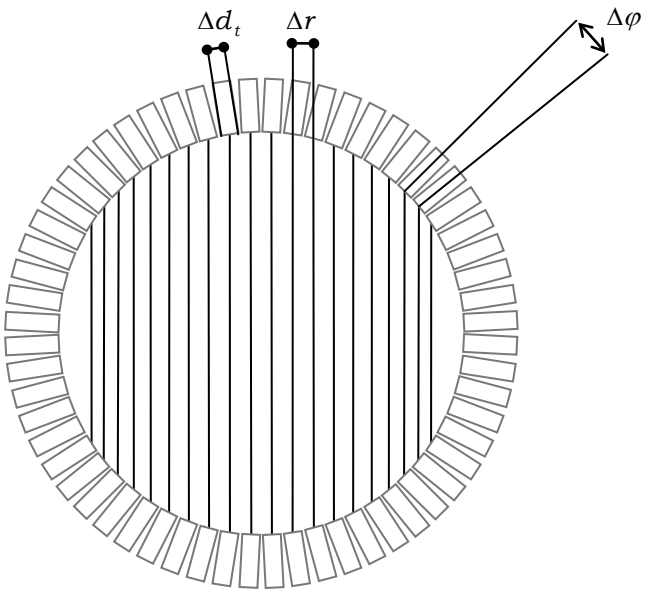

Fig. 4.10: Effect of discrete detection elements on the sampling along the radial direction.

4.3.2 Random Counts Correction

The total number of Random counts can be estimated directly from Eq. (4.4), by knowing the Singles count rates of each detection element and the acquisition time, or by using a method referred to as the delayed coincidence window technique [Dahlbom, 2012], in which a random delay (considerably greater than τ_c) is added to the time pulses generated by one of the detectors prior to the events being processed by a parallel coincidence circuit that registers the number of random coincidences (see, for instance, [Mertens & Bhend, 1993]).

By subtracting the number of Random counts from the total counts, the counts corrected for Random coincidences are then obtained [Cherry & Dahlbom, 2006].

Although the Random count rate can be estimated by one of the above mentioned methods, and used to correct for Random events, the correction introduces additional noise in the effective True count rate, being then desirable to minimize the number of Random events detected [Dahlbom, 2012], which, for a given scanner geometry and acceptance on the polar acceptance angle, can be achieved by reducing the activity in the field of view and/or the coincidence time window.

4.3.3 Normalization Correction

A modern PET scanner has thousands of individual detection elements with slightly different efficiencies, due to, among others, variations in physical dimensions and light output of each detection element, variations in light collection by the photodetectors and QE along its surface, variations in energy threshold and timing settings, as well as geometric factors which include the dependence of efficiency with the incidence angle of the photons on the detector surface. To correct the acquired counts for these efficiency variations some methods can be employed.

One of the methods consists in performing a scan with a uniform plane source from which all possible LORs are acquired, which are then used to compute the relative efficiencies of each pair of detectors [Cherry & Dahlbom, 2006]. This method has the inconvenience of requiring a very low activity source to minimize errors due to pileup and dead time [Cherry & Dahlbom, 2006]. As a consequence, the time needed to acquire a complete scan with enough statistics to minimize the counting errors is considerably high [Cherry & Dahlbom, 2006].

Another method consists in computing the coincidence efficiency of each pair of detectors by using geometrical empirical factors g_{ij}, with i and j representing the individual detectors against with coincidences are checked, and the individual detection efficiencies of each detector, ε_i and ε_j, which can be obtained from a calibration scan performed with an uniform cylindrical phantom or any other circularly symmetric source centred in the FOV [Cherry & Dahlbom, 2006]. From these data the coincidence efficiency of each pair of detectors can be computed by

$$\varepsilon_{ij} = g_{ij}\,\varepsilon_i\,\varepsilon_j . \tag{4.6}$$

For the former method, the normalization coefficients are computed as the inverse of the relative detection efficiencies, while for the latter one the normalization coefficients are the inverse of the coincidence efficiencies computed from Eq. (4.6) [Cherry & Dahlbom, 2006]. The normalization correction is then performed by

multiplying each LOR or each individual bin of the sinograms by the normalization coefficients.

4.3.4 Dead Time Correction

As mentioned in Section 3.1.3 (page 61), for high count rates, detector dead time and the dead time of the data handling system, which includes not only the dead time of the coincidence circuitry (Section 4.2.1, page 89) but also the real-time sorting of coincidence data into sinograms (if applicable) and the time needed for data to be transferred across the data handling system [Cherry & Dahlbom, 2006], reduces the number of detected events.

Taking Eq. (3.1) and Eq. (3.2), the measured count rates for the two limiting models of dead time behaviour (paralyzable and non-paralyzable) can be given by [Cherry & Dahlbom, 2006]

$$N_{Meas} = N_{True}\, \mathrm{e}^{-R_t \tau_p}, \tag{4.7}$$

$$N_{Meas} = \frac{N_{True}}{1 + R_t \tau_{np}}, \tag{4.8}$$

where N_{Meas} and N_{True} are the measured and true number of counts which can then be computed by solving Eq. (4.7) and Eq. (4.8) for N_{True}.

As said in Section 3.1.3 (page 61), in practice the dead time is a combination of non-paralyzable and paralyzable dead time models, and must be modelled for each scanner [Blanco, 2011].

4.3.5 Attenuation Correction

Due to the interaction of photons within the patient body, True events are decreased due to the escape of one of the annihilation photons from the FOV, or being detected after suffering scatter within the patient or object to be imaged contributing then to the increase of Scattered coincidences. These two effects combined lead to distortions of the activity distribution in the reconstructed image as well as the loss of quantitative information [Dahlbom, 2012]. Considering Fig. 4.11, the probability that each photon escape from an homogeneous medium without undergoing any kind of interaction can be computed from Eq. (2.64) (page 42) holding

$$\begin{aligned} p_1(x) &= \mathrm{e}^{-\mu x} \\ p_2(x) &= \mathrm{e}^{-\mu(D-x)} \end{aligned}. \tag{4.9}$$

The probability that the two photons leave the medium without undergoing any kind of interaction, thus being registered as a True coincidence, is given by

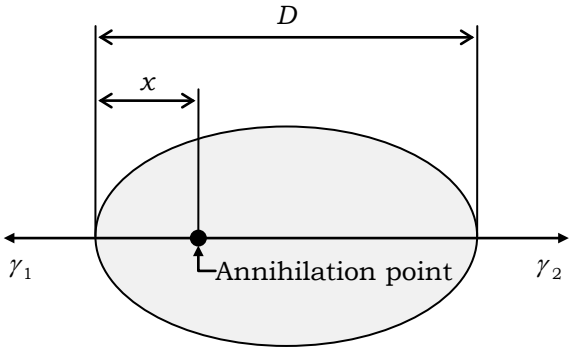

Fig. 4.11: Annihilation photons emitted from a point source within a medium with a constant attenuation coefficient, μ. The medium has a total length D along the annihilation direction and the length traversed by each photon is x for γ_1 and $D-x$ for γ_2.

$$p(x) = p_1(x)\, p_2(x) \quad \Leftrightarrow \quad p(x) = \mathrm{e}^{-\mu x}\, \mathrm{e}^{-\mu(D-x)} \quad \Leftrightarrow \quad p(x) = \mathrm{e}^{-\mu D}. \tag{4.10}$$

So, the probability of a pair of annihilation photons escaping from a homogeneous medium without undergoing any kind of interaction depends only on the total length of the medium traversed by both annihilation photons.

For heterogeneous mediums the probability that a pair of annihilation photons escape the object without undergoing any interaction is given by

$$p(x) = \mathrm{e}^{-\int_0^D \mu(\ell)\, d\ell}. \tag{4.11}$$

This result is a unique characteristic of coincidence detection and greatly simplifies the procedure for attenuation correction [Dahlbom, 2012], which can be achieved by acquiring an attenuation map of the patient or object to be imaged, from which the mean attenuation coefficient along each possible LOR is computed and used in Eq. (4.10) to obtain the attenuation correction factors. The number of coincidence events registered between any given pair of detectors, is then multiplied by the attenuation correction factor, to correct for attenuation.

Since the attenuation correction factors are independent of the source position, depending only on the total length traversed by the pair of annihilation photons, the attenuation map can be obtained by first performing an acquisition with an external source (a long lived radionuclide decaying by β^+ emission) without any attenuation medium placed in the FOV (called blank scan), followed by an acquisition with the patient or object to be imaged in place for PET acquisition. The attenuation correction coefficients are then equal to the ratio of the intensities measured in the blank scan to those measured with the patient placed in the FOV. This procedure has the advantage of computing the attenuation map for the energy of 511 keV photons, not requiring a correction of the attenuation coefficients. The major drawback is the time needed to

acquire the transmission scan, which can range from one third to half the time required to perform a complete PET scan [Dahlbom, 2012].

Since modern PET scanners have a CT prior to it, the CT image can thus be used to generate an almost noiseless attenuation correction map. However, since CTs use X-ray tubes with accelerating potentials ranging from 120 to 140 kV resulting in average X-ray energies of about 70 keV [Dahlbom, 2012], the attenuation map has to be rescaled for 511 keV.

4.3.6 Scatter Correction

Scattered coincidences are only distinguishable from True ones in what total energy deposited for the LOR is concerned [Cherry & Dahlbom, 2006]. For this, Scatter correction is one of the most difficult corrections to perform in a PET scanner [Cherry & Dahlbom, 2006]. Several methods have been proposed to correct for scatter in a PET acquisition.

The most simple and straightforward method assumes that Scattered events have a smooth variation across the FOV and are relatively independent of the source distribution and attenuation medium, the Scatter being then estimated by fitting a smoothly variable function, such as a Gaussian or a polynomial one, to the counts contained in the projection data (the sinograms) registered outside of the patient or object to be imaged, the resulting fitted function being then used to hold the corrected projection data from the uncorrected one by deconvolution [Cherry & Dahlbom, 2006].

In general, the assumption on which this method relies are not valid and the method only hold reasonable results for uniform and symmetrical source distributions such as those used to obtain the correction function [Cherry & Dahlbom, 2006].

Another method employed to correct for Scattered coincidences, consists in using two contiguous energy windows for event discrimination, the upper one being the energy window for accepting True coincidences (for instance 400 to 600 or 650 keV) while the lower one can range from an Low Level Discrimination (LLD) of 250 keV to an Upper Level Discrimination (ULD) equal to the LLD of the True coincidence discrimination, being used to register Scattered events [Cherry & Dahlbom, 2006]. A fraction of the events registered in the lower energy window is then subtracted from the events registered in the upper one [Cherry & Dahlbom, 2006]. To accomplish this, data acquired in calibration scans is used to compute calibration factors that account for the counting efficiency of the two energy windows [Cherry & Dahlbom, 2006].

This method has some drawbacks. First, due to the finite energy resolution of the detectors, both energy windows have a mixture of Scattered and unscattered events,

and, second, the lower energy window is more likely to contain multiple Scattered events that have a different spatial distribution then single Scattered ones, which are more likely to occur in the upper energy window [Cherry & Dahlbom, 2006].

The most accurate methods to correct for Scattered events are those based on simulations using appropriate source and attenuation distributions [Dahlbom, 2012]. The emission data is first reconstructed without scatter correction to hold an approximate distribution of the activity which, along with the attenuation map, can be used to estimate scatter by using a single scatter model, an analytical model or simulation based Monte Carlo (MC) methods[6] [Cherry & Dahlbom, 2006].

The procedure can be repeated iteratively until the desired image quality is attained. The obvious drawback is that it is time consuming, especially if MC methods are used.

4.4 IMAGE RECONSTRUCTION

After acquisition and correction, the coincidence data is fed to a tomographic image reconstruction algorithm, the goal of which is to produce an accurate image of the biodistribution of the radiopharmaceutical so that quantitative information can be retrieved and analysed to support medical diagnosis and treatment.

Two main classes of reconstruction algorithms are employed in PET systems: those based on the mathematics of analytic reconstruction, and those based on iterative reconstruction involving statistical methods. Both classes of methods present advantages and disadvantages.

4.4.1 Analytic Methods

The projection of an activity distribution, described by an analytical function $a(x,y)$, for a given radial distance r from the centre of the activity distribution and azimuthal angle ϕ, is given by [Defrise & Kinahan, 1998]

$$s(r,\phi) = \int_{-\infty}^{+\infty} a(x,y)\,dy_r \,, \tag{4.12}$$

where the integral is computed along the rotated Y direction (see Fig. 4.7 on page 95). For a 2D activity distribution the relation between the coordinates (x,y) of the activity distribution and those of the rotated frame (x_r,y_r) or (r,y_r), is given by [Defrise & Kinahan, 1998]

[6] Monte Carlo simulation methods employ random sampling techniques. The name was given after the Monte Carlo casino which was, and probably still is, the most famous casino where games involving random drawings were played [Buvat & Castiglioni, 2002].

$$\begin{bmatrix} x \\ y \end{bmatrix} = \begin{bmatrix} \cos(\phi) & -\sin(\phi) \\ \sin(\phi) & \cos(\phi) \end{bmatrix} \begin{bmatrix} r \\ y_r \end{bmatrix}, \tag{4.13}$$

and, by inverting Eq. (4.13), the coordinates (r, y_r) can be computed from the coordinates (x, y) and the azimuthal angle ϕ, holding

$$\begin{bmatrix} r \\ y_r \end{bmatrix} = \begin{bmatrix} \cos(\phi) & \sin(\phi) \\ -\sin(\phi) & \cos(\phi) \end{bmatrix} \begin{bmatrix} x \\ y \end{bmatrix}, \tag{4.14}$$

which lead to Eq. (4.1) for the radial distance to the centre of the activity distribution.

If the function $s(r,\phi)$ is known, then an approximation to the activity distribution, $a'(x,y)$, can be obtained by computing [Defrise & Kinahan, 1998]

$$a'(x,y) = \int_0^{\pi} s(r,\phi)\, d\phi\,. \tag{4.15}$$

This procedure, known as Back Projection (BP), must be applied for all possible values of r [Defrise & Kinahan, 1998].

From what was said above and from Section 4.2.2 (page 92), the sinogram in fact contains the complete set of projections obtained for all possible azimuthal angles. However, due to the finite size of the r and ϕ bins the BP must be carried out through a summation rather than by an integral. So, for any given voxel with coordinates (x_i, y_j) in the transverse slice, the activity can be recovered by computing [Cherry & Dahlbom, 2006]

$$a'(x_i, y_j) = \frac{1}{N}\sum_{m=1}^{N} s(r_l, \phi_m) = \frac{1}{N}\sum_{m=1}^{N} s\left(x_i \cos(\phi_m) + y_j \sin(\phi_m), \phi_m\right), \tag{4.16}$$

where N is the number of different equally spaced projection angles over which data have been obtained and $s(r_l, \phi_m)$ is the value of the (l,m) sinogram bin [Cherry & Dahlbom, 2006]. This procedure for computing the activity distribution for a slice from the corresponding sinogram is called pixel-driven BP algorithm, and is the most effective way of preforming BP [Cherry & Dahlbom, 2006].

Another way of performing simple BP consists in back projecting each bin of the sinogram over the image space, by tracing a line along the image matrix corresponding to the coordinates (r_l, ϕ_m) of the sinogram bin (l,m) being projected. If N is the number of counts contained in the sinogram bin (l,m), the value attributed to each pixel (i,j) of the image is given by $N \times w_{ij}$, where w_{ij} is a weighting coefficient which accounts for the fraction of total path length of the projected ray in each image pixel [Cherry & Dahlbom, 2006]. Due to the finite size of the bins of the sinogram, its projection on the image space holds an area. In this case the weighting coefficients can be computed, for instance, as being equal to the fraction of area covered by the

projected bin for each image pixel, the fraction being computed relative to the total area of the sinogram bin contained in the image space. This method of performing BP is called ray-driven BP, and the concept is illustrated in Fig. 4.12.

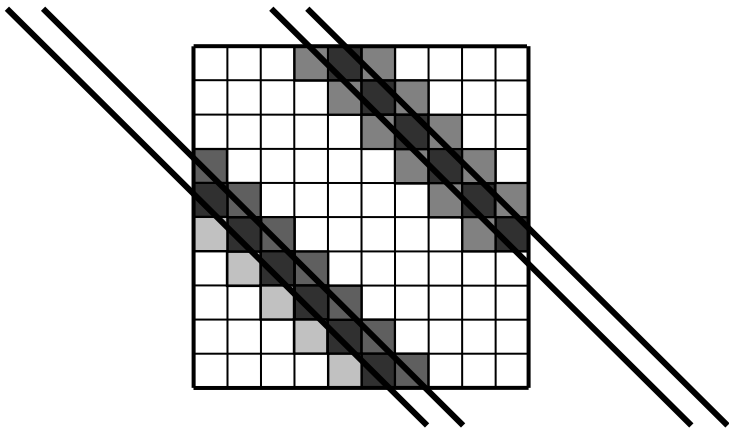

Fig. 4.12: Scheme of the ray-driven BP. Each pixel in the image is attributed a number equal to the product of the number of counts contained in the projection bin (l,m), multiplied by the fraction of total area of the pixel covered by the back projected bin.

The drawback of simple BP is that the activity image obtained, $a'(x_i,y_j)$, is only an approximation of the true activity distribution, $a(x,y)$ [Cherry & Dahlbom, 2006]. In fact, the BP reconstructed activity distribution is mathematically related to the true activity distribution by [Cherry & Dahlbom, 2006]

$$a'(x,y) = a(x,y) \otimes \frac{1}{r}, \tag{4.17}$$

where the symbol ⊗ denotes the convolution operation. So, the BP reconstructed activity distribution is equal to the original one blurred by the $1/r$ factor [Cherry & Dahlbom, 2006], where $r = \sqrt{x^2 + y^2}$ [Dahlbom, 2012]. To eliminate this blurring, one could recur to the 2D Fourier transform of Eq. (4.17), holding [Dahlbom, 2012]

$$A'(\nu_x,\nu_y) = A(\nu_x,\nu_y)\frac{1}{\rho}, \tag{4.18}$$

where the upper case letters represent the Fourier transform of the corresponding lower case one, ν_x and ν_y represent the spatial frequencies of the image along the x and y directions, and $\rho = \sqrt{\nu_x^2 + \nu_y^2}$ [Dahlbom, 2012]. Solving Eq. (4.18) for $A(\nu_x,\nu_y)$ the BP image could then be corrected for the blurring term holding then the true activity distribution

$$a(x,y) = \mathcal{F}^{-1}\left\{\rho\, A'(\nu_x,\nu_y)\right\}, \tag{4.19}$$

with $\mathcal{F}^{-1}$ representing the inverse Fourier transform. The product of ρ by $A'(\nu_x,\nu_y)$

corresponds to filtering the BP reconstructed image with a filter that has a linear response and runs from zero to a given cut-off frequency $\nu_{cut-off}$, known as ramp filter, the shape of which is depicted in Fig. 4.13. This procedure is known as Filtered BP (FBP), and its effect over the reconstructed image is depicted in Fig. 4.14.

In practice, FBP is performed in a different manner that is based on the central section theorem which states that the one-dimensional (1D) Fourier transform of the projection data $s(r,\phi)$ taken along the radial direction for a given value of ϕ (the Fourier transform of a row of the sinogram) is equal to the 2D Fourier transform of the activity distribution $a(x,y)$ evaluated along a radial profile with the same azimuthal angle [Cherry & Dahlbom, 2006], vis.,

$$S(\nu_r,\phi) = A(\nu_x,\nu_y)\Big|_{\nu_x=\nu_r\cos(\phi),\,\nu_y=\nu_r\sin(\phi)}. \tag{4.20}$$

So, instead of first obtaining the BP reconstructed image, computing its Fourier transform, applying the ramp filter in the frequency domain, and computing the

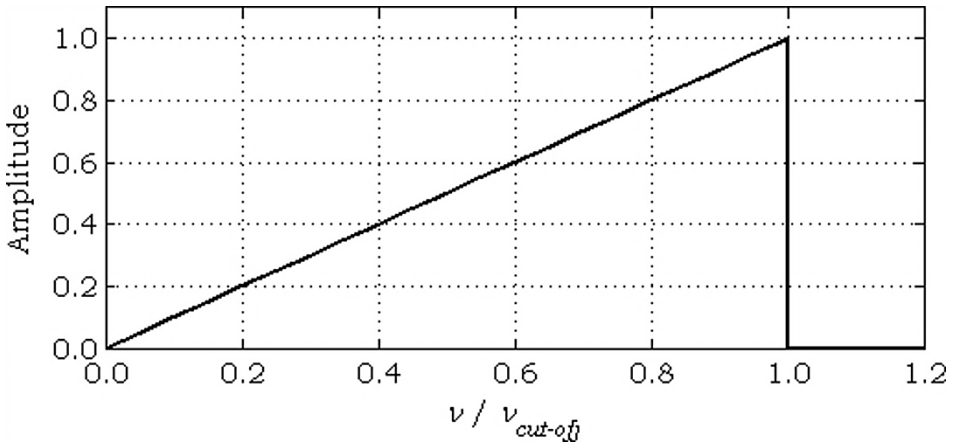

Fig. 4.13: Frequency response of the ramp filter.

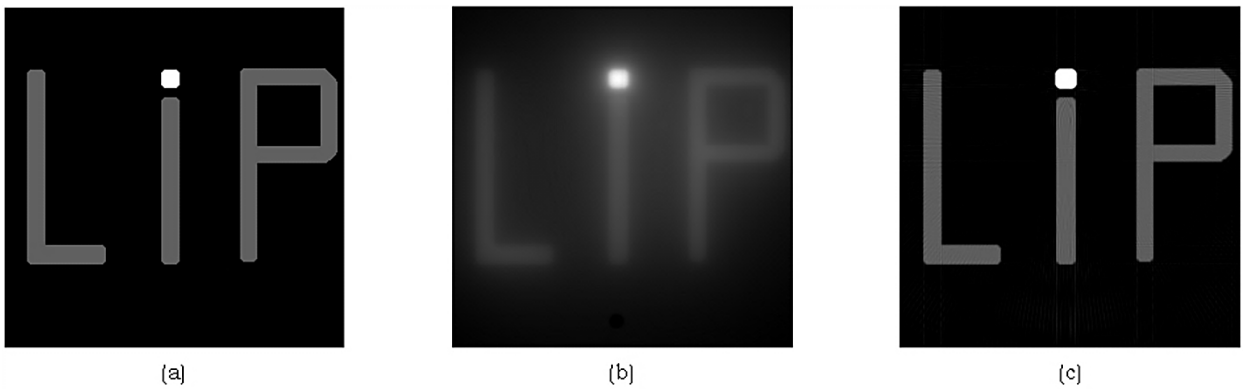

Fig. 4.14: (a) Original object for which the sinogram depicted in Fig. 4.7 (page 95) was obtained. (b) Image reconstructed by BP. (c) Image reconstructed by FBP.
(Adapted from [Blanco, 2011] with consent.)

inverse Fourier transform of the filtered BP image to obtain the FBP one, the reconstruction can be performed in simpler manners, the most effective of which consists in using Eq. (4.16) with $s(r,\phi)$ replaced by $s_f(r,\phi)$ given by [Cherry & Dahlbom, 2006]:

$$s_f(r_l,\phi_m) = \frac{1}{2\pi}\mathcal{F}^{-1}\left\{S(\nu_r,\phi)\left|\nu_r\right|\right\}, \tag{4.21}$$

with the cut-off frequency equal to the Nyquist frequency for the sampling of the sinogram along the radial direction, given by

$$\nu_{cut-off} = \frac{1}{2\Delta r}. \tag{4.22}$$

with Δr the width of the radial bin of the sinogram, which is also constrained by the required spatial resolution such that [Cherry & Dahlbom, 2006]

$$\Delta r \le 0.5 \times \mathrm{FWHM}_{rsr}, \tag{4.23}$$

where FWHM_{rsr} is the *required spatial resolution* of the final reconstructed image.

Combining this result with the requirement that for obtaining a given spatial resolution the image pixel size must be, at maximum, one third of the required FWHM_{rsr} [NEMA, 2001], then one can take the sampling in the radial direction equal to the image pixel size. In this conditions, and with Δx representing the pixel size along both the *X* and *Y* directions, the requirements for the size of the bin of the sinogram along the azimuthal direction is such that [Vandenberghe et al., 2006]

$$\Delta\phi \le \arctan\left(\frac{\Delta x}{R}\right), \tag{4.24}$$

where *R* is the scanner radius. This relation can also be written in term of the number of pixels of the final reconstructed image, ξ, assumed to be equal in both the *X* and *Y* directions as [Vandenberghe et al., 2006]

$$\Delta\phi \le \arctan\left(\frac{2}{\xi}\right). \tag{4.25}$$

What was said concerns only 2D acquisition and reconstruction. For data acquired in 3D mode, and organized in sinograms, a 3D version of the FBP algorithm was developed which is known as 3DRP and is the gold-standard for 3D image reconstruction [Cherry & Dahlbom, 2006]. One of the drawbacks of using a fully 3D algorithm such as 3DRP, with the complete set of sinograms obtained for all possible planes (see Fig. 4.8 on page 96), is the time needed to accomplish the reconstruction. For this, methods globally known as data mashing have been developed. To better

understand these methods one must make use of the so called Michelogram, depicted in Fig. 4.15, and that represents the complete set of sinograms that can be formed for a scanner with sixteen rings. Rows and columns of the Michelogram represent the ring number where each of the photons defining a LOR were detected, and each dot in the Michelogram matrix represent an independent sinogram obtained for the pair of rings involved in the detection of a given LOR.

The number of sinograms can be first reduced by recurring to the same technique used in 2D acquisition mode with increased ring difference to form the direct and cross planes. This corresponds to attributing the LORs to the middle plane between the two rings involved in detection, the Z coordinate of the detection being given the value $\bar{z} = (z_1 + z_2)/2$, with z_1 and z_2 the coordinates of the detection points of the two photons along the axial direction. This data mashing technique is known as Single Slice Rebinning (SSRB) [Daube-Witherspoon & Muehllehner, 1987] and is represented in the Michelogram of Fig. 4.15 by the oblique blue lines connecting the blue dots. Each set of connected dots define independent regions named segments, in which some of the sinograms span for two rings $(s_1 = 2)$ and others span for three rings $(s_2 = 3)$ resulting in segments with a maximum ring difference of five $(\Delta r = s_1 + s_2)$. For each segment, the sinograms connected by the oblique lines are

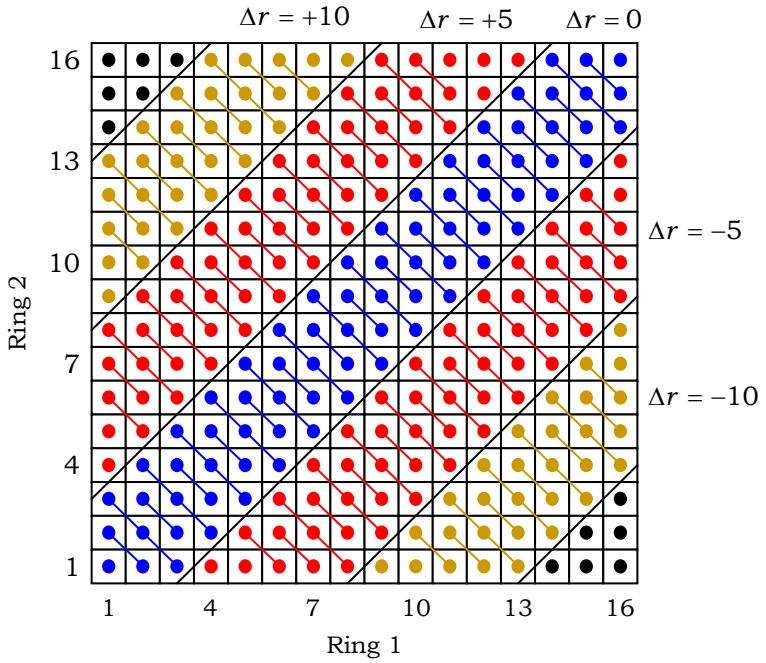

Fig. 4.15: Michelogram for a 16 ring PET scanner. Rows and columns represent the number of the rings where each of the photons of a given LOR were detected, and each dot in the Michelogram represents a complete sinogram obtained for the pair of rings involved in the detection, with the lines connecting the dots representing the mashing of the corresponding sinograms into a single sinogram.

combined, or mashed, into a single sinogram in order to reduce the number of sinograms to be processed by the reconstruction algorithm. As to the maximum ring difference allowed for coincidence detection in the example depicted in Fig. 4.15 is equal to thirteen (the sinograms corresponding to the black dots are not considered for reconstruction). The segments can then be fed to the 3DRP reconstruction algorithm or can be further treated so that only 2D FBP is required for reconstructions.

Although SSRB is a simple and fast data mashing technique, its applicability is limited to small polar angles (~9° [Kinahan & Karp, 1994]). For higher values on the polar acceptance angle and off-axis point sources, SSRB considerably degrades spatial resolution [Cherry & Dahlbom, 2006]. So, to fully convert the 3D data to sets of 2D sinograms that can be reconstructed by 2D FBP faster than would be reconstructed by 3DRP, other rebinning techniques must be used, such as Fourier rebinning (FORE) [Defrise et al., 1997].

4.4.2 Iterative Methods

Iterative reconstruction methods are computationally more demanding than analytic ones. However, the constant improvements in computation speed allowed these methods to replace analytical ones in clinical practice [Comtat, 2012]. The main reason for this is the improved image quality that can be achieved in what concerns the SNR [Dahlbom, 2012].

The basic idea behind iterative reconstruction methods is to obtain the final image representing the true activity distribution by starting from an initial "guess". This initial "guess" is often a blank or grayscale image[7] [Cherry & Dahlbom, 2006]. The next step of an iterative reconstruction algorithm consists in performing the inverse operation of FPB, viz., given the initial "guessed" image the algorithm obtains the projections that such image would generate. This is the reverse operation of BP and, as such, is termed *forward projection*. The projections thus obtained are compared with the acquired ones, and a correction to the data set obtained by forward projecting the initial "guess" image is proposed. This proposed data set is then back projected and a new image is generated, which serves as a new guessed image for the next iteration. The process is then repeated until either a given convergence criterion has been achieved, or a fixed number of iterations have been performed. Fig. 4.16 depicts the general scheme described above.

The two basic components required by an iterative reconstruction algorithm

[7] Since iterative algorithms relay on mathematical operations involving products and divisions, the initial guess should not contain voxels with values equal to zero to avoid divide by zero errors.

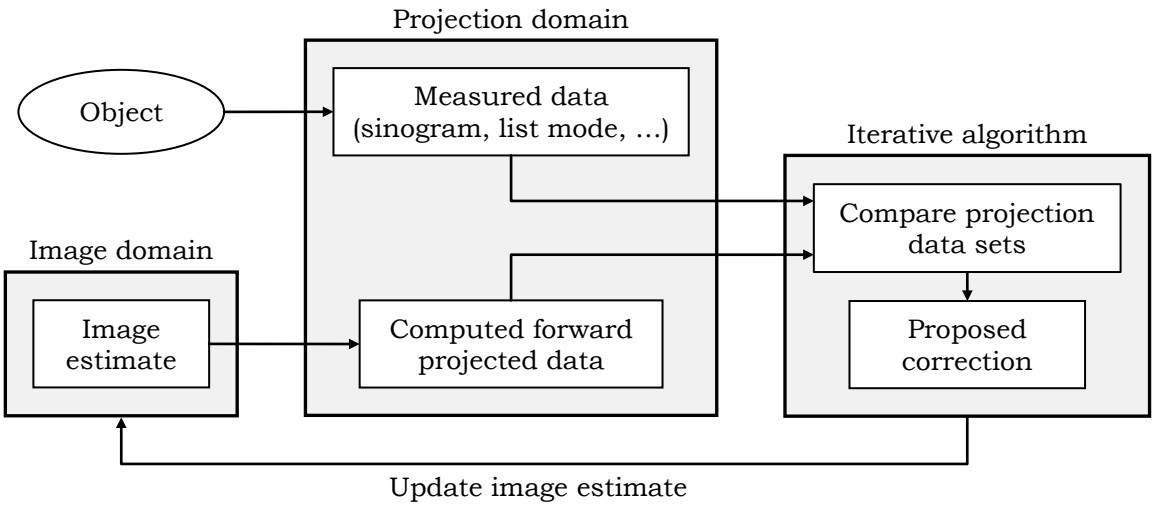

Fig. 4.16: General scheme depicting the steps performed in iterative reconstruction.

include a parameterization of the image to be reconstructed, for instance, a parameterization in terms of the number and size of voxels along each of the three Cartesian coordinates *X*, *Y*, and *Z*, but other parameterizations may be used [Comtat, 2012], and a model for the acquired data [Comtat, 2012], for instance, the discrete nature of data acquisition in a conventional cylindrical PET scanner based on discrete detection elements, or that of scanners based on detectors for which the detection position is essentially continuous. Besides the two aforementioned components, a third one may be desirable, namely a model for the probability distribution function of the measured data [Comtat, 2012]. If this component is available, then the algorithm is termed *statistical*[8] [Comtat, 2012]. These three components together define what is named by *system matrix* [Comtat, 2012], which can be computed numerically, be obtained by measuring the scanner response to point-like sources placed in several positions of the FOV, or by modelling the scanner using MC simulation codes [Comtat, 2012].

Once the system matrix is known, a function relating the acquired data with the reconstructed image must be defined. This function is named *cost function* or *objective function*, the role of which is to compare data obtained from the guessed image by recurring to the system matrix with the real acquired one. Finally, an iterative algorithm is needed to solve the cost function and propose the new data set which is then projected onto the image space.

One of the most widely used iterative reconstruction algorithms are the Maximum Likelihood Expectation Maximization (MLEM), for which the cost function assumes a Poisson distributed noise and computes the likelihood of the projected data

[8] In fact, iterative algorithms are statistical in nature, as will be clear soon.

of the guessed image with the acquired data, trying then to minimize the difference between them, and updating the guess image by using all data simultaneously [Comtat, 2012]. This is simultaneously the major advantage and the major drawback of MLEM. The major advantage since, by updating the image based on the full proposed data set, the convergence is assured, and the major drawback because the convergence is slow [Comtat, 2012].

Another popular iterative reconstruction algorithm is the Ordered Subset Expectation Maximization (OSEM), which is a modification of the MLEM algorithm. The acquired data is first divided is several disjoint subsets so that all image voxel contribute equally to each of them. The subsets are then ordered to be used in turn. One of the subsets is used to update the initial guess image which, after being updated, serves as the guess image to the next subset, which again updates the guess image that will be used as the initial guess to the next subset, and so on. The major advantage of this approach is that it is much faster than the MLEM algorithm because the number of data to be used to update the image is much less as that of the MLEM. The major disadvantage of OSEM, relative to MLEM, is that it does not converge to the maximum likelihood in of noisy data. [Comtat, 2012]

Iterative reconstruction was not used in the present work, and so it will not be further addressed.

4.5 TIME-OF-FLIGHT

As mentioned earlier, detectors with fast response times are preferred to slower ones allowing the reduction of the coincidence time window, with the consequent reduction of the Random counts (Section 4.2.3.3, page 99), which, together with the Scatter counts (Section 4.2.3.2, page 98) degrade the contrast and quality of the reconstructed image [Humm et al., 2003]. Besides, detectors with fast responses times have the advantage of allowing the use of TOF information.

If the detection system had an instantaneous response time, and disregarding the errors due to the detectors intrinsic spatial resolution and annihilation photons acollinearity, TOF could be used to determine the exact point along the LOR where the annihilation occurred, which, by kinematic considerations, would be given by [Vandenberghe & Karp, 2006]

$$(x_{ann}, y_{ann}, z_{ann}) = \frac{(x_1, y_1, z_1) + (x_2, y_2, z_2)}{2} - \frac{\left[(x_2, y_2, z_2) - (x_1, y_1, z_1)\right] c\,\Delta t}{2d}, \qquad (4.26)$$

where $(x_{ann}, y_{ann}, z_{ann})$ are the coordinates of the annihilation point, (x_1, y_1, z_1) and

(x_2, y_2, z_2) are the coordinates of the detection points of both photons, $\Delta t = t_2 - t_1$ is the difference between the two photons detection instants, c is the speed of light, and d is the LOR length. However, due to the timing characteristics of the detection system, which include the detector and associated electronics, the instants of detection of each photon are random variables assumed as presenting a Gaussian distribution with standard deviation σ_t. The difference between two Gaussian distributed random variables (X) with the same standard deviation (σ_X) is also a Gaussian distributed random variable (Y) with standard deviation (σ_Y) given by

$$\sigma_Y = \sqrt{\sigma_X^2 + \sigma_X^2} = \sqrt{2}\,\sigma_X . \tag{4.27}$$

So, from the relation between the standard deviation σ of a Gaussian distribution and the corresponding FWHM, given by

$$FWHM = 2\sqrt{2\ln(2)}\,\sigma , \tag{4.28}$$

one can conclude, that the TOF resolution of a PET system is given by

$$FWHM_{\Delta t} = 4\sqrt{\ln(2)}\,\sigma_t , \tag{4.29}$$

and the precision to which the annihilation point can be computed along the LOR, $FWHM_{\Delta \ell}$, is given by [Moses, 2003]

$$FWHM_{\Delta \ell} = \frac{c}{2} FWHM_{\Delta t} \quad \Leftrightarrow \quad FWHM_{\Delta \ell} = 2c\sqrt{\ln(2)}\,\sigma_t . \tag{4.30}$$

Since reconstruction algorithms rely on the projection of the LOR in the image space, which coincides with the entire FOV, PET systems can take advantage of high TOF resolutions, viz., low values of the $FWHM_{\Delta t}$, to restrict that projection to a smaller region of the FOV, as depicted in Fig. 4.17, which increases the SNR in the reconstructed image [Moses, 2003; Lewellen, 2008], the SNR obtained with TOF information (SNR_{TOF}) being related to the SNR without TOF information $(SNR_{non-TOF})$ by a factor $f_{SNR,TOF} = \sqrt{D/FWHM_{\Delta \ell}}$ with D the diameter of the object being imaged [Conti, 2009], viz.,

$$SNR_{TOF} = \sqrt{\frac{D}{FWHM_{\Delta \ell}}}\, SNR_{non-TOF} . \tag{4.31}$$

Besides, high TOF resolutions can also be used for LOR acceptance and rejection criteria, with improvements on the rejection of Random events (Section 4.2.3.3, page 99) as well as the rejection of long range scattered events (as will be shown in Section 10.3 on page 265, and Section 10.4 on page 275). Table 4.2 summarizes the $FWHM_{\Delta \ell}$ attained for several values of the TOF resolution, expressed by the $FWHM_{\Delta t}$, as well

as by TOF capable reconstruction algorithms in order to restrict the site of annihilation to a smaller portion along the LOR, rather than attributing the LOR to the entire FOV [Moses, 2003].

Even if the reconstruction algorithm does not make use of TOF information, but relies on list mode acquisition, TOF can be very useful in data mashing. As seen in Section 4.4.1 (page 107), SSRB is the simplest method of axially mashing the data projections attributing a given LOR to the plane that lies in the middle of the two detection rings. If the source is much off-axis, and the polar acceptance angle is considerable, then the plane to which the LOR is attributed will be far apart from that where the annihilation occurred, thus leading to a significant loss of resolution along the radial direction. However, if SSRB is modified so that the middle point of detection is not based on the absolute axial positions of the two rings involved in the detection,

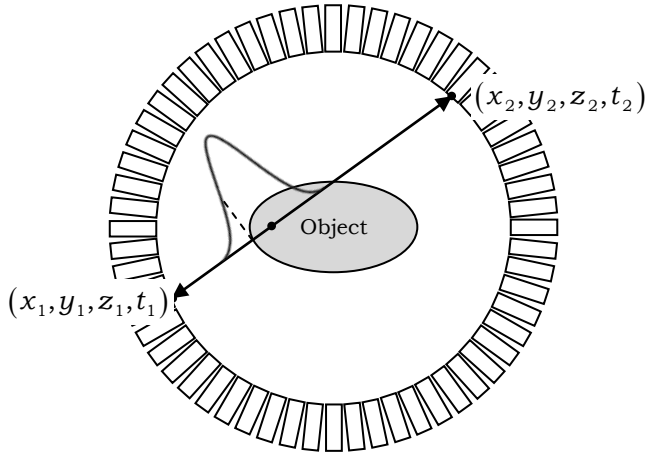

Fig. 4.17: Restriction of the image space projected LOR due to TOF information.

TABLE 4.2: POSITION RESOLUTION ALONG THE LOR $(FWHM_{\Delta\ell})$ FOR SEVERAL TOF RESOLUTIONS $(FWHM_{\Delta t})$

Time resolution [ps]			Position resolution [mm]	
FHMH			FWHM	
600	254.80	180.17	89.9	38.2
500	212.33	150.14	74.9	31.8
400	169.86	120.11	60.0	25.5
300	127.40	90.08	45.0	19.1
200	84.93	60.06	30.0	12.7
100	42.47	30.03	15.0	6.4

but, instead, on the most probable point for annihilation computed from TOF information, then the degradation of spatial resolution will be less severe. This method is the natural extension of SSRB for system with TOF ability, and is known as SSRB-TOF [Vandenberghe & Karp, 2006; Vandenberghe et al., 2006].

Another possibility for performing axial data mashing is to distribute the LOR over more than one plane according to the assumed Gaussian distribution. In this case the LOR will contribute more to the most probable plane, but the uncertainty associated with the annihilation point over the LOR is taken into account by attributing a fraction of the counts to the adjacent planes. Fig. 4.18 depicts the differences in simple SSRB and SSRB-TOF.

Besides allowing to perform axial mashing in a more accurate manner then simple SSRB, TOF information also allows to perform transverse mashing, by reducing the requisites of the sampling on the azimuthal angle, given by Eq. (4.24), which then becomes [Vandenberghe et al., 2006]

$$\Delta\phi \leq \arctan\left(\frac{\Delta x}{\mathrm{FWHM}_{\Delta x}}\right), \tag{4.32}$$

where Δx is the size of the voxel in the transverse plane (assumed to be equal in both the X and Y directions) and $\mathrm{FWHM}_{\Delta x}$ is the position resolution associated to the $\mathrm{FWHM}_{\Delta t}$ TOF resolution. By defining $g = R/\mathrm{FWHM}_{\Delta x}$ where R is the radius of the scanner, Eq. (4.25) can then be substituted by [Vandenberghe et al., 2006]

$$\Delta\phi \leq \arctan\left(\frac{2g}{\xi}\right). \tag{4.33}$$

Further benefits of TOF are related with the performance of PET scanners and will be addressed in the next section, when appropriate.

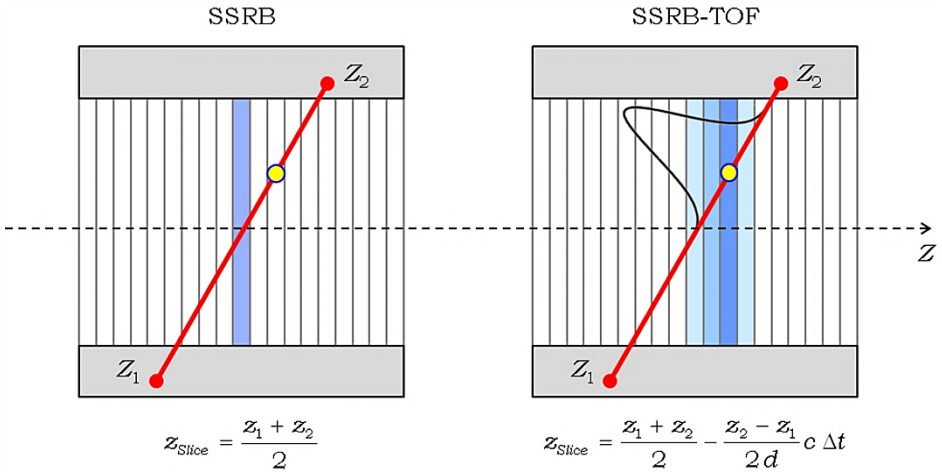

Fig. 4.18: Differences between simple SSRB and SSRB-TOF.

4.6 SCANNER PERFORMANCE TESTS

The performance of PET scanners must ultimately be based on clinical results. However, since the same exact conditions cannot be reproduced in two distinct studies, the assessment of the performance of PET scanners has to be based on test objects (phantoms), and standard procedures must be followed in order to allow quantification and consequent comparison between different PET systems.

The most commonly used procedures for PET performance quantification and comparison are described in the *NEMA NU 2 Performance Measurements of Positron Emission Tomographs*, of which at least four versions exist: the 1994, 2001, 2007 and 2012. These standards include the definition of the phantoms and their positioning in the FOV, radioisotopes and their activities, procedures for data analysis, and results reporting, to be used for several tests aimed to assess spatial resolution, sensitivity, the fraction of accepted LORs that correspond to Scattered events (the SF), total, True, Scatter and Random count rates, True count rates in the absence of noise introduced by Scattered and Random events, which is called the NECR, and also image quality, which is intended to assess the capability of contrast recover of PET systems.

In what follows the performance tests of NEMA NU2-2001 will be addressed, which, with the only exception of the sensitivity test, were those employed in the current work. The major factors impacting on the each of the performance parameters will also be addressed.

4.6.1 Spatial Resolution

The spatial resolution of any imaging system is a measure of its ability in distinguishing between two points placed close one to another. It is widely accepted that the spatial resolution of a PET scanner is affected by two physical factors, positron range and photon acollinearity, and by factors related with the design of the PET system, which include the detector design and decoding, the ability of the detector to measure the DOI, and also the geometry of the PET scanner which influences the sampling of the FOV [Moses, 2011]. Fig. 4.19 depicts the two physical effects accepted to be limiting factor of spatial resolution, as well as the effects of DOI and scanner geometry.

As seen in Section 2.3.2.4 (page 53), the physics of positron emission in β^+ and annihilation with an electron, giving rise to the two annihilation photons, imply that the annihilation point does not coincide with that of the decay. This leads to an annihilation point which is not equal to that of the decay, and that follows a given spatial distribution that limits the spatial resolution, by introducing a blurring in the

image, which for $^{18}_{9}\mathrm{F}$ is equal to 0.54 mm FWHM [Moses, 2011][9].

The other physical phenomenon that limits the spatial resolution is related with the direction of each of the annihilation photons due to the non-zero energy and linear momentum of the positron/electron system immediately before annihilation, as seen in Section 2.3.2.4 (page 53). In the plane defined by the two annihilation photons, the maximum angular aperture of one of the photons is accepted to follow a Gaussian

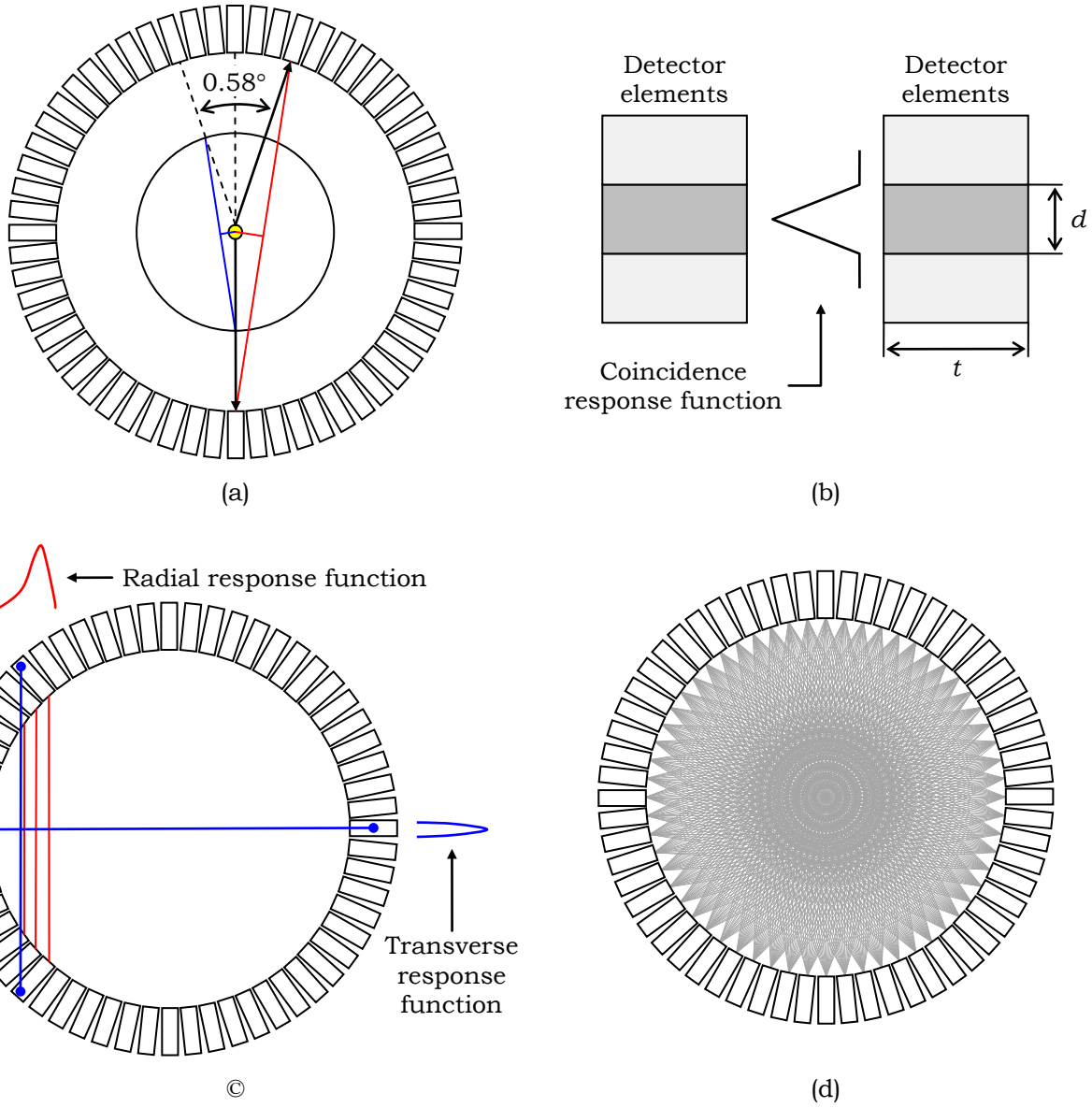

Fig. 4.19: Some effects that are accepted to affect the spatial resolution of a PET system: (a) photon acollinearity, (b) width of the detection elements and its relation with the coincidence response function, (c) DOI, and (d) sampling of the FOV dictated by the scanner geometry.

[9] Other authors report much lower values, more close to the FWHM of the positron range [Levin, 2004].

distribution with 0.58° FWHM [Jan et al., 2004], when taking the direction of the other photon as a reference. This Gaussian distribution in the azimuthal angle is accepted to result in a blurring of the detection position whose FWHM is given by $0.0044 \times R$, with R the scanner radius [Moses, 2011], in the plane defined by the annihilation photons. Fig. 4.19 (a) depicts this effect for an annihilation occurring at the centre of a transaxial plane and considering that the directions of both annihilation points lie in the transaxial plane, showing that, in the referred plane, the error in the distance of the LOR to the annihilation point is smaller for scanners with smaller diameters.

As to the scanner design parameters, the size of the detection elements is the one which most influences the spatial resolution. First, and as depicted in Fig. 4.19 (b), in the plane of the detector surface, the coincidence response function (the coincidence rate as a function of the position [Moses, 2011]) has a triangular profile with a FWHM equal to half the width of the detection elements $(d/2)$ [Moses, 2011]. Second, for detectors using optical multiplexing, as is the case of block detectors, the decoding of the detection element introduces a blur (b) which is assumed to follow a Gaussian distribution with FWHM equal to one-third the width of the element $(b = d/3)$ [Moses, 2011]. For scanners without optical multiplexing, this error is equal to zero [Moses, 2011]. Third, due to the finite thickness of the detection elements, photons impinging them perpendicularly to their surfaces are decoded with the only error given by the two abovementioned limitations. This is depicted the transverse response function in Fig. 4.19 (b). However, photons impinging the detector surface at oblique angles can interact in a deeper position of a neighbour detector. If the detector does not have DOI resolution, and the detection position is attributed to a point close to the detector surface, then a blurring in the radial direction will occur as depicted in Fig. 4.19 (c), which depends on the material from which the detector is made. For detectors based on BGO and LSO, this blur is assumed to follow a Gaussian distribution with a FWHM equal to $12.5 \times r / \sqrt{r^2 + R^2}$, where r and R are the LOR distance to the scanner centre and R is the scanner radius [Moses, 2011].

Another design parameter that influences the spatial resolution of a PET scanner is the sampling of the FOV. Since almost all scanners employ discrete detection elements, and coincidences are checked against pairs of such opposing elements, the FOV is not covered equally by the complete set of possible LORs, the image pixels being then covered by different LOR densities [Moses, 2011]. This effect, depicted in Fig. 4.19 (d) for a hypothetical cylindrical scanner with a total of sixty detection elements, contributes with an empirically determined factor of 1.25 that multiplies by the FWHM of the spatial resolution due to all other effects [Moses, 2011].

Considering all the aforementioned contributions, and using s to represent the FWHM of the positron range, the spatial resolution (FWHM) of a point source placed at a distance r from the centre of the scanner, with radius R, is accepted to be given by [Moses, 2011]

$$\Gamma = 1.25\sqrt{\left(\frac{d}{2}\right)^2 + s^2 + \left(0.0044R\right)^2 + b^2 + \frac{\left(12.5r\right)^2}{r^2 + R^2}}\,. \tag{4.34}$$

The procedure adopted in the NEMA NU2-2001 standards to quantify the spatial resolution of a whole-body PET scanner involves data acquisition, reconstruction and analysis of point sources in air. This is far from being the situation encountered in real PET acquisitions, in which the activity is immersed in a medium thus leading to scatter which degrades the parameter to be measured. However, it allows for the comparison among different scanners on the basis of the best achievable spatial resolution [NEMA, 2001].

The test phantom consists of a small ${}^{18}_{9}\mathrm{F}$ point source created by using a cylindrical capillary tube with an inside diameter of no more than 1 mm and an outside diameter of less than 2 mm. The extent of the source in the capillary must be less than 1 mm, and the activity must be small enough so that neither the losses by dead time are higher than 5% nor the Random count rate exceeds 5% of the prompt count rate.

The phantom must be placed in six different points of the FOV, three of which in the transaxial plane passing through the AFOV centre, and the other three in a transaxial plane at one-fourth of the AFOV. In the transaxial planes the source must be placed in two positions along the *Y* direction (1 and 10 cm) the position along the *X* direction being zero, the other position being along the *X* direction at 10 cm from the centre of the transaxial section, the position along the *Y* direction being then zero. Fig. 4.20 (a) depicts the abovementioned positions. The capillary tube must be aligned with its axis parallel to the scanner axis. Instead of measuring the same source at the six different positions, two acquisitions with three sources in each transaxial plane in turn, or the six sources placed simultaneously at all the six positions, can be performed.

The data must be arranged in transverse sinograms and the polar angle mashing should be performed by SRRB. The sinograms should then be reconstructed using 2D FBP without employing smoothing filters or apodization. The voxel containing the maximum number of counts must be determined, and three profiles should be taken at three orthogonal directions (along the radial, transverse and axial directions, viz., *X*, *Y* and *Z*). For each PSF profile, the maximum value to be used to compute the spatial

resolution must be obtained by fitting a second order polynomial to the pixel of maximum counts and its two nearest neighbours, as depicted in Fig. 4.20 (b). Once the maximum is found, the FWHM must be determined by linear interpolation in both directions using the pixels immediately below and above the half height. Following the same procedure, the FWTM must also be computed.

The spatial resolution must be reported independently for the sources located at 1 and 10 cm off-axis by computing the average spatial resolution from

$$\Gamma_{t,1\,\mathrm{cm}} = \frac{\Gamma_{x,x=0,y=1,z_{center}} + \Gamma_{y,x=0,y=1,z_{center}} + \Gamma_{x,x=0,y=1,z_{1/4\,center}} + \Gamma_{y,x=0,y=1,z_{1/4\,center}}}{4}, \tag{4.35}$$

$$\Gamma_{a,1\,\mathrm{cm}} = \frac{\Gamma_{z,x=0,y=1,z_{center}} + \Gamma_{z,x=0,y=1,z_{1/4\,center}}}{2}, \tag{4.36}$$

$$\Gamma_{tr,10\,\mathrm{cm}} = \frac{\Gamma_{x,x=10,y=0,z_{center}} + \Gamma_{y,x=0,y=10,z_{center}} + \Gamma_{x,x=10,y=0,z_{1/4\,center}} + \Gamma_{y,x=0,y=10,z_{1/4\,center}}}{4}, \tag{4.37}$$

$$\Gamma_{tt,10\,\mathrm{cm}} = \frac{\Gamma_{y,x=10,y=0,z_{center}} + \Gamma_{x,x=0,y=10,z_{center}} + \Gamma_{y,x=10,y=0,z_{1/4\,center}} + \Gamma_{x,x=0,y=10,z_{1/4\,center}}}{4}, \tag{4.38}$$

$$\Gamma_{a,10\,\mathrm{cm}} = \frac{\Gamma_{z,x=10,y=0,z_{center}} + \Gamma_{z,x=0,y=10,z_{center}} + \Gamma_{z,x=10,y=0,z_{1/4\,center}} + \Gamma_{z,x=0,y=10,z_{1/4\,center}}}{4}, \tag{4.39}$$

where $\Gamma_{a,\cdots}$, $\Gamma_{t,\cdots}$, $\Gamma_{tt,\cdots}$ and $\Gamma_{tr,\cdots}$ are the spatial resolutions for the specified positions,

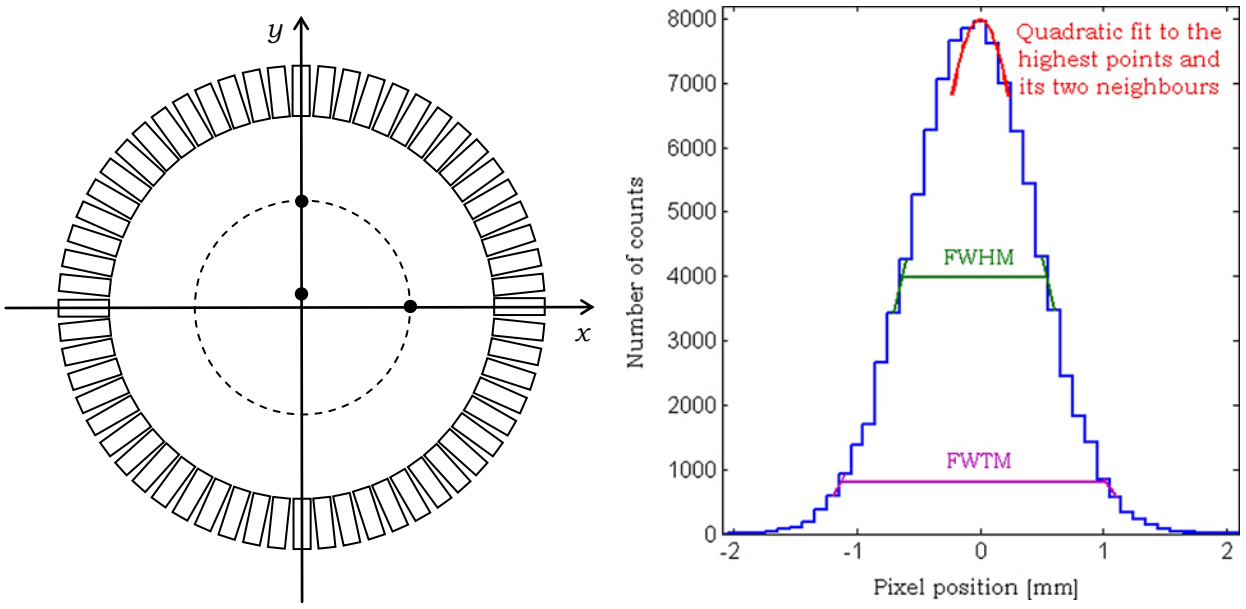

(a) (b)

Fig. 4.20: (a) Location of the point sources in the transverse plane for computing the spatial resolution. (b) PSF profile along a given direction and computation of spatial resolution.

respectively, along the axial direction, in the transaxial plane, in the transaxial plane taken along the transverse direction, and in the transaxial plane taken along the radial direction. $\Gamma_{x,\ldots}$, $\Gamma_{y,\ldots}$ and $\Gamma_{z,\ldots}$ are the spatial resolutions, respectively, along the *X*, *Y* and *Z* directions, taken from each individual PSF. The spatial resolution must be reported independently for the FWHM and for the FWTM.

4.6.2 Sensitivity

The sensitivity of a PET scanner is a measure of the rate at which coincidences are detected for a given value of the total activity in the FOV, and is related both with the intrinsic QE of the detectors and the geometric efficiency of the scanner, which is dictated by the fraction of solid angle subtended by the scanner and seen by the source distribution in the FOV.

Considering a line source centred along the scanner being acquired in full 3D mode, viz., by accepting all possible LORs, independently of their ring difference, and by recurring to Fig. 4.21, which depicts the rings contributing to each direct and cross plane, one can immediately conclude that the geometric efficiency of a PET scanner is not constant throughout the FOV. Assuming that all the detection elements have the same QE, the number of LORs contributing to each plane increases linearly from the scanner periphery to the scanner centre, at least in the absence of any attenuation material, which may reduce the number of LORs available for detection for higher values of the polar acceptance angle, viz., for higher values of the ring difference. So, by squaring the detection efficiency of each detector element (ε), which represents the quantum efficiency of detecting the LOR, and multiplying by the number of LORs acquired around the rings (see Fig. 4.19 (d) on page 120, for a transaxial plane) and by the number of ring differences contributing to each plane, and then dividing by the acquisition time, one can conclude that the slice sensitivity of a PET scanner in full 3D mode presents a triangular profile, with the maximum sensitivity located at the FOV centre, as depicted by the blue line in the left pane of Fig. 4.22. If the maximum ring difference for LOR acceptance is constrained to a value less than the maximum ring difference, then the sensitivity will present a flat plateau as depicted by the green and red lines in the left pane of Fig. 4.22. Due to this flat plateau, to image all slices with the same sensitivity the patient or object to be imaged must be moved across the FOV in steps such that the sensitivity profiles in the axial direction overlap in a manner to achieve a constant slice sensitivity, equal to that of the plateau, as depicted in the right pane of Fig. 4.22.

So, to reduce the number of bed positions that must be acquired in a complete PET scan, and thus the total time needed to complete a full scan, a compromise must be achieved taking into account, at first, the intended sensitivity and the total acquisition time. Besides, the maximum polar acceptance angle to be used in a PET scan must also account for the probability of detecting LORs for which at least one photon suffered scatter within the patient body or object to be imaged, which increases with polar acceptance angle due to the increased LOR length within the object (recall Section 4.3.5 on page 104). By taking the slice activities and summing the total sensitivity of a PET scanner is obtained.

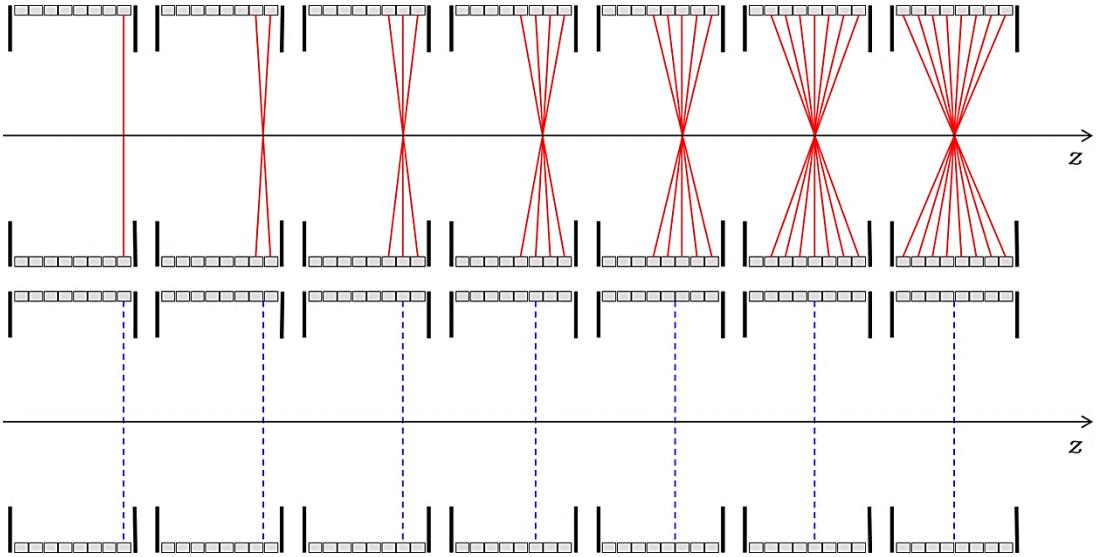

Fig. 4.21: Number of rings contributing to each direct and cross plane.

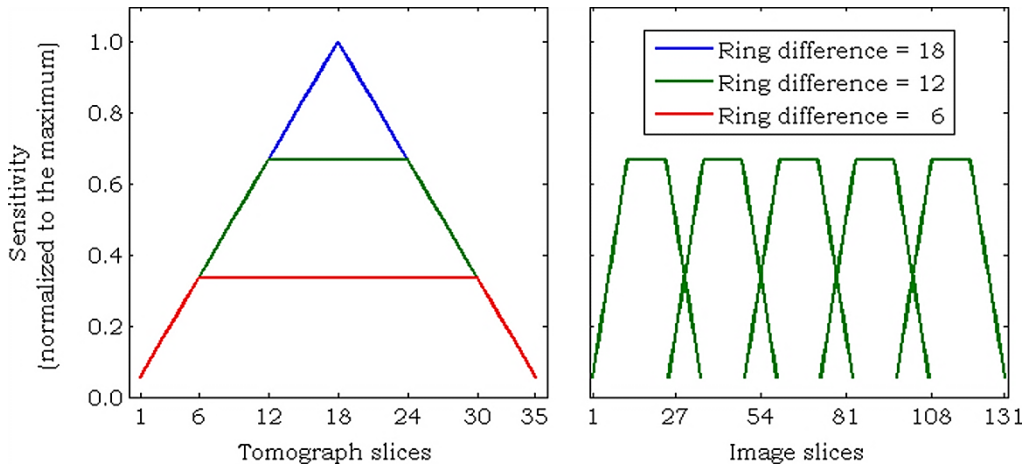

Fig. 4.22: Slice sensitivity for three different ring differences (left pane) and the required overlap of bed positions to achieve an acquisition with constant slice sensitivity for a PET scanner with eighteen detection rings.

The procedures for measuring the slice and total sensitivity of a PET scanner are different in the 1994 and 2001 versions of the NEMA NU2 standards [NEMA, 1994; NEMA, 2001].

4.6.2.1 NEMA NU2-1994 Standards

In the 1994 version of the NEMA NU2 standards, two test phantoms are used: a point source suspended in air over the scanner axis to measure the uniformity of the sensitivity in the axial direction, and a right circular cylinder of virgin Polymethyl Methacrylate (PMMA) with an outside diameter of 203 ± 3 mm, wall thickness of 3 ± 1 mm and inner length of 190 ± 1 mm [NEMA, 1994], filled with water in which a given activity of ${}^{18}_{9}\mathrm{F}$ is diluted and well mixed, to measure the mean planar sensitivity and the total sensitivity. In both phantoms, the activity to be used must be such that the losses due to dead time do not exceed 2%, and the count rate of Random coincidences does not exceed 2% of the count rate of Prompt coincidences. In what follows only the sensitivity test performed with the right circular phantom will be addressed.

The phantom must be centred in the FOV and acquisition must last until at least two hundred thousand counts per slice have been acquired. The LORs must be gathered in sinograms and SSRB (Section 4.4.1, page 107) must be employed to assign each oblique LOR to the corresponding central slice. The sinograms must be corrected for dead time (Section 4.3.4, page 104) and Random counts (Section 4.3.2, page 102), but normalization (Section 4.3.3, page 103), attenuation (Section 4.3.5, page 104) and Scatter (Section 4.3.6, page 106) corrections must not be performed. The total number of counts within the 240 mm central portion[10] of the sinograms of each image slice $\left(C_{i,TOT,240\,\mathrm{mm}}\right)$ comprised in the AFOV, or in the 170 mm central portion of the phantom along the AFOV (whichever is smaller), must be computed and used to determine the sensitivity of each image slice, by using

$$S_i = \frac{C_{i,TOT,240\,\mathrm{mm}}}{T_{acq}\, a_{ave}}\left(1 - SF_i\right), \tag{4.40}$$

where T_{acq} is the total acquisition time, SF_i is the fraction of Scattered coincidences detected in slice i (to be addressed in the next section) and a_{ave} is the average activity concentration in the FOV for the duration of the acquisition, and is given by

$$a_{ave} = \frac{A_{ave}}{V}, \tag{4.41}$$

with V the total volume of the phantom and A_{ave} the activity averaged over the time

[10] Corresponding to a radial distance of 120 mm, comprised between -120 mm and +120 mm.

duration of the scan, and computed by

$$A_{ave} = \frac{A_0}{\ln(2)} \frac{T_{1/2}}{T_{acq}} \left\{ 1 - \exp\left[-\frac{T_{acq}}{T_{1/2}} \right] \right\}, \tag{4.42}$$

where $T_{1/2}$ is the radioisotope half-life (see Section 2.2.1 on page 14), and A_0 is the total activity at the beginning of the acquisition, which is given by

$$A_0 = A_{cal} \exp\left[\frac{T_{cal} - T_0}{T_{1/2}} \ln(2) \right], \tag{4.43}$$

with A_{cal} the activity measured at calibration time (T_{cal}) and T_0 the time at which the scan was started.

The planar sensitivities thus obtained must be plotted against the slice number, so that the planar sensitivities can be addressed easily, and the total sensitivity of the scanner must be obtained by summing all the valid the planar sensitivities. Notice that this method gives the sensitivity to True coincidences. If the sensitivity to Trues plus Scattered coincidences is to be obtained, the term in brackets in Eq. (4.40) has to be ignored.

Fig. 4.23 depicts the positioning of the phantom in the transaxial plane and the central portion of the sinogram that should be used in the computations.

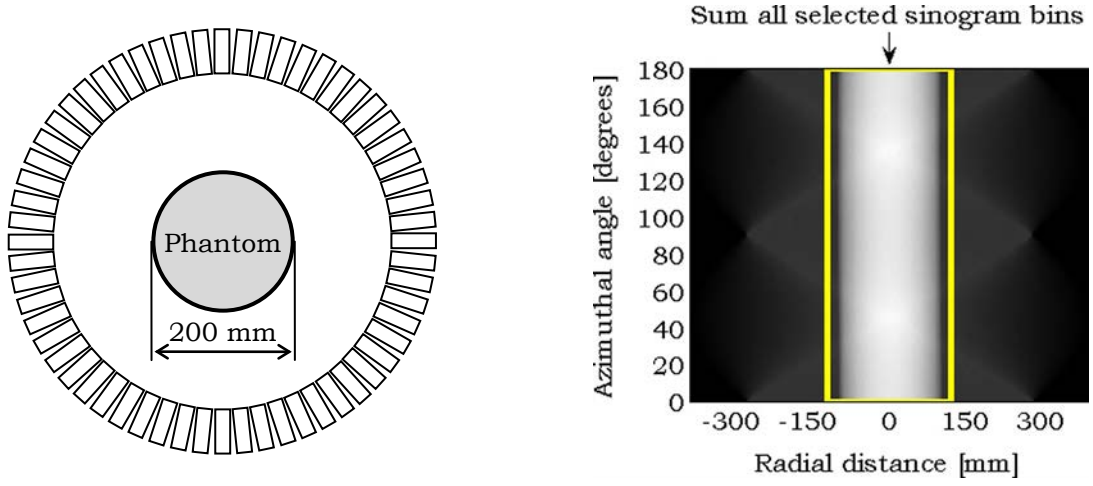

(a) (b)

Fig. 4.23: (a) Positioning of the sensitivity test phantom in the transaxial plane (in the axial direction the phantom is also centred). (b) Sinogram for a given slice.

4.6.2.2 NEMA NU2-2001 Standards

The phantom used in the 2001 version of the NEMA NU2 standards consists in a thin and long plastic tube, with an outside diameter less than 3.9 mm, filled in an

extension of 700 ± 5 mm with water in which a given activity of $^{18}_{9}\mathrm{F}$ is diluted. Again, the activity to be used must comply with criteria regarding losses by dead time, which must be less than 1%, and Random count rates, which must be less than 5% of the Prompt count rate. The tube must then be inserted in a right circular sleeve of Aluminium with 700 mm length and inside and outside diameters of, respectively, 3.9 mm and 6.4 mm, the propose of which is to ensure that positrons emitted by the line source have enough material to be stopped, leading then to annihilation. However, since the Aluminium sleeve leads also to undesirable scatter, the acquisition must be performed with added attenuation material so that it can be possible to extrapolate the sensitivity to zero absorption. This is accomplished by acquiring data with added attenuation material, consisting also of Aluminium sleeves with 700 mm long, which are added in turn to those already placed in the phantom. Table 4.3 resumes the inner and outer diameters of all the five sleeves.

The phantom must be centred in the FOV with its axis aligned with that of the scanner. For each total attenuation thickness, acquisitions must be performed for long enough so that one thousand counts per image plane are obtained. Oblique LORs should be assigned to the corresponding central slice by means of SSRB, and the total number of counts for each slice must be saved. The procedure must then be repeated for an off-axis position in the transaxial plane such that the phantom axis is displaced 10 cm apart the scanner axis. Fig. 4.24 depicts the phantom with the five sleeves and the two positions in the transaxial FOV.

The number of counts obtained for each slice i and thickness of absorbing material t $\left(C_{i,t}\right)$ must be converted first to count rates $\left(R_{i,t}\right)$ by dividing the registered number of counts by the time duration of each corresponding acquisition $\left(T_{acq,t}\right)$, and the count rates thus obtained must be corrected for source decay by

$$R_{Corr,i,t} = R_{i,t} \times 2^{(T_t - T_{cal})/T_{1/2}}, \tag{4.44}$$

where T_t and T_{cal} are, respectively, the time at which the acquisition with sleeve t was initiated and the time of source calibration, and $T_{1/2}$ is the radioisotope half-life. After count rate correction, for each slice and number of sleeves, the total count rate for each thickness of absorbing material must be computed by summing the count rates of all slices,

$$R_{Corr,t} = \sum_i R_{Corr,i,t}, \tag{4.45}$$

and a fit must be performed to the data thus obtained by using

$$R_{Corr,t} = R_{Corr,0}\, \mathrm{e}^{-2\mu x_t}, \tag{4.46}$$

where x_t is the total thickness of absorbing material for a given number of sleeves surrounding the line source, and $R_{Corr,0}$ and μ are the unknowns to be obtained from the fit, the latter being allowed to vary to compensate for the scatter, and the former being the count rate in the absence of absorbing material, from which the total sensitivity must be computed by

$$S_{tot} = \frac{R_{Corr,0}}{A_{cal}}, \tag{4.47}$$

with A_{cal} the total source activity measured at the time of calibration.

Besides the total sensitivity, the slice sensitivity should also be reported. For that, data obtained with the first sleeve should be used holding for the slice sensitivity

$$S_i = \frac{R_{Corr,i,1}}{R_{Corr,1}} S_{tot}, \tag{4.48}$$

with

$$R_{Corr,1} = \sum_i R_{Corr,i,1}, \tag{4.49}$$

TABLE 4.3: INNER AND OUTER DIAMETERS OF THE FIVE ALUMINIUM SLEEVES USED IN THE NEMA NU2-2001 SENSITIVITY TEST. (DIMENSIONS IN MILLIMETRES.)

Sleeve number	Inside diameter	Outside diameter
1	3.9	6.4
2	7.0	9.5
3	10.2	12.7
4	13.4	15.9
5	16.6	19.1

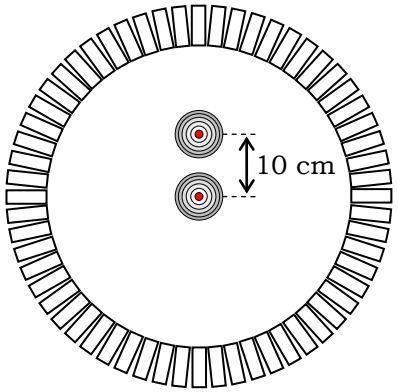

Fig. 4.24: Sensitivity phantom with its axis aligned with the scanner axial axis and placed with a 10 cm offset. (Phantom and dimensions not in scale with those of the scanner).

4.6.2.3 Effect of Time-of-Flight Information on Sensitivity

As mentioned in Section 4.5 (page 115), TOF information, while not improving spatial resolution [Moses, 2003], improves the SNR in the final reconstructed image [Moses, 2003; Conti, 2009]. This improvement is due to the reduction of variance of acquired data, which can be translated by a gain factor in the sensitivity given by [Moses, 2003; Conti, 2009]

$$g_{TOF} = \frac{2D}{c\,FWHM_{\Delta t}} \quad \Leftrightarrow \quad g_{TOF} = \frac{D}{FWHM_{\Delta \ell}}, \tag{4.50}$$

where D is the diameter of the object to be imaged, with $FWHM_{\Delta t}$ and $FWHM_{\Delta \ell}$ given by Eq. (4.29) and Eq. (4.30) (Section 4.5, page 115). While this factor can be applied to sensitivities obtained by the NEMA NU2-1994 standards for which the phantom has a non-negligible diameter, it cannot be applied to the 2001 version of the standards, due to the extremely small diameter of the phantom when compared to the position resolution attained by TOF. In fact, if it was applied, considering the phantom diameter, and taking into account the relatively low TOF resolutions of a few hundred picoseconds achievable with current technology, the factor computed by (4.50) would lead to a decrease in the planar and total sensitivities to True coincidences.

4.6.2.4 Differences Between the 1994 and 2001 Versions of the NEMA NU2 Standards

Besides the obvious differences in the two methods, there are others that deserve to be mentioned, and which are related with the SF.

First, by explicitly using the SF in Eq. (4.40) the 1994 version of the NEMA NU2 standards allows to obtain the sensitivity both to True events and to True plus Scattered ones, while the 2001 version does not allow that.

Second, the SF is related not only with the fraction of scattered events incoming from the patient body or object to be imaged, but also with the fraction of events detected and that suffered scatter in the detectors. As a consequence, the 1994 version of the NEMA NU2 standards may allow inferring the capability of a PET scanner to acquire data that will lead to reasonable image quality, at least to some limited extent determined by low activities for which the Random counts can be neglected when compared with the Prompt ones. For the 2001 version of the NEMA NU2 standards this inference may eventually not be possible.

Apart the influence of Random counts at higher activities, the aforementioned inability is related with the nature of scatter in the detectors. For detectors based on high density materials with high photofractions and energy resolution, such as those based on inorganic scintillators and employed in currently available commercial PET

scanners, the inference of image quality based on planar sensitivity data, may eventually be possible. However, for PET scanners based on different detector technology, such as RPC detectors which do not have energy resolution to actively reject scatter in the detector, and for which the photon interaction process leading to detection is almost exclusively Compton scattering, with the added drawback that the probability of detection per photon interaction is very low, this inference may eventually not to be possible, or at least not to be as straightforward as in the case of inorganic scintillators.

Summarizing, while the sensitivity obtained by the 1994 version of the NEMA NU2 standards give a measure of the overall capability of a PET scanner to detect True coincidences, the 2001 version measures only the ability of the scanner to detect coincidences for which none of the annihilation photons suffered scatter in the patient body or object to be imaged.

4.6.3 Scatter Fraction

As mentioned before (Section 4.2.3.2, page 98), Scattered coincidences degrade the spatial resolution and contrast of the final reconstructed image. As such, it is necessary to have knowledge of the fraction of Prompt coincidences that corresponds to Scattered ones. This is the goal of the performance test that will be described in the following.

The phantom used to access the SF (equal to the quotient between the number of Scattered and the number of Prompt events), consists in a solid right circular cylinder of polyethylene with a density of 0.96±0.01, an axial length of 700±5 mm and a diameter of 203±3 mm in which an hole with a diameter of 6.4±0.2 mm is drilled parallel to the central axis of the phantom but displaced 45±1 mm from it, to accommodate an insert consisting in a polyethylene tube, or a plastic tube coated with polyethylene, with at least 800 mm long, and inside and outside diameters of, respectively, 3.2±0.2 mm and 4.8±0.2 mm. The 700±5 mm central portion of the line insert must be filled with the source consisting in a given activity concentration of $^{18}_{9}\mathrm{F}$ diluted and well mixed in water. The activity to be used must be low enough so that the count losses due to dead time and the Random count rates are less than 1% of the Trues count rate[11]. Fig. 4.25 depicts the phantom geometry.

The phantom must be placed in the patient bed with the line source oriented so that it is closer to the bed, being then centred both in the transaxial and axial FOV, to

[11] Since the same phantom is used in count rates, NECR and count losses measurements, it is usual to start with a high activity and then use the last scans for computing the SF.

a precision within 5 mm[12], and at least five hundred thousand Prompt coincidences should be acquired, while maintaining the acquisition time below one-fourth the half-life of the radionuclide. So, if needed to collect enough statistics, several acquisitions may be performed observing the maximum acquisition time, each acquisition being then processed independently prior to the final computation of SF.

The coincidences obtained, and uncorrected for the factors mentioned in Section 4.3 (page 101), must then be arranged in sinograms for each transverse slice of the scanner if this has an axial length less than that of the phantom or, otherwise, for the 650 mm central portion of the phantom, and oblique LORs should be assigned to the corresponding slice by means of SSRB, respecting the maximum ring difference pretended.

All the pixels of the sinograms thus obtained and located further than 120 mm from the sinogram centre must be zeroed (Fig. 4.26 (a)). The location of the line source in the sinograms must then be determined by finding, for each azimuthal angle ϕ, the radial bin containing the maximum value. Once found, the radial bins of the sinograms must be shifted so that, for each azimuthal angle ϕ, the bin containing the maximum value is aligned with the centre of the sinogram (Fig. 4.26 (b)). A sum projection must then be determined from the shifted sinograms so that each bin in the projection, corresponding to a given radial distance r, contains the sum of the counts for all azimuthal angles ϕ of the sinogram (Fig. 4.26 (c)). The fractional values of the radial bins corresponding to -20 and +20 mm, $r_{-20\,\mathrm{mm}}$ and $r_{+20\,\mathrm{mm}}$, shall be determined and the counts at the left and right bins of each of the fractional values thus found, (respectively, $C_{L,-20\,\mathrm{mm}}$ and $C_{R,-20\,\mathrm{mm}}$, and $C_{L,+20\,\mathrm{mm}}$ and $C_{R,+20\,\mathrm{mm}}$) must be used to

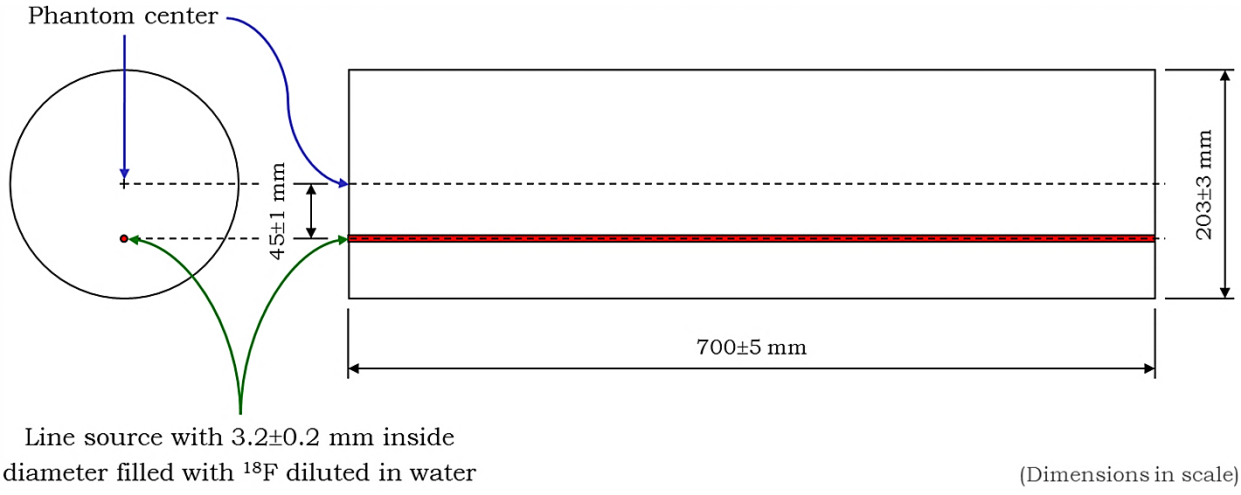

Fig. 4.25: SF phantom. (Dimensions are in scale.)

[12] From Fig. 4.20 (page 125), this is equivalent to say that the line source should be placed in the point with coordinates $(x,y) = (0,-45)$ mm .

compute, by linear interpolation, the counts $C_{-20\,\mathrm{mm}}$ and $C_{+20\,\mathrm{mm}}$, respectively, for $r_{-20\,\mathrm{mm}}$ and $r_{+20\,\mathrm{mm}}$ (green line of Fig. 4.26 (c)). By computing the average value of these two counts and multiplying it by the number of radial bins comprised between them, including the fractional values corresponding to $r_{-20\,\mathrm{mm}}$ and $r_{+20\,\mathrm{mm}}$, and summing the total counts located outside the central 40 mm strip (red curve of Fig. 4.26 (c)), the total number of Scattered and Random coincidences, $C_{S+R,i,j}$ with i and j representing, respectively, the slice and acquisition number, is obtained[13]. The total number of counts of each slice i and acquisition j, $C_{TOT,i,j}$, must also be obtained by summing all the counts contained in the corresponding sinogram projection. With this two values, $C_{S+R,i,j}$ and $C_{TOT,i,j}$, the SF for each slice i, SF_i, is computed by

$$SF_i = \frac{\sum_j C_{S+R,i,j}}{\sum_j C_{TOT,i,j}}, \tag{4.51}$$

and the total SF is computed as the weighted average of the slice SFs by

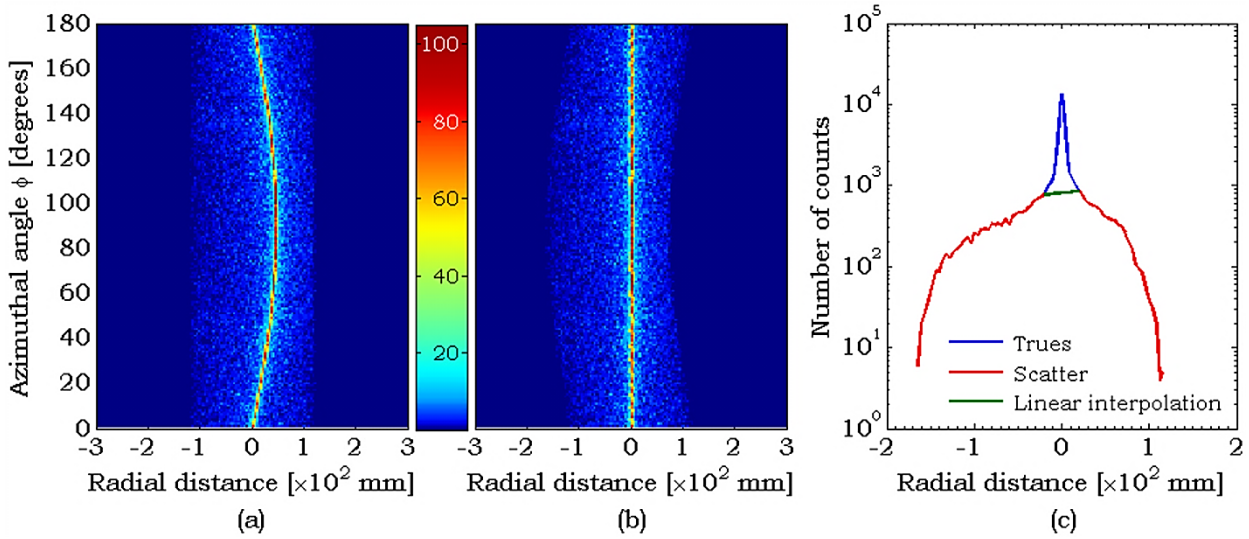

Fig. 4.26: Processing of sinograms to obtain the SF. (a) Zeroing of sinogram bins for which the radial distance is greater than 120 mm. (b) Shifting of sinogram in the radial direction so that the pixel with the highest count be aligned with the sinogram centre. (c) Sinogram projection obtained by summing the bins of all azimuthal angles for each radial bin, which also depicts the line obtained by linear interpolation (green) to find the counts between the -20 and +20 mm radial distances, and that serve to distinguish between the True counts (blue curve) and Scattered plus Random counts (green and red curves).
(Data retrieved from a simulation performed in the scope of the current work.)

[13] If the activity is low enough so that the Random counts are negligible, the counts thus obtained correspond to Scattered coincidences. For higher activities, for which the Random coincidences cannot be neglected, the counts thus obtained correspond to Scattered plus Random coincidences.

$$SF = \frac{\sum_{i,j} C_{S+R,i,j}}{\sum_{i,j} C_{TOT,i,j}}. \tag{4.52}$$

4.6.4 Count Rates, Noise Equivalent Count Rate and Count Losses

Contrary to the performance tests described so far, which make use of very low activities in the FOV, so that count losses due to dead time and Random coincidences can be neglected, the activities present in the FOV in clinical practice are high enough to imply that Random counts be corrected. Moreover, the sensitivity test as performed by the NEMA NU2-2001 standards do not account for scatter in the detector. Since in clinical practice both effects (Random and Scattered events) are present, they must be corrected prior to image reconstruction, as mentioned in Section 4.3 (page 101). However, this corrections increase the statistical noise in the net True counts rate [Dahlbom, 2012]. The net True count rate that is attained after Random and Scattered events correction can however be assessed by means of the NECR performance parameter, which can be expressed mathematically by [Dahlbom, 2012]

$$NECR = \frac{R_T^2}{R_T + R_S + k\, f\, R_R}. \tag{4.53}$$

where the upper case R represent count rates with the indexes representing the corresponding events (T for True, S for Scattered, and R for Random coincidences), f is the fraction of the sinogram, or of the FOV width, subtended by the object to be imaged [Dahlbom, 2012], and which is usually equal to one, and k take the value one if the Random coincidences are corrected on the basis of Single events count rate, while taking the value two if Random correction is performed by the delayed coincidence window method [Dahlbom, 2012].

Moreover, the NECR is directly proportional to the square of the SNR in the reconstructed image [Dahlbom, 2012]. Since for detectors with TOF capability the SNR of the image reconstructed using TOF information is directly proportional to the SNR obtained by reconstruction without considering the TOF information, the proportionality constant being the square root of Eq. (4.50) (compare with Eq. (4.31)), the NECR of TOF capable scanners can be obtained from the NECR computed by the procedure which will be described in the following by multiplying it by the TOF gain $\left(g_{TOF}\right)$ given in Eq. (4.50) [Moses, 2003; Conti, 2009], viz.,

$$NECR_{TOF} = \frac{D}{FWHM_{\Delta\ell}} NECR_{non-TOF}. \tag{4.54}$$

The procedure adopted in the NEMA NU2-2001 standards for computing the Prompt, True, Scatter and Random count rates, from which the NECR can then be computed, is the same as that employed for computing the SF. By starting with a high activity concentration, acquisitions are performed, with the SF phantom placed as in the SF performance test, for time intervals not larger than one fourth of the radionuclide half-life, and, for each acquisition, the projections of the registered counts are computed in exactly the same manner as explained for the SF, holding the counts $C_{S+R,i,j}$ and $C_{TOT,i,j}$.

From the total counts, $C_{TOT,i,j}$, the Prompt count rate per slice is computed by

$$R_{TOT,i,j} = \frac{C_{TOT,i,j}}{T_{acq,j}}, \tag{4.55}$$

where $T_{acq,j}$ is the time duration of the acquisition *j*, and the total Prompt count rate is computed by summing the slice count rates thus obtained for all valid slices,

$$R_{TOT,j} = \sum_i R_{TOT,i,j} \,. \tag{4.56}$$

The True event rate for each slice is computed by

$$R_{T,i,j} = \frac{C_{TOT,i,j} - C_{S+R,i,j}}{T_{acq,j}}, \tag{4.57}$$

and the total True count rate is again obtained by summing over all valid slices,

$$R_{T,j} = \sum_i R_{T,i,j} \,. \tag{4.58}$$

As to the Random count rate for each slice, can be obtained by subtracting from the slice Prompt count rate, the fraction of Prompt count rates in the slice due to scatter and the True count rates in the slice, and then normalize the result thus obtained to the fraction of True plus Random events $\left(1 - SF_i\right)$, holding

$$R_{R,i,j} = R_{TOT,i,j} - \frac{R_{T,i,j}}{1 - SF_i}, \tag{4.59}$$

where SF_i is the SF computed as described in Section 4.6.3 (page 131), viz., obtained for a low activity, which is to say that the SF is considered to be independent of the activity present in the FOV. Again, the total Random count rate is obtained by summing the slice Random rates for all valid slices, viz.,

$$R_{R,j} = \sum_i R_{R,i,j} \,, \tag{4.60}$$

The Scatter count rate for each slice if simply obtained from the True count rate by multiplying it by the slice SF and then normalizing the result to the fraction of

Random plus Trues counts, holding then

$$R_{S,i,j} = \frac{SF_i}{1 - SF_i} R_{T,i,j}, \tag{4.61}$$

the total Scatter count rate being then equal to the sum of the Scatter count rate extended to all valid slices

$$R_{S,j} = \sum_i R_{S,i,j} \ . \tag{4.62}$$

To obtain the non-TOF NECR for each slice the above mentioned count rates do not have to be all computed. In fact, for scanners that perform the Random correction on the basis of the Single event rates, only the True and Prompt rates for each valid slice are needed to compute the non-TOF NECR, which is then given by

$$NECR_{non-TOF,i,j} = \frac{R_{T,i,j}^2}{R_{TOT,i,j}}, \tag{4.63}$$

while for scanners employing the delayed coincidence time window for Random correction, the NECR for each slice, without considering TOF information, is given by

$$NECR_{non-TOF,i,j} = \frac{R_{T,ij}^2}{R_{TOT,i,j} + R_{R,i,j}}, \tag{4.64}$$

In both cases, the total NECR without considering the gain factor due to the use of TOF information in the reconstruction algorithm is given by the sum of the corresponding NECR for each slice, extended to all valid slices, viz.,

$$NECR_{non-TOF,j} = \sum_i NECR_{non-TOF,i,j} \ . \tag{4.65}$$

Notice that if the aforementioned fraction of the sinogram, or of the FOV width, subtended by object to be imaged (f) is not equal to one, $R_{TOT,i,j}$ in the denominator of Eq. (4.63) and Eq. (4.64) must then be replaced by

$$R_{TOT,i,j} \mapsto R_{T,i,j} + R_{S,i,j} + k\, f\, R_{R,i,j} \, . \tag{4.66}$$

with *k* and *f* replaced by the corresponding values.

Since the Random count rates depend on the total activity in the FOV, the above mentioned count rates, as well as the NECR, need to be computed for different activities and then plotted has a function of the average activity concentration which, for each acquisition *j*, must be computed as explained in Section 4.6.2.1 (page 126), with *V* of equation (4.31) equal to the total volume of the phantom $(22000\,\mathrm{cm}^3)$ [NEMA, 2001].

Besides the abovementioned plots, the peak values of the True count rates and of

the NECR should also be computed and reported, along with the activity concentrations at which they occur.

Finally, and not covered by the NEMA NU2-2001 standards, if the NECR is to be given taking the TOF gain into account, that should be explicitly stated, and the diameter of the phantom should be taken as the object diameter.

4.6.5 Accuracy of Dead Time and Random Corrections

The data obtained in the tests described in Sections 4.6.3 (page 131) and 4.6.4 (page 134) can yet be used to test the accuracy of corrections performed prior to image reconstruction, namely in what count losses and Random count corrections are concerned. For that, all the valid slices used in the aforementioned tests must be individually reconstructed after all corrections have been applied, and a circular Region Of Interest (ROI), with 180 mm diameter and centred on the transaxial FOV (and not in the line source), shall be drawn in the reconstructed image. For each slice, the count rates of the defined ROI must be computed by

$$R_{ROI,i,j} = \frac{C_{ROI,i,j}}{T_{acq,j}}, \tag{4.67}$$

where $C_{ROI,i,j}$ are the total counts registered in the selected ROI for each slice *i* and acquisition *j*.

With the three acquisitions performed at low Prompt count rates, viz., low activities in the FOV, for which the losses due to dead time and the Random count rate can be regarded as negligible, the count rate should be obtained by

$$R_{Ext,i,j} = \frac{A_{ave,j}}{3}\sum_{k=1}^{3}\frac{R_{ROI,i,k}}{A_{ave,k}}, \tag{4.68}$$

with A_{ave} given by Eq. (4.42). The count rate thus obtained is considered to be the extrapolated count rate in the absence of the losses for which the test was conceived.

The data obtained from Eq. (4.67) and Eq. (4.68) is then used to compute the relative count error by

$$\Delta r_{i,j} = 100\left(\frac{R_{ROI,i,j}}{R_{Ext,i,j}} - 1\right)\%, \tag{4.69}$$

which must then be tabulated along with the effective activity concentration $a_{eff,j}$ (the activity concentration in the line source and not in the phantom), and a plot of $\Delta r_{i,j}$ against $a_{eff,j}$ should also be given, from which the maximum value of $\left|\Delta r_{i,j}\right|$ at the activity concentration of peak NECR $\left(a_{NEC,peak}\right)$, or below that value if the maximum error occurs for an activity concentration below that of the peak NECR, should then be

computed and reported.

Since modelling a complete PET system by means of simulations is not only a hard task as well as probably an impossible one, if nothing else, due to the computational requirements, this test must be performed with real PET systems. For that, the test was not, neither is foreseen to be, performed in the scope of the current work, and was mentioned only for completeness.

4.6.6 Image Quality and Accuracy of Attenuation and Scatter Corrections

This test is intended to compare the image quality of different PET scanners by acquiring data with a phantom that simulates a clinical imaging situation, and makes use of two phantoms.

One of the phantoms resembles a portion of the torso with an inside length of at least 180 mm, and transaxial dimensions as depicted in Fig. 4.27 (a), which accommodate, via an insert, six fillable spheres with wall thicknesses no more than 1 mm, and internal diameters and positioned as depicted in Fig. 4.27 (b). The set of six spheres must be centred in the transaxial plane so that the centre of the circle that passes through the centre of the spheres is centred with the phantom centre, as depicted in Fig. 4.27 (c). In the axial direction, the spheres must be placed so that their centres are located at a distance of 70±10 mm from one of the inner transaxial surfaces of the body phantom. A cylindrical insert with an outer length equal to the inner length of the torso phantom, outer diameter of 50±2 mm and wall thickness of less than 4 mm, filled with a material with low atomic number and average density of 0.30±0.10, is centred in the phantom with the aim of simulating the attenuation of lung. Fig. 4.27 (d) depicts a picture of this phantom assembled. The other phantom used in the test is the SF phantom described in Section 4.6.3 (page 131), which must be placed in the head side of the body phantom, and abutting it, to simulate a clinical acquisition in which the activity distribution extends beyond the scanner FOV.

The source to be used in all different portions of the assembled phantoms consists of $^{18}_{9}\mathrm{F}$ diluted and well mixed in water. An activity concentration of $5.3\,\mathrm{kBq\,cm^{-3}}$ must be used to fill the body phantom for simulating background and the line source of the SF phantom must be filled with an activity of 116 MBq, so that the effective activity concentration is equal to that used to fill the body phantom. The spheres numbered as five and six in Fig. 4.27 (b) are intended to simulate cold lesions and must be filled with water, while the spheres numbered from one to four are intended to simulate hot lesions and must be filled with an activity concentration equal to four and eight times that of the background concentration. For each

concentration used in the hot lesions spheres, an acquisition must be performed with a time duration given by

$$T_{T,E} = \frac{60}{L}\Delta L \,[\text{minutes}], \tag{4.70}$$

where $L = 100$ cm corresponding to the total axial distance covered in a typical whole-body PET scan and ΔL is the length of the axial steps of the bed used in an whole-body scan.

Acquired data must be corrected for all factors mentioned in Section 4.3 (page 101) and reconstructed using all the parameters recommended by the scanner manufacturer for whole-body studies, which include the size of the image matrix and voxel, reconstruction algorithm, and filter or smoothing applied.

For data analysis, the transverse slice centred on the spheres must be used, in which circular ROIs must then be drawn centred in each of the spheres so that the diameter of each ROI is as close as possible to the inner diameter of the spheres. A second set of twelve ROIs, with the same diameters as those mentioned, must then be drawn concentrically in points distributed across the background region of the

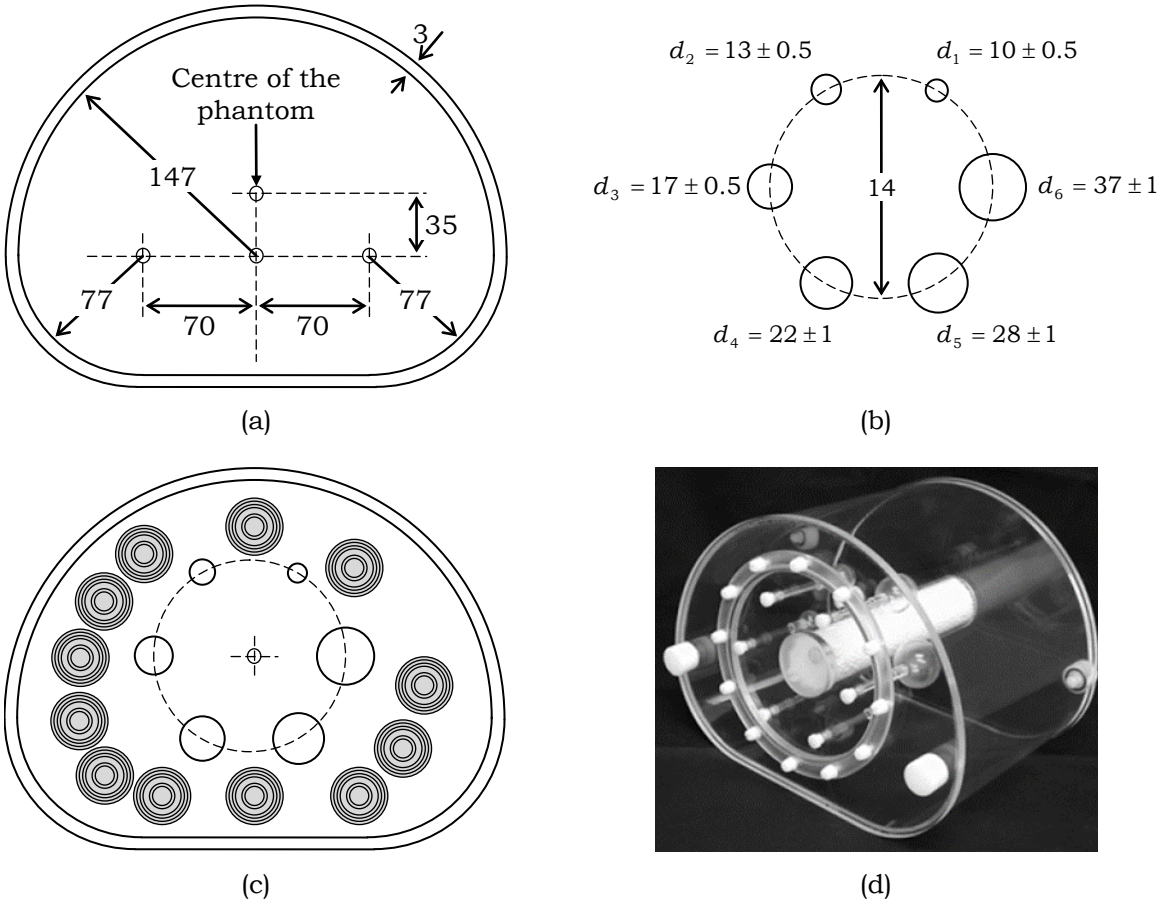

Fig. 4.27: Image quality phantom. All dimensions are in millimetres and not in scale.

phantom so that the edge of the larger diameter ROIs are placed 15 mm apart the inner edge of the phantom and of any of the test spheres. This second set of ROIs shall also be drawn on the neighbour slices of the central one as close as possible to ±1 cm and ±2 cm from the central slice used for analysis.

The average number of counts contained in ROIs drawn for each hot sphere *j* $\left(C_{H,j}\right)$, and the average number of counts contained in all the corresponding background ROIs $\left(C_{B,j}\right)$, shall be obtained and used to compute the contrast recovery of each hot sphere, by

$$CR_{H,j} = \frac{\frac{C_{H,j}}{C_{B,j}} - 1}{\frac{a_H}{a_B} - 1} \times 100\,[\%], \tag{4.71}$$

with a_H and a_B the activity concentrations of, respectively, the hot spheres and the background, and the percentage of contrast recovery for the cold spheres must be computed from

$$CR_{C,j} = \left(1 - \frac{C_{C,j}}{C_{B,j}}\right) \times 100\,[\%], \tag{4.72}$$

where $C_{C,j}$ is the average number of counts recorded in the ROIs defined for the cold spheres.

Besides the percentage contrast recovers, the percentage of background variability for each sphere *j* must also be reported and is computed from

$$BV_j = \frac{SD_j}{C_{B,j}} \times 100\,[\%], \tag{4.73}$$

with

$$SD_j = \sqrt{\frac{\sum_{k=1}^{K}\left(C_{B,j,k} - C_{B,j}\right)^2}{K-1}}, \tag{4.74}$$

where $K = 60$ is the total number of background ROIs (twelve background ROIs for each sphere in five different slices).

To determine the accuracy of attenuation and scatter corrections, a circular ROI with 30±2 mm diameter shall be drawn centred in the lung insert at each slice *i* and the corresponding average number of counts $\left(C_{lung,i}\right)$ shall then be computed for each slice. Twelve ROIs with the same diameter as that centred in the lung insert should be drawn in the background region, at the same locations used to access the contrast recovery parameter, and the average number of background counts $\left(C_{B,i}\right)$ for each

slice must then be computed. With the obtained data, the residual error of the attenuation and scatter corrections is given by

$$\Delta C_{lung,i} = \frac{C_{lung,i}}{C_{B,i}} \times 100\,[\%]. \tag{4.75}$$

As with the test described in Section 4.6.5 (page 137), this test was also not performed in the scope of the current work and was described for completeness.

4.7 STATE OF THE ART POSITRON EMISSION TOMOGRAPHY SCANNERS

The most recent and state of the art PET scanners with TOF capability, commercialized by the three major manufacturers, are the Gemini TF [Surti et al., 2007] from Philips, the Discovery 690 [Kemp et al., 2009; Bettinardi et al., 2011] from General Electric, and Biograph mCT [Jakoby et al., 2011] from Siemens.

The Properties of these scanners are resumed in Table 4.4, and Table 4.5 resumes the published results of the NEMA NU2 performance tests.

TABLE 4.4: MAIN PROPERTIES OF THE THREE COMMERCIALLY AVAILABLE STATE OF THE ART PET SCANNERS

	Gemini TF	**Discovery 690**	**Biograph mCT**
Dimensions	(mm)	(mm)	(mm)
Diameter	903.4	810	605
Axial Length	180	157	218
Detector			
Crystal type	LYSO	LYSO	LSO
Blocks in the transaxial direction	28 flat modules coupled to continuous light guide	64	48
Blocks in the axial direction		4	4
Detection elements per block/module	23×44	9×6	13×13
Volume of the detection elements (mm^3)	4×4×22	4.2×6.3×25	4×4×20
Energy resolution ($FWHM_{(\%511\ keV)}$)	11.5	12.4	11.5
Energy window (LLD – ULD in keV)	440 – 665	425 – 650	435 – 650
Timing performance			
Coincidence time window (ns)	6	4.9	4.1
TOF resolution – FWHM (ps)	585	544.3	527.5

TABLE 4.5: PUBLISHED DATA OF THE PERFORMANCE PARAMETERS ASSESSED BY MEANS OF THE NEMA NU2 STANDARDS

	Gemini TF				**Discovery 690**				**Biograph mCT**			
NEMA NU2 performance (version)	2001				2007				2007			
Spatial resolution	FWHM		FWTM		FWHM		FWTM		FWHM		FWTM	
Transverse @ 1 cm (mm)	4.8		9.7		4.7		8.83		4.4		8.6	
Axial @ 1 cm (mm)	4.8		9.6		4.74		10.91		4.4		8.7	
Transverse radial @ 10 cm (mm)	5.2		10.3		5.34		10.07		5.2		9.4	
Transverse tangential @ 10 cm (mm)	5.2		10.2		4.79		8.96		4.7		9.2	
Axial @ 10 cm (mm)	4.8		9.6		5.55		11.14		4.7		10.9	
Sensitivity @ 0 cm (kcps/MBq)	6.6				7.4				9.7			
Sensitivity @ 10 cm (kcps/MBq)	—				7.6				9.5			
SF (%)	27				37				33.2			
Peak NECR (kcps @ kBq/cm^3)	125 @ 17.4				139.1 @ 29.0				180.3 @ 28.3			
Image quality	Non-TOF[a]		TOF		Non-TOF		TOF		Non-TOF		TOF	
	CR	BV	CR	BV	CR	BV	CR	BV	CR	BV	CR	BV
10 mm sphere diameter (%)	23	6.3	35	4.8	40.7	5.0	51.6	5.0	35.0	5.9	41.2	5.0
13 mm sphere diameter (%)	34	5.9	44	4.6	69.9	4.5	83.4	4.6	54.7	4.8	55.9	4.4
17 mm sphere diameter (%)	60	5.1	66	4.1	77.6	3.9	88.3	4.1	69.6	3.8	73.1	3.8
22 mm sphere diameter (%)	62	4.4	65	3.7	85.3	3.3	94.5	3.7	63.8	2.4	72.7	2.8
28 mm sphere diameter (%)	68	3.6	59	3.3	65.9	2.7	74.5	3.5	63.8	2.4	75.7	2.8
37 mm sphere diameter (%)	78	2.9	70	3.0	73.8	2.1	79.8	3.4	73.7	2.0	83.4	2.5
Lung residual (%)	—		—		—		—		18.4		11.3	

CHAPTER 5
RESISTIVE PLATE CHAMBER DETECTORS DEVELOPED FOR POSITRON EMISSION TOMOGRAPHY

First developed by Santonico and Cardarelli in 1981 [Santonico & Cardarelli, 1981], RPCs are gaseous detectors with parallel plate electrodes, one of which, at least, must be made of a highly resistive material. Several different configurations exist for RPC detectors. However, in what follows, mention will be made only to the concepts involved in those developed for the proposed PET system, and that were the ones on which the simulations of the present work were based.

5.1 SINGLE-GAP RESISTIVE PLATE CHAMBER DETECTOR

One of the possible layouts of a timing RPC detector[1] with position readout consists of two parallel plate resistive electrodes, with a volumetric resistivity of $\sim 10^{12}\ \Omega\,\mathrm{cm}$, separated by a precise small gap[2] established by interposing appropriate spacers, made of an insulator material, between the resistive electrodes. The gap is filled with an appropriate gas mixture, kept at atmospheric pressure for convenience [Blanco, 2011], forming then the sensitive region of the detector, in which a uniform electric field, with intensity $E_0 \sim 10\ \mathrm{MV\,m^{-1}}$, is established by applying a high voltage potential difference to a pair of opposing electrodes, with volumetric resistivity of $\sim 10^{9}\ \Omega\,\mathrm{cm}$, placed directly on top of the outermost surface of the parallel plate resistive ones. A polyimide film, with volumetric resistivity of $\sim 10^{16}\ \Omega\,\mathrm{cm}$, is then placed on top of each high voltage electrode in order to protect and insulate the electrodes for signal collection from the high voltage ones. The signal collection electrodes consist in a series of metallic strips, with a given width and pitch, which may be separated by guard strips made of an isolator material, located in opposing sides of the RPC detector, and oriented orthogonally relative to each other, assembled on a printed circuit collecting the signals to the electronic readout boards. Fig. 5.1

[1] Timing RPC detectors allow measuring the instants of particle detection with a high resolution, thus allowing the use of TOF information in PET applications (see Section 4.5 on page 118).

[2] Typically, sub-millimetric.

depicts the aforementioned scheme, along with a scheme of the processes that lead to signal induction in the collecting electrodes.

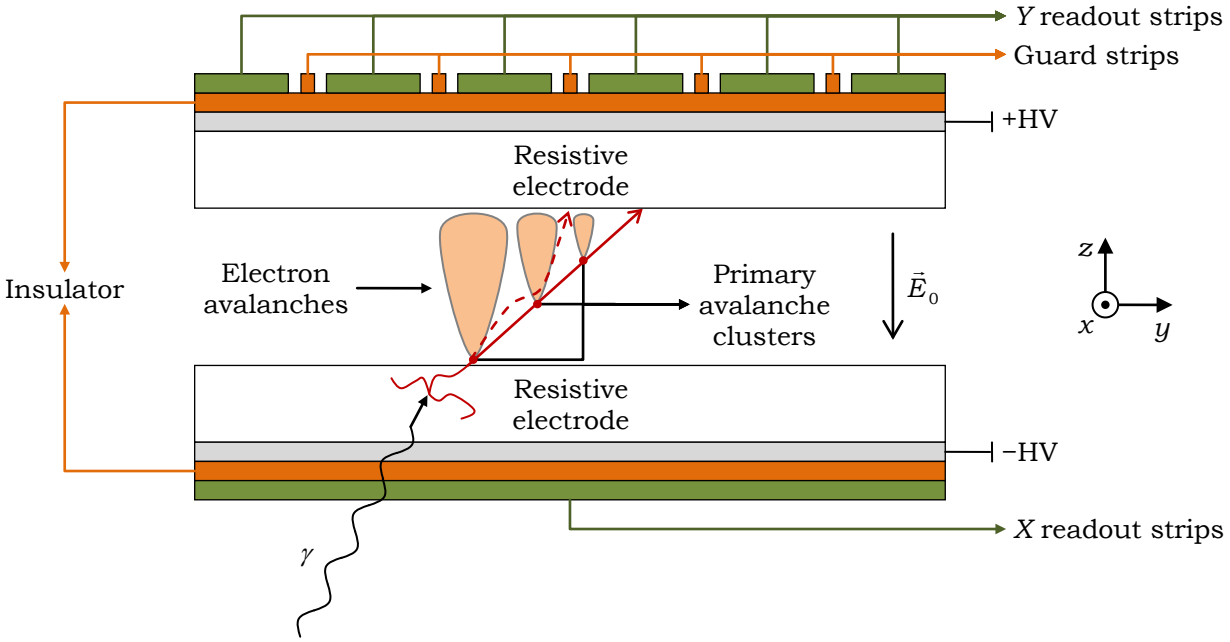

Fig. 5.1: Basic scheme of a single gap RPC detector containing two resistive parallel plate electrodes separated by a gas gap, which forms the active region of the detector and in which a uniform electric field is applied by means of two high voltage electrodes, placed on top of the outer surfaces of the resistive parallel plates, followed by isolation layers on top of which metallic strips for signal collection, possibly separated by isolator guard strips, are placed in opposing sides do the detector and orthogonally to each other.

5.1.1 Primary Physics Processes Leading to Detection

For detection of charged particles, the particles passing through the gap directly ionize the gas there contained creating primary clusters of electron/positive ion pairs which, for highly energetic charged particles, can be regarded as lying along the linear momentum direction of the incident particle (solid red line of Fig. 5.1). The cross sections of the gas mixture for the several interaction processes that a photon can undergo are much smaller than those for charged particles, and the probability of a photon to directly ionize the gas is negligible[3] when compared to that of highly energetic charged particles. So, uncharged particles must first be converted to charged ones, which have a higher interaction probability in the gas mixture being then capable of creating primary electron/positive ion clusters.

The above mentioned conversion may be accomplished by the converter plate

[3] For 511 keV photons, which are those of interest in the present work, but not for low energy photons.

principle [Bateman et al., 1980], which is based on the interaction of the uncharged particles in an appropriate medium, for which the cross sections of the physics processes leading to ionization are some orders of magnitude higher than those of the low density gas medium for the particle intended to be detected. In the case of the RPCs here discussed, this conversion is performed in the resistive plate electrodes, which are made of a highly resistive glass, such as soda lime or borosilicate glass.

Photons interacting in the resistive plate electrodes lead to primary ionizations[4] with consequent creation of δ-rays that will produce further ionizations and more δ-rays, in an electronic cascade process, the great majority of which will be stopped in the resistive electrodes. Nevertheless, a few of those electrons may eventually escape from the resistive plate electrodes and reach the gas gap, where they will be accelerated by the electric field, eventually acquiring sufficient energy to produce primary electron/positive ion clusters.

Due to the low energy of the extracted electrons, their paths in the gas gap are far from being a straight line along their momentum directions, rather having a random path. However, due to the electric field established in the gap, and in the absence of an external magnetic field, the extracted electrons will drift in the field direction [Blanco, 2011], which implies that their tracks are shifted inwards the momentum direction relative to the resistive electrode surface, and toward the normal of the resistive plate direction (dashed red line of Fig. 5.1).

5.1.2 Charge Multiplication in the Gas Gap

Under the influence of the external electric field applied across the gap, primary electrons will drift to the anode, eventually acquiring enough energy to produce further ionizations in collisions with the gas molecules, the produced electrons undergoing then the same processes in cascade and generating the so called Townsend avalanche [Fonte, 2012]. Besides the constant motion along the direction of the externally applied electric field, electrons are also subjected to diffusion due to random collisions caused by thermal motion [Blanco, 2011]. Assuming that the diffusion process is isotropic and characterized by a single diffusion constant D_e, the avalanche growth, in a deterministic approach, will then be axisymmetric around the direction of the externally applied electric field. Taking this direction as that of the Z axis (see dotted line of Fig. 5.2), the avalanche charge density due to electrons at an

[4] For the low effective atomic number of the materials typically used in timing RPCs for detection of photons with energies up to 511 keV, the interaction process leading to ionization of the resistive plate electrodes is almost exclusively Compton scattering (see cross sections for borosilicate and soda lime glasses in Fig. 2.24, page 46).

instant t in a point defined by the position vector $\vec{r}$ relative to that where the primary electron was created is given by [Fonte, 2012]

$$n_e(\vec{r},t) = \mathrm{e}^{\alpha v_e t} \frac{\exp\left(-\frac{r^2}{4D_e t}\right)}{4\pi D_e t} \frac{\exp\left[-\frac{(z-vt)^2}{4D_e t}\right]}{\sqrt{4\pi D_e t}}, \tag{5.1}$$

where r is the distance to the Z axis, and z the distances along it relative to the point where the primary electron of the avalanche was created, α is the first Townsend coefficient[5], and $v = v_e + \alpha D_e$ is the velocity along the Z axis (drift plus diffusion) of the point of the avalanche with higher electronic density [Fonte, 2012].

During the avalanche development, some gas molecules may capture free electrons from the avalanche forming then negative ions. This process, the probability of which is given by the attachment coefficient[6] η, is named electron attachment and affects the exponential growth of the avalanche given by Eq. (5.1), in which the first Townsend coefficient α must then be replaced by the effective Townsend coefficient, given by $\alpha_{eff} = \alpha - \eta$.

Unless they recombine together, both positive and negative ions produced during the avalanche growth will drift toward the cathode and anode, respectively, with drift velocities that are about one thousand times lower than that of electrons[7] [Fonte, 2012], not producing further ionizations for the values of E_0 usually employed in timing RPC detectors [Fonte, 2012]. So, in the time taken for electrons to travel from the starting point of the avalanche to the anode, the charge distribution of the positive and negative ions can be regarded as being essentially static [Fonte, 2012].

5.1.2.1 Space-Charge Effect

Both positive and negative ions tend to be located in the centre of the avalanche (hereinafter referred to as the avalanche body) due to their lower electric mobilities[8], when compared to that of electrons, leading to the establishment of an electric field by the avalanche charge distribution that, at some stage of the amplification process, may attain intensities comparable to that of the externally applied electric field, which

5 The first Townsend coefficient is the number of ionizing collisions per unit length undertaken by an electron under the influence of an electric field, and is equal to the reciprocal of the ionization mean free path [Blanco, 2011].

6 The attachment coefficient represents the number of free electrons that, drifting under the influence of the externally applied electric field, will undergo electron attachment per unit length [Blanco, 2011].

7 Reasonable values for the drift velocities are ~10 cm/μs for electrons and ~10 cm/ms for ions [Fonte, 2012].

8 The drift velocity v_d of a charged particle in a uniform electric field is related to the field intensity E_0 by $v_d = \mu/E_0$, where μ is the electric mobility of the charged particle.

will then be perturbed [Bromley, 1994; Blanco, 2011]. At this stage, the charge carriers in the avalanche body will sense an electric field (E_2 in Fig. 5.2) whose intensity is lower than that of the externally applied one (E_0 in Fig. 5.2) with a consequent reduction of the gas amplification gain in this region [Bromley, 1994; Blanco, 2011]. As to the head and tail of the avalanche, the electric field created by the charge carriers combines with the externally applied one, resulting in electric fields having higher intensities (E_1 and E_3 of Fig. 5.2) than that of the externally applied one (E_0 in Fig. 5.2), and can lead to an increase of the gas gain in these regions [Blanco, 2011]. The aforementioned effect is known as space-charge effect and plays a major role in the behaviour of RPC detectors [Blanco, 2011].

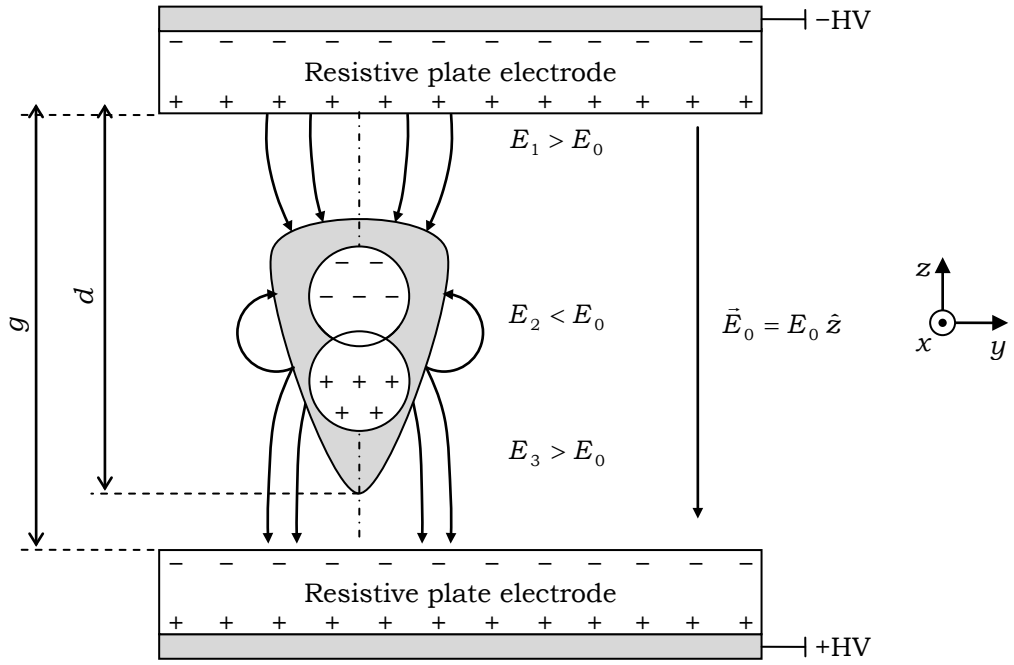

Fig. 5.2: Schematic representation of an avalanche with the modified electric field due to the avalanche charge distribution. E_1, E_2 and E_3 are the intensities of the modified electric field in the three regions of the avalanche. This effect is known as space charge effect.

5.1.2.2 Avalanche Mode of Operation

If the number of electrons contained at the head of the avalanche remains at low values, the space-charge effect at the head of the avalanche is compensated by that of the avalanche body (see Fig. 5.2), which will tend to slow down the electrons of the avalanche head and, consequently, lower the gas gain. The avalanche then remains in the stage of development depicted in Fig. 5.2 until it reaches the electrodes [Bromley, 1994; Blanco, 2011]. The RPC detector is then said to operate in avalanche mode, as is the case of those developed for the RPC TOF-PET scanner, which are characterized

by relatively small avalanche charges (~10 pC), allowing count rates per unit area of detection up to $3\ \mathrm{kHz\,cm^{-2}}$ [Neves, 2008].

5.1.2.3 Streamer Mode of Operation

If the number of electrons at the avalanche head reaches a critical value, the gas gain in that region can increase such that the avalanche does not remain at the development stage depicted in Fig. 5.2. Streamers may then arise from the avalanche head to the anode, resulting in larger pulses than those arising in the avalanche mode of operation [Fonte, 2012].

In avalanche mode of operation, it is normal that a small fraction of streamers arise [Fonte, 2012]. However, if the fraction of streamers become dominant, than the avalanche becomes uncontrolled and the RPC is said to operate in streamer mode, which is characterized by higher avalanche charges (from tenths of pC up to a few nC) and higher recovering times that reduce the maximum allowed count rate per unit area to a maximum of $\sim 300\ \mathrm{Hz\,cm^{-2}}$ [Neves, 2008].

5.1.2.4 Why Resistive Plates

In the limit, streamers may lead to the formation of a highly conductive plasma channel connecting the anode to the cathode [Fonte, 2012]. If the electrodes were both metallic, as is the case of Parallel Plate Chamber detectors[9], the highly conductive electrodes would discharge globally with a strong current burst through the gas gap leading to a spark.

The use of resistive electrodes limits the amount of charge that can flow through the high conductive plasma channel, inhibiting a global discharge from the anode to the cathode, which will be then contained locally in the electrode, resulting in local stunted sparks [Fonte, 2012].

5.1.3 Gas Mixture

The gas mixture usually employed in timing RPC detectors is composed of tetrafluoroethane ($C_2H_2F_4$), iso-butane (iso-C_4H_{10}), and sulfur hexafluoride (SF_6), in volume proportions of 85:5:10. The $C_2H_2F_4$ presents a high primary ionization density also acting as a quencher of ionizations due to low energy photons resulting from electronic deexcitation, while the SF_6 is a high electronegative gas that seems to act as a quencher of the fast avalanche growth by capturing free electrons.

As to the iso-C_4H_{10}, it does not change the RPC behaviour, being thought to slow

[9] Parallel Plate Chamber (PPC) detectors are the full metallic version of RPC detectors [Fonte, 2012].

the aging of RPC detectors [Neves, 2008]. For this, other mixtures that do not contain iso-C_4H_{10} are also used in timing RPCs. One of those mixtures consists of $C_2H_2F_4$ and SF_6 with volume proportions of 90:10, respectively.

5.2 SIGNAL INDUCTION

An accurate treatment of the signal induction in the pickup electrodes is out of the scope of the present work and can be found in [Fonte, 2012]. In what follows, a simple description, the detailed treatment of which can also be found in [Fonte, 2012], will be made to allow the understanding of the electronics involved in time and position readout, addressed in Section 5.4 (page 155), and which is needed to understand the implementation of the processing of the simulation produced data to account for the detection readout.

The moving charge carriers of the avalanche in the gas gap will induce a time varying current in the pickup electrodes that flows to both ends of the pickup electrodes, thus producing a current which has contributions from the electrons as well as from the positive and negative ions. The full computation of this current taking into account the space charge effect can only be performed numerically [Fonte, 2012]. However, qualitative and somehow quantitative useful results can be obtained with a simple model of electron amplification, in which the avalanche size is small enough to do not be affected by space-charge effects, and diffusion is neglected [Fonte, 2012]. In these limits, the currents induced by electrons as well as positive and negative ions are given by [Fonte, 2012]

$$I_e(t) = \gamma v_e \, \mathrm{e}^{\alpha_{eff} v_e t} \qquad \text{for} \quad 0 \le t \le T_e \,, \tag{5.2}$$

$$I_{i,+}(t) = \begin{cases} \gamma v_{i,+} \dfrac{1}{\alpha_{eff}} \left(\alpha \, \mathrm{e}^{\alpha_{eff} d} - \eta \right) & \text{for} \quad T_e \le t \le T'_{i,+} \\ \gamma v_{i,+} \dfrac{\alpha}{\alpha_{eff}} \left[\mathrm{e}^{\alpha_{eff} d} - \mathrm{e}^{\alpha_{eff} (d - g + v_{i,+} t)} \right] & \text{for} \quad T'_{i,+} < t \le T_{i,+} \end{cases}, \tag{5.3}$$

$$I_{i,-}(t) = \gamma v_{i,-} \frac{\eta}{\alpha_{eff}} \left[\mathrm{e}^{\alpha_{eff} (d - v_{i,-} t)} - 1 \right] \qquad \text{for} \quad T_e \le t \le T_{i,-} \,, \tag{5.4}$$

where g is the thickness of the gas gap (see Fig. 5.2 on page 149), d is the amplification distance along the Z axis (see Fig. 5.2 on page 149), v_e, $v_{i,+}$ and $v_{i,-}$ are the drift velocities of electrons, and positive and negative ions, respectively, $T_e = d/v_e$ is the transit time of the electrons, $T'_{i,+} = (g-d)/v_{i,+}$ and $T_{i,+} = g/v_{i,+}$ are the minimum and maximum transit times of positive ions, and $T_{i,-} = d/v_{i,-}$ is the transit time of the negative ions. For times not comprised in the time intervals of the above expressions

the currents can be considered as being equal to zero.

The yet undefined constant γ is the induction coefficient, which depends on the exact geometry of the RPC detector and on the electrical properties of the resistive plates. For a regular multi-gap RPC detector (see Section 5.3 on page 153) comprising N gaps each with a thickness g, and $N+1$ resistive electrodes each with a thickness ℓ and relative permittivity ε_r, with infinite dimensions in the XY plane containing a single infinite size strip both in the X and Y directions, the induction factor is given by [Fonte, 2012]

$$f_{ind.} = \frac{e}{N\,g + \dfrac{(N+1)\,\ell}{\varepsilon_r}}. \tag{5.5}$$

This expression can easily be adapted for non-regular multi-gap RPC detectors, with gas gaps and resistive plates having different thicknesses, with the resistive electrodes being also made of different materials [Fonte, 2012].

Fig. 5.3 depicts the times, shapes and relative intensities of the currents given by Eq. (5.2) to Eq. (5.4) for $\alpha = 40\ \text{mm}^{-1}$, $\eta = 10\ \text{mm}^{-1}$, $g = 0.35\ \text{mm}$, $d = 0.2\ \text{mm}$, $v_e = 130\ \text{mm}\,\mu\text{s}^{-1}$ and $v_{i,+} = v_{i,-} = 0.3\ \text{mm}\,\mu\text{s}^{-1}$ [Fonte, 2000]. As it can be seen, the current induced by electrons has a fast rise and fall time and a peak intensity that is $\sim 10^3$ higher than that induced by the positive ions, the former determining the time resolution of the detector, while the latter will be used to compute the centroid of the total charge of the avalanches generated in the gas gaps, thus determining the

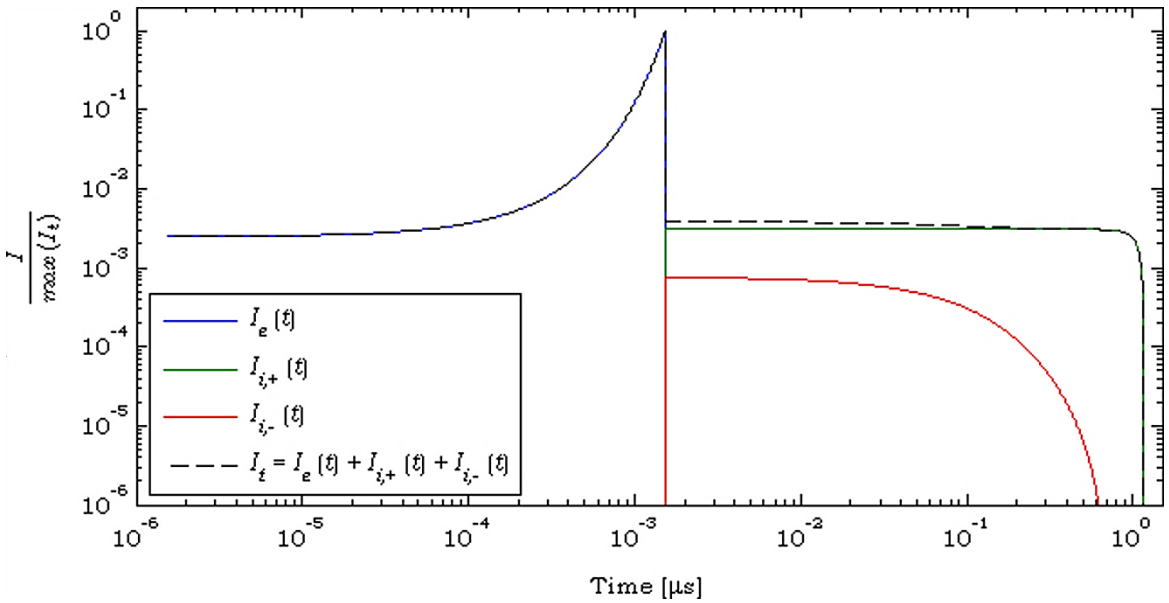

Fig. 5.3: Induced currents (electrons, positive and negative ions, and total), normalized to the maximum total current, obtained from Eq. (5.2) to Eq. (5.4) with $\alpha = 40\ \text{mm}^{-1}$, $\eta = 10\ \text{mm}^{-1}$, $g = 0.35\ \text{mm}$, $d = 0.20\ \text{mm}$, $v_e = 130\ \text{mm}\,\mu\text{s}^{-1}$ and $v_{i,+} = v_{i,+} = 0.3\ \text{mm}\,\mu\text{s}^{-1}$.

minimum time required between successive events for the position to be computed with the required precision. As to the negative ions, their contribution to the total induced signal is almost negligible.

5.3 MULTI-GAP RESISTIVE PLATE CHAMBER DETECTOR

As seen in the previous sections, the detection efficiency of an RPC detector for detection of photons depends on the combined efficiency of several distinct processes: photon interaction in the resistive plates, extraction of electrons from the resistive plates to the gas gaps, creation of primary electron/positive ion clusters in the gas gap due to collisions of the extracted electrons with the gas molecules, avalanche multiplication so that enough charge is created to induce a measurable signal in the pickup electrodes. This depends on the induction factor γ (Eq. (5.5)) which, on average, depends on the detector geometry. So, it is not surprising that while having detection efficiencies of up to 75% for 0.3 mm thick gaps for Minimum Ionizing Particles [Fonte & Peskov, 2002; Blanco et al., 2003b], which are minimum ionizing particles, single-gap RPC detectors have very low detection efficiencies for photons with energies up to 511 keV (< 1.6% for an eight gap RPC, leading to < 0.2% per gap [Blanco et al., 2009]). This is mainly due to the low interaction probability of photons with the thin resistive plate electrodes. Moreover, augmenting the resistive plate thickness will not solve the problem of detection efficiency, since, then, the probability of electron extraction will be very low. In fact, for a given detection system based on RPC detectors with a given geometry, there is an optimum thickness for the resistive plates that maximizes the detection efficiency[10]. A solution to improve the detection efficiency could be to stack several single-gap RPC detectors with optimized resistive plate thicknesses. However, this solution is not cost effective due to the increased electronic requirements.

A more cost effective solution consists in stacking several resistive plate electrodes, with optimized thickness, that are then read by the same set of pickup electrodes. However, the detector cannot have an arbitrary number of resistive plates since the induction factor roughly decreases in the inverse proportion of the number of gaps as it can be seen from Eq. (5.5). Moreover, and contrary to what happens in the case of highly energetic charged particles, which ionize the gas of almost all gaps it traverses, thus producing a higher total avalanche charge for a multi-gap RPC detector which may induce a signal even in RPC detectors with a high number of resistive

[10] Results obtained by simulations performed in GEANT4 for photons impinging perpendicularly a stack of glasses, without accounting for the complete geometry of the detector, can be found in [Blanco et al., 2009].

plates read by the same pickup electrodes, the number of ionized gaps in the case of photon detection will be small, even for a high number of resistive plates, and almost certainly equal to one for an RPC detector with five to ten gaps, only the probability of interaction and electron extraction in a single detector being augmented. Besides, with the increase of the number of gaps, and consequently the distance of the avalanche to one or both pickup electrodes, the profile of charge induced in the readout electrodes will be wider, eventually compromising the intrinsic spatial resolution of the detector. So, even in the case of multi-gap RPCs, several detectors with a limited number of gas gaps have to be stacked in order to achieve detection efficiencies compatible with those required by a PET scanner.

For the above mentioned reasons, the most cost effective solution for multi-gap RPC detectors aimed for the detection of photons, consists in augmenting the number of gaps to an acceptable value while maintaining the electronics to the minimum requirements necessary to collect the induced signals, which can be achieved with an arrangement as that presented in Fig. 5.4, in which the detector is divided in two independent detection modules with a common pickup electrode with the strips aligned in one direction (the *X* direction in the presented case, which is used to

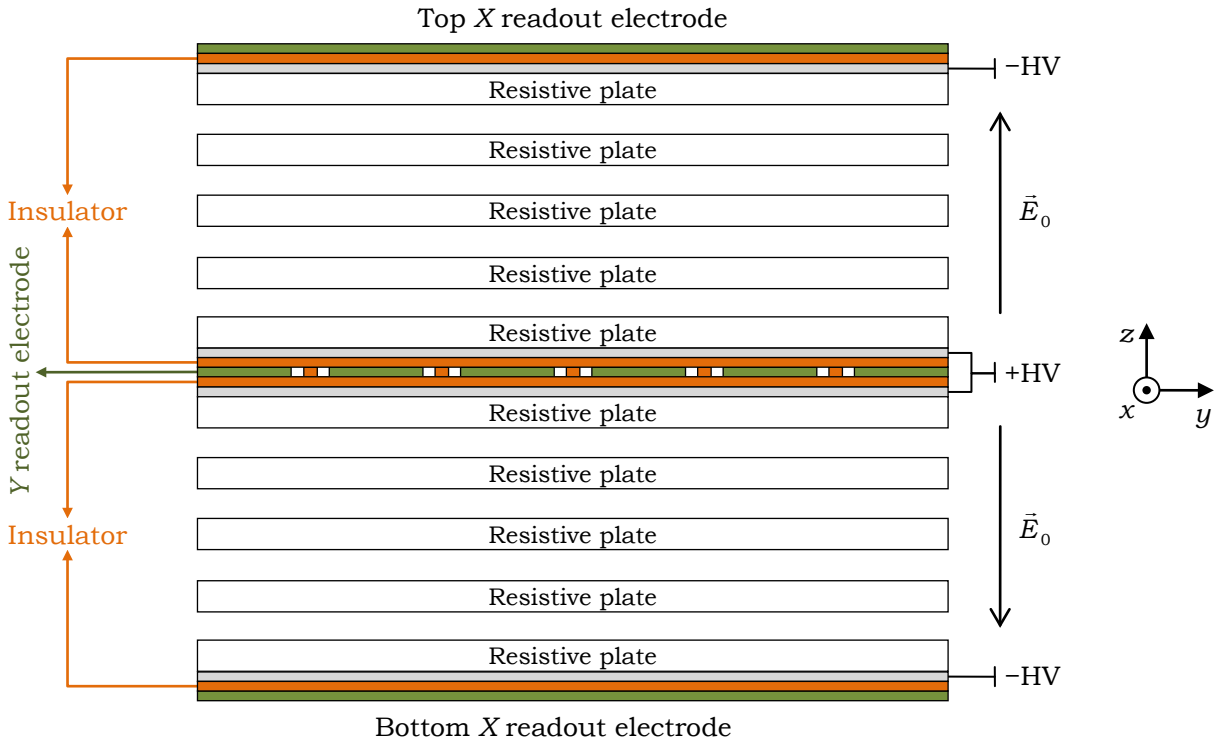

Fig. 5.4: Scheme of a multi-gap RPC detector consisting of two detection modules with two sets of independent *X* readout strips and a set of common *Y* readout strips. This scheme allows to distinguish in which detection module the photon was detected, and eventually the gap where avalanches were developed by comparing the charge induced in the *X* and *Y* pickup strips.

measure the instants of photon detection, a coarse position of the avalanche centroid along the *X* direction and the fine position of the avalanche centroid along the *Y* direction), and two sets of independent pickup electrodes aligned in the other direction (the *Y* direction in the presented case), which is used to measure the fine position of the avalanche centroid along the *X* direction). This scheme allows improving the detection efficiency with the lowest electronic requirements while allowing distinguishing the detection module in which the photon interacted, thus providing some DOI resolution by attributing the detection along the *Z* direction to the midpoint of the corresponding detection module, or even by identifying the gap in which the detection occurred by comparing the induced signal on the *X* and *Y* pickup electrodes. (Notice that the *X* aligned strips form the *Y* readout electrode, since they are used to read the fine position along the *Y* direction, while the *Y* aligned strips form the *X* readout electrode, since they are used to read the fine position along the *X* direction.)

5.4 TIME AND POSITION READOUT

Several schemes can be employed to read the signal induced in the pickup strips. In what follows only the one employed in the detectors developed for the RPC TOF-PET scanner, and used in the processing of the simulation data preformed in the current work, will be mentioned, the details of which can be found in [Fonte et al., 2010].

Before proceeding, and in order to use the terminology commonly employed in PET and already introduced in Chapter 4, it is worth to mention that the *X* and *Y* oriented pickup strips are aligned along the scanner axial and transaxial directions, respectively.

5.4.1 Readout Scheme of the *X* (Axially) Aligned Strips

The strips aligned along the *X* (axial) direction (comprising the *Y* readout electrode) with a given width and pitch (currently equal to 2 mm) are grouped in sets of n_Y (currently 15) contiguous strips forming the basic readout unit (hereinafter referred to as a readout subsection) depicted in Fig. 5.5 (page 156), and which is used to measure detection times and coarse *X* (axial) and fine *Y* (transaxial) positions[11].

At one of the subsection ends (hereinafter referred to as the left end, *L*) the readout electronics of the subsection, consisting basically of a current amplifier, generates a valid time signal, t_L, if the current rises above a suitable threshold, which

[11] The total length of the readout subsections is not limited to that of a single RPC detector. The readout electronics depicted in Fig. 5.5 can be placed at opposing ends of several detectors aligned and interconnected along the *X* (axial) direction.

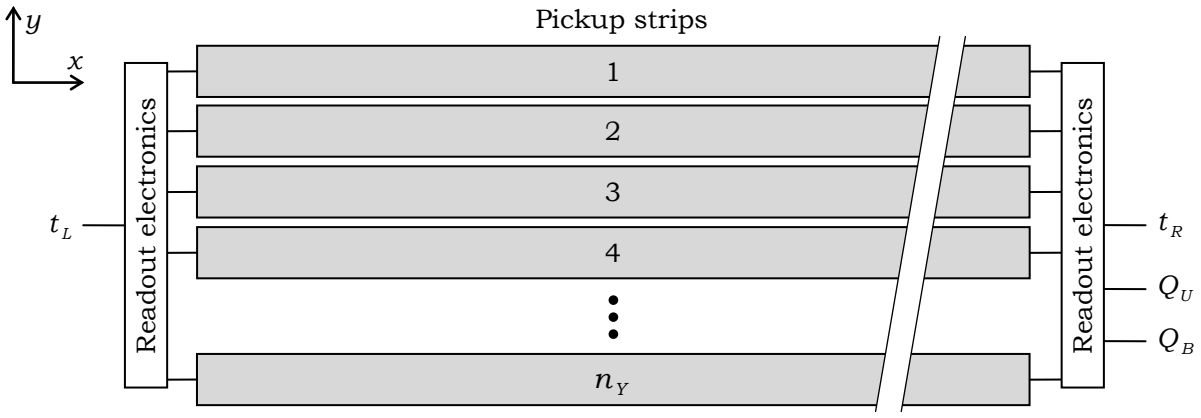

Fig. 5.5: Block diagram of the basic readout unit (subsection) of the *Y* (axially aligned) pickup strips, depicting the time signals obtained at the left (t_L) and right (t_R) sides of the strips and the fraction of charge collected at the upper (Q_U) and bottom ends (Q_B) of the subsection. (Adapted from [Fonte et al., 2010]).

is set according to the current induced by the electrons of the avalanches, as depicted in Fig. 5.3 (page 152). At the opposing end of the subsection (hereinafter referred to as the right end, *R*) the readout electronics generates three signals, one of which is also a time signal generated as that of the left side. The other two signals, are generated by a capacitive division chain that essentially integrates the current induced by the positive and negative ions of the avalanches (Section 5.2, page 151, and Fig. 5.3, page 152), leading to two charge signals: one for the position dependent fraction of the induced charge flowing to the upper end (Q_U), and one for the complementary fraction flowing to the bottom end (Q_B) portions of the subsection.

A given number of consecutive subsections (currently 3) are then grouped to form an independent readout section as depicted in Fig. 5.6.

The time signals from each of the ends of the subsections are analogically summed through wired-ORs resulting in single time signals for each of the readout section ends, t_L and t_R. These signals, which are also encoded with information that allows identifying the subsection in which they occurred, are then fed to a digitizer module.

With this scheme a single time signal is generated for each of the readout section ends while permitting to identify the subsection where the detection occurred, thus allowing computing a coarse position of the detection point along the *Y* (transaxial) and *X* (axial) directions. The coarse position along the *Y* (transaxial) direction is simply taken as the subsection centre corresponding to a maximum error at the detector level of $0.5 \times n_Y \times y_{pitch}$ (currently equal to 15 mm) with y_{pitch} the pitch between the strips aligned along the *X* (axial) direction. The coarse position along the *X* (axial) direction

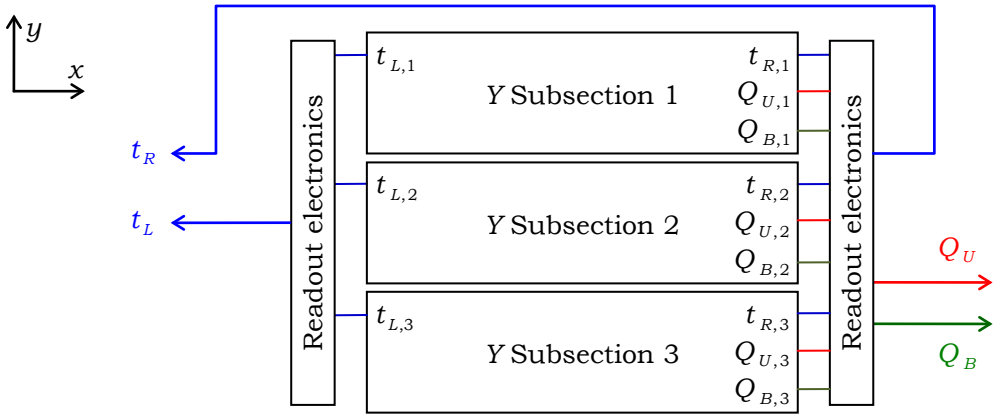

Fig. 5.6: Block diagram of each independent readout section of the detector. The time signal t_R is given by a wired-OR that analogically sums the times $t_{R,1}$, $t_{R,2}$ and $t_{R,3}$. Likewise, the time signals $t_{L,1}$, $t_{L,2}$ and $t_{L,3}$ are analogically summed by a wired-OR, and encoded with information that allows to identify the subsection (Adapted from [Fonte et al., 2010]).

can be computed from the detection times through

$$x_{coarse} = \frac{v}{2}(t_L - t_R)x_{center}, \tag{5.6}$$

where $v \simeq c/2$, with c the light speed, is the propagation speed of the time signals along the X (axially) aligned strips [Neves, 2008] and x_{center} is the absolute position of the strips centre along the X (axial) direction, relative to an appropriate reference frame (for instance, the scanner reference frame). Due to the time resolution of the current amplifiers currently used to measure the detection times, which follows a ~45 ps σ Gaussian distribution, the X_{coarse} variable follows a ~1 cm σ Gaussian distribution.

As to the upper $(Q_{U,1}$, $Q_{U,2}$ and $Q_{U,3})$ and bottom $(Q_{B,1}$, $Q_{B,2}$ and $Q_{B,3})$ charge signals, are combined in single upper (Q_U) and bottom (Q_B) charge signals, which are also sent to a digitizer module. From these charge signals the fine position along the Y (transaxial) direction is obtained by linear interpolation of the upper and bottom charges, through

$$y_{fine} = \frac{Q_U - Q_B}{Q_U + Q_B}\frac{y_{width}}{2} + y_{center}, \tag{5.7}$$

where y_{width} is the width of the subsection (currently equal to 30 mm) and y_{center} is the absolute position of the subsection centre along the Y (transaxial) direction, relative to an appropriate reference frame (for instance, the scanner reference frame).

5.4.2 Readout Scheme of the *Y* (Transaxially) Aligned Strips

The readout of the strips aligned along the Y (transaxial) direction (used to read

the position along the X direction), depicted in Fig. 5.7, is performed differently from those aligned along the X (axial) direction and only makes use of charge amplifiers. A set of n_X (currently 10) contiguous strips with a given width and pitch (currently equal to 2 mm) are connected in an interleaved manner to an appropriate number of charge amplifiers forming then larger X (axial) readout sections.

Once the coarse position along the X (axial) direction is known, the X (axial) readout subsection is identified, and the charge collected at the corresponding charge amplifier is used to compute the fine X (axial) position by

$$x_{fine} = \frac{Q_{L,i} - Q_{R,i}}{Q_{L,i} + Q_{R,i}} \frac{x_{width}}{2} + x_{center}, \tag{5.8}$$

where the subscript i identifies the larger section to which the X (axial) subsection belongs, x_{width} is the subsection width, and x_{center} is the position of the centre of the subsection relative to an appropriate reference frame (for instance, the origin of the scanner reference frame), which can be computed from the x_{coarse} position and the width of the subsections, x_{width}, by

$$x_{center} = \mathrm{sgn}\left(x_{coarse}\right) \left| \left\lfloor \frac{x_{coarse}}{x_{width}} \right\rfloor + 0.5 \right| x_{width}, \tag{5.9}$$

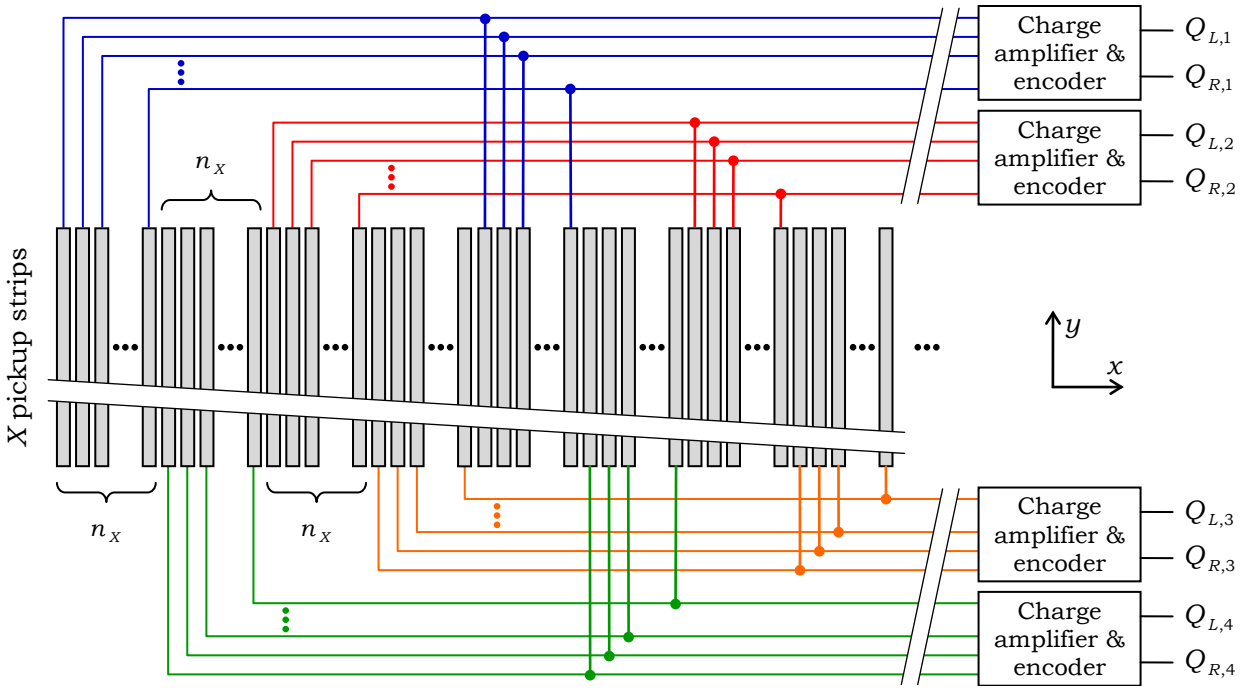

Fig. 5.7: Block diagram of the readout of the Y (transaxially) aligned strips used to determine the fine position along the X (axial) direction. The readout is performed by an appropriate number of charge amplifiers read in a cyclic manner from which the charges in the left and right portions of the readout sections are obtained.

where $\mathrm{sgn}(X)$ and $\lfloor X \rfloor$ are, respectively, the sign and floor functions.

5.4.3 Detector Dead Time

To avoid retriggering time signals due to signal reflections at the strip ends (see Fig. 5.3 on page 152), the comparators placed at both ends of the *Y* (transaxial) readout subsections impose a τ_{ts} non-paralyzable dead time window[12] if the fast component of the current induced in the pickup electrodes rises above the triggering threshold (hereinafter this dead time will be referred to as the dead time for time signals). So, if a second photon interacts in the same subsection of the RPC detector during the τ_{ts} dead time for time signals, the corresponding time cannot be determined. In this case the times given at the left and right ends of the subsection (t_L and t_R in Fig. 5.5, page 156) will correspond to those of the first signal reaching each of the subsection ends.

Two or more photons can also be detected in different subsections of the same readout section during the τ_{ts} dead time window for time signals that has been opened in the first triggered subsection, or cross talk between adjacent subsections (or even sections) can occur. In this case, each subsection will impose, at each of its ends, its own τ_{ts} non-paralyzable dead times for time signals returning then the corresponding left and right times ($t_{L,i}$ and $t_{R,i}$ of Fig. 5.6 on page 157, with the subscript i denoting the subsection) as described in the above paragraph. However, since the timing signals of all the subsections of a given section are analogically summed through wired-ORs, it is not possible to distinguish the individual times coming from each subsection. In this case, the times at both ends of the subsections will give rise to single detection times for the left and right ends of the entire readout section (t_L and t_R in Fig. 5.6, page 157) which are equal to the lowest times measured at each of the readout section ends. So, in practice, each readout section has a single τ_{ts} non-paralyzable dead time for time signals during which a single valid detection time can be read at each of the readout section ends.

A second dead time, equal in both the *Y* (transaxial) and *X* (axial) readout sections, arises due to the shape and timing of the voltage signals generated by the charge amplifiers, and the time needed to unequivocally identify the *X* (axial) and *Y* (transaxial) positions of the charge centroid of the avalanche. The complete treatment of this dead time, hereinafter referred to as the dead time for position signals, and denoted by τ_{ps}, is out of the scope of the present work. However, useful qualitative and somewhat quantitative results for the understanding of the origin of the τ_{ps} dead

[12] Currently $\tau_{ts} = 0.2$ μs

time for charge signals can be obtained in the limit of small diffusionless avalanches (see Section 5.2 on page 151). By integrating Eq. (5.2) to Eq. (5.4) from zero to a given instant *t*, the time dependent charges induced in the pickup electrodes by the electrons and positive and negative ions are given by [Fonte, 2012]

$$Q_e(t) = \gamma \frac{1}{\alpha_{eff}} \left(\mathrm{e}^{\alpha_{eff} v_e t} - 1 \right) \qquad \text{for} \quad 0 \le t \le T_e \,, \tag{5.10}$$

$$Q_{i,+}(t) = \begin{cases} \gamma v_{i,+} \dfrac{1}{\alpha_{eff}} \left(\alpha \, \mathrm{e}^{\alpha_{eff} d} - \eta \right) t & \text{for} \quad T_e \le t \le T'_{i,+} \\ \gamma \left[v_{i,+} \dfrac{1}{\alpha_{eff}} \left(\alpha \, \mathrm{e}^{\alpha_{eff} d} t - \eta T'_{i,+} \right) \right. & \\ \left. \quad - \dfrac{\alpha}{\alpha_{eff}^2} \mathrm{e}^{\alpha_{eff}(d-g)} \left(\mathrm{e}^{\alpha_{eff} v_{i,+} t} - \mathrm{e}^{\alpha_{eff} v_{i,+} T'_{i,+}} \right) \right] & \text{for} \quad T'_{i,+} \le t \le T_{i,+} \end{cases} , \tag{5.11}$$

$$Q_{i,-}(t) = \gamma \frac{\eta}{\alpha_{eff}^2} \left[\mathrm{e}^{\alpha_{eff} d} \left(1 - \mathrm{e}^{-\alpha_{eff} v_{i,-} t} \right) - \alpha_{eff} v_{i,-} t \right] \qquad \text{for} \quad T_e \le t \le T_{i,-} \,, \tag{5.12}$$

with all the quantities already defined in Section 5.2 (page 151). Neglecting the discharge of the capacitor of the charge amplifier, for times above those corresponding to the upper limits of the time intervals of Eq. (5.10) to Eq. (5.12), the output signal will be the same as that of the corresponding upper time limits: $Q_e(t > T_e) = Q_e(T_e)$, $Q_{i,+}(t > T_{i,+}) = Q_{i,+}(T_{i,+})$ and $Q_{i,-}(t > T_{i,-}) = Q_{i,-}(T_{i,-})$. Fig. 5.8 depicts the curves from Eq. (5.10) to Eq. (5.12) obtained with the same set of parameters used in Fig. 5.3 (page 152) ($\alpha = 40\ \mathrm{mm}^{-1}$, $\eta = 10\ \mathrm{mm}^{-1}$, $g = 0.35\ \mathrm{mm}$, $d = 0.2\ \mathrm{mm}$, $v_e = 130\ \mathrm{mm\,\mu s}^{-1}$ and $v_{i,+} = v_{i,-} = 0.3\ \mathrm{mm\,\mu s}^{-1}$), for a total charge collection time $t_{collection} = 2\tau_{Q,rise}$ with $\tau_{Q,rise} = 1\ \mu\mathrm{s}$, in this example, the time needed to fully collect the charge induced by the avalanches.

The voltage signal returned from the output of the charge amplifier, which is proportional to the total charge collected over time, is first digitized and then filtered, giving rise to a signal as that depicted in Fig. 5.9 for three different events, each with a $\tau_{Q,rise}$ rise time, separated by a $\tau_{Q,plateau}$ steady time. To determine the fine position in both the *X* (transaxial) and *Y* (axial) directions, the charge signal is analysed to detect and quantify the charge plateaus occurring before and after the signal rise due to the time varying charge induced by the avalanche propagation in the gas gaps, and detection is assumed if a difference of charge is found between the plateaus.

To improve the SNR, the signal corresponding to the plateau portions has to be averaged for a specified time $\tau_{Q,plateu}$. So, for measuring accurately the position of the centroid of the avalanche, a total time given by $\tau_{ps} = \tau_{Q,rise} + 2\tau_{Q,plateau}$ is needed, which

corresponds to the total dead time for position signals[13]. Notice that the τ_{ps} paralyzable dead time is not a physical dead time in the sense of limiting the count rate of the detector.This dead time only limits the capability to discriminate the fine position of the centroid of the charge distribution in the gas gaps, which cannot be obtained if pileup occurs in the charge signals. However, for each pair of valid times at the opposing ends of the *X* (axially) aligned readout sections, a coarse position can always be obtained. So, the only physical dead time of the RPC detector is the non-paralyzable dead time for time signals referred to in Section 5.4.1 (page 155).

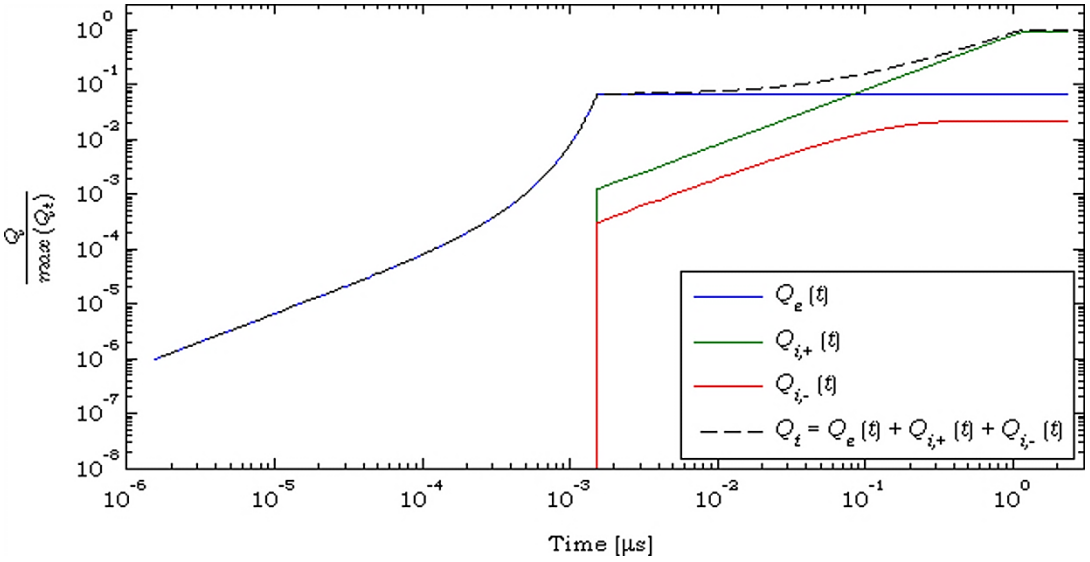

Fig. 5.8: Collected charges (electrons, positive and negative ions, and total), normalized to the maximum total charge, obtained from Eq. (5.10)to Eq. (5.12), with $\alpha = 40\ \text{mm}^{-1}$, $\eta = 10\ \text{mm}^{-1}$, $g = 0.35\ \text{mm}$, $d = 0.20\ \text{mm}$, $v_e = 130\ \text{mm}\,\mu\text{s}^{-1}$ and $v_{i,+} = v_{i,+} = 0.3\ \text{mm}\,\mu\text{s}^{-1}$.

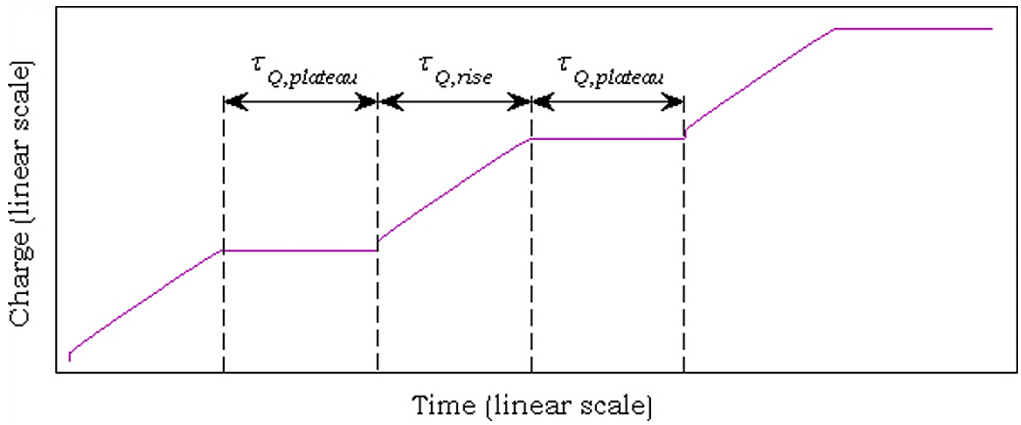

Fig. 5.9: Total collected charge (dashed line of Fig. 5.8) for three induced signals separated with a rise time equal to $\tau_{Q,rise}$ followed by a plateau $\tau_{Q,plateau}$.

[13] Currently $\tau_{Q,rise} = 1\ \mu\text{s}$, $\tau_{Q,plateau} = 1\ \mu\text{s}$ which implies $\tau_{ps} = 3\ \mu s$.

5.5 FINAL CONSIDERATIONS ON DETECTION EFFICIENCY AND TIME, POSITION AND ENERGY RESOLUTION

For a measurable signal to be induced in the pickup strips, the total charge of the avalanche must reach a minimum value which, for a given gas mixture, depends on the intensity of the externally applied electric field, and on the amplification distance (d in Fig. 5.2, on page 149). Considering the typical values of the externally applied electric field employed in timing RPC detectors, $\left(\sim 10\ \mathrm{MV\,m^{-1}}\right)$, the minimum amplification distance is ~0.1 mm [Lippman et al., 2009], which implies that the electrons extracted to the anode side of the gas gaps must have kinetic energies greater than 1 keV along the field direction. Since the probability of electron extraction from the resistive plate electrodes is not equal in the backward and forward directions, the latter being higher than the former (see Section 7.2.2 on page 224), there may exist a difference in the detection efficiencies of the two detection modules depicted in Fig. 5.4 (page 154), the one for which the incident photon impinges the anode side of the resistive plates being more efficient than the other. So, symmetric multi-gap timing RPC detectors as those depicted in Fig. 5.4 (page 154), for which the thickness of the gas gap is about ~0.3 mm, although being more cost-effective in what concerns the readout electronics, may present a drawback in the detection efficiency when compared to multi-gap timing RPC detectors with a single detection module (the upper or bottom detection module of Fig. 5.4 on page 154), since the latter can be stacked such that the cathodes of the resistive plates face the side from which photons impinge the detector, in which case all the extracted electrons can eventually be amplified in the gas gap, even if their kinetic energies are equal to zero.

As mentioned at the end of Section 5.4.1 (page 155), the intrinsic time resolution of the current amplifiers used to measure the instants of photon detection implies that the detection times at both ends of the strips follow a ~45 ps σ Gaussian distribution, which implies a time resolution of ~105 ps FWHM (see Eq. (4.28) on page 116). However, this is the timing resolution for measuring signals once they have been induced in the pickup strips, and not the time resolution for detecting single events. This latter has contributions from both the timing electronics and the time fluctuations intrinsic to the photon detection, which include the statistical variations in the time from photon interaction to electron extraction, the time-of-flight of the extracted electron in the gas gap, the time span where the charge is deposited in the gas gap and the dynamics of the avalanche growth [Lippman et al., 2009]. For the above mentioned reasons, the time resolution of single events has to be determined indirectly from the time resolution of coincidence detection of annihilation photons

which, for a 0.3 mm gap thickness, was experimentally measured and found to approximately follow a Gaussian distribution with 300 ps FWHM, for a single gap RPC detector with a 0.3 mm thick gas gaps separating a glass electrode from an aluminium one [Blanco et al., 2003a]. The same value was found for a double module multi-gap RPC detector as that presented in Fig. 5.4, with each detection module having five 0.2 mm thick gaps delimited by six 0.4 mm thick glasses [Neves, 2008], suggesting that the time resolution of timing RPC detectors for detection of photons is roughly independent of the geometric parameters of the detectors, viz., independent of the resistive floating electrodes and gas gap thicknesses. So, by applying the properties of the Gaussian distribution already introduced in Section 4.5 (page 115), and by solving Eq. (4.29) (page 116) for σ_t, one may conclude that the instants of photon detection follow approximately a 90 ps σ Gaussian distribution.

Although the pickup electrodes consist of a series of strips with a finite width and pitch, the intrinsic spatial resolution of an RPC detector is much less than the strips pitch. A first non-optimized RPC detector developed for proof of concept of the RPC TOF-PET, and having strips with 1 mm pitch, showed an intrinsic spatial resolution of 0.47 mm FWHM after image reconstruction of a point source [Blanco et al., 2006], and the more recently developed detector referred to in the last paragraph also showed submillimeter intrinsic spatial resolution by direct charge injection in the pickup strips (0.2 and 0.6 mm FWHM along *X* and *Y* directions), and also by measuring the spatial resolution obtained by the coincidence detection, between the RPC detector and a crystal detector, of photons coming from the decay of a $^{22}_{11}\mathrm{Na}$ point like source (0.6 mm FWHM) [Neves, 2008].

Finally, mention must be made to the fact that, due to the nature of the physics processes involved in the detection of radiation with RPC detectors, these do not have energy resolution, and, so, it is not possible to reject photons on the basis of detected energy as in the case of crystal detectors. However, RPC detectors for detection of photons in coincidence present an energy sensitivity equivalent to an energy discrimination threshold of 300 keV in terms of rejection of coincidences involving scattered photons [Blanco et al., 2003a].

CHAPTER 6
SOFTWARE DEVELOPED FOR THE SIMULATION OF A POSITRON EMISSION TOMOGRAPHY SYSTEM BASED ON RESISTIVE PLATE CHAMBER DETECTORS

The constant improvement in computer performance and the advent of High Performance Computing (HPC) clusters, combined with the development of reliable MC codes for particle transport, have changed the research paradigm in several areas of particle physics. Complex experiments are now simulated prior to their experimental setup in order to optimize detectors, study and acquaint for physical factors influencing the expected experimental outcome, and for testing triggering and data acquisition strategies. Medical Physics (MP), of which Nuclear Medicine (NM) in general, and PET in particular, is just an example, is one of the many research areas in which MC codes have been and are used successfully.

Several well-documented general propose MC codes extensively tested against experimental data are available for simulation of almost any problem involving the interaction of radiation with matter. Those codes, usually consisting of a set of libraries developed on programming languages such as FORTRAN or C/C++, are updated on a regular basis and make use of the most up to date theoretical physics models of radiation interaction with matter, complemented with empirical ones driven by experimental data, and have a vast community of users from very different fields of radiation physics. One of those codes is GEANT4 [Agostinelli et al., 2003; Allison et al., 2006], consisting of a set of C++ routines for the simulation of particle transport across matter.

While general propose MC codes such as GEANT4 allow for the simulation of almost any system for which radiation interaction is the main concern, usually do not provide simulation routines for specific tasks as those present in NM imaging equipment. Among those tasks is the time dependence due to the radioactive source decay as well as patient and/or detector motions, the encoding of detection positions performed by the detectors used in NM imaging systems, detector dead time and signal pileup, and all the electronic processing chain undergone by signals from which

single detected events are formed, and, in PET applications, the detection of annihilation photons in coincidence. Although a GEANT4 based program developed from scratch can implement all the aforementioned tasks, their implementation is a very time consuming programming work. For this, simulation driven studies in NM are usually performed recurring to dedicated MC codes developed from scratch or from a general propose MC code, that implement a command or script based interface for definition of the physics, geometry, and acquisition processing, thus not requiring the user to have a prior knowledge and/or skills of programing languages, and eliminating the very time consuming task of programming.

Two of the most well-known MC codes used in NM are the Simulation System for Emission Tomography (SimSET) [Harrison et al., 1993; Harrison, 2011] and GATE [Jan et al., 2004]. The first one is a self-contained code developed from scratch and implementing its own routines for geometry definition, radioactive decay, interaction of radiation with matter, among others, while the second one is a program developed on top of GEANT4, thus taking full advantage of the GEANT4 tools in what concerns the geometry, particles, physics, simulation management, among others, and adding the NM specific functionalities based on the GEANT4 own routines for hits recording and electronic readout processing, along with time management inherent to radioactive decay as well as patient and/or imaging system movements during the acquisition of a full tomographic data set.

Despite SimSET and GATE had been used for simulating PET systems based on RPC detectors [Blanco et al., 2003a; Torres-Espallardo et al., 2011], both MC codes have some drawbacks for this propose. First, both programs were developed and are maintained with the aim of simulating imaging systems based on current and predictable future detector technology employed in NM imaging systems, which is based on crystal detectors, being time consuming to adapt to different detector technologies for which the physical processes leading to photon detection are substantially different, as is the case of RPC detectors. Second, and at least in the case of GATE, the simulation of the same experimental setup with different activities imply the full simulation of the underlying detection processes, which is an extremely time consuming computational task.

For the two aforementioned reasons, and scarce computational resources, it was found preferable to develop a program from scratch using the GEANT4 toolkit to simulate particle transport through a human full-body RPC TOF-PET system, which could also be used to simulate individual detectors. Simulation-produced data was processed by a set of routines, developed externally to GEANT4, to account for source activity, detector readout and coincidence processing. With this approach, the same

simulation-produced data set could be used to test for different detector readout strategies, with a tremendous reduction of computation time.

6.1 THE GEANT4 TOOLKIT

The development of any large scale software code, particularly object oriented codes such as those for which C++ is targeted, must observe some basic principles, the most important of which is to split the code in small independent logical units[1], which can be individual classes or sets of classes designed to perform related tasks. Developed and maintained by world-wide collaboration, and hosted by the European Organization for Nuclear Research (CERN), GEANT4 is a toolkit consisting in a complete set of C++ classes designed to simulate the passage of particles through matter, and developed according to the abovementioned principle.

The GEANT4 toolkit classes can be divided in eight different categories: Run and Event, Tracking and Track, Geometry and Magnetic Field, Particle Definition and Matter, Physics, Hits and Digitization, Visualization and Interfaces [Geant4 Collaboration, 2008a].

6.1.1 Run and Event

In GEANT4, a *run*, defined by the *G4Run* class, is the top most unit of simulation which is created when the simulation is started, and is managed by the *run manager*, defined by the *G4RunManager* class, which is a singleton object[2] created at the very beginning of a GEANT4 program and that controls the complete simulation. During each *run*, the selected and configured physics processes for the simulation, the geometry across which particles are to be tracked, and the sensitive areas of the geometry used to trigger particle interactions, cannot be changed.

Each *run* is composed by a user defined number of *events*, implemented by the *G4Event* class, each consisting in a single or a set of particles generated by a *primary generator*, derived from the *G4VUserPrimaryGeneratorAction* abstract class and that must contain a *particle gun*, defined by the *G4ParticleGun*, *G4SingleParticleSource* or

[1] The term independent is used in the sense that a given set of classes must encapsulate all the necessary code to deal with well-defined small tasks. However, those sets of classes may be used by other different set of classes to accomplish a global task that go far beyond those accomplished by the individual small tasks.

[2] A singleton object is an object of a class designed according to the singleton programing pattern, in which only an object of the singleton class can be instantiated. In C++, singleton classes are implemented by including a static pointer to the class, which is initialized to *null*, and implementing a class function which returns the object static pointer. If this pointer is still *null*, the function first creates the object and assigns its address to the static pointer.

G4GeneralParticleSource classes, and that is responsible for the creation of *primary particles* of a given type and with a given spatial and momentum distributions. *Events*, which are managed by an *event manager*, defined by the *G4EventManager* singleton class, are processed until all the *primary particles* as well as the *secondary particles*, created due to the interaction of primary and secondary particles, escape from the geometry, are brought into rest, are explicitly killed, or until the *event* is explicitly killed.

6.1.2 Tracking and Track

A *track*, defined by the *G4Track* class, is attributed to each primary particle (and secondary particles) and passed from the *event manager* to the *tracking manager*, defined by the *G4TrackingManager* class, which stores the *track* in a first in first out *track stack*, defined by the *G4TrackStack* class. Each *track* is processed from the very beginning of its creation until the particle leaves the geometry, is brought into rest or is explicitly killed. Only then the *tracking manager* pushes from the *track stack* the top-most *track* to be processed. However, the order of *track* processing can be changed, for instance, by suspending the processing of the current *track*, in which case the top-most *track* in the *track stack* is pushed back to be processed, the suspended *track* being resumed at the end of the processing of the pushed *track*. This mechanism can be applied successively, allowing to process all the *secondary particles* created in a given interaction process prior to resuming the processing of the suspended *track*. Although GEANT4 keeps a record of the history of the interactions occurred in a given event, this scheme was found to allow an easier control over the history of interaction processes.

For processing each *track*, the *tracking manager* invokes a *stepping manager*, defined by the *G4SteppingManager* class, which takes the current position and linear momentum of the particle and proposes a *step length* equal to the mean free path of the particle along its linear momentum direction, computed from the interaction cross sections for the particle being processed and material of the volume where the particle is located. This proposed *step length* is than compared against an eventual maximum *step length* restriction imposed by the user, and the distance from the current particle position to the boundary of the next volume element in the simulation geometry, computed along the linear momentum direction. The *step* applied to the *track* being processed is then taken as the smallest of the three abovementioned *step lengths*.

6.1.3 Geometry and Magnetic and Electric Fields

The GEANT4 geometry definition is compliant with the Standard for the Exchange

of Product Model Data (STEP)[3] and can be implemented using Constructive Solid Geometry (CSG) and/or Boundary Represented solids (BREPs). The first one can be used to define geometries composed of sets of well-defined geometric solids, while the second can be used to construct more complex geometries such as those imported from Computer Added Design (CAD) systems.

The geometry definition can be implemented in a single class, the *user detector construction*, derived from the *G4VUserDetectorConstruction* abstract class, or spread over several smaller classes. In this case, the *user detector construction* class, an object of which must be given as a parameter to the *run manager*, is responsible for the creation of the geometry objects implemented in the smaller classes.

GEANT4 makes the distinction between three elements of the geometry:

- *Solids*, derived from the *G4VSolid* abstract class, which are mere geometric representations of *volumes* with arbitrary shapes such as, among many others, parallelepipeds, spheres and cones, and that can be constructed from several specific classes, or by combining two solids via the Boolean operations of union, subtraction and intersection;
- *Logical volumes*, derived from the *G4LogicalVolume* class, which consist of a *solid* to which a material is attributed and that can also be defined as being a *sensitive detector* and/or have a magnetic or electric field;
- *Physical volumes*, derived from the *G4VPhysicalVolume* abstract class, which consist in the placement of a particular *logical volume* in another *logical volume*.

With this hierarchy, a given *solid* can be used to create several *logical volumes* with different materials, to which *sensitive detectors* and magnetic and/or electric fields can also be associated, and a given *logical volume* can be placed in different regions of the geometry thus leading to several *physical volumes*.

All GEANT4 geometries have to define what is called the *world volume*, which limits the volume used by GEANT4 for particle *tracking*, such that any particle leaving the world volume will be killed. The *world volume*, which is the only *physical volume* that it is not placed relative to any other volume, can have an arbitrary shape and the dimensions must be such that the complete geometrical setup to be simulated is contained in it.

To associate a given *logical volume* with a *sensitive detector*, it is necessary to create a *sensitive detector* object, defined by a class derived from the

[3] ISO standard that defines the protocol for exchanging geometrical data between CAD systems.

G4VSensitiveDetector abstract class, containing several functions, the most important of which are:

- *Initialize*, which is called at the beginning of each *event*, and that can be used to initialize variables for extracting information from individual interactions in the *sensitive detector*;
- *ProcessHits*, which is triggered whenever the end point of a given *step* falls in the *sensitive detector*, and that can be used to collect information on the type of particle and interaction, as well as all the available information for the start and end points of the *step*, the *pre step point* and the *post step point*, that triggered the function, such as particle positions, linear momentums, energies and velocities;
- *EndOfEvent*, which is called at the end of each *event* processing, and that can be used to further process the information collected in the *ProcessHits* function, to save the collected information to be further processed outside the simulation program, or simply do nothing.

Magnetic or electric fields can also be associated to *logical volumes*. For that, a *field* object, derived from the *G4Field* abstract class, must be created which contains three functions:

- *IsGravityActive*, which must return true if gravity effects are to be considered;
- *DoesFieldChangeEnergy*, which must return *true* for electric fields and *false* for pure magnetic fields;
- *GetFieldValue*, to which the Cartesian coordinates of the point where the field is to be computed and, in the case of time varying fields, the time for which the field must be computed[4], must also be given and the field intensity must be returned.

When defining the simulation geometry, attention must be paid to the positioning of the different *physical volumes* since their boundaries cannot overlap. However, *physical volumes* can be placed inside each other, even in a very tight setup, with the limits of the inner volume being exactly equal to the limits of the corresponding container volume.

Several methods are available to place *physical volumes* in the geometry. In all of

[4] GEANT4 implements time flow for *events* but not for *runs*. For *events*, the time is initialized when the *event* is created, and the flow of time is computed by kinematic considerations. For *runs*, the user must implement at least the time flow from the beginning of the simulation to each generated *event*. The total time from the beginning of the *run* can then be given by the sum of the time at which the *event* was created with the time since the beginning of the *event*.

them the placement is performed relative to the coordinate system of an existing *logical volume*[5]. The position of the volume being placed, which is called the daughter volume, is performed by specifying the coordinates of the origin of the coordinate system of the daughter volume relative to the coordinate system of the parent volume. Additionally, a rotation matrix can also be given, specifying the rotation of the coordinate system of the daughter volume relative to that of the parent volume.

The easiest and most direct method to place *physical volumes* in the geometry consists in placing a given *logical volume* in a specified position of a parent *logical volume*. This is performed by creating a *physical volume placement* object through the *G4PVPlacement* class, and should be used to place a single or a reduced number of identical *logical volumes*.

Another possibility to create *physical volumes* is to use *replicated* copies of a given *logical volume.* The *replicated logical volume*s, placed in the geometry by creating an object of the *G4PVReplica* class, must follow a well-defined pattern which is specified by a set of parameters defining the spacing and rotation of each volume of the *replica*. Being advantageous over individual placement of *physical volumes* in the case of several equal *logical volumes* with a regular distribution in space, has the disadvantage of not allowing *replicated* volumes inside other *replicated* volumes.

When multiple *replication* levels are required, *parameterized* volumes can be used, which are placed in the geometry by creating an object of the *G4PVParameterised* class. A *parameterized* volume consists in a parent *logical volume* inside of which the several copies of the daughter volumes being *parameterized* are placed. The daughter volumes can have different sizes, shapes, orientation in space, be made of different materials, and their positions do not need to follow a regular pattern. Based on the *copy number* of the *parameterized* volumes, all the aforementioned properties must be computed and returned from a user defined object of a class derived from one of two abstract classes: the *G4VPVParameterisation* and the *G4VNestedParameterisation*. The basic difference between these two *parameterization* classes is that the second one allows the material of the daughter volumes to depend also on the *copy number* of the parent volume when a *parameterized* volume is located inside another replicated volume, which can be a *parameterized* volume or a *replica* volume.

Yet another method used to place *physical volumes* in simulation geometries is to use *assembly volumes*. In this method a set of *logical volumes* are created and positioned relative to each other in a parent *logical volume*, but not placed in the

[5] Exception made to the *world physical volume*, which is the top most physical volume of a simulation.

simulation. The parent *logical volume* can then be treated as a single volume, which is placed in the simulation geometry by calling the *MakeImprint* function of the *G4AssemblyVolume* class. As soon as the *assembly volume* is placed in the geometry, the parent *logical volume* of the *assembly* is no longer available, and each daughter *logical volume* contained in the *assembly* is placed as an independent *physical volume*. To access each of the *physical volumes* placed by the *assembly*, an object of the *G4Assembly* class must be used.

6.1.4 Particles Definition and Matter

In GEANT4 particles can be categorized as *primary*, which are those generated by the *primary generator* and that are fired by a *particle gun*, and *secondary*, which are those generated by interaction processes with matter or by decay processes. So, in a given simulation, GEANT4 has to be aware of all the particles generated by the *primary generator* as well as those generated as a result of interaction and decay processes.

A set of specific functions can be used to define each individual particle and thus activating only those that are intended to be simulated. Alternatively, a set of functions can be used to create all the particles of a given type: *bosons*, *leptons*, *mesons*, *baryons*, *ions* and *short lived particles*.

GEANT4 also defines two test particles, or probes, named *geantino* and *charged geantino*, that do not interact with matter and that can be used to test the geometry definition (*geantino*), the propagation of charged particles in magnetic and electric fields (*charged geantino*), or the implementation of *sensitive detectors.*

GEANT4 has a set of classes to define isotopes (*G4Isotope*), elements (*G4Element*) and materials (*G4Material*). Isotopes are defined by specifying the atomic and mass numbers, and the molar mass of the isotope. After isotopes have been created, elements can thus be constructed by adding all the isotopes, specifying their relative abundance in number of atoms per unit volume. As to materials, can be constructed in three different ways:

- From a single element, in which case the atomic number, molar mass, density, physical state (undefined, solid, liquid or gas), temperature and pressure must be given;
- From several elements and/or materials, in which case the density, the number of components (single elements or materials), physical state, temperature and pressure should be given:
  - If materials are to be defined from their constituent elements, these can be added by specifying the number of atoms of the element present in the

material or their fraction by weight in the material;
    - If materials are to be defined by other materials and elements, the material components must be added by specifying their fraction by weight.
- By defining the mean atomic number, molar mass, density, physical state, temperature and pressure.

The third method is used, for instance, to define vacuum, but can be used to specify any material for which the aforementioned parameters are known. However, attention must be paid to some limitations that this definition may impose on the simulation of interaction processes. For instance, if a physics process involving the need of experimental information on atomic data is to be simulated, such as atomic deexcitation with emission of fluorescence or auger electrons, it is important to know with which element the interaction occurred, and this is not possible if the material is defined in this manner. So, the first two methods for defining materials are preferable to the third one.

Alternatively, GEANT4 has a database with several materials, which can be used to define the materials of the volumes that compose the simulation geometry.

6.1.5 Physics

In GEANT4, *physics processes* are associated to individual particles. So, All GEANT4 programs have to declare and setup the physics processes that are intended to be simulated for the defined particles. This is performed in a *user physics list* object, ultimately derived from the *G4VUserPhysicsList* abstract class, which must first define the particles to be used in the simulation, and then assign them the relevant physics processes to be simulated.

Depending on the complexity of the *physics processes* to be declared, the *physics list* can be implemented in a single class or spread over several smaller classes. In this case, the *user physics list* class must perform all the necessary actions to implement the physics processes that are spread over the several smaller classes. After being created, the *user physics list* object must be passed to the *run manager*.

6.1.5.1 Basics of Physics Processes

All the GEANT4 physics process classes are derived from a *process* abstract base class, the *G4VProcess* class, which have three basic functions:

- *AlongStepDoIt*, that implements the physics to be applied for particles along a *step*, viz., in flight;
- *PostStepDoIt*, which is invoked at the endpoint of each *step* if the process has

produced the minimum step length, for instance, a volume boundary crossing, or if the process is forced to occur, which is the case of interaction processes that produce *secondary particles* or elastic processes for which the direction of the incident particle is changed;

- *AtRestDoIt*, which is invoked when a particle is brought to rest and the process has produced the minimum step length or is forced to occur, such as in positron annihilation.

Some *physics processes* can be implemented by different *physics models*, usually valid for distinct energies ranges. In this case, several *physics models* can be associated with a given *physics process*. This is accomplished by creating the objects corresponding to each *physics model*, setting then the lower and upper limits of the energy range for which the model is to be applied, and registering the *physics model* in the *physics process*. If multiple *physics models* are to be used in a given *physics process*, attention must be paid to the energy range of each *physics model*, since the *physics process* will be simulated only if the corresponding particle energy is contained in the energy range defined by the union of the energy ranges specified for each *physics model*. For this, the energy ranges of *physics models* must overlap for the full energy range of the particle to be covered. The extent of energy overlapping for the different *physics models* can be larger or smaller, and in the overlapped energy region GEANT4 decides which of the *physics models* should be used by the *physics process*.

6.1.5.2 Physics Processes

There are seven major categories of physics processes in GEANT4: electromagnetic, hadronic, decay, photo-lepton-hadron, optical, parameterization and transportation. In what follows, only those processes relevant for the present work will be mentioned.

6.1.5.2.1 Transportation

The *transportation* process is responsible for computing the distance from the current particle position to the geometrical limits of the current *physical volume*. This distance is called the *safety* and defines a geometric *step length* limitation. Besides, the *transportation* process is also responsible for the computation of the particles time-of-flight, based on the particles initial velocities, being also responsible for the propagation of charged particles in magnetic and electric fields. For this, the *transportation* process has to be defined and initialized in all *physics lists* to be used in GEANT4 simulations.

6.1.5.2.2 Hadronic Processes

Hadronic processes are aimed to simulate the interaction of hadrons in materials. The only hadronic process with relevance for the current work is the radioactive decay of nuclei, which is simulated by data-driven empirical models using the Evaluated Nuclear Structure Data File (ENSDF), from which information on half-lives, nuclear level structure, decay branching ratios, and energy of the decay process are retrieved. In GEANT4 version 9.2 three radioactive decay modes are defined: α decay, β decay (both β^- and β^+) and electron capture. Besides, if the daughter nucleus of a decay process remains in an excited state, the nuclear de-excitation is also simulated.

The simulation of radioactive decay of nuclei is performed on particles of the type *ion*, and requires four parameters to be given: the atomic number, the mass number, the net charge and the kinetic energy of the isotope. Since ions are hadrons, for simulations involving nuclear decay, the list of particles to be used in the simulation must include, at least the parent and daughter ions to be simulated, as well as all the particles resulting from the nuclear decay, such as, for instance, neutrinos[6] in the case of β decay. Besides, since the parent isotope (in atomic or ion form) can have kinetic energy, and the daughter nuclide will have at least kinetic recoil energy, hadronic and ionic physics processes have also to be implemented if the interaction of the parent and daughter nuclides with matter is of concern.

As mentioned, nuclear decay processes take into account the energy of the decay process. In the case of β decay, the maximum energy of the emitted β particles is retrieved from the ENSDF data files and used as a parameter to random sampling the energy of the β particle from the Fermi distribution of β decay, referred to in Section 2.2.2.2 (page 18).

6.1.5.2.3 Electromagnetic Processes

For the simulation of the relevant electromagnetic processes in the present work, three main physics packages are available:

- The *Standard Electromagnetic Package* (SEP), which implements physics models for the simulation of electromagnetic interactions of photons (photoelectric absorption, Compton scattering, and pair production), electrons (ionization and bremsstrahlung) and positrons (the same processes as those of electrons plus positron annihilation), and that is also used for the simulation of other leptons, as well as hadrons, in the energy range from 1 keV to 10 PeV [Burkhardt et al., 2004], also providing a sub package for optical photons production and interaction [Burkhardt et al., 2004]. SEP also implements the

[6] In this context neutrinos refer both to neutrino and antineutrino.

Coulomb scattering of all charged particles, which can be modelled as Single Coulomb Scattering or as Multiple Coulomb Scattering, this last being the more commonly used since it is computationally less demanding;

- The *Low Energy Package* (LEP), based on the EEDL and the Evaluated Photons Data Library (EPDL), which is used for the simulation of interaction processes of photons (photoelectric absorption, Compton and Rayleigh scattering, and pair production), electrons and positrons (ionization and bremsstrahlung), in the energy range from 250 eV to 100 GeV [Chauvie et al., 2004]. LEP also implements physics models for the electromagnetic processes of hadrons, ions included [Chauvie et al., 2004].
- The low energy electromagnetic models based on the physics of electromagnetic interactions implemented in the PENELOPE general propose MC code [Salvat et al., 2001], for the simulation of photon interactions (photoelectric absorption, Compton and Rayleigh scattering and pair production), electrons (ionization and bremsstrahlung) and positrons (the same processes as those of electrons plus positron annihilation).

In all the aforementioned physics packages, positron annihilation does not take into account photon acollinearity. However, photon acollinearity can be easily implemented in any user defined physics list by deriving a new class from the *G4eplusAnnihilation* class, which is the class used for positron annihilation in the SEP package, and implementing the photon acollinearity in the *AtRestDoIt* function, which is the one responsible for generating the two annihilation photons. This is the approach used in GATE, which implements positron annihilation by modelling photon acollinearity as a 0.58° FWHM Gaussian blur, corresponding to experimental values measured in water [Jan et al., 2004].

6.1.5.2.4 Production and Tracking Thresholds (Cuts)

The production of *secondary particles* is performed by the configured and activated physics processes for each particle, the implementations of which impose intrinsic limits for the *production thresholds* of *secondary particles*. Nevertheless, each particle can define a recommended *production threshold*, which in GEANT4 is called a *production cut*, independent of the physics processes and that is specified in range rather than in energy[7]. For this, in GEANT4 *production cuts* are usually referred as *range cut*s. The advantage of specifying production cuts in range, rather than in energy, is an accurate control of the space position in which one desires to track the

[7] The cut in range is then converted to cut in energy for each material used in the geometry definition.

effects of particle interactions, independently of the material. If the production cuts where specified in energy, the spatial accuracy would be lost, since the production of secondary particles would be based on energy released, which depended on the materials.

The recommended *production cuts* for each particle, which are settled in the *SetCuts* function of the *physics list*, are used by some physics processes as their intrinsic limits for the production of *secondary particles*. This is the case, for instance, of Compton scattering, photoelectric absorption, ionization and bremsstrahlung processes. However, some physics processes ignore the *production cuts* and will produce the *secondary particles* independently of their range in the material. This is the case of β^+ decay, for which the positron will always be created, even if its range is well below the recommended *production cut*, in order to allow for the annihilation process to occur with the consequent emission of the two annihilation photons.

The complete scheme used by GEANT4 to decide if secondary particles are produced and tracked is as follows:

- If the intrinsic limits of the physics process is greater than or equal to the particle recommended *production threshold*, then the secondary particles production is governed solely by the physics process intrinsic limits, and no further actions have to be performed by GEANT4;
- If the intrinsic limits of the physics process is below the suggested *production threshold*, then the *secondary particle* production is performed based on what was settled by the *ApplyCut* function of the *particle definition*:
  - If the OFF option was passed to the *ApplyCut* function, then all the *secondary particles* are passed to the *track stack* and will be processed regardless of their initial energy, in which case energy conservation is respected as long as the physics processes know how to handle the *secondary particles* they produce, and the GEANT4 kernel will accept the best that the physics processes can do, disregarding simulation accuracy and precision;
  - If the ON option was passed to the *ApplyCut* function, then the *tracking manager* checks the range of each *secondary particle* against the *production threshold* and against the *safety* criterion:
    - If the particle range is greater than the minimum of the recommended *production cut* and the *safety* criterion, then the particle will be stacked for tracking;
    - If the particle range is less than the minimum of the recommended

production cut and the safety criterion, GEANT4 will check if a *GoodForTracking* flag has been settled for the produced *secondary particle*, in which case the particle is stacked for tracking;

- If the *GoodForTracking* flag was not settled, then the kinetic energy of the *secondary particle* is zeroed and attributed to a local energy deposition, and GEANT4 checks if any action has to be performed for the *secondary particle* at rest.

This scheme for *secondary particle* production ensures that the *production cuts* are always respected, but taking into account volume boundary constraints and the implementation of *physics processes* that can settle the *GoodForTracking* flag, also assuring the proper implementation of energy conservation.

The boundary constraint, or *safety*, deserves an explicit reference. Since the particle recommended *production cuts* can be greater than the *safety* parameter, by setting the range to the minimum of the mean free path and the *safety*, secondary particles can be created even if their range is below the particle recommended value, allowing them to reach sensitive regions of the geometry, being then available for producing *hits*.

6.1.6 Hits and Digitization

GEANT4 has two special classes that facilitate the task of collecting information related with interactions occurring in *sensitive detectors*. Those classes are the *G4VHit* abstract class, from which concrete classes must be derived to store the needed information of particle interaction in *sensitive detectors*, called *hits*, and the *G4THitsCollection* template class, from which concrete classes must be derived to store all the *hits* of a given type generated in a single *event*.

Typically, in the *Initialize* process of the *sensitive detector*, a new object derived from the *G4THitsCollection* template class is created to hold the concrete *hits* object, the implementation of which is derived from the *G4VHit* abstract class. The newly created *hits collection* can then be added to an object of the *G4HCofThisEvent* class that is passed by GEANT4 to the *Initialize* function of the *sensitive detector*, so that all the recorded *hits* for a given *event* can be stored for later processing. In the *ProcessHits* function of the *sensitive detector*, the user must then implement the necessary code to trigger the interactions that must be considered as *hits*. This includes the selection of all the conditions that must be met by the generated *secondary particles* for which *hits* must be collected. The user must then create a *hit* object in which the information related to the interaction should be stored. In the

EndOfEvent function of the *sensitive detector*, the *hits collection* object, created in the *Initialize* function, can be used for further processing by a digitizer module, to save the *hits* generated in the *event* to a file, or simply do nothing and be postponed for later processing all the hits originated by a given number of events. If the hits collection is not to be kept for further processing, then the user must ensure that the hits collection created in the *Initialize* function is properly destroyed in order to release the allocated memory.

For a given sensitive detector, several *hits collections* can be created and used to store *hits*. Those *hits collections* can be of the same type or, more usually, of different types, for instance, a *hits collection* to store *photon hits* and a *hits collection* to store *electron hits*. On the other end, the same *hits* and *hits collection* classes can be used to store *hits* on different *sensitive detectors*.

Hits can be processed by a *digitizer*, which is used to simulate electronic acquisition circuitry, such as Analog to Digital Converters (ADCs), Time to Digital Converters (TDCs), detector pile up, trigger logic, and readout schemes. *Digitizer* objects, which must be created from concrete classes derived from the *G4VDigitizerModule* abstract class, are not associated with any volume of the geometry and, as such, are not triggered by any sort of GEANT4 generated software events. It is the user responsibility to decide where in the code, and when, to create a *digitizer* object and invoke the corresponding *Digitize* function in order to initiate the *digitization* of the *hits* generated in the *sensitive detectors*. Those *hits* are accessible through the *run manager*, which can be retrieved from anywhere in the code by invoking the *GetRunManager* function of the *G4RunManager* class. The result of the digitizer process is a *digit*, which is a concrete object of the *G4VDigi* abstract class, and is stored in a *digit collection* object, which is an object of a concrete class derived from the *G4TDigiCollection* abstract class, as *hits* are stored in a *hits collection* object. The *digit collection* resulting from a *digitizer* processing can be used in other *digitizer* objects for further processing, or saved to a file.

6.1.7 Visualisation

GEANT4 has a set of classes that deal with the visualization of the geometry, particle trajectories and *hits*. The most used visualization drivers include the Open Graphics Library (OpenGL), the Fukui Renderer Drawer for Academic WritiNgs (DAWN) and the Virtual Reality Modelling Language (VRML).

For visualizing DAWN produced images, an appropriate postscript viewer is needed, while for visualizing VRML produced models, an appropriate VRML viewer is

needed. As to OpenGL, the visualization is preformed directly from inside the GEANT4 program, being sufficient to have installed an appropriate OpenGL library.

6.1.8 Interfaces

This category of classes handles the production of the graphical user interfaces available for GEANT4, the interaction with external software, and yet the *user defined interfaces* for passing parameters from the GEANT4 command line, or from scripts implemented in ASCII files, to the program. Since the developed program makes intensive use of *interface messengers*, it is worth mentioning how they work and are implemented. For that purpose, let *UIMClassA* be the *interface messenger* class of *ClassA* for which parameters are to be passed and retrieved, and let *m_pClassA* and *m_pUIMClassA* be pointers to the *ClassA* and *UIMClassA* objects, respectively

ClassA definition and implementation requirements:

- Declare the *m_pUIMClassA* pointer as a member variable;
- Implement a set of *Set* and *Get* functions, used to set and retrieve the *ClassA* variables that are allowed to be settled by the *UIMClassA*;
- The constructer must instantiate a new *UIMClassA* object, to which the *this* pointer of the *ClassA* object must be passed;

UIMClassA definition and implementation requirements:

- Must declare:
  - The *m_pClassA* pointer as a member variable;
  - A set of *interface command* pointers as member variables;
- The constructer must:
  - Accept a pointer to a *ClassA* object, and assign it to the *m_pClassA* pointer;
  - Create the user *interface commands* through which the *ClassA* variables will be settled;
- The interface *commands* must:
  - Be of the appropriate type for the variables of *ClassA* for which they are intended to operate on;
  - Be settled as a hierarchic tree terminating with the command to be used for setting the variable of the *ClassA* for which it was created;
  - Specify the GEANT4 running state or states during which they are available (*PreInit*, *Init*, *Idle*, *GeomClosed*, *EventProc*, *Quit* and *Abort*);
- Must implement the *SetNewValue* function, which must check which *interface command* was issued, and then set the appropriate variable of the *ClassA* object.

6.2 GEANT4 DEVELOPED PROGRAM FOR DETAILED SIMULATIONS OF RESISTIVE PLATE CHAMBER DETECTORS AND OF THE RESISTIVE PLATE CHAMBER TIME-OF-FLIGHT POSITRON EMISSION TOMOGRAPHY SCANNER

In the present section a brief description of the GEANT4 program developed for the detailed simulation of RPC detectors, and the RPC TOF-PET scanner, will be given, in which several aspects of the GEANT4 toolkit, referred to in Section 6.1 (page 167), will be mentioned.

6.2.1 The *main* Function

As in any C++ program, the entry point of a GEANT4 program is the *main* function, where some specific objects have to be initialized so that the GEANT4 toolkit can take control of the simulation process. One of those objects is the *run manager*, which controls the flow of the entire simulation and initializes other manager objects, being also responsible for managing initialization procedures, including random number generators and methods in *user initialization* objects that must be passed to the *run manager*. Once the *run manager* object is created, some objects have to be initialized and passed to it. Two mandatory *initialization* objects, and one mandatory *user action* object, must be passed to the *run manager* through the functions *SetUserInitialization* and *SetUserAction*, respectively. The two mandatory initialization objects are the *geometry definition* and the *physics list*, and the mandatory user action is the *user primary generator*.

Other optional user actions can also be passed to the *run manager*, such as the *user run action*, the *user event action*, the *user stacking action*, the *user tracking action* and the *user stepping action*. These user actions allow the user to take some control of the corresponding processes (*run*, *event*, *stacking*, *tracking* and *stepping*). Of these, only the *user run action* was used.

Once the mandatory and optional *initialization* and *user action* objects were passed to the run action, the *visualization modules* and the *messenger interface* are initialized. Then the program checks if a *script* has been passed to the program. If not, a *terminal interface* is initialized in order to allow the user to interact with the program, and the program will terminate execution only when the *exit* command is issued in the command line of the GEANT4 *terminal*. If a script has been passed to the program, an execution command is launched, with the script as a parameter, and the program will stop execution as soon as the simulation ends.

At the end of program execution, the *main* function ensures that all the objects

declared and created in it are properly deleted, so that the memory is released, thus avoiding memory leaks.

6.2.2 Physics List

The *physics list* was defined as a *modular physics list* in which the several physics categories were spread over distinct classes: *main physics list*, *particles physics list*, *gamma physics list*, *electron physics list*, *hadron physics list*, *ions physics list* and *decay physics list*. Besides, a set of *interface messenger* classes were defined to allow changing the physics setup without the need to recompile the code, which allows launching several instances of the program with different scripts for testing proposes and fine tuning of the parameters that influence the accuracy of simulations.

The complete set of parameters available for the *physics list*, and relevant for the present work, can be found in Appendix A.

6.2.2.1 Main Physics List

The *main physics list* is the one of which an object is constructed and passed to the *run manager* in the *main* function. This class contains pointers to all the *physics sub-lists*, Boolean variables specifying if a given *physics sub-list* is to be activated, and variables to hold the default *range cuts* to be applied to all particles, as well as a Boolean variable to flag if the lower energy used to compute the production cuts should be settled to a user specified value or be left as the GEANT4 default value. All these parameters can be settled via the *main physics list interface messenger*, either in the GEANT4 command line or through a script.

The *main physics list* has a *ConstructParticle* function, which calls the corresponding function of the *particle physics sub-list*, and a *ConstructProcess* function, which calls the corresponding function of the remaining *physics sub-lists*, which then set all the physics previously selected for simulation. The main physics list also has a *SetCuts* function in which the default, gamma, electron and positron production *range cuts* are settled.

6.2.2.2 Particles Physics List

The *particle physics list* class encapsulates particle construction and constructs all the particles available in GEANT4.

6.2.2.3 γ Physics List

The *gamma physics list* is responsible for constructing all the *physics processes* that the user wants to activate for the simulation of photon interactions with matter.

For that propose, an *interface messenger* was developed, which allows the user to activate each process individually, as well as while choosing the physics package to be used in the simulation of the corresponding interaction.

The available processes are Rayleigh and Compton scattering, photoelectric absorption, and gamma conversion (or pair production). For each process the user can select one of the three physics packages referred to in Section 6.1.5.2.3 (page 175), with the exception of Rayleigh scattering, which is available only in the LEP and PENELOPE physics packages. The selection is performed through the *gamma physics list interface messenger*, which also allows the user to specify the *range cut* to be used for the production of secondary photons.

For the LEP and PENELOPE packages, atomic deexcitation through fluorescence emission is activated by default, and the user can select, via the *gamma physics list interface messenger*, the energy cuts to be used for fluorescence production as well as the energy cuts to be used for production of secondary electrons emitted due to photoelectric absorption. As to deexcitation through the emission of Auger electrons, the user can activate or deactivate the process through the *gamma physics list interface messenger*.

6.2.2.4 Electron and Positron Physics List

The *electron physics list* is responsible for constructing the *physics processes* that the user wants to activate for the simulation of electron and positron interactions with matter. Therefore, an *interface messenger* was developed that allows the user to activate each process individually and for each of the particles, while choosing the physics package to be used in the simulation of the corresponding interaction. The available processes for both particles are multiple scattering, ionization and bremsstrahlung. For positrons, the annihilation process is also available.

The user can select to disable the simulation of multiple scattering or to activate the multiple scattering process provided by the SEP physics package, either the general multiple scattering physics applicable to all charged particles, or the multiple scattering physics specific for electrons. As to ionization and bremsstrahlung processes, the user may select to deactivate each one of them, or use the SEP, LEP or PENELOPE packages.

For the ionization and bremsstrahlung processes, with the low energy extensions provided by LEP and PENELOPE physics packages, the user can further select to simulate atomic deexcitation by using fluorescence and/or auger electrons, as well as set the low energy cuts for the production of secondary electrons (in the case of ionization) and photons (in the case of ionization and bremsstrahlung).

For positron annihilation, the user can chose to deactivate the process, or use the PENELOPE package, the SEP package without photon acollinearity, or the SEP package with photon acollinearity provided by the GATE annihilation routine.

6.2.2.5 Hadron, Ion and Decay Physics Lists

The *hadron* and *ion physics lists* were implemented to allow for simulations of hadron therapy, as well as the radioactive decay, which is implemented in the decay physics list. Both the *hadron* and *ion physics lists*, implement multiple scattering, ionization, both based on SEP and LEP physics, as well as several *physics models* for elastic and inelastic *physics processes*, which are irrelevant for PET physics. For this, no mention will be made to the options available in these two *physics lists*, the defaults of which are based on the SEP physics package and can be activated by setting the hadron and ion physics processes in the *main physics list* (Section 6.2.2.1, page 182). As to the *decay physics list*, which does not has user configurable parameters, implements the decay process for all particles for which the process is applicable, as well as the radioactive decay process for all ions.

6.2.3 Materials and Geometry Definition

To handle the materials used in the simulation, a singleton class of Materials was developed, in which the naturally occurring isotopes of all the elements from which materials are made are first created, followed by the creation of the elements, by specifying their isotopic natural abundances. The elements were then used to define all the compounds, by considering their chemical formulas and mass densities, and both were used to define the mixtures needed for the simulation, by specifying the fraction by mass of each element and/or compound in the mixture, and its mass density.

As to the geometry of the detection system was implemented by recurring to successive parameterized volumes, while the phantoms geometry was implemented by using assembly volumes.

6.2.3.1 Resistive Plate Chamber Detectors and Scanner

Fig. 6.1 depicts a scheme of the complete RPC TOF-PET scanner, which has a hollow parallelepipedic geometry with the bore being delimited by four detection heads[8], juxtaposed in the scanner corners. Each detection head consists of a hollow case with a given thickness, inside of which a given number of RPC detectors are

[8] The term head is adopted in an analogy to the flat detection heads of conventional gamma cameras.

stacked, with their surfaces parallel to the heads surfaces. The RPC detector was implemented as consisting of one or two detection modules, depending if it was intended to simulate a multi-gap RPC with just one detection module, viz., having its independent transaxial and axial readout electrodes, or if it was intended to simulate a multi-gap RPC detector with a common transaxial readout electrode and two separate axial readout electrodes, as depicted in Fig. 5.4 (page 154). The direction of the incoming annihilation photons relative to the detection head, RPC detector and detection module surfaces are also presented in Fig. 6.1.

A set of four parameter classes, along with the corresponding *interface messenger* classes, were implemented in order to allow script-based setup of the geometric parameters and materials. Those classes hold all the relevant information needed to construct *RPC detection modules*, *RPC detectors*, *scanner detection heads* and the *scanner*, as presented in Fig. 6.1. An abstract class was defined for implementing all the needed variables to store the *parameterizations*, and the functions needed by GEANT4 to retrieve the *parameterization* information. The concrete *parameterizations*

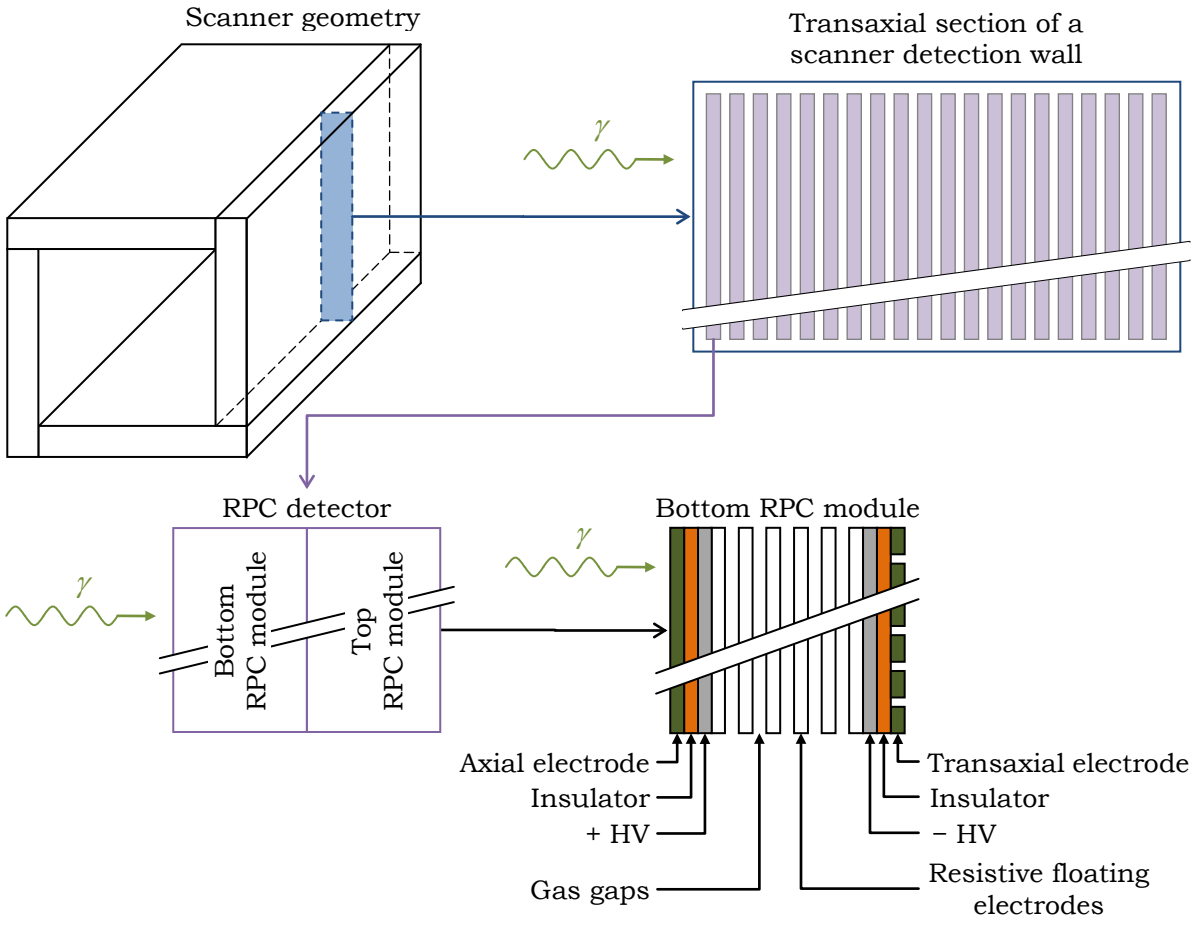

Fig. 6.1: Schematic diagram of the RPC-PET scanner, showing a section of a detection wall, a section of an RPC detector, and a section of an RPC detection module.

describing the *RPC detection modules*, *RPC detectors*, *scanner heads* and *scanner* geometry, where derived from the *parameterization* abstract base class and only implement the procedures needed to store the parameters of each element of the geometry in the member variables defined in the *parameterization* abstract base class.

With this highly configurable and *parameterized* implementation of the scanner geometry, the same code could be used to simulate both a long AFOV human PET scanner and a small animal one, as well as some experimental setups used for testing prototype RPC detectors, and coincidence acquisition by two opposing detection heads of the small animal PET prototype under development, allowing the comparison of experimental results with simulation-driven ones.

The complete set of options available for defining the scanner geometry is listed in Appendix B.

6.2.3.1.1 Resistive Plate Chamber Detection Module

The RPC detection *module* is defined has having the two readout electrodes with the strips for reading the signal induced by electron avalanches (Section 5.2, page 151, and Section 5.4, page 155), insulators and high voltage layers, and a given number of resistive floating electrodes, as depicted in Fig. 5.4 (page 154) and Fig. 6.1. The materials and thicknesses of each readout electrode, insulators, and high voltage layers, are all independently configurable through the *module interface messenger*, which also allows setting the number, material and thickness of the resistive electrodes and gas gaps. The height (measured along the transaxial direction) and width (measured along the axial direction) of the readout electrodes, insulators, and high voltage electrodes, are all equal and configurable through the *module interface messenger*, which also allows to independently set the corresponding dimensions of the geometric block containing the resistive floating electrodes and gas gaps. Besides, the *module interface messenger* also allows to independently set the pitch of the axially and transaxially aligned strips, placed on the transaxial and axial readout electrodes, respectively, in which the signals due to the electron avalanches created in the gas gaps are induced.

The detection module is implemented as a *parameterization* of the several layers with proper materials and dimensions, with the singleton *RPC sensitive detector* object (Section 6.2.5.2, page 191) assigned to all the individual layers.

6.2.3.1.2 Resistive Plate Chamber Detector

The RPC detector is defined as being a parallelepiped made of a given material, which can be settled to any available one, but should be settled to the gas contained

in the gas gaps, with one or two detection modules. If the detector is defined as having two detection modules, as in Fig. 5.4 (page 154), both will share the same transaxial readout electrode and attention must be paid when defining its thickness, which must be equal to half of its real value. The detector dimensions are computed from the module dimensions, the height and width being equal to those of the RPC detection module, and the thickness being the product of the number of detection modules by the detection module thickness.

The detector is defined as a *parameterized volume* even if it has only one detection module. In the case of being defined as having two detection modules, the top one (Fig. 5.4 on page 154) is first rotated by 180° so that its transaxial readout electrode is located on top of the same electrode of the bottom module, thus guaranteeing that its total thickness is twice that specified, as mentioned above.

6.2.3.1.3 Detection Head

The detection head is defined as being a hollow parallelepiped with a given wall thickness and material. The referred parameters are configurable through the *head interface messenger*, allowing also to specify the material contained in the detection head case, which should be equal to the gas contained in the gas gaps, the number of detectors and the corresponding spacing along the radial, transaxial and axial directions, as well as the spacing of the outer most detectors to the inner walls of the detection head box. The dimensions of the detection head are computed from the dimensions of each detector, the spacing between adjacent detectors, the margins of the outermost detectors to the inner walls of the detection head, and the thickness of the detection head box.

The detection head is defined as a *parameterized volume* in which each detector is repeated in a regular pattern along the radial, transaxial and axial directions of the detection head, according to the specified parameters.

6.2.3.1.4 Scanner

The scanner is defined as being a hollow parallelepiped made of a given material, that should be settled to air, and a given number of detection heads (one[9] to four), that can be defined through the *scanner interface messenger*, which also allows to define a margin to be settled between two adjacent detection heads (usually settled to zero). The dimensions of the scanner, including the outer dimensions and the size of the bore, are computed from the detection head dimensions and the spacing between

[9] A single detection head can be, and was, used for simulating a complete detection head to optimize the detector parameters without the influence of scattered radiation in the remaining detection heads, and without the need to develop a separate program for that propose.

adjacent detection heads.

The scanner is defined as a *parameterized volume* in which the detection heads are placed. If the number of detection heads is defined as being equal to one, only the right-hand vertical head (Fig. 6.1) is placed in the geometry. If two detection heads are specified, one is placed as being the right vertical one (Fig. 6.1) while the other is rotated by 180° anti-clockwise around the axial direction and placed as the left vertical detection head (Fig. 6.1). In the remaining cases (three[10] and four detection heads), the detection heads are rotated anti-clockwise around the axial direction, in steps of 90°, and placed in the corresponding scanner location.

6.2.3.2 Phantoms

Phantoms were implemented as *assembly volumes*, which are placed in the geometry at end of the detector construction. To simplify the process of adding phantoms to the program, an abstract base class was developed, which implements all the variables and functions common to all phantoms, including, among others, a function to place the phantom *assembly* with the appropriate rotation in the appropriate location of the global geometry, and a function that assigns a singleton *phantom sensitive detector* object to all phantoms that are placed in the geometry. Each particular phantom is then derived from the above-mentioned phantom abstract base class, and must implement all of its virtual functions for creating and computing individual phantom solid rotations and translations, as well as defining the phantoms logical volumes to which the appropriate materials must be associated.

Three phantom classes and the corresponding *phantom interface messengers* were created:

- The *spatial resolution phantom*, consisting in a sphere or in a right circular cylinder, with core dimensions and materials, and shell thickness and materials, defined through the corresponding *interface messenger*;
- The *sensitivity phantom*, consisting in a right circular cylindrical phantom with core dimension and materials, and shell thickness and materials, defined through the corresponding *interface messenger*, which also allows to activate up to five cylindrical sleeves with arbitrary material, the corresponding thicknesses and spacing being defined according to the NEMA NU2-2001 standards, the remaining dimensions being computed so that the sleeves surround the phantom;

[10] Three detection heads placed at right angles do not make much sense for PET applications. However, no restriction was made, for what it is available for testing proposes, if needed.

- The *Scatter Fraction, count losses, and Randoms measurement phantom* (hereinafter referred to as the SF phantom), consisting of a solid right circular cylinder with dimensions and material defined through the corresponding *interface messenger*, which also allows to specify the diameter and transaxial position of the hole drilled along the axial direction, as well as the dimensions and material of the line insert core, and the thickness and material of the line insert shell.

The *phantom interface messengers* also allow defining the phantoms position and rotation relative to the scanner coordinate system.

To manage the phantoms, a singleton class based on the *factory programing pattern*[11] was developed, which allows adding as many phantoms as the user wishes, by specifying the phantom type and attributing a name to it, which will be used to set the several phantom parameters. At the end of the detector construction, a pointer to the *phantom factory* singleton object, created in the beginning of the *main* function, is retrieved and used to cycle through all the added phantoms to place them in the geometry.

The complete set of parameters for defining phantoms, and adding them to the geometry, are listed in Appendix C.

6.2.4 User Primary Generator

The declaration of the implemented *user primary generator* has a member variable which is a pointer to a *G4GeneralParticleSource* object, the class constructor and destructor, the *GeneratePrimaries* function, which is called by GEANT4 in the very beginning of each event, in order for the *primary particles* to be created, and a function which returns the identifier of the source.

The constructer of the *primary generator* simply creates a *general particle source* object and assigns its address to the corresponding member variable of the *primary generator*, while the destructor simply deletes this object.

As to the *GeneratePrimaries* function, simply calls the *GeneratePrimaryVertex* of the *general particle source* object created in the constructor, which encapsulates all the necessary actions to create primary particles, including the choice of the primary particle to be produced, its position, energy and linear momentum direction. All these options are settled by the *general particle source interface messenger*, which allows specifying point like, surface and volumetric sources, both with a given random

[11] The factory programming pattern is an object-oriented design pattern aimed to implement objects without specifying the exact class from which the object is to be created.

distribution, and a specified rotation relative to the coordinate system of the world volume. So, the source distribution is specified independently from the phantom geometry, and attention must be paid so that the source distribution and orientation coincides with the volume of the phantom where it is supposed to be confined.

6.2.5 Sensitive Detectors and Hits

Two *sensitive detectors* classes where defined: one for the phantoms (*phantom sensitive detector*), and the other one for the RPC detectors (*RPC sensitive detector*). Both are based on the singleton programing pattern, in order to be easily accessible from any part of the code without having to invoke the *run manager*, and also to allow the assignment of the same *sensitive detector* to any volume of the geometry.

Five *hit* classes where implemented, named *phantom hits*, *primary photon hits*, *all photon hits*, *electron hits* and *RPC hits*, all of which are used only by the *RPC sensitive detector*. So, the *phantom sensitive detector* does not create any hits.

The complete set of parameters stored in each of the abovementioned hits classes are resumed in Appendix D.

6.2.5.1 Phantom

The same *phantom sensitive detector* object is assigned to all phantoms used in the simulation, and triggers:

- The radioactive decay, if the process is defined, storing the coordinates of the point where the decay occurred;
- The positron annihilation, if the *primary particles* consist of radioactive nucleus or positrons, storing the coordinates of the point where the annihilation took place;
- The creation of *primary* photons, if the *primary particles* consist of photons, storing the coordinates of the point where the photons were created;
- Photon interactions, storing the number of Rayleigh and Compton interactions undergone by each photon in the phantom.

The points of radioactive decay, positron annihilation or primary photon creation, depending on the *primary particle* defined for the *user primary generator*, are stored in single variables of the *phantom sensitive detector* object, while the number of photon interactions is stored in separate arrays for the Rayleigh and Compton scattering, which have as many entries as photon *tracks* created in the phantom. Besides the aforementioned information, the *phantom sensitive detector* also stores, in member variables, the *event identifier* (*eventID*) and the *track identifier* (*trackID*) of each photon

track, the first being stored in a single variable, and the second in an array as in the case of the number of interactions.

When a given *track* gives rise to *secondary particles* due to interactions in the phantom, the track is suspended and each of the *secondary particles* is completely processed, the suspended track being then resumed. Besides, the *ProcessHits* function kills all the tracks corresponding to particles other than nucleus, positrons, electrons and photons. Although not killing electron tracks, the *ProcessHits* function of the *phantom sensitive detector* does not perform any action for electron tracks. The reason for not killing electron tracks is that, in this way, electrons are allowed to produce bremsstrahlung and fluorescence photons (if LEP or PENELOPE physics where selected, and fluorescence production was activated) which are then processed as any other photon.

6.2.5.2 Resistive Plate Chamber Detector

The *RPC sensitive detector* is assigned to each layer of the RPC detection modules, the RPC detectors, the detection heads and the scanner, and triggers the interaction of photons, electrons and positrons. If the particle triggering the *ProcessHits* function of the *RPC sensitive detector* is a positron, the track is killed and no further processing is performed. If the track corresponds to a photon or an electron, then the *ProcessHits* function calls, respectively, the *ProcessGammaHits* or the *ProcessElectronHits* functions, defined in the *RPC sensitive detector* class. For the remaining particles defined in the *physics list*, the *ProcessHits* function of the *RPC sensitive detector* does not perform any action.

During the several processing stages of the *RPC sensitive detector*, several hits are created, which can be saved to ASCII or binary files when the *EndOfEvent* function of the *RPC sensitive detector* is called by GEANT4. For each interaction, several parameters are stored, which will be described in the next two sections. Among those, are the coordinates of some relevant points, which are sketched in Fig. 6.2 (page 192).

6.2.5.2.1 Processing of the Photon Interactions

The *ProcessGammaHits* function first gets the photon *trackID* and the starting and ending points of the *step* being processed (*preStepPoint*, and *postStepPoint*, respectively), from which the names of the *physical volumes* where those points are located, the names of the interaction processes that occurred in those points, and the *status* of the *track* in each point are also retrieved. If the *postStepPoint status* indicates that the particle has reached the *world* boundary, then the *ProcessGammaHits* function returns the control to the *ProcessHits* function that, in turn, returns the

control to GEANT4 so that it can take the necessary actions to kill the *track*.

If the photon has not reached the *world* boundary, the *ProcessHits* function of the *RPC sensitive detector* checks if the photon being processed is entering the scanner and if its *trackID* is different from the last photon *trackID*. If both conditions are met, then the last *trackID* is updated to the new one and a set of counters corresponding to the number of interaction of a given type that a photon with up to 511 keV can undergo (Rayleigh and Compton scattering, and photoelectric absorption), as well as the total number of interactions, are initialized to zero. After that, the *ProcessGammaHits* function calls a *CreatePhantomHit* function which, after gathering the *RPC* and *phantom sensitive detectors* information, creates a *phantom hit* (Appendix D.1) containing the *eventID*, the *identifier* of the *primary particles* (*sourceID*) generated by the *primary generator*, the identifier of the *parent track* (*parentID*), the *trackID*, the source and annihilation positions[12], the number of Rayleigh and Compton interactions and the total number of interactions in the phantom (in different variables), the time

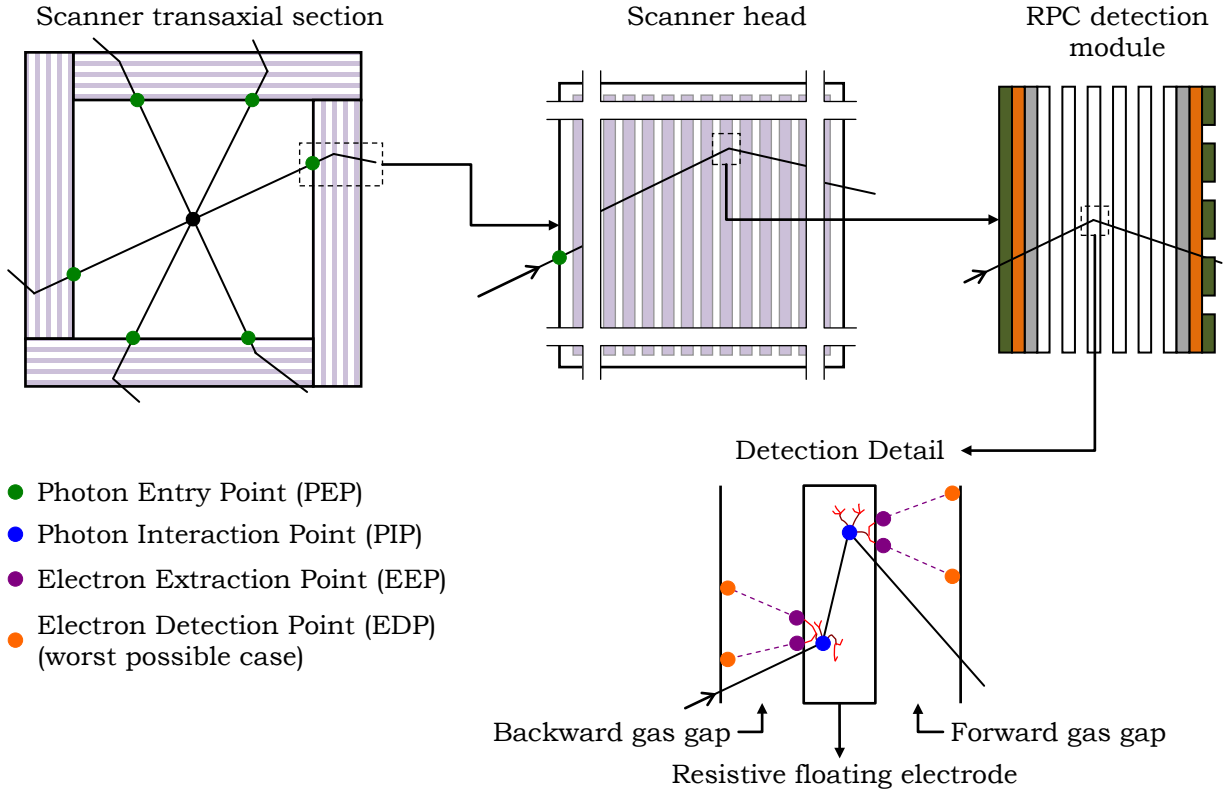

Fig. 6.2: Sketch of particle tracking and recorded points for each *RPC hit*.

[12] If the *primary particles* consist of radioactive nucleus, the source position corresponds to that where the radioactive decay occurred, while the positron annihilation position is that where positron annihilation took place. If the *primary particles* consist of positrons, both source and annihilation positions are made equal to the point in which annihilation occurred. If the *primary particles* consist of photons, the source and annihilation positions are made equal to the point where the photon was created by the *primary generator*.

at which the photon entered the scanner computed from the beginning of the *event*, the incident photon energy, the Photon Entry Point (PEP) (Fig. 6.2) and the linear momentum direction at the scanner entry point.

After the aforementioned initialization procedure, the *RPC sensitive detector* verifies if the photon interaction that triggered the *ProcessHits* function was due to a *primary* or *secondary photon*[13]. If the *trackID* corresponds to a *primary photon*, the interaction that triggered the *ProcessHits* function is checked against the three above mentioned *physics processes*, and the corresponding interaction counter, as well as the counter of the total number of interactions, are incremented, after which the function *CreatePrimaryPhotonHit* is called in order to create a *primary photon hit* containing twenty seven parameters (Appendix D.2): the *eventID*, *parentID*, *trackID*, the identifiers of the RPC module layer (*layerID*), RPC detector module (*moduleID*), RPC detector (*detectorID*) and scanner head (*headID*) where the interaction occurred[14], the number of interactions of each type that the photon suffered in the phantom and in the detector (in two separate sets of variables, one for the phantom and the other for the scanner), the time since the beginning of the event, the energy of the incident photon, the energy transferred from the incident photon to the medium and the energy deposited in the medium, the Photon Interaction Point (PIP) (Fig. 6.2), and the incoming and outgoing photon linear momentum directions.

The *ProcessGammaHits* function creates then a *hit* for the photon interaction regardless of this having its origin in a *primary* or *secondary photon*, containing all the information contained in the *primary photon hits*, less the information concerning the number of interactions by each interaction process in the phantom and in the scanner (Appendix D.3). With this scheme of hits storage, it is easier to acquaint for the hits generated by *primary photons* as well as those generated by *secondary photons* produced by bremsstrahlung, or if the LEP or PENELOPE physics models with fluorescence emission are used in the simulation.

6.2.5.2.2 Processing of the Electron Interactions

The *ProcessElectronHits* function first gets the *postStepPoint* of the *step* being processed and the name of the *physical volume* where the interaction occurred. If this

[13] In this context, *primary photons* are those for which the corresponding *trackID* is equal to that of the annihilation photons (if the primary particles consist of radioactive nucleus or positrons) or to that of single photons (if the *primary generator* created photons as primary particles), while *secondary photons* are those created as a consequence of interaction processes, in which case the *trackID* differs from those corresponding to *primary photons*.

[14] The referred parameters are collected if the interaction took place in a layer of an RPC detection module. If the interaction occurred in a physical volume different from that corresponding to an RPC detection module layer, then the identifiers of all the physical volumes hierarchically bellow (RPC detector, scanner head and scanner) the one where the interaction took place are set to -1.

contains the text "ResPlate", then the interaction took place in a resistive floating electrode[15] (Fig. 6.2), and the *ProcessElectronHits* function verifies if the interaction produced secondary particles, in which case the current electron track is suspended in order for the newly created *track*s to be fully processed. If the interaction did not occurred in a resistive floating electrode, the program verifies if the name of the *physical volume* where the interaction took place contains the text "GasGap"[16], in which case an *electron hit* and an *RPC hit* are created, and the electron track being processed is flagged to be killed. If the electron that triggered the *ProcessElectronHits* function was neither created in the resistive floating electrode nor in the gas gap, the corresponding *track* is flagged to be killed and no further actions are taken, since it was verified that those electrons do not reach a gas gap.

The *electron hit* (Appendix D.4) contains all the *primary photon hit* information of the *primary photon* that lead to the electron *track* being processed, the *all photon hit* information of the photon leading to the electron hit being processed, plus twenty one parameters related to the electron that produced the *hit*, which include: the identifier of the parent *track* giving rise to the *electron hit* (*electParentID*), the identifier of the electron *track* (*electTrackID*), the number of electron hits originated by the primary photon that gave rise to the current *electTrackID* (*electHitID*), the *layerID*, the *moduleID*, the *detectorID* and the *headID* of the *physical volume* where the *electron hit* took place[17], the time since the beginning of the *event* at which the *hit* occurred , the energy of the electron extracted from the resistive floating electrode to the gas gap, the Electron Extraction Point (EEP) (Fig. 6.2), and the linear momentum direction of the extracted electron. Besides, two other points are computed and stored in the *electron hit*: the Electron Detection Point (EDP) (Fig. 6.2), and the Electron Assignment Point (EAP).

The *RPC hit* (Appendix D.5) contains forty nine parameters which include all those contained in the *primary photon hit*, and those of the *electron hit* concerning the electron information.

Mention must be made to the EDP and EAP. As electron avalanches in the gas gaps were not simulated, the centroid of the detection point was chosen to be the one

---

[15] The name of each resistive floating electrode layer contains the "ResPlate" text followed by the text "_layer_#", where # represents the number of the resistive float electrode.

[16] The name of each gas gap layer contains the "GasGap" text followed by the text "_layer_#", where # represents the number of the gas gap.

[17] Contrary to *photon hits* (both *primary* and *all*), which can occur in any *physical volume* to which the *RPC sensitive detector* is attached to, electron hits (in the sense here attributed) can only occur in a gas gap layer of an *RPC detection module*. So, all the referred identifiers (*layerID*, *moduleID*, *detectorID* and *headID*) are valid and saved with their corresponding values.

on the opposite side of the gas gap, computed along the linear momentum direction from the electron extraction point, since this is the one which maximizes the error in the readout position, and hence the parallax error. The point thus computed is the above mentioned EDP. Concerning the EAP, and due to the detector design, it is always possible to know in which *RPC detection module* the electron avalanche occurred, but not in which gas gap it took place. So, the radial position of the EAP is always taken as the mid-point of the *RPC detection module*, corresponding to a maximum DOI error, and hence to a DOI resolution, equal to half the thickness of the detection module. As to the positions in the transaxial and axial directions, and despite being essentially continuous, were binned to the middle of the readout strips, as this also maximizes the readout position error, and hence the parallax error.

6.2.6 User Run Action

Since the collected *hits* referred to in Section 6.2.5 (page 190) should be saved to disk, the *RPC user run action*, hereinafter referred to as the *RPC run action*, has been implemented. It has Boolean variables that can be settled through the *RPC run action interface messenger*, allowing the user to specify which *hits* to be saved (*phantom*, *primary photon*, *all photon*, *electron* and *RPC hits*), in which format should be saved (ASCII, binary or both), as well as the name of the file, excluding the extension, which is appended to the specified name (".txt" for ASCII files, and ".dat" for binary files). Besides, the *RPC run action* allows setting the seed of the random number generator used by GEANT4 in the following way. If the seed is given as a non-zero positive integer, it will be used as the initial seed for the random number generator. If the seed is set to zero, then the *RPC user run action* computes the seed as being the product of three values: the identifier of the instantiated process, the time retrieved from the system, and the identifier of the run.

The automatic setting of the seed, based not only on execution start time but also on the process identifier, is an important issue when running the code in massive HPC clusters. If the execution start time was given as the seed to be used by GEANT4, then all processes launched in a given job could, with a high probability, have the same seed, which would not result in better statistics, but in several simulated data with exactly the same information. By multiplying the execution start time by the process identifier the result will be, with a high probability, a different seed for each process belonging to the same job, and also for processes launched by different jobs[18]. Although this may not be the best solution for very large scale simulations, it seems

[18] In order to have enough statistics, a complete simulation may require hundreds of jobs with many processes each.

suited for the needs of the present work[19].

The parameters that can be settled for the run action are listed in Appendix E.

6.3 SOFTWARE DEVELOPED FOR PROCESSING THE SIMULATION DATA

In order to acquire good statistics with a given phantom, several independent *runs* were simulated by launching several instances of the GEANT4 developed program in several cores of the HPC cluster of the Advanced Computing Laboratory of the University of Coimbra [LCA-UC, 2009], and also in the HPC facility of the Laboratory of Instrumentation and Experimental Particle Physics [LIP-CA, 2007]. For each run, the *hits* selected to be stored were saved with a fixed pattern, consisting of a name terminated with a number that identifies the *run*. For processing the simulation data generated by all *runs*, a set of routines was developed externally to GEANT4, which cycles through the *runs*, processing each one independently, the processing results being then combined to form the final results of the simulation. Those routines account, among other things, for decay instants, processing of *Single hits* to account for detector readout, first level triggering to reduce the number of valid *Single events*, and coincidence processing.

In the present Section these routines will be briefly described, along with some results obtained to point out the options taken in the processing of the simulation data. The complete sequence of simulation data processing will also be mentioned, along with the most important options that can be activated or deactivated in the programs developed to fully process the simulation data sets.

6.3.1 Processing of the Decay Instants and Detection Time Jitter

As mentioned in the introduction of the present Chapter and also on footnote 4 on page 170, GEANT4 accounts only for time flow of individual *events*, not accounting for time flow through the entire simulation of a given *run*, and much less in a simulation with several independent *runs*. So, even if time flow of individual runs had been implemented in GEANT4, it would be necessary to implement a scheme for dealing with time flow in hundreds of independent runs launched in different cores of an HPC cluster. The alternative to deal with the decay of radioactive sources is to perform the time management in programs developed for post-processing of simulation data. This was the approach taken in the present work, since it is far easier

[19] Each instance of a run stores its own log file containing all the initialization procedures issued by GEANT4, as well as the seed used in simulation, which is preceded by an identifying string for easy identification and automated processing, to verify if there existed two processes with the same seed.

to implement, with the advantage of allowing to use the same simulation data set to test for the effect of different source activities in the final results, without the need of simulating the entire passage of particles through matter, which, depending on the phantom being processed, can account for up to half the total computational time needed to fully process a run, including the post-processing stage.

The routine developed for processing the instants at which each event was created, accepts the total number of simulated runs, the *run* to be processed, and a structure (Appendix F) containing, among others, the number of simulated *events* in each *run*, the decay constant, the branching ratio, a variable to select whether branching ratios should be applied, and the initial activity of the radionuclide to be used for processing the decay instants. Using the total number of simulated *runs* and the data contained in the above mentioned structure, the routine computes, in a deterministic approach, the time needed to produce the total number of simulated *events*. This is performed by setting $t_s = 0$ s on Eq. (2.17) (page 16) and solving for t_e, which holds

$$t_e = -\frac{1}{\lambda_t}\ln\left(1 - \frac{n \times N \times \lambda_t}{BR \times A_0}\right), \tag{6.1}$$

where n is the total number of simulated *runs*, N is the number of simulated events per *run*, and BR is the β^+ branching ratio of the radionuclide to be simulated, which is used only if the variable holding the branching ratio processing is set to *true*[20]. Since $A_0 = \lambda_t N_0$, the argument of the logarithmic function can be negative if the total number of simulated decays $(n \times N)$ is larger than the number of radioactive nucleus (N_0) present in a radioactive sample with an initial activity equal to A_0. In this case a flag is settled to signal that each *run* must be processed as an independent acquisition with start time equal to zero and end time equal to that obtained from Eq. (6.1) for a single *run*, viz., with $n = 1$.

After the abovementioned procedure, the start and end times of the run being processed, denoted by i (with $i = 1, 2, \cdots, n$), are computed from

$$t_{s,i} = -\frac{1}{\lambda_t}\ln\left[1 - \frac{(i-1) \times N \times \lambda_t}{BR \times A_0}\right] \quad , \quad t_{e,i} = -\frac{1}{\lambda_t}\ln\left[1 - \frac{i \times N \times \lambda_t}{BR \times A_0}\right]. \tag{6.2}$$

The computed times are then used to create an array with $M = 1000$ bins

[20] If the primary particles simulated consist of radioactive nuclei, the use of branching ratios should be set to false, since GEANT4 simulates all the decay processes, accounting for the positron branching ratio. The details of the implementation of the structure defining the source parameters, and given in Appendix F, explains how the number of simulated positrons and the number of simulated decays are computed from the input parameters taking into account the branching ratio.

$\left(\tilde{A}_1 \cdots \tilde{A}_M\right)$, each having a fixed time width $\Delta t = \left(t_{e,i} - t_{s,i}\right)/M$. With the time intervals thus obtained, Eq. (2.17) (page 16) is computed and normalized such that $\tilde{A}_1 = 1$ and $\tilde{A}_M = 0$, the array $\tilde{A}$ being then checked for strictly decreasing monotonicity. If this criterion is not met, the number of bins is decreased by one $(M = M - 1)$. The process is then repeated until the strictly decreasing monotonicity criterion is met, with a lower limit of two on the final value of *M*. Fig. 6.3, depicts the flow chart of the described process.

Once this procedure is completed, *N* random numbers are drawn from a uniform distribution and compared against the normalized values of $\tilde{A}$, in order to find the time interval for which each of the *N* uniformly distributed random numbers is larger than a given value of $\tilde{A}$. Once the bin of $\tilde{A}$ is found, the decay instant for the event is computed so that it is equal to the time corresponding to the lower limit of the bin plus the product of the bin width, Δt, by a second random number drawn also from an uniform distribution. The times thus obtained are then added to those stored in the *hits* files (see Section 6.2.5 on page 190), by attributing the same randomly drawn time to all the *Single hits* with the same *eventID*. Fig. 6.4 depicts the results obtained with the aforementioned procedure for three radioisotopes, namely $^{11}_{6}\mathrm{C}$, $^{15}_{8}\mathrm{O}$ and $^{18}_{9}\mathrm{F}$, with an initial activity $A_0 = 180$ MBq (5 mCi). Simulations were also performed for initial source activities of 37 kBq (1 μCi), 18.5 MBq (0.5 mCi) and 37 MBq (1 mCi) with the same overall results as those presented in Fig. 6.4, namely, the exponential fit recovered both the initial source activity and the decay constant of the radionuclide.

After processing the decay instants, and updating the above mentioned times, a time jitter, randomly drawn from a Gaussian distribution with standard deviation σ_{event}, was added to the stored times of each *Single hit*, in order to take into account

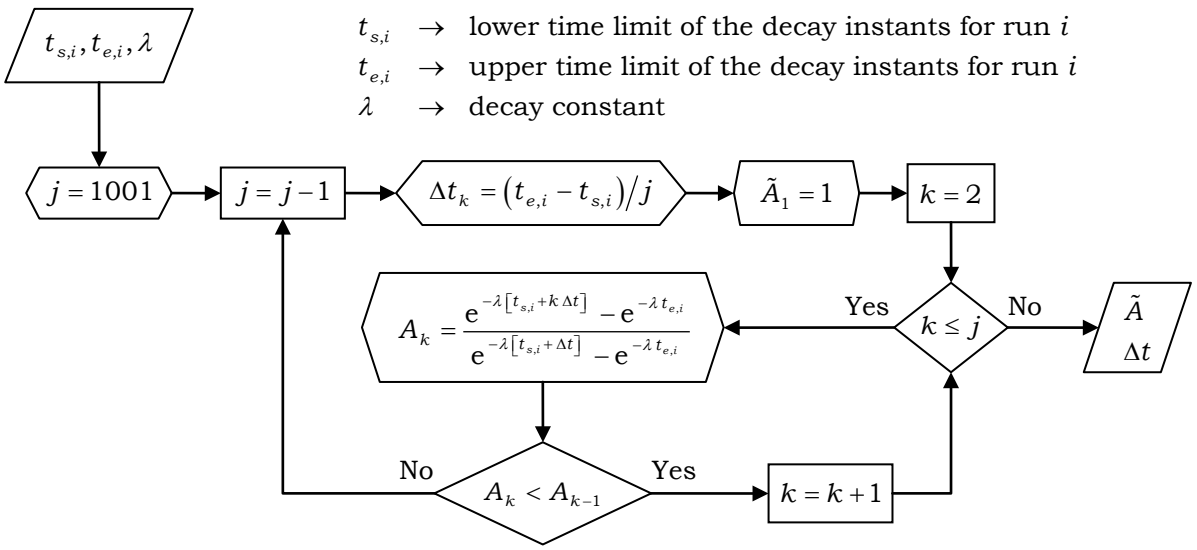

Fig. 6.3: Flow chart for setting the bins from which the random decay times are drawn.

the detection time jitter. The value of σ_{event} was computed by solving (4.29) (page 116) for σ_t, and using the time resolution experimentally measured with pairs of RPC detectors for testing proposes, and found to follow a Gaussian distribution with 300 ps FWHM, independently of the geometric parameters of the detectors, holding then a $\sigma_{event} = 90$ ps.

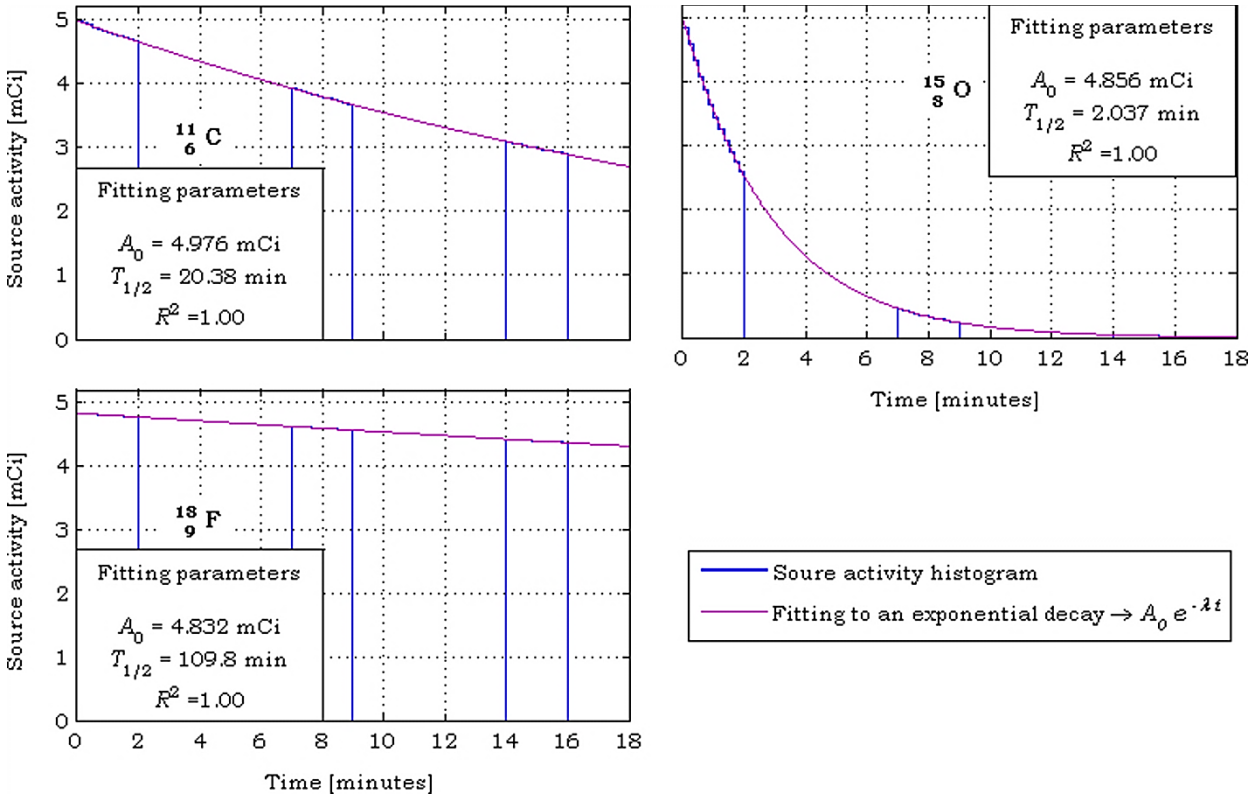

Fig. 6.4: Decay times randomly drawn from an exponential distribution. For each radionuclide, decay instants were drawn for the time intervals $[0, 2]$, $[7, 9]$ and $[14, 18]$ minutes and the fit was performed to the histogram data, taking into account only those time intervals.

6.3.2 Processing of the Detector Readout

The processing of the readout of the detector is based on a data structure that must be carefully set to match some of the parameters specified for the simulation, and some parameters specific to account for the processing of dead time. This structure is fully documented in Appendix G.

After the decay times and the detection time jitters have been set, the simulation data is processed to account for the detector readout. This is performed by several routines, one of which allows computing the EDP from the EEP and the corresponding linear momentum direction, if a different method than that employed in the GEANT4 program is desired to compute the EDP. A second routine computes the EAP from the

EDP, if a different binning than that employed in the simulation is pretended. In both routines, this is performed by first rotating all coordinate points of the several detection heads so that they refer to the right vertical detection head of Fig. 6.1 (page 185), the processing being then performed in the same coordinate system. At the end of both computations, the coordinate points are rotated back to their original positions, and the data if fed to a routine to account for the readout as explained in Section 5.4 (page 155), and that will be briefly resumed in the following.

As mentioned in Section 6.2.3.1 (page 184), each RPC detector has a transaxial readout electrode and one or two axial readout electrodes, depending if the RPC detector is formed, respectively, by a single detection module or by two juxtaposed detection modules, in which case the transaxial readout electrode is shared by the two detection modules. In both cases (one or two detection modules), the detector has at least one axial readout electrode, on which the strips are aligned in the transaxial direction of the scanner, and a single transaxial readout electrode with the strips aligned along the axial direction of the scanner, which, as mentioned in Sections 5.3 (page 153) and 5.4 (page 155), imposes a non-paralyzable dead time for the readout of time signals, and a paralyzable dead time for accurate determination of the detection position. The readout scheme explained in Section 5.4 (page 155), and depicted in Fig. 5.5 (page 156), Fig. 5.6 (page 157) and Fig. 5.7 (page 158), can be combined in a single simplified scheme as depicted in Fig. 6.5.

To account for the dead times of each independent readout section of each detector in each detection head, the coordinates of the EAP are again rotated to be referred to the same detection head as mentioned above. After this first procedure, a loop is used to cycle through all *headID*s, and retrieve the hits corresponding to the detection head being processed, the data being then used in a second nested loop that cycle through all *detectorID*s, and retrieve all hits from the corresponding detector. A third nested loop is then used to retrieve the data of each readout section, based on the transaxial coordinates of each hit and on a structure containing, among others, the number of readout sections that each detector contains and the dimensions of each readout section. The selected data is then sorted in ascending time order to be processed twice, in sequence, and by the same two routines, to account first for a τ_{ts} non-paralyzable dead time for the time signals, and only then to account for the τ_{ps} dead time on the position signals.

The first of the abovementioned routines used for dead time processing (*ApplyDeadTimeModel*) receives as parameters the readout section data sorted in ascending time order and a structure containing the parameters for dead time

processing, which include, among others, the width of the dead time window and the dead time model (non-paralyzable or paralyzable), and returns a two column array containing, in the first column, the indexes of the events opening a dead time window, and, in the second column, the indexes of the last event in the dead time window opened by the events in the first column.

The second routine (*ApplyDeadTimePolicy*), takes as parameters the readout section data, the two column array returned from the first routine, and the same structure containing the parameters for dead time processing, which also include the processing options to be applied in case of pileup, both to the time and position of the final Single event to be returned. For the position of the Single event, three options are available: average all (*averageAll*), reject all (*rejectAll*), and coarse position (*coarsePosition*). For the time of the Single event, two options are available: average all (*averageAll*), and accept first (*acceptFirst*).

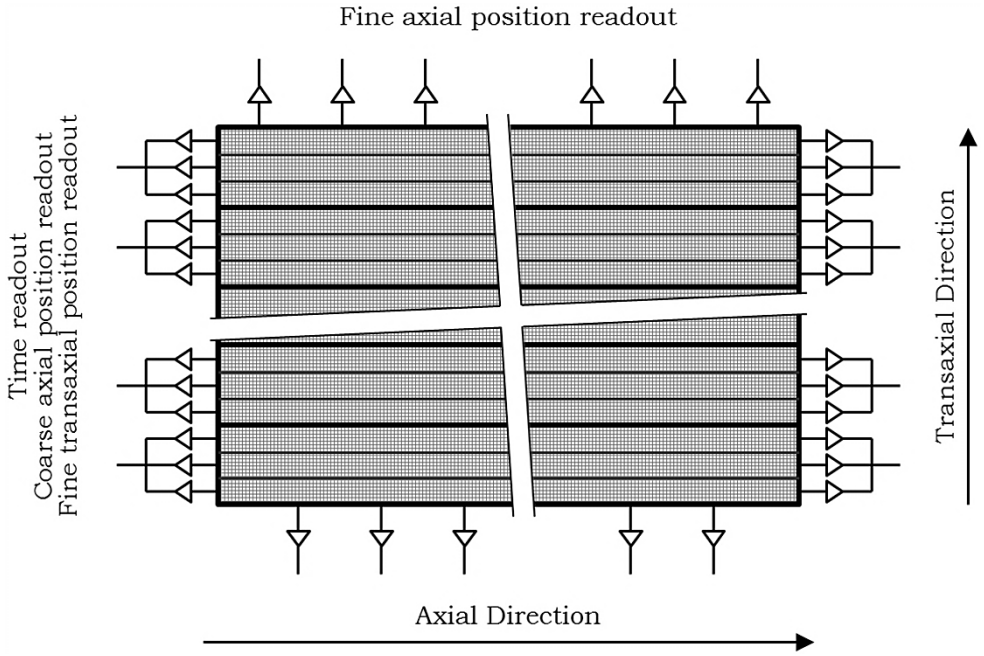

Fig. 6.5: Simplified scheme of the readout of each RPC detector, where the fine mesh represents both the axially and transaxially aligned readout strips. The smaller transaxial sections, containing a set of axially aligned strips, represent the readout subsections referred to in Section 5.4.1 (Fig. 5.5, page 156), and allow to measure detection times, coarse axial (1 cm σ Gaussian distribution) and coarse transaxial position (binned to the subsection centre). The larger transaxial sections represent the independent readout sections referred to in Section 5.4.1 (Fig. 5.6, page 157), and are used to measure the fine transaxial position. The vertically placed amplifiers represent independent groups of readout sections of the fine axial position as described in Section 5.4.2 (Fig. 5.7, page 158), and independent for each axially aligned readout section. For RPC detectors with two detection modules, the axially aligned strips are placed in the central transaxial readout electrode, shared by both detection modules.

For the processing of the dead time for time signals, the *averageAll* option is used for the position of the Single event resulting from the single hits that are found in the same dead time window, and the *acceptFirst* option is used, so that the time of detection of the Single event is that of the first hit in case of pileup.

For the processing of the dead time for the position signals, which is only performed after the procedure to account for the dead time on the time signals, the *rejectAll* option rejects all the events for which pileup occurred, and the *coarsePosition* is used to accept all the events falling in a given dead time window as consisting in Single events for which only the coarse position can be known. As mentioned in Section 5.4.1 (page 155), the coarse position along the axial direction consists in the EAP blurred by a 1 cm σ Gaussian distribution, while in the transaxial direction consists in the midpoint of the subsection. As to the detection time of the Single event returned in case the *coarsePosition* was specified, corresponds to the detection time of the corresponding Single hit.

Fig. 6.6 depicts the sequence for processing the detector dead time and Fig. 6.7 an illustrative example of the outcome of this processing.

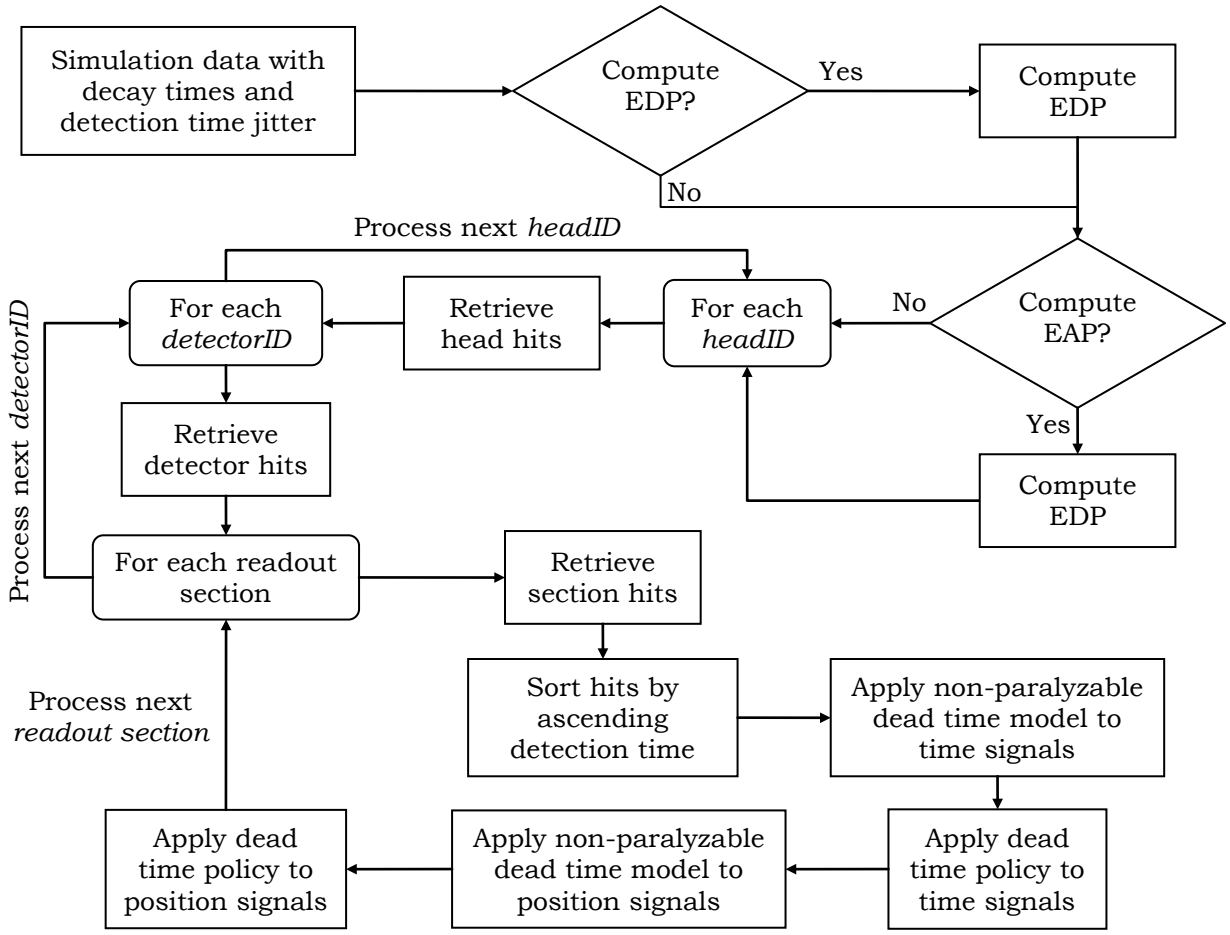

Fig. 6.6: Flow diagram for processing the dead time from the simulated Single hits.

As mentioned previously, the same *ApplyDeadTimeModel* routine is used to process both the non-paralyzable and the paralyzable dead time models. For that, the routine starts by creating a two column array (*allPulses*) initialized to zero, with as many rows as the number of N_t events to be processed. Then, a counter (i) is initialized to the first index of the array holding the N_t detection times sorted in ascending time order, and a loop through all events is executed while the i^{th} event being processed is less than the total number of events $(i < N_t)$.

At the beginning of each cycle of the abovementioned loop, a *lastPulse* variable is set to the event being processed $(lastPulse = i)$ and an incremental loop (j) is started in the event immediately after that being processed $(j = i+1)$. This loop then checks if the time difference between the event being processed $(j, j+1, j+2, \cdots, N_t)$ and the *lastPulse* event is greater than the length of the dead time window (τ), viz., verifies if $t[j] - t[lastPulse] > \tau$. If so, the inner incremental loop (j) is cancelled and the control is returned to the outer loop (i), which then sets the first and second columns of the i^{th} row of the *allPulses* array to, respectively, i and $j-1$, viz., $allPulses[i][1] = i$ and $allPulses[i][2] = j-1$, after which sets $i = j$. If the condition $t[j] - t[lastPulse] > \tau$ is not met, then the routine verifies if the dead time model is set to paralyzable and, if so, updates the *lastPulse* variable to the j counter $(lastPulse = j)$.

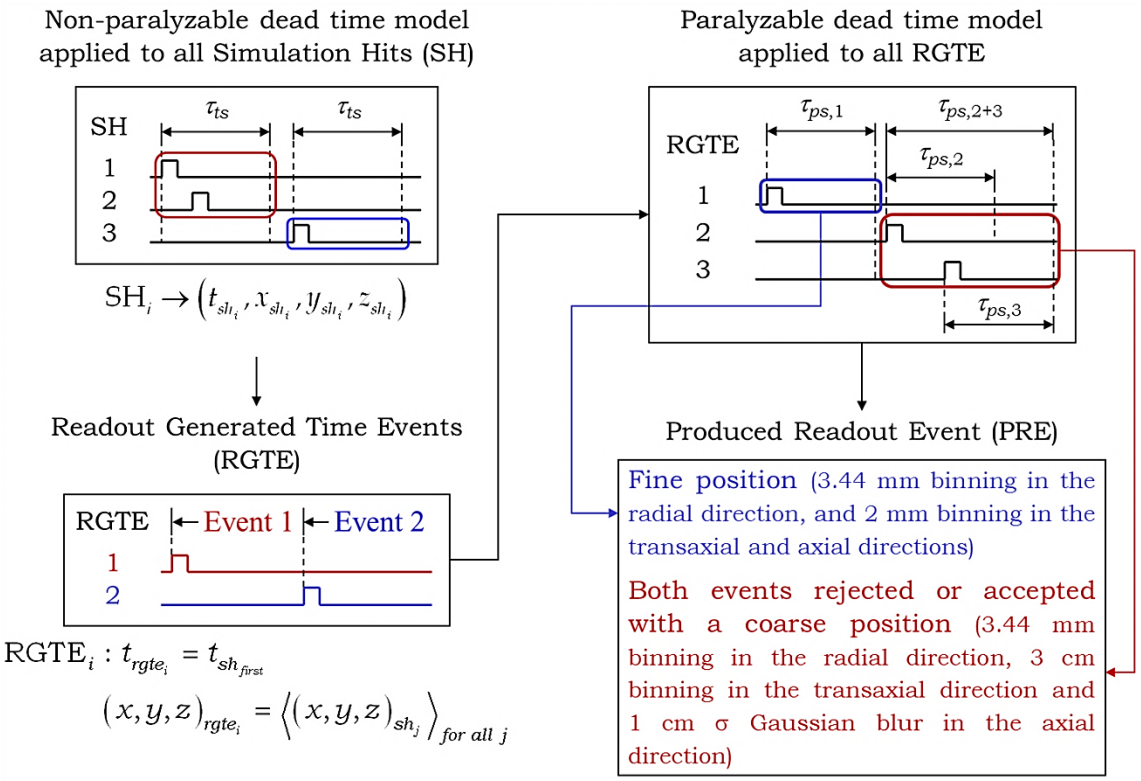

Fig. 6.7: Example of the outcome of the dead time processing, starting from simulated Single hits to the final Single events.

At the end of the outer loop the routine verifies if the *lastPulse* processed and the second column of the *lastPulse* processed is less than the N_t time events, viz., $lastPulse < N_t \wedge allPulses[lastPulse][2] < N_t$. If so, the N_t event is then added to both columns of the last row of the *allPulses* variable, viz. $allPulses[N_t][1] = N_t$ and $allPulses[N_t][2] = N_t$. Finally, the routine adds both columns of the *allPulses* variable and retains only those rows for which the resulting value is different from zero, viz., retains the rows for which $allPulses[row][1] + allPulses[row][2] > 0$.

Fig. 6.8 depicts the flow chart of the *ApplyDeadTimeModel* routine.

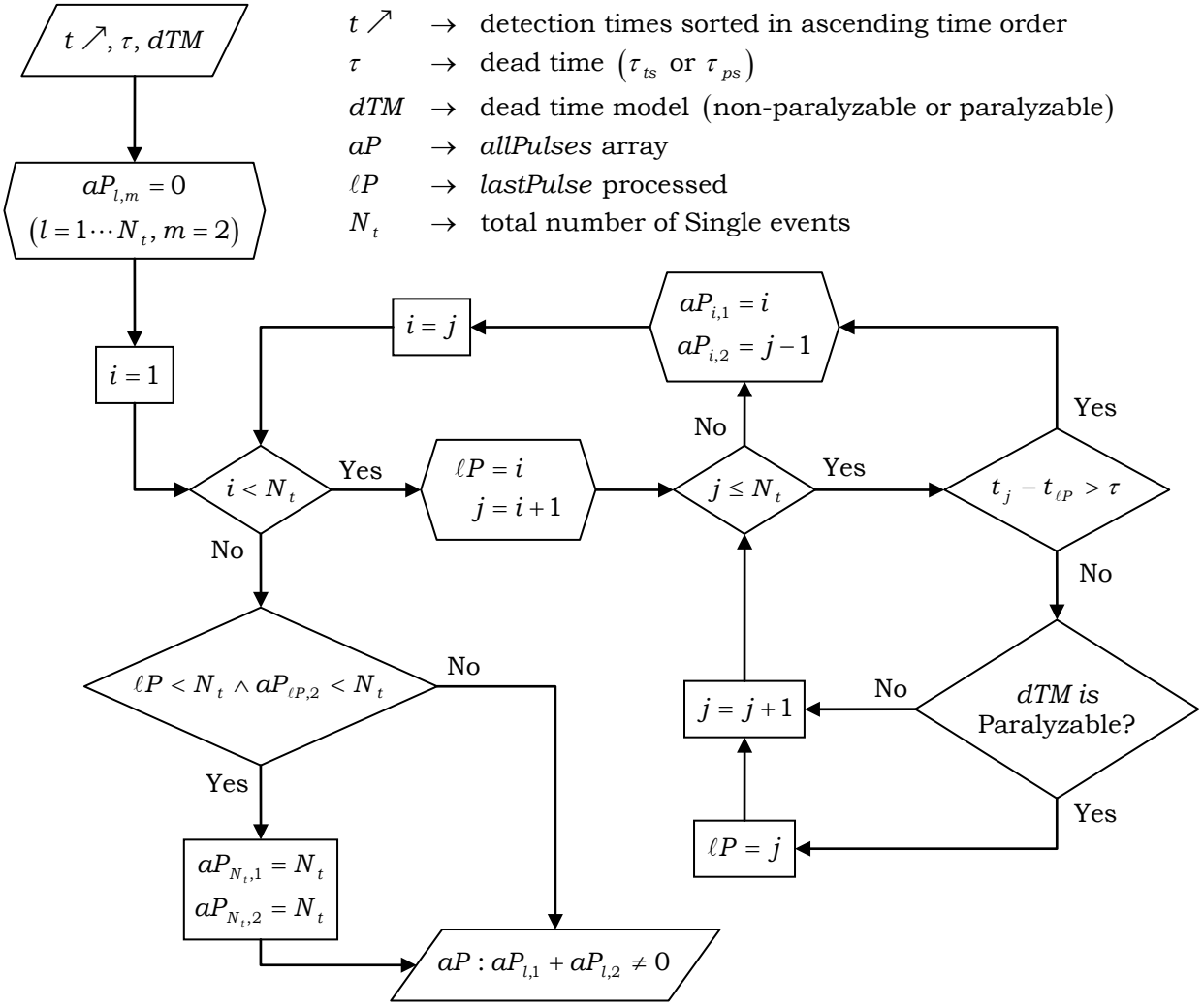

Fig. 6.8: Flow diagram of the *ApplyDeadTimeModel* routine.

6.3.3 Removal of Multiple Events

As mentioned previously, and as it can be seen in Fig. 2.9 (page 27), Fig. 2.21 (page 37), Fig. 2.22 (page 40) and Fig. 2.24 (page 44), for soda lime and borosilicate glass, which are the materials used in the resistive electrodes of the RPCs under

development for the RPC TOF-PET scanner, photons interact in RPC detectors almost exclusively by Compton scattering. As a consequence, it may happens that a given photon give rise to more than one hit in the same detector, or in a different one. Moreover, the same photon interaction can lead to more than one electron being extracted to the gas gap, thus leading to as many hits as electrons extracted.

Multiple hits arising from multiple electrons being extracted to a given gas gap, as a consequence of a single photon interaction, will eventually give rise to a Single event after the processing stage to account for the τ_{ts} non-paralyzable dead time for the time signals, described in the last section.

As to multiple hits arising from multiple interactions of the same photon in the same readout section and, eventually, a negligible fraction of those due to multiple electron extraction and not gathered in a Single event during the processing stage to account for the τ_{ts} non-paralyzable dead time for time signals, will result in multiple Single events in the same detector. If the *rejectAll* option is used to process the τ_{ps} paralyzable dead time for position signals, then those events will eventually be discarded and not considered for further processing. However, if the *coarsePosition* option is used for processing the paralyzable dead time for position signals, then those multiple hits will result in multiple Single events due to the same photon. This is what happens with multiple hits occurring due to multiple photons interacting in different detectors, since, in this case, different readout sections are involved in the detection.

The aforementioned multiple events can contribute in two opposing ways to the final coincidence data. If the incident photon scatters in the forward direction with small deviation from its initial trajectory, the multiple events may contribute to falsely augment the number of LORs that pass close to the annihilation points, thus contributing as True coincidences. If the incident photon scatters with a considerable deviation from the incident direction, then the LORs will contribute to Scattered coincidences.

Since RPC detectors do not have energy resolution, having however an excellent time resolution for Single events, a scheme based on simple kinematics was implemented to remove the multiple Single events that may arise after completion of the processing to account for both non-paralyzable and paralyzable dead times. First, all the Single events are sorted in ascending time order and then a MTW coincidence sorter (see Fig. 4.4 on page 92) is performed, with a time window computed from

$$\Delta t_{MHR} = \frac{\Delta \ell_{max.}}{c}, \tag{6.3}$$

where $\Delta \ell_{max.}$ is the maximum flight path length that a photon can have between

consecutive interactions, which is equal to the maximum diagonal of the scanner. The outcome of this process is a two column array containing in the first column the sorted indexes of all Single events, and in the second column the indexes of the last event found in coincidence with the corresponding one in the first column[21].

The first column is then subtracted from the second, and all the entries equal to zero are removed from the valid events since they cannot be in coincidence with any other event. The events for which coincidences were found (Single or Multiple coincidences) are retained as valid events for further processing, which consist in first forming all possible pairs out of all Single events found in coincidence. This pairs are again organized in a two column array with the first column containing the event with the lower detection time, and the second column containing the event with the higher detection time. For each of the formed pairs, the time difference and distance between the Single events found in coincidence is then computed as

$$\begin{aligned} \Delta t_{pair} &= t_{second} - t_{first} \\ d_{pair} &= \sqrt{\left(x_{second} - x_{first}\right)^2 + \left(y_{second} - y_{first}\right)^2 + \left(z_{second} - z_{first}\right)^2}, \end{aligned} \tag{6.4}$$

where (x_i, y_i, z_i) are the coordinates of the detection points returned from all the previous processing stages (for a real RPC detector, the coordinates returned by the readout electronics). Then, for each pair, the time needed for a photon to travel along a straight line from the detection point of the *first* photon to the detection point of the *second* photon is computed from

$$\Delta t_{light} = \frac{d_{pair}}{c}, \tag{6.5}$$

and compared to a minimum and a maximum time given by

$$\begin{cases} t_{min.} = \max\left(0, \Delta t_{light} - f_{lower}\,\sigma_t\right) \\ t_{max.} = \Delta t_{light} + f_{upper}\,\sigma_t \end{cases}, \tag{6.6}$$

with f_{lower} and f_{upper} parameters for setting a rejection band about the light speed, and σ_t the detector time resolution for Single events. The index of the event corresponding to the *second* photon, viz., the one in the second column of the array having a higher detection time, is then set to zero if

$$t_{min.} \le \Delta t_{pair} \le t_{max.}. \tag{6.7}$$

In the end of the process, the indexes contained in the two column array are reshaped to a single column vector, which is then sorted in ascending order of the

[21] If no other event is found in coincidence with a given event of the first columns, the corresponding entry in the second column will be equal to that of the first one.

indexes of the Single events, and the difference between each successive element in the array $(event_{i+1} - event_i)$ is computed. Those entries in the array for which the aforementioned difference is positive are taken as the Single events to be retained, while all the other events are discarded. This guaranties that a given Single event is not retained twice, that a major fraction of the events for which the kinematics of a single photon travelling through the scanner, and with a time difference and distance between them compatible with that of the light speed, are eliminated from the original data set, and also that all events that cannot be part of a coincidence performed with a smaller time window are also excluded from the original data set. The process can be repeated iteratively a given number of times or until a given convergence criterion is achieved. The first option was the one employed in the present work.

The structure used by the routine that performs the operations described above is listed in Appendix H.

Graphically, the above mentioned procedure is equivalent to reject all events that lie in a rejection band delimited by two lines with slopes equal to the inverse of the speed of light $(1/c)$, and that intercept the time axis of the time vs. distance plot at times equal to $-f_{lower}\,\sigma_t$ and $f_{upper}\,\sigma_t$ as depicted in Fig. 6.9.

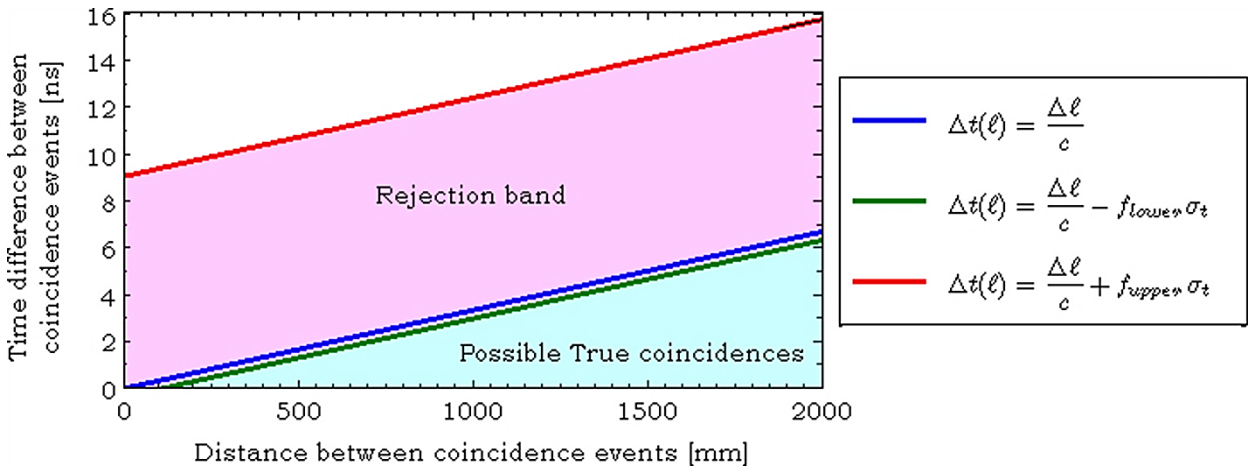

Fig. 6.9: Graphical depiction of the band used for rejecting multiple events, and events that cannot take part of a True coincidence event.

6.3.4 Coincidence Processing

The routine developed for processing Single events in order to form coincidence events, accepts the events returned from the previous processing stages and a structure (Appendix I) containing a set of parameters that specify how the coincidences must be performed. These parameters include, among others, the width of the time window used for coincidence processing and the coincidence sorter type,

which can be one of those mentioned in Section 4.2.1 (page 89) and depicted in Fig. 4.4 (page 92), namely the STW and MTW coincidence sorters. The routine then sorts the input data in ascending time order, and performs the coincidences using the two parameters mentioned above, returning then the input data sorted in ascending time order, and two arrays with two columns each. One of the arrays holds the coincidence events for which only two Single events where found in coincidence, and the other contains all possible single pairs of events in coincidence, out of those found in Multiple coincidence.

The array holding the indexes of coincidence events for which only two Single events where found in coincidence is used to extract, from the array holding the input data sorted in ascending time order, a coincidence data set which was named Accepted Single Coincidence Pairs (ASCP).

The array holding the indexes of all possible pairs of Single events found in coincidence out of the Multiple coincidence events is used to retrieve, from the array of input data sorted in ascending time order, a coincidence data set which was named Accepted Multiple Coincidence Pairs (AMCP).

Both sets of coincidence data (the ASCP and the AMCP) are then concatenated into a single data set which contains All Accepted Coincidence Pairs (AACP), from which all duplicate coincidence pairs are removed.

These three data sets are saved to disk in binary files for being independently processed at a later stage, to account for the performance tests according to the NEMA NU2 standards. Each of the data sets are saved in a two dimensional array containing as many rows as coincidence events, with the columns representing different variables as listed in Appendix J.

The flow chart for coincidence processing is depicted in Fig. 6.10.

6.4 SOFTWARE DEVELOPED FOR PROCESSING COINCIDENCE DATA TO OBTAIN THE NEMA NU2-2001 PERFORMANCE PARAMETERS

A set of routines was developed in order to automate the process of computing the performance parameters according to the NEMA NU2 standards. Those routines concern the spatial resolution, SF, count rates and NECR performed by the 2001 version of the standards. As to the sensitivity test following the NEMA NU2-1994, it was performed prior to the simulations including the detailed geometry of the RPC TOF-PET scanner were started, and its processing does not follow the same sequence of procedures employed in the detailed simulations of the RPC TOF-PET scanner.

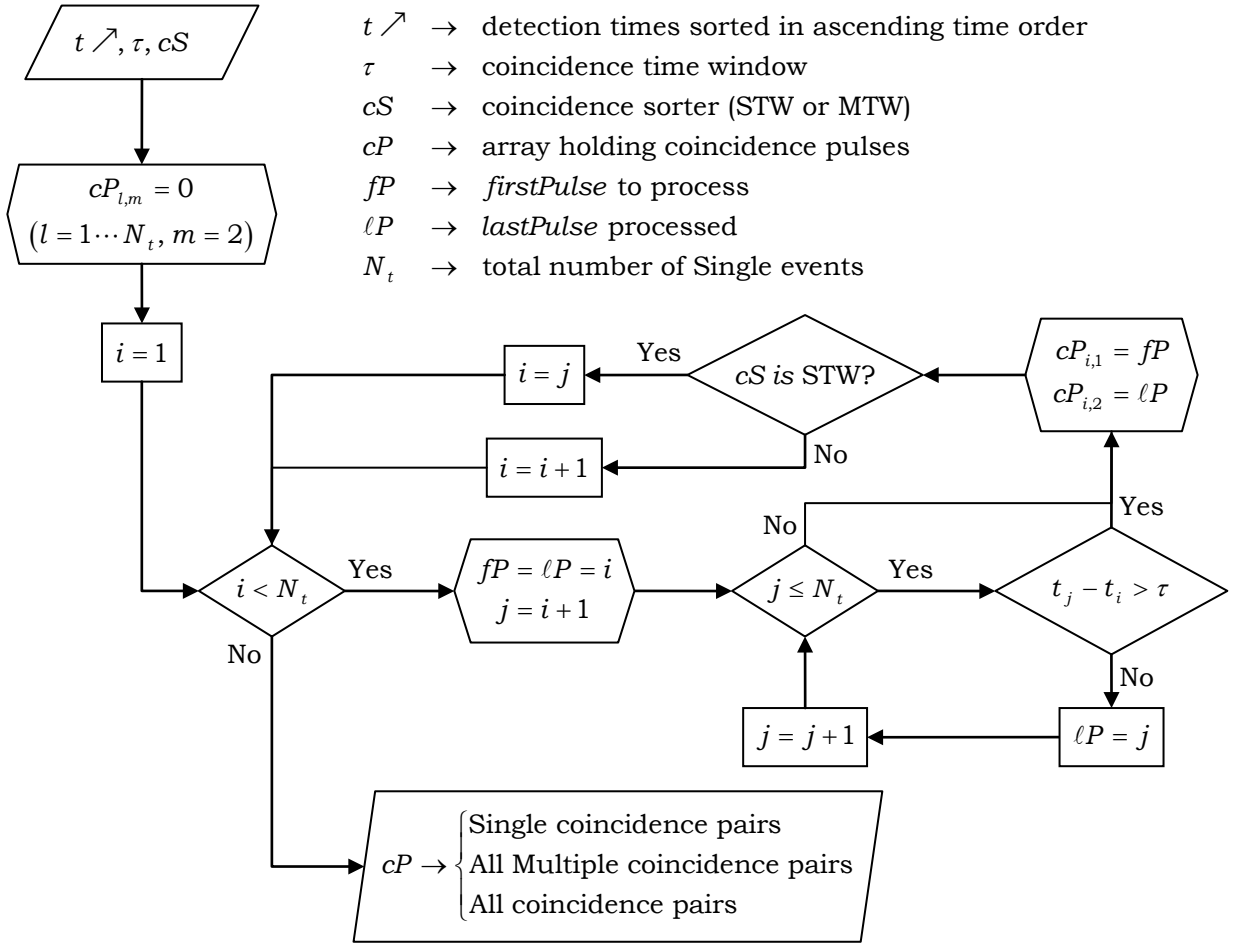

Fig. 6.10: Flow chart of the coincidence sorter.

For the remaining tests, the coincidence data generated by the complete processing of Single events returned by the simulation, according to the sequence described in the last Section, is first processed so that the set of LORs to be used to account for the performance tests is selected on the basis of the criteria specified in the structure holding the coincidence options given in Appendix I. The resulting set of coincidences is then processed to account for the performance tests.

6.4.1 Constraining Coincidence Data to the Scanner Geometry

The first constraint imposed on coincidence data is that the detection points defining a given LOR must be located on different detection heads (see Fig. 6.1 on page 185). This is simply performed by comparing the *headID* of the two Single events defining the LOR and accepting those LORs for which they are different.

6.4.2 Constraining the Polar Acceptance Angle

The LORs resulting from the first stage of geometric constraining are then tested

for the constraint imposed by the polar acceptance angle to be used. This constrain is performed so that only the LORs with a polar angle less than or equal to that specified in the options for acceptance of coincidence data are retained. The polar acceptance angle is computed as defined in Fig. 4.1 (d) (page 89), viz., is specified in the *YZ* plane as in cylindrical PET systems, which use a ring difference, thus holding a polar acceptance angle specified in a 2D mode rather than in full 3D mode.

6.4.3 Retrieving Valid Coincidences Based on Geometric Criteria

Once the two aforementioned constraints have been applied, coincidence data is checked against geometric criteria for acceptance. The three available options for this constraint are the acceptance of those LORs that cross the scanner bore (*none* option in the *type* field of the *Rejection* structure listed in Appendix I.4), the acceptance of those LORs that cross a given volume centred in a given point of the FOV (*geometric* option in the *type* field of the *Rejection* structure listed in Appendix I.4, with the volume specified by the remaining parameters of that same structure), and the acceptance of those LORs for which the point reconstructed by direct TOF lies inside a given volume centred in a given point of the FOV (*geometric_tof* option in the *type* field of the *Rejection* structure listed in Appendix I.4, with the volume specified as in *geometric* rejection).

For any of the above constraints, a second restriction, which was named *time_space*, can also be imposed on the LORs to be accepted, and that consists in first performing the abovementioned rejection followed by the rejection of those LORs for which the corresponding points in the time/distance plot of Fig. 6.9 (page 207) is above the line corresponding to the light speed line. While this restriction may eventually make sense for the *none* and *geometric* rejection methods, it is of no use for the *geometric_tof* method, as will be clear soon.

6.4.3.1 Bore Acceptance and Geometric Acceptance

If the *type* option of the *Rejection* data structure (Appendix I.4) is equal to *none* or *geometric*, the selection of LORs is mathematically performed in exactly the same way, with the differences being eventually in the length of the volume and the shape and size of its cross section, as well as the coordinates of its centre. For the *none* option, the volume consists in a right circular cylinder centred in the FOV with an axial length equal to the scanner AFOV and a diameter equal to the product of the inner width of the scanner transaxial FOV (distance between two parallel detection heads) by the *bore_fraction* field of the substructure *Scanner* of the structure defining the scanner parameters (Appendix G.4). For the *geometric* option, the shape is that of a right

elliptical (or circular) cylinder with minor and major axis given by the *dx* and *dy* fields of the *EllipticalVolume* substructure listed in Appendix I.4, and a total length along the axial direction given by the *dz* parameter of the same substructure, the volume being centred in the point defined by the substructure *Centre* (Appendix I.4).

Considering Fig. 6.11, the LOR defined by the points (x_1,y_1,z_1) and (x_2,y_2,z_2), crosses the acceptance volume if two different points, (x'_1,y'_1,z'_1) and (x'_2,y'_2,z'_2), computed along the 3D symmetric unit vectors $(\hat{x}_1,\hat{y}_1,\hat{z}_1)$ and $(\hat{x}_2,\hat{y}_2,\hat{z}_2)$, lying on the surface of the acceptance volume can be found. This can be first performed in the transaxial plane by verifying the interception of the LOR projected in the transaxial plane with the ellipse that defines the cross section of the acceptance volume, and then, for those LORs that intercept the ellipse, requiring that at least one of the values of the Z coordinate, z'_1 or z'_2, of the interception points of the LOR with the surface of the right elliptical cylinder, computed along the unit vectors $(\hat{x}_1,\hat{y}_1,\hat{z}_1)$ and $(\hat{x}_2,\hat{y}_2,\hat{z}_2)$, is within the limits of the volume along the axial direction.

Since, mathematically, the circular and elliptical cross sections are similar in treatment, the latter being more general, the elliptical cross section centred in an arbitrary point with coordinates (C_x,C_y) was used as the basis for computing the intersection of the LOR with the volume of interest.

The computation relies in the interception of the transaxial projection of a 3D line, defined in its parametric form by

$$(x,y,z)=(x_i,y_i,z_i)+(\hat{x}_i,\hat{y}_i,\hat{z}_i)t_i \quad \text{with} \quad i=\{1,2\}, \tag{6.8}$$

where t_i is the parameter that defines the LOR, with an ellipse defined by

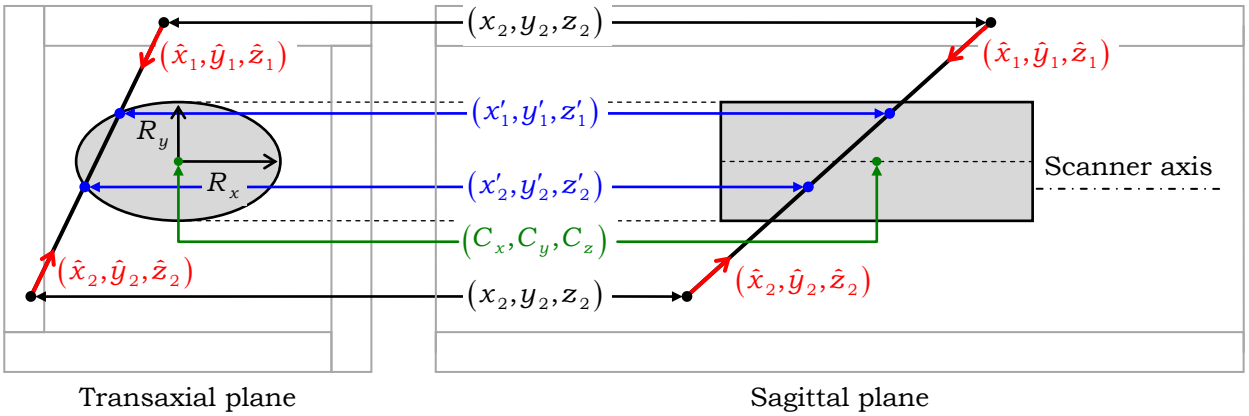

Fig. 6.11: Sketch of the geometric rejection performed to a right elliptical cylinder volume with an elliptical cross section with semi-axis R_x and R_y, and a length *dz*, with its centre placed at an arbitrary point in the FOV, defined by the coordinates (C_x,C_y,C_z). If $R_x=R_y=R$, then the volume for acceptance is a right circular cylinder.

$$\frac{(x-C_x)^2}{R_x^2}+\frac{(y-C_y)^2}{R_y^2}=1\,, \tag{6.9}$$

where $R_x = dx/2$ and $R_y = dy/2$.

Taking into account one of the two possible unit vectors, pointing from one of the LOR points to the other, defined by

$$\begin{cases} (\hat{x}_1,\hat{y}_1,\hat{z}_1)=\dfrac{(x_2,y_2,z_2)-(x_1,y_1,z_1)}{\sqrt{\left[(x_1,y_1,z_1)-(x_2,y_2,z_2)\right]\cdot\left[(x_1,y_1,z_1)-(x_2,y_2,z_2)\right]}} \\ (\hat{x}_2,\hat{y}_2,\hat{z}_2)=\dfrac{(x_1,y_1,z_1)-(x_2,y_2,z_2)}{\sqrt{\left[(x_1,y_1,z_1)-(x_2,y_2,z_2)\right]\cdot\left[(x_1,y_1,z_1)-(x_2,y_2,z_2)\right]}} \end{cases}, \tag{6.10}$$

where the dot inside the square root is the vector inner product operator, and defining the auxiliary variables

$$\begin{cases} a_i=(\hat{x}_i\,R_y)^2+(\hat{y}_i\,R_x)^2 \\ b_i=2\left[(x_i-C_x)\,\hat{x}_i\,R_y^2+(y_i-C_y)\,\hat{y}_i\,R_x^2\right] \\ c_i=\left[(x_i-C_x)\,R_y\right]^2+\left[(y_i-C_y)\,R_x\right]^2-(R_x\,R_y)^2 \\ D_i=b_i^2-4\,a_i\,c_i \end{cases}, \tag{6.11}$$

The LORs that intercept the ellipse in the transaxial projection plane can be obtained from the variable D_i in the above equation, which is such that

$$\begin{cases} D_i<0 & \text{the LOR do not intercept the ellipse} \\ D_i=0 & \text{the LOR is tagent to the ellipse} \\ D_i>0 & \text{the LOR intercepts the ellipse} \end{cases}. \tag{6.12}$$

From this first step, only the LORs that intercept the ellipse in the transaxial plane are retained and used to compute the interception with the volume along the axial (*Z*) direction. For that, the 3D parameters of the line are computed from

$$\begin{cases} t_{i,-}=\dfrac{-b_i-\sqrt{D_i}}{2\,a_i} \\ t_{i,+}=\dfrac{-b_i+\sqrt{D_i}}{2\,a_i} \end{cases}. \tag{6.13}$$

Since it is required that the LOR intercepts the volume for acceptance, and that both points defining the LOR lie outside the region of interest, then both parameters,

$t_{i,-}$ and $t_{i,+}$ must be positive[22], which thus ensure that the LOR crosses the elliptical cylindrical volume, and that it is not formed by a pair of events detected at the same side of the elliptical cylindrical volume. So, the second criteria for accepting LORs passing through the volume of interest is given by

$$t_{i,-} \geq 0 \quad \wedge \quad t_{i,+} \geq 0 . \tag{6.14}$$

Two parameters for defining the interception of the LOR with the volume, $t_{i,-}$ and $t_{i,+}$, imply two points on the volume surface. The smallest line parameter gives the point closest to the LOR point used to compute the parameters, and the highest line parameter gives the other one.

For reasons related with implementation details and generality (Section 6.4.4, page 214), it was opted to compute the line parameters for both points of the LOR. In this case, the line parameter to be retained for each LOR point is the smallest of those satisfying Eq. (6.14), viz., for each of the two points that define the LOR, (x_1, y_1, z_1) and (x_2, y_2, z_2), the line parameters are given by

$$\begin{cases} t_1 = \min(t_{1,-}, t_{1,+}) & \text{with} \quad t_{1,-} \geq 0 \quad \wedge \quad t_{1,+} \geq 0 \\ t_2 = \min(t_{2,-}, t_{2,+}) & \text{with} \quad t_{2,-} \geq 0 \quad \wedge \quad t_{2,+} \geq 0 \end{cases} . \tag{6.15}$$

From these two line parameters, the axial coordinates of the interception with the surface of the right elliptical cylinder are obtained, and the LOR is finally accepted if

$$C_z - \frac{dz}{2} \leq z'_1 \leq C_z + \frac{dz}{2} \quad \vee \quad C_z - \frac{dz}{2} \leq z'_2 \leq C_z + \frac{dz}{2} . \tag{6.16}$$

6.4.3.2 Geometric Time-Of-Flight Acceptance

If the rejection method is specified as being of type *geometric_tof*, then Eq. (4.26) is used to compute the most probable point of annihilation along the LOR, and the coincidence is accepted if

$$\frac{(x_{TOF} - C_x)^2}{R_x^2} + \frac{(y_{TOF} - C_y)^2}{R_y^2} < 1 \quad \wedge \quad C_z - \frac{dz}{2} \leq z_{TOF} \leq C_z + \frac{dz}{2} . \tag{6.17}$$

The second condition constrains the direct TOF reconstructed point along the axial direction, while the first imply that, in the transaxial plane, the TOF reconstructed point is inside the ellipse that defines the cross section of the acceptance volume.

If the point obtained by direct TOF reconstruction is inside the volume of

[22] A negative value of $t_{i,-}$ or $t_{i,+}$ imply to take a way along the LOR that is symmetric to that defined by the unit vector, in order to reach the ellipse.

interest, then the position of the LOR in a time/distance plot, such as that of Fig. 6.9 (page 207), will be always below the light speed line. So, as stated at the end of the introduction of Section 6.4.3 (page 210), it is of no use to add the *time_space* string to the *geometric_tof* one.

6.4.4 Data Rebinning

A routine to perform the rebinning of inclined LORs, by both SSRB and SSRB_TOF (Section 4.4.1, page 107, Section 4.5, page 115, and Fig. 4.18 on page 118), was developed, in which the SSRB_TOF is performed by applying Eq. (4.26) to the axial coordinate, and attributing to both points defining the LOR the z_{TOF} coordinate, instead of distributing the LOR through the neighbouring slices according to the Gaussian distribution of the z_{TOF}, as depicted in Fig. 4.18 (page 118). As to SSRB, is computed by simply setting the Z coordinate of both detection points to the average value of their Z coordinates

A third rebinning method, named *SSRB_Modified*, was also implemented, in which the coincidence data is first reshaped, in exactly the same way as described in Section 6.4.3.1 (page 210), so that the detection points of the LORs lie in the surface of a right circular cylinder. The reason for performing the reshaping of the LOR points into a right circular cylindrical surface, is related to the fact that, to achieve a reasonable detection efficiency, the RPC TOF-PET scanner needs to stack several RPC detectors, implying detection depths that are much thicker than the crystal detection elements employed in commercial PET scanners.

Making use of Fig. 6.12 (a), the maximum deviation produced by SSRB in the axial coordinate due to the DOI is given by

$$\Delta\bar{z}_{max.} = \frac{\tan(\theta)\Delta y_{max.}}{2}. \tag{6.18}$$

Considering two maximum detection thicknesses of $\Delta y_{max.,1}$ and $\Delta y_{max.,2}$, the deviation in the axial position, due to SSRB, of the detector with thickness $\Delta y_{max.,2}$ to that with thickness $\Delta y_{max.,1}$, relative to the latter, is a constant given by

$$\Delta\bar{z}_{rel,1} = \frac{\Delta y_{max.,2} - \Delta y_{max.,1}}{\Delta y_{max.,1}}. \tag{6.19}$$

Using the data contained in Appendix B for the complete definition of the RPC TOF-PET scanner, the maximum difference in the detection points along the radial direction is equal to 137.6 mm, against the 25 mm of the thicker crystals employed in the PET scanners resumed in Table 4.4 (page 142), and Eq. (6.19) holds a deviation of ~4.50 (~450%) for the RPC TOF-PET scanner relative to typical commercial crystal

based scanners. Fig. 6.12 (b) depicts a plot of Eq. (6.18) for polar acceptance angles ranging from zero to seventy degrees, and an inset for the range of zero to ten degrees, which is close to that reported as the maximum allowed polar acceptance angle of ~9° for SSRB for not compromising spatial resolution along the axial direction [Kinahan & Karp, 1994].

Taking into account the typical thickness of the slices used in crystal PET scanners (of about 2 mm, which is half the axial pitch of the detection elements), and the depth of the detection elements, it is clear from the inset that a maximum value of ~10° on the polar acceptance angle is required for the spatial resolution along the axial direction not to be compromised due to the lack of DOI information. Moreover, it is also clear why LORs were reshaped so that they lied in the surface of a cylinder prior to performing SSRB.

For the sensitivity, SF, count rates and NECR performance tests, which employ a continuous source distribution along the axial direction, the SSRB method or the *SSRB_Modified*, with the surface for reshaping coincidence data being a right circular cylinder centred in the scanner axis, can both be applied without loss of information. However, for tests involving image reconstruction, two choices are possible. If the polar acceptance angle used for LOR acceptance is restricted so that its influence for off-axis sources does not compromise the spatial resolution along the axial direction, the reshaping can also be performed to the surface of a right circular cylinder centred in

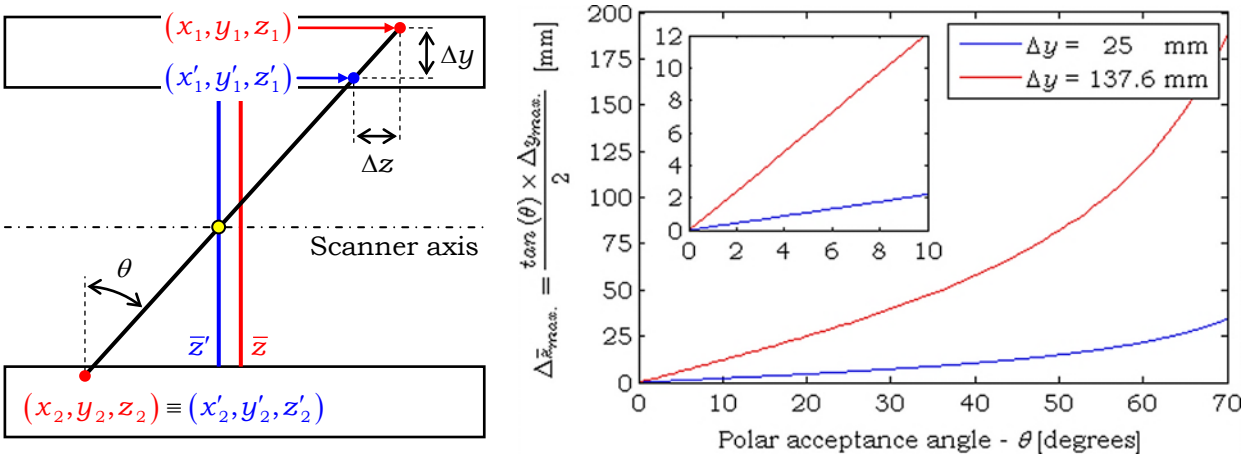

(a) (b)

Fig. 6.12: Influence of DOI and polar acceptance angle on LOR assignment by means of SSRB, for a point source located in the axis of the scanner. Pane (a) represents the geometry in a sagittal plane, and pane (b) depicts the plot of the maximum deviation in the average axial position for values of Δy equal to 25 and 137.6 mm, along with an inset tailored for the values of the polar acceptance angle for which SSRB is considered as reliable in what concerns the degradation of spatial resolution in the axial direction [Kinahan & Karp, 1994].

the FOV. However, if higher values of the polar acceptance angle are to be used in order to take full advantage of a full-body length AFOV scanner, then it may eventually be preferable to centre the reshaping surface on the point of interest or in a neighbourhood of it. In this case, if not taken the necessary precautions in setting the radius of the surface so that all the detection points lie outside it, Eq. (6.15) with $t_{i,-}$ and $t_{i,+}$ given by Eq. (6.13) may result in the rejection of valid LORs. So, to avoid errors that may eventually arise in setting the dimensions of the surface for reshaping the LORs, Eq. (6.13) was changed holding $t'_{i,-}$ and $t'_{i,+}$ given by

$$\begin{cases} t'_{i,-} = \operatorname{sgn}\left(\dfrac{\left(x_i - C_x\right)^2}{R_x^2} + \dfrac{\left(y_i - C_y\right)^2}{R_y^2} - 1 \right) t_{i,-} \\ t'_{i,+} = \operatorname{sgn}\left(\dfrac{\left(x_i - C_x\right)^2}{R_x^2} + \dfrac{\left(y_i - C_y\right)^2}{R_y^2} - 1 \right) t_{i,+} \end{cases}, \tag{6.20}$$

where *sgn* is the sign function, which is positive, negative or zero if the points lie outside, inside or on the surface of the volume used for reshaping. So, the effect of the *sgn* function is to redirect the walking over the LOR to the appropriate direction, depending on the position of the LOR points relative to the volume enclosed by the reshaping surface.

6.4.5 Sinogram Construction

For constructing the sinograms required by some of the NEMA NU2 performance tests, a function was developed which accepts the coincidence data and a structure containing four parameters resumed in Appendix K.

The routine takes into account the pretended rebinning method, as described in the previous section, and applies it to the coincidence data prior to constructing the sinograms. After the rebinning has been performed, the radial distance and the azimuthal angle of each LOR are computed, respectively, from Eq. (4.1) and Eq. (4.2) (page 94), respectively. The computed values are then used to produce 3D histograms with a radial, azimuthal and axial binning specified by the *voxelSize* and *numBins* of the structure referred in Appendix K. If the azimuthal binning given in the referred structure is set to zero, the routine uses Eq. (4.25) for computing the azimuthal sampling, and sets the azimuthal binning accordingly.

6.4.6 Sensitivity Test

As mentioned previously, the Sensitivity test was performed prior to the development of the GEANT4 program for simulation of the detailed geometry of the RPC

TOF-PET scanner. The goal was to study the behaviour of the sensitivity with increased axial length, both for crystal based scanners and the RPC TOF-PET scanner, and compare the expected sensitivities. This will be addressed in Chapter 8.

6.4.7 Spatial Resolution

For computing the spatial resolution, a routine was developed that takes all the sinograms produced and the structure containing the parameters for their construction (Appendix K). The routine then reconstructs the image using the FBP algorithm provided by Matlab.

The reconstructed image is then passed to a second routine that accepts also as input the structure containing the parameters for sinogram construction, the fractional level at which the spatial resolution must be computed (for instance, 0.5 for FWHM and 0.1 for FWTM), a Boolean variable specifying if the PSFs are to be computed through the point of highest intensity or through a specified point of the reconstructed image. The routine then applies the procedure described in Section 4.6.1 (page 119)[23], returning the three orthogonal PSFs, the coordinates of the points at which the specified fractional level occurs, and the spatial resolution.

This will be addressed in Chapter 9.

6.4.8 Scatter Fraction, Count Rates and Noise Equivalent Count Rate Tests

Since the processing of data for computing the SF, count rates and NECR is performed in the same exact way, a single routine was developed, which takes into account the complete set of parameters being processed, such as the dead time of the detector for the position signals, the policy for acceptance and rejection of position signals for which pileup occurred, the removal of multiple events, the coincidence sorter type, and data set to be processed (ASCP, AMCP or AACP), as well as the activity of the source. Based on all the input parameters, the routine retrieves the coincidence data files to first compute the SF with a low activity concentration in the phantom, as described in Section 4.6.3 (page 131), and latter retrieves the corresponding SF file for performing the computations as described in Section 4.6.4 (page 134), with the exception of the sinograms shifting, which can be performed in three different ways, one of which consists on the method described in Section 4.6.4 (page 134).

The other two methods rely on a single sinogram for performing the radial shifting, differing only in the method used to compute that sinogram, which, in one

[23] With the exception of the point through which the PSFs must be retrieved if the Boolean variable is set to true, in which the coordinates passed to the routine are used to retrieve the three orthogonal PSFs.

case, is equal to the sum of all the transaxial sinograms that are used for computing the performance parameters, and, in the other, is produced by directly applying Eq. (4.1) using the (x,y) coordinates of the centre of the line source, which, in the case of simulated data, are accurately known. In this last case, the sinogram is constructed with the same exact binning of that employed for the construction of the sinograms of each slice. The produced sinogram is then used to compute the radial shifting to be applied to each of the axial sinograms.

Owing to low statistics due to computation time and storage restrictions, it was found that the shifting performed by using each individual sinogram, as described in the NEMA NU2-2001 standards, could lead to the attribution of Scatter and/or Random counts to the central portion of the shifted sinograms, thus erroneously increasing the number of True counts. For this, the last method described for performing the radial shifting was adopted for processing the SF and count rates.

CHAPTER 7
OPTIMIZATION OF THE RESISTIVE PLATE CHAMBER DETECTOR AND PRELIMINARY TESTS OF THE RESISTIVE PLATE CHAMBER TIME-OF-FLIGHT POSITRON EMISSION TOMOGRAPHY SCANNER

In the present Chapter, the optimization of the RPC detector, in what concerns the thickness of the resistive electrodes, will be addressed, after which an analysis of the RPC TOF-PET scanner will be performed to address some parameters of more fundamental nature than those given by the NEMA NU2 standards.

7.1 SETUP EMPLOYED IN THE SIMULATIONS

Since the full set of parameters employed in the GEANT4 developed program were the same for both the optimization of the thickness of the resistive electrodes and the preliminary tests performed with the full scanner geometry, these last being equal to those employed in the simulation of SF, count rates and NECR performance tests, it was opted to list them in the present Chapter, with a reminder whenever the parameters for the two tests here discussed differed. Also the full set of phantom configurations employed in the SF, count rates and NECR performance tests will be given in the present section, thus avoiding repetition in Chapter 10.

7.1.1 Physics

The physics lists implemented in the GEANT4 developed program, were activated according to the values contained in the "Default" column of the table specified in Appendix A.1., thus allowing for the decay of radioactive nuclei.

The parameters for the interaction of photons, electrons, positrons, Hadrons and Ions were also set to those of the "Default" columns presented in Appendixes A.2 through A.5. As such, for those simulations that made use of radioactive nuclei as the primary particles, the positron range was accounted for, and, for those simulations involving the annihilation of positron/electron pairs, the GATE annihilation routine was employed, thus accounting for the photon acollinearity. As to Rayleigh scattering, and since the SEP does not provide it, the LEP extensions were activates.

7.1.2 Detector and Scanner Geometry

In what follows, the values listed, and the complete geometry of the scanner, applies only to the simulation of the RPC TOF-PET scanner. For the optimization of the detector, the parameters where all the same, with two exceptions: the thickness of the resistive electrodes, which was varied, thus leading to different thickness of those mentioned bellow, and the number of detection heads defined for the scanner was equal to one (see Appendix B.3).

The scanner geometry (Section 6.2.3.1, page 184) was defined as listed in the "Default" column of tables presented in Appendix B, leading to an active detection volume of 3.44×1000×2400 mm^3 (radial×transaxial×axial) for each detection module. From the abovementioned dimensions, the active detection volume of each RPC detector can be found as having been equal to 6.88×1000×2400 mm^3. Since each detection head was defined as having a stack of twenty detectors in the radial direction, and without spacing between them, the total volume for detection in each detection head was of 137.6×1000×2400 mm^3. As to the outer volume of each detection head, it can be found as having been equal to 143.6×1008×2408 mm^3. This value takes into account the outer dimensions of each RPC detector (6.88×1002×2002 mm^3), the margins between the walls of the detection head and the detectors (2 mm in both the transaxial and axial directions), as well as the thickness of the walls of the detection head case (1 mm). From the outer dimensions of the detection head, and taking into account that no spacing between adjacent detection heads was set, the outer scanner dimensions were of 1151.6 mm and 2408 mm. Finally, from the outer thickness (radial) and width (transaxial) of the scanner, and the corresponding dimensions of the detection heads, the diameter of the scanner bore, defined in this context as the circle inscribed in the square that defines the inner dimensions of the scanner, was of 864.4 mm.

7.1.3 Phantom Geometry

For the optimization of the detector, no phantom was employed in the simulations. For the tests involving the complete RPC TOF-PET scanner, the phantom for the SF, count losses and NECR performance tests, defined in accordance to the NEMA NU2-2001 standards (Fig. 4.25 on page 132), was employed, the parameters of which are listed in the "Default" column of Appendix C.4.

In addition, for the SF, count rates and NECR performance tests, an axially extended version of the NEMA NU2-2001 SF phantom, with all the parameters defined as given in Appendix C.4 with the exception of the axial length, which was set to

1800 mm, was also used. So, and except for the axial length, both phantoms targeted for the SF, count rates and NECR performance tests, consisted in solid right circular cylinders with a diameter of 200 mm, with a 6.8 mm diameter hole drilled along the axial direction and 45 mm off-centre, containing an annulus-like insert, with inner and outer diameters of 3.2 and 4.8 mm, respectively.

7.1.4 Materials

The walls of the head case were defined as being of Aluminium, the space inside the head case being filled with the gas mixture usually employed in timing RPC detectors, namely, a mixture of Tetrafluoroethane $(C_2H_2F_4,)$, Sulphur Hexafluoride (SF_6) and Isobutane $(\text{iso-}C_4H_{10})$, in volume proportions of 0.85:0.10:0.05, leading to a mass proportion of 0.832:0.028:0.140, which was also used to define the material of the RPC detector in which the several layers were placed.

The insulator and conductor layers of each RPC detection module, were defined as being made of polyamide $(C_{22}H_{10}N_2O_5)$ films[1], and the layer that serve as support for the readout strips, defined as being made of Aluminium, was set to biaxially-oriented polyethylene terephthalate $(\text{BoPET} - (C_{10}H_8O_4)_n)$ film[2]. As to the gas gaps, were set to the abovementioned gas mixture, and the material employed in the floating resistive electrodes was set to soda lime glass.

The materials employed in the definition of the phantoms targeted for the SF, count rate and NECR performance tests were those specified in the NEMA NU2-2001 standards, namely, the right circular cylinder, and the walls of the line insert, were defined as being made of polyethylene, while the core of the line insert was considered to be filled with water.

As to the *world* volume, it was considered to be made of air.

7.1.5 Primary Particles and Source Distribution

For the optimization of the resistive electrodes thickness, the primary particles consisted of 511 keV photons. For the simulations involving the complete RPC TOF-PET scanner, and the SF, count rate and NECR phantoms, the source consisted in ${}^{18}_{9}F$ nuclei at rest, uniformly distributed in the volume of a cylinder with dimensions equal to the inner core of the line insert, and centred within it.

7.1.6 Simulated Runs

For the simulation of the complete system, a total of 600 runs were simulated for

[1] The name attributed to the material was Kapton, a brand of polyamide films.
[2] The name attributed to the material was Mylar, a brand of BoPET films.

both phantoms (the 700 mm length standard NEMA NU2-2001 phantom, and the 1800 mm axially extended version), in order to obtain sufficient statistics for the SF, count rates and NECR performance tests, but only five runs were employed in the preliminary tests.

In both cases, the parameters employed in the definition of each run, were those listed in the "Default" column of the table presented in Appendix E, with the exception of the *savePhantomHitsBinaryData* parameter, which was not activated for the optimization of the RPC detector, and was activated for a single run of the simulations performed with the SF, count rate and NECR phantoms.

For each run, a total of 10^6 events were simulated, with one photon fired onto the single detection head, for the optimization of the RPC detector, and one $^{18}_{9}\mathrm{F}$ decay per simulated event, for the simulations performed with the SF, count rates and NECR NEMA NU2-2001 phantom, as well as for the simulations performed with the 1800 mm axially extended phantom.

7.2 OPTIMIZATION OF THE DETECTION EFFICIENCY

The detection efficiency of an RPC detector for 511 keV photons depends on the balance between two opposing requirements. First, the resistive electrodes, which serve as converters of photons into electrons, must be thick enough to increase the probability of photon interaction. Second, the converter plates must be thin enough so that the δ-rays, arising from the collisions of primary electrons due to the interaction of photons, can penetrate the material from the points where they are created, and reach the surface of the electrodes, eventually being extracted to the gas gap.

7.2.1 Previous Studies on the Detection Efficiency

The dependence of the detection efficiency on the thickness of the resistive plates and the energy of the incident photons, has been thoroughly studied, mainly by Blanco [Blanco et al., 2009; Blanco, 2011], for photons impinging perpendicularly the surface of several stacks of converter plates of three different materials (glass, lead glass and lead). The detection efficiency as a function of the energy of the incident photon, for a fixed thickness of the converter plates (400 μm), and for the optimum thickness found for a given number of converter plates and materials, was also studied. The results obtained have shown that, for a given material, the thickness that maximizes the detection efficiency, for 511 keV photons, depends on the number of converter plates present in the stack, as depicted in the top row of Fig. 7.1, for three different materials, and also that the detection efficiency, for a given thickness of the

converter plates, depends on the energy of the incident photons, as depicted in the bottom row of Fig. 7.1. These latter plots are for the optimum thickness of the converter plates, for the corresponding material and number of converter plates. As it can be seen, there is a strong dependency of the detection efficiency with the energy of the incident photons, that is stronger for glass than for lead glass and lead, which present a tendency for reaching a plateau for energy. For instance, for a stack of 201 glass plates defining 200 gas gaps, the detection efficiency for 511 keV photons is of ~30%, being of ~20% for 400 keV photons, while for lead glass and lead, this difference is of ~5%.

This dependency of the detection efficiency on the incident photon energy is very important for PET applications. As stated previously, at the end of Section 5.5 (page 162), RPC detectors do not have energy resolution, not allowing thus to reject events on the basis of an energy window, as is employed in PET scanners with crystal based detectors. However, the strong dependency of the detection efficiency on the energy of the incident photons, leads to the rejection of events scattered in the patient or object to be imaged. However, this is not by itself a guarantee that RPC detectors can be used successfully in PET scanners. In fact, the negligible cross section for photoelectric absorption presented by glass, the material commonly employed in the resistive

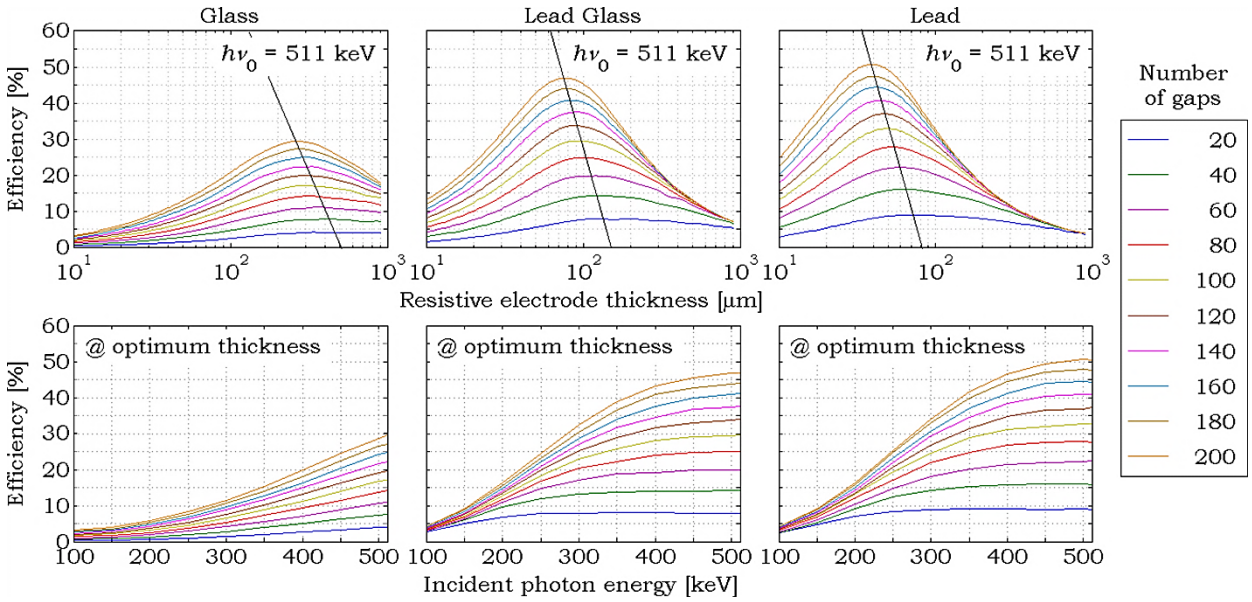

Fig. 7.1: Dependence of the detection efficiency of a stack of converter plates, for 511 keV photons impinging perpendicularly the first converter plate of the stack, as a function of the converter plate thickness, for several materials and number of converter plates (top row), and detection efficiency as a function of the incident photon energy for stacks with different numbers of 400 μm thick converter plates. (Data kindly ceded by Alberto Blanco, and that can be found in [Blanco et al., 2009; Blanco, 2011].)

electrodes, leads to a detection based on Compton scattering, which may compromise the use of RPC detectors in PET applications. Blanco also addressed this point by computing the Misidentified Fraction (MIF) of events [Blanco et al., 2009; Blanco, 2011] which may be given by

$$MIF_{\Delta r} = \frac{N_{out\ of\ \Delta r}}{N_{detected}}, \tag{7.1}$$

where $N_{detected}$ is the total number of events detected, and $N_{out\ of\ \Delta r}$ is the number of events detected farther than a given distance Δr of the point where the interaction leading to detection occurred. This distance may be computed in 2D mode as being, for instance, the distance of the detection point projected in the surface of the resistive electrode to the detection point projected in the same plane, or more accurately in full 3D mode, for instance, as the distance of the detection point to the point where the photon leading to detection interacted, or the distance from the detection point to the line defined by the flight path of the incident photon that lead to detection. This last was used by Blanco, who found values for $MIF_{1\,mm}$ of about 20% for stacks of 201 glass plates (200 gas gaps) with the optimum thickness, showing also that the $MIF_{1\,mm}$ depended on the plate thickness [Blanco et al., 2009; Blanco, 2011]. Moreover, the definition of MIF also leads to a dependence of this parameter with the thickness of the gas gaps and the DOI resolution of the RPC detector.

7.2.2 Optimization of the Glass Thickness for a Complete Resistive Plate Chamber Detection Head

The thorough study conducted by Blanco has led to very important results concerning the optimum thickness for a given number of converter plates. However, eventually it may not be straightforward to extrapolate the results for an RPC detector with a specific geometry. There are some reasons, as follows.

The values reported by [Blanco et al., 2009] were obtained for a stack of glasses from which electrons can always be extracted to the forward and backward gaps, with the only exception of the first and last glasses of the stack, the former extracting electrons only to the forward gap, and the latter extracting electrons only to the backward gap. This is not the case of RPC detectors based on double module geometry, as those developed and under study for the RPC TOF-PET scanner, and depicted in Fig. 5.4 (page 154), in which two sets of five gaps are delimited by two sets of six glasses. In each of the readout modules, the first glass (the one on the side from which the photon impinges the detector) only contribute with electrons being extracted to the forward gap, and the last glass (the one farther from the side from which the

photon impinges the detector) only contribute with electrons being extracted to the backward gap. So, each detector has two glasses that only contribute with electrons extracted to the forward gap, and two glasses that only contribute with electrons being extracted to the backward gap. In addition, RPC detectors have other materials interposed between the two detection modules, and between adjacent detectors: the insulator, conductive and readout layers.

From the above, the optimum thickness of the resistive electrodes must, in principle, be determined by considering the complete detection geometry, instead of a stack of floating resistive electrodes alone. This was performed by detailed simulations, in GEANT4, of a single detection head, with the full set of RPC detectors that are intended to be employed in the RPC TOF-PET scanner, and by firing a total of 10^6 photons with 511 keV, such that the angles of incidence of the photons impinging the detection head, which ranged from 0° to 60°, were uniformly distributed in a spherical shell, rather than with photons impinging perpendicularly the detector surface, which may lead to different results. In fact, a previous study performed with a single 400 μm thick glass plate, which was then the thickness of the glasses employed in the RPC detectors for testing purposes, showed that the extraction efficiency depended both on the energy of the impinging photons, and on the angle of incidence, as depicted in Fig. 7.2 (page 226).

The results concerning the optimum thickness of the glass plates and the MIF are depicted in Fig. 7.3 (page 227). As it can be seen, the maximum efficiency, found by simulation, was obtained for a resistive electrode thickness of 200 μm. Concerning the MIF, it was computed for the EEP, the EDP and the EAP. Although the latter is the one with practical interest, the MIF for the other two points allows gaining some insight on the effects introduced by each stage of the detection. As it can be seen from the plots, for a given point, the MIF was higher for smaller bins than for higher ones, having been worse for the point of detection assignment, which was computed as explained in Section 6.2.5.2.2 (page 193), and depicted in Fig. 6.2 (page 192), and which was binned to 2 mm in the transaxial and axial directions, and to the centre of the RPC detection module, thus resulting in a radial binning that depended on the thickness of the glass plates.

7.3 ANALYSIS OF THE RAW DATA TO ACQUAINT FOR THE EFFECTS INTRODUCED BY THE DETECTION SYSTEM

Prior to account for the source activity and the detector readout in the processing stages, the simulation raw data was analysed to acquaint for the effects of the

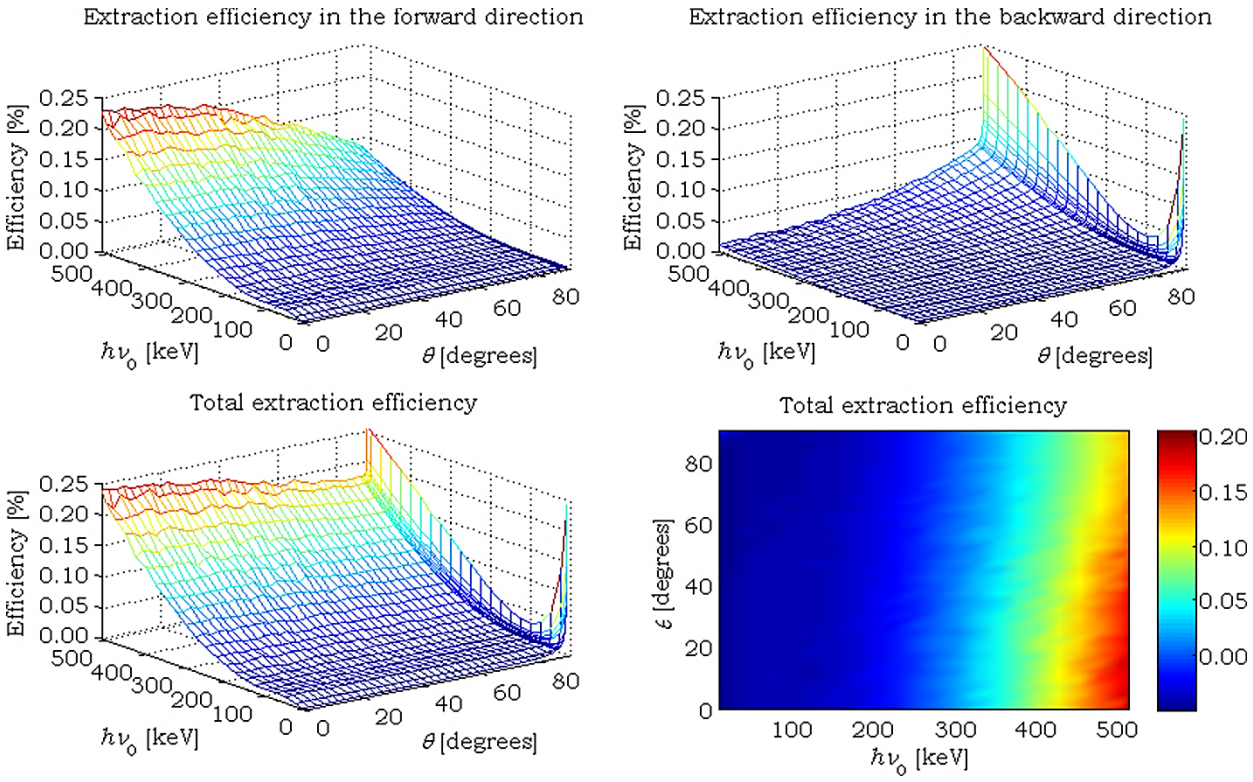

Fig. 7.2: Extraction efficiency for a single 400 μm thick glass plate, as a function of the incident photon energy and angle of incidence. The top left plot depicts the extraction efficiency in the forward direction, the top right plot depicts the extraction efficiency in the backward direction, and the plots on the bottom row depict the total extraction efficiency.

detection system. This was performed by first sorting the simulation raw data by the event ID, then by the ID of the particle that gave rise to the primary photon, followed by the ID of the primary photon, and finally by the number identifying the hit originated by the primary photon. With the raw data sorted in this way, the indexes of the photons corresponding to pairs of photons, originated in the same annihilation, were identified as those with equal IDs for the event and the particle originating the primary photons, different IDs for the primary photon, and a single hit in the detector. The retrieved photons were then removed from the raw data, and the indexes of the photons giving rise to a single hit were obtained by imposing the conditions of different IDs for the event and the primary photon. The indexes of the remaining hits, which correspond to photons that gave rise to more than one hit, were then stored in a two column array, with the first column corresponding to the first hit of a given photon, and the second column corresponding to the last hit of that same photon.

Table 7.1 (page 228) depicts an example of the ordering process for some hits of one of the simulated runs, along with the classification of the hits according to the abovementioned scheme.

From the above described procedure and Table 7.1 (page 228), if two photons arising from the same annihilation are detected with one of the photons having more than one hit, then the photons are not classified as a pair, but instead as a multiple and a single hit (event ID 189 of Table 7.1, on page 228) or two multiple hits (event ID 157 of Table 7.1, on page 228). This classification procedure allows accounting for the fact that, eventually, these pairs of photons would give rise to multiple coincidences, which are usually discarded in PET, as mentioned in Section 4.2.3.4 (page 100).

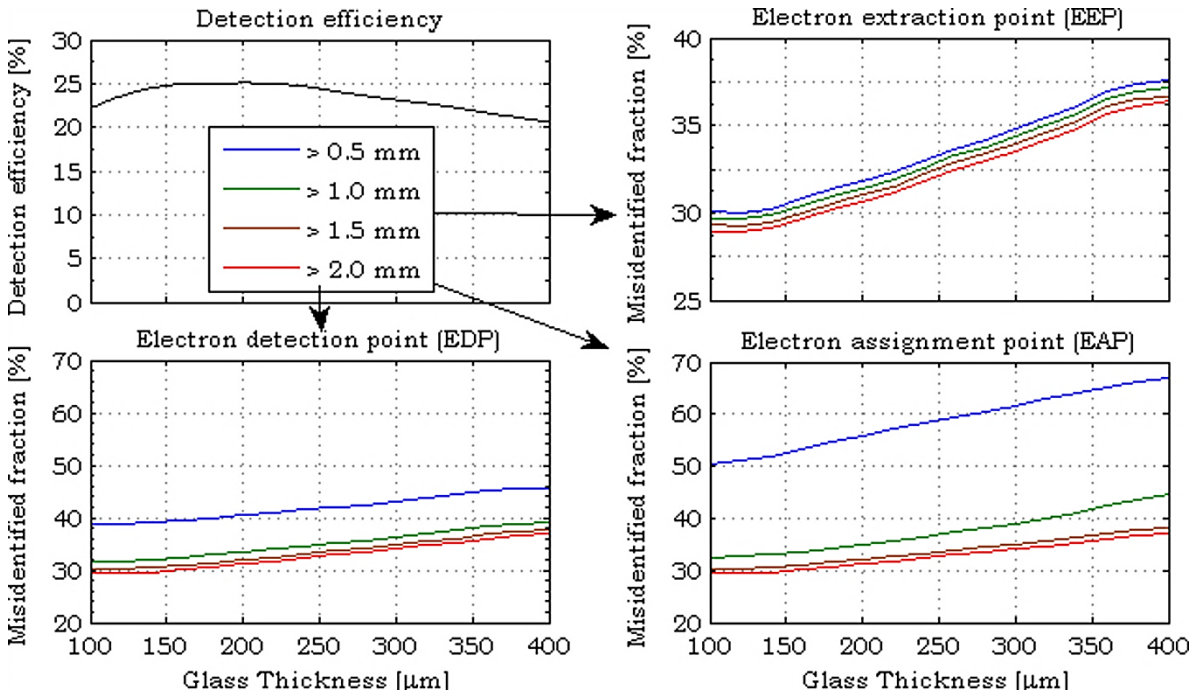

Fig. 7.3: Detection efficiency of an RPC detection head, for 511 keV photons, as a function of the thickness of the glass plates (top left). The angular distribution of the photons impinging the detection head was uniformly sampled over a spherical shell, with angles ranging from 0° to 60°. Also depicted are the MIFs computed for the EEP (top right), EDP (bottom left) and EAP (bottom right), which was binned to 2 mm in the transaxial and axial directions, and to the centre of the RPC detection module, in the radial direction. The MIFs were computed as the distance of the corresponding points to the lines defined by the flight paths of the incident photons, for four different binning: 0.5, 1.0, 1.5 and 2.0 mm.

7.3.1 Energy Spectrum of Detected Photons

From the obtained data, several plots have been produced to account for parameters such as the energy spectrum of the incident photons, for all photons reaching the scanner surface, the energy spectrum of photons reaching the scanner surface and being detected, and the energy spectrum of the photons immediately before the interaction leading to electron extraction.

Fig. 7.4 depicts such plots, obtained from the data corresponding to a single run with 10^6 simulated decays with the 700 mm length SF NEMA NU2-2001 phantom, for all the photons that leaved the phantom and reached the scanner surface (PEP_{all}), all the photons that reached the scanner surface and were detected $(PEP_{detected})$, and for all detected photons, in which case the energy considered was that of the photons immediately before the interaction that lead to electron extraction. For the photons

TABLE 7.1: EXAMPLE OF THE SORTING PERFORMED TO THE SIMULATION RAW DATA FOR SOME HITS, ALONG WITH THE CLASSIFICATION OF EACH HIT. DATA IS GROUPED BY COLOURS, ACCORDING TO THEIR CLASSIFICATION, AND FURTHER GROUPED BY EVENT ID, WITH HORIZONTAL LINES FOR DISAMBIGUATION.

Event ID	Parent ID	Photon ID	Hit ID	Classification
5	4	24	1	M
5	4	24	2	
8	4	18	1	S
32	4	9	1	S
37	4	7	1	P
37	4	8	1	
40	4	12	1	S
41	4	22	1	P
41	4	23	1	
45	4	15	1	S
62	4	16	1	S
87	4	25	1	P
87	4	26	1	
90	4	15	1	S
93	4	20	1	S
96	4	12	1	P
96	4	13	1	
157	4	23	1	M
157	4	23	2	
157	4	24	1	M
157	4	24	2	
189	4	25	1	S
189	4	26	1	M
189	4	26	2	
189	4	26	3	
193	4	26	1	S
201	4	10	1	S
208	4	10	1	M
208	4	10	2	
208	4	10	3	

with multiple hits, only the first hit was considered. The plots depicted in the top row represent the energy spectrum (left) and the cumulative energy spectrum (right), while the plots in the bottom row represent the deviation of the corresponding plots on the top row relative to all the photons that reached the detector surface, viz., $(PEP_{\det ected} - PEP_{all})/PEP_{all}$ (green curves) and $(PDP - PEP_{all})/PEP_{all}$ (red curves), the magenta curve representing the deviation of the *PDP* curves relative to those of the $PEP_{\det ected}$, viz., $(PDP - PEP_{\det ected})/PEP_{\det ected}$.

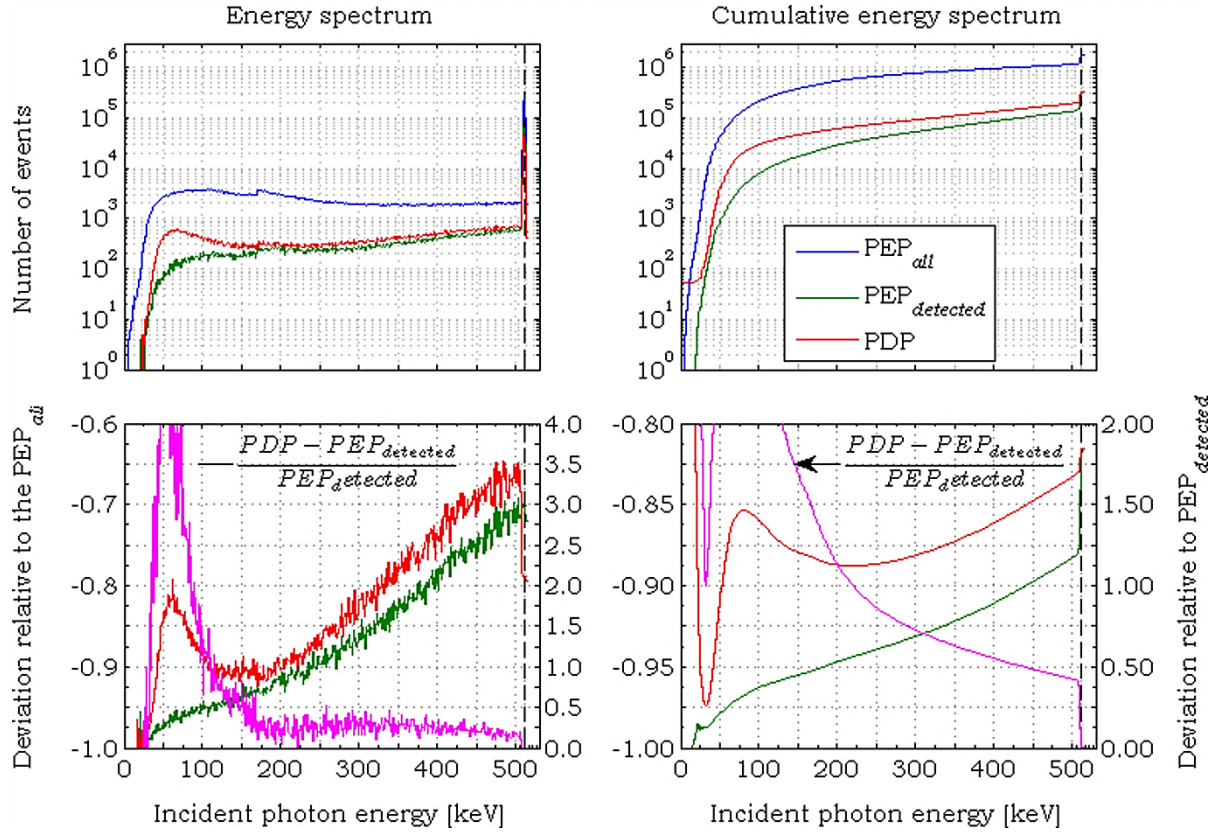

Fig. 7.4: Energy spectrum (top left), cumulative energy spectrum (top right), relative deviation of energy spectrum (bottom left), and cumulative energy spectrum (bottom right), for a single run with 10^6 simulated decays. For convenience, the legend is place only in the cumulative energy spectrum. On the top plots, the PEP_{all} curves represent the energy all the photons that leaved the phantom and reached the scanner surface, the $PEP_{detected}$ curves represent the energy of all the photons that reached the detector surface and were detected, and the *PDP* curves represent the energy of all detected photons immediately before the interaction leading to electron extraction. The green and red curves of the bottom plots refer also to $PEP_{detected}$ and *PDP*, representing the deviation of the corresponding curve of the top plots relative to that for the PEP_{all}, viz., $(PEP_{\det ected} - PEP_{all})/PEP_{all}$ and $(PDP - PEP_{all})/PEP_{all}$, and must be read in the left *Y* axis. As to the magenta curve, depicted in the bottom plots, represents also the deviation of the energy of the *PDP* curves of the corresponding top plots, but relative to the $PEP_{detected}$, viz., $(PDP - PEP_{\det ected})/PEP_{\det cted}$, and must be read on the right *Y* axes.

From the green curve of the bottom left plot, it can be seen that, as expected, the RPC TOF-PET scanner has a detection efficiency which depends on the energy of the incident photons, and, from the red and magenta curves of the bottom left plot, it can be seen that the detection process shifts the energy of the detected photons to lower values, relative to those of the incident photons, thus introducing unwanted scatter that may compromise the SF and NECR. Notice, however, that an important amount of scattered events in the detection system led to the detection of very low energy photons (less than about 200 keV), which have lost a great amount of their initial energy, and thus have suffered considerable deviation from their initial flight paths inside the detection system, eventually contributing to a constant scatter background spread across the scanner, which may not compromise the spatial resolution, and may have a small impact on the contrast of the final reconstructed image.

From the bottom right plot, it can also be seen that, for the simulated geometry (including the scanner and the phantom), the global detection efficiency was found to be between 18% and 19% (the value computed from the raw data was 18.42%).

The energy spectrum of the photons entering the scanner and, consequently, the energy spectrum of the detected photons, may eventually be shifted to higher energies by adding a given thickness of an absorbing material at the scanner surface. Preliminary results obtained by adding several lead thicknesses on top of the detection heads (Fig. 7.5), indicate a considerable percentual reduction of the number of low energy photons impinging the scanner surface and being detected (left plots of Fig. 7.5), and also a considerable percentual reduction of the photons detected with low energy. However, this reduction is also accompanied by a reduction of the 511 keV photons that are detected, and may imply the use of smaller thicknesses of absorber, to minimize the impact of the absorber in the 511 keV photons. Further studies, with smaller absorber thicknesses, need to be performed, and the performance parameters must be assessed with the added absorber.

7.3.2 Number of Hits Produced by Detected Photons

The data, classified as depicted in Table 7.1 (page 228), was also used to obtain the number of hits that each photon gave rise to, the number of interactions that each individual photon has undergone in the scanner prior to detection, the number of interactions in the scanner suffered by each photon forming a pair, and the average number of interactions for photon pairs, as well as the number of interactions that photons giving rise to multiple hits have undergone between each hit produced. Fig. 7.6 (page 232) depicts the plots for the aforementioned quantities.

In the top left plot of Fig. 7.6 (page 232), it can be seen that more than 90% (91.11%) of the photons gave rise to a single hit in the detector, the remaining giving rise to two or more hits, of which 94.26% correspond to exactly two hits.

From the top right plot of Fig. 7.6 (page 232), it can be seen that more than 60% (63.53%) of the hits were produced by photons that have undergone a single interaction in the detector, the remaining having undergone two or more interactions. Of these, 51.32%, 19.17%, 9.68%, 6.13% and 4.27% have undergone, respectively, 2, 3, 4, 5, and 6 interactions in the detector, prior to the one that gave rise to a hit.

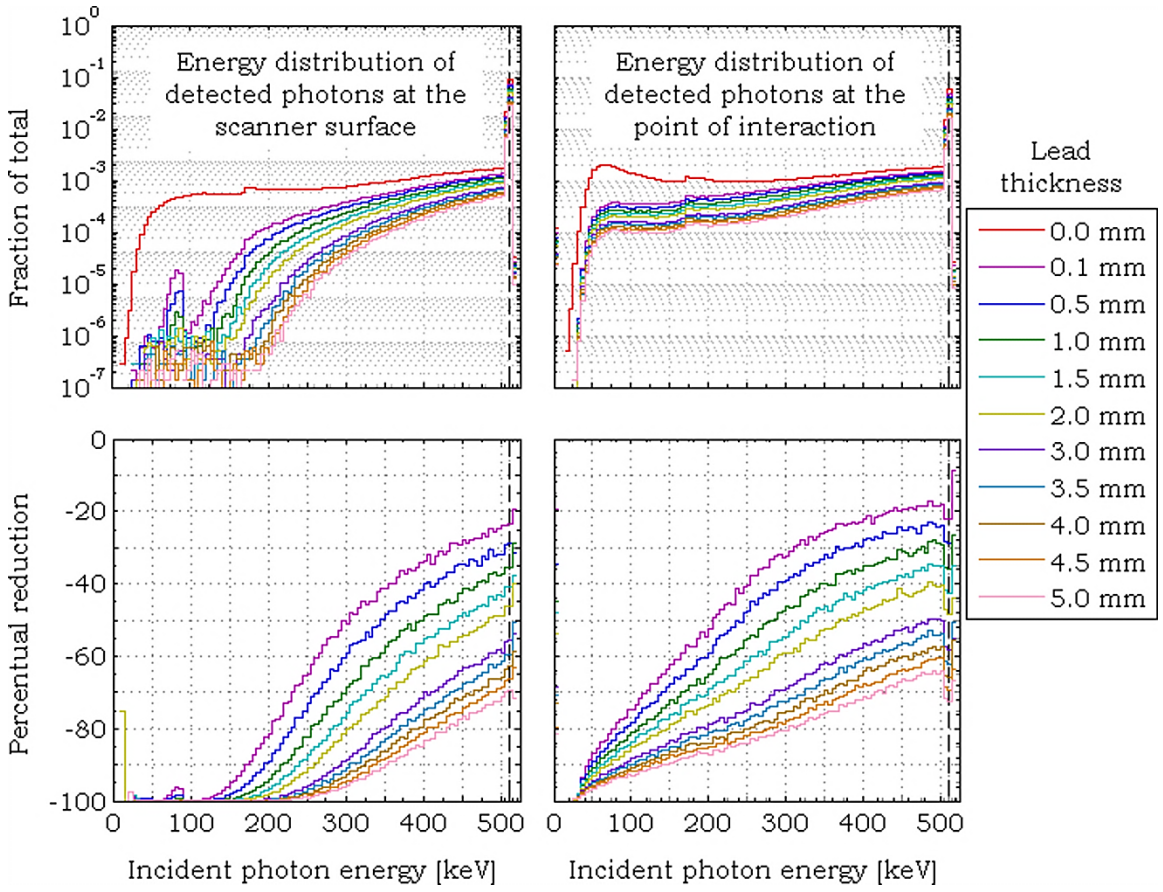

Fig. 7.5: The top left plot depicts the energy spectrum of photons impinging the scanner surface and being detected, without any additional absorber material (0.0 mm curve), and by adding different thicknesses of lead to the scanner surface, normalized to the total number of photons impinging the scanner surface. The top right plot depicts the same information, but for the energy of the photons immediately before the interaction that gave rise to electrons being extracted to the gas gap, and is normalized to the total number of detected photons without added absorber material (0.0 mm). The bottom left plot depicts the percentual reduction of the energy spectrum obtained for the several thicknesses of lead, relative to the corresponding energy spectrum without absorber. The bottom right plot depicts the same information, but for the energy of the photons immediately before the interaction leading to electrons being extracted to the gas gap.

Since each photon taking part in a pair is indistinguishable from the total set of photons, the aforementioned percentages are the same for these photons, as it can be seen from the *SP* curves depicted in the bottom left plot of Fig. 7.6. As to the average number of interactions undergone by photon pairs , depicted by the *AP* curves of the same plot, it can be found that almost 40% (39.04%) of the photon pairs have undergone a single interaction in the detector. This value corresponds to the percentage of pairs coming from the phantom that are detected without suffering scatter in the detector. Of the remaining 60.96% photon pairs, 38.55%, 20.62%, 12.17%, 7.88% and 5.74% have undergone, respectively, 1.5, 2.0, 2.5, 3.0 and 3.5 average number of interactions prior to detection.

From the bottom right plot of Fig. 7.6, it can be seen that, for more than 10% (12.24%) of the photons giving rise to multiple hits, the incident photon did not suffer any interaction in the detector between consecutive hits, which is only possible if these events correspond to multiple electron extractions by the same interaction, as it has been confirmed. These hits, which correspond to 1.09% of the total detected

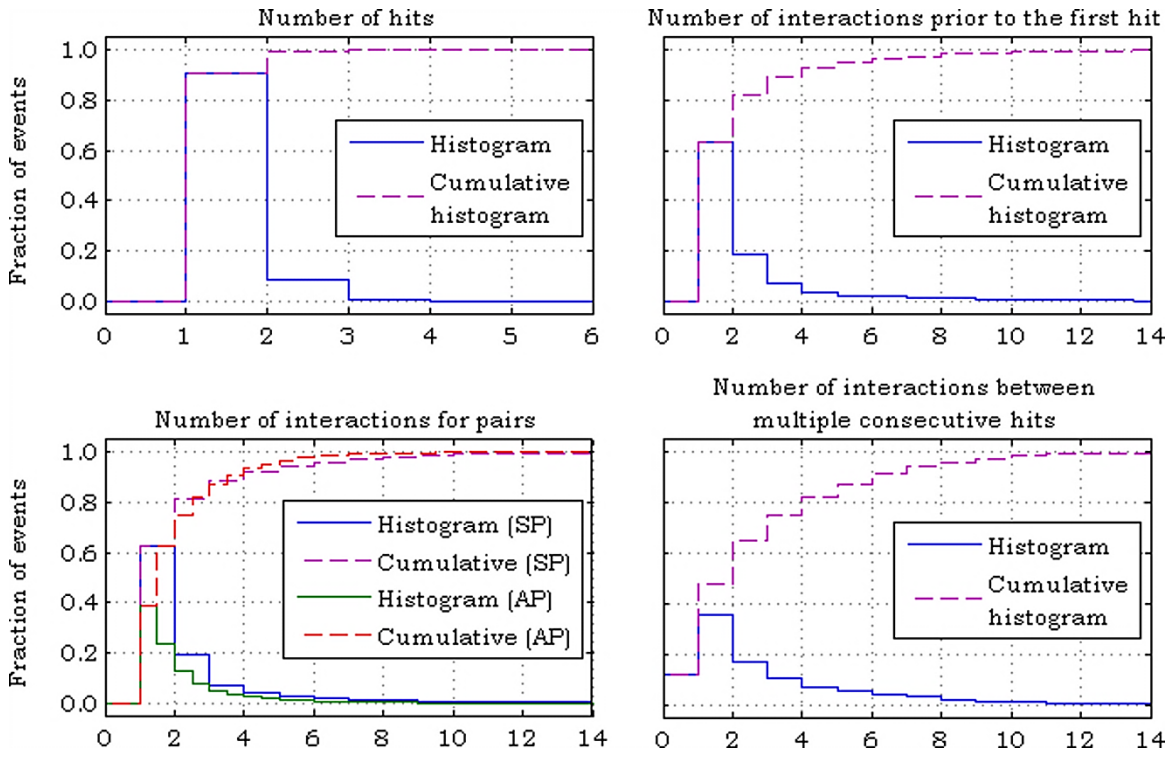

Fig. 7.6: Histograms depicting the number of hits that each photon gave rise to (top left), the number of interactions that a photon has undergone in the detector prior to give rise to an hit (top right), the number of interactions prior to detection undergone in the detector by single photons (SP) that make part of a pair, and the mean number of interactions for photon pairs (AP) (bottom left), and the number of interactions between consecutive hits for photons that gave rise to multiple hits (bottom right).

photons, will eventually be removed by the readout of the detector due to the τ_{ts} non-paralyzable dead time on the time signals. The remaining 87.76% of the photons giving rise to more than one hit, and which represent 7.80% of the detected photons, will have a time/distance signature that is above the line defined by the light speed (Fig. 6.9 on page 207) as depicted in Fig. 7.7.

Finally, Fig. 7.8 (page 234) depicts the colour maps relating the number of interactions undergone by each detected photon with the energy, normalized to the maximum value obtained to the total number of interactions.

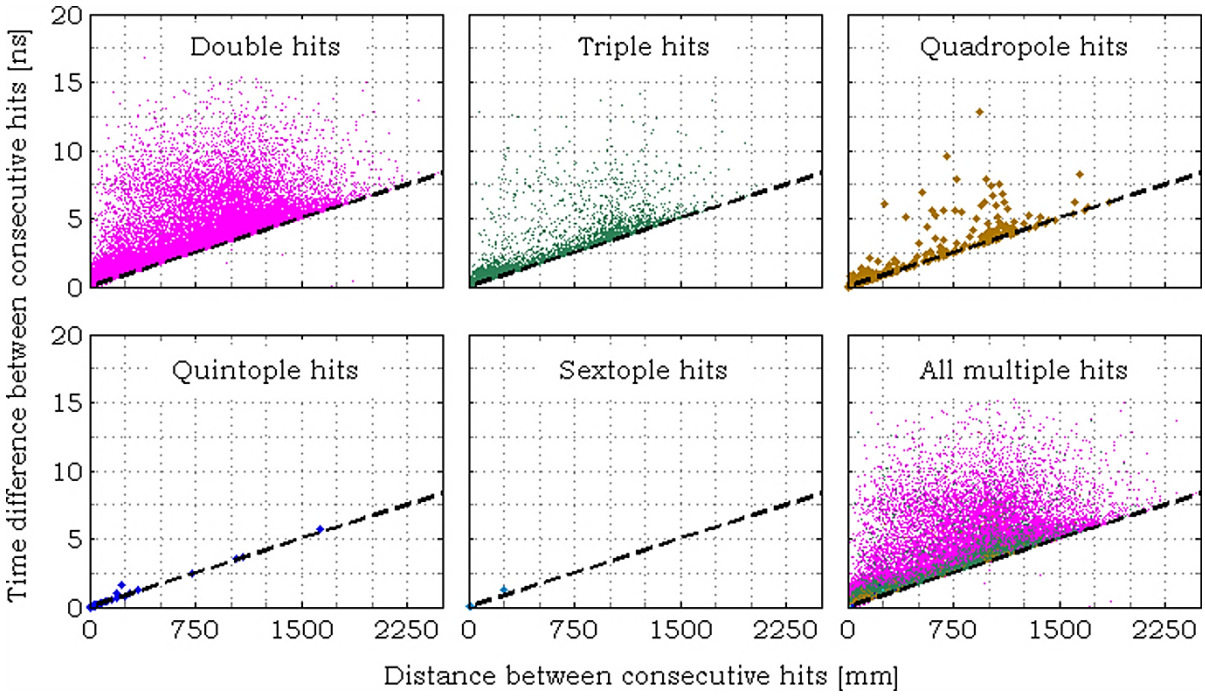

Fig. 7.7: Time/distance patterns of multiple consecutive hits.

7.4 EFFECT OF DEAD TIME AND MULTIPLE EVENTS REMOVAL ON SIMULATION RAW DATA

To study the effects of the detector dead time on the number of photons detected, the simulation data was processed to account for the decay times by considering activities ranging from 37 kBq (1 μCi) to 370 MBq (10 mCi), followed by the $\tau_{ts} = 200$ ns non-paralyzable dead time for time signals, and four different values of the dead time for position signals, $\tau_{ps} = \{0.0, 0.5, 1.0, 3.0\}$ μs, both rejecting all the photons for which pileup occurred, and accepting them with a coarse position. The obtained data set was stored, and a second data set was obtained by processing the stored data to account for the multiple events removal as described in Section 6.3.3

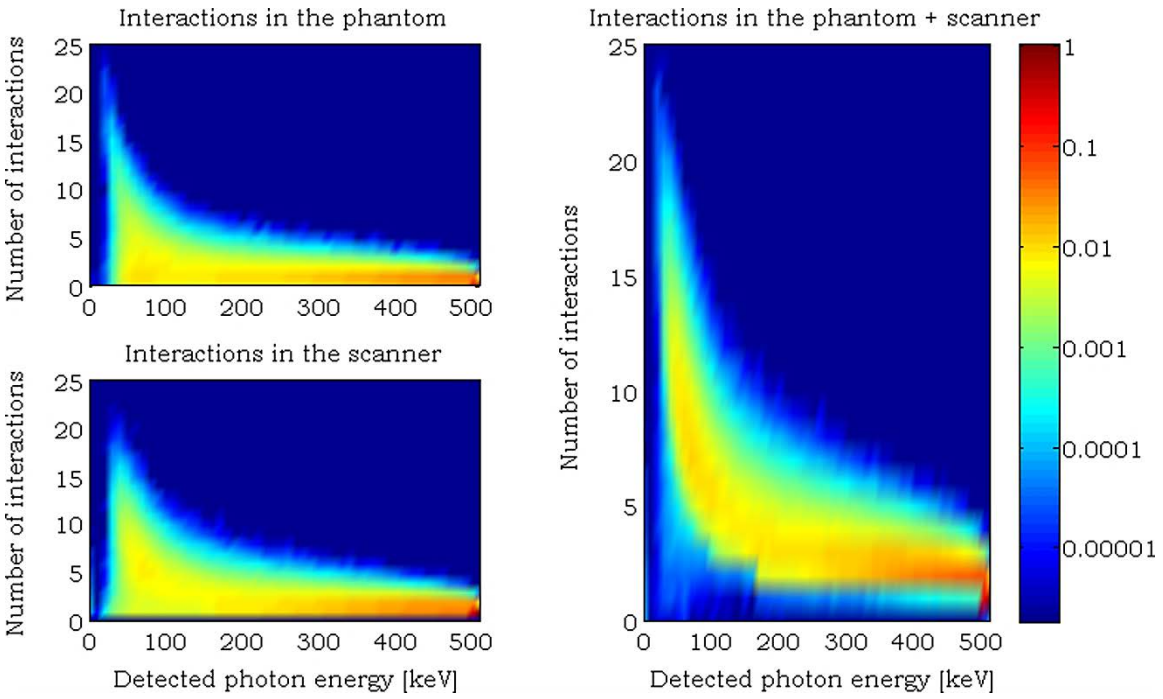

Fig. 7.8: Colour maps depicting the number of interactions undergone by each photon until detection as a function of the energy of the detected photon. The top left plot depicts the number of interactions in the phantom, the bottom left plot depicts the number of interactions in the scanner, and the right plot depicts the total number of interactions (phantom plus scanner). The colour maps were obtained by considering only the first hit of each detected photon, and are in logarithmic scale, normalized to the maximum of the right colour map.

(page 204), so that the effects of the procedure on the simulation data could be accessed.

After the abovementioned processing, each data set, obtained for the different combinations of the processing parameters, was sorted as explained in Section 7.3 (page 225), and the data concerning the photons giving rise to a single hit, pairs of photons and photons with multiple hits was retrieved (e.g. Table 7.1, page 228).

The data set processed with a total activity of 37 kBq (1 μCi) and a $\tau_{ps} = 0.0$ μs paralyzable dead time on the position signals, so that pileup due to different detected photons could be considered negligible, was then used to produce a plot with the same information contained in the bottom right plot of Fig. 7.6 (page 232), showing that the hits contained in the first bin were reduced to zero by the τ_{ts} non-paralyzable dead time on the position signals, as expected and depicted in the right plot of Fig. 7.9, along with the bottom right plot of Fig. 7.6 (page 232) for easier comparison of the effects of the τ_{ts} non-paralyzable dead time for the time signals.

As to the remaining processed data, comprising a total of eighteen activities for the source, four values for the τ_{ps} paralyzable dead time for the position signals, and

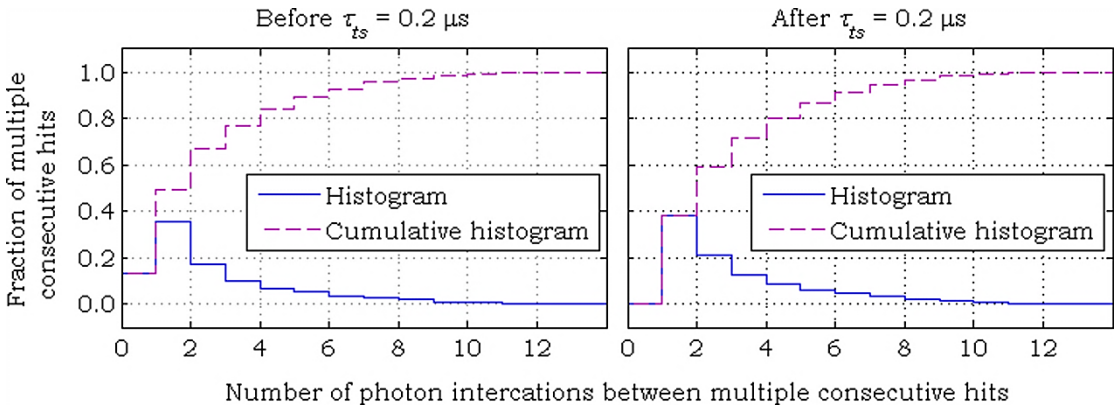

Fig. 7.9: Number of interactions between consecutive hits for photons that gave rise to multiple hits, obtained from the simulation raw data (left plot), and from the data processed by considering a total activity of 37 kBq (1 μCi), after applying the $\tau_{ts} = 200$ ns non-paralyzable dead time for time signals.

the processing with and without the removal of multiple events, was then used to address the effects of the dead time and multiple events removal on the simulation raw data. This was performed by computing the percentual reduction of each one of the four categories of events, relative to the corresponding values obtained from the raw data.

The results are depicted in Fig. 7.10 (page 236), showing, as expected, the reduction of all the four quantities with the increase of the total activity in the FOV (depicted in the plots as the activity concentration in the phantom), the percentual reduction having been higher for higher values of the τ_{ps} paralyzable dead time for the position signals. Moreover, the results obtained by accepting all events for which pileup for the position signals occurred, were all equal to those obtained with $\tau_{ps} = 0.0$ μs, as also expected, since, in this case only, the τ_{ts} non-paralyzable dead time for the time signals reduces the number of detected and accepted events.

As to the percentual reductions of the above mentioned quantities after applying the multiple events removal, relative to those obtained after processing the data to account for the detector readout but without performing the removal of multiple events, are depicted in Fig. 7.11 (page 237).

As it can be seen, the procedure for removal of multiple events, caused by multiple interactions of the same photon, is effective in reducing the total number of events detected, the number of Single events, as well as the number of Single events due to multiple hits produced by the same photon, although it also reduces the number of photon pairs. However, it was verified that this latter reduction decreases with the decrease of the value used for the f_{lower} parameter (recall Section 6.3.3 on

page 204, in particular Eq. (6.6) on page 206 and Fig. 6.9 on page 207). This is due to the fact that, with the increase of the f_{lower} parameter, the region for rejecting multiple events overlaps the region for allowed coincidences. Yet, the pairs that were removed by the procedure were confirmed to correspond to long range Scattered events, for which the time difference between photon pairs is higher than the lower limit imposed for the removal of multiple events, as depicted in Fig. 6.9 (page 207).

One may then conclude that the removal process is effective in reducing the number of Single events, and may eventually be implemented as a first level triggering to substantially reduce the number of Single events to be sent from the scanner front end electronics to a small dedicated HPC cluster, to be promptly processed on the fly, or to be stored for later processing.

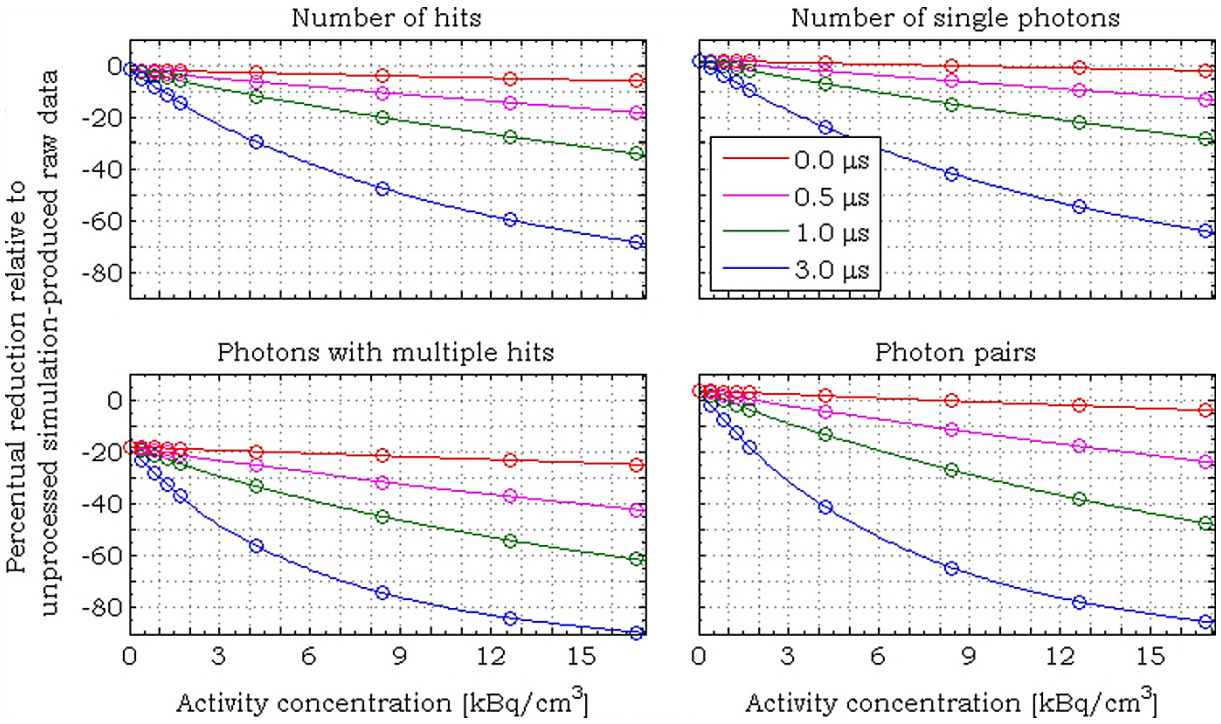

Fig. 7.10: Percentual reduction, due to dead time, of the number of hits, number of single photons, photons with multiple hits, and photon pairs, for all values of τ_{ps}, as a function of activity concentration, relative to the same quantities of the simulation raw data.

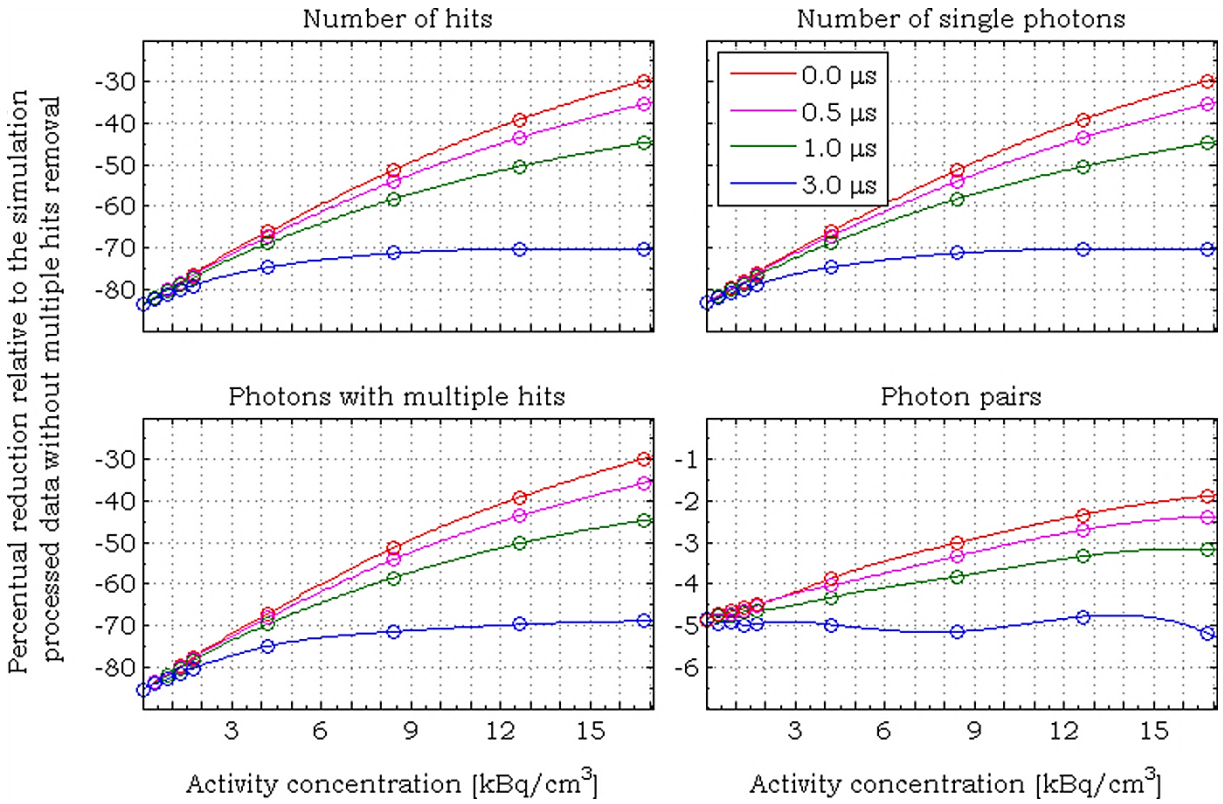

Fig. 7.11: Percentual reduction of the number of hits, number of single photons, photons with multiple hits and photon pairs, for all values of τ_{ps}, as a function of activity concentration, obtained after processing for the removal of multiple events, relative to the same quantities obtained prior to the multiple events removal.

CHAPTER 8

SENSITIVITY OF WIDE-AXIAL FIELD OF VIEW POSITRON EMISSION TOMOGRAPHY SCANNERS BASED ON SCINTILLATION AND RESISTIVE PLATE CHAMBER DETECTORS, ASSESSED BY SIMULATIONS, FOLLOWING A NEMA-LIKE MEASUREMENT

The present Chapter addresses the sensitivity advantage of a wide AFOV PET scanner based on crystal detectors and on RPC detectors, by means of simulations, carried out with a program developed with the GEANT4 toolkit.

The simulations that led to the assessment of the expected sensitivity of a wide AFOV PET scanner were performed prior to the development of the GEANT4 program for the detailed simulation of the RPC TOF-PET system. The goal was then to gain some knowledge on the expected increase of the sensitivity with the AFOV and the polar acceptance angle, extending previous studies performed by [Badawi et al., 2000], and later by [Eriksson et al., 2006], toward a full-body PET scanner, as proposed by [Crosetto, 2003]. The study was partially motivated by the prospect of applying RPCs to a full-body AFOV TOF-PET system.

8.1 ANALYTICAL MODEL OF THE 3D TRUE SENSITIVITY

As mentioned in the beginning of section 4.6.2 (page 124), the 3D Trues sensitivity of a PET scanner is proportional to the fraction of solid angle subtended by the scanner and seen by the source distribution in the FOV, which can be modelled mathematically by recurring to Fig. 8.1 (a), that depicts half of a sagittal plane of a cylindrical PET scanner with radius R and length L, as well as a cylindrical phantom with diameter d and length ℓ.

The fraction of the differential solid angle subtended by a differential annular surface defined by the vector $d\vec{s}$, perpendicular to the surface, and seen by a point from which a position vector $\vec{r}$ of the surface element ds can be defined, is given by

$$\frac{d\Omega}{4\pi} = \frac{1}{4\pi}\frac{\vec{r}\cdot\vec{ds}}{r^2}. \qquad (8.1)$$

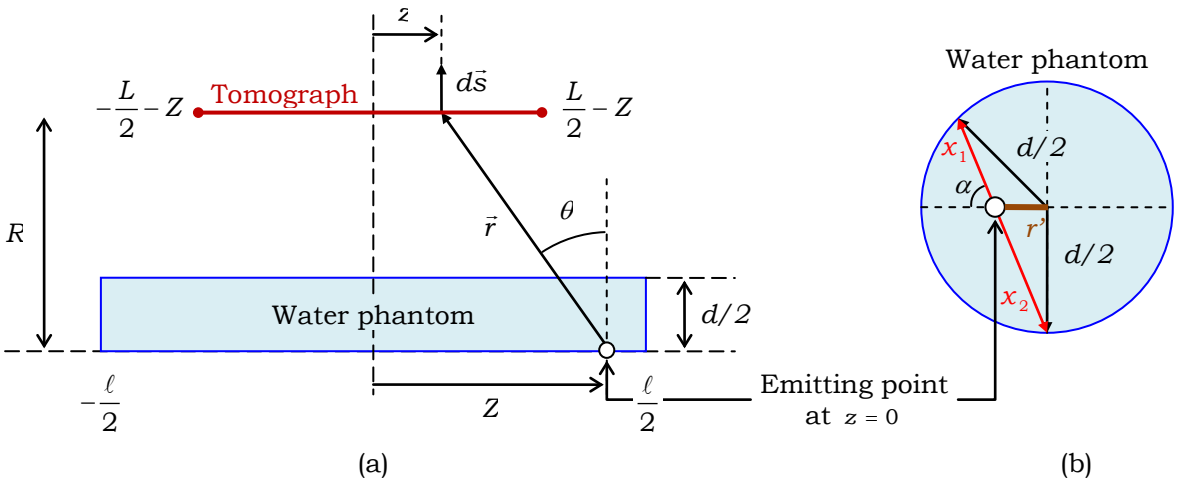

Fig. 8.1: (a) Simple geometrical model of a cylindrical PET scanner with radius R and length L, imaging a cylindrical phantom of diameter d and length ℓ, centred and aligned with the axial axis of the tomograph. (b) Geometrical definition of the paths x_1 and x_2 of each photon defining a LOR and of other quantities appearing in equations.

Recurring to Fig. 8.1 (a), and employing cylindrical coordinates, for a point located over the scanner axis at an axial coordinate Z from the centre of the tomograph, and seen by a cylindrical surface with radius R extending from $z=-L/2$ to $z=+L/2$, the inner product $\vec{r}\cdot\vec{ds}$ can be found to be given by

$$\begin{cases} \vec{r}\cdot d\vec{s} = \cos(\theta)\, ds \\ \cos(\theta) = \dfrac{R}{r} \\ ds = 2\pi R\, dz \end{cases} \quad \Rightarrow \quad \vec{r}\cdot d\vec{s} = \frac{2\pi R^2}{r} dz\,. \tag{8.2}$$

Taking into account that $r=\sqrt{R^2+(Z-z)^2}$, Eq. (8.1) can then be written as

$$\frac{d\Omega}{4\pi} = \frac{R^2}{2\left[R^2+(Z-z)^2\right]^{3/2}}\, dz\,. \tag{8.3}$$

This is also a reasonable approximation of the fraction of the differential solid angle subtended by the scanner and seen by any point in a cylindrical phantom if $d << 2R$. With this approximation, if it were not for the attenuation in the phantom, the 3D sensitivity to True coincidences would be simply proportional to the product of the cross sectional area of the phantom by the integral of Eq. (8.3) extended to all possible solid angles for which a LOR can be defined. However, the attenuation in the phantom reduces the number of True LORs accepted by the scanner. For this, the sensitivity is proportional to the product of the solid angle by the transmission factor of LORs through the phantom volume, which can be approximately obtained by

recurring to Fig. 8.1 (b) and assuming, coarsely, that, for all inclined photon paths, the attenuation scales with the inverse of $\cos(\theta)$. In this condition, the transmission factor, equal to the fraction of LORs for which both annihilation photons do not suffer any interaction in the phantom, averaged over the transaxial surface of the phantom, is given by

$$T(Z-z) = \int_0^{d/2} r' \int_0^{2\pi} \mathrm{e}^{-\mu\rho(x_1+x_2)/\cos[\Theta(Z-z)]}\, d\alpha\, dr' , \tag{8.4}$$

where μ is the mass attenuation coefficient for 511 keV photons, ρ is the mass density of the phantom material, $\Theta(Z-z) = \arctan[(Z-z)/R]$ gives the maximum polar acceptance angle for given values of Z and z, and x_1 and x_2 are given by

$$\begin{aligned} x_1 &= -r'\cos(\alpha) + \frac{1}{2}\sqrt{4r'^2\left[\cos^2(\alpha)-1\right]+d^2} \\ x_2 &= r'\cos(\alpha) + \frac{1}{2}\sqrt{4r'^2\left[\cos^2(\alpha)-1\right]+d^2} \end{aligned} \quad . \tag{8.5}$$

For $d = 200$ mm and $\ell = 1750$ mm, Eq. (8.4) predicts a value of $\langle T \rangle_\theta = 11\%$ for the transmission averaged over all polar acceptance angles, while the simulation yielded an average transmission over the phantom of $\langle T \rangle_{\text{phantom}} = 9.4\%$. In view of the approximate nature of the calculation, these values may be regarded as being in reasonable agreement, but suggest that the model somewhat underestimates the photon attenuation.

Using Eq. (8.3) and Eq. (8.4), the 3D Trues sensitivity are then given by

$$S = \beta\,\varepsilon^2\,\frac{\pi d^2}{4} \times 2\int_{Z_1}^{0}\int_{z_1}^{z_2} \frac{R^2\, T(Z-z)}{2\left[R^2+(Z-z)^2\right]^{3/2}}\, dz\, dZ . \tag{8.6}$$

where β is the positron branching ratio of the source and ε is the quantum detection efficiency for 511 keV photons. This expression, which must be computed numerically, is in units of observed count rate (counts per second - cps) per unit of activity concentration in the phantom (Bq/unit volume), and should be multiplied by 37, and the geometrical dimensions expressed in centimetre, if the more customary units of kcps/(mCi/cm^3) are to be used. As to the limits of integration, the one of the outer integral is given by

$$Z_1 = \max\left(-\frac{L}{2}, -\frac{\ell}{2}\right), \tag{8.7}$$

while those of the inner integral are given by

$$z_1 = \max\left[-\frac{L}{2},\, Z - R\tan(\theta)\right] \quad , \quad z_2 = \min\left[\frac{L}{2}+2Z,\, Z + R\tan(\theta)\right]. \tag{8.8}$$

The inner integral (in z) of Eq. (8.6) holds a function that gives the slice sensitivity profiles as a function of Z. However, the profiles are only correct for values of Z such that $\max\left(-L/2\,;-\ell/2\right) \le Z \le 0$. This is why the upper limit in (8.6) is equal to zero, and the double integrals are multiplied by the factor 2.

Fig. 8.2 presents the 3D Trues sensitivity obtained by Eq. (8.6), with the limits of integration given by Eq. (8.8), as a function of the AFOV for several limiting values of the polar acceptance angle, normalized to that obtained for a value of $L = 150$ mm and $\theta = 5°$. As it can clearly be seen, a gain of two orders of magnitude is to be expected for a full-body length PET scanner operating in full 3D mode.

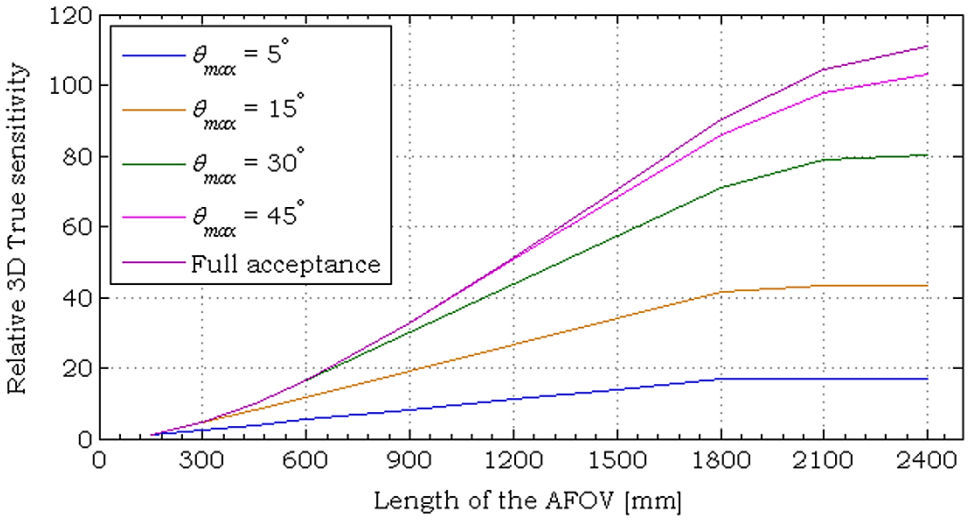

Fig. 8.2: 3D True sensitivity as a function of the length of the AFOV, for several values of the polar acceptance angle. The curves are all normalized to the value obtained for a value of $L = 150$ mm and a value of $\theta_{\max} = 5°$.

8.2 GEANT4 DEVELOPED PROGRAM FOR THE SIMULATIONS CONCERNING THE SENSITIVITY

In the present section a brief description of the GEANT4 program developed for the simulations concerning the assessment of the sensitivity with the length of the AFOV and the polar acceptance angle, for a PET scanner based on crystal detectors and on RPC detectors, will be mentioned.

8.2.1 Physics List

The physics lists employed were based on the SEP physics models, and included Compton scattering, photoelectric absorption and pair production processes for the simulation of the interaction of photons, and the multiple scattering, ionization and

bremsstrahlung processes for the interaction of electrons and positrons. For positron annihilation, the GEANT4 routine without photon acollinearity was used. Hadron, ion and decay processes where not activated.

As to the range cuts, it were set to 1.0 mm for photons and 2.0 mm for electrons and positrons.

8.2.2 Scanner Geometry and Materials

The detectors were not modelled in the GEANT4 developed program. Instead, the scanner was defined as a solid tungsten annulus with 927 mm inner diameter, a thickness of 30 mm, the length having been varied from 150 mm to 2400 mm, in steps of 150 mm for lengths less than or equal to 600 mm, and in steps of 300 mm for lengths comprised between 600 and 2400 mm.

End-shields were defined as being 1 cm thick tungsten absorbers, with an inner diameter of 600 mm (as in [Badawi et al., 2000]), and an outer diameter equal to the annulus outer diameter.

8.2.3 Phantom Geometry and Materials

The standard NEMA NU2-1994 sensitivity phantom (Section 4.6.2.1, page 126), with an outer diameter of 200 mm, a thickness of 3 mm, and an outer length of 190 mm, was used for validation proposes, while for all other simulations an extended version of the phantom, with an outer length of 1750 mm, was used. In both cases, the phantoms were defined to have their axis aligned with that of the scanner, being centred in the FOV.

As to the materials of both phantoms, were defined to match those described in Section 4.6.2.1, page 126.

8.2.4 Primary Particles and Source Distribution

The primary particles consisted of positrons at rest uniformly distributed in the phantom core volume.

8.2.5 Particle Tracking and Hits

Photons and secondary particles were fully tracked in the phantoms. Photons impinging the surface of the annulus defining the scanner were killed, as well as any secondary particle there produced, and the coordinates of the photon entry points were taken as those of detection.

As to the end-shields, photons and secondary particles were fully tracked for

validation proposes (150 mm length AFOV with the standard NEMA NU2-1994 phantom), being killed in all other simulations, leading then to ideal absorbers (as in [Badawi et al., 2000]).

8.2.6 Simulation runs

For validation proposes, a total of 50 runs were simulated, while for all other simulations a total of 100 runs, were simulated. In both cases, each run consisted of 10^6 events.

8.3 PROCESSING OF SIMULATION DATA

With the exception of the processing to account for the detection of single photons, the processing of the simulation to account for the 3D Trues sensitivity was performed in exactly the same manner for the crystal based scanner and for the scanner based on RPC detectors. In what follows the procedures employed in the post-processing of simulation data will be addressed, and mention will be made whenever the procedure applies to a specific detector.

8.3.1 Processing of Single Events to Account for the Detector Segmentation

Photons were first assigned to a module-block-crystal, according to the architecture of the GE Advance tomograph, which has 56 detection modules disposed in a ring, each module having 2 and 3 blocks detectors along the, respectively, transaxial and axial directions, with individual dimensions of 25×50×30 mm^3 (transaxial×axial×radial). Each block detector has 6×6 monolithic crystals with individual dimensions of $\sim 4 \times 8 \times 30$ mm^3, read by 4 PMTs, holding then 18 rings along the axial direction, each ring having 672 individual BGO crystals. As to the total number of crystals, is equal to 12096 crystals, defining an AFOV with $L = 152$ mm and a transaxial FOV with $R = 463.5$ mm. Scanner details can be found in [Schmidtlein et al., 2006].

Although the aforementioned segmentation is strictly valid for the GE Advance scanner, the same segmentation was also applied to single events for processing the simulation raw data for the RPC TOF-PET scanner.

8.3.2 Source Definition

For randomly drawing the decay times to account for the radioactive decay, the procedure described in Section 6.3.1 (page 196) was employed, with the source defined

as listed in the "Default" column of the table depicted in Appendix F, except in what concerns the parameters *useBranchRatio*, *numSimPositrons*, and *activity*. The first two were set to, respectively, true and 10^6, while the third was set so that, for each phantom, the activity concentration was equal to $\sim 67.3\ \mathrm{Bq/cm^3}$ $(\sim 1.82\ \mathrm{nCi/cm^3})$.

8.3.3 Detection Efficiency

After the aforementioned procedure to account for the detector segmentation, single photons were processed to account for detection efficiency. The procedure for each detector type (crystal based block detector and RPC detector) will be described in the following.

8.3.3.1 Crystal Based Block Detectors

Single photons were randomly removed to account for a packing fraction of ~0.86, computed as the ratio between the total volume of BGO crystal in the GE Advance scanner, given by $56 \times 2 \times n_{axial} \times 6 \times 6 \times 4 \times 8 \times 30$, and the total volume of an annulus with a length of 150 mm, and inner and outer radios of, respectively, 463.5 mm and 493.5 mm.

Single photons resulting from the above mentioned procedure were then randomly remove to account for the mean detection efficiency of the BGO block detectors, which was considered to be equal to 0.92 [Badawi et al., 2000].

A 100 keV threshold was then applied in order to model the scanner discrimination electronics [Schmidtlein et al., 2006], the resulting photons having been then affected by a Gaussian blur with 20% FWHM resolution at 511 keV, following which a 0.914 correction factor was applied to individual photons (by randomly removing them) so as to compensate for the simplifications in the simulation of the detection processing.

At the end of this processing chain, an LLD (of 300 or 400 keV) was then applied, the HLD having been of 650 keV.

8.3.3.2 Resistive Plate Chamber Detectors

For the RPC detectors, photons were randomly removed according to the detection efficiencies given from a 6th degree polynomial fit to the extraction efficiencies obtained by simulation of stacks of 61 and 121 glass plates with individual thicknesses of 400 μm. Fig. 8.3 (page 246) depicts the aforementioned efficiencies and the polynomial fit employed.

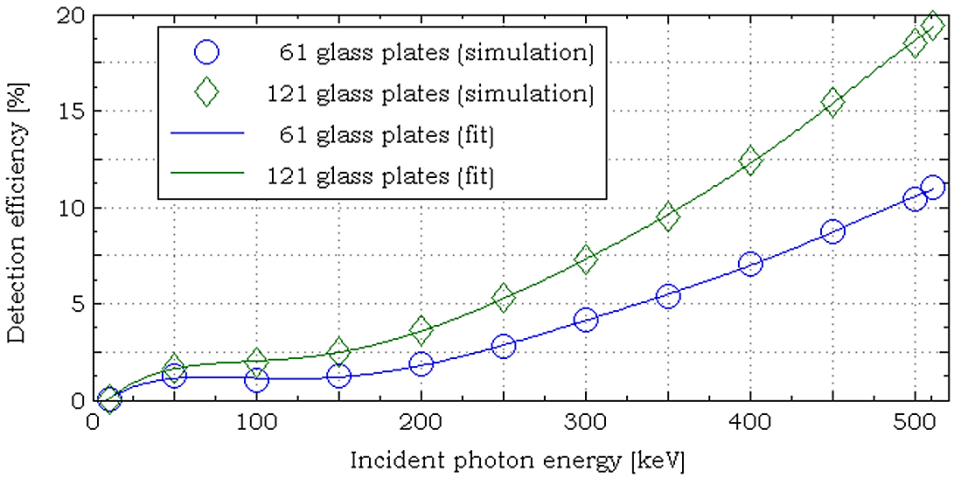

Fig. 8.3: Detection efficiencies obtained by simulation (markers) for stacks of 61 and 121 glass plates with individual thicknesses of 400 μm, and corresponding fits (solid lines) to a 6th degree polynomial function.

8.3.4 Coincidence Processing

For both systems and phantoms, the coincidences were performed by a 12.5 ns STW coincidence sorter with rejection of Multiple coincidences, and acceptance of all LORs that traversed the scanner bore.

Inclined LORs were then assigned by SSBR (Section 6.4.4, page 214) to slices with ~4.29 mm thick along the axial direction, and sinograms were constructed as described in Section 6.4.5 (page 216), width a radial binning of 4 mm and azimuthal angular binning of 1 °. The procedure described in Section 4.6.2.1 (page 126) was then employed to compute the 3D slice sensitivities and the 3D total sensitivity, using the SF obtained as the ratio of accepted Scattered to Trues plus Scatter events, which, owing to the fact that interactions in the detector were not simulated, does not account for the scatter in the detector.

8.4 VALIDATION PROCEDURE

The simulation was validated by comparison of the Trues and Trues plus Scatter count rates, and the Trues and Trues plus Scatter 3D sensitivities obtained by simulation of a 150 mm long AFOV scanner based on crystal detectors, with the standard NEMA NU2-1994 sensitivity phantom, and published data for the GE Advance scanner [Lewellen et al., 1995; Badawi et al., 2000], obtained with the same phantom. The results are presented in Table 8.1, showing a quite satisfactory agreement between the simulations and the measurements. Similar data for the axially extended phantom is shown on the rightmost column. In this case, the

sensitivity to Trues plus Scatter is higher than that obtained with the NEMA phantom, while the sensitivity to Trues remains unchanged. This is owed to the substantial increase of the activity outside the field of view, giving rise to more Scattered LORs.

TABLE 8.1: SIMULATED AND MEASURED VALUES OF COUNT RATES AND 3D SENSITIVITIES FOLLOWING THE NEMA NU2-1994 STANDARDS FOR SENSITIVITY ASSESSMENT, WITH THE STANDARD PHANTOM.

Parameter	**NEMA NU2-1994 phantom**		**Extended phantom**
	Simulated	**Measured**	**Simulated**
Single count rate [kcps]	794.141[a]	750.615[c]	—
Trues + Scatter count rate [kcps]	43.913[a]	41.163[c]	—
3D Trues sensitivity $(\theta \approx 5.7°)$ [kcps/(μCi/cm³)]	1013[b]	1020[d]	1032
3D Trues + Scatter sensitivity $(\theta \approx 5.7°)$ [kcps/(μCi/cm³)]	1557[b]	1570[d]	1786
3D Trues sensitivity $(\theta \approx 8.7°)$ [kcps/(μCi/cm³)]	1160[b]	1284[d]	1180
3D Trues + Scatter sensitivity $(\theta \approx 8.7°)$ [kcps/(μCi/cm³)]	1782[b]	1920[d]	2024

[a] Simulation results obtained by considering an LLD of 400 keV

[b] Simulation results obtained by considering an LLD of 300 keV

[c] Data retrieved from [Badawi et al., 2000].

[d] Data retrieved from [Lewellen et al., 1995].

8.5 EXPECTED INCREASE OF THE SENSITIVITY WITH THE AXIAL FIELD OF VIEW AND THE POLAR ACCEPTANCE ANGLE

After the validation procedure described in the previous section, simulation data obtained with the extended phantom for several values of the AFOV, ranging from 150 to 2400 mm, was processed to account for detection considering both crystal based and RPC detectors, and the 3D Trues sensitivities for several values of the polar acceptance angle, were then computed.

8.5.1 Scanner based on Inorganic Scintillation Crystal Block Detectors

For crystal based detectors, an LLD of 400 keV was used, and the 3D Trues sensitivities were normalized to the value of $1032\ \mathrm{kcps}/(\mu\mathrm{Ci}/\mathrm{cm}^3)$, obtained for an AFOV of 150 mm with a maximum polar acceptance angle of 5.7° (see Table 2.1), corresponding in the GE Advance scanner to a maximum ring difference of 11. The results are depicted in Fig. 8.4 (page 248), showing a reasonable agreement with those

obtained with the analytical model and depicted in Fig. 8.2, and confirming the expected increase of two orders of magnitude in the 3D Trues sensitivity for a full-body length PET scanner based on crystal detectors operated in full 3D mode. Also presented, for comparison, is an inset with the results obtained for a value of the polar acceptance angle of 5.7° and the results obtained by [Badawi et al., 2000], which were appropriately renormalized, showing a reasonable agreement between the simulation results of the present work and that of [Badawi et al., 2000].

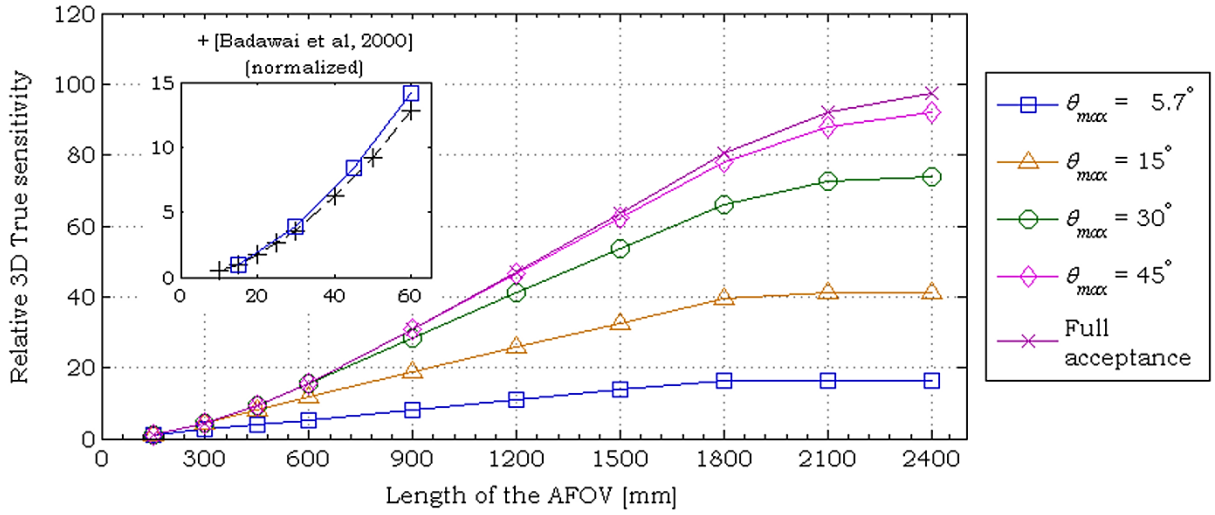

Fig. 8.4: Relative 3D True sensitivity as a function of the length of the AFOV for several values of the polar acceptance angle, obtained for the 1750 mm axially extended phantom, and by considering crystal based detectors. All values were normalized to that obtained with an AFOV of 15 cm and a polar acceptance angle of 5.7° (see Table 2.1 for absolute values). The inset shows a comparison of the results obtained in the present work with those obtained by [Badawi et al., 2000], after applying the appropriate renormalization.

8.5.2 Scanner Based on Resistive Plate Chamber Detectors

The results obtained for the 3D Trues sensitivities when the detection was processed to account for the detection efficiencies of RPC detectors, are depicted in Fig. 8.5 without considering a gain factor due to TOF information. As it can be seen, and in what the NEMA NU2-1994 3D True sensitivity is of concern, for the RPC TOF-PET system to be advantageous over current PET systems based on inorganic crystal detectors, the number of converter plates must be greater than 61, the AFOV must be greater than 1200 mm, and the polar acceptance angle must be at least of 15°. The advantage is more notorious if a full-body length AFOV of 2400 mm and full acceptance on the polar acceptance angle are to be considered, for which the expected NEMA NU2-1994 3D Trues sensitivity of the RPC TOF-PET system presents a gain of

~5 relative to current PET systems based on inorganic crystal detectors. However, if a gain factor of 4.4 due to TOF information, and obtained from Eq. (4.50) (page 130) by setting $D = 200$ mm (the phantom diameter) and $FWHM_{\Delta\ell} = 45$ mm (see Table 4.2 on page 117), corresponding to a TOF resolution of 300 ps FWHM, then the gain in the NEMA NU2-1994 3D Trues sensitivity is of ~22 when compared to current PET systems based on inorganic crystal detectors, as it can be seen in Fig. 8.6 (page 250).

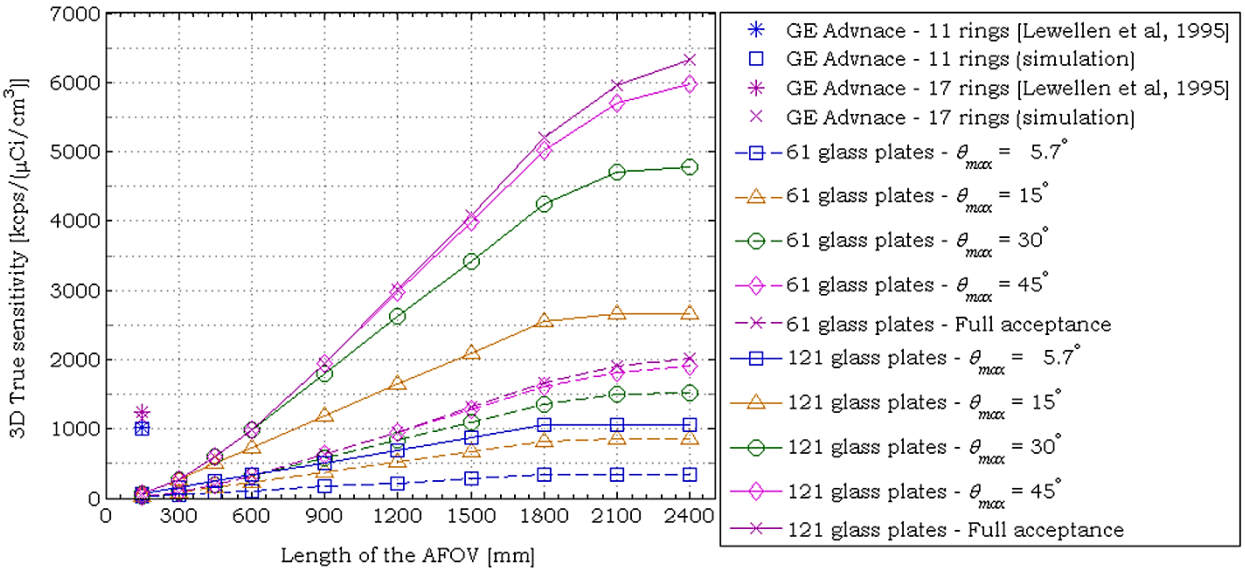

Fig. 8.5: Absolute 3D True sensitivity as a function of the length of the AFOV length for several values of the polar acceptance angle, obtained for the 1750 mm axially extended phantom, and by considering RPC detectors with 61 and 121 glass plates with individual thickness of 400 μm, and without considering a gain factor due to TOF information.

8.6 FRACTION OF ACCEPTED SCATTER DUE TO THE INCREASED AXIAL FIELD OF VIEW AND POLAR ACCEPTANCE ANGLE

The fraction of Scattered coincidences accepted by both the crystal and the RPC based systems, and which do not account for scatter in the detectors, was computed as the ratio between the Scattered coincidences and the Scattered plus Trues coincidences. The results obtained for both systems (crystal and RPC based detectors) are depicted in Fig. 8.7 (page 250). As it can be readily seen, due to the energy resolution presented by inorganic crystal scintillation detectors, the fraction of Scattered coincidences accepted by the crystal based PET system is expected to be lower than that for the RPC based ones. However, in both cases, the fraction of accepted coincidences is fairly independent of the AFOV and the value employed for the polar acceptance angle.

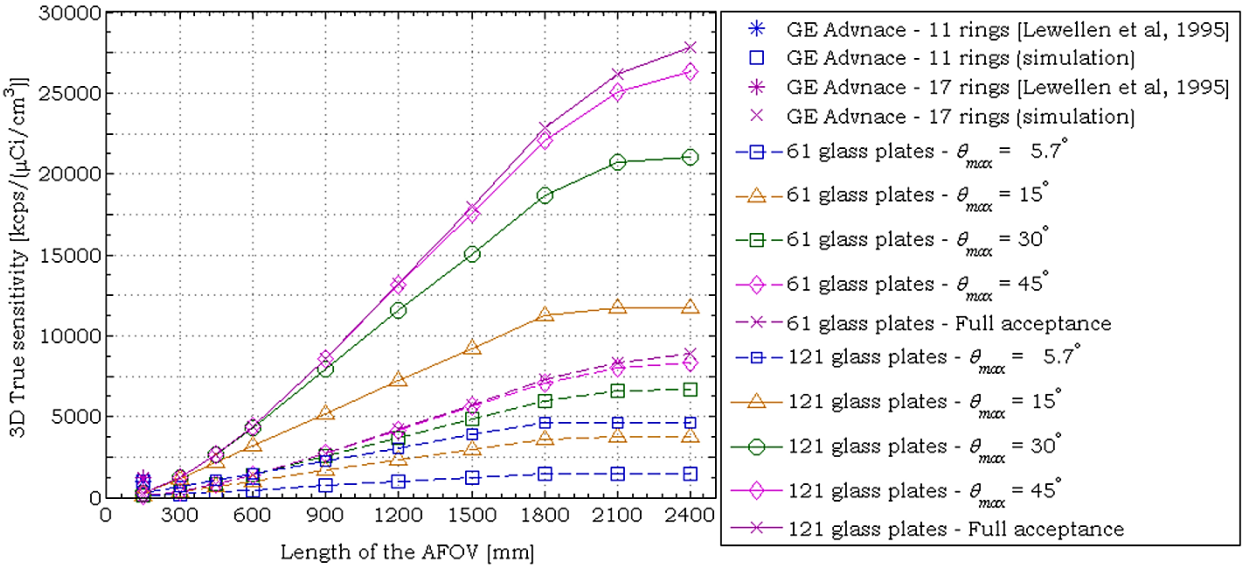

Fig. 8.6: Absolute 3D True sensitivity as a function of the length of the AFOV length for several values of the polar acceptance angle, obtained for the 1750 mm axially extended phantom, and by considering RPC detectors with 61 and 121 glass plates with individual thickness of 400 μm, and considering a 4.4 gain factor due to TOF information, by setting $D = 200$ mm (the phantom diameter) and $FWHM_{\Delta\ell} = 45$ mm (see Table 4.2 on page 117), corresponding to a TOF resolution of 300 ps FWHM

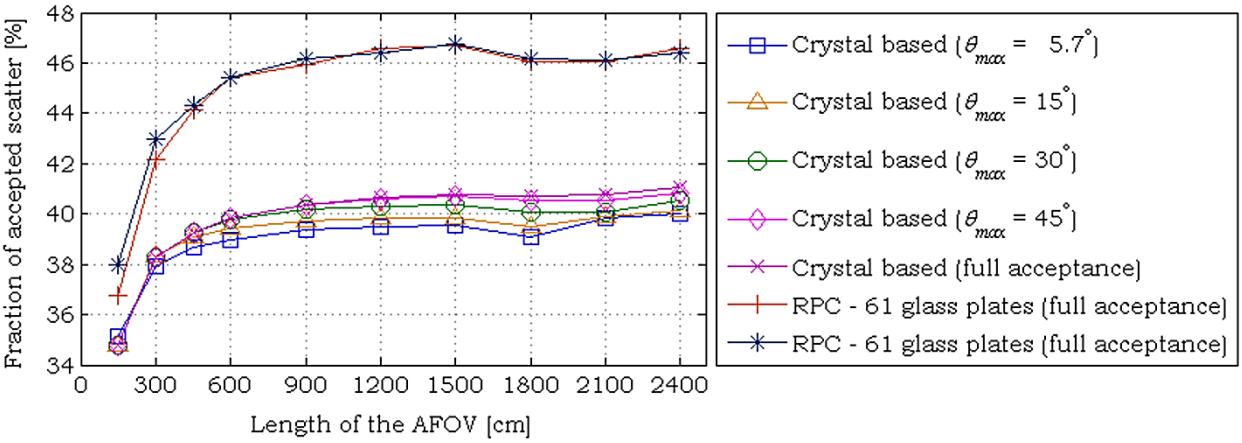

Fig. 8.7: Fraction of accepted Scattered coincidences, computed as the ratio between the Scattered coincidences to Scattered plus Trues coincidences, for a crystal and RPC based PET system as a function of the length of the AFOV for several values of the polar acceptance angle. Data was obtained with the 1750 mm length phantom, and in the case of crystal based detectors an LLD of 400 keV was considered.

CHAPTER 9
SPATIAL RESOLUTION OF A FULL-BODY LENGTH RESISTIVE PLATE CHAMBER TIME-OF-FLIGHT POSITRON EMISSION TOMOGRAPHY SCANNER, ASSESSED BY MEANS OF DETAILED SIMULATIONS, FOLLOWING A NEMA-LIKE MEASUREMENT

The present Chapter addresses the spatial resolution, by means of detailed simulations carried out with the GEANT4 program developed as described in Section 6.2 (page 181), the post-processing of simulation data made as explained in Section 6.3 (page 196), and the processing of coincidence data performed as explained in Sections 6.4.1 (page 209) through 6.4.5 (page 216).

9.1 SIMULATION SETUP

The setup employed in the simulations to account for the spatial resolution of the RPC TOF-PET system was mainly that described in Section 7.1, with some minor exceptions, which will be addressed in the following.

9.1.1 Physics

Hadron, ion and decay physics were not activated. For positron annihilation physics two routines were used: the one implemented in the SEP of GEANT4, which assumes that the annihilation photons are emitted in exact opposite directions, and the one implemented in GATE, which accounts for the photon acollinearity.

9.1.2 Scanner Geometry

The RPC detectors were defined as consisting in single detection modules, and the detection heads were defined to have 40 single module RPC detectors along the radial direction. As seen on Section 6.3.2 (page 199) this only influences the number of readout sections along the radial direction, with the possible consequence being in the reduction of pileup due to dead time for timing and position signals. However, and as will be seen on Chapter 10, for the low activities required by the NEMA NU2-2001

standards, pileup and dead time are of no concern.

9.1.3 Phantom Geometry

The phantom was defined by setting the parameters listed in Appendix C.2 so that it consisted in a sphere with a 1 μm diameter water core, enclosed in a PMMA shell with 2 mm outer diameter, placed in the centre of the scanner and at a point lying on the same transaxial plane but with an offset of 10 cm, in both the *X* and the *Y* directions.

9.1.4 Primary Particles and Source Distribution

The source consisted of positrons at rest uniformly distributed in the phantom core volume, meaning that the positron range was not accounted for.

9.2 SETUP EMPLOYED IN THE POST-PROCESSING STAGE PRIOR TO THE EVALUATION OF THE SPATIAL RESOLUTION

For each phantom and combination of the simulation parameters (positron annihilation physics), the simulation raw data was processed by the set of routines described in Section 6.3 on page 196, and from Section 6.4.1 on page 209, to Section 6.4.5 on page 216, to account for the radioactive decay and the detector readout. The removal of multiple Single events arising from multiple photon interactions in the detector was not performed. In what follows, the relevant set of parameters employed in the post-processing of simulation data will be addressed.

9.2.1 Source Definition

For randomly drawing the decay times to account for the radioactive decay, the source was defined as listed in the "Default" column of the table depicted in Appendix F, namely, all the parameters were set to match those of $^{18}_{9}\mathrm{F}$. The only exception to the default parameters was the total activity, which was set to 370 kBq (10 μCi).

9.2.2 Detector Readout

Simulation data, processed to account for the source activity, was then processed to account for the detector readout with a $\tau_{ts} = 200$ ns non-paralyzable dead time for the timing signals and a $\tau_{ps} = 1$ μs paralyzable dead time for the position signals, as explained in Section 6.3.2 (page 199).

The processing made use of the structure given in Appendix G, with the substructures "Module", "Detector", "Head" and "Scanner", defined as given from

Appendixes G.1 through G.4, the exception being the "*number_of_modules*" and the "*Number.radial*" parameters of the "Detector" substructure, which were set to 1 and 40, respectively. As to the parameters of the "Readout" substructure, were defined as in Appendix G.5, the exceptions being the parameters "*Dead_Time.Position.window*" and "*Sections.num_transaxial*", which were set to 1 μs and 3, respectively.

9.2.3 Coincidence Processing

For processing the coincidences, a STW coincidence sorter (Section 4.2.1, page 89, and Section 6.3.4, page 207) with 4 ns duration was used, and Multiple coincidences were rejected.

To gain some insight on the effects on the spatial resolution of the several physical processes leading to detection, LORs were formed for all the points referred to in Section 6.2.5.2 (page 191), and depicted in Fig. 6.2 (page 192), viz., the PEP, the PIP, the EEP, the EDP, and the EAP. This latter was binned to 3.44 mm in the radial direction, and to 0.0, 1.0 and 2.0 mm in the axial and transaxial directions.

9.3 SETUP EMPLOYED FOR PROCESSING COINCIDENCE DATA TO OBTAIN THE SPATIAL RESOLUTION

Coincidence data obtained for each phantom position, annihilation procedure, and each point used to define the LORs, were stored without imposing any constraints on the acceptance of valid LORs. These constraints were performed during the processing stage to account for the spatial resolution, which was carried out according to the NEMA NU2-2001 standards (Section 4.6.1, page 119), employing the procedure described from Section 6.4.1 (page 209) to Section 6.4.5 (page 216) and in Section 6.4.7 (page 217).

9.3.1 Rejection of Coincidences on the Basis of Geometric Constraints

Following the geometric constraint imposed on the coincidence data, referred to in Section 6.4.1 (page 209), the constraint referred to in Section 6.4.2 (page 209) was performed by accepting the LORs for which the polar acceptance angle, computed in 2D mode, was less than or equal to 9°. The third geometric constraint was then performed by setting the "*type*" field of the rejection substructure, listed in Appendix I.4, to *none*, leading then to the acceptance of all LORs that crossed the scanner bore.

9.3.2 Rebinning and Sinogram Construction

Coincidence data returned from the previous processing stages, were then

processed to account for the rebinning performed as described in Section 6.4.4 (page 214), following which the sinograms were constructed as described in Section 6.4.5 (page 216).

To avoid axial distortions for off-axis sources, the *SSRB_Modified* method (see Section 6.4.4 on page 214) was employed, and all detection points were translated so that the source was centred in the sinogram and image space.

After rebinning the inclined LORs, 2D sinograms were produced and reconstructed by 2D FBP. The sinogram radial binning was made equal to the image voxel size, and, whenever statistics allowed it, made equal to, at least, one fourth the expected image spatial resolution. As to the binning in the azimuthal angle, it was set according to Eq. (4.25) (page 111).

9.3.3 Image Reconstruction and Assessment of the Spatial Resolution

All sinograms obtained for each phantom position, annihilation procedure and point used to define the LORs, were then reconstructed by FBP, and PSFs in the *X*, *Y* and *Z* directions were drawn, passing through the maximum of the image. For each PSF, the maximum, FWHM, and FWTM, were computed according to the NEMA NU2-2001 procedure (see Section 4.6.1 on page 119).

9.4 RESULTS OBTAINED FOR THE SPATIAL RESOLUTION

Table 9.1 resumes the image spatial resolutions obtained, computed as the mean of the spatial resolution for each direction (*X*, *Y* and *Z*) for the two simulated phantom positions and annihilation routines, along with the corresponding standard deviations, and Fig. 9.1 depicts the reconstructed image for the EAP binned to 2 mm in the axial and transaxial direction, for the phantom positioned 100 mm off-axis in both the *X* and *Y* directions, along with the PSFs for the three Cartesian directions, and considering the photon acollinearity.

As it can be seen, the physically-limited image spatial resolution for the full-body AFOV RPC TOF-PET is expected to be of ~2 mm FWHM, including detection-process and acollinearity errors. Except for the case of the EEP, it was not observed a strong dependency of spatial resolution on the photon acollinearity. Besides, the observed effect in all cases is much less than that generally assumed in the literature. Therefore, this study indicates that the attainable resolution will be dominated by the accuracy of the readout system.

TABLE 9.1: MEAN AND STANDARD DEVIATION OF THE SPATIAL RESOLUTION, COMPUTED AS THE FWHM AND THE FWTM, OF A POINT SOURCE SIMULATED WITH AND WITHOUT CONSIDERING PHOTON ACOLLINEARITY FOR THE DIFFERENT POINTS EMPLOYED TO DEFINE THE LORS: PEP, PDP, EEP, EDP AND EAP . THIS LATTER WAS BINNED TO 3.44 mm IN THE RADIAL DIRECTION AND TO 0.0, 1.0 AND 2.0 mm IN THE AXIAL AND TRANSAXIAL DIRECTIONS.

PEP [μm]	PDP [μm]	EEP [μm]	EDP [mm]	EAP [mm]		
				0	1	2
FWHM – Without Photon Acollinearity						
1.0±0.0	1.0±0.0	3.0±0.1	0.3±0.0	0.5±0.1	1.1±0.1	1.7±0.0
FWHM – With Photon Acollinearity						
1.1±0.0	1.1±0.1	39.9±1.7	0.5±0.0	0.9±0.1	1.4±0.0	2.1±0.1
FWTM – Without Photon Acollinearity						
1.3±0.0	1.3±0.0	13.0±1.0	0.7±0.1	2.1±0.9	2.8±0.7	3.4±0.2
FWTM – With Photon Acollinearity						
3.0±0.2	3.1±0.4	140.2±18.1	1.3±0.6	3.1±0.4	3.9±0.4	4.8±0.3

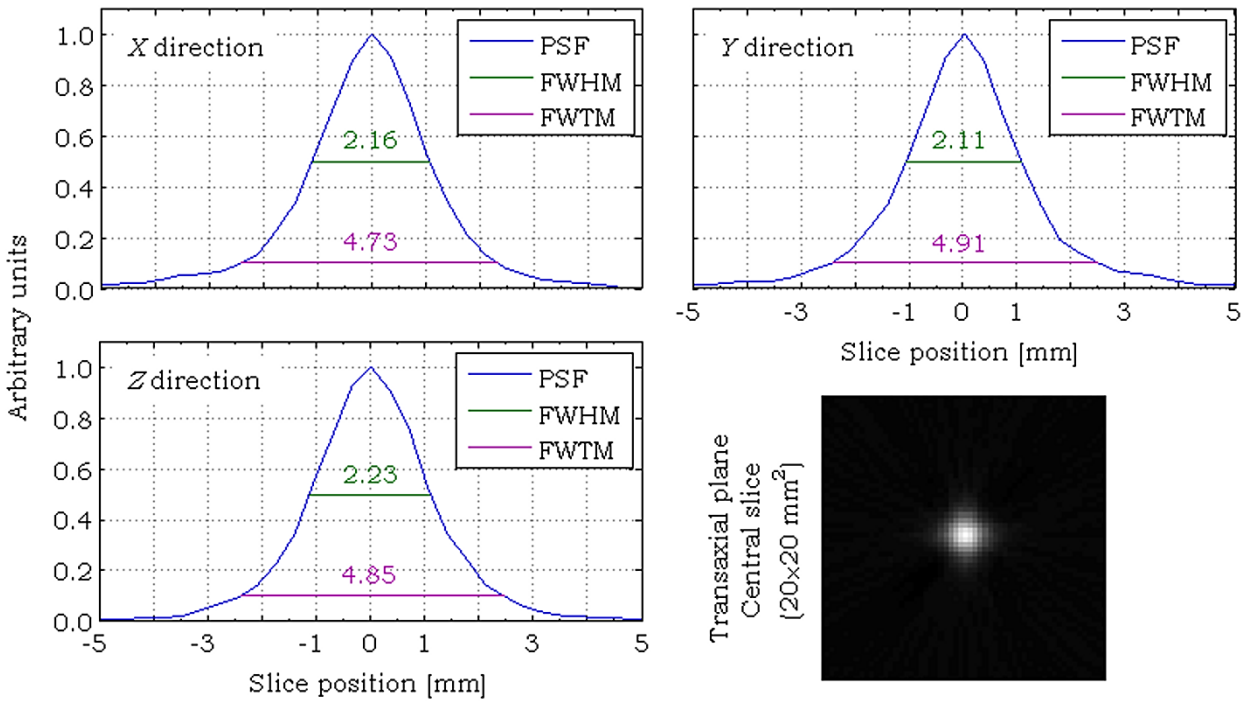

Fig. 9.1: Reconstructed image (bottom left) for the EAP binned to 2 mm in the axial and transaxial direction, for the phantom positioned 100 mm off-axis in both the *X* and *Y* directions and by considering photon acollinearity, along with the PSFs for the three Cartesian directions.

9.5 THE EFFECT OF PHOTON ACOLLINEARITY ON THE SPATIAL RESOLUTION

Contrary to what was expected, and commonly accepted, the results presented in the last Section do not show the effect of the photon acollinearity on the spatial resolution, as mentioned in Section 4.6.1 (page 119), and which is accepted to limit the spatial resolution to $0.0044 \times R$, with R the radius of the scanner [Moses, 2011]. In the present case, and considering a diameter of 864.4 mm for the cylinder inscribed in the scanner bore, the photon acollinearity was expected to introduce a blur for the PEP of ~1.9 mm FWHM. Instead, the spatial resolution, measured as the FWHM, with a point-like source with 1.0 μm diameter, was of 1.1 μm, and very similar to that measured when photon acollinearity was not taken into account.

Some insight can be gained on this by creating a set of coincidence data affected by a Gaussian distribution with 0.58° FWHM on the direction of one of the annihilation photons relative to the direction of the other, as implemented in the GATE annihilation routine. For an ideal cylindrical scanner with a radius of 500 mm, and without segmentation in the detection elements, the spatial resolution should then be limited to a value of ~2.2 mm, due to the photon acollinearity.

Ideal coincidence data as described above was mathematically created by randomly drawing annihilation points considered to be uniformly distributed in a spherical volume with a diameter of 100 μm, centred in the FOV of a scanner with 1000 mm diameter by 2400 mm long, and assuming that the instants of detection of the two photons, computed from light kinematics, were known exactly. The direct TOF reconstructed points were then computed, and the distance from the annihilation points to the TOF reconstructed ones, was obtained. Also obtained were the distances of the annihilation points to the LORs. Fig. 9.2 depicts such distributions, as well as the corresponding signed distributions, computed from the absolute distances by multiplying them by the sign of the blurring angle. As it can be seen, the FWHM for both distributions is the same, and equal to 2.91 mm.

However, the presented distributions are not the PSFs of the reconstructed image acquired in full 3D mode. These can only be obtained by reconstructing the image and taking the intensity profiles along three orthogonal directions passing through the point of maximum intensity. This was performed by creating an image matrix from the direct TOF reconstructed points, as well as by following the complete procedure given in the NEMA NU2-2001 standards, and described in Section 4.6.1 (page 119), with the rebinning performed by SSRB using TOF information (see Section 4.5 on page 115, Fig. 4.18 on page 118), and with full acceptance on the polar acceptance angle. The

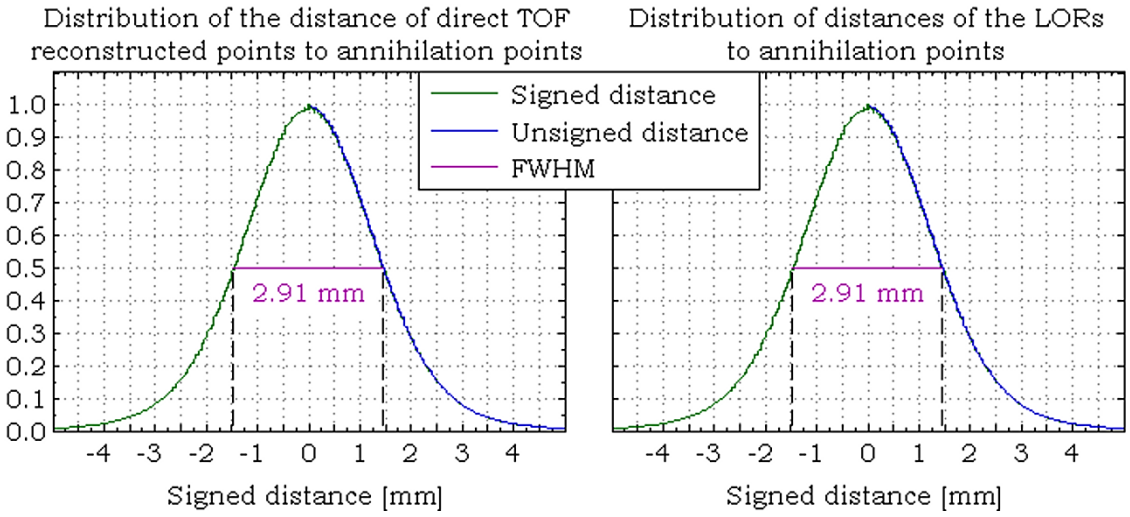

Fig. 9.2: Distance from annihilation points to the direct TOF reconstructed points (left pane) and to the LORs (right pane). The absolute distances are presented by the blue curves, while the green curves present the signed distances, computed from the unsigned ones by multiplying them by the signal of the blurring angle drawn from a Gaussian distribution with 0.58° FWHM. Also presented are the corresponding FWHM of the distributions of the distances.

PSFs thus obtained for the *X*, *Y* and *Z* directions are depicted in Fig. 9.3 (page 258), and the corresponding images of the transaxial plane passing through the centre of the source are depicted in Fig. 9.4 (page 258). Considering the three PSFs, the FWHM obtained by direct TOF reconstruction was of 97.6±3.5 μm, having been of 103.7±12.0 μm for the FBP reconstructed image.

These results indicate that, for full 3D acquisition mode, if the direction of one of the annihilation photons relative to the direction of the other follows a Gaussian distribution with 0.58° FWHM, then the effect of the photon acollinearity, alone, in the image spatial resolution is much less than the currently accepted value of $0.0044 \times R$, with R the radius of the scanner.

This deserves further experimental investigation with a full 3D acquisition system composed of detectors with high intrinsic 3D spatial resolution, such as those employed in the RPC small animal PET prototype under development, and that is in the final stage of testing with phantoms, and which is expected to be used in the first pre-clinical trials by the end of 2014.

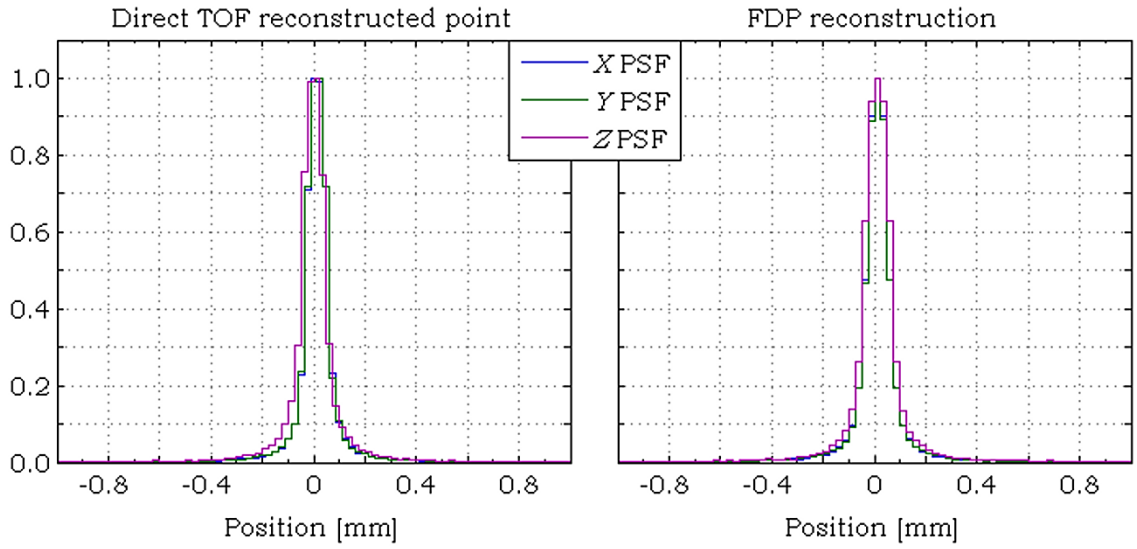

Fig. 9.3: PSFs obtained from images of the direct TOF reconstructed points (left pane), and by FBP reconstruction (right pane) of 2D sinograms after performing the SSRB using TOF information, as explained in Section 4.5 (page 115) and depicted in Fig. 4.18 (page 118), and accepting all possible values of the polar acceptance angle. Considering the three PSFs, the FWHM obtained by direct TOF reconstruction was of 96.9±3.1 μm, being of 91.5±18.4 μm for the FBP reconstructed image.

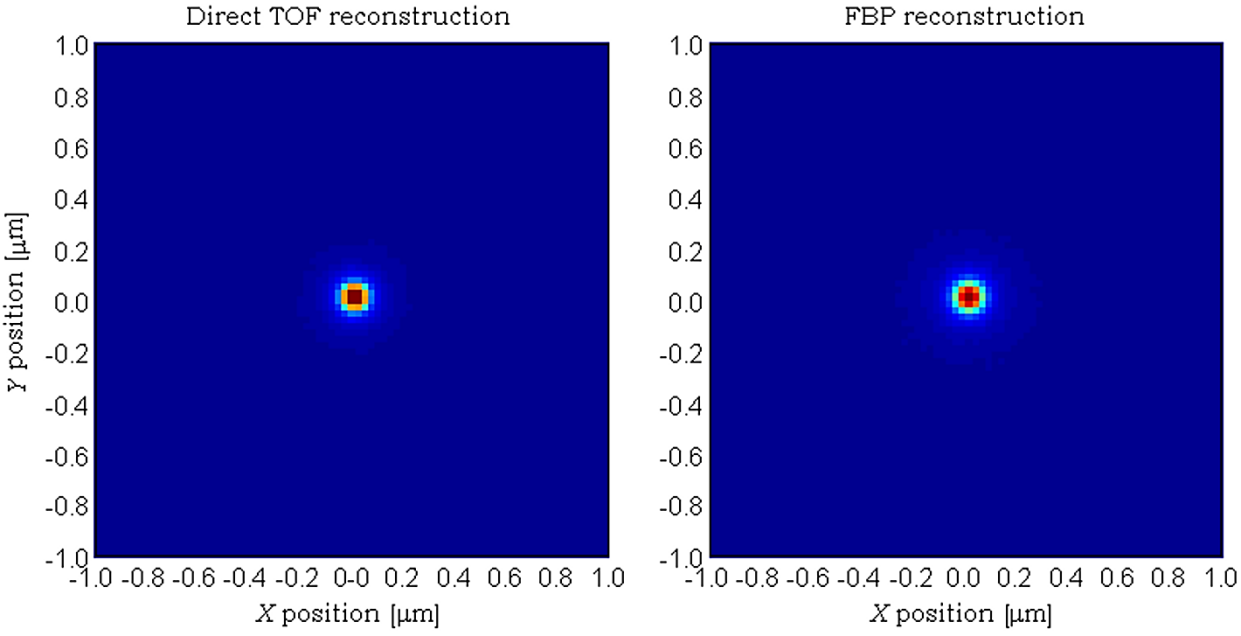

Fig. 9.4: Direct TOF (left pane) and FPB (right pane) reconstructed images of LORs obtained mathematically from a spherical source with 100 μm placed in the centre of the FOV and considering photon acollinearity given by a Gaussian distribution with 0.58° FWHM.

CHAPTER 10
SCATTER FRACTION, COUNT RATES AND NOISE EQUIVALENT COUNT RATE, OF A FULL-BODY LENGTH RESISTIVE PLATE CHAMBER TIME-OF-FLIGHT POSITRON EMISSION TOMOGRAPHY SCANNER, ASSESSED BY MEANS OF DETAILED SIMULATIONS, FOLLOWING THE NEMA NU2-2001 STANDARDS

The present Chapter addresses the NEMA NU2-2001 SF, count rates and NECR performance tests (Section 4.6.3, page 131, and 4.6.4, page 134), by means of detailed simulations, carried out with the GEANT4 program developed as described in Section 6.2 (page 181), the post-processing of simulation data made as explained in Section 6.3 (page 196), and the processing of coincidence data performed as explained in Sections 6.4.1 (page 209) through 6.4.5 (page 216). As to the setup employed in the simulations, it was already referred to in Section 7.1 (page 219).

10.1 SETUP EMPLOYED IN THE POST-PROCESSING STAGE PRIOR TO THE EVALUATION OF THE PERFORMANCE PARAMETERS

For each phantom, the simulation raw data was processed with several possible combinations of some of the processing parameters that are configurable. In the present Section, the set of relevant parameters (defined in Section 6.3 on page 196, and from Section 6.4.1 on page 209, to Section 6.4.5 on page 216) used for processing the simulation raw data, to account for the radioactive decay, the detector readout, the removal of multiple Single events arising from multiple photon interactions in the detector, as well as the removal of Single events that cannot take part of coincidences, and the coincidence processing, will be addressed.

10.1.1 Source Definition

For randomly drawing the decay times to account for the radioactive decay, the source was defined as listed in the "Default" column of the table depicted in Appendix F, namely, all the parameters were set to match those of $^{18}_{9}\mathrm{F}$. The only exception to

the default parameters was the total activity.

For the SF test, a total activity of 37 kBq (1 μCi) was used, so that the count losses due to dead time, and the Random count rates, met the requirements imposed by the NEMA NU2-2001 standards, and mentioned in Section 4.6.3 (page 210), namely, the referred losses must be less than 1% of the True events count rates. Since, for the referred activity, the number of $^{18}_{9}\mathrm{F}$ nuclei initially present in the phantom is $\sim 352\times10^{6}$, less than the 600×10^{6} simulated events, for the propose of randomly drawing the decay times, each run was processed as an independent acquisition with ~28 seconds long.

For the count rates and NECR performance tests, the total phantom activities included that employed for the SF test, plus 17 activities, ranging from 9.25 MBq (0.25 mCi) to 370 MBq (10 mCi). Since, for source activities equal to or greater than 9.25 MBq (0.25 mCi), the total number of radioactive nuclei present in the phantom is greater than the total number of simulated events, the 600 runs were processed as single acquisitions, in what concerns the randomly drawing of the decay times, with total duration ranging from ~1.7 seconds, for a total activity of 370 MBq (10 mCi), to ~67.3 seconds, for a total activity of 9.25 MBq (0.25 mCi), which met the requirements of the NEMA NU2-2001, standards that impose a total acquisition time less than one-fourth the half-life of the radionuclide.

The complete set of simulated activities is listed in Table 10.1, along with the corresponding activity concentrations for each of the simulated phantoms.

10.1.2 Detector Readout

Simulation data processed to account for each source activity; was then processed to account for the detector readout, with a $\tau_{ts} = 200\ \mathrm{ns}$ non-paralyzable dead time for the time signals, and the τ_{ps} paralyzable dead time for the position signals, as explained in Section 6.3.2 (page 199).

The processing made use of the structure explained in Appendix G, with the substructures “Module”, “Detector”, “Head” and “Scanner”, defined as given from Appendixes G.1 through G.4, which are in accordance with the parameters used to define the complete geometry of the scanner, already addressed in Section 7.1.2 (page 220).

As to the parameters of the “Readout” substructure, were defined as in Appendix G.5, the exceptions being the “*Dead_Time.Position.window*” parameter, which defines the τ_{ps} paralyzable dead time for the position signals, and on the parameter “*Dead_Time.Position.coordinates_policy*”, which defines how to handle events for which

TABLE 10.1: ABSOLUTE ACTIVITIES EMPLOYED IN POST-PROCESSING OF SIMULATION DATA FOR THE SF, COUNT RATES, AND NECR PERFORMANCE TESTS, AND CORRESPONDING ACTIVITY CONCENTRATIONS FOR THE 700 mm LENGTH NEMA NU2-2001, AND THE 1800 mm AXIALLY EXTENDED ONE.

Total source activity		**Activity concentration**			
		700 mm length Phantom		**1800 mm length Phantom**	
MBq	**mCi**	**kBq/cm³**	**nCi/cm³**	**kBq/cm³**	**nCi/cm³**
37×10^{-3}	10^{-3}	1.68×10^{-3}	45.5×10^{-3}	0.654×10^{-3}	17.7×10^{-3}
9.25	0.25	0.421	11.368	0.164	4.421
18.50	0.50	0.841	22.736	0.327	8.842
27.75	0.75	1.262	34.105	0.491	13.263
37.00	1.00	1.682	45.473	0.654	17.684
55.50	1.50	2.524	68.209	0.981	26.526
74.00	2.00	3.365	90.946	1.309	35.368
92.50	2.50	4.206	113.682	1.636	44.210
111.00	3.00	5.047	136.419	1.963	53.052
129.50	3.50	5.889	159.155	2.290	61.894
148.00	4.00	6.730	181.891	2.617	70.736
166.50	4.50	7.571	204.628	2.944	79.577
185.00	5.00	8.412	227.364	3.272	88.419
222.00	6.00	10.095	272.837	3.926	106.103
259.00	7.00	11.777	318.310	4.580	123.787
296.00	8.00	13.460	363.783	5.234	141.471
333.00	9.00	15.142	409.256	5.889	159.155
370.00	10.00	16.825	454.728	6.543	176.839

pileup on the positions signals occur.

For the parameter defining the τ_{ps} dead time for position signals, four different values were employed: 0.0, 0.5, 1.0 and 3.0 μs, this latter corresponding to the dead time of the RPC detectors developed for testing proposes. As to the remaining values, served, primarily, to study the dependence of the expected performance of the RPC TOF-PET scanner with the paralyzable dead time for the position signals, but allowed to gain some insight for the development of future detectors.

For the parameter defining how to handle Single events for which pileup on the position signals occurred, the two available options were used: *rejectAll*, leading to data sets that were named Pileup Event Rejection (PER), and *coarsePosition*, leading to data sets that were named Pileup Event Acceptance with Coarse Position (PEACP). This latter was intended to study the extent to which the NECR could be compromised

by the acceptance, with a coarse position, of position signals for which pileup occurred.

As to the width of the readout sections, and the binning performed for the events for which pileup in the position signal occurred, it were set as in the "Default" column of Appendix G.5, which imply 10 readout sections in the transaxial direction, with a width of 100 mm each, and subdivided in 3 subsections, 20 readout sections in the radial direction, corresponding to the 20 stacked RPC detectors, and a single readout section in the axial direction. So, considering the four detection heads, a total of 800 readout sections were considered.

10.1.3 Removal of Multiple Single Events

Simulation data, processed to account for the τ_{ts}, and each of the τ_{ps} dead times, was then processed with and without performing the removal of multiple Single events[1] due to multiple photon interactions, as well as the Single events that cannot be in coincidence with other events, as explained in Section 6.3.3 (page 204). The goal was to address the effect of the removal procedure on the SF, count rates and NECR.

10.1.4 Coincidence Processing

For processing the coincidences, a coincidence time window of 5 ns was used, as listed in the "Default" column of the table presented in Appendix I.2, for the "*time*" parameter. As to the "*type*" parameter of the same structure, the two allowed values ("*singleTimeWindow*" and "*multipleTimeWindow*"), corresponding to the STW and MTW coincidence sorters (Section 4.2.1, page 89, and Section 6.3.4, page 207), were used. As mentioned at the end of Section 6.3.4 (page 207), for each of the coincidence sorters, three sets of data were saved: ASCP, AMCP and AACP.

Concerning the points used to define the LORs (Section 6.2.5.2 on page 191, and Fig. 6.2 on page 192), the values of the "Default" column of the table listed in Appendix I.1 were employed, leading to the coincidence data being obtained only for the EAP, which is the one known in practice.

10.2 SETUP EMPLOYED FOR PROCESSING COINCIDENCE DATA TO OBTAIN THE PERFORMANCE PARAMETERS

The coincidence data obtained for each phantom, and each combination of the processing parameters, referred to in the last Section (18 source activities, 4 dead

[1] In what follows, WMER will refer to With Multiple Events Rejection, with WoMER referring to Without Multiple Events Rejection.

times, 2 criteria for dealing with pileup for the position signals, 2 options for the removal of multiple events, 2 coincidence sorters, and 3 data sets, the ASCP, AMCP and AACP), were stored without imposing any constraints on the acceptance of valid LORs. These constraints were performed during the processing stage to account for the performance parameters, which was carried out according to the NEMA NU2-2001 standards (Section 4.6.3, page 131, and Section 4.6.4, page 134), employing the procedure described from Section 6.4.1 (page 209) to Section 6.4.6 (page 216).

10.2.1 Rejection of Coincidences on the Basis of Geometric Constraints

Following the first geometric constraint imposed on the coincidence data, referred to in Section 6.4.1 (page 209), the second constraint, referred to in Section 6.4.2 (page 209), was performed by accepting the LORs for which the polar acceptance angle, computed in 2D mode, was less than or equal to 5°, 15°, 25°, 35°, 45° and 90°, this latter corresponding to full acceptance on the polar acceptance angle. The third geometric constraint was then performed with four of the six possible rejection methods explained in Section 6.4.3 (page 210), by setting the *type* field of the rejection substructure, listed in Appendix I.4, to *none*, *none_time_space*, *geometric*, and *geometric_tof*.

For the Geometric Rjection (GR) and the Geometric TOF Rejection (GTOFR), the volume of interest was defined as a right circular cylinder enclosing each phantom, with a 20 mm margin to the phantom edges, holding then a diameter of 240 mm, and lengths of 740 mm, for the standard NEMA NU2-2001 phantom, and 1840 mm, for the axially extended one. The two rejection methods that yielded the better results, GR and GTOFR, are depicted in Fig. 10.1.

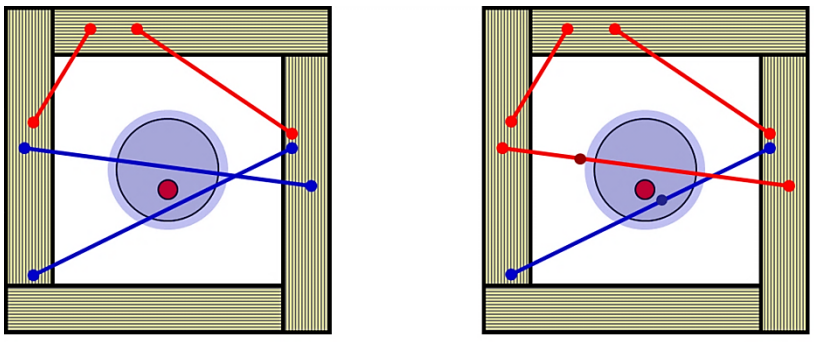

(a) Geometric rejection (GR)

(b) Geometric TOF rejection (GTOFR)

Fig. 10.1. Coincidence rejection/acceptance criteria: a) GR and b) GTOFR. Dots in the scanner heads represent the readout detection points. Red and blue lines represent rejected and accepted LORs, respectively. Dots in the bore represent direct TOF reconstructed points.

Concerning the *none_time_space* constraint, it was used as a first approach to improve the SF and NECR, which yielded poor performance results after processing the coincidences with a STW coincidence sorter and the *none* constraint option, and after analysing the time/distance patterns of each type of event, obtained for the standard NEMA NU2-2001 phantom, with a total activity of 37 kBq (1 μCi) and the *none* rejection option, yielding the plots depicted in Fig. 10.2.

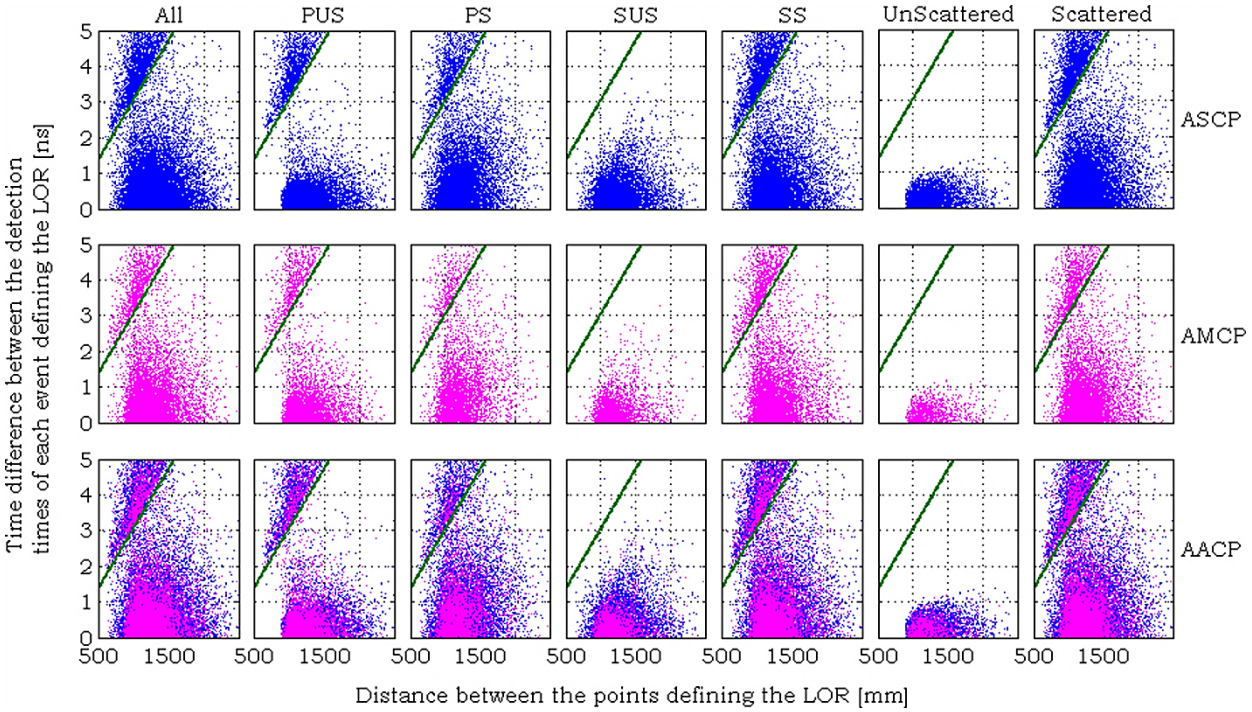

Fig. 10.2: Time difference between the detection times of each event defining the LOR vs. distance between the detection points defining the LOR, for the three data sets: ASCP (top row), AMCP (middle row) and AACP (bottom row). The plots were obtained with the standard NEMA NU2-2001 phantom, for a total activity in the FOV equal to 37 kBq (1 μCi), after constraining the valid LORs to the scanner bore. Each column depicts different types of events according to the following nomenclature: All - all events, PUS - Phantom UnScattered events, PS - Phantom Scattered events, SUS - Scanner UnScattered events, SS - Scanner Scattered events, UnScattered - all unscattered events, Scattered - all scattered events. Random are not shown, since they were found to be negligible.

10.2.2 Rebinning and Sinogram Construction

Coincidence data returned from the previous processing stages, were then processed to account for the rebinning performed as described in Section 6.4.4 (page 214), following which the sinograms were constructed as described in Section 6.4.5 (page 216). The settings employed for these two stages of coincidence processing, were those listed in the “Default” column of Appendix K, resulting in SSRB, followed by the

construction of sinograms for 4 mm thick slices, with a radial binning of 4 mm, and an azimuthal angular binning of 1°. The sinograms were then used to obtain the performance parameters as described in Sections 4.6.3 (page 131) and 4.6.4 (page 134), with the radial shifting of the sinograms performed as mentioned in Section 6.4.6 (page 216) and Fig. 4.26 (page 133).

10.3 RESULTS OBTAINED FOR THE SCATTER FRACTION

All the data sets produced, for each phantom, with all the different possible combinations of the parameters described in Sections 10.1 (page 259) and 10.2 (page 262), were systematically analysed. However, there is no easy way of summarizing the full set of results obtained for the SF, and, thus, in the following, only some of the results obtained with the GR and the GTOFR, depicted in Fig. 10.1 (page 263), and with full acceptance on the polar acceptance angle, will be addressed, since were those holding the best results.

By direct analysis of the first column of the array holding the coincidence data (Appendix J), it was found that, for all the three data sets (ASCP, AMCP and AACP), the fraction of Random events was less than 0.01% of the Prompt coincidences, and less than 0.1% of the True events, as required by the NEMA NU2-2001 standards. This is owing to the small amount of activity present in the FOV (37 kBq), which roughly holds 185×10^{-6} decays during the 5 ns time window used to perform coincidences, making very improbable the detection of Random coincidences, with the added consequence of the SF being independent of the τ_{ps} values employed for the dead time for position signals, and of the PER and PEACP criteria for handling the pileup for the position signals.

The complete set of results obtained for the SF with the abovementioned conditions, and for the standard 700 mm long NEMA NU2-2001 phantom, are listed in Table 10.2, from which it can be seen that the procedure for the removal of multiple events systematically decreased the SF for the GR and the ASCP and AACP data sets, having a negligible effect on the SF of those same data sets when the GTOFR was employed. This is due to the fact that the GTOFR imposes a rejection on the coincidence data that is more stringent than that employed in the procedure for the removal of multiple events, and with a shorter coincidence time window.

TABLE 10.2: COMPLETE LIST OF THE SFS OBTAINED FOR THE STANDARD NEMA NU2-2001 PHANTOM, FOR THE SET OF PROCESSING PARAMETERS LISTED, AND FULL ACCEPTANCE ON THE POLAR ACCEPTANCE ANGLE.

Set of parameters				WioMER				Percentual variation				WiMER			
				Dead Time [μs]				Dead Time [μs]				Dead Time [μs]			
DTP	**CS**	**RT**	**DS**	**0.0**	**0.5**	**1.0**	**3.0**	**0.0**	**0.5**	**1.0**	**3.0**	**0.0**	**0.5**	**1.0**	**3.0**
PER	STW	GR	ASCP	53.2	53.2	53.2	53.2	-1.67	-1.67	-1.66	-1.66	52.3	52.3	52.3	52.3
PEACP	STW	GR	ASCP	53.2	53.2	53.2	53.2	-1.67	-1.67	-1.67	-1.67	52.3	52.3	52.3	52.3
PER	MTW	GR	ASCP	55.6	55.6	55.6	55.6	-1.61	-1.61	-1.58	-1.60	54.7	54.7	54.7	54.7
PEACP	MTW	GR	ASCP	55.6	55.6	55.6	55.6	-1.61	-1.61	-1.61	-1.61	54.7	54.7	54.7	54.7
PER	STW	GTOFR	ASCP	46.5	46.5	46.5	46.5	-0.15	-0.19	-0.21	-0.24	46.4	46.4	46.4	46.4
PEACP	STW	GTOFR	ASCP	46.5	46.5	46.5	46.5	-0.15	-0.17	-0.17	-0.17	46.4	46.4	46.4	46.4
PER	MTW	GTOFR	ASCP	48.9	48.9	48.9	48.8	-0.17	-0.19	-0.17	-0.16	48.8	48.8	48.8	48.8
PEACP	MTW	GTOFR	ASCP	48.9	48.9	48.9	48.9	-0.17	-0.20	-0.21	-0.19	48.8	48.8	48.8	48.8
PER	STW	GR	AMCP	65.6	65.6	65.6	65.6	1.16	1.16	1.16	1.15	66.4	66.4	66.4	66.4
PEACP	STW	GR	AMCP	65.6	65.6	65.6	65.6	1.16	1.17	1.16	1.16	66.4	66.4	66.4	66.4
PER	MTW	GR	AMCP	65.6	65.6	65.6	65.6	1.13	1.14	1.15	1.15	66.4	66.4	66.4	66.4
PEACP	MTW	GR	AMCP	65.6	65.6	65.6	65.6	1.13	1.14	1.14	1.14	66.4	66.4	66.4	66.4
PER	STW	GTOFR	AMCP	58.3	58.3	58.3	58.3	1.95	1.93	1.96	1.94	59.4	59.4	59.4	59.5
PEACP	STW	GTOFR	AMCP	58.3	58.3	58.3	58.3	1.95	2.00	1.95	1.97	59.4	59.5	59.5	59.5
PER	MTW	GTOFR	AMCP	58.3	58.3	58.3	58.3	1.96	1.98	1.94	1.98	59.5	59.5	59.5	59.4
PEACP	MTW	GTOFR	AMCP	58.3	58.3	58.3	58.3	1.96	1.90	1.93	1.94	59.5	59.5	59.5	59.4
PER	STW	GR	AACP	56.4	56.4	56.4	56.4	-1.19	-1.20	-1.19	-1.19	55.7	55.7	55.7	55.7
PEACP	STW	GR	AACP	56.4	56.4	56.4	56.4	-1.19	-1.19	-1.20	-1.19	55.7	55.7	55.7	55.7
PER	MTW	GR	AACP	58.0	58.0	58.0	58.0	-1.14	-1.14	-1.11	-1.13	57.4	57.4	57.4	57.4
PEACP	MTW	GR	AACP	58.0	58.0	58.0	58.0	-1.14	-1.13	-1.14	-1.13	57.4	57.4	57.4	57.4
PER	STW	GTOFR	AACP	49.4	49.4	49.4	49.4	0.02	-0.01	-0.01	-0.05	49.4	49.4	49.4	49.4
PEACP	STW	GTOFR	AACP	49.4	49.4	49.4	49.4	0.02	0.02	0.00	0.01	49.4	49.4	49.4	49.4
PER	MTW	GTOFR	AACP	51.1	51.1	51.1	51.0	0.06	0.05	0.06	0.07	51.1	51.1	51.1	51.1
PEACP	MTW	GTOFR	AACP	51.1	51.1	51.1	51.1	0.06	0.03	0.03	0.04	51.1	51.1	51.1	51.1

DTP: Dead Time Policy **CS**: Coincidence Sorter **RT**: Rejection Type **DS**: Data Set

As to the AMCP data set, the removal of multiple events systematically increases the SF, owing to the removal of Single events arising from photons scattered in the forward direction, which, after forming all the possible combinations of single coincidence events, would result in more than one LOR arising from the same annihilation being accounted as a True event.

So, in what concerns the SF, the removal of multiple events is useless if the GTOFR is to be employed.

As to the coincidence sorter, it can be observed that the MTW leads to a slight systematic increase of the SFs for the ASCP and AACP data sets, relative to those observed, for the same data sets in the same conditions, for the STW coincidence sorter. For the AMCP data set, the coincidence sorter employed does not influence the SF. The absence of difference between the coincidence sorters in this latter data set, is explained by the fact that the AMCP data set only contains single coincidences retrieved from the Multiple coincidences, which contribute to the increase of Scatter, while the increase in the SF on the former data sets, is due to the increase of Multiple coincidences that are formed by the MTW coincidence sorter, relative to those formed by the STW one (see, for instance, the example of the single coincidence pairs formed by both coincidence sorters, depicted in Fig. 4.4 on page 92).

Concerning the geometric rejection method employed, it is clear that the GTOFR is capable of improving the SF for any of the three data sets. This is due to the fact that, long range scatter leads to the formation of LORs for which the distance between the two detection points defining the LOR is smaller than the time difference between the instants of detection of the two photons, leading then to direct TOF reconstructed points that lie outside the volume for acceptance of valid events.

As to the fairly small increase in the SF obtained for the AACP data set, relative to that obtained for the ASCP one, and that is comprised between 5.5% and 6.0% for the STW coincidence sorter, and between 4.1% and 4.6% for the MTW one, despite including the AMCP data set, which has SFs increased by 17.6% (GR plus MTW) and 24.8% (GTOFR plus STW), is due to the fact that, the AMCP data set contains ~31% of the events contained in the ASCP data set, and ~23% of the events contained in the AACP data set, thus not influencing drastically the SF obtained for the AACP, when compared to that obtained for the ASCP.

Given the independence of the SF with the values of the τ_{ps} dead time for the position signals, and with the PER and PEACP criteria for dealing with pileup events, the data of Table 10.2 (page 266) can be summarized in a more readable manner, by taking the average and standard deviation of the SF over all values of the dead time

and pileup handling criteria, for each of the remaining combinations on the parameters employed to process the SF. Table 10.3 resumes the data of Table 10.2 (page 266) in this way, but without the standard deviations, which were found to be no more than 0.01%, for any of the combinations of the remaining processing parameters. Also presented are the percentual deviations of the SFs accessed with the MTW coincidence sorter, relative to those assessed with the STW coincidence sorter, the percentual deviations of the SFs assessed with the GTOFR, relative to those assessed with the GR, and the percentual deviations of the SF assessed WMER, relative to those assessed WoMER.

Simulation processed data was also analysed, by direct assessment of the True and Scattered coincidences, retrieved from the coincidence data files, after applying the processing stages that led to the results of Table 10.2 (page 266) and Table 10.3. The analysis was performed on the basis of the average energy of the coincidence event for each set of LORs (those that correspond to Scattered events and those that

TABLE 10.3: SCATTER FRACTION (IN %) FOR THE STANDARD NEMA NU2-2001 PHANTOM, WITH FULL ACCEPTANCE ON THE POLAR ACCEPTANCE ANGLE. DATA CORRESPONDS TO THE AVERAGE TAKEN OVER ALL VALUES OF THE SF FOUND IN TABLE 10.2 (PAGE 266), FOR THE COMBINATION OF PROCESSING PARAMETERS LISTED IN THE FIRST TWO ROWS AND IN THE FIRST COLUMN OF THE PRESENT TABLE, AND THE ROW ABOVE THE RESULTS. ALSO GIVEN ARE THE PERCENTUAL DEVIATIONS OF THE SFS OBTAINED WITH MTW, RELATIVE TO THOSE OBTAINED WITH STW $\left[RD_1 = 100 \times (SF_{MTW} - SF_{STW})/SF_{STW}\right]$, THE PERCENTUAL DEVIATIONS OF THE SFS OBTAINED WITH GTOFR, RELATIVE TO THOSE OBTAINED WITH GR $\left[RD_2 = 100 \times (SF_{GTOFR} - SF_{GR})/SF_{GR}\right]$, AND THE PERCENTUAL DEVIATIONS OF THE SF OBTAINED WMER RELATIVE TO THOSE OBTAINED WOMER $\left[100 \times (SF_{WMER} - SF_{WoMER})/SF_{WoMER}\right]$.

Rejection method	**ASCP**			**AMCP**			**AACP**		
	STW	**MTW**	RD_1	**STW**	**MTW**	RD_1	**STW**	**MTW**	RD_1
					WoMER				
GR	54.0	56.4	4.4	66.3	66.3	0.0	57.1	58.8	2.9
GTOFR	47.3	49.6	5.0	59.0	59.0	0.0	50.2	51.8	3.3
RD_2	-12.4	-11.9		-10.9	-11.0		-12.2	-11.8	
					WMER				
GR	53.1	55.5	4.5	67.0	67.0	0.0	56.5	58.1	2.9
GTOFR	47.2	49.5	5.0	60.1	60.1	0.0	50.2	51.9	3.4
RD_2	-11.1	-10.7		-10.3	-10.3		-11.2	-10.8	
					Percentual deviation of WMER relative to WoMER				
GR	-1.6	-1.5		1.1	1.1		-1.1	-1.1	
GTOFR	-0.2	-0.2		1.9	1.9		0.0	0.0	

correspond to True events), computed as the average of the energy of the two photons forming the coincidences. The results were then plotted in histograms as those depicted in Fig. 10.3, which were obtained by processing 20 simulation runs, with a $\tau_{ps} = 3.0$ μs dead time for the position signals, acceptance of pileup events with coarse position, WoMER, full acceptance on the polar acceptance angle, followed by the GTOFR. As it can be seen from the plots corresponding to the ASCP and AACP data sets, the MTW coincidence sorter slightly increases the fraction of Scattered events, with a consequent slight decrease in the fraction of True events. The percentual increases of the Scattered events obtained with the MTW coincidence sorter, relative to those obtained with the STW coincidence sorter, computed directly from the coincidence data, were found to be of 10.13% for the ASCP data set, and of 7.28% for the AACP data set. As to the percentual increases for the True events obtained for the MTW coincidence sorter, relative to those found for the STW coincidence sorter, were of 0.83% for the ASCP data set, and of 0.66% for the AACP data set.

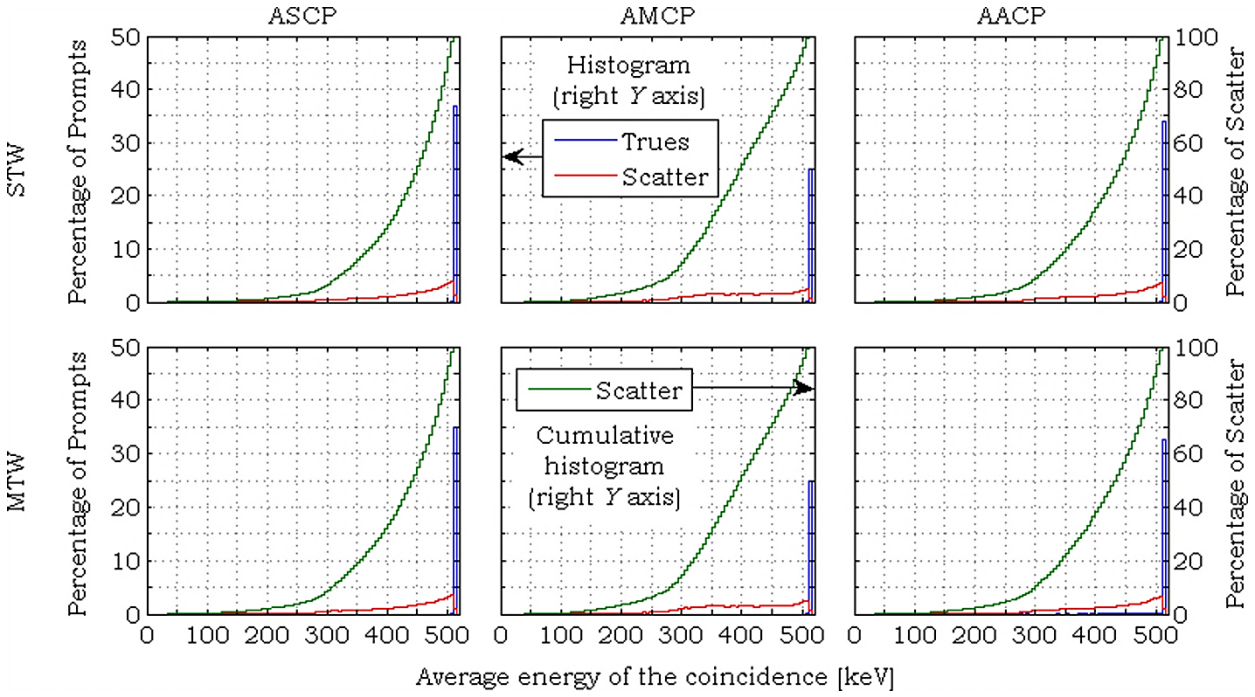

Fig. 10.3. Energy distribution of the coincidence events, computed as the average of the energy of the photons forming a coincidence. The plots were obtained by processing 20 runs with a $\tau_{ps} = 3.0$ μs , acceptance of pileup events with coarse position, WoMER, full acceptance on the polar acceptance angle, and GTOFR. The top and bottom rows correspond to, respectively, the STW and MTW coincidence sorters, while the first, second and third columns correspond to, respectively, the ASCP, AMCP and AACP data sets. Blue and red curves are normalized to the number of Prompt events of each data set and coincidence sorter, and should be read in the left *Y* axis. Green curves are normalized to the number of Scattered events of each data set and coincidence sorter, and should be read on the right *Y* axis.

These results may seem in apparent disagreement with those listed in Table 10.2 (page 266) and Table 10.3 (page 268). However, the aforementioned percentual increases were obtained on the basis of the information available by simulation, from which a coincidence can be classified as Scattered if at least one of the photons that define the corresponding LOR has undergone at least one interaction in the phantom or in the scanner, regardless of the energy lost by the photon in the interaction process, and, consequently, the deviation suffered by the scattered photon from its initial flight path. This is not the case of the NEMA NU2-2001 standards, in which the 40 mm large central portion of the radial binning of the sinograms is considered to compute the number of True counts, thus including small angle scattered LORs.

As to the slice profiles of the SFs, for the standard NEMA NU2-2001 phantom, are depicted in Fig. 10.4, for all data sets (ASCP, AMCP and AACP), the two coincidence sorters employed (STW and MTW), and the two rejection methods under discussion (GR and GTOFR), by performing the removal of multiple events (WMER). As it can be seen, the SFs are almost constant throughout the central portion of the

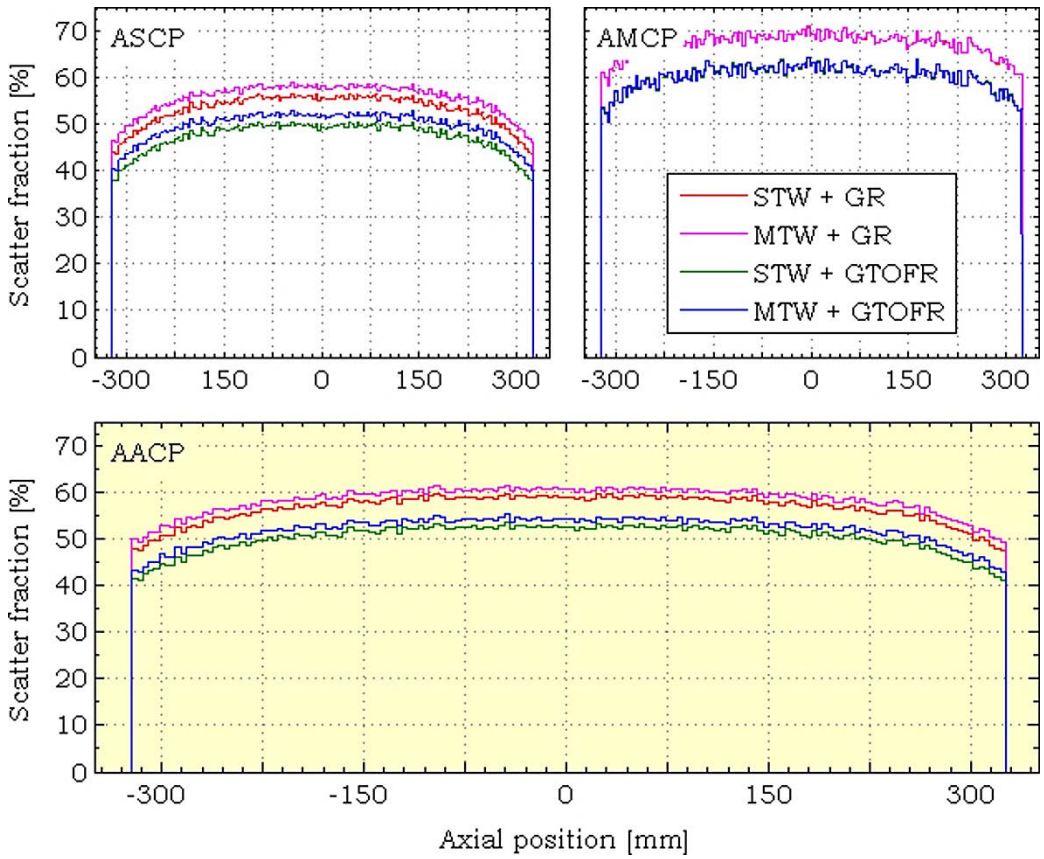

Fig. 10.4: Scatter fraction profiles obtained for the standard NEMA NU2 - 2001 phantom, for a $\tau_{ps} = 3.0$ μs dead time for the position signals, acceptance of pileup events with coarse positions, WMER, for all the combinations of the remaining parameters.

phantom, decreasing in its extremities. This effect is caused by the shorter absorption thickness available at the phantom edges in the axial directions, which means that, if a phantom axially larger than the scanner axial length had been employed, the SFs listed in Table 10.2 (page 266) and Table 10.3 (page 268) would have been larger.

All the results presented so far, fully listed in Table 10.2 (page 266) and summarized in Table 10.3 (page 268), refer only to the standard NEMA NU2-2001 phantom. The SFs obtained for the 1800 mm axially extended phantom, presented exactly the same trends, but with slightly different results, as it can be seen from Table 10.4, which summarizes the results obtained for the 1800 mm axially extended phantom.

As it can be seen, for the GR rejection method, the removal of multiple events percentually performs marginally better for the axially extended phantom than for the standard NEMA NU2-2001phantom, for all the three data sets (ASCP, AMCP and

TABLE 10.4: SCATTER FRACTION (IN %), FOR THE 1800 mm AXIALLY EXTENDED PHANTOM, AND FULL ACCEPTANCE ON THE POLAR ACCEPTANCE ANGLE. DATA CORRESPONDS TO THE AVERAGE TAKEN OVER ALL VALUES OF THE SFS OBTAINED FOR THE COMBINATION OF THE PROCESSING PARAMETERS LISTED IN THE FIRST TWO ROWS AND IN THE FIRST COLUMN OF THE PRESENT TABLE, AND THE ROW ABOVE THE RESULTS. ALSO GIVEN ARE THE PERCENTUAL DEVIATIONS OF THE SF OBTAINED FOR THE MTW COINCIDENCE SORTER, RELATIVE TO THOSE WITH THE STW $\left[RD_1 = 100 \times (SF_{MTW} - SF_{STW})/SF_{STW}\right]$, THE PERCENTUAL DEVIATIONS OF THE SF OBTAINED WITH GTOFR, RELATIVE TO THOSE WITH GR $\left[RD_2 = 100 \times (SF_{GTOFR} - SF_{GR})/SF_{GR}\right]$, AND THE PERCENTUAL DEVIATIONS OF THE SF OBTAINED WITH WMER, RELATIVE TO THOSE OBTAINED WITH WOMER $\left[100 \times (SF_{WMER} - SF_{WoMER})/SF_{WoMER}\right]$.

Rejection method	**ASCP**			**AMCP**			**AACP**		
	STW	**MTW**	RD_1	**STW**	**MTW**	RD_1	**STW**	**MTW**	RD_1
					WoMER				
GR	57.3	59.5	3.8	68.4	68.4	0.0	60.1	61.6	2.5
GTOFR	49.4	51.7	4.5	60.6	60.6	0.0	52.1	53.7	3.0
RD_2	-13.7	-13.1		-11.4	-11.5		-13.2	-12.8	
					WMER				
GR	56.1	58.3	3.9	69.0	69.0	0.0	59.1	60.7	2.6
GTOFR	49.4	51.6	4.5	61.6	61.7	0.0	52.1	53.7	3.1
RD_2	-12.0	-11.5		-10.6	-10.6		-11.9	-11.5	
					Percentual deviation of WMER relative to WoMER				
GR	-2.1	-2.0		0.8	0.8		-1.6	-1.5	
GTOFR	-0.2	-0.2		1.7	1.8		0.0	0.0	

AACP), and performs equally well with the GTOFR, for both phantoms. As to the rejection method, GTOFR percentually performs slightly better than GR, in comparison to the standard NEMA NU2-2001 phantom, for the ASCP and AACP data sets, performing percentually equally better for the AMCP data set. Concerning the coincidence sorter, the MTW percentually increases less the SF for the axially extended phantom than it does for the standard NEMA NU2-2001 phantom. However, the SFs obtained with the axially extended phantom are systematically higher than those found for the standard NEMA NU2-2001 phantom, as it can be seen from Table 10.5, which lists the percentual increases of the SFs obtained with the axially extended phantom, relative to those obtained with the standard NEMA NU2-2001 phantom. These increases in the SFs, for the axially extended phantom, are due to the increased Scatter in the phantom along the axial direction, combined with a more extensive flat plateau of the slice SFs, as depicted in Fig. 10.5.

When comparing the values obtained for the expected SF of the RPC TOF-PET scanner, for the different combinations of the processing parameters, with those presented by the current state of the art PET scanners listed in Table 4.5 (page 143), it can be seen that the RPC TOF-PET is expected to perform much worse. However, the referred scanners have energy resolution, the SFs being usually reported for stringent values of the LLD. For instance, the Philips Gemini TF scanner is reported to present a SF, obtained with the standard NEMA NU2-2001 phantom, of ~30% for an LLD of 440 keV, being of ~42% for an LLD of ~357 keV [Surti et al., 2007]. Still, the SF found for the RPC TOF-PET scanner is worse than the worse value reported by [Surti et al.,

TABLE 10.5: PERCENTUAL DEVIATIONS OF THE SFS OBTAINED FOR THE 1800 mm AXIALLY EXTENDED PHANTOM, RELATIVE TO THOSE FOUND FOR THE STANDARD NEMA NU2-2001 PHANTOM, COMPUTED AS $100 \times \left(SF_{1800\ \mathrm{mm}} - SF_{700\ \mathrm{mm}}\right) / SF_{700\ \mathrm{mm}}$.

Rejection method	**ASCP**		**AMCP**		**AACP**	
	STW	**MTW**	**STW**	**MTW**	**STW**	**MTW**
			WoMER			
GR	6.1	5.5	3.3	3.3	5.1	4.8
GTOFR	4.6	4.1	2.7	2.7	3.9	3.6
			WMER			
GR	5.6	5.0	2.9	2.9	4.7	4.4
GTOFR	4.6	4.1	2.5	2.5	3.9	3.6

2007], for the Philips Gemini TF scanner.

In order to determine the nature of Scatter in terms of range, so as to evaluate the possible impact that it may have on the quality of the final reconstructed images, the 3D distance from the LORs to the annihilation points were computed and plotted in histograms. Fig. 10.6 (page 274) depicts these histograms, for all the three coincidence data sets (ASCP, AMCP and AACP), normalized to the total number of events of each data set, obtained for the standard NEMA NU2-2001 phantom with a total activity of 37 kBq (1 μCi), processed with a $\tau_{ps} = 3.0$ μs dead time for the position signals and rejecting all events for which pileup occurred, followed by the removal of multiple events, the coincidences having been performed with the MTW coincidence sorter, full acceptance on the polar acceptance angle, and with the GTOFR. Also presented are the LOR volume densities as a function of the distance of the LORs to the annihilation points, obtained by dividing the histograms of the distance of the LORs to the annihilation points by the volume of the spherical shell with inner and outer radius equal to the bin edges. The plots suggest that the Scatter contributes to

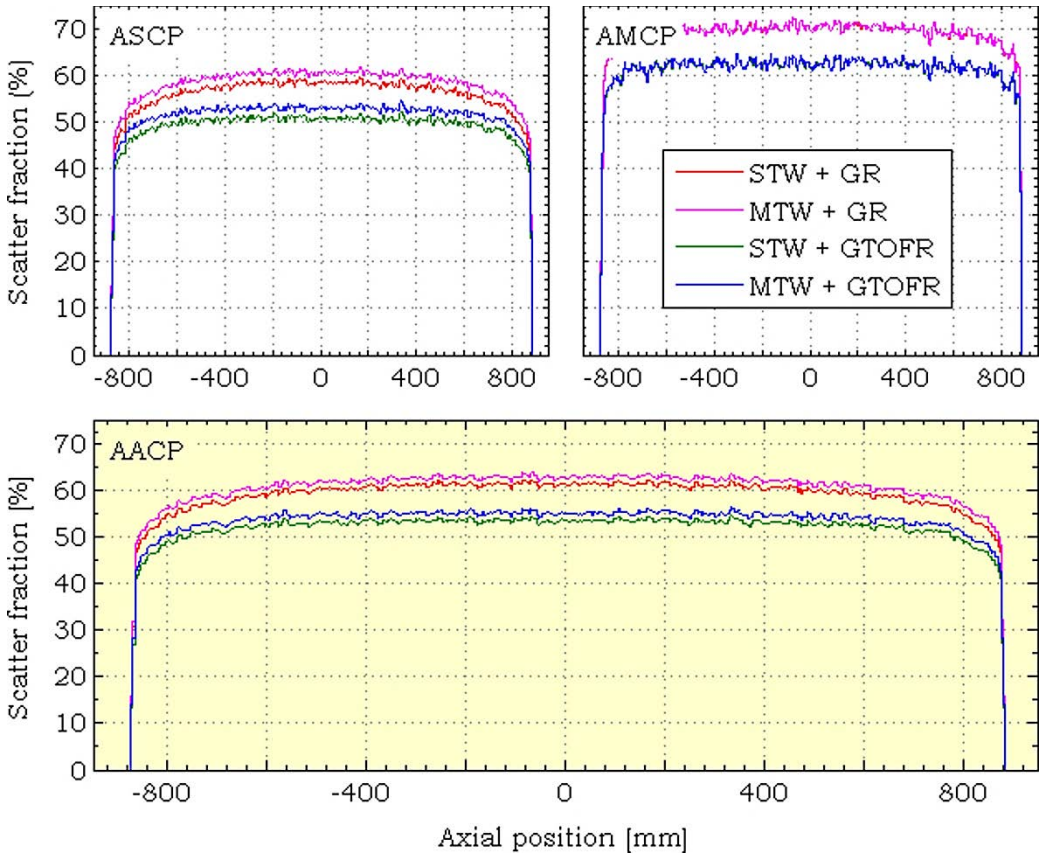

Fig. 10.5: Scatter fraction profiles obtained for the 1800 mm axially extended phantom, for a $\tau_{ps} = 3.0$ μs dead time for the position signals, acceptance of pileup events with coarse positions, WMER, for all the combinations of remaining parameters.

long-range diffuse background that does not compromise image quality.

As mentioned in Section 10.2.1 (page 263), simulation data was processed by considering six different polar angles for acceptance of LORs (5°, 15°, 25°, 35°, 45° and 90°), and by employing the *none*, *none_time_space*, *geometric* and *geometric_tof* options, for rejection of coincidence data, and in the beginning of the present section it was said that only the results for GR and GTOFR were to be presented.

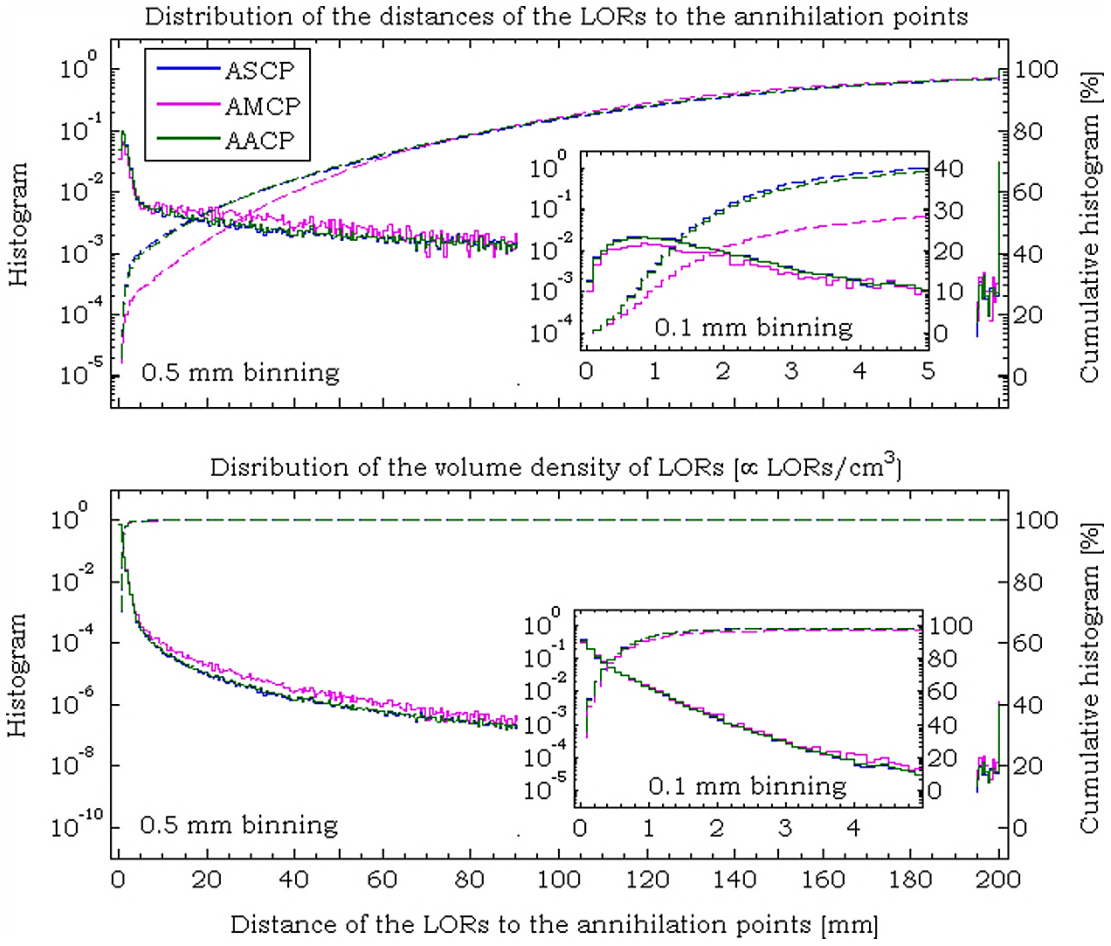

Fig. 10.6: Distribution (solid lines - left *Y* axis) of the distances of the LORs to the annihilation points (top), and of the volume density of the LORs (bottom), as a function of the distances to the annihilation points, obtained by dividing the histograms of the distances of the LORs to the annihilation points by the volumes of the spherical shells with inner and outer radius equal do the bin edges, for all the three coincidence data sets (ASCP, AMCP and AACP). The dashed lines represent the corresponding cumulative distributions, and should be read at the right *Y* axis. Plots were obtained for the standard NEMA NU2-2001 phantom, for a total activity equal to 37 kBq (1 μCi), and processed with a $\tau_{ps} = 3.0$ μs dead time for the position signals, which were rejected in case of pileup, WMER, the coincidences having been performed by using the MTW coincidence sorter, full acceptance on the polar acceptance angle, and the GTOFR. The bin widths of the main plots and insets are equal to 0.5 mm and 0.1 mm, respectively.

Concerning the results obtained for all the rejection methods tested, the one holding the best results, in what concerns the SF, was the GTOFR. Moreover, GTOFR was found to be independent of the value employed for the acceptance on the polar acceptance angle, while the other methods showed a slight increase with this parameter. Fig. 10.7 depicts the SFs obtained for the standard NEMA NU2-2001 phantom, processed with a $\tau_{ps} = 3.0$ µs dead time for position signals, by accepting

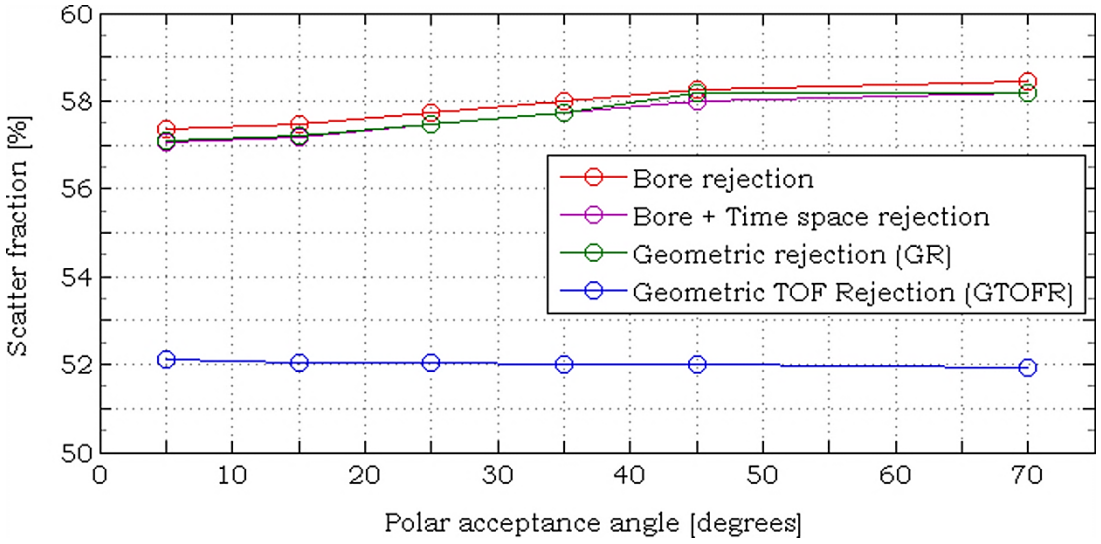

Fig. 10.7: Scatter fractions for the standard NEMA NU2-2001 phantom, obtained for the AACP data set, by processing the simulation data with a $\tau_{ps} = 3.0$ µs dead time on the position signals, accepting with a coarse position all the Single events for which pileup occurred, followed by the removal of multiple events, with the coincidences performed by the MTW coincidence sorter.

with a coarse position all the Single events for which pileup occurred, followed by the removal of multiple events, for the AACP data set.

10.4 COUNT RATES

The results of the previous section suggest that, for the RPC TOF-PET scanner, the optimum scheme for processing the raw data to hold the coincidences, so that the SF remains at the minimum possible value, consists in performing a STW coincidence sorter with full acceptance on the polar acceptance angle, rejecting all the multiple coincidences, and accepting only those LORs for which the direct TOF reconstructed point lies inside a tight volume surrounding the object being imaged. However, the optimum processing scheme is not necessarily the one that gives the lower SF, but the one that increases NECR, as long as spatial resolution and image quality will not be compromised, both for lower count rates and for higher ones.

So, to assess the best strategy to maximize the NECR, the simulation data, obtained for both phantoms (standard NEMA NU2-2001 and extended), was processed to account for each source activity (Table 10.1, page 261) and all the possible combination of the previously mentioned processing parameters. The Prompt, Trues, Scatter and Random count rates, along with the NECR, were then computed according to the NEMA NU2-2001 standards.

As in the previous section, the several results obtained were systematically studied to account for the effects of each combination of the processing parameters. However, the results are more difficult to resume in tables, and to be considered in a systematic manner, as in the previous section. For this, in the present Section, the effects of a more limited set of the processing parameters on the count rates, excluding NECR, will be addressed.

The set of parameters chosen was based on the achievable gains concerning the reduction of the Scatter and Random count rates, and also on the increase of the True count rates, or, at least, less severe reductions. For that, the results obtained with the four values of the τ_{ps} dead time for position signals, and rejecting the events for which pileup occurred (the PER criterion), followed by the removal of multiple events, will be addressed, first by employing the STW coincidence sorter, full acceptance on the polar acceptance angle, and the rejection of LORs based on the GR and the GTOFR methods, for all the three data sets of coincidences (ASCP, AMCP and AACP). This set of parameters allowed gaining some insight on the ability of GTOFR, which was the rejection method that best performed for the SF test, to reduce the Scatter and Random count rates. Moreover, the results will be presented in the form of plots.

Fig. 10.8 depicts the Trues count rates for the three coincidence data sets (ASCP, AMCP and AACP), obtained with the set of parameters previously mentioned, along with the percentual variations of count rates obtained with GTOFR relative to those obtained with GR. As it can be seen, for all data sets (ASCP, AMCP and AACP), the Trues count rate obtained with GTOFR are reduced by ~1% to ~5% when compared to those obtained with GR. This is due to the removal of Scattered and Random events that were accounted for as True coincidences, and also to the removal of a small fraction of True events for which the TOF reconstructed points fall outside of the volume of interest.

Concerning the ASCP data set, it can be seen that, for the simulated activity concentrations, the Trues count rate present a maximum value of about 300 kcps[2], for an activity concentration of $6.7\,\mathrm{kBq\,cm^{-3}}$, when the paralyzable dead time for the

[2] kcps = kilo counts per second

position signals was set to $\tau_{ps} = 3.0$ μs, while increasing toward a maximum for the remaining values employed in the processing of the dead time for the position signals.

On one hand, the increase of the activity in the FOV leads to an increase in the number of pileup events that are discarded with the PER acceptance criteria, which was the one employed for the data presented in Fig. 10.8. This effect is evidenced by the increase of the True count rates with the decrease of the dead time for the position signals, for the same value of the activity concentration. On the other hand, the increase in the activity concentration leads to an increase of the Single count rate,

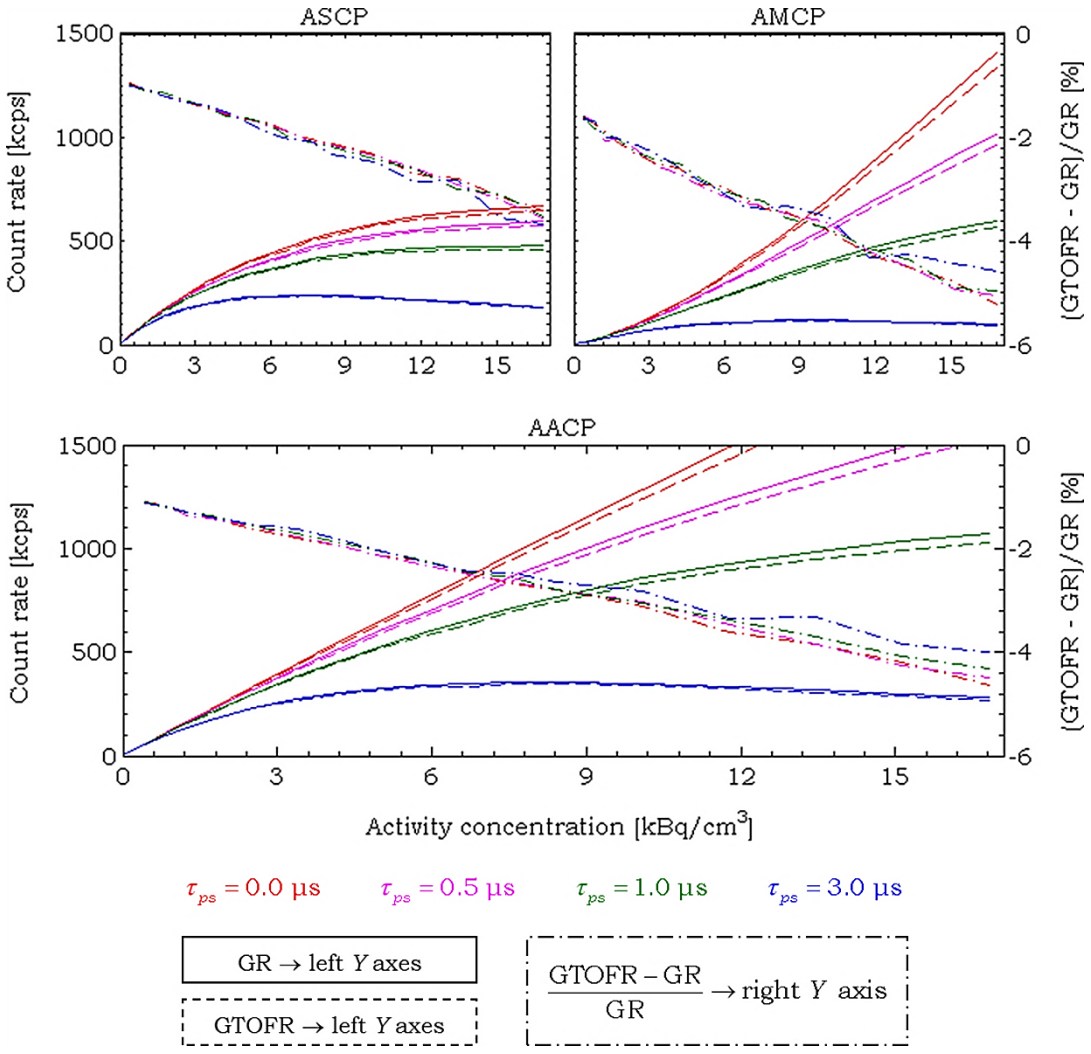

Fig. 10.8: Trues count rates as a function of activity concentration for the standard NEMA NU2-2001 phantom, obtained for values of the dead time for position signals of $\tau_{ps} = 0.0, 0.5, 1.0$ and 3.0 μs and rejecting pileup events, followed by the removal of multiple events, with the coincidences performed by the STW coincidence sorter, for full acceptance on the polar acceptance angle, and employing the GR and the GTOFR. Also presented are the percentual reductions of the True count rates as a function of the activity concentration in the phantom, obtained with the GTOFR relative to those obtained with the GR.

with a consequent increase in the number of Multiple coincidences, which then lowers the number of single pairs of photons being registered in coincidence.

This latter effect is evidenced by the increase of the Trues count rate contained in the AMCP data set, with the increase of the total activity present in the FOV and the decrease of the τ_{ps} paralyzable dead time for position signals. In the limit of no dead time for the position signals, the Trues count rate contained in the AMCP data set is expected to increase with the total activity present in the FOV. As the value of the paralyzable dead time for the position signals increases, the effect of pileup becomes dominant and the Trues Count rate of the AMCP data set, after reaching a maximum, start to decrease with the increased activity in the FOV. For the $\tau_{ps} = 3.0\ \mu s$ dead time for the position signals, the True count rate of the AMCP data set was found to have a maximum value of ~114 kcps for an activity concentration of $\sim 10\ \mathrm{kBq\,cm^{-3}}$.

As to the AACP data set, it presents a trend that is the combination of those presented by the ASCP and AMCP data sets. The maximum True count rate found, for a value of $\tau_{ps} = 3.0\ \mu s$ dead time for the position signals, was of 346 kcps, for an activity concentration of $7.6\ \mathrm{kBq\,cm^{-3}}$. For the remaining values employed for the dead time for position signals, and for the simulated range of activity concentrations, the Trues count rate do not present a maximum, almost constantly increasing with the activity concentration if no dead time for the position signals existed.

Since Scattered coincidences are undistinguishable from True ones, in the sense that both are formed by two photons arising from the same annihilation, what was said for the True count rates also applies to the Scatter count rates, depicted in Fig. 10.9, with the only difference that the GTOFR is capable of rejecting Scattered events from ~20% to ~30%, relative to the GR.

As to the effects on the Random count rate of the dead time for position signals, and of the method employed to reject coincidences, are depicted in Fig. 10.10 (page 280). As it can be seen, if it were not for the dead time, the Random count rate would present a significant increase with the increase of the total activity present in the FOV, as mentioned in Section 4.2.3.3 (page 99).

The percentual reduction of more than 70%, achieved with the GTOFR, relative to that achieved with the GR, was much greater than that achieved for the Scatter count rates. This can be explained by the fact that GR only discards coincidences for which the corresponding LOR do not cross the volume of interest, while GTOFR additionally reject those coincidence events for which the relation between the time difference in the detection instants of the two photons and the length of the LOR does not place the direct TOF reconstructed point inside the volume of interest. Since the Random events are not correlated by the aforementioned relation, the probability that the

corresponding points reconstructed by direct TOF do not lie inside the volume of interest, is greater for the Random events than for the Scattered events, for which that probability is significant only if long range scatter occurs.

Concerning the AMCP data set, and for all the combinations of the processing parameters, some slices contained negative values, which were zeroed before being summed to compute the total Random count rate. While this does not affect the NECR computation, it affects the Scatter and Random count rates, the effect being more pronounced for the latter for lower activity concentrations, depending also on the τ_{ps} dead time for position signals, with longer values of τ_{ps} keeping this influence up to

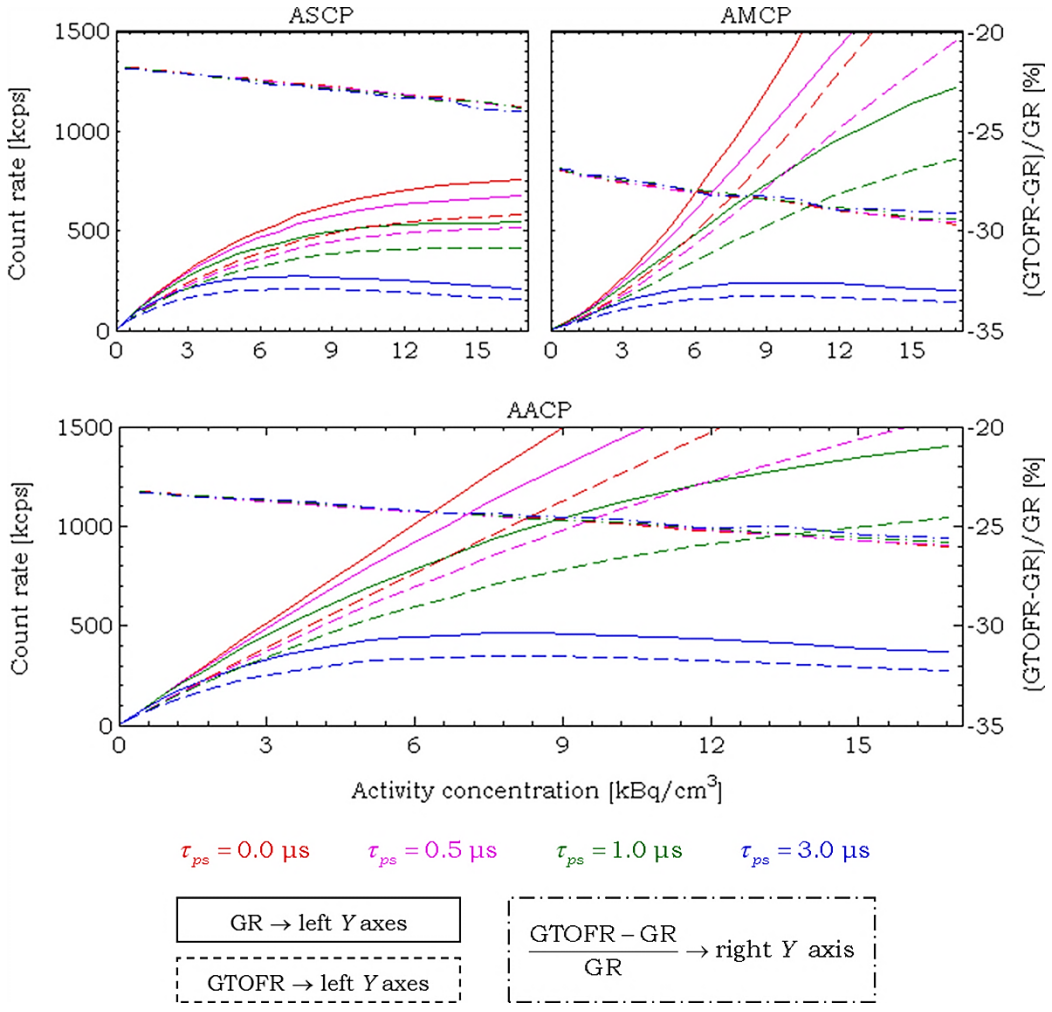

Fig. 10.9: Scatter count rates as a function of activity concentration for the standard NEMA NU2-2001 phantom, obtained for values of the dead time for position signals of $\tau_{ps} = 0.0, 0.5, 1.0$ and 3.0 μs and rejecting pileup events, followed by the removal of multiple events, with the coincidences performed by the STW coincidence sorter, for full acceptance on the polar acceptance angle, and employing the GR and the GTOFR. Also presented are the percentual reductions of the Scatter count rates as a function of the activity concentration in the phantom, obtained with the GTOFR relative to those obtained with the GR.

higher concentration activities. Nevertheless, when slice SF obtained with the ASCP data set was used (maintaining the remaining processing parameters), no negative Random count rates were found for the slices of the AMCP data sets.

Plotting the Prompt, Trues, Scatter and Random slice count rates for both processing cases (slice SFs obtained from the AMCP and from the ASCP data sets), it was verified that the Scatter plus Random count rate was the same for all slices. Since SF for the ASCP data set is lower than that for the AMCP data set, the result suggested that the SF for AMCP is dependent on activity concentration. This was confirmed by direct analysis of coincidence data, which showed that, for the AMCP

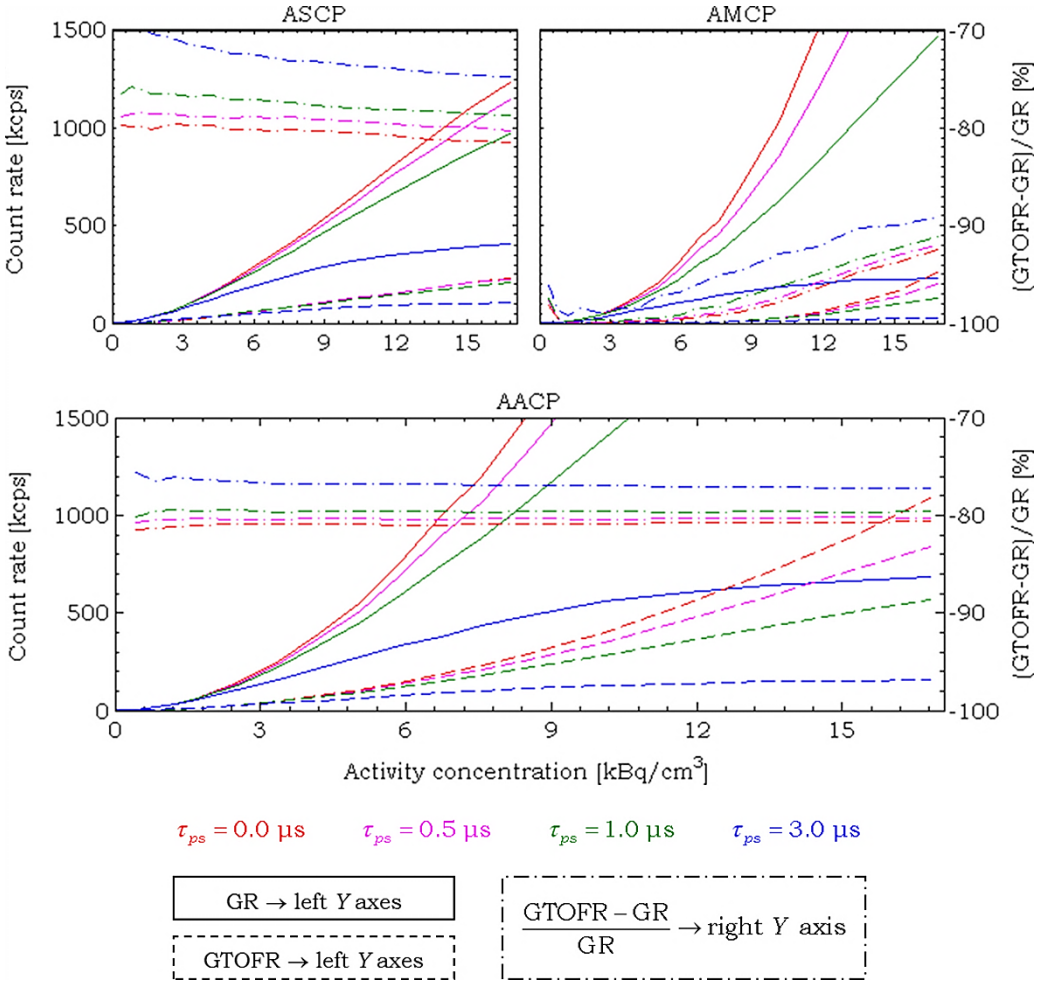

Fig. 10.10: Random count rates as a function of activity concentration for the standard NEMA NU2-2001 phantom, obtained for values of the dead time for position signals of $\tau_{ps} = 0.0, 0.5, 1.0, 3.0$ μs and rejecting the pileup events, followed by the removal of multiple events, with the coincidences performed by the STW coincidence sorter for full acceptance on the polar acceptance angle and employing the GR and GTOFR methods. Also presented are the percentual reductions of the Trues counts rates as a function of the activity concentration in the phantom, obtained with the GTOFR relative to those obtained with the GR.

data set, unlike for the ASCP and AACP data sets, the ratios of Scatter to Trues plus Scatter, and of Scatter to Prompt coincidences, decreased as the activity concentration increased. This effect was verified to be much more significant for the GTOFR than for the GR.

From the above, and as Fig. 10.8 (page 277), Fig. 10.9 (page 279) and Fig. 10.10 (page 280) show, in spite of the combined Scatter and Random count rate content for the AMCP data set being higher than the True count rate, they are roughly of the same order of magnitude, which suggest that Multiple coincidences should not be discarded, since NECR benefits from True count rates by squaring it, while depending inversely on the first power of the Prompt count rates.

The results obtained so far concern only the STW coincidence sorter, which was the one that led to the best results for the SF. To test if this was also the case for the count rates, and consequently for the NECR, the simulation data was processed with the same set of parameters that led to the final results presented throughout the present Section, with the only difference being on the coincidence sorter, which was set to the MTW. Fig. 10.11 (page 282) depicts the percentual variation of the Trues, Scatter and Random count rates, obtained with the MTW coincidence sorter relative to those obtained with the STW, and by considering only the AACP data set with the GTOFR, showing a systematic increase in all the count rates, with the increase being greater for the Scatter than for the Trues and Random count rates.

10.5 NOISE EQUIVALENT COUNT RATE

The assessment of the NECR was performed by processing the simulation data for all the set of parameters that were employed in the remaining tests. Although for the NECR a table could be given with the values found for the peak NECR, along with the concentration at which they occurred, for each combination of the processing parameters, as seen previously, and with the exception for the $\tau_{ps} = 3.0$ µs dead time on the position signals, the Trues and Scatter count rates addressed so far do not present such peaks. Moreover, the peak NECR alone is not the best indicator of the performance in clinical practice. For instance, the peak NECR for the Philips Gemini TF, the GE Discovery 690 and the Siemens Biograph mCT, are reported to be of, respectively, 125 kcps [Surti et al., 2007], 139.1 kcps [Bettinardi et al., 2011] and 180.3 kcps [Jakoby et al., 2011]. These values were achieved with the 700 mm length NEMA NU2 phantom, for activity concentrations of, respectively, 17.4 $\mathrm{kBq\,cm^{-3}}$ [Surti et al., 2007], 29.0 $\mathrm{kBq\,cm^{-3}}$ [Bettinardi et al., 2011] and 28.3 $\mathrm{kBq\,cm^{-3}}$ [Jakoby et al., 2011], corresponding to total activities in the phantom of, respectively, 382.6 MBq

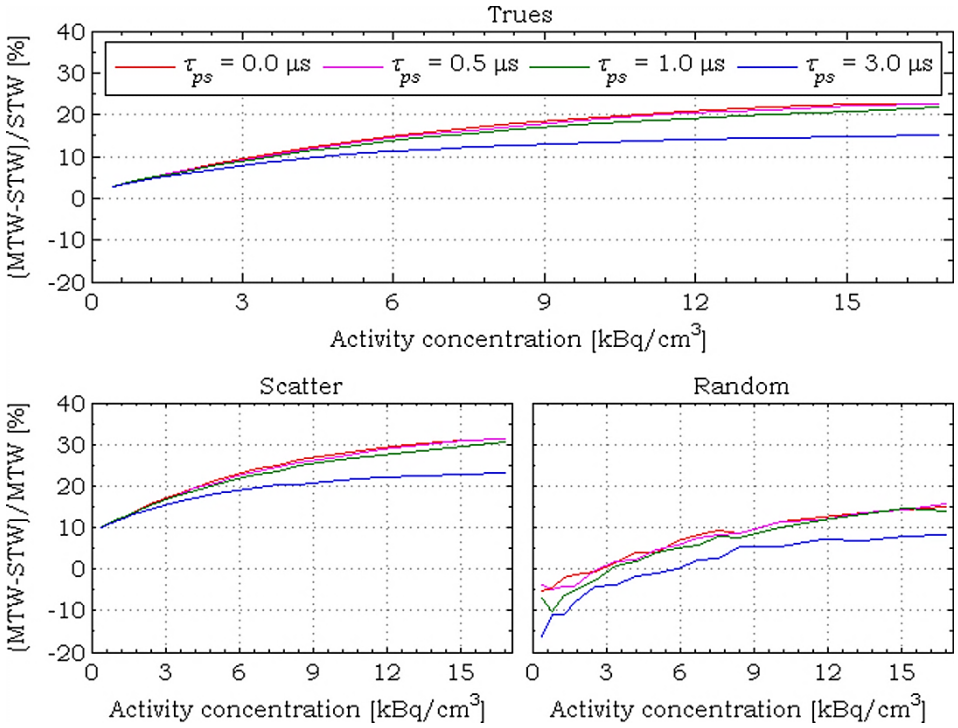

Fig. 10.11: Percentual deviation, as a function of the activity concentration, for the Trues, Scatter and Random count rates, obtained for the AACP data set processed with the MTW coincidence sorter, relative to those obtained with the STW coincidence sorter. The simulation data was processed for the standard NEMA NU2-2001 phantom, for values of the dead time for position signals of $\tau_{ps} = 0.0, 0.5, 1.0$ and 3.0 μs , by rejecting the pileup events, followed by the removal of multiple events, for full acceptance on the polar acceptance angle, and employing the GTOFR.

(10.3 mCi), 637.7 MBq (17.2 mCi) and 622.3 MBq (16.8 mCi).

For oncological studies performed with FDG, the total activities injected to patients usually range from 185 MBq (5 mCi) to 370 MBq (10 mCi), the patient laying down at rest for approximately one hour prior to the study. Considering the radioactive decay of $^{18}_{9}\mathrm{F}$ and neglecting the effective decay constant, which also includes the biological excretion, the total activity present in the patient at the time of the exam will be usually comprised between 127 MBq (3.4 mCi) and 253 MBq (6.8 mCi). If the volumes of $\sim 40\times10^3$ cm^3 and $\sim 75\times10^3$ cm^3, referred to by [Surti et al., 2007] as corresponding to those of average and heavy patients[3], are used to compute the activity concentrations, then the activity concentration in the patient[4], at

[3] The axially extended phantom employed in the present works has total volume of $\sim 56\times10^3$ cm^3, and thus comprised between the mentioned values. Although, the diameter is still 200 mm, which may be less than the total body thickness of the average patient.

[4] The concentrations give refer to the total average activity concentration. The concentrations found at some organs one hour past the injection [Crespo et al., 2012], may be higher than the total average concentration.

the time of the exam, will be roughly comprised between $\sim 3.2\,\mathrm{kBq\,cm^{-3}}$ and $\sim 6.3\,\mathrm{kBq\,cm^{-3}}$, for the average patients, and between $\sim 1.7\,\mathrm{kBq\,cm^{-3}}$ and $\sim 3.4\,\mathrm{kBq\,cm^{-3}}$, for the heavy patients, respectively. So, the peak NECR is a good indicator of the maximum performance that a PET scanner can achieve, but is not so good to account for the performance in clinical practice, which is better assessed by analysing the NECR curves for the range of activity concentrations employed in clinical practice.

For the above mentioned reasons, it was opted to present only the results

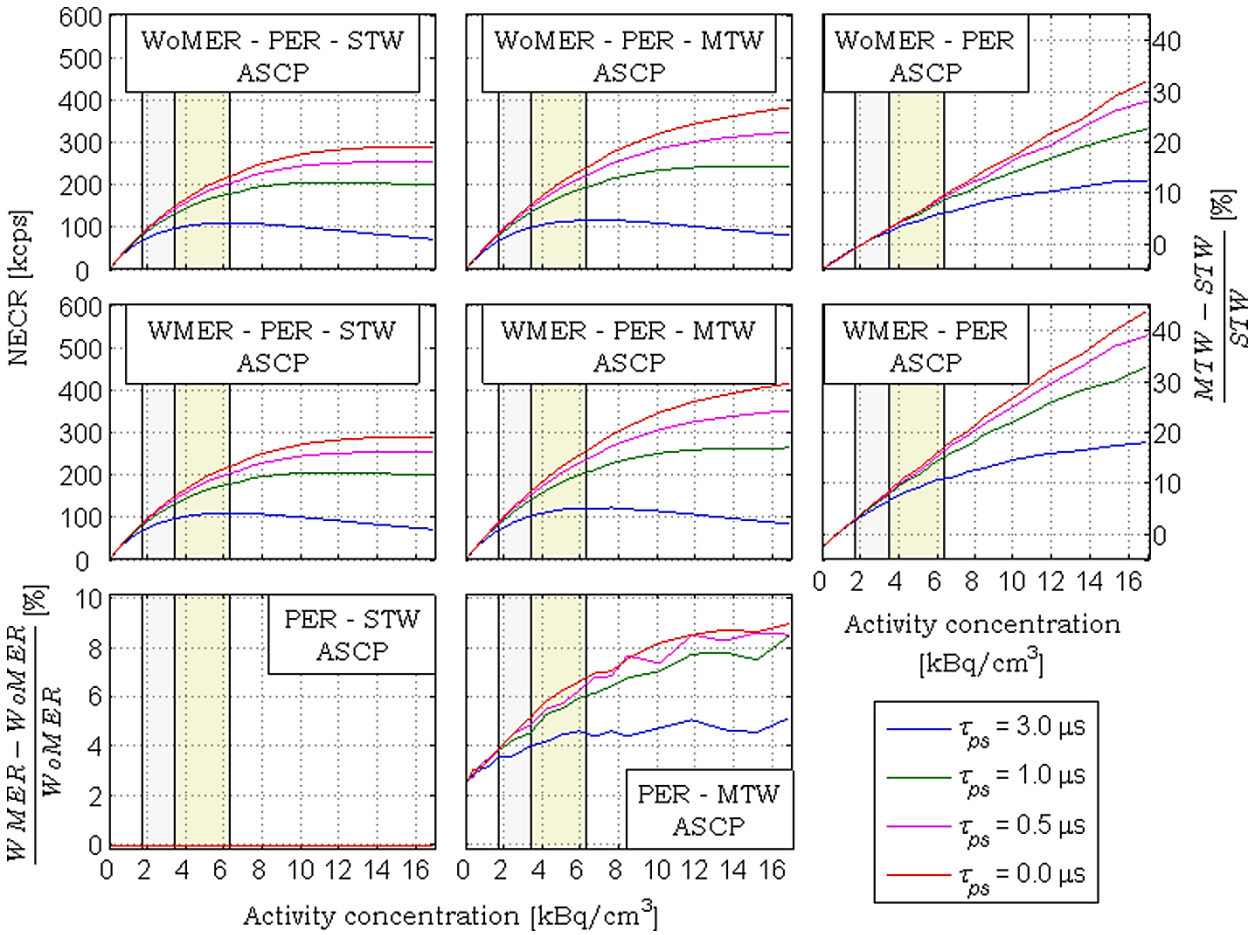

Fig. 10.12: NECR curves for the ASCP data set, obtained with the standard NEMA NU2-2001 phantom, and all the combinations of the remaining parameters, with the exception of the criterion to deal with pileup events, which was set to PER. The vertical black solid lines represent the activity concentrations previously mentioned as being those present in the patient at the time of the exam ($1.70\,\mathrm{kBq\,cm^{-3}}$, $3.45\,\mathrm{kBq\,cm^{-3}}$ and $6.30\,\mathrm{kBq\,cm^{-3}}$). The two plots in the bottom represent the percentual deviation of the NECR with the removal of multiple events relative to those without the removal, and the two right plots represent the percentual deviation of the NECR obtained for the MTW coincidence sorter relative to that obtained with the STW coincidence sorter. The shaded areas represent the previously mentioned activity concentrations for the standard NEMA NU2-2001 phantom (see text above).

obtained by means of plots, which are depicted in Fig. 10.12 (ASCP data set), Fig. 10.13 (AMCP data set), and Fig. 10.14 (AACP data set, on page 285), for the standard NEMA NU2-2001 phantom, processed with the PER criterion for acceptance of pileup events, full acceptance on the polar acceptance angle, with the GTOFR rejection method, and all the combinations of the remaining parameters employed in the processing of simulation data.

As it can be seen, the MTW coincidence sorter improves the NECR for the three data sets (ASCP, AMCP and AACP), the improvement being greater for lower values of

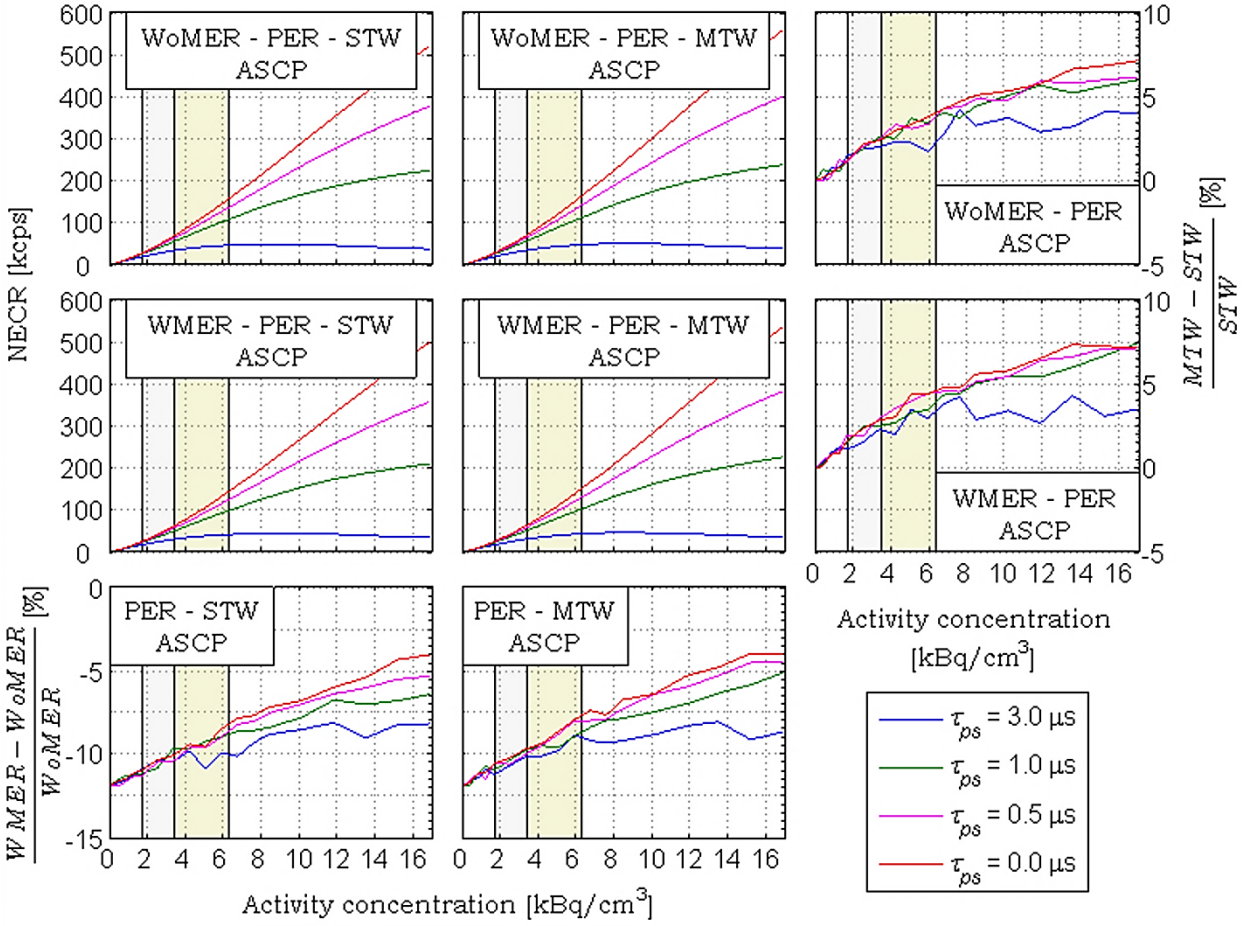

Fig. 10.13: NECR curves for the AMCP data set, obtained with the standard NEMA NU2-2001 phantom, and all the combinations of the remaining parameters, with the exception of the criterion to deal with pileup events, which was set to PER. The vertical black solid lines represent the activity concentrations previously mentioned as being those present in the patient at the time of the exam (1.70 kBq cm^{-3}, 3.45 kBq cm^{-3} and 6.30 kBq cm^{-3}. The two plots in the bottom represent the percentual deviation of the NECR with the removal of multiple events relative to those without the removal, and the two right plots represent the percentual deviation of the NECR obtained for the MTW coincidence sorter relative to that obtained with the STW coincidence sorter. The shaded areas represent the previously mentioned activity concentrations for the standard NEMA NU2-2001 phantom (see text above).

the τ_{ps} dead time for position signals than for higher ones. As to the removal of multiple events, it has no influence on the NECR curves of the ASCP and AACP data sets for the STW coincidence sorter, slightly increasing the NECR of the ASCP data set for the MTW coincidence sorter, decreasing it for the AMCP data set for both coincidence sorters, and marginally increasing the NECR of the AACP data set for the MTW coincidence sorter.

Concerning the dependence of the NECR on the polar acceptance angle, it was verified that the former increases with the increase of the latter, as depicted in Fig.

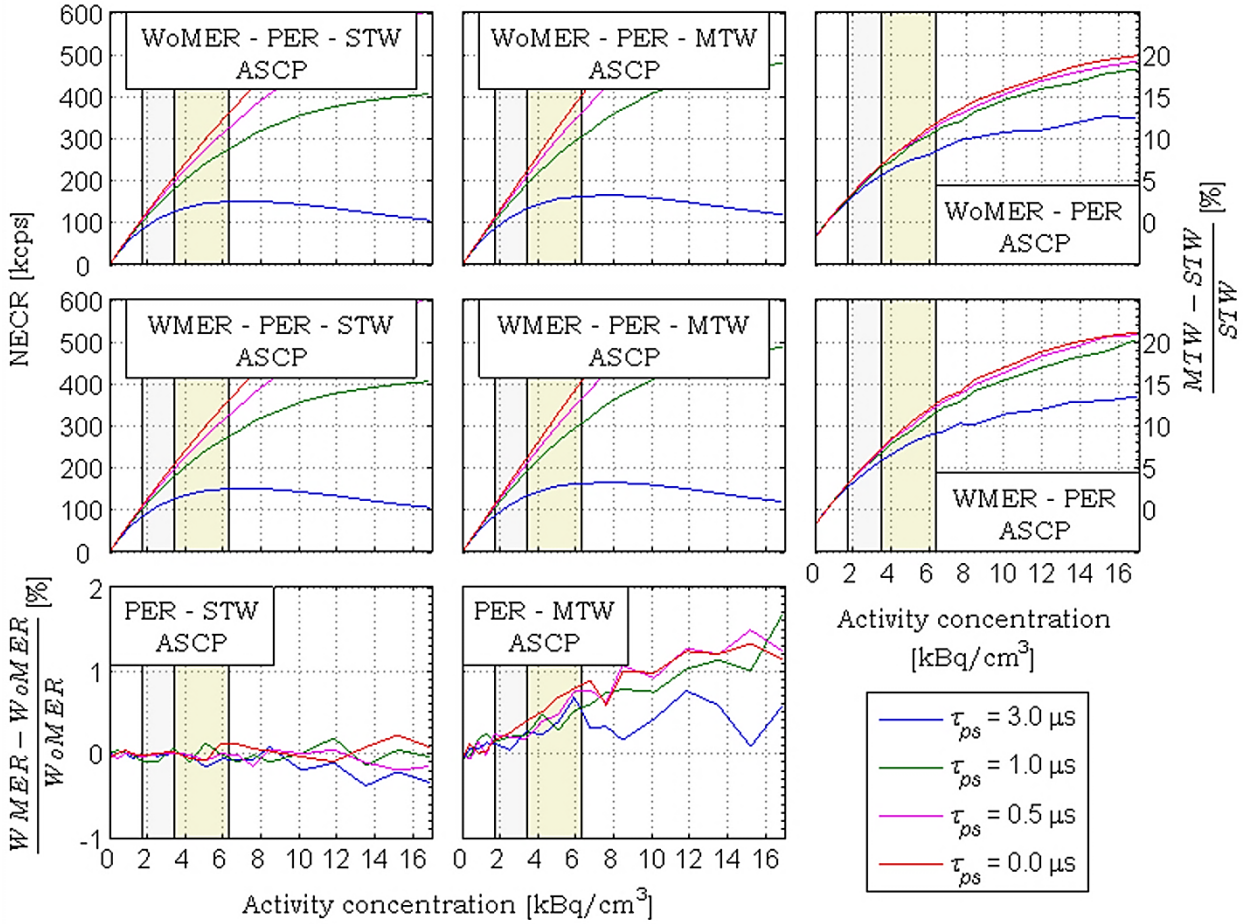

Fig. 10.14: NECR curves for the AACP data set, obtained with the standard NEMA NU2-2001 phantom, and all the combinations of the remaining parameters, with the exception of the criterion to deal with pileup events, which was set to PER. The vertical black solid lines represent the activity concentrations previously mentioned as being those present in the patient at the time of the exam (1.70 kBq cm^{-3}, 3.45 kBq cm^{-3} and 6.30 kBq cm^{-3}. The two plots in the bottom represent the percentual deviation of the NECR with the removal of multiple events relative to those without the removal, and the two right plots represent the percentual deviation of the NECR obtained for the MTW coincidence sorter relative to that obtained with the STW coincidence sorter. The shaded areas represent the previously mentioned activity concentrations for the standard NEMA NU2-2001 phantom (see text above).

10.15 (page 286), for the standard NEMA NU2-2001 phantom, processed with a value of $\tau_{ps} = 3.0$ μs for the dead time on the position signals, followed by the rejection of multiple events, with the coincidences performed by the MTW coincidence sorter and employing the GTOFR, for the AACP data set.

Once found the processing scheme that maximizes the NECR, this parameter was compared with that of the Philips Gemini TF scanner, the curves of this latter having been obtained by retrieving the data from the plots presented in [Surti et al., 2007], with the *grabit* routine [Doke, 2007] for Matlab. The results obtained for the AACP data set, with the PER criterion for dealing with pileup events, followed by the removal of multiple events, and both coincidence sorters (STW and MTW), are depicted in Fig. 10.16 (NECR curves) and in Fig. 10.17 on page 288 (expected gain in NECR of

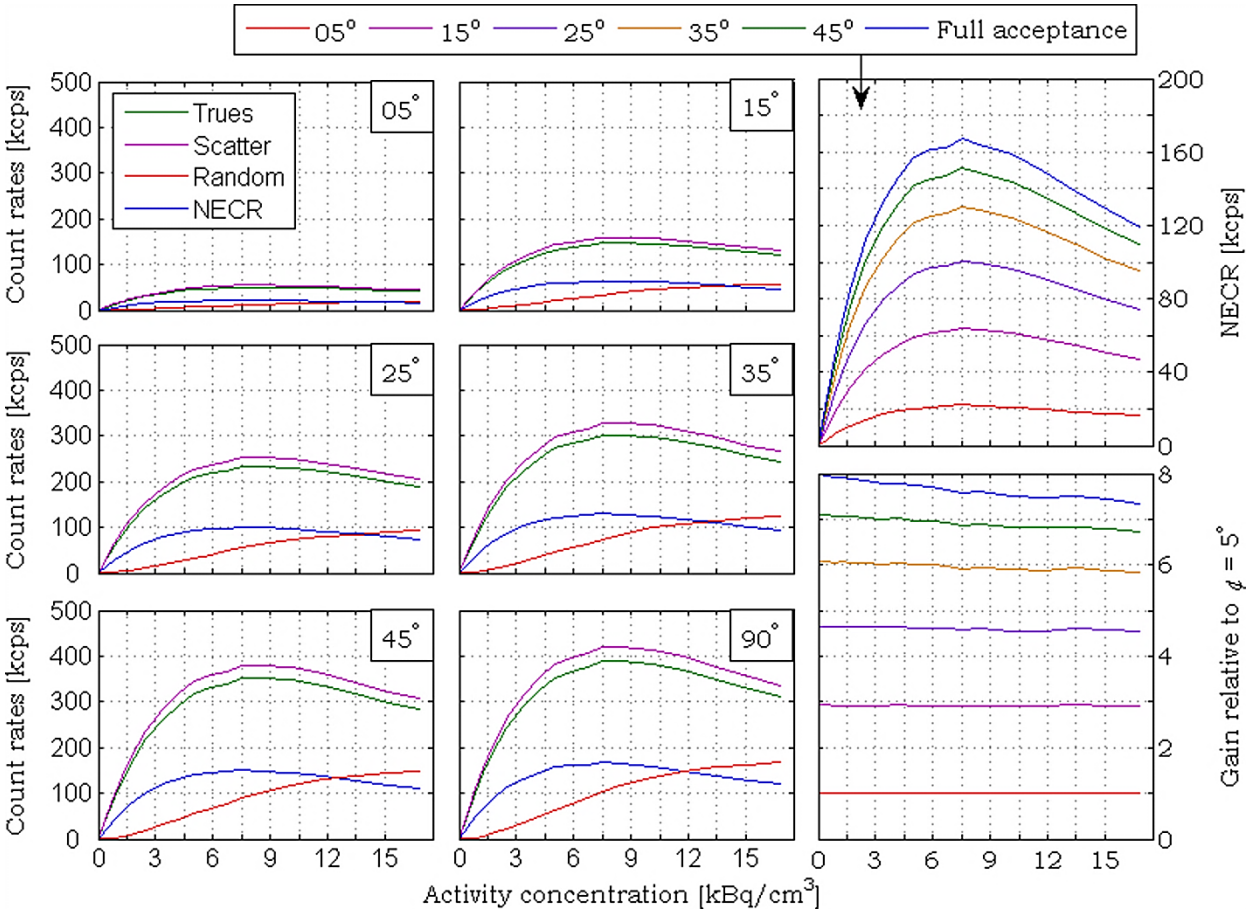

Fig. 10.15: True, Scatter and Random count rates, along with NECR (smaller plots), for several values of the polar acceptance angle, NECR curves (top right plot), and percentual gain in NECR (bottom right plot), relative that obtained for a value of 5° on the polar acceptance angle. The plots were obtained for the standard NEMA NU2-2001 phantom, processed with a value of $\tau_{ps} = 3.0$ μs for the dead time for position signals, by rejecting pileup events, followed by the removal of multiple events, with the coincidences performed by MTW coincidence sorter, and rejection of LORs done with GTOFR.

the RPC TOF-PET, relative to that of the Philips Gemini TF), for both the standard NEMA NU2-2001 and the 1800 mm axially extended phantoms.

For a value of $\tau_{ps} = 3.0\ \mu s$ for the dead time for position signals, which is the current value presented by the RPC detectors developed for testing proposes, and rejecting the events found in pileup (PER), the NECR computed for the standard NEMA NU2-2001 phantom presented a peak value of ~167 kcps at $\sim 7.6\ kBq\,cm^{-3}$, which is about 2.0 times greater than that published for the Philips Gemini TF scanner, for the same phantom and activity concentration [Surti et al., 2007]. However, for a value of $\tau_{ps} = 1.0\ \mu s$, which is seemingly achievable with dedicated efforts for speeding up the

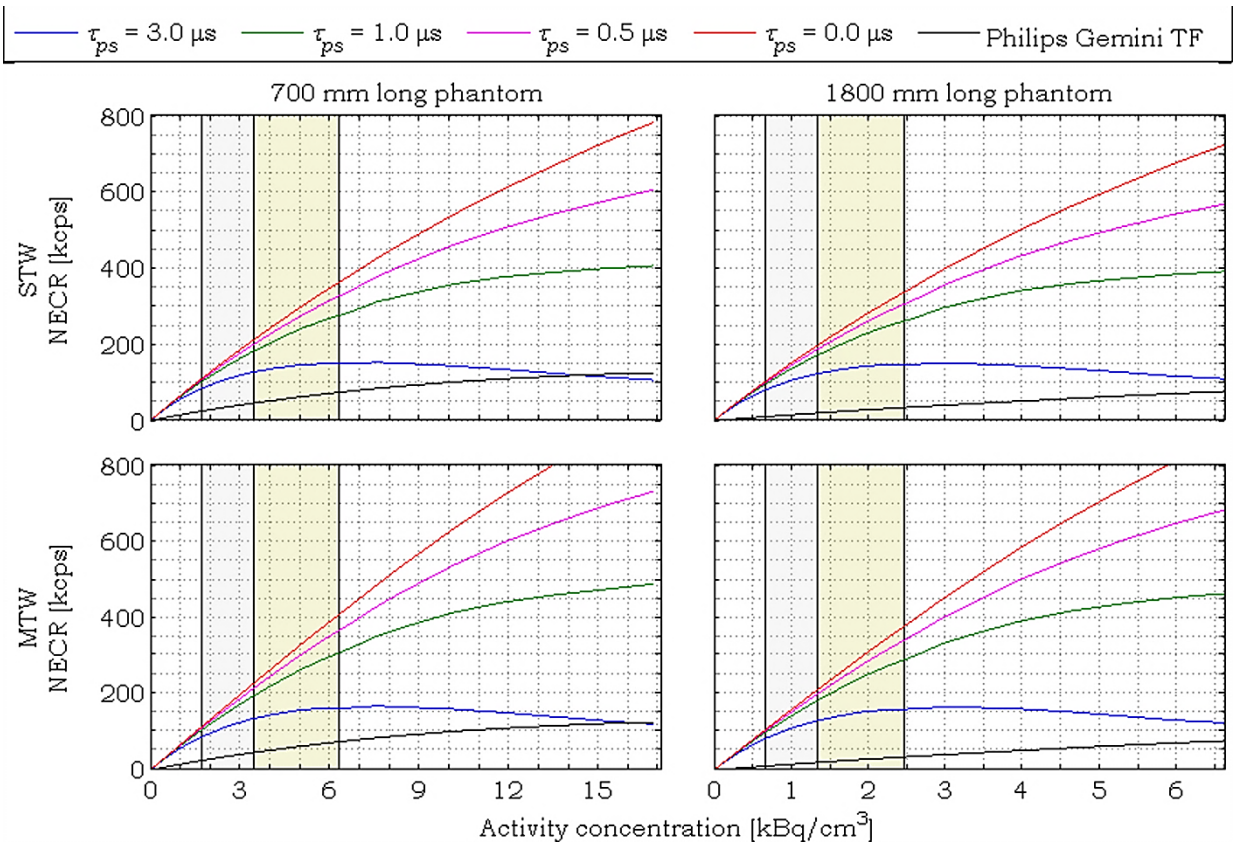

Fig. 10.16: NECR curves expected for the RPC TOF-PET scanner and published for the Philips Gemini TF scanner [Surti et al., 2007], for the AACP data set, for all the processed values of the τ_{ps} paralyzable dead time for position signals, with the PER criteria for handling pileup events, followed by the removal of multiple events, the coincidences performed by the STW and MTW coincidence sorters, with full acceptance on the polar acceptance angle, and rejection performed by the GTOFR. The plots on the left columns refer to the standard NEMA NU2-2001 phantom while those on the right column refer to the 1800 mm axially extended phantom. The top plots represent the NECR curves for the STW coincidence sorter, and the bottom plots represent the NECR curves for the MTW coincidence sorter. The shaded areas represent the previously mentioned activity concentrations for both phantoms (see text above).

electronics, no peak NECR was found for the range of simulated activity concentrations, the NECR increasing up to 485 kcps at 16.8 $kBq\,cm^{-3}$, being about 349 kcps for an activity concentration of ~ 7.6 $kBq\,cm^{-3}$, representing a gain of about 4.2 relative to the NECR reported for the Philips Gemini TF scanner, with the same phantom and activity concentration [Surti et al., 2007].

Considering the 180 cm long extended phantom, the NECR curves obtained, when plotted against the total activity in the phantom (hence in the FOV), are similar to those obtained with the standard NEMA NU2-2001 phantom, although presenting a slight decrease in the NECR for all values of τ_{ps}, relative to those observed with the standard NEMA NU2-2001 phantom. This decrease was confirmed to be a

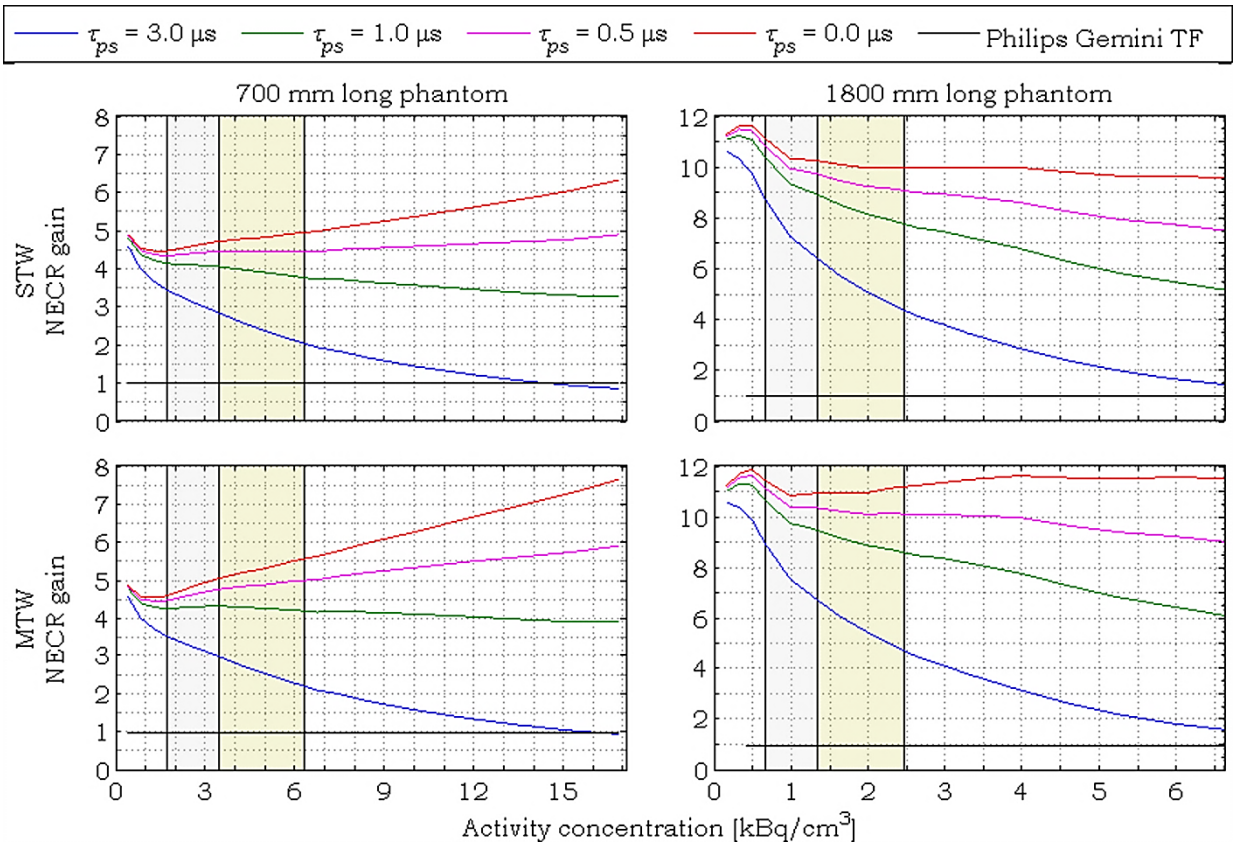

Fig. 10.17: Expected gain in NECR for the RPC TOF-PET scanner relative to that of the Philips Gemini TF scanner [Surti et al., 2007], for the AACP data set, for all the processed values of the τ_{ps} paralyzable dead time for position signals, with the PER criteria for handling pileup events, followed by the removal of multiple events, the coincidences performed by the STW and MTW coincidence sorters, with full acceptance on the polar acceptance angle, and rejection performed by the GTOFR. The plots on the left columns refer to the standard NEMA NU2-2001 phantom while those on the right column refer to the 1800 mm axially extended phantom. The top plots represent the NECR gain curves for the STW coincidence sorter, and the bottom plots represent the NECR gain curves for the MTW coincidence sorter. The shaded areas represent the previously mentioned activity concentrations for both phantoms (see text above).

consequence of the decreased geometric efficiency due to smaller solid angle coverage near the scanner ends, and also to the increased SF for the 1800 mm length phantom, when compared to that obtained with the standard NEMA NU2-2001 phantom.

Since for the same total activity present in the phantom, the activity concentrations are reduced to about 0.39 (700/1800) those present in the standard NEMA NU2-2001 phantom, the peak NECR for $\tau_{ps} = 3.0\,\mu s$ occurred at an activity concentration of $\sim 3.0\,kBq\,cm^{-3}$ $(81.08\,nCi\,cm^{-3})$, presenting a value of ~164 kcps, to which corresponds a gain in the NECR of ~5.5 relative to that reported for the Philips Gemini TF scanner at the same activity concentration, with the standard NEMA NU2-2001 phantom [Surti et al., 2007]. For a value of 1.0 μs for τ_{ps}, the NECR for the same activity concentration $(3.0\,kBq\,cm^{-3} \rightarrow 81.08\,nCi\,cm^{-3})$, was found to be of about 330 kcps, representing a gain of ~8.3 when compared to the NECR reported for the Philips Gemini TF scanner [Surti et al., 2007].

Concerning the NECR values obtained, for the simulated activity concentrations, by accepting with a coarse position all those Single events for which pileup on the position signals occurred (PEACP), it turned out to be independent of the value of τ_{ps} employed for processing the simulation data, being equal to the corresponding values obtained for the same phantoms processed with a τ_{ps} value of 0.0 μs and employing the PER criterion for rejecting Single events found in pileup. This can be explained by the errors introduced by the coarse position at the line source location, and by the method employed by the NEMA NU2-2001 to assess the NECR.

The maximum transaxial error at the detector level, due to event pileup, is equal to half the width of the readout subsections in the transaxial direction. Since the width of the active area for detection in the transaxial direction was set to 1000 mm, and a total of 10 transaxial sections were considered, each being divided in three subsections, the referred maximum error is of about 16.7 mm. This will be also the maximum error at the line source location for a particular LOR that is perpendicular to the surface of the detection heads, with both photons being detected with a coarse position with the maximum error being in the same direction. If all possible azimuthal directions, and combinations of errors in the transaxial direction, were taken and averaged, the maximum error at the source location would be smaller than the abovementioned value. Moreover, the line source has a diameter of 3.2 mm, and the central portion of the sinograms used in the NECR performance test for counting LORs as True events is 40 mm wide, corresponding to 20 mm radial distances from the LORs to the line source location. For this, True LORs accepted with a coarse transaxial position will fall in the central portion of the sinograms, thus being counted

as True events. As to the 1 cm σ Gaussian blur in the axial direction, introduced at the detector level due to the acceptance of Single events that are found in pileup, besides being smaller at the line source location, mainly when averaged for all possible LORs, it has the sole effect of attributing a particular LOR to a different slice. Since the total NECR is computed by summing the NECR values found for all slices lying in the FOV, or in the central portion of the phantom, with a margin of 25 mm from the phantom edges, the total NECR will still account for the LORs erroneously attributed to different slices from those at which the LORs would have been assigned if the fine position was known.

For the above mentioned reasons, further investigation is needed to test the spatial resolution and image quality when the PEACP criteria for dealing with Single events found in pileup is employed. However, to gain some insight for the possible impact that the PEACP criterion may have on the spatial resolution and quality of the final reconstructed images, the histograms of the distances of the LORs to the annihilation points, and the volume density of the LORs, was obtained, as in Fig. 10.6 (page 274). Fig. 10.18 depicts such plot for the simulation data obtained with the standard NEMA NU2-2001 phantom, processed with a total activity of 92.5 MBq (2.5 mCi), to which corresponds an activity concentration of $4.2\,\mathrm{kBq\,cm^{-3}}$ $\left(113.7\,\mathrm{nCi\,cm^{-3}}\right)$, with a value of $\tau_{ps} = 3.0\,\mu\mathrm{s}$ for the dead time on the position signals and the PEACP criterion for dealing with Single events for which pileup occurred, followed by the removal of multiple events, with the coincidences performed with the MTW coincidence sorter and full acceptance on the polar acceptance angle, with the rejection of LORs performed by GTOFR. The results obtained for the volume density of the LORs seems promising, in what the usability of the PEACP criterion for handling with pileup events is of concern.

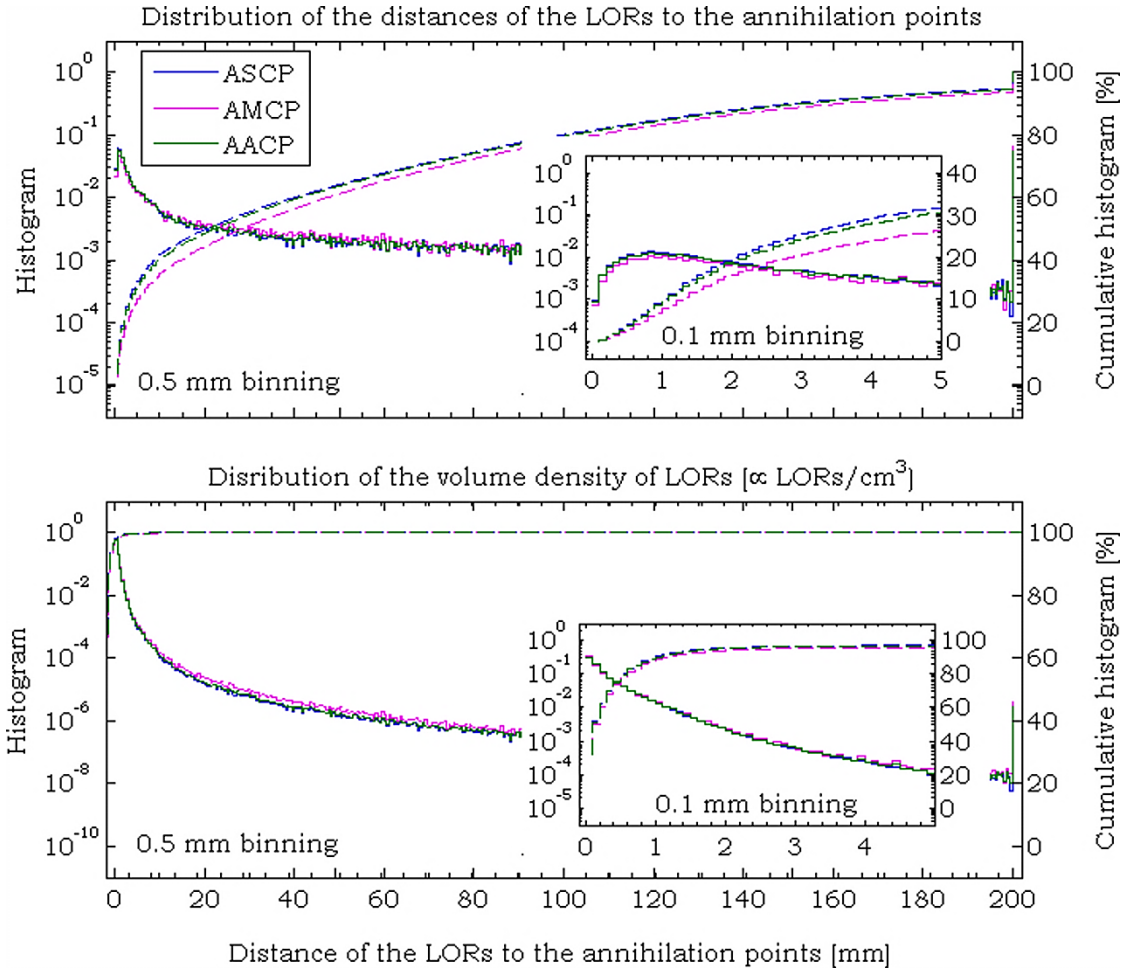

Fig. 10.18. Distribution of the distances of the LORs to the annihilation points (top), and the volume density of the LORs (bottom), as a function of the distances to the annihilation points, obtained by dividing the histograms of the distances of the LORs to the annihilation points by the volumes of the spherical shells with inner and outer radius equal do the bin edges, for all the three coincidence data sets (ASCP, AMCP and AACP). Plots were obtained for the standard NEMA NU2-2001 phantom, for a total activity in the phantom equal to 92.5 kBq (2.5 mCi), corresponding to an activity concentration of $4.2\ \mathrm{kBq\,cm^{-3}}$ $\left(113.7\ \mathrm{nCi\,cm^{-3}}\right)$, and processed with a $\tau_{ps} = 3.0\ \mu\mathrm{s}$ dead time for the position signals followed by the PEACP criterion for handling pileup events, followed by the removal of multiple events, the coincidences having been performed by using an MTW coincidence sorter, full acceptance on the polar acceptance angle, with the rejection of LORs performed by GTOFR. The bin widths of the plots and insets are equal to 0.5 mm and 0.1 mm, respectively.

CHAPTER 11
CONCLUSIONS

The aim of the present work was to assess the performance parameters of a PET scanner with 2400 mm long AFOV, based on RPC detectors, by means of simulations with the GEANT4 toolkit.

The dependence of the sensitivity to True coincidences of a PET scanner, based on BGO detectors, with the polar angle for accepting coincidences and the length of the AFOV, was studied by simulation, and complemented by an approximate analytical model, aiming at a full-body human PET system with an AFOV of about 2400 mm long. Simulations were performed with the GEANT4 toolkit and followed closely the NEMA NU-2-1994 standards. The scanner was defined as a tungsten annulus for retrieving the photon entry points, and a set of correction factors were applied to account for packing fraction and detection efficiency, according to the segmentation of the GE Advance tomograph.

The results obtained showed that the sensitivity to True events is dominated by the solid angle, growing strongly with the AFOV and with the polar acceptance angle, while the SF was found to be almost independent from the geometry, depending however on the value for the polar acceptance angle.

The sensitivity relative to that of the GE Advance PET scanner, increased by a factor of about 100 for a 2400 mm length AFOV, with full acceptance on the polar acceptance angle, and without considering a gain factor due to TOF information. The SF was found to increase slightly, from the 35% reported for the GE Advance tomograph, up to 41% for the 2400 mm long AFOV scanner, being almost independent of the AFOV for a given value of the polar acceptance angle, but increasing with this parameter. As to the results obtained with the approximate analytical model, they were in reasonable agreement with those found by simulation, showing the same trend with the polar acceptance angle and the length of the AFOV, but not the same absolute values, since no normalization was employed.

A similar study was conducted for a scanner based on RPC detectors, which presents an excellent intrinsic spatial resolution of 0.47 mm FWHM, and also an

excellent time resolution of 300 ps FWHM for photon pairs. The scanner was modelled as described above, and the detection efficiencies were obtained by simulation of a stack of 121 (61) glass plates, each with a thickness of 400 μm, separated by 120 (60) gas gaps, each with a thickness of 350 μm.

The sensitivity of the RPC TOF-PET scanner to True coincidences was found to follow the same trends as for the BGO based PET scanner, but with lower sensitivities due to the lower detection efficiency of the former detectors relative to the latter.

For a 2400 mm long AFOV RPC TOF-PET scanner with full acceptance on the polar acceptance angle, and based on the detection efficiencies computed for the stack of 61 glass plates, the sensitivity was found to be up to 7.3 (or 1.7) times higher than that of the GE Advance tomograph if a TOF gain factor of 4.4 is considered (without the TOF gain factor), with the SF ranging from 36.8% for a 150 mm long AFOV up to 46.6% for the 2400 mm long AFOV.

For the stack of 121 glass plates the Trues sensitivity of a 2400 mm long AFOV RPC TOF-PET scanner was found to be up to 20 (or 5) times higher than that of the GE Advance tomograph, if a TOF gain of 4.4 was considered (without TOF gain), with the SF ranging from 38% for the 150 mm long AFOV, up to 46.4% for the 2400 mm long AFOV. However, these SFs do not include scatter in the detector, accounting only for the fraction of scatter from the phantom accepted by the scanner.

With the aim of parameterizing the detection in each glass plate, and then save computation time in the simulations, by killing all the electron tracks leaving only those of photons, a study was conducted to assess the extraction efficiencies of a single glass plate, in the forward and backward directions, as a function of the incident photon energy and angle relative to the direction perpendicular to the surface of the glass plates. With the parameterization in the form of a 2D array, the efficiencies could then be computed by bilinear or even spline interpolation. However, the bilinear interpolation did not hold the same results, leading to increased detection efficiencies, and to an increase of the computation time, which worsened for the spline interpolation. However, the study led to interesting results, which were also in accordance with the detection efficiency observed for experimental RPC detectors.

It was found that the extraction efficiencies in the forward and backward directions are very different, strongly depending on both the angle with which the photons impinge on the detector surface, and the photon energy. The extraction efficiency in the forward direction was found to be considerably higher than that in the backward direction for values of the incidence angle up to 60°, starting then to decrease. However, the extraction efficiency in the backward direction starts to

increase significantly for energies of the incident photon above a few hundred keV.

From this study, the possibility of developing the RPC TOF-PET scanner with the detectors aligned around a cylindrical annulus, and with appropriate angular pitch, was still raised, and some drawings for the mechanical arrangement were done. However, since it was concluded that this arrangement would pose problems regarding the mechanical stability of the scanner, it has been abandoned, in favour of a parallelepipedic shape. Yet, a more detailed study of this arrangement may lead to the conclusion that the effort of solving the problems related to the mechanical stability may be worth attention

Following the above mentioned simulations, the optimization of an RPC detector to be employed in the development of a human PET scanner, with a parallelepipedic shape and 2400 mm long AFOV, defined by four detection heads, with the RPC detector faces aligned parallel to the cases of the detection heads, was performed by detailed simulations in GEANT4.

The detection head consisted of a stack of 20 RPC detectors formed by two detection modules, each containing 5 gaps with 350 μm thick and delimited by 6 glass plates. The layers of insulators, high voltage electrodes and signal pickup electrodes, with the correct thicknesses and materials, were also defined.

Based on the results previously obtained for the single glass plate, 511 keV photons were fired with an angular distribution, relative to the perpendicular to the detection head surface, comprised between 0° and 60° degrees, and sampled such that the edges of the unit vectors defining the initial direction of the photons were uniformly distributed over the surface of a sphere.

The simulation data obtained was then processed to account for the detector readout by considering a $\tau_{ts} = 200$ ns non-paralyzable dead time for the time signals, so that the extraction of multiple electrons into the same gas gap did not falsely increase the detection efficiency. The detection efficiency was computed as the quotient of the Single events, returned from the detector readout processing stage, by the total number of photons fired. The procedure was repeated for several glass plate thicknesses, and the thickness that maximized the detection efficiency was then computed by spline interpolation between the obtained efficiencies, holding a value of 200 μm, with a MIF of about 32% for a 2 mm binning on the distance of the LORs to the annihilation points. Fortunately, 200 μm borosilicate glasses are readily available on the market, and the cross sections for photon interactions are indistinguishable from those of soda lime glass, which was the material used to define the glass plates.

The spatial resolution of the scanner with the structure described in the previous

procedure for optimization of the glass plates thickness, was then assessed, with a minor modification in the RPC detectors, and hence in the detection heads, which contained a stack of 40 RPC detectors with 6 glass plates with individual thicknesses of 200 μm, separated by 5 gas gaps with individual thicknesses of 350 μm, corresponding to the detection modules mentioned above. The phantom consisted of a spherical core with 1 μm diameter surrounded by a 2 mm diameter shell of PMMA, with the source consisting of positrons at rest, uniformly distributed in the phantom core volume. The annihilation was performed both with and without considering photon acollinearity.

The simulation data was processed to account for detector readout as implemented in RPC detectors for testing proposes, the coincidences were performed by a STW coincidence sorter, and only those LORs traversing the scanner bore with a polar angle equal to less than 9° were accepted.

The spatial resolution was then assessed according to the prescriptions of the NEMA NU2-2001 standards, but considering a single point placed in the central slice of the scanner and 100 mm off-axis in both directions of the transaxial plane.

For the readout position, and considering photon acollinearity, a spatial resolution of 0.9, 1.4 and 2.1 mm was found for a detector binning along the transaxial and axial directions of, respectively, 0, 1 and 2 mm, and a detector binning along the radial direction of 3.44 mm. These results allow concluding that the RPC TOF-PET scanner is expected to achieve higher spatial resolutions than those attained by the currently available state of the art PET scanners, if the position signal can be considered as being essentially continuous or if a binning of 1 mm is required in both the axial and transaxial directions, or at least reach the same spatial resolution, if the detector binning in the transaxial and axial directions has to be set to 2 mm.

Finally, the SF, count rates and NECR of a full body RPC TOF-PET scanner was assessed following the NEMA NU2-2001 standards, and compared to the same parameters of commercially available state of the art PET scanners. The study was conducted by detailed simulations with GEANT4, considering the current design of the RPC detectors developed for testing proposes, and several triggering strategies for accepting Single events found in pileup (PER and PEACP), the removal of multiple events arising from multiple interactions of the same photon, the coincidences being then processed with both the STW and the MTW coincidence sorters, and imposing different values for the polar acceptance angle, followed by geometric constraining of the LORs by different methods that included, among others, the GR and the GTOFR, and by analysing three different data sets (ASCP, AMCP and AACP).

The best combination of the processing parameters was found to be the removal of multiple events by a time/distance relation based on simple kinematics of light, the coincidences being then performed by a MTW coincidence sorter for full acceptance on the polar acceptance angle, followed by the constraining of LORs to those for which the direct TOF reconstructed point fall inside a tight region of interest surrounding the phantom, and finally accepting all possible pairs of coincidences. This is further supported by the fact that, for low activity concentrations, about 45% of all possible single pairs of photons that can be formed from the AMCP data set correspond to True events.

The SF obtained for the standard NEMA NU2-2001 phantom was found to be 51.8%, which is about 40% to 92% higher than those reported for three state of the art commercially available PET scanners with TOF information, for the same phantom. However, it was also found that the scatter in the detector is long- range, which possibly may not compromise the quality of the final reconstructed image. For the 1800 mm axially extended phantom the SF obtained, with the same set of processing parameters, was found to be 53.7%, which is about 45% to 99% higher than those presented by the aforementioned state of the art PET scanners.

As to the NECR, it was found to strongly depend on the τ_{ps} paralyzable dead time for position signals. For the current value of $\tau_{ps} = 3.0\ \mu s$, and for the standard NEMA NU2-2001 phantom, a peak NECR of ~167 kcps at $\sim 7.6\ kBq\,cm^{-3}$ was found, which is about 2.0 times higher than the one published for the Philips Gemini TF scanner with the same phantom and activity concentration. However, for a value of $\tau_{ps} = 1.0\ \mu s$, which is seemingly achievable with dedicated efforts for speeding up the electronics, no peak NECR was found for the range of simulated activity concentrations, the NECR increasing up to 485 kcps at $16.8\ kBq\,cm^{-3}$, being of about 349 kcps for an activity concentration of $\sim 7.6\ kBq\,cm^{-3}$, representing a gain of about 4.2 relative to the NECR reported for the Philips Gemini TF scanner with the same phantom and activity concentration.

For the 1800 mm long extended phantom, the peak NECR for $\tau_{ps} = 3.0\ \mu s$ was of ~164 kcps for an activity concentration of $\sim 3.0\ kBq\,cm^{-3}$ $\left(81.08\ nCi\,cm^{-3}\right)$, corresponding to a gain in NECR of ~5.5 relative to that reported for the Philips Gemini TF scanner at the same activity concentration with the standard NEMA NU2-2001 phantom. For a value of 1.0 μs for τ_{ps}, the NECR for the same activity concentration $\left(3.0\ kBq\,cm^{-3} \rightarrow 81.08\ nCi\,cm^{-3}\right)$ was found to be of about 330 kcps, representing a gain of ~8.3 when compared to the NECR reported for the Philips Gemini TF scanner.

It was also verified that, by adding a thin lead foil to the detection head, the energy spectrum of photons immediately before the interaction leading to detection is hardened, with the consequent shifting of the spectrum toward higher energies. This raises the hope of improving the values obtained for the SF and NECR. For instance, it may be possible that a thinner lead foil interposed between each RPC detector could lead to improved results relative to those obtained with a single lead foil placed at the scanner surface. However, it was also verified that the fraction of photons detected with 511 keV decreases with the increase of the lead foil thickness. So, detailed studies are needed to assess the best way of performing the energy hardening and, consequently, of increasing the energy sensitivity of the detection system, in order to compensate for the lack of energy resolution of the RPC detectors.

The results resumed so far allow concluding that the RPC TOF-PET scanner is expected to outperform currently available commercial state of the art PET scanners.

BIBLIOGRAPHY

Abrunhosa A. & Prata M. I. (2008), "Radiofármacos: desenvolvimento e principais aplicações". In Lima J. J. P. d., editor *Física em Medicina Nuclear*, Ch. 4, pp. 119-59. Imprensa da Universidade de Coimbra, Coimbra, Portugal, Abril 2008. ISBN: 978-989-8074-26-3.

Adam L.-E., Karp J. S., Daube-Witherspoon M. E. & Smith R. J. (2001), "Performance of a Whole-Body PET Scanner Using Curve-Plate NaI(Tl) Detectors". *Journal of Nuclear Medicine*, vol. 42, no. 12, pp. 1821-30, 1 December 2001.

Agostinelli S., Allison J., Amako K. . A. J., Araujo H., Arce P. et al. (2003), "Geant4—a simulation toolkit". *Nuclear Instruments and Methods in Physics Research A*, vol. 506, iss. 3, pp. 250-303, 1 July 2003. DOI: 10.1016/S0168-9002(03)01368-8.

Allison J., Amako K., Apostolakis J., Araujo H., Dubois P. A. et al. (2006), "Geant4 developments and applications". *IEEE Transactions on Nuclear Science*, vol. 53, iss. 1, pp. 270 - 278, February 2006. DOI: 10.1109/TNS.2006.869826.

Angeli I. (1999), *Table of nuclear root mean square charge radii*. Technical report INDC(HUN)-033. International Atomic Energy Agency, International Nuclear Data Committee, Nuclear Data Section, Wagramer Strasse 5, A-1400, Vienna, Austria, September 1999. (Available at http://www-nds.iaea.org/publications/indc/indc-hun-0033.pdf, retrieved at 17:22 on 10 September 2012.)

Attix F. H. (1986), "Introduction to Radiological Physics and Radiation Dosimetry". Ch. Gamma- and X-Ray Interactions in Matter, pp. 124-59. John Wiley & Sons, Inc., November 1986. ISBN: 978-0-471-01146-0.

Badawi R. , Kohlmyer S. G., Harrison R. L., Vannoy S. D. & Lewellen T. K. (2000), "The Effect of Camera Geometry on Singles Flux, Scatter Fraction and Trues and Randoms Sensitivity for Cylindrical 3D PET - a Simulation Study". *IEEE Transactions on Nuclear Science*, vol. 47, iss. 3, pp. 1228-32, June 2000. DOI: 10.1109/23.856575.

Bateman J. E., Connolly J. F., Stephenson R. & Flesher A. C. (1980), "The development of the Rutherford laboratory MWPC positron camera". *Nuclear Instruments and Methods*, vol. 176, iss. 1-2, pp. 83-88, 1 October 1980. DOI: 10.1016/0029-554X(80)90685-0.

Bell Z. W. (2012), "Scintillation Counters". In Grupen C. & Buvat I., editors *Handbook of Particle Detection and Imaging*, Ch. 15, pp. 349-75. Springer-Verlag, Germany, 2012. ISBN: 978-3-642-13270-4.

Berger M. J., Coursey J. S., Zucker M. A. & Chang J. (2005), *Stopping-Power and Range Tables for Electrons, Protons, and Helium Ions*. Available at http://www.nist.gov/pml/data/star/index.cfm. Accessed on 7 July 2013.

Berger M. J., Hubbell J. H. . S. S. M., Chang J., Coursey J. S., Sukumar R. et al. (2011), *XCOM: Photon Cross Sections Database*. Available at http://www.nist.gov/pml/data/xcom/index.cfm. Accessed on 10 March 2013.

Bettinardi V., Presotto L., Rapisarda E., Picchio M., Gianolli L. & Gilardi M. C. (2011), "Physical Performance of the new hybrid PET=CT Discovery-690". *Medical Physics*, vol. 38, iss. 10, pp. 5394-411, October 2011. DOI: 10.1118/1.3635220.

Blanco A. (2011), *A Small Animal PET Prototype With Sub-Millimetre Spatial Resolution Based on tRPCs*. PhD Thesis. Universidade de Santiago de Compostela, Facultad de Física, Departamento de Física de Partículas, Santiago de Compostela, Galicia, Spain, Diciembre 2011. (Available at http://hdl.handle.net/10347/3688, on 01/04/2013 at 00:55.)

Blanco A., Carolino N., Correia C. M. B. A., Fazendeiro L., Ferreira N. C. et al. (2006), "RPC-PET: A New Very High Resolution PET Technology". *IEEE Transactions on Nuclear Science*, vol. 53, iss. 5, pp. 2489-94, October 2006. DOI: 10.1109/TNS.2006.876005.

Blanco A., Chepel V., Ferreira-Marques R., Fonte P., Lopes M. I. et al. (2003a), "Perspectives for positron emission tomography with RPCs". *Nuclear Instruments and Methods in Physics Research A*, vol. 508, iss. 1-2, p. 88–93, DOI: 10.1016/S0168-9002(03)01283-X.

Blanco A., Couceiro M., Crespo P., Ferreira N. C., Marques R. F. et al. (2009), "Efficiency of RPC detectors for whole-body human TOF-PET". *Nuclear Instruments and Methods in Physics Research A*, vol. 602, iss. 3, p. 780–783, 1 May 2009. DOI: 10.1016/j.nima.2008.12.134.

Blanco A., Marques R. F., Finck C., Fonte P., Gobbi A. & Policarpo A. (2003b), "Single-Gap Timing RPCs with Bidimensional Position Sensitive Readout Very Accurate TOF systems". *Nuclear Instruments and Methods in Physics Research A*, vol. 508, iss. 1-2, pp. 70-74, DOI: 10.1016/S0168-9002(03)01279-8.

Born M. (1990), *Atomic Physics*, 8th edition. Translated by: R. J. Blin-Stoyle & J. M. Radcliffe. Dover Publications Inc., London, UK, 1 May 1990. ISBN: 978-0486659848.

Bromley J. T. (1994), *Investigation of the Operation of Resistive Plate Chambers*. MSc. University of Manchester, Faculty of Science and Engineering, Department of Physics and Astronomy, Manchester, United Kingdom, September 1994. (Available at http://www.hep.man.ac.uk/theses/jane.ps.gz)

Brucer M. (1978), "Nuclear Medicine Begins with a Boa Constrictor". *Journal of Nuclear Medicine*, vol. 19, No. 6, pp. 581-98, 1978.

Burkhardt H., Grichine V. M., Gumplinger P., Ivanchenko V. N., Kokoulin R. P. et al. (2004), "Geant4 Standard Electromagnetic Package for HEP applications". In *Proceedings of the IEEE Nuclear Science Symposium and Medical Imaging Conference*, Rome, Italy, 16-22 October 2004 2004, pp. 1907-1910, Vol. 3. DOI: 10.1109/NSSMIC.2004.1462617.

Buvat I. & Castiglioni I. (2002), "Monte Carlo simulations in SPET and PET". *The Quarterly Journal of Nuclear Medicine*, vol. 46, no. 1, pp. 48-61, March 2002.

Carron N. J. (2007), *An Introduction to the Passage of Energetic Particles to Matter*. Taylor & Francis, 2007. ISBN: 978-0-7503-0935-6.

Charpak G., Bouclier R., Bressani T., Favier J. & Zupančič Č. (1968), "The use of multiwire proportional counters to select and localize charged particles". *Nuclear Instruments and Methods*, vol. 62, iss. 3, pp. 262-68, 1 July 1968. DOI: 10.1016/0029-554X(68)90371-6.

Chauvie S., Guatelli S., Ivanchenko V., Longo F., Mantero A. et al. (2004), "Geant4 Low Energy Electromagnetic Physics". In *Proceedings of the IEEE Nuclear Science Science Symposium and Medical Imaging Conferece*, Rome, Italy, 16-22 October 2004 2004, pp. 1881-1885, Vol.3. DOI: 10.1109/NSSMIC.2004.1462612.

Cherry S. R. & Dahlbom M. (2006), *PET: Physics, Instrumentation, and Scanners*. Editor: M. E. Phelps. Springer Science+Business Media, LLC, USA, 2006. ISBN: 978-0-387-32302-2.

Chinn G. & Levin C. S. (2008), "A Method to Reject Random Coincidences and Extract True from Multiple Coincidences in PET using 3-D Detectors". In *Proceedings of the 2008 IEEE Nuclear Science Symposium and Medica Image Conference*, Dresden, Germany, 19-25 October 2008 2008, pp. M10-414. DOI: 10.1109/NSSMIC.2008.4774418.

Comtat C. (2012), "Image Reconstruction". In Grupen C. & Buvat I., editors *Handbook of Particle Detection and Imaging*, Ch. 39, pp. 973-1006. Springer-Verlag, Germany, 2012. ISBN: 978-3-642-13270-4.

Conti M. (2009), "State of the art and challenges of time-of-flight PET". *Physica Medica*, vol. 25, iss. 1, pp. 1-11, March 2009. DOI: 10.1016/j.ejmp.2008.10.001.

Conti M., Bendriem B., Casey M., Eriksson L., Jakoby B. et al. (2006), "Performance of a high sensitivity PET scanner based on LSO panel detectors". *IEEE Transactions on Nuclear Science*, vol. 53, iss. 3, pp. 1136-42, June 2006. DOI: 10.1109/TNS.2006.875153.

Couceiro M., Crespo P., Marques R. F. & Fonte P. (2012), "Scatter Fraction, Count Rates, and Noise Equivalent Count Rate of an RPC TOF-PET System: Simulation Study Following the NEMA NU2-2001 Standards". In *Proceedings of the IEEE 2012 Nuclear Science Symposium and Medical Imaging Conference*, Anaheim, CaliforniaUSA, 29 October - 3 November 2012 2012.

Coursey J. S., Schwab D. J., Tsai J. J. & Dragoset R. A. (2011), *Atomic Weights and Isotopic Compositions with Relative Atomic Masses*. Available at http://www.nist.gov/pml/data/comp.cfm. Accessed on 8 February 2013.

Crespo P., Reis J., Couceiro M., Blanco A., Ferreira N. C. et al. (2012), "Whole-Body Single-Bed Time-of-Flight RPC-PET: Simulation of Axial and Planar Sensitivities With NEMA and Anthropomorphic Phantoms". *IEEE Transactions on Nuclear Science*, vol. 59, iss. 3, pp. 520-29, June 2012. DOI: 10.1109/TNS.2012.2182677.

Crosetto D. B. (2003), "The 3D Complete Body Screening (3D-CBS) Features and Implementation". In *Proceedings of the IEEE Nuclear Science Symposium and Medical Imaging Conference*, Portland, OregonUSA, 19-25 October 2003, pp. 2415 - 2419. DOI: 10.1109/NSSMIC.2003.1352382.

Dahlbom M. (2012), "PET Imaging: Basics and New Trends". In Grupen C. & Buvat I., editors *Handbook of Particle Detection and Imaging*, Ch. 38, pp. 935-71. Springer-Verlag, Germany, 2012. ISBN: 978-3-642-13270-4.

Daube-Witherspoon M. E. & Muehllehner G. (1987), "Treatment of Axial Data in Three-Dimensional PET". *Journal of Nuclear Medicine*, vol. 28, no. 11, pp. 1717-24, November 1987.

Defrise M. & Kinahan P. E. (1998), "Data Acquisition and Image Reconstruction for 3D PET". In Bendriem B. & Townsend D. W., editors *The Theory and Practive of 3D PET*, Ch. 2, pp. 11-53. Kluwer Academic Publishers, Netherlands, 29 June 1998. ISBN: 978-0792351085.

Defrise M., Kinahan P. E., Townsend D. W., Michel C., Sibomana M. & Newport D. F. (1997), "Exact and Approximate Rebinning Algorithms for 3-D PET Data". *IEEE Transacions on Nuclear Science*, vol. 16, iss. 2, pp. 145-58, April 1997. DOI: 10.1109/42.563660.

Doke J. (2007, *GRABIT - Extracts data points from an image file*. Available at http://www.mathworks.com/matlabcentral/fileexchange/7173-grabit. Accessed on 23 February 2012.

Eberhardt C. (2006, *Photomultiplier tube*. Available at http://en.wikipedia.org/wiki/File:Photomultipliertube.svg. Accessed on 14 June 2013.

Eisberg R. M. & Resnick R. (1985), *Quantum Physics of Atoms, Molecules, Solids, Nuclei and Particles*, 2nd edition. John Wiley & Sons, Inc., New York, USA, 1985. ISBN: 0-471-87373-X.

Eriksson L., Townsend D., Conti M., Eriksson M., Bohm C. et al. (2006), "Future instrumentation in positron emission tomography". In *Proceedings of the IEEE Nuclear Science Symposium and Medical Imaging Conference*, San Diego, CaliforniaUSA, 29 October - 1 November 2006, pp. 2542-45. DOI: 10.1109/NSSMIC.2006.354427.

Eriksson L., Wienhard K. & Dahlbom M. (1994), "A Simple Data Loss Model for Positron Camera Systems". *IEEE Transactions on Nuclear Science*, vol. 41, iss. 4, pp. 1566-70, August 1994. DOI: 10.1109/23.322950.

Evans R. D. (1955), *The Atomic Nucleus*. Tata McGraw-Hill Publishing Company Ltd., India, 1955.

Fonte P. (2000), "High-resolution timing of MIPs with RPCs - a model". *Nuclear Instruments and Methods in Physics Research A*, vol. 456, iss. 1-2, pp. 6-10, 21 December 2000. DOI: 10.1016/S0168-9002(00)00953-0.

Fonte P. (2012), "Review of RPC simulation and modelling". In *Proceedings of the XI workshop on Resistive Plate Chambers and Related Detectors (RPC2012)*, INFN-Laboratori Nazionali di Frascati, Italy, 5-10 February 2012 2012. (Available at http://pos.sissa.it/archive/conferences/159/033/RPC2012_033.pdf, Consulted in 14 May 2013.)

Fonte P., Lopes L., Blanco A. & Couceiro M. (2010), *Dispositivo para Tomografia de Emissão de Positrões com tempo de voo de corpo inteiro num único varrimento e correspondente método de leitura*. Portuguesa patent no. 104303. Assignee: Laboratório de Instrumentação e Física Experimental de Partículas.

Fonte P. & Peskov V. (2002), "High-resolution TOF with RPCs". *Nuclear Instruments and Methods in Physics Research A*, vol. 477, iss. 1-3, pp. 17-22, 21 January 2002. DOI: 10.1016/S0168-9002(01)01914-3.

Geant4 Collaboration (2008a), *Geant4 User's Guide for Application Developers - Geant4 version 9.2*.

Geant4 Collaboration (2008b), *Physics Reference Manual - Geant4 version 9.2*.

Griffiths D. (2008), *Introduction to Elementary Particles*, 2nd edition. Wiley-VCH Verlag GmbH & Co., Germany, 13 October 2008. ISBN: 978-3-527-40601-2.

Guyton A. C. (1990), *Textbook of Medical Physiology*, 8th edition. Harcourt College Pub, October 1990. ISBN: 978-0721630878.

Harrison R. (2011), *Simulation System for Emission Tomography (SimSET) Home Page*. Available at http://depts.washington.edu/simset/html/simset_main.html. Accessed on 13 April 2013.

Harrison R. L., Vannoy S. D., R. H. D., Gillipsie S. B., S. K. M. & Lewellen T. K. (1993), "Preliminary experience with the photon history generator module of a public domain simulation system for emission tomography". In *Proceedings of the IEEE Nuclear Science Symposium and Medical Imaging Conference*, San Francisco, USA, 31 October - 6 November 1993 1993, pp. 1154-58. DOI: 10.1109/NSSMIC.1993.701828.

Heitler W. (2010), *The Quantum Theory of Radiation*, 3rd edition. Dover Publications, Inc., New York, USA, 18 October 2010. ISBN: 978-0486645582.

Hubbell J. H. & Øverbø I. (1979), "Relativistic Atomic Form Factors and Photon Coherent Scatter Cross Sections". *Journal of Physical and Chemical Reference Data*, vol. 8, no. 1, pp. 69-105, 1979. DOI: 10.1063/1.555593. (Available at http://www.nist.gov/data/PDFfiles/jpcrd133.pdf)

Hubbell J. H., Veigele W. J., Briggs E. A., Brown R. T., Cromer D. T. & Howerron R. J. (1975), "Atomic Form Factors, Incoherent Scattering Functions, and Photon Scattering Cross Sections". *Journal of Physical and Chemical Reference Data*, vol. 4, no. 3, pp. 471-538, 1975. DOI: 10.1063/1.555523. (Available at http://www.nist.gov/data/PDFfiles/jpcrd67.pdf)

Humm J. L., Rosenfeld A. & Del Guerra A. (2003), "From PET detectors to PET scanners". *European Journal of Nuclear Medicine and Molecular Imaging*, vol. 30, iss. 11, pp. 1574-97, November 2003. DOI: 10.1007/s00259-003-1266-2.

Jakoby B. W., Bercier Y., Conti M., Casey M. E., Bendriem B. & Townsend D. W. (2011), "Physical and clinical performance of the mCT time-of-flight PET/CT scanner". *Physics in Medicine and Biology*, vol. 56, no. 8, p. 2375–2389, 22 March 2011. DOI: 10.1088/0031-9155/56/8/004.

Jan S., Santin G., Strul D., Staelens S., Assié K. et al. (2004), "GATE: a simulation toolkit for PET and SPECT". *Physics in Medicine and Biology*, vol. 49, no. 19, p. 4543–4561, 2004. DOI: 10.1088/0031-9155/49/19/007.

Jeavons A. P., Chandler R. A. & Dettmar C. A. R. (1999), "A 3D HIDAC-PET Camera with Sub-millimetre Resolution for Imaging Small Animals". *IEEE Transactions on Nuclear Science*, vol. 46, no. 3, pp. 468-73, June 1999. DOI: 10.1109/23.775564.

Johnston B. D., McDaniel D. L. & Colsher J. G. (1994), *Gamma Ray Detector for PET Scanner*. US patent no. 5300782. Assignee: General Electric Company.

Karp J. S., Muehllehner G., Mankoff D. A., Ordonez C. E., Ollinger J. M. et al. (1990), "Continuous-Slice PENN-PET: A Positron Tomograph with Volume Imaging Capability". *Journal of Nuclear Medicine*, vol. 31, no. 5, pp. 617-27, 1 May 1990.

Kemp B., Williams J., Ruter R., Lowe V. & Mullan B. (2009), "Performance measurements of a whole body PET/CT system with time-of-flight capability". *The Journal of Nuclear Medicine*, vol. 50, Supl. 2, p. 1546, 2009.

Kinahan P. E. & Karp J. S. (1994), "Figures of merit for comparing reconstruction algorithms with a volume-imaging PET scanner". *Physics in Medicine an Biology*, vol. 39, iss. 3, pp. 631-42, March 1994. DOI: 10.1088/0031-9155/39/3/024.

Knoll G. F. (2010), *Radiation Detection and Measurement*, 4th edition. John Wiley & Sons, Inc., USA, 16 August 2010. ISBN: 978-0470131480.

Krane K. S. (1988), *Introductory Nuclear Physics*. John Wiley & Sons, Inc., 1988. ISBN: 0-471-80553-X.

Križan P. (2012), "Photon Detectors". In Grupen C. & Buvat I., editors *Handbook of Particle Detection and Imaging*, Ch. 13, pp. 297-311. Springer-Verlag, Germany, 2012. ISBN: 978-3-642-13270-4.

LCA-UC (2009), *Advanced Computing Laboratory*. Available at http://www.uc.pt/lca/. Accessed on 9 July 2013.

Levin C. (2004), "Basic Physics of Radionuclide Imaging". In Wernick M. N. & Aarsvold J. N., editors *Emission Tomography: The Fundamentals of PET and SPECT*, Ch. 4, pp. 53-88. Elsevier Academic Press, San Diego, California, USA, 2004. ISBN: 0-12-744482-3.

Lewellen T. K. (2008), "Recent developments in PET detector technology". *Physics in Medicine and Biology*, vol. 53, no. 17, p. R287–R317, 7 September 2008. DOI: 10.1088/0031-9155/53/17/R01.

Lewellen T. K., Kohlmyer S. G., Miyaoka R. S., Kaplan M. S., Stearns C. W. & Schubert S. F. (1995), "Investigation of the performance of the General Electric Advance positron emission tomograph in 3D mode". In *Proceedings of the IEEE Nuclear Science Symposium and Medical Imaging Conference*, San Francisco, CaliforniaUSA, 21-28 October 1995, pp. 1786-90. DOI: 10.1109/NSSMIC.1995.501931.

LIP-CA (2007), *Laboratory of Instrumentation and Experimental Particle Physics Computing facility*. Available at http://coimbra.lip.pt/computing/. Accessed on 9 July 2013.

Lippman C., Vincke H. & Riegler W. (2009), "Simulation of RPC performance for 511 keV photon detection". *Nuclear Instruments and Methods in Physics Research A*, vol. 602, iss. 3, pp. 735-39, 1 May 2009. DOI: 10.1016/j.nima.2008.12.102.

Mertens J. D. & Bhend W. L. (1993), *Coincidence Detector for a PET Scanner*. Patent no. 5241181. Assignee: General ELectric Company.

Mohr P. J., Taylor B. N. & Newell D. B. (2012), "CODATA Recommended Values of the Fundamental Physical Constants: 2010". *Reviews of Modern Physics*, vol. 84, iss. 4, pp. 1527-605, 13 November 2012. DOI: 10.1103/RevModPhys.84.1527.

Moses W. W. (2003), "Time of Flight in PET Revisited". *IEEE Transactions on Nuclear Science*, vol. 50, no. 5, pp. 1325-30, October 2003. DOI: 10.1109/TNS.2003.817319.

Moses W. W. (2011), "Fundamental limits of spatial resolution in PET". *Nuclear Instruments and Methods in Physics Research A*, vol. 648, Sup. 1, p. S236–S240, 21 August 2011. DOI: 10.1016/j.nima.2010.11.092.

Moses W. W. & Derenzo S. E. (1996), "Scintilators for positron emission tomography". In *Proceedings of the SCINT 95, International Conference on Inorganic Scintillators and Their Applications*, Delft, The Netherlands, 28 August - 1 September, 1995 1996. Editors: P. Dorenbos & C. W. Van Eijk. Coronet Books. ISBN: 978-9040712159.

Moskal P. B. T., Białas P., Ciszewska M., Czerwiński E., Heczko A. et al. (2012), "TOF-PET detector concept based on organic scintillators". *Nuclear Medicine Review*, vol. 15, Supl. C, pp. C81-84, 2012. DOI: 10.5603/NMR.2012.0003.

NEMA (1994), *NEMA Standards Publication NU2-1994: Performance Measurements of Positron Emission Tomographs*. Technical report NEMA NU2-1994. National Electrical Manufacturers Association, Rosslyn, Virginia, USA, 1994.

NEMA (2001), *NEMA Standards Publication NU2-2001: Performance Measurements of Positron Emission Tomographs*. Technical report NEMA NU2-2001. National Electrical Manufacturers Association, Rosslyn, Virginia, USA, 2001.

Neves J. A. D. (2008), *Desenvolvimento de um protótipo RPC-PET*. MSc. Universidade de Coimbra, Faculdade de Ciências e Tecnologia, Departamento de Física, Coimbra, Portugal, Junho 2008. (Available at https://estudogeral.sib.uc.pt/handle/10316/12250)

Pedroso de Lima A. & Gordo P. M. (2008), "Física do Positrão". In Pedroso de Lima J. J., editor *Física em Medicina Nuclear*, Ch. 3, pp. 91-118. Imprensa da Universidade de Coimbra, Coimbra, Portugal, 2008. ISBN: 978-989-8074-26-3.

Reis J. (2008), *Simulação da Biodistribuição, Aniquilação e Escape de Fotões PET no Corpo Humano*. MSc. Universidade de Coimbra, Faculdade de Ciências e Tecnologia, Departamento de Física, Coimbra, Portugal, September 2008. (Available at https://estudogeral.sib.uc.pt/jspui/handle/10316/12258)

Saint-Gobain Crystals (2011, *Scintilation Products: Organic Scintilation Materials and Detectors*. Available at http://www.detectors.saint-gobain.com/uploadedFiles/SGdetectors/Documents/Brochures/Organics-Brochure.pdf. Accessed on 14 June 2013.

Salvat F., Fernández-Varea J. M., Acosta E. & Josep S. (2001), *PENELOPE: A Code System for Monte Carlo Simulation of Electron and Photon Transport*. Organization for Economic Co-operation and Development, Nuclear Energy Agency, France, 2001. (Available at https://www.oecd-nea.org/dbprog/nea3388-penelope.pdf, Available online on 15 April 2013.)

Santonico R. & Cardarelli R. (1981), "Development of resistive plate counters". *Nuclear Instruments and Methods in Physics Research*, vol. 187, iss. 2-3, p. 377–380, 15 August 1981. DOI: 10.1016/0029-554X(81)90363-3.

Schäfers K. P., Reader A. J., Kriens M., Knoess C., Schober O. & Schäfers M. (2005), "Performance Evaluation of the 32-Module quadHIDAC Small-Animal PET Scanner". *The Journal of Nuclear Medicine*, vol. 46, no. 6, pp. 996-1004, June 2005.

Schmidtlein C. R., Kirov A. S., Nehmeh S. A., Erdi Y. E., Humm J. L. et al. (2006), "Validation of GATE Monte Carlo simulations of the GE Advance/Discovery LS PET scanners". *Medical Physics*, vol. 33, iss. 1, pp. 198-208, January 2006. DOI: 10.1118/1.2089447.

Segars W. P. (2001), *Development and Application of the new Dynamic NURBS-Based Cardiac-Torso (NCAT) Phantom*. PhD. University of North Carolina, Department of Biomedical Engineering, Chapel Hill, North Carolina, USA, 2001. (Available at http://www.bme.unc.edu/~wsegars/segars_NCAT_dis.pdf)

Shehad N. N., Athanasiades A., Martin C. S. & Sun L. (2006), "Small Animal PET Camera Design Based on 2-mm Straw Detectors". In *Proceedings of the IEEE 2006 Nuclear Science Symposium and Medical Imaging Conference*, San Diego, CaliforniaUSA, 29 October - 1 November 2006, pp. 2462-68. DOI: 10.1109/NSSMIC.2006.354410.

Solovov V. N., Hitachi A., Chepel V., Lopes M. I., Marques R. F. & Policarpo A. J. P. L. (2000), "Detection of scintillation light of liquid xenon with a LAAPD". In *Proceedings of the IEEE 2000 Nuclear Science Symposium and Medical Image Conference*, Lyon, France, 15-20 October 2000 2000, pp. 7/58-7/62 vol.1. DOI: 10.1109/NSSMIC.2000.949288.

Sonzogni A. (2013), *Chart of Nuclides*. Available at http://www.nndc.bnl.gov/chart/. Accessed on 9 February 2013.

Srivastava B. B. (2005), "Beta-Decay". In Srivastava B. B. *Fundamentals of Nuclear Physics*, Ch. 12, pp. 189-252. Rastogi Publications, New Delhi, India, 1 December 2005. ISBN: 978-8171338283.

St. James S. T. & Thompson C. J. (2005), "Investigation of the block effect in LSO detectors". In *Proceedings of the IEEE 2005 Nuclear Science Symposium and Medical Imaging Conference*, Fajardo, Puerto Rico, 23-29 October 2005 2005, pp. 2474-77. DOI: 10.1109/NSSMIC.2005.1596842.

St. James S. T., Thompson C. J., Tomic N. & Kemp B. (2004), "Investigation of the block effect in positron emission tomography". In *Proceedings of the IEEE 2004 Nuclear Science Symposium and Medical Image Conference*, Rome, Italy, 16-22 October 2004 2004, pp. 3370-74. DOI: 10.1109/NSSMIC.2004.1466459.

Surti S. & Karp J. S. (2004), "Imaging Characteristics of a 3-Dimensional GSO Whole-Body PET Camera". *The Journal of Nuclear Medicine*, vol. 45, no. 6, pp. 1040-49, June 2004.

Surti S., Kuhn A., Werner M. E., Perkins A. E., Kolthammer J. & Karp J. S. (2007), "Performance of Philips Gemini TF PET/CT Scanner with Special Consideration for Its Time-of-Flight Imaging Capabilities". *The Journal of Nuclear Medicine*, vol. 43, no. 3, p. 471–480, March 2007.

Toki W. H. (1990), "Review of Straw Chambers". In *Proceedings of the 5th International Conference on Instrumentation for Colliding-beam Physics*, Novosibirsk, USSR, 15 - 21 March 1990 1990. (Available at http://www.slac.stanford.edu/cgi-wrap/getdoc/slac-pub-5232.pdf)

Torres-Espallardo I., Gillam J. E., Solevi P., Cabello J., Llosa G. et al. (2011), "Simulation study of Resistive-Plate-Chambers based PET for hadron-therapy monitoring". In *Proceedings of the IEEE Nuclear Science Symposium and Medical Imaging Conference*, Valencia, Spain, 23-29 October 2011 2011, pp. 3529-33. DOI: 10.1109/NSSMIC.2011.6153662.

Vandenberghe S., Daube-Witherspoon M. E., Lewitt R. M. & Karp J. S. (2006), "Fast reconstruction of 3D time-of-flight PET data by axial rebinning and transverse mashing". *Physics in Medicine and Biology*, vol. 51, iss. 6, p. 1603–1621, 21 March 2006. DOI: 10.1088/0031-9155/51/6/017.

Vandenberghe S. & Karp J. (2006), "Rebinning and reconstruction techniques for 3D TOF-PET". *Nuclear Instruments and Methods in Physics Research A*, vol. 569, iss. 2, p. 421–424, 2 December 2006. DOI: 10.1016/j.nima.2006.08.065.

Winter M. (2012), *Periodic Table of the Elements*. Available at http://www.webelements.com. Accessed on 20 May 2013.

Yoshida E. & Yamaya T. (2013), *Coincidence Determination Method and Apparatus of PET Device*. Patent no. US 2013/0009064 A1. Assignee: National Institute of Radiological Sciences.

Zanzonico P. (2004), "Positron emission tomography: a review of basic principles, scanner design and performance, and current systems". *Seminars in Nuclear Medicine*, vol. 34, iss. 2, pp. 87-111, April 2004. DOI: 10.1053/j.semnuclmed.2003.12.002.

APPENDIX A
PARAMETERS FOR DEFINITION OF THE PHYSICS LIST FOR USE WITH THE GEANT4 DEVELOPED PROGRAM

This appendix contains the complete set of commands available for definition of the physics to be used in the simulations.

A.1 MAIN PHYSICS LIST

The parameters for setting the main physics list are available under the "/Physics/" command tree, which will be omitted in the next table.

The "Default" column presents the values usually employed in simulations. The last entry in the table is only available and used if the last but one is set to *true*.

Command	Value type	Default
activateGammaPhysics	Boolean	true
activateElectronPhysics		true
activateHadronPhysics		true
activateDecayPhysics		true
setDefaultRangeCut	Double with a unit	1 mm
useLowEnergyCut	Boolean	false
setLowEnergyCut	Double with a unit	250 eV

A.2 γ PHYSICS LIST

The commands available for setting the physics processes and associated parameters for the simulation of photons are available through the command tree "/Physics/Gamma/", which will be omitted in the next table.

The "Default" column presents the values usually employed in simulations. Parameters under the "LowEnPhotoElectric/" command tree are only available if the LEP (*lowenergy*) or the PENELOPE (*penelope*) physics models have been chosen, and

are deactivated and not used if the SEP (*standard*) is selected. For these parameters, the "Default" column presents the values used when the LEP (*lowenergy*) or the PENELOPE (*penelope*) physics models are activated.

Command	Value type	Default
setCut	Double with a unit	20.0 μm
rayleighProcess	in, lo, pe	lo
comptonProcess	in, st, lo, pe	st
photoelectricProcess	in, st, lo, pe	st
conversionProcess	in, st, lo, pe	st
LowEnPhotoElectric/useScndPhotonCut	Boolean	true
LowEnPhotoElectric/useScndElctCut		true
LowEnPhotoElectric/useAuger		true
LowEnPhotoElectric/setScndPhotonCut	Double with a unit	250 eV
LowEnPhotoElectric/setScndElctCut		250 eV

in: inactive st: standard lo: lowenergy pe: penelope

A.3 ELECTRON PHYSICS LIST

The commands available for setting the physics processes and associated parameters for the simulation of electrons are available through the command tree "/Physics/Electron/", which will be omitted from the next table.

The "Default" column presents the values usually employed in simulations. Parameters under the "LowEnIonization/" and "LowEnBremsstrahlung/" command trees are only available if the LEP (*lowenergy*) or PENELOPE (*penelope*) physics models are chosen, and are deactivated and not used if the SEP (*standard*) is selected. For these parameters, the "Default" column presents the values used when the LEP (*lowenergy*) or the PENELOPE (*penelope*) physics models are activated.

Command	Value type	Default
setCut	Double with a unit	450 nm
multiplescatteringProcess	in, st, st_e	st
ionizationProcess	in, st, lo, pe	st
bremsstrahlungProcess	in, st, lo, pe	st
LowEnIonization/useScndPhotonCut	Boolean	true

Command	Value type	Default
LowEnIonization/useScndElctCut	Boolean	true
LowEnIonization/useAuger		true
LowEnIonization/useFluorescence		true
LowEnIonization/setScndPhotonCut	Double with a unit	250 eV
LowEnIonization/setScndElctCut		250 eV
LowEnBremsstrahlung/useScndPhotonCut	Boolean	true
LowEnBremsstrahlung/setScndPhotonCut	Double with a unit	250 eV

in: inactive st: standard st_e: standard_e lo: lowenergy pe: penelope

A.4 POSITRON PHYSICS LIST

The commands available for setting the physics processes and associated parameters for the simulation of positrons are available through the command tree "/Physics/Positron/", which will be omitted from the next table.

The "Default" column presents the values usually employed in simulations. Parameters under the "LowEnBremsstrahlung/" command tree are only available if the LEP (*lowenergy*) or the PENELOPE (*penelope*) physics models have been chosen, and are deactivated and not used if the SEP (*standard*) is selected. For these parameters, the "Default" column presents the values used when the LEP (*lowenergy*) or the PENELOPE (*penelope*) physics models are activated.

Command	Value type	Default
setCut	Double with a unit	1 mm
multiplescatteringProcess	in, st, st_e	st
ionizationProcess	in, st, lo, pe	st
bremsstrahlungProcess	in, st, lo, pe	st
annihilationProcess	in, st, st_ac, pe	st_ac
LowEnBremsstrahlung/useXRayCut	Boolean	true
LowEnBremsstrahlung/setXRayCut	Double with a unit	250 eV

in: inactive st: standard st_ac: standard_accolinear lo: lowenergy pe: penelope

A.5 HADRON, ION AND DECAY PHYSICS LIST

Hadron and ion physics where used only to allow for the decay of radioactive nuclei. Both implement the *multiple scattering* and *ionization* processes and the SEP physics was always used.

As to the decay physics list, it has no settable parameters, being enough to activate the Decay, Hadron and Ion physics lists, as in the table of Appendix A.1, so that nuclear decay can be used.

APPENDIX B
PARAMETERS FOR DEFINITION OF THE SCANNER GEOMETRY IN THE GEANT4 DEVELOPED PROGRAM

This appendix contains the complete set of commands available for definition of the scanner geometry, including *RPC detection modules*, *RPC detectors*, *detection heads*, and the *scanner*. Values in the "Default" column of all the tables here presented are those usually employed in simulations, and alternative options will not be mentioned.

B.1 RESISTIVE PLATE CHAMBER DETECTION MODULE

The commands available for setting the geometry and materials of the *RPC detection modules* are all under the "/RPC/Module/" command tree, which will be omitted in the next table. The thicknesses of the transaxial electrode and support medium are half of those found in real detectors, since the detector is usually set as a double module detector.

Command	Default
setContainerMaterial	RPCGasMixture
setTotalLength	2402 mm
setTotalWidth	1002 mm
setSensitiveLength	2400 mm
setSensitiveWidth	1000 mm
setAxialPixelSize	1 μm
setTransaxialPixelSize	1 μm
AxialElectrode/OuterInsulation/setMaterial	Kapton
AxialElectrode/OuterInsulation/setThickness	85 μm
AxialElectrode/setStipsMaterial	Aluminium
AxialElectrode/setStripsThickness	20 μm
AxialElectrode/setSupportMaterial	Mylar

Command	Default
AxialElectrode/setSupportThickness	50 μm
AxialElectrode/InnerInsulation/setMaterial	Kapton
AxialElectrode/InnerInsulation/setThickness	100 μm
AxialElectrode/Conductor/setMaterial	Kapton
AxialElectrode/Conductor/setThickness	50 μm
GlassPlates/setMaterial	SodaLimeGlass
GlassPlates/setNumber	6
GlassPlates/setThickness	200 μm
GasGap/setMaterial	RPCGasMixture
GasGap/setThickness	350 μm
TransaxialElectrode/Conductor/setMaterial	Kapton
TransaxialElectrode/Conductor/setThickness	50 μm
TransaxialElectrode/InnerInsulation/setMaterial	Kapton
TransaxialElectrode/InnerInsulation/setThickness	100 μm
TransaxialElectrode/setSupportMaterial	Mylar
TransaxialElectrode/setSupportThickness	25 μm
TransaxialElectrode/setStipsMaterial	Aluminium
TransaxialElectrode/setStripsThickness	10 μm
TransaxialElectrode/OuterInsulation/setMaterial	Kapton
TransaxialElectrode/OuteInsulation/setThickness	0 μm

B.2 RESISTIVE PLATE CHAMBER DETECTOR

The commands available for setting the geometry and materials of *RPC detectors* are all under the "/RPC/Detector/" command tree, which will be omitted in the next table.

Command	Default
setMaterial	RPCGasMixture
setNumberOfModules	2

B.3 DETECTION HEADS

The commands available for setting the geometry and materials of the scanner

detection heads are all under the "/RPC/Head/" command tree, which will be omitted in the next table.

Command	Default
setWallThickness	1 mm
setWallMaterial	Aluminium
setFillMaterial	RPCGasMixture
setNumberOfDetectorsRadial	20
setNumberOfDetectorsTransaxial	1
setNumberOfDetectorsAxial	1
setDetectorSpacingRadial	0 μm
setDetectorSpacingTransaxial	0 μm
setDetectorSpacingAxial	0 μm
setDetectorMarginRadial	2 mm
setDetectorMarginTransaxial	2 mm
setDetectorMarginAxial	2 mm

B.4 SCANNER

The commands available for setting the geometry and materials of the *scanner* are all under the "/RPC/Scanner/" command tree, which will be omitted in the next table.

Command	Default
setMaterial	Air
setNumberOfHeads	4
setHeadSpacing	0 mm
setCenterX	0 mm
setCenterY	0 mm
setCenterZ	0 mm

APPENDIX C
PARAMETERS FOR DEFINITION OF THE PHANTOM GEOMETRY IN THE GEANT4 DEVELOPED PROGRAM

This appendix contains the complete set of commands available for definition of phantoms and their insertion in the final geometry. Values given are those usually employed in simulations, and alternate options will not be mentioned.

C.1 INITIALIZING A NEW PHANTOM TO BE PLACED IN THE GEOMETRY

The phantom factory class is responsible for managing and keeping track of all phantoms used in the geometry. This is accomplished through the commands listed in the following table, and that are all under the "/Phantom/" command tree, which will be omitted in the next table.

With the exception of the last row in the table, which must be set to true if the phantom is to be included in the simulation, the "Example" column depicts how one of the implemented phantoms can be initialized. If the last row of the table is set to false, the phantom is created in the phantom factory with the corresponding default parameters, but will not be placed in the simulation geometry.

Command	Example
setNewPhantomType	Sphere_1mm_00X_10Y_00Z
setNewPhantomName	NEMASpatialResolutionPhantom
addNewPhantom	true

Once the phantom is created, the name attributed to the phantom is added as a new level entry in the phantom command tree, through which the phantom parameters must be set. In the remaining sections of this Appendix, it will be assumed that the newly created phantom was attributed the name "PhantomName" meaning that the available phantom parameters are under "/Phantom/PhantomName/".

C.2 SPATIAL RESOLUTION PHANTOM

The commands available for setting the geometry and materials of the spatial resolution phantom are all under the "/Phantom/PhantomName/" command tree, which will be omitted in the next table. The "Example" column presents the default values used to create NEMA NU2-2001 phantoms. The parameter *setShape* can only assume the values "Sphere" and "Cylinder".

Command	Example
setShape	Cylinder
setPosition	0.0 1.0 0.0 cm
setRotation	0.0 0.0 0.0 deg
Core/setMaterial	Water
Core/setDiameter	1 mm
Core/setLength	1 mm
Shell/setMaterial	SodaLimeGlass
Shell/setThickness	0.5 mm

C.3 SENSITIVITY PHANTOM

The commands available for setting the geometry and materials of the sensitivity phantom are all under the "/Phantom/PhantomName/" command tree, which will be omitted in the next table. The "Example" column presents the default values used to create NEMA NU2-2001 phantoms.

Command	Example
setPosition	0.0 0.0 0.0 cm
setRotation	0.0 0.0 0.0 deg
Core/setMaterial	Water
Core/setAxialWidth	700.0 mm
Core/setDiameter	1.0 mm
CoreShell/setMaterial	HDPE
CoreShell/setCoreShellThickness	1.0 mm
Sleeves/setMaterial	Aluminium
Sleeves/setNumber	1 [from 0 to 5]

C.4 SCATTER FRACTION, COUNT LOSSES AND COUNT RATES PHANTOM

The commands available for setting the geometry and materials of the SF phantom are all under the "/Phantom/PhantomName/" command tree, which will be omitted in the next table. The "Example" column presents the default values used to create NEMA NU2-2001 phantoms.

Command	Example
setPosition	0.0 0.0 0.0 mm
setRotation	0.0 0.0 0.0 deg
Insert/Core/setMaterial	Water
Insert/Core/setDiameter	3.2 mm
Insert/Core/setLength	700 mm
Insert/Shell/setMaterial	HDPE
Insert/Shell/setThickness	0.8 mm
Cylinder/setMaterial	HDPE
Cylinder/setDiameter	200 mm
Cylinder/setLength	701.6 mm
Cylinder/setHoleDiameter	6.4 mm
Cylinder/setHolePosition	0.0 -45.0 0.0 mm

APPENDIX D
VARIABLES CONTAINED IN EACH HITS CLASS

This appendix contains the complete set of data saved for each of the hit classes used in the GEANT4 developed program.

D.1 PHANTOM HITS

Column	Variable	Type	Units
1	m_nEventID	Integer	–
2	m_vSourcePosition_X	Double	mm
3	m_vSourcePosition_Y	Double	mm
4	m_vSourcePosition_Z	Double	mm
5	m_vAnnihilationPosition_X	Double	mm
6	m_vAnnihilationPosition_Y	Double	mm
7	m_vAnnihilationPosition_Z	Double	mm
8	m_nParentID	Integer	–
9	m_nTrackID	Integer	–
10	m_nNumRayleighInter	Integer	–
11	m_nNumComptonInter	Integer	–
12	m_nNumTotalInter	Integer	–
13	m_fTime	Double	ns
14	m_fEnergy	Double	keV
15	m_vGlobalPosition_X	Double	mm
16	m_vGlobalPosition_Y	Double	mm
17	m_vGlobalPosition_Z	Double	mm
18	m_vMomentumDirection_X	Double	–
19	m_vMomentumDirection_Y	Double	–
20	m_vMomentumDirection_Z	Integer	–

D.2 PRIMARY PHOTON HITS

Column	Variable	Type	Units
1	m_nEventID	Integer	–
2	m_nParentID	Integer	–
3	m_nTrackID	Integer	–
4	m_nLayerID	Integer	–
5	m_nModuleID	Integer	–
6	m_nDetectorID	Integer	–
7	m_nHeadID	Integer	–
8	m_nPhantomNumRaylInter	Integer	–
9	m_nPhantomNumCompInter	Integer	–
10	m_nPhantomTotalInter	Integer	–
11	m_nScannerNumRaylInter	Integer	–
12	m_nScannerNumCompInter	Integer	–
13	m_nScannerNumPhotoInter	Integer	–
14	m_nScannerNumTotalInter	Integer	–
15	m_fGlobalTime	Double	ns
16	m_fEnergy	Double	keV
17	m_fEnergyTransf	Double	keV
18	m_fEnergyDep	Double	keV
19	m_vGlobalPosition_X	Double	mm
20	m_vGlobalPosition_Y	Double	mm
21	m_vGlobalPosition_Z	Double	mm
22	m_vIncomingMomDir_X	Double	–
23	m_vIncomingMomDir_Y	Double	–
24	m_vIncomingMomDir_Z	Double	–
25	m_vOutgoingMomDir_X	Double	–
26	m_vOutgoingMomDir_Y	Double	–
27	m_vOutgoingMomDir_Z	Double	–

D.3 ALL PHOTON HITS

Column	Variable	Type	Units
1	m_nEventID	Integer	–
2	m_nParentID	Integer	–
3	m_nTrackID	Integer	–
4	m_nLayerID	Integer	–
5	m_nModuleID	Integer	–
6	m_nDetectorID	Integer	–
7	m_nHeadID	Integer	–
8	m_fGlobalTime	Double	ns
9	m_fEnergy	Double	keV
10	m_fEnergyTransf	Double	keV
11	m_fEnergyDep	Double	keV
12	m_vGlobalPos_X	Double	mm
13	m_vGlobalPos_Y	Double	mm
14	m_vGlobalPos_Z	Double	mm
15	m_vIncomingMomDir_X	Double	–
16	m_vIncomingMomDir_Y	Double	–
17	m_vIncomingMomDir_Z	Double	–
18	m_vOutgoingMomDir_X	Double	–
19	m_vOutgoingMomDir_Y	Double	–
20	m_vOutgoingMomDir_Z	Double	–

D.4 ELECTRON HITS

Column	Variable	Type	Units
1	m_nEventID	Integer	–
2	m_nPrimPhotParentID	Integer	–
3	m_nPrimPhotTrackID	Integer	–
4	m_nPrimPhotLayerID	Integer	–
5	m_nPrimPhotModuleID	Integer	–
6	m_nPrimPhotDetectorID	Integer	–
7	m_nPrimPhotHeadID	Integer	–

Column	Variable	Type	Units
8	m_nPrimPhotPhantomNumRaylInter	Integer	–
9	m_nPrimPhotPhantomNumCompInter	Integer	–
10	m_nPrimPhotPhantomNumTotalInter	Integer	–
11	m_nPrimPhotScannerNumRaylInter	Integer	–
12	m_nPrimPhotScannerNumCompInter	Integer	–
13	m_nPrimPhotScannerNumPhotoInter	Integer	–
14	m_nPrimPhotScannerNumTotalInter	Integer	–
15	m_fPrimPhotGlobalTime	Double	ns
16	m_fPrimPhotEnergy	Double	keV
17	m_fPrimPhotEnergyTransf	Double	keV
18	m_fPrimPhotEnergyDep	Double	keV
19	m_vPrimPhotGlobalPos_X	Double	mm
20	m_vPrimPhotGlobalPos_Y	Double	mm
21	m_vPrimPhotGlobalPos_Z	Double	mm
22	m_vPrimPhotInMomDir_X	Double	–
23	m_vPrimPhotInMomDir_Y	Double	–
24	m_vPrimPhotInMomDir_Z	Double	–
25	m_vPrimPhotOutMomDir_X	Double	–
26	m_vPrimPhotOutMomDir_Y	Double	–
27	m_vPrimPhotOutMomDir_Z	Double	–
28	m_nPhotParentID	Integer	–
29	m_nPhotTrackID	Integer	–
30	m_nPhotLayerID	Integer	–
31	m_nPhotModuleID	Integer	–
32	m_nPhotDetectorID	Integer	–
33	m_nPhotHeadID	Integer	–
34	m_fPhotGlobalTime	Double	ns
35	m_fPhotEnergy	Double	keV
36	m_fPhotEnergyTransf	Double	keV
37	m_fPhotEnergyDep	Double	keV
38	m_vPhotGlobalPos_X	Double	mm

Column	Variable	Type	Units
39	m_vPhotGlobalPos_Y	Double	mm
40	m_vPhotGlobalPos_Z	Double	mm
41	m_vPhotInMomDir_X	Double	–
42	m_vPhotInMomDir_Y	Double	–
43	m_vPhotInMomDir_Z	Double	–
44	m_vPhotOutMomDir_X	Double	–
45	m_vPhotOutMomDir_Y	Double	–
46	m_vPhotOutMomDir_Z	Double	–
47	m_nElectParentID	Integer	–
48	m_nElectTrackID	Integer	–
49	m_nElectHitID	Integer	–
50	m_nElectLayerID	Integer	–
51	m_nElectModuleID	Integer	–
52	m_nElectDetectorID	Integer	–
53	m_nElectHeadID	Integer	–
54	m_fElectExtTime	Double	ns
55	m_fElectExtEnergy	Double	keV
56	m_vElectExtPos_X	Double	mm
57	m_vElectExtPos_Y	Double	mm
58	m_vElectExtPos_Z	Double	mm
89	m_vElectDetPos_X	Double	mm
60	m_vElectDetPos_Y	Double	mm
61	m_vElectDetPos_Z	Double	mm
62	m_vElectAssPos_X	Double	mm
63	m_vElectAssPos_Y	Double	mm
64	m_vElectAssPos_Z	Double	mm
65	m_vElectExtMomDir_X	Double	–
66	m_vElectExtMomDir_Y	Double	–
67	m_vElectExtMomDir_Z	Double	–

D.5 RPC HITS

Column	Variable	Type	Units
1	m_nEventID	Integer	–
2	m_vSourcePosition_X	Double	mm
3	m_vSourcePosition_Y	Double	mm
4	m_vSourcePosition_Z	Double	mm
5	m_vAnnihilationPosition_X	Double	mm
6	m_vAnnihilationPosition_Y	Double	mm
7	m_vAnnihilationPosition_Z	Double	mm
8	m_nPrimPhotParentID	Integer	–
9	m_nPrimPhotID	Integer	–
10	m_nPrimPhotPhantomNumRaylInter	Integer	–
11	m_nPrimPhotPhantomNumCompInter	Integer	–
12	m_nPrimPhotPhantomNumTotalInter	Integer	–
13	m_fPrimPhotScannerEntryEnergy	Double	keV
14	m_vPrimPhotScannerEntryPos_X	Double	mm
15	m_vPrimPhotScannerEntryPos_Y	Double	mm
16	m_vPrimPhotScannerEntryPos_Z	Double	mm
17	m_vPrimPhotScannerEntryMomDir_X	Double	–
18	m_vPrimPhotScannerEntryMomDir_Y	Double	–
19	m_vPrimPhotScannerEntryMomDir_Z	Double	–
20	m_nPrimPhotScannerNumRaylInter	Integer	–
21	m_nPrimPhotScannerNumCompInter	Integer	–
22	m_nPrimPhotScannerNumPhotoInter	Integer	–
23	m_nPrimPhotScannerNumTotalInter	Integer	–
24	m_fPrimPhotDetTime	Double	ns
25	m_fPrimPhotDetEnergy	Double	keV
26	m_fPrimPhotDetEnergyTransf	Double	keV
27	m_fPrimPhotDetEnergyDep	Double	keV
28	m_vPrimPhotDetPos_X	Double	mm
29	m_vPrimPhotDetPos_Y	Double	mm
30	m_vPrimPhotDetPos_Z	Double	mm

Column	Variable	Type	Units
31	m_nHitID	Integer	–
32	m_nElectGapID	Integer	–
33	m_nElectModuleID	Integer	–
34	m_nElectDetectorID	Integer	–
35	m_nElectHeadID	Integer	–
36	m_fElectExtTime	Double	ns
37	m_fElectExtEnergy	Double	keV
38	m_vElectExtPos_X	Double	mm
39	m_vElectExtPos_Y	Double	mm
40	m_vElectExtPos_Z	Double	mm
41	m_vElectDetPos_X	Double	mm
42	m_vElectDetPos_Y	Double	mm
43	m_vElectDetPos_Z	Double	mm
44	m_vElectAssPos_X	Double	mm
45	m_vElectAssPos_Y	Double	mm
46	m_vElectAssPos_Z	Double	mm
47	m_vElectExtMomDir_X	Double	–
48	m_vElectExtMomDir_Y	Double	–
49	m_vElectExtMomDir_Z	Double	–

APPENDIX E
PARAMETERS FOR THE RUN ACTION IN THE GEANT4 DEVELOPED PROGRAM

This appendix contains the complete set of parameters that can be settled for the *run action*, for which the command tree is "/RunAction/", and will be omitted in the following table.

Command	Example
savePrimPhotHitsASCIIData	false
savePrimPhotHitsBinaryData	false
setPrimPhotHitsDataFileName	Primary-Photon-Hits-Data
saveAllPhotHitsASCIIData	false
saveAllPhotHitsBinaryData	false
setAllPhotHitsDataFileName	All-Photon-Hits-Data
saveElectHitsASCIIData	false
saveElectHitsBinaryData	false
setElectHitsDataFileName	Electron-Hits-Data
saveRPCHitsASCIIData	false
saveRPCHitsBinaryData	true
setRPCHitsDataFileName	RPC-Hits-Data
savePhantomHitsASCIIData	false
savePhantomHitsBinaryData	false
setPhantomHitsDataFileName	Phantom-Hits-Data
setRunSeed	0

APPENDIX F
PARAMETERS FOR DEFINITION OF A RADIOACTIVE SOURCE FOR USE IN THE POST-PROCESSING OF SIMULATION DATA

This appendix contains the data structure used for defining the radioactive source, along with an example of the values of the parameters.

The routine that returns the source parameters (*Get_Source_Options*) accept as parameters the activity in Bq, the number of simulated positrons, and the name of the radionuclide, and returns the parameters resumed in the following table, for the case of $^{18}_{9}\mathrm{F}$. With the exception of the *activity* and the *useBranchRatio* parameters, the column "Default" presents the values used in all simulations performed in the current work.

Parameter	User definable	Internal unit	Default
activity	Yes	Bq	37000
halfLife	No	s	6588
meanLife	No	s	halfLife/ln(2)
decayConst	No	s^{-1}	ln(2)/halfLife
branchRatio	No	–	0.967
useBranchRatio	Yes	–	false
numSimPositrons[(a)]	Yes	–	0.967×10^6
numSimDecays[(b)]	No	–	10^6

(a) If *useBranchRatio* is set to false, *numSimPositrons* is set to *branchRatio*×*numSimPositrons* and *numSimDecays* is set to the value entered in *numSimPositrons*.

(b) If *useBranchRatio* is set to true, *numSimDecays* is set to *numSimPositrons*/*branchRatio*.

APPENDIX G
PARAMETERS FOR DEFINITION OF THE SCANNER GEOMETRY AND READOUT FOR POST-PROCESSING OF SIMULATION DATA

The structure containing the complete set of parameters required for the post-processing of simulation data has four inner substructures (*Module*, *Detector*, *Head* and *Scanner*), for which the parameters must be carefully set so that the information agrees with that used in the simulation and presented on Appendix B. A fifth substructure contains the parameters related with the processing of simulation data according to the readout implemented in the RPC detector.

The five substructures will be presented in the next sections, along with the parameters used in most of the simulations performed.

G.1 *MODULE* SUBSTRUCTURE

The data contained in this substructure cannot be changed through a function call and must be carefully set prior to start processing the simulation data so that they match the corresponding information passed to the GEANT4 developed program during the simulation.

The values presented are those employed in most of the simulations and post-processing

Parameter	Internal unit	Default
gap_thickness	mm	0.350
Dimensions.Inner.length	mm	2400
Dimensions.Inner.width	mm	1000
Dimensions.Inner.thickness	mm	3.44
Dimensions.Outer.length	mm	2402
Dimentions.Outer.width	mm	1002
Dimensions.Outer.thickness	mm	Dimensions.Inner.thickness

G.2 *DETECTOR* SUBSTRUCTURE

The data contained in this substructure cannot be changed through a function call and must be carefully set prior to start processing the simulation data so that it matches the corresponding information passed to the GEANT4 developed program during the simulation.

The values presented are those employed in most of the simulations and post-processing

Parameter	Internal unit	Default
number_of_modules	–	2
Dimensions.Inner.length	mm	Auto computed
Dimensions.Inner.width	mm	Auto computed
Dimensions.Inner.thickness	mm	Auto computed
Dimensions.Outer.length	mm	Auto computed
Dimensions.Outer.width	mm	Auto computed
Dimensions.Outer.thickness	mm	Auto computed
Number.axial	–	1
Number.transaxial	–	1
Number.radial	–	20
Spacing.axial	mm	0
Spacing.transaxial	mm	0
Spacing.radial	mm	0.3
Margin.axial	mm	2
Margin.transaxial	mm	2
Margin.radial	mm	2

G.3 *HEAD* SUBSTRUCTURE

The data contained in this substructure cannot be changed through a function call and must be carefully set prior to start processing the simulation data so that it matches the corresponding information passed to the GEANT4 developed program during the simulation.

The values presented are those employed in most of the simulations and post-processing.

Parameter	Internal unit	Default
wall_thickness	mm	1
Spacing	mm	0
Number	–	4
Dimensions.Inner.length	mm	Auto computed
Dimensions.Inner.width	mm	Auto computed
Dimensions.Inner.thickness	mm	Auto computed
Dimensions.Outer.length	mm	Auto computed
Dimensions.Outer.width	mm	Auto computed
Dimentions.Outer.thickness	mm	Auto computed

G.4 *SCANNER* SUBSTRUCTURE

The data contained in this substructure cannot be changed through a function call and must be carefully set prior to start processing the simulation data so that it matches the corresponding information passed to the GEANT4 developed program during the simulation.

The values presented are those employed in most of the simulations and post-processing.

Parameter	Internal unit	Default
bore_fraction	–	0.8
Dimensions.Inner.length	mm	Auto computed
Dimensions.Inner.width	mm	Auto computed
Dimensions.Inner.thickness	mm	Auto computed
Dimensions.Outer.length	mm	Auto computed
Dimensions.Outer.width	mm	Auto computed
Dimensions.Outer.thickness	mm	Auto computed
Center.X	mm	0
Center.Y	mm	0
Center.Z	mm	0

G.5 *READOUT* SUBSTRUCTURE

Some data contained in this substructure can be changed through a function call. This data is presented in blue colour with an appropriate reference and the complete set of available options will be given when applicable. The remaining data must be carefully set prior to start processing the simulation data so that it matches the pretended set of parameters for readout processing.

The values presented are those employed in most of the simulations and post-processing.

Parameter	Internal unit	Default
Detection.time_jitter	s	90×10^{-12}
Detection.detection_point_correction	–	opositeSide
Dead_Time.Time.window	s	200×10^{-9}
Dead_Time.Time.jitter	–	0
Dead_Time.Time.model	–	nonParalyzable
Dead_Time.Time.coordinates_policy	–	averageAll
Dead_Time.Time.coarse_resolution_axial	mm	0
Dead_Time.Time.coarse_resolution_transaxial	mm	0
Dead_Time.Time.time_policy	–	acceptFirst
Dead_Time.Position.window	s	3×10^{-6}
Dead_Time.Position.jitter	s	0
Dead_Time.Position.model	–	paralyzable
Dead_Time.Position.coordinates_policy[a]	–	coarsePosition
Dead_Time.Position.coarse_resolution_axial[b]	mm	10
Dead_Time.Position.coarse_resolution_transaxial[c]	mm	30
Dead_Time.Position.time_policy	–	acceptFirst
Sections.type	–	Equal
Sections.reference_detector	–	0
Sections.num_axial	–	1
Sections.num_transaxial	–	10
Sections.num_radial	–	20
Binning.axial_pixel_size	mm	2
Binning.transaxial_pixel_size	mm	2

Parameter	Internal unit	Default
Binning.radial_pizel_size	mm	Auto computed

(a) Available options are: *rejectAll* and *coarsePosition*.

(b) The coarse_resolution_axial must be set to the standard deviation of the Gaussian distribution of the coarse axial position given by RPC detectors.

(c) The coarse_resolution_transaxial must be set equal to the width of the readout sections along the transaxial direction

APPENDIX H

PARAMETERS FOR PROCESSING THE REMOVAL OF MULTIPLE SINGLE EVENTS CAUSED BY MULTIPLE PHOTON INTERACTIONS AND REDUCTION OF THE SINGLE EVENTS DATA SET

This appendix contains the data structure used for processing the removal of multiple events caused by multiple interactions of the same incident photon and also to reduce the number of Single events by rejecting those that definitely cannot be paired to form coincidences.

The "Default" column presents the parameters used whenever the removal of multiple events was performed.

Parameter	User definable	Internal unit	Default
removeMultipleHits	Yes	–	true
useAllHeads	Yes	–	true
numberOfIterations	Yes	–	5
lowerRemoveBand	Yes	–	4
upperRemoveBand	Yes	–	100

APPENDIX I
PARAMETERS FOR PERFORMING AND ACCEPTING COINCIDENCES

The structure containing the complete set of parameters required for the post-processing of simulation data contain five substructures (*PointForCoincidence*, *Sorter*, *Multiples*, *Rejection* and *Acceptance*).

The five substructures will be presented in the next sections, along with the parameters used in most of the post-processing performed.

I.1 *POINTFORCOINCIDENCE* SUBSTRUCTURE

The data contained in this substructure specifies which points of the hits data should be used to assign the coordinates points of detection to LORs.

Parameter	Unit	Default
phtEntPnt	–	false
phtDetPnt	–	false
elctExtPnt	–	false
elctDetPnt	–	false
elctDetPntWithDOI	–	false
elctReadPnt	–	true

I.2 *SORTER* SUBSTRUCTURE

The data contained in this substructure specify the parameters needed to perform the coincidence sorter, for which no other substructure is used.

Parameter	Unit	Default
Type[a]	–	singleTimeWindow
time	s	5×10^{-9}

[a] Available options are: *singleTimeWindow* and *multipleTimeWindow*

I.3 *MULTIPLES* SUBSTRUCTURE

The Multiples substructure contains only the *policy* parameter which can take the values *rejectAll* and *acceptAll*. Since the coincidence sorter routine returns Single and Multiple coincidences in separate arrays, the option used was always the *acceptAll*, the multiple coincidences being further processed or rejected as wanted.

I.4 *REJECTION* SUBSTRUCTURE

The data contained in this substructure is used to reject LORs based on some geometrical parameters, excluding the polar acceptance angle. The values presented in the "Default" column are just examples of those employed in most of the post-processing.

Parameter	Unit	Default
type[a]	–	geometric_tof
EllipticalVolume.Centre.X	mm	0
EllipticalVolume.Centre.Y	mm	0
EllipticalVolume.Centre.Y	mm	0
EllipticalVolume.dx[b]	mm	400
EllipticalVolume.dy[c]	mm	400
EllipticalVolume.dz[d]	mm	700

[a] Available options are: *none* (reject LORs that do not pass through the scanner bore), *geometric* (reject LORs that do not cross the right elliptical cylindrical volume defined by the fields of the *ElipticalVolume* substructure), *geometric_tof* (reject the LORs for which the direct TOF reconstructed point does not fall inside the right elliptical cylindrical volume defined by the parameters of the *ElipticalVolume* substructure).

[b] Major axis of the cross section of the right elliptical cylinder.

[c] Minor axis of the cross section of the right elliptical cylinder.

[d] Total length of the right elliptical cylinder.

I.5 *ACCEPTANCE* SUBSTRUCTURE

The parameters defined in this substructure refer to the polar acceptance angle.

Parameter	Unit	Default
angle_value	deg	90
angle_type	–	2D

APPENDIX J
VARIABLES CONTAINED IN THE COINCIDENCE DATA FILES

This appendix contains the complete set of data saved for each coincidence event. The data is organized in a two dimensional array with a row for each coincidence event, and the columns holding the data listed in the following table, in which γ_1 and γ_2 will be used to refer to the two events detected in coincidence.

Column	Variable	Type	Units
1	Type of coincidence event[a]	Integer	–
2	Scattered in phantom	Boolean	–
3	Scattered in detector		–
4	Source position along the X direction[b]	Double	mm
5	Source position along the Y direction[b]	Double	mm
6	Source position along the Z direction[b]	Double	mm
7	Annihilation position along the X direction[b]	Double	mm
8	Annihilation position along the Y direction[b]	Double	mm
9	Annihilation position along the Z direction[b]	Double	mm
10	ID of the detector for γ_1	Integer	–
11	ID of the detection head for γ_1	Integer	–
12	Detection time for γ_1	Double	s
13	Detection position of γ_1 along the X direction	Double	mm
14	Detection position of γ_1 along the Y direction	Double	mm
15	Detection position of γ_1 along the Z direction	Double	mm
16	ID of the detector for γ_2	Integer	–
17	ID of the detection head for γ_2	Integer	–
18	Detection time for γ_2	Double	s

Column	Variable	Type	Units
19	Detection position of γ_2 along the X direction	Double	mm
20	Detection position of γ_2 along the Y direction	Double	mm
21	Detection position of γ_2 along the Z direction	Double	mm
22	Energy of γ_1	Double	keV
23	Energy of γ_2	Double	keV

(a) 0 – Random coincidence, 1 – True coincidence, 2 – Scattered coincidence.

(b) Equal to zero is the LOR is a Random coincidence event.

APPENDIX K
PARAMETERS FOR THE CONSTRUCTION OF SINOGRAMS

This appendix contains the data structure used for defining sinograms from the coincidence data

Parameter	User definable	Internal unit	Default
voxelSize[a]	Yes	mm	4
numBins[b]	Yes	–	151×600×180
sinogramCentre[c]	Yes	mm	$(0,0,0)$
rebinningMethod[d]	Yes	–	SSRB

[a] Size of the image voxel, which is equal in all the three directions.

[b] Number of bins of the sinogram given as $N_r \times N_z \times N_\phi$, where N_r is the number of radial bins of the sinogram with size equal to the *voxelSize*, N_z is the number of slices along the *Z* direction, and N_ϕ is the number of bins along the azimuthal direction, and which is set according to Eq. (4.25) if N_ϕ is set to zero.

[c] The point on which the complete set of sinograms should be centred.

[d] Valid options are: *SSRB*, consisting in the usual SSRB method applied to the obtained detection points; *SSRB_Modified*, in which the detection points are reshaped to the surface of a right circular cylinder centred in *sinogramCentre* and with a diameter equal to the product of the voxel size by the number of radial bins; *SSRB_TOF*, which performs SSRB by computing the direct TOF reconstructed point along the axial direction.